New materials for Spin Electronics

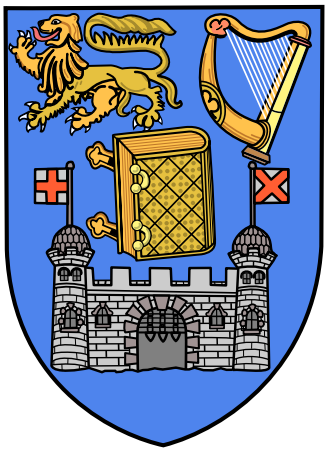

A thesis submitted to the University of Dublin, Trinity College in application for the degree of Doctor of Philosophy by

Davide Betto

School of Physics

Trinity College Dublin

April 2015

Declaration

I declare that this thesis has not been submitted as an exercise for a degree at this or any other university and it is entirely my own work.

I agree to deposit this thesis in the University's open access institutional repository or allow the Library to do so on my behalf, subject to Irish Copyright Legislation and Trinity College Library conditions of use and acknowledgement.

_____

Davide Betto

There is no emotion, there is peace.
There is no ignorance, there is knowledge.
There is no passion, there is serenity.
There is no chaos, there is harmony.
There is no death, there is the Force.

Jedi Code, established by Odan-Urr and transcribed by Homonix Rectonia during the Early Manderon Period.

Summary

Magnetic components are currently widely used in electronic devices, especially in the field of data storage. The need for downscaling the lateral dimensions of every component following Moore's law brings new challenges and will preclude the use of the currently employed materials and structures. The study presented is concerned with the investigation of new materials for future use in spin electronics devices.

The first part focuses on full and half Heuser alloys Mn_3Ga, Mn_2Ga and the unprecedented hybrid Mn_2Ru_xGa. We investigated Mn_3Ga in the $D0_{22}$ cubic structure with large tetragonal distortion using x-ray absorption and magnetic circular dichroism (XAS/XMCD). We found that two different magnetic moments are present: the main component shows high perpendicular magnetic anisotropy (PMA), while a second, smaller one is oriented in the plane and posses no anisotropy. This configuration is due to the canted magnetic moment on one sublattice. The decomposition of the total magnetisation into the site-specific moments has been possible through the measurement of samples of Mn_3Ga, $Mn_{2.5}Ga$ and Mn_2Ga at several angles of incidence of the x-rays.

We then investigated the properties of the first half-metallic compensated ferrimagnet, Mn_2Ru_xGa. The two Mn sublattices are antiferromagnetically coupled and their moments cancel out almost perfectly. At the same time they are crystallographically inequivalent and only electrons with a definite spin participate in the electric conduction, making Mn_2Ru_xGa a half-metal. The transport and magnetic properties have been studied by anomalous Hall effect (AHE) and by XAS/XMCD. We found that it is possible to tune the magnetic moment and the spin polarisation by Ru concentration x and tetragonal distortion c/a. This material is free from stray fields and unaffected by external magnetic perturbations. In addition, the very high spin polarisation should also lead to high magnetoresistance ratio if used in a magnetic tunnel junction device.

Finally, we studied the spin-orbit torques of heavy metals with high spin-orbit coupling in order to investigate the possibility of the current-induced switching of an adjacent magnetic element. These torques arise from the spin Hall effect and from the Rashba effect. In particular we analysed materials such as W and Pt employing different methods in order to determine the validity of each method. The figure of merit used is the spin Hall angle, which measures the efficiency of the spin-orbit interaction in converting charge current into spin current. The literature values for the spin Hall angle of these metals vary of orders of magnitude, depending on the technique used. We found that the spin Hall angle of Pt assumes approximatively the same value regardless of the technique used, while the determination of the spin Hall angle for Ta and W gives very different results depending on the technique. Some types of measurement, such as the spin pumping from a ferromagnet and detection by inverse spin Hall effect or the harmonic Hall voltage measurement, are not reliable with these materials. We found an unusually high planar Hall resistance in W that could be at the origin of these unreliabilities.

Acknowledgement

The path I followed during this PhD has not been the most straight and direct one, far from it! There have been some difficult moments (a lot), some happy ones (a few), some changes of direction and more than once someone had to kick me to push me over an obstacle. It is time now to thank everyone who has been important during this journey. I'll try not to forget anybody but, in case that happens, I hope the relevant person will forgive my mistake.

Of course, I have to thank Prof. Mike Coey and Prof. Plamen Stamenov for giving me the opportunity to come to Dublin and join Group D. Your guidance and supervision have been key to my professional and personal development. If only I could fully understand when Plamen is trying to explain me how the world works...

I would like to thank all the people in the Magnetism and Spin Electronics group for the help and the support they gave me during these years. In particular I would like to thank Yong-Chang Lau and Kiril Borisov, friends and partners that shared a great deal of work, together with Dr. Gwenael Atcheson and Dr. Nivetha Thiyagarajah, who guided me and is able to understand my nerdy jokes. A special thank has to go to Dr. Karsten Rode, who helped me both professionally and humanly, basically showing me the way all the time in spite of my never-ending flow of questions. Thanks to Dr. Rémy Lassalle-Balier, my first supervisor and the person who brought me in Dublin in the first place.

Thanks to Jane and Stephen, Pelin, Karl, João, José and Stephen, who made me smile and lightened the burden I was carrying.

Many thanks to some people working in my group or in others, or part of the technical staff: in no particular order Nigel, Venky, Lorena, Gavin, Peter, Chris, Mike, Neal, Shaun, Emma and Karsten.

Thanks to my Italian friends, who always supported me and still believe that I am a smart guy. I missed you in the last three years. Again, in no particular order: Squiz & Elena, Andrea & Federica, Gabri & Linda, Ivan, il Monte & Desi, Fede & Annica, Marco, Marco & Federica, Dodi & Lisa, Lorenzo, Anna, Cri, Teo, Davide & Kristina, Mez, Petra, Alessia and Miki.

Last but not least, thanks to my family and my parents. I don't have to say why, thanks for everything.

Davide

Contents

List of Acronyms **xxi**

List of Symbols **xxv**

List of Space Groups and Atomic Structures **xxxv**

1 Introduction **1**
1.1 Future prospects and challenges . . . 2
1.2 Materials for spin electronics . . . 3
1.2.1 Heusler alloys . . . 3
1.2.2 Heavy metals with high spin-orbit coupling . . . 5
1.3 PhD project . . . 5

2 Theory **7**
2.1 Magnetism of the electron . . . 7
2.1.1 Spin-orbit coupling . . . 11
2.1.2 Ferromagnetism, Stoner model and local moments . . . 11
2.1.3 Exchange energy . . . 12
2.1.4 Zeeman energy . . . 13
2.1.5 Magnetic anisotropy . . . 13
2.1.6 Magneto-crystalline anisotropy, shape anisotropy and coercivity . . . 13
2.2 Magnetisation dynamics . . . 14
2.2.1 Landau-Lifshitz-Gilbert equation and the macrospin model . . . 14
2.2.2 Spin transfer torque . . . 19
2.3 Transport . . . 22
2.3.1 Anisotropic magnetoresistance . . . 22
2.3.2 Planar Hall effect . . . 23
2.3.3 Spin currents . . . 24
2.3.4 Spin pumping . . . 24
2.3.5 Rashba Hamiltonian . . . 27
2.3.6 Hall effect, anomalous Hall effect and spin Hall effect . . . 28
2.3.7 Torques and effective fields from spin-orbit interactions . . . 32
2.3.8 Spin rectification . . . 33
2.3.9 Spin electronics . . . 37
2.4 X-ray spectroscopy . . . 39
2.4.1 Interaction of x-rays with matter . . . 39

2.4.2 Atomic multiplets . . . 40
2.4.3 Crystal field . . . 42
2.4.4 Spin-orbit coupling . . . 47
2.4.5 X-ray absorption with atomic multiplets . . . 47
2.4.6 Charge transfer . . . 48
References . . . 50

3 Experimental methods **57**
3.1 Material deposition . . . 57
3.1.1 Sputtering . . . 57
3.1.2 Evaporation . . . 61
3.2 Lithography methods . . . 63
3.2.1 Resist types . . . 63
3.2.2 UV lithography . . . 64
3.2.3 Mask fabrication . . . 66
3.3 Patterning methods . . . 66
3.3.1 Lift-off . . . 66
3.3.2 Ion milling . . . 67
3.4 X-ray-based characterisation techniques . . . 69
3.4.1 Light sources and monochromators . . . 69
3.4.2 X-ray absorption spectroscopy (XAS) and x-ray magnetic circular dichroism (XMCD) 70
3.4.3 Extended x-ray absorption fine structure (EXAFS) . . . 73
3.4.4 X-ray photoelectron spectroscopy (XPS) and UV photoelectron spectroscopy (UPS) 76
3.5 Transport measurements . . . 80
3.5.1 Hall voltage techniques . . . 80
3.6 Ferromagnetic resonance techniques . . . 81
3.6.1 Ferromagnetic resonance . . . 81
3.6.2 Spin torque FMR . . . 87
3.6.3 Inverse spin Hall effect . . . 89
3.7 Other characterisation techniques . . . 95
3.7.1 Atomic force microscope . . . 95
3.7.2 SQUID . . . 95
3.7.3 X-ray diffraction and reflectometry . . . 97
References . . . 99

4 Heusler alloys **104**
4.1 Introduction . . . 105
4.2 DO_{22} $Mn_{3-x}Ga$ . . . 108
4.2.1 Review of characteristics . . . 108
4.2.2 XAS and XMCD . . . 113
4.2.3 Conclusions . . . 122
4.3 Mn_2Ru_xGa . . . 123
4.3.1 Introduction . . . 123
4.3.2 Growth and properties . . . 124
4.3.3 Transport properties . . . 126
4.3.4 XAS ans XMCD measurements . . . 135

4.3.5 X-ray and UV photoelectron spectroscopy . . . 141
4.3.6 EXAFS measurements . . . 142
4.3.7 Mn_2Ru_xGa-based MTJ . . . 149
4.4 Future work . . . 153
References . . . 154

5 Heavy metals, spin Hall effect and spin-orbit torques 159
5.1 Literature review . . . 159
5.2 Alternating current Hall technique . . . 161
5.2.1 Theory . . . 161
5.2.2 Low field measurements: theory . . . 164
5.2.3 Samples . . . 166
5.2.4 Low field measurements: results . . . 167
5.2.5 High field measurements: results . . . 174
5.3 Planar Hall effect of HM/FM bilayers . . . 185
5.4 Direct current Hall technique . . . 187
5.4.1 Theory . . . 188
5.4.2 Measurements results and conclusions . . . 189
5.5 Current-induced switching of PMA structures . . . 189
5.5.1 Theory . . . 190
5.5.2 Measurement results . . . 191
5.6 Ørsted field calculation . . . 193
5.7 Spin torque-FMR technique . . . 194
5.7.1 Theory . . . 194
5.7.2 Results . . . 196
5.8 ISHE and Spin pumping technique . . . 198
5.8.1 Conclusions . . . 200
5.9 Future work . . . 202
References . . . 202

6 Conclusions and outlook 207

A Resist details 209

B Device fabrication steps 210
B.0.1 Hall bars . . . 210
B.0.2 MTJ samples . . . 213

C Beamline details 216

D $C1_b$ $Mn_{3-x}Ga$ 218
D.0.3 Review of characteristics . . . 218
D.0.4 XAS and XMCD . . . 219
D.0.5 Conclusions . . . 223
References . . . 223

Appendices 209

Publications **225**

List of Figures

1.1 Top: schematic of an MTJ device. Bottom: exploded view of a magnetic random acces memory (MRAM) cell, used for data storage. 3

1.2 Periodic table and elements that can be used to form a Heusler alloy. Blue elements can be X atoms, red elements can be Y atoms, while green elements can be Z atoms. 4

2.1 Schematic representation of the orbital momentum for an electron in a d state, corresponding to $l = 2$ and $m_l = -2, \ldots, +2$. 9

2.2 Schematic representation of the coupling of orbital and magnetic momenta. 10

2.3 Hysteresis loop for a ferromagnetic material with perpendicular magnetic anisotropy (out-of-plane easy axis). Remanence magnetisation, saturation magnetisation M_{s}, anisotropy field H_{an} and coercive field H_{c} are indicated. 15

2.4 Precession of the magnetic moment around a magnetic field. 16

2.5 Precession of the magnetic moment around a magnetic field considering a damping term. 17

2.6 Scattering of unpolarised electrons at the interface between a non magnetic and a ferromagnetic layer. 20

2.7 Spin transfer torque between non-collinearly magnetised ferromagnetic layers. 20

2.8 Schematic for the measurement of the anisotropic magnetoresistance (AMR) in a magnetic sample. 23

2.9 Schematic for the measurement of the planar Hall effect (PHE) in a magnetic sample. . . 24

2.10 Schematic illustration of the spin pumping process achieved through ac excitation of the magnetisation of a FM layer. H_{ex} and m are the fixed external field and the reduced magnetic moment, J_{s} is the spin current. From ref. [41]. 25

2.11 Decay of the spin current J_{s} as a function of the distance from the FM/NM interface ($z = 0$) for different values of the spin diffusion length λ_{sf}. 26

2.12 Representation of the Fermi surfaces for majority and minority electrons in a ferromagnet without Rashba interations, a non magnetic metal with Rashba interactions and in a ferromagnet with Rashba interactions. From ref. [49]. 28

2.13 Schematic for the measurement of the anomalous Hall effect (AHE) in a magnetic sample. 29

2.14 Schematic of the three mechanisms that give rise to the anomalous Hall effect. From ref. [51]. 30

2.15 Representation of the spin Hall effect in a thin layer and in cylindrical wire. The injection of a charge current in presence of spin-orbit interaction results in a spin accumulation at the edges of the samples. In a thin layer the accumulation has opposite sign at opposite edges, while in a wire the spins wind around the surface. From ref. [52]. 31

2.16 Schematic of a non magnetic heavy metal/ferromagnetic metals bilayer with (a) in-plane and (b) out-of-plane magnetisation. J_c is the charge current injected in-plane, J_s is the resulting spin current. $\tau_{\text{anti-damping}}$ and $\tau_{\text{field-like}}$ are the two torques acting on the magnetic moment. Equivalently, in panels (c) and (d) the effective fields $H_{\text{anti-damping}}$ and $H_{\text{field-like}}$ are displayed. 33
2.17 Example of symmetric and antisymmetric Lorentzian lineshapes with $\Delta = 1$. 34
2.18 Coordinate system for a long narrow strip of a soft ferromagnetic metal. The static field H_{ex} is applied in plane at an angle θ_H with the $\hat{z}'$ axis. The rf current and electric field are along the strip length $\hat{z}'$. 36
2.19 Schematics of a GMR and of a TMR cells. 37
2.20 Ion in octahedral symmetry. The surrounding charges are located at $(0, d, d)$, $(0, -d, -d)$, $(0, d, -d)$, $(0, -d, d)$, $(0, 0, d)$ and $(0, 0, -d)$ with d the distance from the central ion. . . . 43
2.21 Ion in tetrahedral symmetry. The surrounding charges are located at $(-d/2, -d/2, -d/2)$, $(d/2, d/2, -d/2)$, $(d/2, -d/2, d/2)$ and $(-d/2, d/2, d/2)$, with d the edge of the cube. . . . 44
2.22 Ion in octahedral symmetry with tetragonal distortion. The surrounding charges are located at $(0, d, d)$, $(0, -d, -d)$, $(0, d, -d)$, $(0, -d, d)$, $(0, 0, d+\delta)$ and $(0, 0, -d-\delta)$ with d the distance from the central ion in octahedral symmetry and δ the tetragonal distortion. 45
2.23 Schematic of $2p$ XAS and XPS energy levels and transitions. In XPS experiments (left) the charge transfer configuration lies below the $3d^N$ configuration. The situation is opposite for the levels in XAS experiments. From ref. [69]. 51

3.1 The Shamrock sputtering tool. 58
3.2 Inside view of the "Shamrock" Chamber A. On the left and the right there are the six guns, while at the top there is the wafer loader and at the bottom the ion gun. 59
3.3 Inside view of Chamber B. In clockwise direction, starting from the bottom left there are: one TFT gun, a cluster with three dc guns, the other TFT gun, the wafer loader, the other dc cluster and the rf gun. 60
3.4 Picture of a cluster in Chamber B with three dc guns. 61
3.5 Picture of a TFT gun in Chamber B. 62
3.6 The Temescal FC2000 evaporation tool. 62
3.7 Proximity effect due to backscattering of light in UV lithography. 65
3.8 The OAI Model 800 CE mask aligner for UV lithography. 65
3.9 Undercut profile obtained using a double layer of resist. 66
3.10 Steps of the lift-off process. 67
3.11 The Millatron ion milling tool. 68
3.12 Hiden end-point-detection data from the milling of an MRG-based MTJ stack (see sec. B). The etching has been performed in steps with wait times in order to avoid the overheating of the resist. This is the reason why the curves have this particular shape. 68
3.13 The Millatron ion milling tool chamber. On the right there is the ion gun that provides the accelerated Ar^+ particles. At the top of the chamber there is the inlet for the end-point detection. 69
3.14 Schematic of an experimental XMCD setup at a beamline. From ref. [7]. 70
3.15 Different methods for measurements of XAS spectra. 71
3.16 XAS(blue) and XMCD(red) signals with decomposition of the total area for L_2 and L_3 edges. The spectra shows have been taken from a Mn_3Ga sample. 72

3.17 Simplified view of the multiple scattering of an outgoing wave off neighbouring atoms. The red atom is the source of the wave, which travels towards the other atoms, gets diffracted and bounces back towards the original source or towards other atoms. The amplitude of the outgoing spherical wave is weakened after each diffraction. From ref. [14] 74
3.18 Example of EXAFS absorption spectra from the Mn K edge. a) raw data. b) corrected data: the curve have been normalised to the edge jump and the decreasing background subtracted in order to empathise the oscillations. 74
3.19 Fourier transform of corrected EXAFS signal extracted from the K edge absorption of Ga, Mn and Ru of a $Mn_2Ru_{0.5}Ga$ sample. 77
3.20 XPS data obtained using the K_α emission line of Al. 78
3.21 Schematic illustration of the two types of Hall voltage measurements performed on our samples. (a) Thin film with corner-contacs. (b) Patterned Hall bar. 81
3.22 The setup for electrically-induced fmr measurements. 82
3.23 Close up view of the gap of the electromagnet setup used for FMR measurements. The two GSG probes are used to contact the lithographically defined antennas. 83
3.24 (a) Schematic illustration of the sample setups used for broadband FMR measurements. H_{ex} is the external in-plane magnetic field, I_{rf} is the rf current and h_{rf} is the resulting Ørsted field. (b) Precession of the magnetic moment M around the external field. 84
3.25 Schematic of the broadband FMR setup. An antenna is patterned on the sample and contacted using GSG picoprobes. The sample is placed in the gap of an electromagnet and connected to a vector network analyser (VNA) port, which injects an rf current in the antenna. Both magnetic field and rf frequency are swept during the measurement and the reflected signal is detected. 84
3.26 Broadband FMR spectra for a CoFeB sample with in-plane magnetisation. The noise at low field is due to the formation of magnetic domains. 85
3.27 Electric and magnetic field configuration of a TE_{102} rectangular cavity used for FMR measurements. 85
3.28 Electric and magnetic field configuration of a TE_{011} cylindrical cavity used for FMR measurements. 85
3.29 Schematic of the coupling between the cavity and the waveguide. In order to fine-tune the system, it is possible to vary the position of a teflon screw in correspondence of the iris. . 86
3.30 Schematic of the cavity FMR setup. The sample is placed in the centre of a microwave cavity. The rf resonance mode of the cavity ($\sim$9.6 GHz) is excited by a klystron and the reflected power is detected using a magic tee and a diode. The cavity is placed in the gap of an electromagnet that provides a dc external field. An ac magnetic field is superimposed, modulated at the frequency (100 kHz) of the reference signal of a lock-in amplifier (LIA). The diode signal, modulated at this frequency, is detected by the LIA and recorded while the dc magnetic field is swept. 87
3.31 Schematic of the ST-FMR measurement setup. A signal generator sends a microwave signal into the sample through a bias tee. The source is chopped at high frequency using the first reference signal of a wave generator. The sample is placed in the gap of an electromagnet and the magnetic field is modulated at low frequency using the second reference signal of the wave generator. The rectified dc voltage produced by the sample is detected at the other end of the bias tee by two lock-in amplifiers in cascade. 88

3.32 Schematic of the HM/FM bilayer used for ST-FMR measurements. (a) Front view with Ørsted field acting on the FM layer produced by the charge current in the HM layer. (b) Spin injection and effective fields acting on the magnetic moment. φ is the polar angle of the equilibrium position of the in-plane magnetic moment. The direction of the Ørsted and Rashba fields is parallel to the polarisation of the spin current, while the antidamping effective field is pointing out-of-plane. 88
3.33 Schematic illustration of the spin pumping process achieved through ac excitation of the magnetisation of a FM layer, used in ISHE experiments. H_{ex}, h_{rf} and M are the fixed external and the rf fields and the magnetic moment, respectively. J_{c} and J_{s} are the charge and spin current, respectively. 90
3.34 Schematic of the ISHE-spin pumping setup. The sample is placed in the centre of a microwave cavity. The rf resonance mode of the cavity ($\sim$9.7 GHz) is excited by a klystron and the reflected power is detected using a magic tee and a diode. The cavity is placed in the gap of an electromagnet that provides a dc external field. An ac magnetic field is superimposed, modulated at the frequency (100 kHz) of the reference signal of a lock-in amplifier (LIA). The diode signal, modulated at this frequency, is detected by the LIA and recorded while the dc magnetic field is swept. The dc voltage building up at the edges of the samples is recorded by a nanovoltmeter. 91
3.35 Measurement configuration for the ISHE-spin pumping in a TE_{011} cavity. (a) Schematic of the cavity with the rf $\vec{h}$ and $\vec{e}$ fields and the external $\vec{H}_{\mathrm{ex}}$ field. The black pads on the sample represent the electrical contacts. (b) Top view of the sample in the cavity in a centred position (top) and off-centre position (bottom). The electric field seen by the sample is different in the two situations. 91
3.36 Effect of the AHE on the ISHE-spin pumping measurement. (a) Dc voltage generation induced by the AHE when $H_{\mathrm{ex}} < H_{\mathrm{res}}$ (b) Dc voltage generation induced by the AHE when $H_{\mathrm{ex}} > H_{\mathrm{res}}$. The top and bottom figures show the effect after half a period of oscillation. We suppose a phase shift of 180° between the rf electric and magnetic fields. . 92
3.37 Equivalent electric circuit of the FM/HM bilayer. R_{FM} and R_{HM} are the resistances of the ferromagnetic and heavy metal layers respectively. I_c is the charge current generated by the ISHE. 93
3.38 DPPH peak-to-peak height of the FMR resonance and fitting with eq 3.24. 94
3.39 FMR signals of the bilayer FM/HM and of the DPPH paramagnetic powder. The scaling of the x axis is not the same for the two plots. 95
3.40 AFM scan of a MRG sample. The root mean square roughness is about 20 pm. Some particles of dust are visible. 96
3.41 Schematic representation of Bragg's law of diffraction. Incident x-ray beams at an angle θ are reflected from parallel atomic planes with lattice parameter d. 97
3.42 Ewald's sphere. The incident wavevector $\vec{k}_{\mathrm{in}}$ is drawn starting from the origin of the reciprocal lattice O at the angle of incidence on the lattice. A sphere with the radius of the vector is drawn from the end of $\vec{k}_{\mathrm{in}}$, which has angle of incidence ω. A diffraction peak is observed for all $\vec{k}_{\mathrm{out}}$ connecting a point of the reciprocal lattice falling on the sphere and the end of $\vec{k}_{\mathrm{in}}$. The difference between the two vectors is a reciprocal lattice vector $\vec{Q}$. The angle 2θ is the angle between the incident and outgoing vectors. 98

4.1 Schematic of the band structure of a half metal. The minority spin band has a gap Δ at the fermi level E_{F}. 105

4.2 Schematic representation of the hybridisation of the d orbitals in a full Heusler alloy. The notation used is the same as in Tab. 4.1. From ref. [2]. 107
4.3 a) $L2_1$ crystal structure for a "normal" Heusler alloy b) $L2_1$ crystal structure for an "inverse" Heusler alloy. 108
4.4 $C1_b$ crystal structure for a half Heusler alloy. 109
4.5 DO_{22} crystal structure for an Heusler alloy. Note that $a_{DO_{22}} \approx a_{L2_1}$ 109
4.6 X-ray diffraction of $Mn_{3-x}Ga$ films on $SrTiO_3$ (left) and on MgO (right) substrates. The curves are offset for clarity. 110
4.7 DO_{22} crystal structure of Mn_3Ga. The arrows indicate the direction of the magnetic moments on each site. In the perfectly ordered crystal, the central atom in the unit cell is always Ga. 111
4.8 SQUID magnetometry of a Mn_3Ga thin film sample on STO at 300 K. The loop with in-plane applied field shows a small in-plane moment. 112
4.9 Real-space amplitude and phase of the EXAFS signal at both Mn and Ga edges. Each panel contains the experimental Fourier transform amplitude and phase (marks) and the fit based on the FEFF models as discussed in the text. Within each panel, the upper manifold corresponds to $\vec{E} \perp \vec{c}$ and the lower to $\vec{E} \parallel \vec{c}$. 114
4.10 Comparison of the L_3 pre-edge of Mn in Mn_3Ga (60 nm)/MgO (5 nm), Mn^{2+}(MnO), Mn^{4+}(MnO_2) and Mn-metal. 115
4.11 Schematic of the experimental setup for XAS and XMCD measurements with definition of the angles. 116
4.12 XAS spectrum of Mn_3Ga (60 nm)/MgO (5 nm) at the $L_{3,2}$ edges and the contributions from the 4d and 2b sites obtained using the decomposition method described in the text. . 117
4.13 XMCD spectrum of Mn_3Ga (60 nm)/MgO (5 nm) at the $L_{3,2}$ edges and the contributions from the 4d and 2b sites obtained using the decomposition method described in the text. . 118
4.14 $Mn_{2.5}Ga$ (60 nm)/MgO (5 nm) experimental XAS spectra and simulation using the extracted contribution from the 4d and 2b sites. 119
4.15 $Mn_{2.5}Ga$ (60 nm)/MgO (5 nm) experimental XMCD spectra and simulation using the extracted contribution from the 4d and 2b sites. 119
4.16 Total spin moment for Mn_3Ga (60 nm)/MgO (5 nm) with the applied magnetic field parallel and perpendicular to the wave vector $\vec{k}$. The experimental values have been extracted using the sum rules on the recorded spectra. The lines are simultaneous fits to the data in this figure and the 4d contribution shown in Fig. 4.17. 120
4.17 Absolute value of the sample spin moment deconvoluted to the two Mn positions. The solid line relative to the 2b moment is a guide to the eye, while the line relative to the 4d moment is a simultaneous fit using this data set and the two data sets presented in Fig. 4.16. 120
4.18 Site-specific orbital moments in Mn_3Ga (60 nm)/MgO (5 nm). The solid lines are obtained by fitting the data with a cosine function to account for the angular projection of the moment on $\vec{k}$. They allow us to determine the magnitude of the orbital moment at each Mn position. 121
4.19 Mn_3Ga (60 nm)/MgO (5 nm) total orbital moment derived directly from the sum rules. The solid line corresponds to the sum of the site-specific orbital moments as shown in Fig. 4.18. 122
4.20 Experimentally observed, site-specific, magnetic structure of Mn_3Ga (60 nm)/MgO (5 nm). The figure is to scale, noting that the 4d $\vec{S}$ and $\vec{L}$ have been multiplied by a factor of 2 and 20, respectively, and the 2b $\vec{L}$ by a factor of 10. 123

4.21 XRD pattern of $L2_1$ Mn_2RuGa grown on a MgO (001) substrate. 125
4.22 Reciprocal space mapping scan of an MRG sample around the (204) peak. The inset shows the logatimic intensity profile of the peaks at constant q_z for the MRG (204) and the MgO (113) peaks. 126
4.23 Variation of Curie temperature T_C and moment with Ru concentration x and number of valence electrons per formula unit N_v. The half-metallic region is lightly shaded. The black and blue lines are guide to the eye, while the red straight line has a slope of $2\,\mu_B$/f.u./Ru. The lower panel shows the variation of the lattice parameter c, normal to the substrate, as a function of x. The line is a linear fit of the data, excluding the first point. 127
4.24 Schematic density of states showing the effect of Ru addition in Mn_2Ru_xGa, which illustrated the Fermi level crossing the spin gap. The numbers between square brackets indicate the total number of electronic states in the respective bands and the occupancy of the bands is given by the white numbers. 128
4.25 Anomalous Hall effect of Mn_2RuGa with $\Delta c/a$ =1.92 % and different x. The loops have been measured at room temperature and have been shifted for clarity. The AHE resistance changes sign between $x = 0.62$ and $x = 0.73$. At $x = 0.69$ the magnetisation is practically zero, making it almost impossible to influence it with an external magnetic field, hence the AHE voltage is a flat line. The measurements have been performed at room temperature. 128
4.26 Anomalous Hall effect of Mn_2RuGa with $\Delta c/a$ =1.92 % and $x = 1$ measured at different temperatures. The loops have been shifted for clarity. The AHE resistance changes sign between 300 and 350 K. 129
4.27 Temperature derivative of the AHE resistance $\partial R_{xy}/\partial T$ as a function of the temperature for samples of varying Ru concentration x and same $\Delta c/a$ ∼1.9 %. The maxima in the curves are indicated with arrows and correspond to the compensation temperature T_{comp}. 130
4.28 Coercive field H_c as a function of the temperature for samples of varying Ru concentration x and same $\Delta c/a$ ∼1.9 %. The maxima in the curves correspond to the compensation temperature T_{comp}. 131
4.29 Temperature derivative of the AHE resistance $\partial R_{xy}/\partial T$ as a function of the temperature for samples of varying strain $\Delta c/a$ and same Ru concentration $x \sim 1$. The maxima in the curves are indicated with arrows and correspond to the compensation temperature T_{comp}. 131
4.30 Temperature derivative of the coercive field H_c as a function of the temperature for samples of varying strain $\Delta c/a$ and same Ru concentration $x \sim 1$. The maxima in the curves correspond to the compensation temperature T_{comp}. 132
4.31 Absolute values of the anomalous Hall angle (AHA) as a function of temperature for the two sets of samples. All straight lines are obtained through linear regression of the data. The solid lines correspond to samples with same $x \sim 1$, while the dashed lines correspond to samples with same $\Delta c/a$ ∼1.9 %. 133
4.32 Anomalous Hall angle (AHA) as a function of temperature for the two sets of samples. The solid lines correspond to samples with same $x \sim 1$, while the dashed lines correspond to samples with same $\Delta c/a$ ∼1.9 %. Negative values correspond to the switching of the magnetisation of the samples. The sample with $\Delta c/a$ =3.6 % has an estimated Curie temperature T_C of only ∼200 K and it is not possible to reach compensation. 133
4.33 Left y axis: anomalous Hall angle (AHA) as a function of Ru concentration x, as extracted from AHE measurements at 300 K. The black line is a guide to the eye, while the blue one is a linear fit of the data. Right y axis: ρ_{xy} and ρ_{xx} as a function of x. 134

4.34 Left y axis: anomalous Hall angle (AHA) as a function of strain $\Delta c/a$, as extracted from AHE measurements at 300 K for samples with $x \sim 1$. The lines are linear fits of the data. Right y axis: ρ_{xy} and ρ_{xx} as a function of $\Delta c/a$. 134
4.35 The isotropic x-ray absorption and dichroism spectra for a typical Mn_2Ru_xGa sample. The calculated contribution from each crystallographic position is shown in thin dotted/dashed lines. The dichroic spectra for each site has opposite sign for the two positions $4a$ and $4c$, confirming their antiferromagnetic ordering. 136
4.36 Temperature dependence of the magnetisation (absolute values) of a selected sample, with $x = 0.98$. The change of sign of the magnetisation occurs at $T_{\mathrm{comp}} \sim 310$ K in good agreement with the compensation temperature measured by spontaneous Hall effect. The lines are guides to the eye only. At $T = 300$ K, the sample is almost perfectly compensated, and we were unable to achieve even partial magnetic saturation with the maximum applied field available ($\mu_0 H = 6.8$ T), hence the observed spin moments tend towards 0. 137
4.37 Temperature dependence of the Mn $4c$ magnetisation as a function of the temperature and linear fitting. The inset shows the extrapolated values of the Curie temperature T_{C}. Some data points, corresponding to the compensation temperature, have not been included in the fits since they are not reliable, as explained below. 138
4.38 The isotropic x-ray absorption and dichroism spectra for a typical Mn_2Ru_xGa sample with switched magnetic moment. The calculated contribution from each crystallographic position is opposite with respect to the spectra of Fig. 4.35. 138
4.39 X-ray absorption spectra for samples of Mn_2Ru_xGa with $x \sim 1$ as a function of temperature. The spectra have been shifted for clarity. The features reverse at 200 K, where the magnetic moment is close to zero and no clear signal is detected. 139
4.40 Evolution of the absolute value of the magnetic moments at of the two Mn positions, extrapolated to $T = 0$ K, with Ru concentration x. The solid lines are linear regressions to the data sets. In the case of Mn $4c$, we identify a change of slope in the vicinity of $x = 0.7$, corresponding to the onset of filling the minority spin channel of Mn in this position. . . 140
4.41 Site-specific magnetisation (absolute values) extrapolated to $T = 0$ K as a function of c/a ratio for the samples with their spin moments translated to a virtual $x = 1.0$ Ru concentration as discussed in the text. The solid lines are guides to the eye only. 141
4.42 XPS spectra of a Mn_2Ru_xGa sample close to compensation. The low resolution does not allow us to clearly distinguish the position of the charge transfer satellite peak. 142
4.43 UPS spectra of two Mn_2Ru_xGa samples with different Ru concentration x. Although the spectral resolution is not very high, there is a clear difference in the valence band DOS for the two samples, indicated by the arrow. 143
4.44 XANES and EXAFS spectra for the K edges of Ga, Mn and Ru. The data shown are for sample thickness varying from 4 nm to 70 nm and for in-plane (red, solid) and out-of-plane (blue, dotted) light polarisation. It was not possible to measure the in-plane spectra for the samples with lowest thicknesses because of the low signal-to-noise ratio, due to the extremely small interaction volume in that configuration. 144
4.45 EXAFS spectra of Fig. 4.44 in reciprocal space. The data shown are for sample thickness varying from 4 nm to 70 nm and for in-plane (red, solid) and out-of-plane (blue, dotted) light polarisation. It was not possible to measure the in-plane spectra for the samples with lowest thicknesses because of the low signal-to-noise ratio, due to the extremely small interaction volume in that configuration. 145

4.46 Fourier transform of the EXAFS spectra of Fig. 4.45. The data shown are for sample thickness varying from 4 nm to 70 nm and for in-plane (red, solid) and out-of-plane (blue, dotted) light polarisation. It was not possible to measure the in-plane spectra for the samples with lowest thicknesses because of the low signal-to-noise ratio, due to the extremely small interaction volume in that configuration. 146

4.47 Fourier transform of the EXAFS spectra and fits using the reverse Monte Carlo model on the Ga edge. The fits consider only the 1st shell of neighbouring atoms. Both modulus and the imaginary parts of the Fourier transforms are shown. 147

4.48 Results of the analysis of the EXAFS data for Ga. a) Percentage of Mn in the 1st shell in-plane and out-of-plane as a function of sample thickness. b) Number of Mn in the 2nd shell in-plane and out-of-plane as a function of sample thickness. c) Ga-Mn and Ga-Ru distances (1st shell) in-plane and out-of-plane as a function of sample thickness. d) Ga-Mn distances (2nd shell) in-plane and out-of-plane as a function of sample thickness. 148

4.49 X-ray absorption spectra for samples of Mn_2Ru_xGa with different oxide capping layers. The last spectra has been rescaled for clarity. It is possible to clearly distinguish additional peaks on the $L_{3,2}$ edges that indicate the oxidation of the Mn atoms. 150

4.50 X-ray photoelectron spectra for MRG samples with different oxide capping layers. (a) Ru ^3d edges. (b) Ga ^2p edges. (c) Valence band. The double peak labelled Ga^3p consists of the $^3p_{3/2}$ and $^3p_{1/2}$ peaks. (d) Mn ^2p edges. In the last frame the effect of the Mn atoms oxidation are recognizable in the MRG/MgO/Al_2O_3 sample. 151

4.51 10 mm × 10 mm sample of MRG-based MTJ stack after the patterning process. The bottom contact is in common to all the devices. 152

4.52 MTJ resistance as a function of the perpendicular applied field. The very high resistance of the stack make it difficult to obtain a very high signal-to-noise ratio. The arrows represent the orientation of the magnetic moment of the MRG (blue) and CoFeB (red) layers. . . . 153

5.1 Schematic illustration of the sample and measurement geometry. A Hall bar is patterned from a stack of thin films consisting in a HM layer (blue), a FM layer (red) and an insulating oxide (green). The coordinate system uses spherical coordinates. $\vec{M}$ is the magnetisation vector and $\vec{H}_{ex}$ is the external applied field. 160

5.2 Schematic of a non magnetic heavy metal/ferromagnetic metals bilayer with out-of-plane magnetisation. On the left, $\tau_\perp$ and $\tau_\parallel$ are shown. Equivalently, the effective fields $H_\perp$ and $H_\parallel$ are displayed on the right. 161

5.3 A patterned Hall bar used for spin-orbit torques measurements. 166

5.4 Normalised anomalous Hall signal as a function of a perpendicular applied field for W/CoFeB/MgO, Pt/CoFeB/MgO and β-Ta/CoFeB/MgO samples. The complete remanence indicates the presence of PMA. 167

5.5 First harmonic signal V_ω as a function of the in-plane applied field for β-Ta/CoFeB/MgO, Pt/CoFeB/MgO and β-W/CoFeB/MgO samples. The data (blue circles) are fitted with a parabolic function (red curves). The upper panel corresponds to initial magnetisation pointing in the $+\hat{z}$ direction, while the lower panel corresponds to initial magnetisation pointing in the $-\hat{z}$ direction. 169

5.6 Second harmonic signal $V_{2\omega}$ as a function of the in-plane applied field in the longitudinal configuration ($\phi_H = 0$) for β-Ta/CoFeB/MgO, Pt/CoFeB/MgO and β-W/CoFeB/MgO samples. The data (blue circles) are fitted with a linear function (red lines). The upper panel corresponds to initial magnetisation pointing in the $+\hat{z}$ direction, while the lower panel corresponds to initial magnetisation pointing in the $-\hat{z}$ direction. 171

5.7 Second harmonic signal $V_{2\omega}$ as a function of the in-plane applied field in the transverse configuration ($\phi_H = \pi/2$) for β-Ta/CoFeB/MgO, Pt/CoFeB/MgO and β-W/CoFeB/MgO samples. The data (blue circles) are fitted with a linear function (red lines). The upper panel corresponds to initial magnetisation pointing in the $+\hat{z}$ direction, while the lower panel corresponds to initial magnetisation pointing in the $-\hat{z}$ direction. 172

5.8 Spin-orbit effective fields $\mu_0 H_{\text{eff}}$ per 10^{10}A m^{-2} as a function of the HM layer thickness for W, β-Ta and Pt. The extracted values take into account the PHE; the ratio $\xi = R_{\text{PHE}}/R_{\text{AHE}}$ is shown in the inset. 173

5.9 First(blue) and second (red) harmonic Hall signal as a function of the in-plane applied field ($\theta_H = 88°$) for a Pt/CoFeB/MgO sample in longitudinal ($\varphi_H = 0°$) and transverse configuration ($\varphi_H = 90°$). 175

5.10 First(blue) and second (red) harmonic Hall signal as a function of the in-plane applied field ($\theta_H = 88°$) for a α-Ta/CoFeB/MgO sample in longitudinal ($\varphi_H = 0°$) and transverse configuration ($\varphi_H = 90°$). 176

5.11 First(blue) and second (red) harmonic Hall signal as a function of the in-plane applied field ($\theta_H = 88°$) for the annealed β-Ta/CoFeB/MgO sample in longitudinal ($\varphi_H = 0°$) and transverse configuration ($\varphi_H = 90°$). 177

5.12 First(blue) and second (red) harmonic Hall signal as a function of the in-plane applied field ($\theta_H = 88°$) for the unannealed β-Ta/CoFeB/MgO sample in longitudinal ($\varphi_H = 0°$) and transverse configuration ($\varphi_H = 90°$). 178

5.13 Normalised second harmonic Hall signal as a function of the perpendicular applied field for W/CoFeB/MgO, Pt/CoFeB/MgO and β-Ta/CoFeB/MgO samples. These voltages results from the anomalous Nernst effect (ANE) originating from out-of-plane temperature gradients. 179

5.14 Estimated longitudinal ($\mu_0 H_{\parallel}$) (a) and transverse ($\mu_0 H_{\perp}$) (b) effective field for a Pt/CoFeB/MgO sample as a function of the injected current density. 181

5.15 Estimated longitudinal ($\mu_0 H_{\parallel}$) (a) and transverse ($\mu_0 H_{\perp}$) (b) effective field for an annealed α-Ta/CoFeB/MgO sample as a function of the injected current density. 182

5.16 Estimated longitudinal ($\mu_0 H_{\parallel}$) (a) and transverse ($\mu_0 H_{\perp}$) (b) effective field for an annealed β-Ta/CoFeB/MgO sample as a function of the injected current density. 183

5.17 Estimated longitudinal ($\mu_0 H_{\parallel}$) (a) and transverse ($\mu_0 H_{\perp}$) (b) effective field for a unannealed β-Ta/CoFeB/MgO sample as a function of the injected current density. 184

5.18 Measured AHE, AMR and PHE for a W/CoFeB/ Al_2O_3 sample. The spike at low field in the AHE loop is probably due to domain nucleation. 185

5.19 Results from dc Hall measurements on a Pt/CoFeB/MgO/Ta sample. (a): normalised Hall voltage V_{H} as a function of an in-plane applied field for longitudinal and transverse configurations. (b): estimated effective fields $\mu_0 H_{\parallel}$ and $\mu_0 H_{\perp}$ as a function of θ(direction of the FM magnetic moment). The grey areas indicate the regions where the data are not reliable. 190

5.20 Schematic illustration of an up-down domain wall (red dots = down moments, blue dots = up moments). In (a) the Dzyaloshinskii-Moriya interaction (DMI) fixes the chirality (left-handed) of the domain walls. The directions of the spin Hall effective fields acting on the left and right sections on the wall is indicated, where we have $m \approx \pm m_x$. In this case, there is no domain nucleation/annihilation but only a displacement, hence no reversal of the magnetisation is possible. In (b) an external field is applied along $\hat{x}$, imposing the chirality of the domain walls. Therefore, nucleation or annihilation of the domain is possible under the effect of a spin-orbit field. From ref. [35]. 192
5.21 Current switching of the magnetisation of W/CoFeB/MgO as a function of an injected pulsed current with 25 mT and −25 mT longitudinal applied field $\mu_0 H_{\text{ex}}$. 193
5.22 Schematic illustration of the coordinate system for the calculation of the Ørsted field. The current is assumed to flow in the bottom (blue) layer, while the profile of the field is calculated in the upper layer (red). 194
5.23 ST-FMR signal for a W/CoFeB sample. The measured dc voltage is decomposed into an antisymmetric and a symmetric Lorentzians. 195
5.24 ST-FMR signal for a Cu (10)/NiFe (10) sample (thickness in nm). The measured dc voltage has an almost perfect antisymmetric lineshape, with the best results obtained at the frequency of 7 GHz. The inset shows a plot of the excitation frequency against the resonance field and the fit using Kittel law 2.38. 196
5.25 Thickness dependence of the spin Hall angle of Pt, fitted using eq. 5.47. The inset shows a representative dataset for the change in the linewidth Δ with the injected dc current. . . 197
5.26 Thickness dependence of the spin Hall angle of W (absolute value), fitted using eq. 5.47. The inset shows a representative dataset for the change in the linewidth Δ with the injected dc current. 197
5.27 Dc voltage signal of a NiFe-only sample measured in the rf cavity. The signal, originating from the anomalous Hall effect, has an almost completely antisymmetric lineshape, indicating that the phase between the electric and magnetic field is $\pi/2$. 199
5.28 Dc voltage signal of a Pt/NiFe sample measured in the rf cavity. The signal is divided into an antisymmetric Lorentzian, arising from the AHE, and a symmetric Lorentzian, arising from the ISHE. 199
5.29 Ferromagnetic resonance of the NiFe-only and the Pt/NiFe sample. The latter shows a broader linewidth, resulting from the additional damping due to the spin pumping. 200
5.30 Dc voltage signal of a CoFeB-only sample measured in the rf cavity. The signal is a mixture of antisymmetric and symmetric Lorentzians, indicating that the phase between the electric and magnetic field is ∼20°. 201
5.31 Dc voltage signal of a Ta/CoFeB sample measured in the rf cavity. The signal is divided into an antisymmetric Lorentzian. 201
5.32 Ferromagnetic resonance of the CoFeB and the Ta/CoFeB sample. The latter shows a broader linewidth, resulting from the additional damping due to the spin pumping effect. 202

B.1 Schematic of a sample used for ST-FMR experiments. The red bar of magnetic material is contacted by two coupled microstrips. The contacts make a 45° turn in order to make it possible to apply the field with an angle of 45° in the plane with respect to the bar using our rf setup. 211
B.2 Step-by-step fabrication process of the Hall bars samples for spin Hall measurements. 212
B.3 Step-by-step fabrication process of the MTJ samples. 215

D.1 XRD pattern of $C1_b$ Mn_2Ga grown on a V (001) seed layer. 218
D.2 Atomic force microscope scans of a 10 x 10 µm surface area of Mn_3Ga sample. The film is granular and discontinuous, with several pin-holes. 219
D.3 XPS spectra of a Mn_2Ga showing the $2p$ peaks of V. The presence of these peaks is a further confirmation of the granular nature of the thin film. 220
D.4 XAS spectra for $Mn_{3-x}Ga$ samples. The curve in orange is the difference between the Mn_3Ga and Mn_2Ga spectra, that we attribute to the additional Mn atoms in the first alloy. No clear spectral signature due to these atoms is visible. 220
D.5 XMCD spectra for $Mn_{3-x}Ga$ samples. The curve in orange is the difference between the Mn_3Ga and Mn_2Ga spectra, that we attribute to the additional Mn atoms in the first alloy. This signal resemble the one of a tetrahedrally coordinated Mn atom. 221
D.6 Fit of the XAS spectra for Mn_2Ga and Mn_3Ga. The Mn_3Ga one shows more contribution from a tetrahedrally coordinated site. 222
D.7 Fit of the XMCD spectra for Mn_2Ga and Mn_3Ga. The Mn_3Ga one shows more contribution from a tetrahedrally coordinated site. 222
D.8 SQUID data for Mn_2Ga, $Mn_{2.5}Ga$ and Mn_3Ga measured with applied out-of-plane and in-plane field at room temperature. 223

List of Tables

2.1 Ground states in weak octahedral field for d electrons [24]. 45
2.2 Energy of the single-electron $3d$ orbitals in strong tetragonal field 46
2.3 High-spin and low-spin parameters for $3d^4$ to $3d^7$ configurations in strong octahedral field 46
2.4 Direct product table for the O_h point group. Square brackets [ ] are used to indicate antisymmetrized products of a degenerate representation with itself. 47

3.1 Typical deposition parameters for some materials used in this work 60

4.1 Representation in O_h symmetry of orbitals from the $X - X$ interaction and from the Y atom. Subscripts $1, 2, 3, 4$ and 5 refer to d orbitals xy, yz, zx, $3z^2 - r^2$ and $x^2 - y^2$ and to p orbitals of $\hat{x}$, $\hat{y}$ and $\hat{z}$ symmetry, respectively. The subscripts a and b refer to the two non-equivalent X atoms in the unit cell. 106
4.2 Summary of macroscopic parameters 111
4.3 Interatomic distances and magnetic coupling 113
4.4 Correlation between tetragonal distortion $\Delta c/a$ and thickness of MRG samples with $x \sim 1$ 124
4.5 List of samples measured by XAS/XMCD 135
4.6 List of samples measured by EXAFS 143

5.1 List of samples measured with harmonic Hall measurements 167
5.2 Results of the low-field harmonic Hall measurements 174
5.3 PHE and AMR summary 186

D.1 List of samples measured by XAS/XMCD 223

List of Acronyms

ac	Alternating current
AFM	Atomic force microscope
AHA	Anomalous Hall angle
AHE	Anomalous Hall effect
AMR	Anisotropic magneto resistance
ANE	Anomalous Nernst effect
ARPES	Angle-resolved photoelectron spectroscopy
ARUPS	Angle-resolved UV photoelectron spectroscopy
BCC	Body centered cubic
BE	Binding energy
CSM	Vibrating sample magnetometer
dc	Direct current
DMI	Dzyaloshinskii-Moriya interaction
DOS	Density of states
DPPH	α-α-diphenyl-β-picryl-hydrazyl
EXAFS	Extended x-ray absorption fine structure
FCC	Face centered cubic
FM	Ferromagnetic layer
FMR	Ferromagnetic resonance
FWHM	Full width at half maximum
GMR	Giant magneto resistance
GS	Ground-signal

GSG	Ground-signal-ground
HM	Heavy metal layer
ISHE	Inverse spin Hall effect
LIA	Lock-in amplifier
LLG	Landau-Lifshitz-Gilbert
MFM	Magnetic force microscope
MRAM	Magnetic random access memory
MRG	Mn_2Ru_xGa
MTJ	Magnetic tunnel junction
NM	Non magnetic layer
PMA	Perpendicular magnetic anisotropy
PPMS	Physical properties measurement system
rf	Radio frequency
RSM	Reciprocal space mapping
SHA	Spin Hall angle
SHE	Spin Hall effect
SQUID	Superconducting quantum interference device
STFMR	Spin torque ferromagnetic resonance
STT	Spin transfer torque
TE	Transverse electric
TEY	Total electron yeld
TM	Transverse magnetic
TMR	Tunnelling magneto resistance
UHV	Ultra high vacuum
UPS	UV photoelectron spectroscopy
UV	Ultra-violet light
VNA	Vector network analyser

XAS	X-ray absorption spectroscopy
XLD	X-ray linear dichroism
XMCD	X-ray magnetic circular dichroism
XPS	X-ray photoelectron spectroscopy
XRD	X-ray diffraction
XRR	X-ray reflectivity

List of Symbols

a	Annihilation operator in second quantisation formalism
$a \times b \times d$	Dimensions (rectangular cavity) [m^3]
$a^\dagger$	Creation operator in second quantisation formalism
A	Exchange constant (for micromagnetics) [$\mathrm{J\,m^{-1}}$]
A_{ij}	Polder susceptibility coefficient ($i, j = xx, xy, yy$) [dimensionless]
a	In-plane lattice constant [m]
α	Gilbert damping parameter [dimensionless]
$\alpha_{\mathbf{eff}}$	Effective Gilbert damping parameter [dimensionless]
α	Set of all quantum numbers apart from J and M [dimensionless]
A	Amplitude of the antisymmetric Lorentzian lineshape [V]
$\vec{A}$	Vector potential of electromagnetic radiation ($\vec{B} = \vec{\nabla} \times \vec{A}$) [$\mathrm{V\,s\,m^{-1}}$=$\mathrm{T\,m}$]
B	Racah parameter for electron-electron repulsion = $((9F^2 + 5F^4)/441)$ [dimensionless]
c	Speed of light = $2.998 \times 10^8 \mathrm{m\,s^{-1}}$
$\overline{\overline{\chi}}$	Polder susceptibility tensor [dimensionless]
$\chi(E/k)$	EXAFS signal = $((\mu(E) - \mu_0(E))/\Delta\mu_0)$ [dimensionless]
c	Out-of-plane lattice constant [m]
c_{lm}	Coefficients for spherical harmonics expansion [V]
Δ	Energy difference between the lowest levels in $3d^N$ and $3d^{N+1}$ configurations [J]]
$\Delta c/a$	Tetragonal distortion = $((c - a)/a)$ [dimensionless]
$\Delta_{\mathbf{f}}$	Energy difference between the $3d^{N+1}\underline{L}$ and $3d^{N+2}\underline{L}$ configurations in the final state [J]
Δ	Band gap at the Fermi level [J]
ΔH	Linewidth of the resonance at constant frequency [$\mathrm{A\,m^{-1}}$]
$\Delta_{\mathbf{i}}$	Energy difference between the $3d^N$ and $3d^{N+1}$ configurations in the initial state = (Δ) [J]

Δ	Linewidth of a Lorentzian lineshape [$\mathrm{A\,m^{-1}}$]
$\Delta\mu_0(E)$	Increase in the absorption coefficient in correspondence of an edge [dimensionless]
$\int \Delta\mu_{L3/L2}$	Area of the L_3/L_2 edge in XMCD measurement [dimensionless]
$\Delta\omega$	Linewidth of the resonance at constant applied field [$\mathrm{rad\,s^{-1}}$]
D	Density of states [$\mathrm{J^{-1}\,m^{-3}}$]
D	Diffusion constant [$\mathrm{m^2\,s^{-1}}$]
Dq	Crystal field splitting energy parameter for octahedral symmetry [J]
Ds	Crystal field splitting energy parameter for D_{4h} symmetry [J]
d	Crystal lattice parameter [m]
d	Thickness of the HM layer [m]
Dt	Crystal field splitting energy parameter for D_{4h} symmetry [J]
E	Energy [J]
e	Electronic charge $= 1.6022 \times 10^{-19}\mathrm{C}$
$E_{\mathbf{c}}$	Energy of a core level [J]
$E_{\mathbf{F}}$	Fermi level [J]
$\vec{E}$	Electric field [$\mathrm{V\,m^{-1}}$]
$\vec{e}$	Rf/electromagnetic electric field [$\mathrm{V\,m^{-1}}$]
ϵ	Energy of a state [J]
ϵ_r	Relative permittivity of a material [dimensionless]
ϵ_0	Permittivity of free space $= (1/\mu_0 c^2) = 8.854 \times 10^{-12}\mathrm{C\,V^{-1}\,m^{-1}}$
η	Rashba coefficient [dimensionless]
η	Single electron spin-orbit coefficient [dimensionless]
F^2	Slater parameter for electron-electron repulsion [dimensionless]
F^4	Slater parameter for electron-electron repulsion [dimensionless]
$F_{\mathbf{a}}$	Antisymmetric Lorentzian lineshape $= (F_{\mathrm{s}}(H_{\mathrm{ex}})(H_{\mathrm{ex}} - H_{\mathrm{res}})/\Delta)$ [dimensionless]
$f(E)$	Fermi-Dirac distribution [dimensionless]
$f(k)$	Complex backscattering amplitude in EXAFS [dimensionless]
$F(r)$	Fourier transform [m]
$F_{\mathbf{s}}$	Symmetric Lorentzian lineshape $= (\Delta^2/[\Delta^2 + (H_{\mathrm{ex}} - H_{\mathrm{res}})^2])$ [dimensionless]

g	Landé factor [dimensionless]
G^1	Slater parameter for electron-electron repulsion [dimensionless]
G^3	Slater parameter for electron-electron repulsion [dimensionless]
γ_0	Gyromagnetic ratio $= (ge/2m_\mathrm{e}) = 28.024\,\mathrm{GHz\,T^{-1}}$ for spin-only electrons ($g = 2$)
Γ	Label for a particular symmetry representation [dimensionless]
Γ_{dip}	Symmetry representation for the dipolar operator [dimensionless]
$\Gamma_{i/f}$	Symmetry representation for the initial/final state in an electronic transition [dimensionless]
Γ	Torque [$\mathrm{A\,m^{-1}\,s^{-1}}$]
$g^{\uparrow\downarrow}_{\mathbf{eff}}$	Effective spin mixing conductance [$\Omega^{-1}\,\mathrm{m}$]
$G_{\mathbf{p/ap}}$	Electrical conductance for parallel/antiparallel configurations [Ω^{-1}]
$g^{\uparrow\downarrow}$	Spin mixing conductance [$\Omega^{-1}\,\mathrm{m}$]
$\mathcal{H}$	Hamiltonian operator
$\mathcal{H}_{\mathbf{AIM}}$	Anderson impurity model Hamiltonian
$\mathcal{H}_{\mathbf{i/f}}$	Anderson impurity model Hamiltonian for the initial/final states
$H_{\mathbf{an}}$	Anisotropy field $= (2k_\mathrm{an}/\mu_0 M_\mathrm{s})$ [$\mathrm{A\,m^{-1}}$]
$\hbar$	Reduced Planck constant $= 1.0546 \times 10^{-34}\,\mathrm{J\,s}$
$H_{\mathbf{c}}$	Coercive field [$\mathrm{A\,m^{-1}}$]
$H_{\mathbf{demag}}$	Demagnetising field $= (\overline{\overline{N}}\vec{M})$ [$\mathrm{A\,m^{-1}}$]
$H_{\mathbf{eff}}$	Effective field [$\mathrm{A\,m^{-1}}$]
$\vec{H}_\parallel$	Antidamping effective field $\propto (\hat{y})$ [$\mathrm{A\,m^{-1}}$]
$\vec{H}_\perp$	Field-like effective field $\propto (\hat{y})$ [$\mathrm{A\,m^{-1}}$]
$H_{\mathbf{ex}}$	External applied field [$\mathrm{A\,m^{-1}}$]
$\vec{h}$	Rf/electromagnetic magnetic field [$\mathrm{A\,m^{-1}}$]
$H_{\mathbf{i}}$	Effective in-plane anisotropy field $= (2K_\mathrm{i}/M_\mathrm{s})$ [$\mathrm{A\,m^{-1}}$]
$H_{\mathbf{k}}$	Effective out-of-plane anisotropy field $= (2K_\mathrm{eff}/M_\mathrm{s})$ [$\mathrm{A\,m^{-1}}$]
(h, k, l)	Miller indexes that define a diffraction peak [dimensionless]
$H_{\mathbf{res}}$	Resonance external field [$\mathrm{A\,m^{-1}}$]
$h_{\mathbf{rf}}$	Rf magnetic field [$\mathrm{A\,m^{-1}}$]
$\mathcal{H}_{\mathbf{so}}$	Spin-orbit Hamiltonian
$I_{\mathbf{ac}}$	Ac injected current [A]

$I_{\mathbf{dc}}$	Dc injected current [A]
$I_{\mathbf{rf}}$	Rf injected current [A]
$\vec{J_{\mathbf{c}}}$	Charge current density [$\mathrm{A\,m^{-2}\,s^{-1}}$]
$J_{\mathbf{ex}}$	Exchange energy [J]
$\vec{J}$	Multi-electron total momentum [J s]
$\vec{j}$	Single electron total momentum [J s]
J	Multi-electron total momentum quantum number [$\hbar$]
j	Single electron total momentum quantum number [$\hbar$]
$J_{\mathbf{rf}}$	Rf current density [$\mathrm{A\,m^{-2}}$]
$\vec{J_{\mathbf{s}}}$	Spin current density [$\mathrm{J\,s\,m^{-2}\,s^{-1}}$]
$j(E)$	Measured XPS signal [dimensionless]
$K_{\mathbf{an}}$	Anisotropy constant [$\mathrm{J\,m^{-3}}$]
k_{B}	Boltzmann constant = $1.3807 \times 10^{-23}\mathrm{J\,K^{-1}}$
$K_{\mathbf{eff}}$	Effective out-of-plane anisotropy constant = $(K_{\mathrm{u}} - 1/2(N_z - N_x)M_{\mathrm{s}}^2)$ [J]
$K_{\mathbf{i}}$	In-plane shape anisotropy constant = $(1/2(N_x - N_y)M_{\mathrm{s}}^2)$ [J]
K	Shape factor in Scherrer equation [dimensionless]
$K(E)$	Universal inelastic loss function for Touhaard's background in XPS [dimensionless]
$K_{\mathbf{u}}$	Uniaxial ou-of-plane anisotropy constant [J]
$\vec{k}$	Wave vector of electrons or photons [$\mathrm{m^{-1}}$]
$\Lambda(k)$	Energy dependent mean free path in EXAFS [m]
λ	Lifshitz damping parameter [dimensionless]
$\lambda_{\mathbf{sf}}$	Spin diffusion length [m]
λ	Multi-electron spin-orbit coupling constant [dimensionless]
λ	Electromagnetic wavelength [m]
l	Length of the sample [m]
L	Length (cylindrical cavity) [m]
$\vec{L}$	Multi-electron orbital momentum [J s]
$\vec{l}$	Single electron orbital momentum [J s]
$\mathfrak{l}$	Orbital momentum operator

L	Multi-electron orbital quantum number [$\hbar$]
l	Single electron orbital quantum number [$\hbar$]
$\langle L \rangle$	Orbital moment (expectation value) from XMCD sum rules [μ_{B}]
$\vec{M}$	Local magnetisation [$\mathrm{A\,m^{-1}}$]
$\vec{m}$	Reduced magnetisation = $(\vec{M}/M_{\mathrm{s}})$ [dimensionless]
$M_{\mathbf{s}}$	Saturation magnetisation [$\mathrm{A\,m^{-1}}$]
$m_{\mathbf{e}}$	Electronic mass = $9.109 \times 10^{-31}\mathrm{kg}$
$M_{\mathbf{eff}}$	Effective (rf) magnetisation [$\mathrm{A\,m^{-1}}$]
M_L	Multi-electron orbital magnetic quantum number [J s]
$\vec{m}$	Rf-varying magnetisation component [$\mathrm{A\,m^{-1}}$]
M_S	Multi-electron spin magnetic quantum number [J s]
M	Multi-electron total magnetic quantum number [J s]
$\mu_0(E)$	Smoothly varying background of the absorption coefficient in EXAFS [dimensionless]
$\mu_{\mathbf{B}}$	Bohr magneton = $(e\hbar/2m_{\mathrm{e}}) = 9.274 \times 10^{-24}\mathrm{A\,m^2}$
$\mu(E)$	Absorption coefficient in EXAFS [dimensionless]
μ	Electron mobility [$\mathrm{m^2\,V^{-1}\,s^{-1}}$]
$\vec{\mu}$	Electronic magnetic moment [$\mathrm{A\,m^2}$]
μ_r	Relative permeability of a material [dimensionless]
$\vec{\mu}$	Spin accumulation [$\mathrm{A\,m^{-1}\,m^{-3}}$]
$\int \mu$	Area of the total XAS measurement [dimensionless]
μ_0	Permeability of free space = $4\pi \times 10^{-7}\mathrm{T\,m\,A^{-1}}$
$\overline{\overline{N}}$	Demagnetising tensor [dimensionless]
n	Electronic density [$\mathrm{m^{-3}}$]
$N_{\mathbf{h}}$	Number of holes in the $3d$ band [dimensionless]
n	Order of the reflection in x-ray diffraction [dimensionless]
n	Refractive index [dimensionless]
N_R	Coordination number of the shell of atoms at distance R from the central atom [dimensionless]
$n_{\uparrow\downarrow}$	Density of $\uparrow$ or $\downarrow$ electrons [$\mathrm{m^{-3}}$]
$N_{\mathbf{v}}$	Number of electrons in the valence band [dimensionless]
$N_{\downarrow}$	Number of $\downarrow$ electrons in the valence band [dimensionless]

$N_\uparrow$	Number of $\uparrow$ electrons in the valence band [dimensionless]
ω	Frequency [$\mathrm{rad\,s^{-1}}$]
$\omega_{\mathbf{res}}$	Resonance frequency [$\mathrm{rad\,s^{-1}}$]
Φ_0	Magnetic flux quanta $= 2.068 \times 10^{-15}$Wb
φ	Azimuthal angle in spherical coordinates [rad]
ϕ_H	Azimuthal angle for the external field $\vec{H}_{\mathrm{ex}}$ [rad]
$\phi_{\mathbf{i/f}}$	Initial/final states wavefunctions [dimensionless]
ϕ	Azimuthal angle for the reduced magnetic moment $\vec{m}$ [rad]
Φ	Phase shift between $\vec{h}$ and $\vec{e}$ in FMR [rad]
$\phi(\vec{r})$	Electronic wave function
ϕ	Angle of incidence of the x-rays with respect to the normal of the sample surface in XMCD [rad]
$\vec{p}$	Particle momentum [$\mathrm{kg\,m\,s^{-1}}$]
P	Spin polarisation $= ((D_\uparrow - D_\downarrow)/(D_\uparrow + D_\downarrow))$ [dimensionless]
P	Injected power [W]
$\vec{p}_{\mathbf{q}}$	Light-polarisation-dependent effective dipole moment [dimensionless]
Q**-factor**	Quality factor of an rf cavity [dimensionless]
q_i	Charge flow in the direction $\hat{i}$ [$\mathrm{m^{-2}\,s^{-1}}$]
q_{ij}	Spin flow in the direction $\hat{i}$ with polarisation $\hat{j}$ [$\mathrm{m^{-2}\,s^{-1}}$]
q	Polarisation of the light ($q = 0, \pm 1$) [dimensionless]
$\vec{Q}$	Vector of the reciprocal lattice in x-ray diffraction $= \vec{k}_{\mathrm{out}} - \vec{k}_{\mathrm{in}}$ [$\mathrm{m^{-1}}$]
$\vec{Q}^{\uparrow/\downarrow}$	Charge quadrupole moment for $\uparrow$ / $\downarrow$ electrons [dimensionless]
$\vec{r}$	Position [m]
$R_{\mathbf{AHE}}$	Anomalous Hall resistance [Ω]
$R_{\mathbf{AMR}}$	Anisotropic magnetoresistance [Ω]
$\vec{R}$	Distance between atoms [m]
$R_{\mathbf{H}}$	Hall coefficient $= (E_y/J_x B_z)$ [$\Omega\,\mathrm{m\,T^{-1}}$]
$R_{\mathbf{HM/FM}}$	Resistance of the HM or FM layer [Ω]
ρ	Electrical resistivity [$\Omega\,\mathrm{m}$]
$\rho_{\mathbf{AHE}}$	Anomalous Hall effect resistivity [$\Omega\,\mathrm{m}$]

$\rho_{\parallel}$	Parallel resistivity ($\vec{M} \parallel J_c$) [$\Omega\,\mathrm{m}$]
$\rho_{\perp}$	Perpendicular resistivity ($\vec{M} \perp J_c$) [$\Omega\,\mathrm{m}$]
ρ_{xx}	Longitudinal resistivity [$\Omega\,\mathrm{m}$]
ρ_{xy}	Transverse resistivity [$\Omega\,\mathrm{m}$]
$R_{\mathbf{p/ap}}$	Electric resistance for parallel/antiparallel configurations [Ω]
$R_{\mathbf{PHE}}$	Planar Hall resistance [Ω]
$\vec{r}_{\mathbf{q}}$	Light-polarisation-dependent effective position operator [dimensionless]
R	Radius (cylindrical cavity) [m]
R	Reflectivity of a surface [dimensionless]
$\mathbb{R}^*$	Reciprocal lattice space
$R_{nl}(r)$	Radial part of a wavefunction [dimensionless]
$R_{\mathbf{xy}}$	Transverse resistance [Ω]
S_0	Overall amplitude factor in EXAFS [dimensionless]
$S_i(E)$	Shirley background for XPS [dimensionless]
$\delta_{\mathbf{c}}$	Central atom phase shift in EXAFS [rad]
σ	Cross-section for light-matter interaction [m^2]
σ	Debye-Waller coefficient in EXAFS [dimensionless]
$\sigma_{\mathbf{HM/FM}}$	Electrical conductivity of the HM or FM layer [$\Omega^{-1}\,\mathrm{m}^{-1}$]
$\sigma_{\mathbf{p/ap}}$	Electrical conductivity for parallel/antiparallel configurations [$\Omega^{-1}\,\mathrm{m}^{-1}$]
$\vec{\sigma}$	Spin current polarisation direction [dimensionless]
$\vec{\sigma}_{\mathbf{s}}$	Spin density [m^{-3}]
$\sigma_{\uparrow\downarrow}$	Electrical conductivity for spin $\uparrow$ / $\downarrow$ electrons [$\Omega^{-1}\,\mathrm{m}^{-1}$]
σ_{xx}	Longitudinal conductivity [$\Omega^{-1}\,\mathrm{m}^{-1}$]
σ_{xy}	Transverse conductivity [$\Omega^{-1}\,\mathrm{m}^{-1}$]
$\vec{S}$	Multi-electron spin momentum [J s]
$\vec{s}$	Single electron spin momentum [J s]
$\mathfrak{s}$	Spin momentum operator
S	Multi-electron spin quantum number [$\hbar$]
s	Single electron spin quantum number [$\hbar$]
S	Amplitude of the symmetric Lorentzian lineshape [V]

$\langle S \rangle$	Spin moment (expectation value) from XMCD sum rules [μ_{B}]
$\langle S \rangle_{\mathbf{eff}}$	Effective (measured) spin moment (expectation value) from XMCD sum rules [μ_{B}]
T	Temperature [K]
T_1	Spin-lattice relaxation time [s]
T_2	Spin-spin relaxation time [s]
$\tau_{\mathbf{el}}$	Electronic scattering relaxation time [s]
$\tau_{\mathbf{ex}}$	Exchange relaxation time = $(\hbar / S J_{\mathrm{ex}})$ [s]
$\tau_{\parallel}$	Antidamping torque $\propto (\vec{m} \times (\hat{y} \times \vec{m}))$ [$\mathrm{A\,m^{-1}\,s^{-1}}$]
$\tau_{\perp}$	Field-like torque $\propto (\vec{m} \times \hat{y})$ [$\mathrm{A\,m^{-1}\,s^{-1}}$]
τ	Size of the particles of crystallites in a sample [m]
$\tau_{\mathbf{sf}}$	Spin-flip relaxation time [s]
$\tau_{\mathbf{so}}$	Torque due to the spin-orbit effect acting on the magnetisation [$\mathrm{A\,m^{-1}\,s^{-1}}$]
$\tau_{\mathbf{tot}}$	Total torque acting on the magnetisation [$\mathrm{A\,m^{-1}\,s^{-1}}$]
$T_{\mathbf{comp}}$	Compensation temperature [K]
$T_{\mathbf{c}}$	Curié temperature [K]
θ	Polar angle in spherical coordinates [rad]
θ_H	Polar angle for the external field $\vec{H}_{\mathrm{ex}}$ [rad]
θ	Polar angle for the reduced magnetic moment $\vec{m}$ [rad]
Θ	Phase shift between $\vec{h}$ and $\vec{m}$ in FMR [rad]
$\theta_{\mathbf{sh}}$	Spin Hall angle [dimensionless]
θ	Angle between the two sublattices magnetic moments in XMCD [rad]
t	Thickness [m]
$t_{\mathbf{i/f}}$	Hopping parameter (transfer integral) for the initial/final states
T	Transition operator [dimensionless]
t	Thickness of the FM layer [m]
t_{vd}	Hopping parameter (transfer integral) between $3d$ and valence band
$\langle T \rangle$	Magnetic dipole moment (expectation value) from XMCD sum rules [μ_{B}]
U_{dd}	Hubbard energy of the interaction between $3d$ electrons
U_{pd}	Hubbard energy of the interaction between $3d$ and $2p$ electrons

V	Volume [m^3]
V_0	Work function [J]
$V_{2\omega}$	Second harmonic voltage [V]
$V_{\mathbf{AHE}}$	Anomalous Hall voltage [V]
$V_{\mathbf{ANE}}$	Anomalous Nernst voltage [V]
$V_{\mathbf{cr}}$	Crystal field potential [V]
$V_{\mathbf{dc}}$	Dc voltage [V]
$v_{\mathbf{F}}$	Fermi velocity [$\mathrm{m\,s}^{-1}$]
$V_{\mathbf{H}}$	Hall (transverse) voltage [V]
V_o	Crystal field potential in octahedral symmetry [V]
V_ω	First harmonic voltage [V]
$V_{\mathbf{PHE}}$	Planar Hall voltage [V]
$\vec{V}$	Electric potential [V]
$V_{\mathbf{R}}$	Zeroth-order expansion of the crystal field potential [V]
$W_{\mathbf{fi}}$	Transition probability between an initial and a final atomic states [dimensionless]
$W(k)$	Window function for the Fourier transform in EXAFS [dimensionless]
X_{220}	Crystal field splitting energy parameter for D_{4h} symmetry = $(-\sqrt{70}Ds)$ [J]
X_{400}	Crystal field splitting energy parameter for D_{4h} symmetry = $(6\sqrt{30}Dq - 7/2\sqrt{30}Dt)$ [J]
X_{40}	Crystal field splitting energy parameter for octahedral symmetry = $(10\sqrt{30}/18Dq)$ [J]
X_{420}	Crystal field splitting energy parameter for D_{4h} symmetry = $(-5/2\sqrt{42}Dt)$ [J]
ξ	Spin-orbit coefficient for spin Hall interaction [dimensionless]
ξ	Ratio between the planar Hall and the anomalous Hall resistances = $(R_{\mathrm{PHE}}/R_{\mathrm{AHE}})$[dimensionless]
X_{nl}	l-th zero of the n-th Bessel function [dimensionless]
X'_{nl}	l-th zero of the derivative of the n-th Bessel function [dimensionless]
$Y_l^m(\theta, \varphi)$	Spherical harmonics [dimensionless]
Z	Atomic mass [dimensionless]

List of Space Groups and Atomic Structures

A_{1g}	Multi-electron totally symmetric representation
a_{1g}	Single electron totally symmetric representation
D_{4h}	Tetragonally distorted octahedral symmetry
e_g	Two-fold degenerated single electron level for octahedral symmetry $= d_{x^2-y^2}, d_{z^2}$
e	Two-fold degenerated single electron level for tetrahedral symmetry $= d_{x^2-y^2}, d_{z^2}$
$\Gamma_7(t_{2g})$	Single electron double group representation coming from an t_{2g} state
$\Gamma_8(e_g)$	Single electron double group representation coming from an e_g state
$\Gamma_8(t_{2g})$	Single electron double group representation coming from an t_{2g} state
O_h	Octahedral symmetry
SO_3	Spherical symmetry
T_{1g}	Multi-electron representation for the dipolar operator in octahedral symmetry
t_{2g}	Three-fold degenerated single electron level for octahedral symmetry $= d_{xy}, d_{yz}, d_{zx}$
t_2	Three-fold degenerated single electron level for tetrahedral symmetry $= d_{xy}, d_{yz}, d_{zx}$
$C1_b$	Cubic crystal structure of a half Heusler alloy, space group $F\bar{4}3m$, number 216
$D0_{22}$	Tetragonally distorted crystal structure of an Heusler alloy, space group $I4/mmm$, number 139
$L2_1$	Cubic crystal structure of an Heusler alloy, space group $Fm\bar{3}m$, number 225
"inverse" $L2_1$	Cubic crystal structure of an "inverse" Heusler alloy, space group $F\bar{4}3m$, number 216

Chapter 1

Introduction

Magnetism is both one of the oldest scientific disciplines and at the forefront of modern nanoscience and nanotechnology. The irreversible, non linear and time dependent response of the magnetisation of a ferromagnet to an external magnetic field, known as the hysteresis loop, has attracted the attention of physicists for a long time. The recent progress in nano and microfabrication opens up new possibilities in the world of magnetism, where quantum mechanical effects and lateral confinement become dominant. In addition, the advances in deposition and growth techniques of crystalline materials now allows us to prepare very high quality crystalline thin films. In this context, it is of paramount importance to understand single-atom interactions, strain and doping effects.

The most known and used spin electronics device, the magnetic tunnel junction (MTJ)[1] is the perfect example of how to exploit these new possibilities. The fabrication of tunnel junctions consisting of ultra-thin layers of magnetic materials and oxide barriers with extremely short lateral dimensions made it possible to realise highly efficient magnetic memory devices. The crystallographic quality of the magnetic (CoFe) and oxide (MgO) layers is key to the functionality of these devices, since this combination of materials gives very high tunnelling magnetoresistance (TMR) ratios.

Moore's law demands an exponential increase of the capacity of silicon technology, requiring the lateral dimensions of electronic devices to shrink more and more. This is not an easy task and it comes with its own problems. The magnetic stability and properties of MTJs degrade rapidly and fabrication issues becomes predominant as their dimensions shrink. In this context, the hunt for new solutions goes through the exploration of new materials and new quantum mechanical effects.

In the first part of this thesis we investigated the properties of Mn-based Heusler alloys, a class of magnetic compounds that has recently attracted the attention of the research community. These intermetallic alloys show a wide range of properties that can be tuned by atomic composition, crystal structure and strain. Ferromagnetic, antiferromagnetic and ferrimagnetic compounds are readily available and some of them show interesting characteristics like perpendicular magnetic anisotropy (PMA) and half metallicity.

The second part of this work is focussed on spin injection mechanisms using the spin Hall and Rashba effects. In modern spin electronic devices, the manipulation of the magnetisation of a magnetic layer is achieved through the injection of a spin polarised current. In MTJ devices, this implies high current densities flowing across an oxide tunnel barrier, which in nano-sized devices can cause dielectric breakdown and increased power consumption. The spin Hall effect allows for the injection of spins perpendicular to the flow of a charge current in a material with high spin-orbit coupling. A typical structure consists of an

[1] A list of acromyms can be found on page xix.

heavy metal layer underneath or on top of a ferromagnetic layer of an MTJ device. In this geometry, the high current density flows in the heavy metal, and a spin current is injected in the ferromagnetic metal, actively modifying its magnetic moment.

1.1 Future prospects and challenges

Following Moore's law, the lateral size of transistors in integrated circuits should halve every 18 months. Similar "laws" apply to data rates and magnetic storage on hard disks. As we have now reached the nanometric scale, the realisation of the various components has become more and more demanding. Apart from the more obvious fabrication problems regarding lithography and patterning, the reduced volume of magnetic elements brings challenges of its own. Magnetic data recording relies on the storage of information in the orientation of the magnetic moment of a perpendicular magnetised bit. The thermal stability of one bit is given by the height of the potential barrier between the $\uparrow$ and the $\downarrow$ configurations, corresponding to bits 0 and 1. That is the energy that it takes to switch between one magnetic state to the other. It is directly related to the perpendicular magnetic anisotropy (PMA) of the material and scales linearly with the volume of the magnetic element. The switching probability due to thermal excitation is given by $\exp(K_{\mathrm{an}}V/k_{\mathrm{B}}T)$[2], where K_{an} is the anisotropy constant, V is the volume, k_{B} is the Boltzmann constant and T is the temperature. Hence, a good figure of merit is given by the ratio $K_{\mathrm{an}}V/k_{\mathrm{B}}T$: modern magnetic storage devices, such as magnetic tunnel junctions, require a ratio of 50 or more in order to retain the stored data for 10 years. As the volume of the magnetic elements decreases, higher values of PMA are required for high thermal stability. Magnetic data storage using perpendicular Co/Pt multilayers fails to reach the required stability for nanometre-sized elements.

In addition, a high PMA will result in a high anisotropy field $H_{\mathrm{an}} = 2K_{\mathrm{an}}/\mu_0 M_{\mathrm{s}}$, where M_{s} is the saturation magnetisation of the magnetic storage layer, which translates in a high resonance frequency. This property could be exploited in spin torque oscillator devices to generate high frequency electric signals from a dc current (see sec. 2.3.9).

The magnetic anisotropy of a magnetic material can be enhanced by alloying $3d$ metals with rare earth elements. The high spin-orbit coupling of the $4f$ shell of these elements results in huge uniaxial anisotropy. The world first rare earth permanent magnets were based on $SmCo_5$, and the material with the best properties and most widely employed is $Nd_2Fe_{12}B$. Sm or Nd provide most of the anisotropy in these materials.

For thin film applications in magnetic recording, amorphous GdCo, possibly with the addition of Mo or Cu, has been investigated [1–3]. It has also been demonstrated [4] that many different rare earth/transition metal (RE/TM) alloys, with RE being Gd, Tb, Dy and Ho and TM being mainly Co and Fe or CoFe alloys, have perpendicular magnetic anisotropy. Moreover it was also reported in Tb/Co and Ho/Co multilayers. Unfortunately, the cost of the materials is often critical for bulk, if not for thin films, applications. The price of rare earth elements is extremely high in comparison to transition metals, and a recent crisis (2008-2010) in the production of Nd sent the cost of NdFeB permanent magnets sky-rocketing. Even if this crisis has now passed, it is clear that the use of rare earth elements is not a suitable choice for future applications. A more viable way to enhance the anisotropy of magnetic elements consists in finding materials with highly distorted crystalline structure. When the out-of-plane lattice parameter c is higher than the in-plane parameter a, a uniaxial magnetic material acquires perpendicular uniaxial or easy-plane anisotropy.

The tunnelling magnetoresistance ratio (TMR) of a MTJ device (Fig. 1.1) is a direct consequence of

[2] A list of symbol can be found on page xxiii.

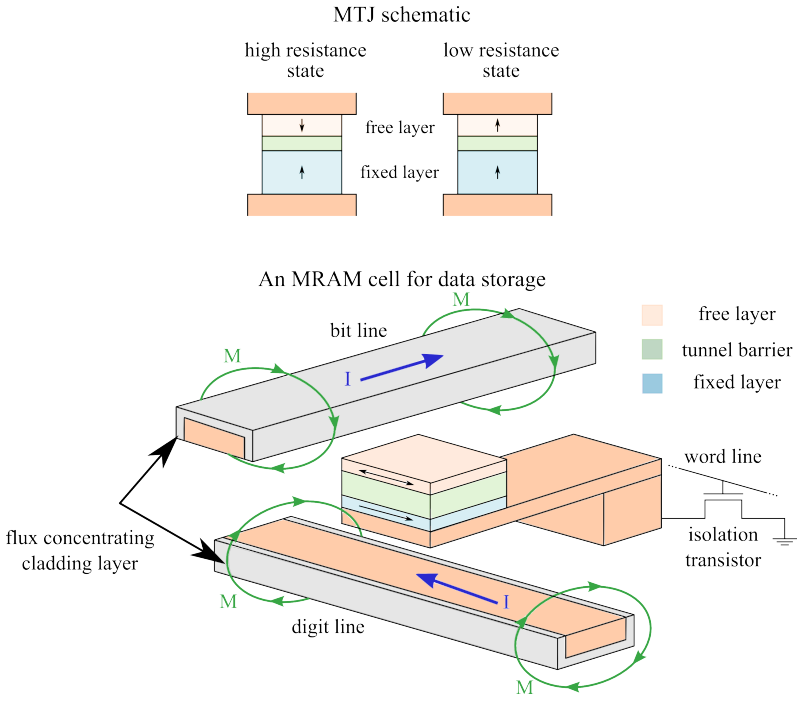

Figure 1.1: Top: schematic of an MTJ device. Bottom: exploded view of a magnetic random acces memory (MRAM) cell, used for data storage.

the spin polarisation at the Fermi level of the ferromagnetic layers that sandwich the insulating barrier (see sec. 2.3.9). "Strong" $3d$ ferromagnetic metals (with a completely spin polarised d band) still don't have high spin polarisation because of the presence of the $4s$ band that is not directly spin-split, adding minority electronic states at the Fermi level. The use of the combination CoFe/MgO/CoFe increases the TMR because of the spin filtering effect of the MgO barrier [5], but the discovery of a new suitable material with very high spin polarisation would allow us to move away from this configuration without sacrificing the TMR ratio.

Another problem is related to the switching of the magnetic element in MTJ by spin transfer torque [6] (STT, see sec 2.2.2). The critical current density required for the switching is of the order of $10^{10}\,\mathrm{A\,m^{-2}}$: such a high current density travelling through the insulating barrier can cause dielectric breakdown and excessive heating. Research is trying to optimise the STT process by finding materials with reduced magnetisation and Gilbert damping which would require less current to switch, but it is also looking for new ways to apply torque on the magnetisation of the free magnetic layer. An interesting prospect is represented by the switching by spin Hall effect, as will be presented in sec. 1.2.2.

1.2 Materials for spin electronics

1.2.1 Heusler alloys

As discussed in the previous section, for magnetic recording the shrinking of the volume of the magnetic elements in MTJ devices will cause problems regarding the thermal stability of the stored data. In order to obtain high data retention, new materials with high PMA are required, as a high anisotropy increases the thermal stability of a magnetic element. In addition, the TMR ratio of MTJs is directly dependent on the spin polarisation at the Fermi level of the ferromagnetic electrodes. A class of material that has

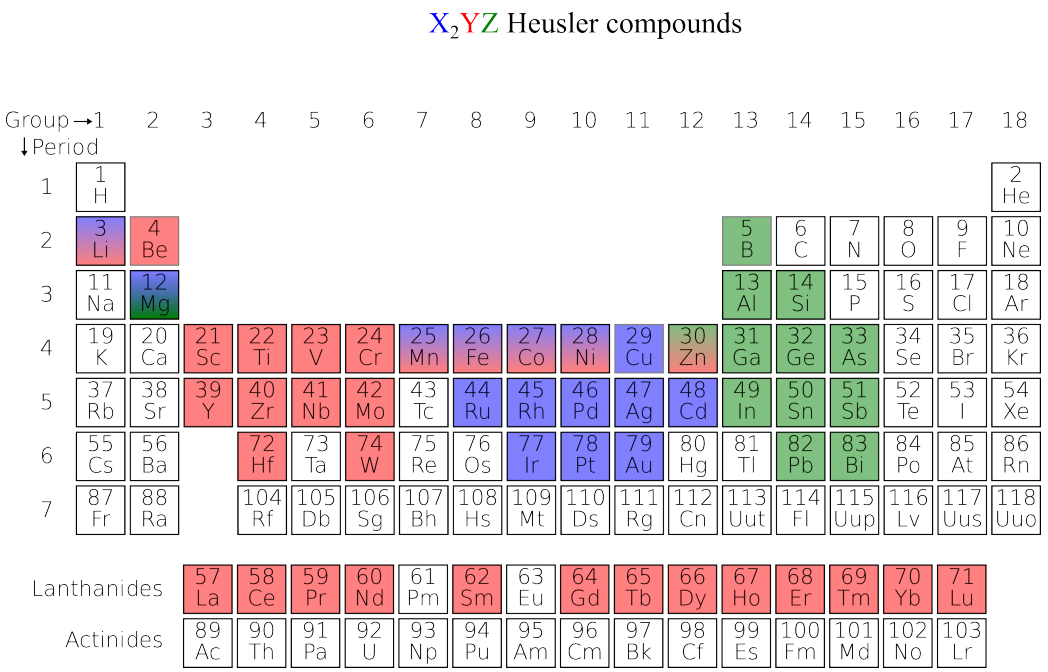

Figure 1.2: Periodic table and elements that can be used to form a Heusler alloy. Blue elements can be X atoms, red elements can be Y atoms, while green elements can be Z atoms.

attracted a lot of attention in the research is the family of Heusler alloys. They are generally cubic intermetallic compounds, but other related materials are uniaxial ferrimagnets with very high PMA and high spin polarisation.

A Heusler compound is a ternary inter-metallic with the general formula XYZ (half Heusler) or X_2YZ (full Heusler), where X and Y typically are transition metals and Z is a main group element [7–9]. The term is named after Friedrich Heusler, a German mining engineer and chemist who studied such an alloy at the beginning of the twentieth century. Fig. 1.2 shows the elements that can be used to form a Heusler alloy together with the positions they usually occupy. A common feature of both XYZ and X_2YZ families are four interpenetrating face-centered cubic sublattices. In the case of full Heusler compounds, the sublattices are fully occupied, whereas one of them is void in half Heusler compounds. The most electropositive atoms fill the octahedral sites, since this is electrostatically preferred. *The properties of Heusler compounds differ completely from those of the contained elements.* Alloys showing ferromagnetism and ferrimagnetism are readily obtained both in bulk and thin film forms.

We have focused our interest in the tetragonally distorted Heusler alloys. While the cubic $L2_1$ Heusler alloys are virtually isotropic, their tetragonal forms can display very high uniaxial magnetic anisotropy along with tunable saturation magnetisation and high spin polarisation. As mentioned in the previous section, the high magneto-crystalline anisotropy could be exploited in magnetic recording or high-frequency applications.

Heusler alloys with 24 valence electrons and half Heusler with 18 electrons are particularly interesting because they have been predicted to be compensated ferrimagnets [10, 11]: the different magnetic sublattices are antiferromagnetically coupled and the magnetic moments cancel each other. In addition, these materials should be half metals, with a spin gap at the Fermi level resulting in 100 % spin polarisation. A compensated half metallic ferrimagnet would be very useful, since it would be fully spin polarised yet free from shape anisotropy, it would create no stray fields and it would be insensitive to external fields. Another important parameter for spin electronic devices is the Gilbert damping parameter α. It

represents the torque that has to be overcome by the STT to obtain magnetisation switching, *i.e.*, the higher is α, the higher is the critical current for STT switching. It has been predicted and experimentally verified [12, 13] that half-metallic Heusler alloys have very small Gilbert damping parameter, due to the spin-gap in the density of states that does not allow spin-flip processes. Because of the 100 % spin polarisation at the Fermi level and low damping make, we expect these kind of compounds to need low critical current densities for STT switching. Several Heusler alloys in their cubic form have been predicted to be a compensated half metal ferrimagnet. Unfortunately, up to now all attempts to fabricate such a material has failed [14–16]: some of these compounds don't crystallise in the cubic structure even in the form of thin films; the presence of defects and some degree of disorder in the occupancy of the crystalline positions inevitably ruins their half-metallicity. In addition, the deposition conditions and the coupling at interfaces greatly influence the spin polarisation in devices [17, 18].

1.2.2 Heavy metals with high spin-orbit coupling

Other materials that could be used in a new type of magnetic devices are non magnetic metals with high spin-orbit coupling. In the simplest approximation this interaction scales as Z^4, where Z is the atomic number. This is the reason why the spin-orbit interaction is stronger in heavy metals such as W, Ta and Pt. Exploiting the spin Hall effect [19] or the Rashba effective field [20], thin layers of these materials could be used as a source of spin currents and to apply a torque on the magnetisation of the free layer in an MTJ. This would allow the switching of the magnetic state without having to pass a high current directly through the tunnel barrier. An example of an application would be a device with a top-pinned ferromagnetic electrode and a free bottom electrode deposited on top of an high spin-orbit coupling material. By passing a charge current in the plane of the heavy metal, a pure spin current normal to the interface is generated and the injected spins could transfer their angular momentum to the magnetisation of the free layer.

1.3 PhD project

My PhD project consisted in investigating the properties of new materials in order to obtain a better understanding with a view to the future use in spin electronic devices. First we studied the Heusler and half Heusler alloys Mn_3Ga and Mn_2Ga. These are antiferromagnets that in the form of thin films crystallise in the $D0_{22}$ tetragonal structure[3]. This can be regarded either as an ordered bcc structure with a huge distortion (c/a ranges from 1.806 to 1.845), or as a slightly distorted ordered fcc structure (c/a ranges from 0.903 to 0.9225). This results in high PMA, with anisotropy fields up to 15 T and uniaxial anisotropy energy of $1.1\,\mathrm{MJ\,m^{-3}}$. Interestingly, we also found a small soft in-plane component of the magnetisation that is due to the canted magnetic moment of one sublattice.

We have also investigated the first half-metallic compensated ferrimagnet Mn_2Ru_xGa. This Heusler alloy grows in the cubic $L2_1$ crystal structure and its magnetic properties can be fully tuned by strain and Ru concentration x. We found that it is possible to obtain almost perfect compensation of the magnetic moment of the two Mn sublattices and very high spin polarisation at the Fermi level. Such a material is free from stray fields and unaffected from external magnetic field perturbation. Its very high spin polarisation would also lead to high TMR ratio if used in a MTJ device and low critical current for STT-based switching.

Finally, we tested heavy metals with high spin-orbit coupling in order to investigate the possibility of using them for STT switching of magnetic material through spin Hall effect or Rashba effect. In particular,

[3] A list of crystal structures can be found on page xxxiii.

we analysed W and Pt with different methods proposed in the literature and determined the validity of each of them.

Chapter 2

Theory

This work investigates the development of novel magnetic materials and their spin dependent transport properties, with a particular focus on compensated Heusler alloys and on the effect of spin injection using the spin Hall effect mechanism.

The phenomena discussed in this work are understood and analysed on the basis of both classical and quantum mechanical theories. Therefore we give a short summary of some of the required theory of magnetism and magnetotransport below. We then analyse basic aspects of the interaction of x-rays with matter, since during this research we used advanced x-ray characterisation techniques.

2.1 Magnetism of the electron

The phenomenon of magnetism finds its true basis in quantum mechanics [21–24]. In this framework, electrons are described by a complex wave function $\phi(\vec{r})$, whose physical significance is that $\phi^*(\vec{r})\phi(\vec{r})\delta^3 r$ gives the probability of finding the electron in an infinitesimal volume $\delta^3 r$ around $\vec{r}$. The basic equation is the Schrödinger equation

$$\mathcal{H}\phi = E\phi \ , \tag{2.1}$$

where $\mathcal{H}$ is the Hamiltonian operator. The eigenvalues of $\mathcal{H}$ are the energy levels E_i for each electronic wave function ϕ_i. The eigenfunctions are orthogonal to each other and form a basis of the system. All physical quantities are described by matrix operators and the procedure to determine the values of these quantities is to diagonalise the operators and find the eigenvalues.

Magnetism is directly connected to the angular momentum of particles. The protons and neutrons in the nuclei of atoms posses much smaller magnetic moments with respect to the electrons because of the much greater nucleon mass. Therefore, in this work we will neglect them and consider electrons only. Each electron is characterised by an orbital angular momentum $\vec{L}$ and by a spin angular momentum $\vec{S}$. The first one is associated with the orbital motion of the particle around the nucleus, while the second one is directly related to the quantum mechanical nature of the particle.

The orbital angular momentum can be understood in both the classical and quantum mechanical pictures. In the first, the orbiting electron produces a current loop that in turn produces a magnetic moment. This moment is given by

$$\vec{\mu} = -\frac{e}{2m_{\mathrm{e}}}\vec{l} \, , \tag{2.2}$$

where m_{e} is the mass of an electron, e is the (positive) electron charge and $\vec{l} = \vec{r} \times \vec{p}$ is the single-electron orbital momentum.

The spin orbital momentum derives directly from the relativistic quantum mechanical nature of the particles. Electrons, like all fermions, posses a spin momentum with quantum number $s = 1/2$. The spin momentum is twice as efficient in generating a magnetic moment as the orbital one. In fact, the magnetic moment arising from the spin of an electron is given by

$$\vec{\mu} = -\frac{e}{m_\mathrm{e}}\vec{s}\,. \tag{2.3}$$

This quantity is known as the Bohr magneton. We will reuse and redefine eq 2.2 and eq. 2.3 in terms of the gyromagnetic ratio and g-factor in sec. 2.2.

From the quantum mechanical point of view, the orbital momentum operator $\mathfrak{l}$ is obtained by replacing the particle momentum $\vec{p}$ with its operator $-\imath\hbar\partial/\partial\vec{r}$, where $\hbar$ is the reduced Planck constant. Therefore, we have

$$\begin{aligned}
\mathfrak{l}_x &= -\imath\hbar\left(\hat{y}\tfrac{\partial}{\partial z} - \hat{z}\tfrac{\partial}{\partial y}\right)\ , \\
\mathfrak{l}_y &= -\imath\hbar\left(\hat{z}\tfrac{\partial}{\partial x} - \hat{x}\tfrac{\partial}{\partial z}\right)\ , \\
\mathfrak{l}_z &= -\imath\hbar\left(\hat{x}\tfrac{\partial}{\partial y} - \hat{y}\tfrac{\partial}{\partial x}\right)\ .
\end{aligned} \tag{2.4}$$

The allowed values of the orbital momentum will be given by the eigenvalues of these operators. By straightforward differentiation it follows then

$$\mathfrak{l}_x\mathfrak{l}_y - \mathfrak{l}_y\mathfrak{l}_x = \hbar^2\left(\hat{x}\frac{\partial}{\partial y} - \hat{y}\frac{\partial}{\partial x}\right) = \imath\hbar\mathfrak{l}_z\ . \tag{2.5}$$

Then, we define the commutation as $[AB] = AB - BA$. Repeating this operation for the other two possible combinations, we derive the commutation relations

$$\begin{aligned}
[\mathfrak{l}_x\mathfrak{l}_y] &= \imath\hbar\mathfrak{l}_z\ , \\
[\mathfrak{l}_y\mathfrak{l}_z] &= \imath\hbar\mathfrak{l}_x\ , \\
[\mathfrak{l}_z\mathfrak{l}_x] &= \imath\hbar\mathfrak{l}_y\ .
\end{aligned} \tag{2.6}$$

Therefore $\mathfrak{l}_x$, $\mathfrak{l}_y$ and $\mathfrak{l}_z$ don't commute with each other and it is not possible to simultaneously know their values. On the contrary, we have that $\mathfrak{l}^2 = \mathfrak{l}\cdot\mathfrak{l} = \mathfrak{l}_x^2 + \mathfrak{l}_y^2 + \mathfrak{l}_z^2$ does commute with $\mathfrak{l}_z$. It is then possible to find wave functions that are eigenfunctions of both $\mathfrak{l}_z$ and $\mathfrak{l}^2$. Using the commutation relations 2.6 the eigenvalues of the orbital momentum are given by the orbital quantum number l and the magnetic orbital quantum number m_l as

$$\langle\mathfrak{l}^2\rangle = \hbar^2 l(l+1) \quad \text{and} \quad \langle\mathfrak{l}_z\rangle = \hbar m_l\ . \tag{2.7}$$

The reduced Planck constant $\hbar$ is sometimes omitted for simplicity in theoretical discussions, when the treatment is done in atomic units. The eigenfunctions are given by the spherical harmonics $Y_l^{m_l}$. In the hydrogen-like atom wavefunctions, the l quantum number is related to the orbital shell of the electron: $l = 0, 1, 2, 3, 4, \ldots$ for $s, p, d, f, g, \ldots$ orbitals, respectively, and it is always an integer number. m_l can assume values between $-l$ and $+l$ at intervals of 1. In Fig. 2.1 the orbital momentum of a d electron is represented as the vector $\vec{l}$: the magnitude of the vector is $\hbar\sqrt{6}$ and the l_z projection varies from $-2\hbar$ to $2\hbar$ as m_l varies. The l_x and l_y components are not eigenstates and oscillate continuously.

The spin momentum behaves in the same way: it can be represented by the spin quantum number s and by the magnetic spin quantum number m_s. The main difference is that s is half-integer and can only

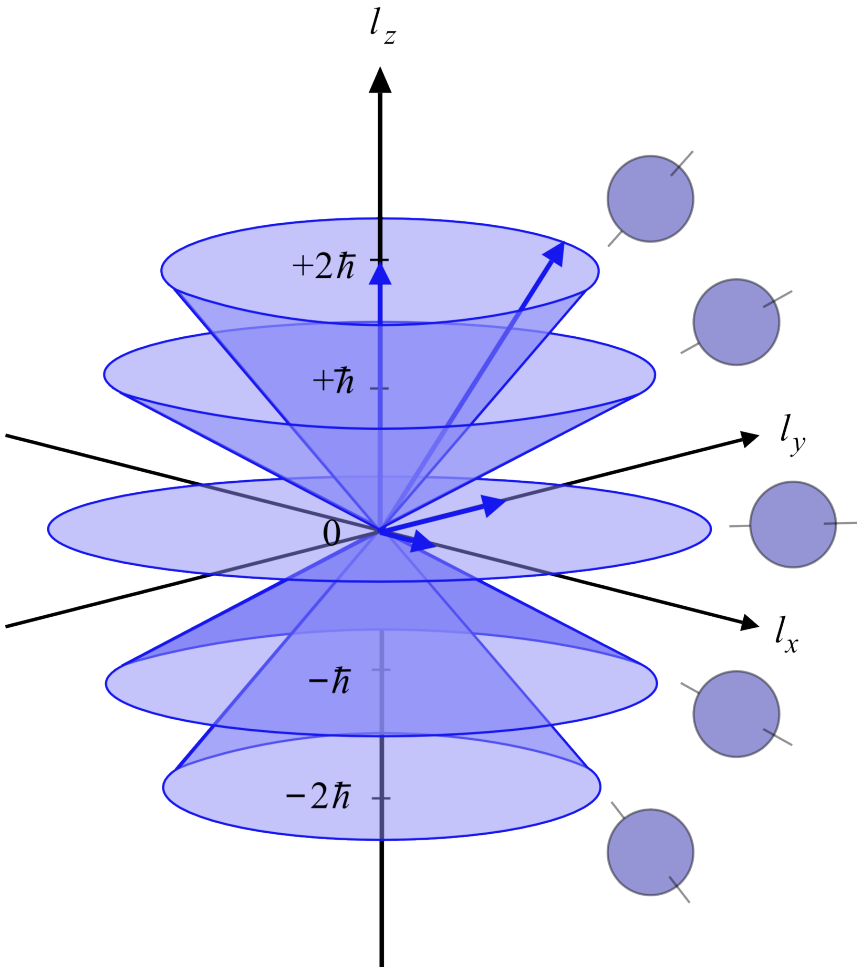

Figure 2.1: Schematic representation of the orbital momentum for an electron in a d state, corresponding to $l = 2$ and $m_l = -2, \ldots, +2$.

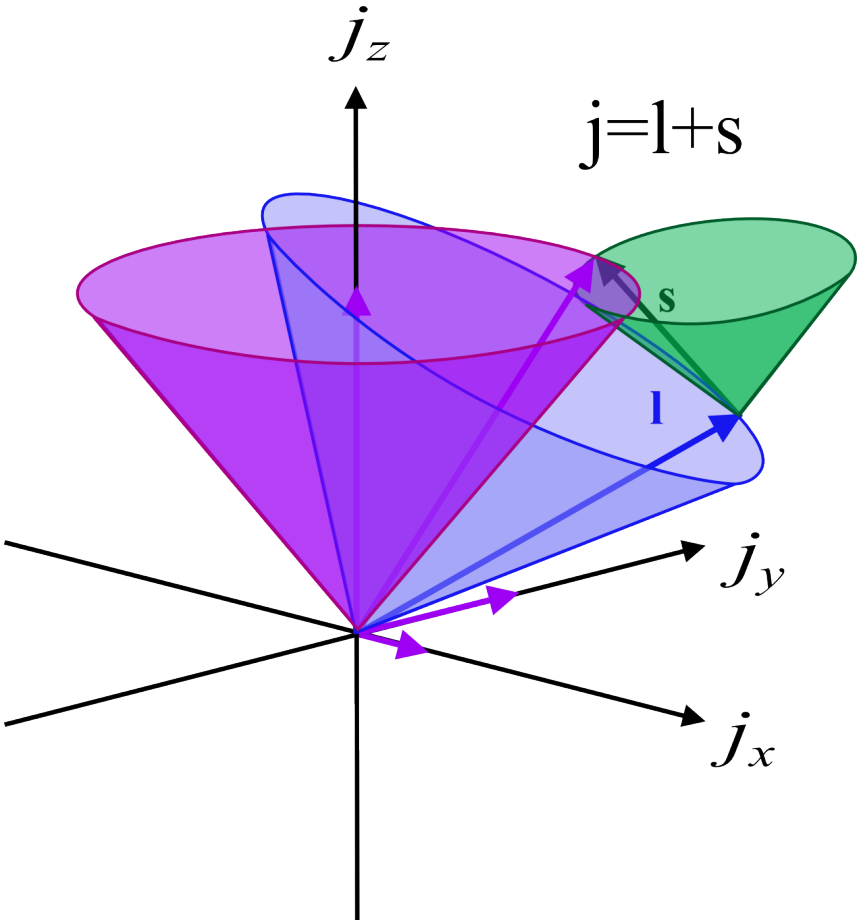

Figure 2.2: Schematic representation of the coupling of orbital and magnetic momenta.

assume the value of 1/2. Therefore we have $m_s = \pm 1/2$.

The total angular momentum of an electron $\vec{j}$ is given by the vectorial sum of the orbital and magnetic momenta. Therefore we have $\vec{j} = \vec{l} + \vec{s}$. The situation is shown in Fig. 2.2. The momentum $\vec{j}$ has the same properties as $\vec{l}$ and $\vec{s}$, therefore it has the correspondent quantum numbers j and $m_j = -j, \ldots, +j$. Since $\vec{l}$ and $\vec{s}$ are vectors, j can assume values $|l - s|, \ldots, l + s$ at intervals of 1.

In a multi-electron atom, the total angular momentum of the atom can be obtained using different coupling schemes. We have been using lower-case letters for the momenta and the quantum numbers of single-electron states, while we will use upper-case letters for multi-electrons states. The most common coupling scheme is the so called Russell-Saunders or LS coupling. In an atom containing N electrons we have that the total angular momentum is given by

$$\vec{J} = \sum_{i=1}^{N} (\vec{l}_i + \vec{s}_i) \ . \tag{2.8}$$

In the LS coupling scheme, the orbital momenta and spin momenta of all the electrons couple separately, and the total $\vec{J}$ is then given by the sum of the total $\vec{L}$ and $\vec{S}$. Therefore we have

$$\vec{L} = \sum_{i=1}^{N} \vec{l}_i \quad \text{and} \quad \vec{S} = \sum_{i=1}^{N} \vec{s}_i \ . \tag{2.9}$$

In the same way we can define the quantum numbers L, S, J and M_L, M_S, M (instead of M_J), respectively.

The LS coupling is valid when l and s are good quantum number for the system, that is in the case of small spin-orbit coupling (see sec. 2.1.1). If that is not the case, the individual orbital and spin momenta of each electron must couple together first, producing N values $\vec{j}_i$. These momenta must be summed together to obtain $\vec{J}$. This is called JJ coupling.

2.1.1 Spin-orbit coupling

The spin-orbit coupling is due to the interaction between the spins of the electrons and the charge of the nucleus it orbits around. The interaction is given by the formula [22]

$$\mathcal{H}_{\text{so}} = -\frac{1}{2}\frac{e\hbar^2}{2mc^2 r}\frac{\mathrm{d}V(r)}{\mathrm{d}r}\vec{S}\cdot\vec{L} = \lambda\vec{S}\cdot\vec{L}\ , \tag{2.10}$$

where $V(r)$ is the electric potential seen by the electron and $\vec{S}$ and $\vec{L}$ are the spin or orbital momenta respectively. The theory of relativity must be considered in order to have $\mathcal{H}_{\text{so}} \neq 0$, since, in the classic limit of $c \to \infty$ it would vanish. λ is usually phenomenologically determined; however for a hydrogen-like atom we have

$$\frac{1}{r}\frac{\mathrm{d}V(r)}{\mathrm{d}r} = \frac{Ze}{4\pi\epsilon_0 r^3}\ , \tag{2.11}$$

with Z the atomic mass and r is the mean radius of the electron orbit. $r^{-3} \propto Z^3$ so that the spin-orbit coupling is proportional to Z^4. This simplified model highlights that the spin-orbit interactions are important in heavy elements (high Z value) while they can be treated as a perturbation in the light ones (low Z value).

The spin-orbit interaction can produce spin-dependent transverse resistivity. It creates an additional component of the velocity of a moving electron. This component is perpendicular to the current flow and has opposite sign for electrons with opposite spins. This results in a spin accumulation in directions perpendicular to the electron current, a phenomena discussed in more detail in sec. 2.3.6.

2.1.2 Ferromagnetism, Stoner model and local moments

The main characteristic of a ferromagnetic material is its spontaneous magnetisation M_{s}, due to the parallel alignment of all the electronic magnetic moments in the crystal lattice. Ferromagnetism was first described phenomenologically by Weiss in terms of an internal molecular magnetic field, proportional to the total magnetisation, that favours the alignment of the moments. Later, quantum mechanics was able to explain this phenomenon considering the Coulomb and exchange interactions in the Hamiltonian for a system of interacting atoms.

The interactions between local magnetic moments are described by the Heisenberg Hamiltonian $\mathcal{H} = -2J_{\text{ex}}\hat{S}_1\cdot\hat{S}_2$, where $\vec{S}_1$ and $\vec{S}_2$ are the spins of the electrons, J_{ex} is the exchange energy and $\hat{S}_1$ and $\hat{S}_2$ are unity vectors indicating the directions of the respective spins. $J_{\text{ex}} > 0$ favours a parallel alignment (ferromagnetism), while $J_{\text{ex}} < 0$ favours an antiparallel alignment (antiferromagnetism).

In a ferromagnetic material, the exchange interaction makes it favourable for the spins to all align in the same directions. The total moment per unit volume is the saturation magnetisation M_{s}. Even in a perfect crystalline system, this totally-aligned configuration is not observed at non-zero temperature. Thermal agitation and entropy cause the spins to randomly misalign, so that the net magnetic moment is less than M_{s}.

In the picture of itinerant electrons, electronic wave functions are delocalised over the crystal lattice and form the band structure. In a ferromagnetic material the bands are split into two sub-bands of

different energy for spin ↑ and spin ↓ electrons respectively. The saturation magnetisation of a material is approximately equal to $M_\mathrm{s} = \mu_\mathrm{B}(n_\uparrow - n_\downarrow)$, where $\mu_\mathrm{B} = (\hbar e)/(2m_\mathrm{e})$ is the Bohr magneton and $n_\uparrow$ and $n_\downarrow$ are the density of electrons for the two sub-bands. This spin-split band structure is energetically favourable if the condition $D(E_\mathrm{F})J_\mathrm{ex} > 1$, with $D(E_\mathrm{F})$ density of states at the Fermi level, is verified. This is known as the Stoner criterion.

The magnetic state of a mesoscopic ferromagnetic material is not as straightforward as one might initially think. The configuration in thermodynamic equilibrium conditions is determined by the minimisation of the total energy of the structure, given by the sum of various components (exchange, anisotropy, demagnetising field, external fields). Spin precession and dynamics are excited when this equilibrium state is perturbed in some way, for example by an external magnetic field. In the following, the main contributions to the total energy are described.

2.1.3 Exchange energy

The exchange interaction between spins of adjacent atoms is related to quantum mechanics and it can be due to several mechanisms [21, 22, 25, 26]. The origin of this interaction derive from the Pauli exclusion principle and the Coulomb repulsion between electrons: two electrons of the same atom cannot occupy the same orbital if they have the same spin and they will lower the electrostatic interaction by staying away from each other as much as possible.

The most common type of exchanges for itinerant electrons in metals are [25, 27]:

- direct exchange between nearest neighbours atoms, which is a result of the superposition of the wave functions of the electrons;
- RKKY interaction, which is an oscillatory coupling between localised moments and delocalised "mobile" electrons;
- double exchange, which arises between ions with both localised and delocalised electrons in different shells.

In insulators, exchange interactions mainly take the form of superexchange, where there is no direct superposition of wave functions of electrons but the interaction is mediated by non magnetic ions in the lattice.

The magnetic configuration of a material of mesoscopic dimensions is usually determined using the micromagnetic model, first introduced by Brown in 1963 [28]. The basis of this model is that a magnet is a continuous medium: the length scales considered is large enough to ignore atomic-scale structures. In this approximation, the magnetisation and other variables are continuously varying functions of the position in the volume of the magnetic element. Micromagnetics can be used to derive the equilibrium magnetic configuration of a system or predict dynamic behaviour of the magnetic moments.

The exchange energy depends on the relative alignment of adjacent spins. Therefore, in the continuum approximation, it can be derived classically by the gradient of the magnetisation in the considered material, using the formula

$$E_\mathrm{ex} = \frac{A}{M_\mathrm{s}^2} \int_V \left(\vec{\nabla} \cdot \vec{M}\right)^2 \mathrm{d}V \ . \tag{2.12}$$

The exchange constant A (positive for ferromagnetic materials, negative for antiferromagnetic materials) is related to the J_ex constant of the Heisemberg Hamiltonian by the averaging of the interactions between adjacent spins in a unit volume in the crystal lattice. $\vec{M}$ is the local magnetisation, M_s is the saturation magnetisation and V is the considered magnetic volume.

2.1.4 Zeeman energy

When an external magnetic field H_{ex} is applied, a magnetic moment will tend to align to it. The additional energy provided by the external field is given by the Zeeman energy [21, 22]

$$E = -\mu_0 \vec{M} \cdot H_{\text{ex}} \ . \tag{2.13}$$

This energy is minimised for the field and the magnetic moment pointing in the same direction.

2.1.5 Magnetic anisotropy

Magnetic anisotropy is the directional dependence of a material's magnetic properties. For the simple case of uniaxial anisotropy, the magnetic moment of a magnetically anisotropic material will tend to align with an easy axis, since by doing so it minimises its energy. The plane perpendicular to the easy axis is defined as the hard plane. The two opposite directions along the easy axis are equivalent. It is also possible that the direction defined by the anisotropy is energetically disadvantageous: in this case we have an hard axis and easy plane anisotropy.

In contrast to an anisotropic material, a magnetically isotropic material has no preferential direction for its magnetic moment unless there is an applied magnetic field. Magnetic anisotropy is a prerequisite for hysteresis in ferromagnets.

There are several sources of magnetic anisotropy:

- magneto-crystalline anisotropy originates from the atomic structure of a crystal, which introduces preferential directions for the magnetization (*vide infra*);
- shape anisotropy origins from the demagnetising field of a magnetic element (*vide infra*);
- magneto-elastic anisotropy, which occurs when strain alters the magnetic behaviour, leading to magnetic anisotropy;
- exchange anisotropy, which occurs when antiferromagnetic and ferromagnetic materials interact.

2.1.6 Magneto-crystalline anisotropy, shape anisotropy and coercivity

Spin-orbit interactions are the main origin of magneto-crystalline anisotropy [21, 22]. In a crystalline transition metal, the orbital momentum $\vec{L}$ is fixed by the crystal symmetry. The form of the spin-orbit Hamiltonian (eq 2.10) implies that there will be a particular direction of $\vec{S}$ that minimises the total energy. The magnetic moment of the atoms will then be oriented preferably in that direction, the easy axis. In the absence of spin-orbit interaction, iron would be perfectly isotropic and would have a perfectly body-centered cubic (bcc) lattice, with no $\vec{L}$ momentum. The spin-orbit interaction stabilises a ground state with $\vec{L} \neq 0$ and a net magnetic moment in some direction.

In the simple case of uniaxial magneto-crystalline anisotropy, with unitary vector $\vec{e_K}$ for the easy axis, the magneto-crystalline energy is written

$$E_{\text{K}} = \int_V -\frac{K_{\text{an}}}{M_{\text{s}}} \vec{M} \cdot \vec{e_K} \mathrm{d}V \ . \tag{2.14}$$

This component of the total energy is then zero when the magnetisation is directed along the easy axis. It is preferable in some cases to express the anisotropy in terms of an equivalent field, *i.e.*,, the external

field that has to be applied so that the Zeeman energy equals the magneto-crystalline anisotropy energy. This anisotropy field is given by

$$H_{\mathrm{an}} = \frac{2K_{\mathrm{an}}}{\mu_0 M_{\mathrm{s}}} \tag{2.15}$$

and it is directed along the easy axis direction.

Another type of anisotropy originates from the demagnetising field. The demagnetising field is generated by the magnetisation of a magnetic element itself. It is equivalent to the stray field of a magnet, with the difference that the first is within the magnet, while the latter is outside it. The demagnetising field of an object with arbitrary shape is difficult to calculate, even in the case of uniform magnetisation. For the special case of ellipsoids in its own coordinate system, it is related to the demagnetising tensor

$$\overline{\overline{N}} = \begin{bmatrix} N_x & 0 & 0 \\ 0 & N_y & 0 \\ 0 & 0 & N_z \end{bmatrix} \tag{2.16}$$

so that we have $\vec{H}_{\mathrm{demag}} = \overline{\overline{N}}\vec{M}$. The components of the tensor $\overline{\overline{N}}$ are related to the shape of the sample and it is common practice to use an approximate demagnetising tensor even in non ellipsoidal objects. Taking into account the fact that the magnetic moment will preferably lie parallel to the longest dimension of the sample and that the sum of the three components must be equal to -1, demagnetising factors for simple shapes can be easily deduced by symmetry. For example, for an isotropic spherical sample we have $N_x = N_y = N_z = -1/3$, while for a thin film in $\hat{x}\hat{y}$ plane we have $N_x = N_y = 0$ and $N_z = -1$. In addition, the anisotropy field can be integrated in the equation by considering an appropriate demagnetisation factor N_i with $\hat{i}$ the easy axis direction.

For ferromagnetic materials, the coercivity is the intensity of the applied magnetic field required to reduce the magnetization of that material to zero after the magnetization of the sample has been driven to saturation along the easy axis. Since the anisotropy and the exchange interaction will stabilise a parallel alignment of the magnetic moments even in zero field (remanence magnetisation) a field with opposite sign is necessary to achieve zero magnetisation (see Fig. 2.3).

Ferromagnetic materials with high coercivity are called magnetically hard materials, and are used to make permanent magnets. Materials with low coercivity are said to be magnetically soft and are used in transformer and inductor cores, recording heads and magnetic shielding.

2.2 Magnetisation dynamics

2.2.1 Landau-Lifshitz-Gilbert equation and the macrospin model

In the classic theory of magnetism, the magnetic moment $\vec{M}$ and the total angular momentum $\vec{J}$ of a charged particle are related by the equation of motion [26, 29–31]

$$\vec{M} = \frac{ge}{2m_{\mathrm{e}}}\vec{J}\,, \tag{2.17}$$

where m_{e} is the mass of the particle, e is the electron charge and g is the Landé factor. In general, the electron charge e can be substituted by the considered particle charge. From now on we will consider e as a positive value and we will add a minus sign in the equation 2.17. The Landé factor results from a first order perturbation theory of an atom under a weak magnetic field and it takes a mean value between the one of a pure orbital-momentum-only particle ($g = 1$) and a pure spin-momentum-only particle ($g = 2$).

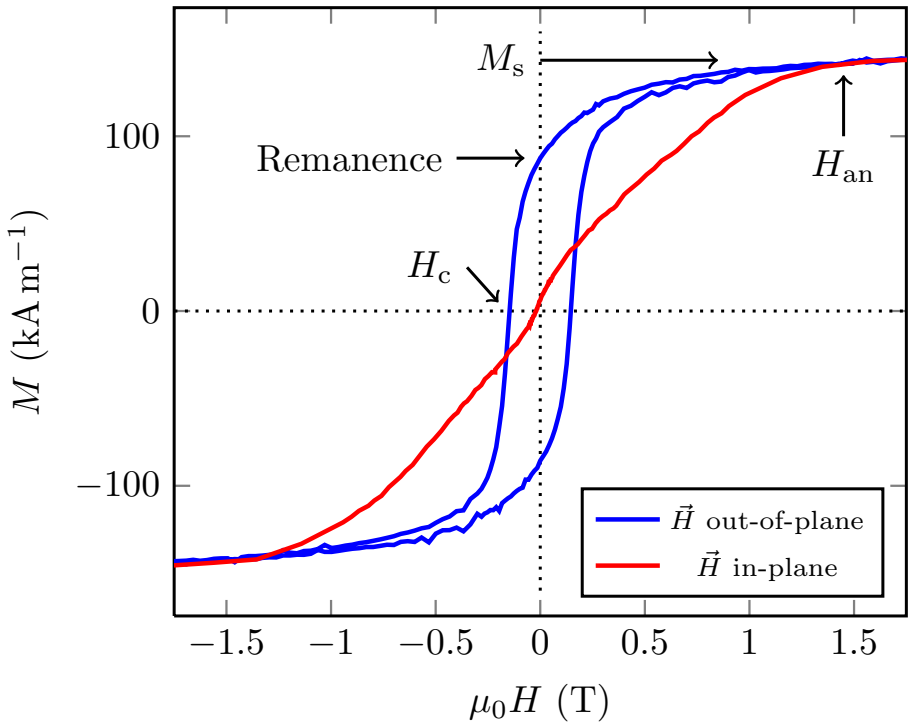

Figure 2.3: Hysteresis loop for a ferromagnetic material with perpendicular magnetic anisotropy (out-of-plane easy axis). Remanence magnetisation, saturation magnetisation M_s, anisotropy field H_{an} and coercive field H_c are indicated.

The exact value is given by the equation

$$g = \frac{3}{2} + \frac{S(S+1) - L(L+1)}{2J(J+1)} \ , \tag{2.18}$$

with L and S respectively orbital and spin quantum numbers. In the case of a *3d* ferromagnetic metal, the electrons of the outer shells have spin 1/2 and no orbital momentum, as it is quenched by the hybridization of the orbitals due to the crystal field. Then, we have the Landé factor almost equal to 2. For rare earth elements on the other hand, magnetism arises from electrons that occupy inner shells of the atoms. These electrons are much less affected by the crystal field and it is then necessary to take into consideration the orbital momentum and derive the correct Landé factor. The ratio between $\vec{M}$ and $\vec{J}$ is called gyromagnetic factor and it is indicated by γ_0. It is given by

$$\gamma_0 = \frac{ge}{2m_e} \ . \tag{2.19}$$

In the case of a ferromagnetic *3d* metal, it's value is between 28 and 30 GHz T^{-1}.

We will follow the derivation given by Gurevich and Melkov [29] for the basic derivation of the ferromagnetic resonance frequency. A magnetic field $\mu_0\vec{H}$ acting on magnetic moment $\vec{M}$ exerts a torque $\vec{\Gamma}$ given by

$$\vec{\Gamma} = \vec{M} \times (\mu_0 \vec{H}) \ . \tag{2.20}$$

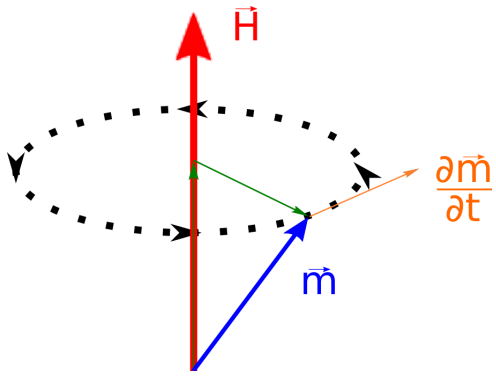

Figure 2.4: Precession of the magnetic moment around a magnetic field.

Since $\Gamma = \partial \vec{J}/\partial t$ and using 2.17 and 2.19 , it follows that

$$\frac{\partial \vec{M}}{\partial t} = -\gamma_0 \mu_0 \vec{M} \times \vec{H} \ . \tag{2.21}$$

The situation is schematised in Fig. 2.4. If $\vec{M}$ and $\vec{H}$ are not aligned, there is a torque acting on the magnetic moment that induces a precession of motion around $\vec{H}$. The equilibrium condition is given by

$$\vec{M} \times \vec{H} = 0 \ . \tag{2.22}$$

The Landau-Lifshitz-Gilbert equation describes the magnetisation dynamics under the effect of an effective field $\vec{H}_{\text{eff}}$. It is often written in the form

$$\frac{\partial \vec{M}}{\partial t} = -\mu_0 \gamma_0 \vec{M} \times \vec{H}_{\text{eff}} + \frac{\alpha}{M_{\text{s}}} \vec{M} \times \frac{\partial \vec{M}}{\partial t} \ . \tag{2.23}$$

The effective field is given by

$$\vec{H}_{\text{eff}} = -\frac{\mathrm{d}E}{\mathrm{d}\vec{M}} \tag{2.24}$$

and sums the external field $\mu_0 \vec{H}_{\text{ex}}$, the magneto-crystalline anisotropy field $\mu_0 \vec{H}_{\text{an}}$ and the demagnetising field $\mu_0 \vec{H}_{\text{demag}}$. The last term in eq 2.23 is the Gilbert damping, a torque that tends to align the magnetisation with the effective field and α is the dimensionless Gilbert damping parameter (typically $\alpha \sim 0.01$). The damping is mainly a phenomenological parameter and is very much sample dependent. The main types of process which produce damping are divided into intrinsic and extrinsic. The intrinsic ones are spin-flip processes mainly due to creation/interaction with phonons and interaction with nuclei due to spin-orbit coupling. The extrinsic ones are due to surface roughness, sample defects and/or Eddy currents, which are usually neglected. It has been predicted and experimentally verified [12, 13] that half-metallic Heusler alloys with cubic crystalline structure have very small damping, due to the spin-gap in the density of states that does not allow spin-flip processes. Heusler alloys will be treated in more detail in chapter 4. The trajectory of a damped precession is shown in Fig. 2.5. By applying $(\vec{M} \cdot)$ on the both sides of eq 2.23, we obtain

$$\vec{M} \cdot \frac{\partial \vec{M}}{\partial t} = \frac{\partial \vec{M}^2}{\partial t} = 0 \ . \tag{2.25}$$

$|\vec{M}|$ is always constant and equal to M_{s}. Eq. 2.23 can be expressed in the equivalent form first proposed

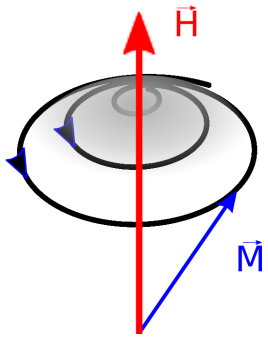

Figure 2.5: Precession of the magnetic moment around a magnetic field considering a damping term.

by Landau and Lifshitz as

$$\frac{\partial \vec{M}}{\partial t} = -\mu_0 \gamma' \vec{M} \times \vec{H}_{\text{eff}} - \frac{\lambda \gamma'}{M_\text{s}} \vec{M} \times (\vec{M} \times \vec{H}) \tag{2.26}$$

with the parameter λ. The two formulations are equivalent: applying $(\vec{M}\times)$ on both sides of eq 2.23, we find

$$\begin{aligned} \vec{M} \times \frac{\partial \vec{M}}{\partial t} &= -\gamma_0 \mu_0 \vec{M} \times (\vec{M} \times \vec{H}) + \frac{\alpha}{M_\text{s}} \vec{M} \times \left(\vec{M} \times \frac{\partial \vec{M}}{\partial t} \right) \\ &= -\gamma_0 \mu_0 \vec{M} \times (\vec{M} \times \vec{H}) + \frac{\alpha}{M_\text{s}} \left(\vec{M} \cdot \frac{\partial \vec{M}}{\partial t} \right) \vec{M} - \alpha \frac{\partial \vec{M}}{\partial t} \\ &= -\gamma_0 \mu_0 \vec{M} \times (\vec{M} \times \vec{H}) - \alpha \frac{\partial \vec{M}}{\partial t} \ . \end{aligned} \tag{2.27}$$

Substituting this result in eq 2.23, we obtain

$$(1+\alpha^2) \frac{\partial \vec{M}}{\partial t} = -\gamma_0 \mu_0 \vec{M} \times \vec{H} - \gamma_0 \frac{\alpha}{M_\text{s}} \vec{M} \times (\vec{M} \times \vec{H}) \ . \tag{2.28}$$

By defining $\lambda = \alpha$ and $\gamma' = \frac{\gamma_0}{1+\lambda^2}$ we find eq 2.26.

Let's now take the effective field and the magnetisation as the sums of steady and alternating parts

$$\vec{H}_{\text{eff}} = \vec{H} + \vec{h} \qquad \text{and} \qquad \vec{M}_{tot} = \vec{M} + \vec{m} \ . \tag{2.29}$$

If we assume that

$$\vec{h} \ll \vec{H} \qquad \text{and} \qquad \vec{m} \ll \vec{M} \tag{2.30}$$

we can substitute 2.29 into 2.23 and neglect second order terms. In addition, we consider that the steady components satisfy the equilibrium condition given by 2.22 and we assume $M \simeq M_\text{s}$. We can now solve a linearised LLG equation to obtain the solution first given by Polder [32]. By defining

$$\omega_M = \mu_0 \gamma_0 M_\text{s} \qquad \text{and} \qquad \omega_0 = \mu_0 \gamma_0 H \tag{2.31}$$

we get

$$\begin{pmatrix} m_x \\ m_y \end{pmatrix} = \overline{\overline{\chi}} \begin{pmatrix} h_x \\ h_y \end{pmatrix} = \begin{bmatrix} \chi & \imath\kappa \\ -\imath\kappa & \chi \end{bmatrix} \begin{pmatrix} h_x \\ h_y \end{pmatrix} \ , \tag{2.32}$$

with

$$\chi = \frac{\omega_M \omega_0}{(\omega_0 - \imath\alpha\omega)^2 - \omega^2} \qquad \text{and} \qquad \kappa = \frac{\omega_M \omega}{(\omega_0 - \imath\alpha\omega)^2 - \omega^2} \ . \tag{2.33}$$

Considering a lossless system ($\alpha = 0$), it is clear from 2.33 that the system shows resonance at the frequency

$$\omega_{\rm res} = \omega_0 = \mu_0 \gamma_0 H \ . \tag{2.34}$$

The effect of damping on the resonance frequency can be estimated deriving the eigenvalues of the Polder susceptibility $\overline{\overline{\chi}}$ (eq. 2.32)

$$\lambda_\pm = \chi \pm \kappa \ , \tag{2.35}$$

where λ_+ is the resonant one. It follows that

$$\Re(\lambda_+) = \lambda' = \frac{\omega_M(\omega_0 - \omega)}{(\omega_0 - \omega)^2 + \omega^2\alpha^2} \qquad \text{and} \qquad \Im(\lambda_+) = \lambda'' = \frac{\omega_M \alpha\omega}{(\omega_0 - \omega)^2 + \omega^2\alpha^2} \ . \tag{2.36}$$

The resonance frequency is given by the value of ω when λ'' is at the maximum: $\lambda''_{\rm max} = \frac{\omega_M}{\alpha\omega_{\rm res}}$. We will call ΔH the width at half maximum of the resonance peak when the frequency of the ac field excitation is kept constant and the steady applied field is slowly swept, and $\Delta\omega$ the width at half maximum of the resonance peak when the steady applied field is kept constant and the frequency of the excitation is slowly swept. Therefore, requiring $\lambda'' = \lambda''_{\rm max}/2$ we obtain

$$\Delta H = \frac{2\alpha\omega_{\rm res}}{\mu_0\gamma_0} \qquad \text{and} \qquad \Delta\omega = 2\alpha\omega_{\rm res} \ . \tag{2.37}$$

In the presence of shape anisotropy or magneto-crystalline anisotropy, effective anisotropy fields must be considered in the derivation of the resonance frequency. A general expression for the resonance frequency has been given by Kittel and is known as the Kittel law [33]

$$\omega^2_{\rm res} = \mu_0^2\gamma_0^2(H_{\rm ex} + H_{\rm an})(H_{\rm ex} + H_{\rm an} + M_{\rm s}) \ , \tag{2.38}$$

with $H_{\rm ex}$ and $H_{\rm an}$ external and magneto-crystalline anisotropy field respectively. In the case of uniaxial magneto-crystalline anisotropy, the anisotropy field is given by $2K_{\rm an}/\mu_0 M_{\rm s}$ and it is directed along the easy axis direction. As discussed in sec. 2.1.6, a general expression for all types of anisotropies can be written as

$$\overline{\overline{N}} = \begin{bmatrix} N_x & 0 & 0 \\ 0 & N_y & 0 \\ 0 & 0 & N_z \end{bmatrix} \tag{2.39}$$

so that we have $\vec{H}_{\rm eff} = \vec{H}_{\rm ex} + \overline{\overline{N}}\vec{M}$ and $\vec{h}_\sim = \vec{h}_\sim + \overline{\overline{N}}\vec{m}_\sim$. By employing the same procedure used above, we get the Polder susceptibility

$$\overline{\overline{\chi}} = \frac{\omega_M \begin{bmatrix} (N_z - N_y)\omega_M - \omega_0 + \imath\alpha\omega & -\imath\omega \\ \imath\omega & (N_z - N_x)\omega_M - \omega_0 + \imath\alpha\omega \end{bmatrix}}{\omega^2 + [(N_z - N_y)\omega_M - \omega_0 + \imath\alpha\omega][(N_x - N_z)\omega_M + \omega_0 - \imath\alpha\omega]} \ . \tag{2.40}$$

This implies that the precessional orbit is not circular any more but it is elliptical, with the ellipticity given by the factor M_x/M_y. In the limit of $\alpha \to 0$ (lossless system) we obtain the resonance frequency as

$$\omega^2_{\rm res} = [\omega_0 + (N_x - N_z)\omega_M][\omega_0 + (N_y - N_z)\omega_M] \ . \tag{2.41}$$

2.2.2 Spin transfer torque

A first explanation of the spin transfer torque (STT) effect has been given by Slonczewski in 1995 [6]. By spin transfer torque he denoted the current-driven angular momentum transfer that was observed in multilayer structures such as giant magnetoresistance devices or magnetic tunnel junctions. The flow of angular momentum in a particular direction associated with an electric current is

$$\frac{\partial J}{\partial t} = n\frac{\hbar}{2}Pv_{\mathrm{d}}(\pi r^2) = \frac{J_{\mathrm{c}}\hbar P(\pi r^2)}{2e} \ , \tag{2.42}$$

where n is the electron density, v_{d} is the drift velocity, $J_{\mathrm{c}} = env_{\mathrm{d}}$ is the charge current density, $\hbar/2$ is the quantum of momentum, P is the spin polarisation of the electron current in the considered direction and r is the radius of the wire. The spin polarisation is the degree to which the electron spins are aligned in a particular direction, usually parallel or anti-parallel to the magnetic moment. Only the conduction electrons are important, hence only the density of states at the Fermi level must be considered. The spin polarisation [34–36] is defined as

$$P = \frac{D_{\uparrow}(E_{\mathrm{F}})v^n_{\uparrow\mathrm{F}} - D_{\downarrow}(E_{\mathrm{F}})v^n_{\downarrow\mathrm{F}}}{D_{\uparrow}(E_{\mathrm{F}})v^n_{\uparrow\mathrm{F}} + D_{\downarrow}(E_{\mathrm{F}})v^n_{\downarrow\mathrm{F}}} \ , \tag{2.43}$$

where $D_{\uparrow\downarrow}(E_{\mathrm{F}})$ is the density of states of $\uparrow$ or $\downarrow$ electrons at the Fermi level and $v_{\uparrow\downarrow\mathrm{F}}$ is the Fermi velocity. The density of states is weighted by the Fermi velocity raised to a factor n. This factor is 0 for spin-polarised photoemission experiments, where the pure DOS is probed using optical transitions, 1 for ballistic transport, when the mean free path of electrons is large compared to the thickness of the layers, and 2 for diffusive transport or tunnelling at low bias. In this work we will usually consider $n = 2$, since we will deal with non-ballistic electronic transport [35]. From equations 2.17 and 2.19, the angular momentum associated with the ferromagnetic layer of thickness t is given by

$$J = \frac{M\pi r^2 t}{\gamma_0} \ . \tag{2.44}$$

When an electron, initially spin-polarised in a direction making an angle θ with respect to the $\hat{x}$ direction and travelling along the $\hat{z}$ direction, enters a ferromagnetic thin film magnetized along $\hat{x}$, it can be either transmitted of reflected, depending on the matching of the spin polarised band structures of the two layers, as shown in Fig. 2.6. The reflectance and transmittance at the interface depend on the orientation of the spin of the electrons. For example, at the Cu-Co interface, the majority spin $\uparrow$ electrons with respect to the Co magnetisation are more easily transmitted than the minority spin $\downarrow$ ones. Those that make it into the ferromagnetic layer sense a strong magnetic field and their spins start to precess, completing many turns as they travel into the metal. By the time the electrons leave the cobalt film, they have scattered several times with the lattice atoms and each one has followed a different path: this means that the $\hat{y}\hat{z}$ components of the spins are completely dephased between one electron and the next, while the $\hat{x}$ components stay unmodified, if we exclude any spin-flip event. This is reasonable if the thickness of the ferromagnetic layer is much less than the spin-diffusion length. The spin-diffusion length is defined as the mean distance that an electron has to travel before experiencing a spin-scattering event, *i.e.*, a scattering event in which the spin is not conserved. Then, only the total $\hat{y}\hat{z}$ component of the electrons angular momentum is lost while they travel through the layer. Since the total angular momentum must be conserved, the lost electronic momentum is transmitted to the lattice at a rate

$$\frac{\partial M}{\partial t} = \frac{J_{\mathrm{c}}\hbar P\gamma_0 \sin\theta}{2eMt} = \frac{J_{\mathrm{c}}P\mu_{\mathrm{B}}\sin\theta}{eMt} \ , \tag{2.45}$$

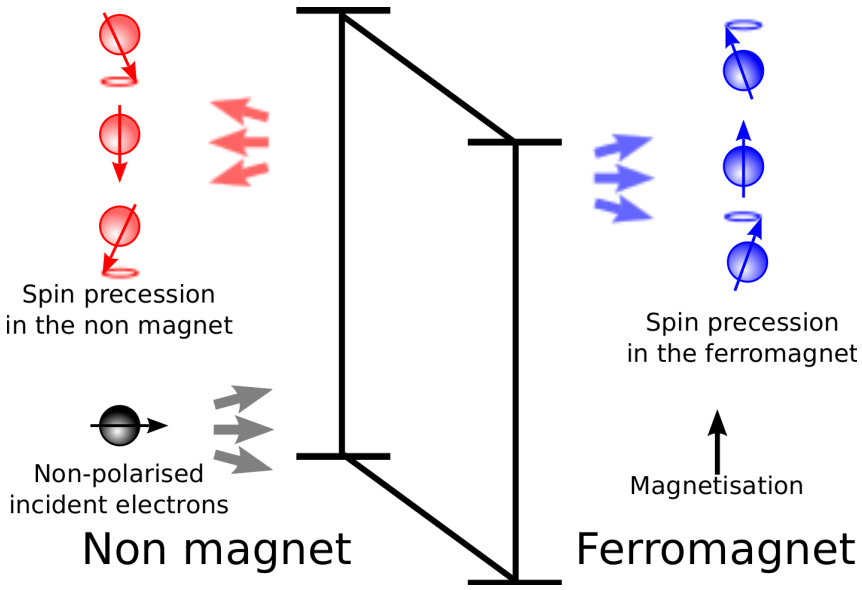

Figure 2.6: Scattering of unpolarised electrons at the interface between a non magnetic and a ferromagnetic layer.

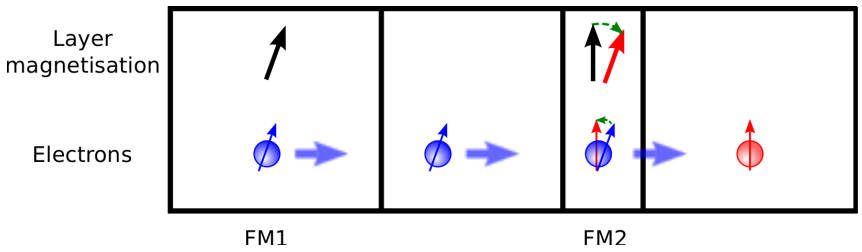

Figure 2.7: Spin transfer torque between non-collinearly magnetised ferromagnetic layers.

if we consider $g \simeq 2$ and the Bohr magneton $\mu_B = (\hbar e)/(2m_e)$. This has little influence on a thick ferromagnetic layer, but if enough current density is provided it can greatly modify the magnetisation of a thin one, aligning it to the spins of the incoming electrons. The spin transfer torque doesn't depend on the area πr^2, so it is a scalable effect.

Let's consider a multilayer composed of two ferromagnetic layers, a thick one and a thin one, separated by a non magnetic layer as shown in Fig. 2.7. The magnetisation of the thick magnetic material is fixed by exchange bias or some other suitable method and it will be denoted as pinned layer, while the magnetisation of the other layer is relatively unconstrained to a particular orientation. Let's send an unpolarised current through the structure, in such a way that the electrons travel first through the thick layer: because of the damping, their spins will get polarised parallel to the magnetisation direction of the material, with no effect on the latter. Then, after having travelled in the non magnetic spacer, they will enter the other ferromagnetic layer. If its magnetisation is already aligned with the one of the thick layer, there is no spin transfer torque. If instead the two magnetisation are not aligned, the electrons will transfer their transverse momentum to the thin layer. This will bring its magnetisation to align with the fixed one. It can be shown that this torque effect can be easily integrated in the Landau-Lifshitz-Gilbert

equation 2.23 by adding the additional term

$$\vec{\Gamma} = \frac{J_c P \mu_B}{e M_s^2 t} \vec{M} \times (\vec{s_e} \times \vec{M}) \ , \tag{2.46}$$

where $\vec{s_e}$ is the direction of the spin of the electron current density. The effect of this additional term is to exert a torque that drives the magnetic moment towards the direction of the polarisation of the current while it precesses. If the effective field is opposite to this polarisation, the additional term can be seen as an extra damping-like term α', that is subtracted to the usual Gilbert damping α. Then, if $\alpha' > \alpha$ the precession brings the magnetic moments to spiral towards the direction of the polarisation of the current instead of the effective field as usual.

This theory implies that the electrons get to the interface with the thin ferromagnetic layer already polarised in a particular direction and that the mentioned layer has uniform magnetisation. A more general approach had been considered by Zhang and Li [37, 38]. In their theory, the electron current can flow initially unpolarised in a ferromagnetic metal with space-dependent magnetisation direction. Denoting with $\vec{\sigma_s}(\vec{r}, t)$ the electron spin density, with $J_s(\vec{r}, t)$ the spin current density and with $\vec{M}(\vec{r}, t)$ the magnetisation of the layer, one can obtain the semiclassical Bloch equation for the continuity of the spin current as

$$\frac{\partial \vec{\sigma_s}}{\partial t} + \vec{\nabla} \cdot \vec{J_s} = -\frac{1}{\tau_{ex} M_s} \vec{\sigma_s} \times \vec{M} - \langle \Gamma(\vec{\sigma_s}) \rangle \ , \tag{2.47}$$

where $\Gamma(\vec{\sigma_s})$ represents the spin relaxation due to scattering processes and $\tau_{ex} = \hbar / S J_{ex}$. $J_s(\vec{r}, t)$ is formally a matrix, taking into account both the spin current direction and its polarisation. The spin density can be split into two component

$$\vec{\sigma_s} = \vec{\sigma_{s0}} + \vec{\delta\sigma_s} = n_0 \frac{\vec{M}}{M_s} + \vec{\delta\sigma_s} \ , \tag{2.48}$$

where n_0 is the local equilibrium spin density whose direction is parallel to the magnetisation. The first term represents the adiabatic spin density when the conduction electron spin relaxes to its equilibrium value (aligned with the magnetisation) instantaneously. Since the dynamics of the magnetisation of the metal is slow compared to that of the electrons, we can assume that the spins of the latter follow the direction of the local moment: this is known as the adiabatic process. The second term represents the deviation from this behaviour: it is the small fraction of the spin density that is not aligned with the magnetisation. Similarly, we can separate the spin current as in the following equation

$$\vec{J_s} = \vec{J_0} + \vec{\delta J_s} = -\frac{\mu_B P}{e} \vec{J_s} \times \frac{\vec{M}}{M_s} + \vec{\delta J_s} \ . \tag{2.49}$$

Again, the first term is the adiabatic part of the spin current, the part whose spin polarisation is parallel to the local magnetisation. The second term is the non-adiabatic part. The scattering term Γ is approximated by a time-relaxation model, such as that $\langle \Gamma \rangle = \vec{\delta\sigma_s} / \tau_{sf}$, with τ_{sf} is the spin-flip relaxation time. Another approximation consists in considering only first order terms of $\vec{\delta\sigma_s}$ with respect to the spin current J_s and to the time derivative of the magnetisation $\partial \vec{M} / \partial t$. In the semiclassical theory of transport, the non-adiabatic spin current density is related to the spin density via the diffusion relation

$$\delta J_s = -D_0 \nabla \vec{\delta\sigma_s} \ , \tag{2.50}$$

with D_0 the diffusion constant. By substituting equations 2.48 and 2.49 into equation 2.47 and assuming a slowly varying magnetisation in space with respect to the transport length scale, one can obtain, for the

non-equilibrium spin density,

$$\delta\vec{\sigma}_{\rm s} = \frac{\tau_{\rm ex}}{1+\xi^2}\left[-\frac{\xi n_0}{M_{\rm s}}\frac{\partial\vec{M}}{\partial t} - \frac{n_0}{M_{\rm s}^2}\vec{M}\times\frac{\partial\vec{M}}{\partial t} + \frac{\mu_{\rm B}P\xi}{eM_{\rm s}}(\vec{J}_{\rm s}\cdot\vec{\nabla})\vec{M} + \frac{\mu_{\rm B}P}{eM_{\rm s}^2}\vec{M}\times(\vec{J}_{\rm s}\cdot\vec{\nabla})\vec{M}\right] , \tag{2.51}$$

where $\xi = \tau_{\rm ex}/\tau_{\rm sf}$. This induced spin density exerts a torque on the magnetisation given by the equation

$$\begin{aligned}\vec{\Gamma} = \frac{1}{1+\xi^2}\Bigg[&- \frac{n_0}{M_{\rm s}}\frac{\partial\vec{M}}{\partial t} + \frac{\xi n_0}{M_{\rm s}^2}\vec{M}\times\frac{\partial\vec{M}}{\partial t} - \frac{\mu_{\rm B}P}{eM_{\rm s}^3}\vec{M}\times[\vec{M}\times(\vec{J}_{\rm s}\cdot\vec{\nabla})\vec{M}] \\ &- \frac{\mu_{\rm B}P\xi}{eM_{\rm s}^2}\vec{M}\times(\vec{J}_{\rm s}\cdot\vec{\nabla})\vec{M}\Bigg] .\end{aligned} \tag{2.52}$$

This torque has to be added to the traditional Landau-Lifshitz-Gilbert equation 2.23. There are four terms to be considered: the first two come from the variation of the magnetisation in time, the last two come from the variation in space and they are proportional to the injected current. The first term can be integrated in the traditional equation by renormalising the gyromagnetic factor, while the second modifies the damping parameter. It is possible then to introduce an effective gyromagnetic ratio $\gamma_{0\,\rm eff}$ and an effective damping parameter $\alpha_{\rm eff}$, given by

$$\gamma_{0\,\rm eff} = \gamma_0(1+\eta)^{-1} \qquad \text{and} \qquad \gamma_{0\,\rm eff}\alpha_{\rm eff} = \gamma_0(\alpha+\xi\eta) , \tag{2.53}$$

where $\eta \equiv (n_0/M_{\rm s})/(1+\xi^2)$. For a typical ferromagnet we have $\xi \approx 10^{-2}$, $\eta \approx 10^{-2}$ and $\eta\xi \approx 10^{-4}$, so these modifications are negligible. This may not be the case in very low moment magnetic materials, such as the one considered in chap. 4. In this case, it may be necessary to modify the gyromagnetic factor and the damping parameter. Considering only the last two terms of equation 2.52 and assuming the current flowing in the $\hat{x}$ direction, the resulting Landau-Lifshitz-Gilbert equation is

$$\frac{\partial\vec{M}}{\partial t} = -\mu_0\gamma_0\vec{M}\times\vec{H}_{\rm eff} + \frac{\alpha}{M_{\rm s}}\vec{M}\times\frac{\partial\vec{M}}{\partial t} - \frac{b_j}{M_{\rm s}^2}\vec{M}\times\left(\vec{M}\times\frac{\partial\vec{M}}{\partial x}\right) - \frac{c_j}{M_{\rm s}}\vec{M}\times\frac{\partial\vec{M}}{\partial x} , \tag{2.54}$$

where $b_j = (jPg\mu_{\rm B})/(2eM_{\rm s})$ and $c_j = (jPg\xi\mu_{\rm B})/(2eM_{\rm s})$. It can be shown that a domain wall is pushed in the flowing electrons direction with initial velocity $v(0) \approx b_j$, while the terminal, steady-state velocity of the motion is given by the non-adiabatic torque $v(\infty) \approx c_j/\alpha$. The first term is usually called anti-damping torque, while the second is called field-like torque.

2.3 Transport

2.3.1 Anisotropic magnetoresistance

A well-known effect resulting from the spin-orbit interaction is the anisotropic magnetoresistance (AMR) [21, 39]. It is a small effect in which the resistance of a magnetic sample depends on the relative orientation of current and magnetisation. Even if small, it is a direct manifestation of the spin-orbit coupling for the conduction electrons and, therefore, it can be used to quantify the spin-orbit interactions. It has been exploited for magnetic sensors and even for magnetic data storage in the early days of spin electronics.

Conduction electrons in $3d$ ferromagnets and their alloys belong to a s-like or a d-like state. The s electrons resemble free electrons and carry most of the current. The d electrons instead have high effective mass, that makes them inefficient in carrying electric current, but the sub-bands for opposite spins are split, with different density of states at the Fermi level for spin $\uparrow$ and spin $\downarrow$ electrons. The s band is

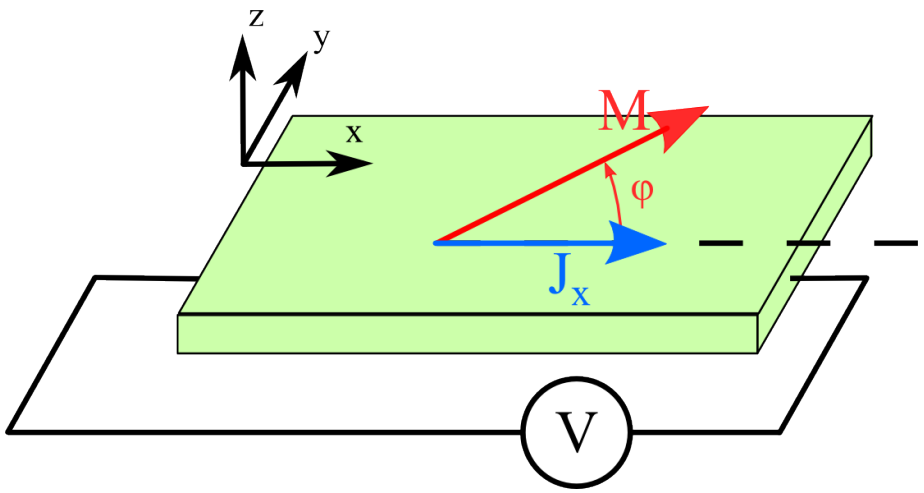

Figure 2.8: Schematic for the measurement of the anisotropic magnetoresistance (AMR) in a magnetic sample.

not directly spin-split, but it can become partially polarised by interaction with the d band. The $s-d$ scattering in a ferromagnet is heavily dependent on the spin of the s electrons. Let's consider a so-called strong ferromagnet, like nickel or cobalt, where the $3d$ minority spin band does not cross the Fermi level (its density of states is zero at E_{F}). In this case, because of the conservation of the electron spin, only majority spin s electrons can actually scatter in a $3d$ band, decreasing their electric mobility. This is true in the absence of spin-flip events, which are much less frequent than phonon scattering in metals.

In the presence of spin-orbit interactions, the spin $\uparrow$ and spin $\downarrow$ states are mixed, since the spin-flip scattering probability increases. This scattering is effective only when the magnetisation direction is parallel to the current direction but not if it is perpendicular to it, since the spin-orbit interaction has the form $\vec{p}\times\vec{S}$. That is why, in general, the resistivity is higher when the current is parallel to the magnetisation, *i.e.*, the AMR is positive.

In general, the electric field $\vec{E}$ in a magnetic material is given as a function of the current $\vec{J}_{\mathrm{c}}$ in the form [39]

$$\vec{E} = \rho_{\perp}\vec{J}_{\mathrm{c}} + \vec{m}(\vec{J}_{\mathrm{c}}\cdot\vec{m})(\rho_{\parallel}-\rho_{\perp}) + \rho_{\mathrm{AHE}}\vec{m}\times\vec{J}_{\mathrm{c}} \tag{2.55}$$

where ρ_{AHE} is anomalous Hall effect resistivity (see sec. 2.3.6) and $\rho_{\parallel}$ and $\rho_{\perp}$ are the resistivities when the current is parallel and perpendicular to the reduced magnetic moment $\vec{m}=\vec{M}/M_{\mathrm{s}}$, respectively. In this section, we will consider only the AMR contribution to the longitudinal resistivity of a sample, *i.e.* we will neglect the anomalous Hall effect term. In this framework, the longitudinal resistivity is expressed as a function of the in-plane angle φ (Fig. 2.8) as

$$\rho_{xx} = \rho_{\perp} + (\rho_{\parallel}-\rho_{\perp})\cos^2\varphi = \rho_{\perp} + \Delta\rho\cos^2\varphi\ . \tag{2.56}$$

2.3.2 Planar Hall effect

A phenomenon that is directly related to the AMR is the planar Hall effect (PHE) [21, 39]: while the AMR is the variation of the longitudinal resistance (ρ_{xx}) as a function of the relative angle between the magnetic moment and the electric current, in the PHE we have a variation of the transverse resistance ρ_{xy}.

Considering the electric current to be directed in the $\hat{x}$ direction (Fig. 2.9), we can resolve the electric

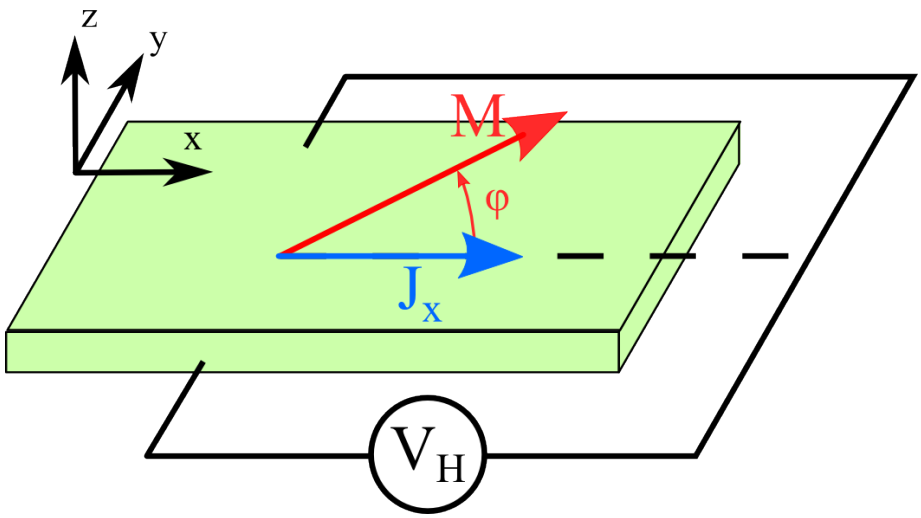

Figure 2.9: Schematic for the measurement of the planar Hall effect (PHE) in a magnetic sample.

field into the components parallel and perpendicular to the magnetic moment as

$$\begin{aligned} E_{\parallel} &= \rho_{\parallel} J_x \cos\varphi \ , \\ E_{\perp} &= \rho_{\perp} J_x \sin\varphi \ . \end{aligned} \tag{2.57}$$

Therefore, the components parallel and perpendicular to the current are

$$\begin{aligned} E_x &= J_x(\rho_{\perp} + \Delta\rho \cos^2\varphi) \ , \\ E_y &= J_x \Delta\rho \sin\varphi\cos\varphi \ . \end{aligned} \tag{2.58}$$

The planar Hall resistivity E_y/J_x is therefore

$$\rho_{xy} = \frac{1}{2}\Delta\rho \sin 2\varphi \ . \tag{2.59}$$

2.3.3 Spin currents

Conventional electronics is charge-based, meaning that it deals with charge currents. This is not the only type of current that can be generated in a magnetic material. A pure spin current carries only spin angular momentum but no electric charge, *i.e.*, no charge current. Let's consider an electron current that flows in one direction and consists only of spin ↑ electrons. Let's add to this current another current of the same magnitude in the opposite direction in which all electrons are instead spin ↓. The result is a current of spins only; there is no net particle and charge transfer, offering advantages like reduced power consumption because of the absence of Joule heating. Pure spin currents can be created using different methods, such as spin pumping from a precessing ferromagnet and spin Hall effect [40–42].

2.3.4 Spin pumping

Spin pumping generates spin currents in a non magnetic layer when it is in contact with a ferromagnet which magnetisation is varying in time. Typically this is achieved by exciting the magnetisation precession

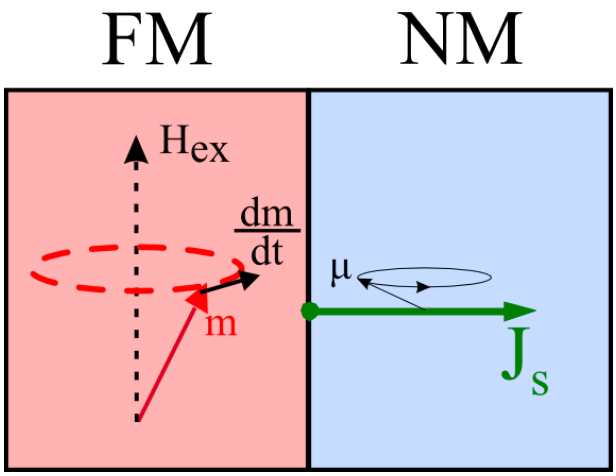

Figure 2.10: Schematic illustration of the spin pumping process achieved through ac excitation of the magnetisation of a FM layer. H_{ex} and m are the fixed external field and the reduced magnetic moment, J_s is the spin current. From ref. [41].

at the resonance frequency by FMR in a bilayer system non-magnetic metal (NM)/ferromagnet (FM) (Fig. 2.10). We will follow the derivation given by Mosendz *et. al.* [42]. The spin pumping current generated at the interface is given by

$$\vec{J}_s^0 = \frac{\hbar}{8\pi}\Re(2g^{\uparrow\downarrow})\left[\vec{m}\times\frac{\partial\vec{m}}{\partial t}\right] , \tag{2.60}$$

where $g^{\uparrow\downarrow}$ is the spin-mixing conductance and $\vec{m} = \vec{M}/M_s$ is the the reduced magnetic moment. The polarisation of the spin current is perpendicular to both the magnetisation direction and its time derivative. Because of the nature of the FMR precession, there is always a polarisation component along the equilibrium position of the magnetic moment. This results in a dc spin current, while the other polarisation components generate ac spin currents. The direction of flow of the spins is normal to the interface. These spin currents generate spin accumulation in the NM layer, with the density $\vec{\mu}_{NM}$ that relaxes over length scale given by the spin diffusion length λ_{sf}, related to the spin-flip time constant τ_{sf}. The propagation of the spin accumulation $\vec{\mu}_{NM}$ is described by the equation

$$\imath\omega\vec{\mu}_{NM} = D\frac{\partial^2\vec{\mu}_{NM}}{\partial z^2} - \frac{\vec{\mu}_{NM}}{\tau_{sf}} , \tag{2.61}$$

where ω is the angular frequency, τ_{sf} is the spin-flip time constant, $\hat{z}$ is the coordinate normal to the interface and $D = v_F^2\tau_{el}/3$ is the electronic diffusion constant. Here τ_{el} is the normal scattering relaxation time for electrons, usually smaller than τ_{sf}. Using the boundary conditions

$$\vec{J}_s^0(z=0) = -D\frac{\partial\vec{\mu}_{NM}}{\partial z}|_{z=0} \quad \text{and} \quad \frac{\partial\vec{\mu}_{NM}}{\partial z}|_{z=t_{NM}} = 0 , \tag{2.62}$$

eq 2.61 gives a spin accumulation profile that decays as we move away from the NM/FM interface, driving a spin current with dc component [43, 44]

$$J_s(z) = J_s^0\frac{\sinh[(z-t_{NM})/\lambda_{sf}]}{\sinh(t_{NM}/\lambda_{sf})} , \tag{2.63}$$

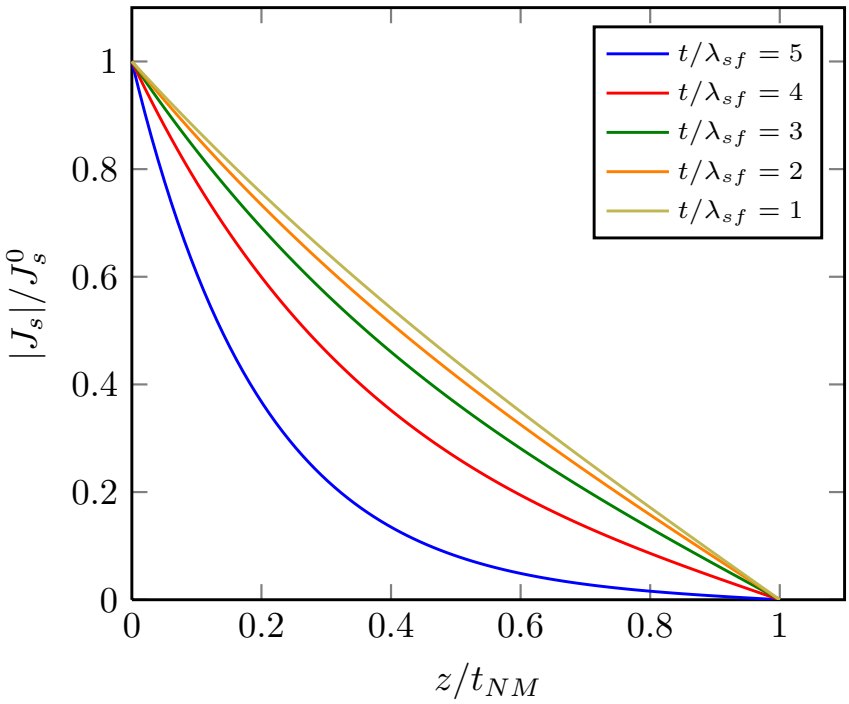

Figure 2.11: Decay of the spin current J_s as a function of the distance from the FM/NM interface ($z = 0$) for different values of the spin diffusion length λ_{sf}.

with t_{NM} thickness of the NM layer. Fig. 2.11 shows the decay of the spin current as we move further away from the interface. The spin accumulation generated in the NM layer results in an additional backflow of spins that reduces the spin pumping current. This effect can be taken into account by considering an effective spin-mixing conductance $g_{\text{eff}}^{\uparrow\downarrow}$ instead of the usual $g^{\uparrow\downarrow}$.

In FMR experiments, the Gilbert damping α in eq 2.23 is a measure of the spin-relaxation mechanisms that bring the magnetisation towards the equilibrium position. The spin pumping can be accounted for by adding a contribution to the damping α_{sp} [45–48]. It can be quantified by measuring the full width at half maximum (FWHM) at constant frequency $\Delta H = \alpha_{\text{eff}}\omega/\gamma_0$ for a NM/FM bilayer and for just the FM layer. For samples in which t_{NM} is sufficiently high to completely dissipate the spin accumulation (spin-sink approximation), the difference in the two values of α_{eff} allows to derive the effective spin-mixing conductance

$$g_{\text{eff}}^{\uparrow\downarrow} = \frac{\gamma_0 \mu_0 M_s t_{\text{FM}}}{g\mu_B \omega}(\Delta H_{\text{NM/FM}} - \Delta H_{\text{FM}}) \ . \tag{2.64}$$

Eq. 2.64 is valid for negligible inhomogeneous contributions to the linewidth. If this approximation is not valid, the sample dependent inhomogeneous linewidths must be subtracted independently.

The dc component of the spin current is polarised parallel to the equilibrium direction of the magnetisation, approximately given by the external field direction for soft magnetic FM. Considering a simple circular precession of the magnetisation at the resonance, the time-average of this current is given by

$$J_s^{dc} = \frac{\hbar\omega}{4\pi}\Re(g_{\text{eff}}^{\uparrow\downarrow})\sin^2\theta \ . \tag{2.65}$$

In thin films, the shape anisotropy forces the magnetisation to lie preferentially in the plane of the film. Hence, the motion is not circular but elliptic and a correction factor must be taken into account. Substituting the ellipticity correction and the expression for the magnetisation precession angle θ, the

spin current density is given by [41]

$$J_{\mathrm{s}}^{dc} = \frac{g_{\mathrm{eff}}^{\uparrow\downarrow}\gamma^2 h_{\mathrm{rf}}^2 \hbar \left[\mu_0 M_{\mathrm{eff}}\gamma + \sqrt{(\mu_0 M_{\mathrm{eff}}\gamma)^2 + 4\omega^2}\right]}{8\pi\alpha^2\left[(\mu_0 M_{\mathrm{s}}\gamma)^2 + 4\omega^2\right]}, \tag{2.66}$$

with h_{rf} the small radio-frequency magnetic field.

2.3.5 Rashba Hamiltonian

One of the effects of the spin-orbit coupling between the electron spin and its angular momentum is the Rashba spin-orbit interaction [20, 49]. This kind of interaction requires broken inversion of symmetry, usually obtained at the interface between two thin films, that generates an effective electric field and potential seen by the electrons. The Rashba effect can create a non-equilibrium spin density and induce spin torque even in a uniformly magnetised material.

Following ref. [49], the Rashba Hamiltonian for a ferromagnetic layer with spin-orbit coupling and breaking of symmetry contains the term

$$\mathcal{H}_{\mathrm{so}} = \frac{\hbar}{2m_{\mathrm{e}}}(\vec{\nabla V} \times \vec{p}) \cdot \vec{s}\,, \tag{2.67}$$

where $\vec{s}$ is the spin of the electron, $-\vec{\nabla V}$ is the effective local electric field and $\vec{p}$ is the momentum. The spin density continuity equation is then given by

$$\frac{\mathrm{d}\vec{s}}{\mathrm{d}t} = -\vec{\nabla}\cdot\vec{J}_{\mathrm{s}} - \frac{J_{\mathrm{ex}}}{\hbar}\vec{M}\times\vec{s} + \frac{1}{2m_{\mathrm{e}}}\langle(\vec{\nabla V}\times\vec{p})\times\vec{s}\rangle\,, \tag{2.68}$$

with $\vec{M}$ is the magnetisation vector, J_{ex} is the exchange constant, $\vec{s}$ is the spin density and $\vec{J}_{\mathrm{s}}$ is the spin current. The symbols $\langle\ldots\rangle$ denotes quantum-mechanical averaging. The system can be described once again with a modified Landau-Lifshit-Gilbert equation 2.23 adding the Rashba spin-orbit torque induced by the non-equilibrium spin density $\vec{\mu}$

$$\frac{\mathrm{d}\vec{M}}{\mathrm{d}t} = -\gamma\vec{M}\times\vec{H} + \alpha\vec{M}\times\frac{\mathrm{d}\vec{M}}{\mathrm{d}t} + \frac{J_{\mathrm{ex}}}{\hbar}\vec{M}\times\vec{\mu}\,. \tag{2.69}$$

In the usual case of a uniformly magnetised layer ($\vec{\nabla}\cdot\vec{J}_{\mathrm{s}} = 0$) in steady state conditions ($\mathrm{d}/\mathrm{d}t = 0$), the Rashba torque is given by

$$\vec{\Gamma} = \frac{J_{\mathrm{ex}}}{\hbar}\vec{M}\times\vec{\mu} = \frac{1}{2m_{\mathrm{e}}}\langle(\vec{\nabla V}\times\vec{p})\times\vec{s}\rangle\,. \tag{2.70}$$

As mentioned previously, the breaking of inversion symmetry usually results from the presence of an interface between two thin film layers. Under this condition, the effective electric field is constant and normal to the interface, *i.e.*, in the $\hat{z}$ direction. We have then $\vec{\nabla V} = \eta\hat{z}$. Substituting this expression into eq. 2.70 gives

$$\vec{\Gamma} = \frac{\eta}{\hbar}\langle(\hat{z}\times\vec{p})\times\vec{s}\rangle\,. \tag{2.71}$$

Usually, in a ferromagnetic material, $\vec{s}$ is in the direction of the net magnetic moment.

Let's consider different systems in order to evaluate the effect of this Hamiltonian (Fig. 2.12). First, if we have a ferromagnet without spin-orbit coupling, the Fermi surfaces of majority and minority spins will be, in the simplest approximation, two spheres of different radii. By applying an electric field, the electrons acquire momentum $\vec{p}$ and the Fermi surfaces shift by an equal amount. This is a rigid shift, so the amount of spin $\uparrow$ and spin $\downarrow$ remains the same, giving no non-equilibrium spin density. Second, we

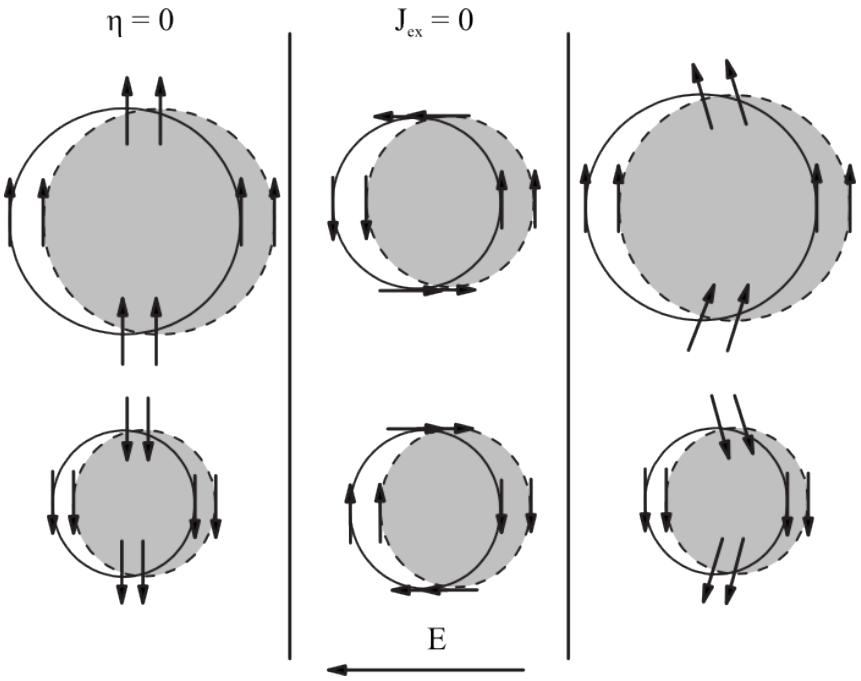

Figure 2.12: Representation of the Fermi surfaces for majority and minority electrons in a ferromagnet without Rashba interations, a non magnetic metal with Rashba interactions and in a ferromagnet with Rashba interactions. From ref. [49].

consider a non-magnetic metal with spin-orbit coupling. The two Fermi surfaces will the have the same radius and the electron spins will be perpendicular to the electron momentum. The effect of the applied electric field will be to displace the surfaces and create a spin density of the same magnitude and opposite sign for each sub-band. Hence, the net spin density will be zero. In the last case, both spin-orbit and exchange interactions are present, resulting in a Rashba torque on the magnetisation. The first produces a non-equilibrium spin density, the latter couples it with the local magnetisation. Further information can be found in ref. [49].

2.3.6 Hall effect, anomalous Hall effect and spin Hall effect

Hall effect

The Hall effect is the generation of a voltage difference in a metal layer, perpendicular to both the applied electric current and the out-of-plane magnetic field H_z. It results from the Lorentz force that deviates the electron trajectory, bending it towards the edges of the layer. The Hall voltage is then given by the cross product $\vec{p}\times\vec{H}$. Since its discovery in 1879, it has been extensively exploited to determine the carrier concentration in metals and semiconductors and to realise Hall probes, used as magnetometers. The Hall coefficient is defined as the ratio

$$R_{\mathrm{H}} = \frac{E_y}{J_x B} \ , \tag{2.72}$$

where E_y is the transverse electric field, J_x is the longitudinal injected current and B is the magnetic field. By setting the Lorentz force $\vec{F}_{\mathrm{L}} = e(\vec{E}) + \vec{v}\times\vec{B})$ to zero, it is easy to obtain

$$R_{\mathrm{H}} = -\frac{1}{ne} \ . \tag{2.73}$$

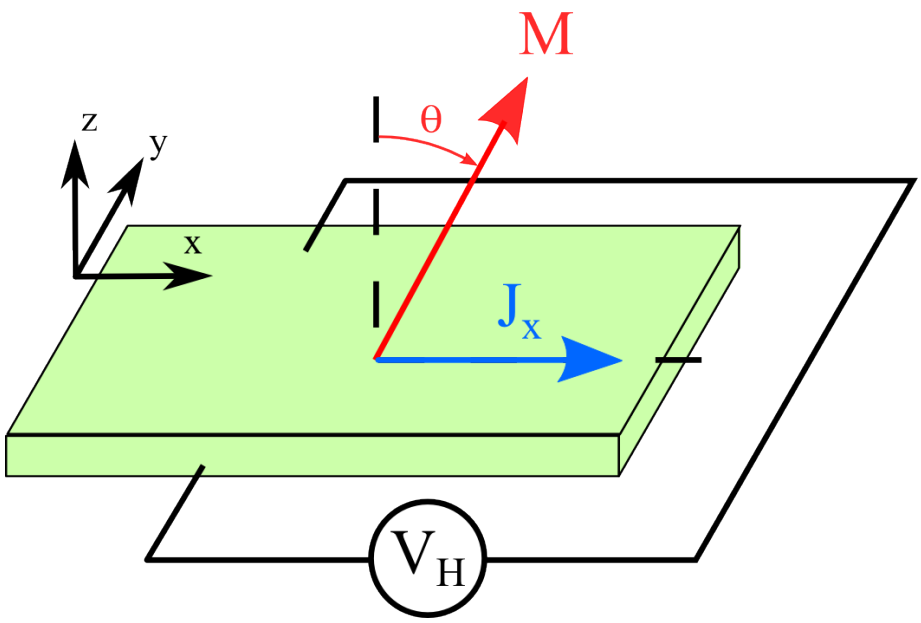

Figure 2.13: Schematic for the measurement of the anomalous Hall effect (AHE) in a magnetic sample.

Therefore, the Hall coefficient can be used to directly measure the carrier concentration n in metals.

Anomalous Hall effect

The anomalous Hall effect (AHE) or extraordinary Hall effect is the additional contribution to the Hall voltage found in ferromagnets due to their own magnetisation [50, 51]. This contribution is usually much more important than the normal Hall effect in metals, especially at room temperature and for external magnetic field values achievable in common experimental setups. An excellent review on this subject can be found in ref. [51].

The anomalous Hall voltage is proportional to the spin polarisation of the conduction electrons along the $\hat{z}$ direction. In normal ferromagnetic materials, this is usually directly related to the total magnetisation, hence there is no qualitative difference between the two. It is in any case important to notice that there might be an AHE in compensated ferrimagnets, because the fact that the total magnetic moment is zero doesn't necessarily mean that the spin polarisation at the Fermi level is zero.

Similarly to the normal Hall effect, the anomalous Hall voltage in ferromagnetic materials is proportional to the cross product $\vec{p}\times\vec{M}$. Hence, if the current is injected in the plane of a thin film, the signal is proportional to the out-of-plane component of the magnetisation M_z (Fig. 2.13). This effect is very useful for characterising the perpendicular magnetisation and magnetic anisotropy of a magnetic layer. In fact, by applying a perpendicular magnetic field it is possible to flip the magnetisation of the layer from one perpendicular direction to the other, effectively changing the sign of the Hall voltage. The signal recorded in a complete field sweep will resemble an hysteretic magnetisation loop.

The origins of the AHE are still under debate. The total Hall resistivity is usually expressed as

$$\rho_{xy} = R_{\mathrm{H}}\mu_0 H_z + \rho_{\mathrm{AHE}} m_z \ , \tag{2.74}$$

where R_0 is the normal Hall coefficient, ρ_{AHE} is the anomalous Hall contribution and $m_z = M_z/M_{\mathrm{s}}$. The current theory of the AHE provides three different mechanisms to explain it, schematised in Fig. 2.14. They all derive from a quantum mechanic treatise of the spin-dependent scattering. The first is an

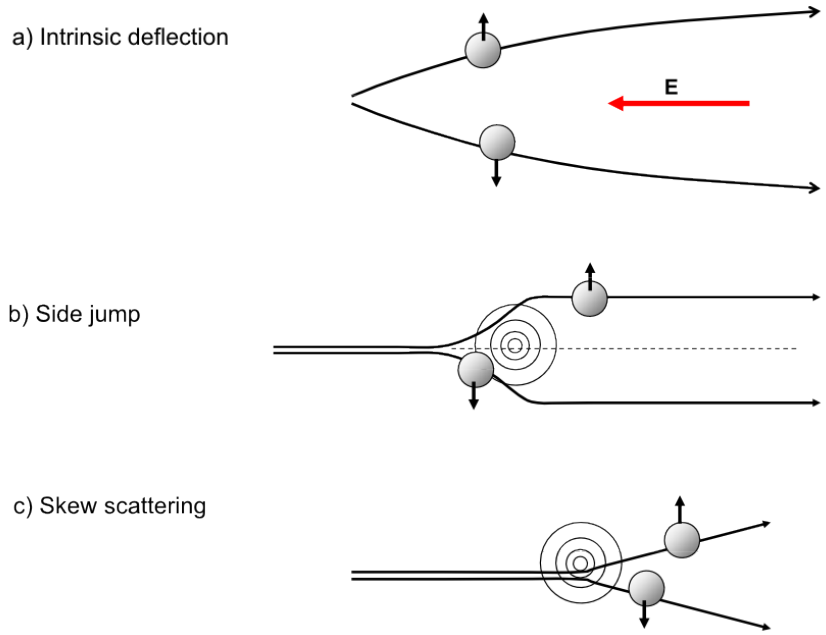

Figure 2.14: Schematic of the three mechanisms that give rise to the anomalous Hall effect. From ref. [51].

intrinsic deflection due to the Berry's phase curvature in the band structure of the metal. The application of an electric field gives rise to a perpendicular velocity of the carriers (anomalous velocity) that does not sum to zero in ferromagnetic materials, where one of the spin sub-bands in less occupied than the other. This contribution is usually referred to as the intrinsic contributions to the AHE since it does not rely on scattering. The dependence of the Hall conductivity σ_{xy} due to this effect is independent on the longitudinal conductivity σ_{xx}, hence the Hall resistivity $\rho_{xy} \approx \sigma_{xy}/\sigma_{xx}^2$ is proportional to ρ_{xx}^2.

Another mechanism is called skew-scattering and it is due to the asymmetric scattering of the carriers as a result of the spin-orbit coupling with the nuclei or magnetic impurities. In fact, in the presence of spin-orbit coupling, either in the disordered or in the perfect-crystal Hamiltonian, asymmetric chiral contributions appear at odd orders in the perturbation expansion [51]. This results in the generation of a current proportional to the longitudinal current driven by the electric field E_x and perpendicular to it and to the magnetisation. This mechanism give a conductivity σ_{xy} proportional to the Bloch states lifetime, hence proportional to σ_{xx}. For this reason, this mechanism is usually the dominant one in the case of nearly perfect crystals. The Hall resistivity ρ_{xy} is now proportional to ρ_{xx}.

The last contribution to the AHE is the side-jump mechanism. It is due to the interaction between an electron and a spherical impurity with spin-orbit coupling. The electron is deflected in opposite direction when approaching and leaving an impurity, hence it will suffer a displacement transverse to its velocity and with opposite sign for opposite spins. Similarly to the skew-scattering, this contribution gives a conductivity that is independent of σ_{xx} and a resistivity that is proportional to ρ_{xx}^2. The common way to determine the origin of the AHE in a material is to verify the relationship between ρ_{xy} and ρ_{xx}: a simple proportional dependence indicates the presence of extrinsic contributions from the skew-scattering, while a quadratic dependence is a sign of the dominance of the intrinsic contribution (Berry's phase) and/or side-jump effect. Such measurements should be carried out at temperatures below 4 K, where impurity scattering dominates and phonons and spin waves scattering are "frozen" and do not contribute to the resistivity. By adjusting the impurity concentration one may hope to change both ρ_{xx} and ρ_{xy} and to

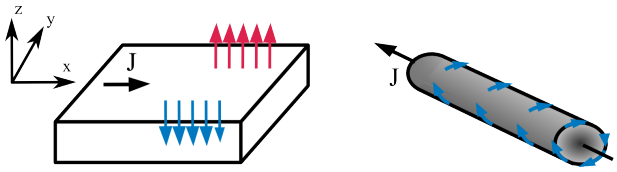

Figure 2.15: Representation of the spin Hall effect in a thin layer and in cylindrical wire. The injection of a charge current in presence of spin-orbit interaction results in a spin accumulation at the edges of the samples. In a thin layer the accumulation has opposite sign at opposite edges, while in a wire the spins wind around the surface. From ref. [52].

determine the scaling law.

The ratio between ρ_{xy} and ρ_{xx} is called anomalous Hall angle (AHA)

$$\text{AHA} = \frac{\rho_{xy}}{\rho_{xx}} = \frac{\sigma_{xy}}{\sigma_{xx}^2 + \sigma_{xy}^2}\frac{1}{\rho_{xx}} \approx \frac{\sigma_{xy}}{\sigma_{xx}^2}\frac{1}{\rho_{xx}} = \frac{\sigma_{xy}}{\sigma_{xx}} \ . \tag{2.75}$$

Spin Hall effect

The spin Hall Effect (SHE) [19, 52–54] consists in the spin accumulation at the edges of a conductor with spin-orbit coupling between the charges and the spins (see Fig. 2.15). While in the normal Hall effect we have carrier accumulation at the edges, in the SHE we have only spin accumulation, hence there is no creation of a transverse electric potential. This spin accumulation is proportional to the current, it changes sign when the latter is reversed and it requires no external magnetic field. The microscopic mechanisms at the origin of the spin Hall effect are the same of the anomalous Hall effect, *i.e.*, skew-scattering, side-jump and Berry phase curvature. For example, the skew-scattering can be seen as the effective magnetic field seen by an electron travelling near a charged centre in the crystal in the presence of spin-orbit coupling. This field is perpendicular to the plane of the electrons trajectories and has opposite sign for electrons travelling to the right or to the left of the centre. The Zeeman energy splitting for spin $\uparrow$ and spin $\downarrow$ is the spin-orbit coupling energy. The scattering angle depends on the spins of the electrons: spin $\uparrow$ and spin $\downarrow$ will be deflected in opposite directions. Hence, an unpolarised charge current will give rise to a spin current perpendicular to it. Below we will give a phenomenological treatment of the spin Hall effect, without taking into consideration the exact mechanisms giving raise to the spin-dependent scattering.

Following Dyakonov [52], we consider a drift and diffusion model and let's define the charge and spin flow densities in the absence of spin-orbit interactions as

$$\begin{aligned} q_i^0 &= -\mu n E_\text{i} - D\frac{\partial n}{\partial x_i} \ , \\ q_{ij}^0 &= -\mu n E_\text{i} P_j - D\frac{\partial P_j}{\partial x_i} \ , \end{aligned} \tag{2.76}$$

where $i, j = \hat{x}, \hat{y}, \hat{z}$, μ and D are the mobility and diffusion coefficient, n is the electron concentration, $\vec{E}$ is the electric field and $\vec{P}$ is the spin polarisation vector. The addition of spin-orbit interaction causes the coupling of the charge and the spin flow, described in general by

$$\begin{aligned} q_i &= q_i^0 + \xi\epsilon_{ijk}q_{jk}^0 \ , \\ q_{ij} &= q_{ij}^0 - \xi\epsilon_{ijk}q_k^0 \ , \end{aligned} \tag{2.77}$$

where ϵ_{ijk} is the unit antisymmetric tensor and ξ is a dimensionless coefficient that gives the strength of

the interaction. Hence, a charge current in the $\hat{x}$ direction induces spin currents in the $\hat{y}\hat{z}$ plane. Eq. 2.77 give the following expressions for the currents

$$\begin{aligned} \frac{\vec{J_c}}{e} &= \mu n\vec{E} + D\vec{\nabla}n + \beta\vec{E}\times\vec{P} + \sigma\vec{\nabla}\times\vec{P} \ , \\ q_{ij} &= -\mu E_i P_j - D\frac{\partial P_j}{\partial x_i} + \epsilon_{ijk}(\beta n E_k + \sigma\frac{\partial n}{\partial x_k}) \ , \end{aligned} \tag{2.78}$$

where $\beta = \xi\mu$ and $\sigma = \xi D$. The continuity equation is then

$$\frac{\partial P_j}{\partial t} + \frac{\partial q_{ij}}{\partial x_i} + \frac{P_j}{\tau_{sf}} = 0 \ . \tag{2.79}$$

In steady state conditions $\frac{\partial P_j}{\partial t} = 0$, electric field along $\hat{x}$ and boundary conditions $\partial P_x/\partial y = 0$, $\partial P_y/\partial y = 0$ and $\partial P_z/\partial y = \beta n E/D$, eq. 2.79 gives the results

$$\begin{aligned} P_z(y) &= P_z(0)\exp\left(-\tfrac{y}{\lambda_{sf}}\right) \ , \\ P_z(0) &= -\tfrac{\beta n E L_{sf}}{D} \ , \\ P_x &= 0 \ , \qquad P_y = 0 \ . \end{aligned} \tag{2.80}$$

with $\lambda_{sf} = \sqrt{D\tau_{sf}}$ is again the spin diffusion length. Typical values range from as small as 1 nm for heavy metals like Ta and Pt to 350 nm in Cu. Hence, spin accumulation is generated in thin atomic layers at the edges of a sample. The width of this layer is comparable to the spin diffusion length, which is very small in a ferromagnet and in materials with high spin-orbit coupling, thus the spin accumulation is confined to the first nanometres of a thin film. This might not be true in non magnetic materials with low spin-orbit coupling, but, of course, in this case the spin Hall effect would be negligible. The polarisation is proportional to the current and it is opposite at opposite edges.

2.3.7 Torques and effective fields from spin-orbit interactions

The spin Hall effect and the Rashba effect produce non-equilibrium spin accumulations at the interfaces between a non magnetic and a ferromagnetic layer. This results in a torque acting on the magnetic moment of the latter.

As discussed in sec. 2.3.5 and sec. 2.3.6, if a charge current J_c is injected in the plane of a thin film bilayer such as represented in Fig. 2.16, the spin-orbit interaction generates a spin current J_s perpendicular to the interface. Its spin polarised is directed in the plane and perpendicular to the current direction. In the case of a perfectly transparent interface, where the interface resistance can be described only by a real function of the angle between the magnetic moment $\vec{m}$ and the spin current polarisation $\vec{\sigma}$, this spin current results in a torque similar to the one described in sec. 2.2.2 in the Slonczewski theory [6]. This torque, named anti-damping since it is opposite to the Gilbert damping term [55] in the LLG equation 2.23, is given by $\frac{J_s\hbar}{2eM_s^2}(\vec{M}\times\vec{\sigma}\times\vec{M})$ with J_s the spin current density and M_s the saturation magnetisation. It is easy to see that it is directed parallel to the spin current polarisation for both in-plane and out-of-plane magnetic moment. From eq 2.71, the Rashba torque is given by $-\frac{\eta e}{2}(\vec{M}\times\vec{\sigma})$ with η the Rashba field coefficient. Therefore, in the case of in-plane magnetisation, it is directed out-of-plane while in the case of out-of-plane magnetisation it is directed along the charge current direction. This torque is often referred to as field-like torque since it is similar to the one produced by the Ørsted field arising from the injected current. The torques are schematised in Fig. 2.16 (a) and (b) [56].

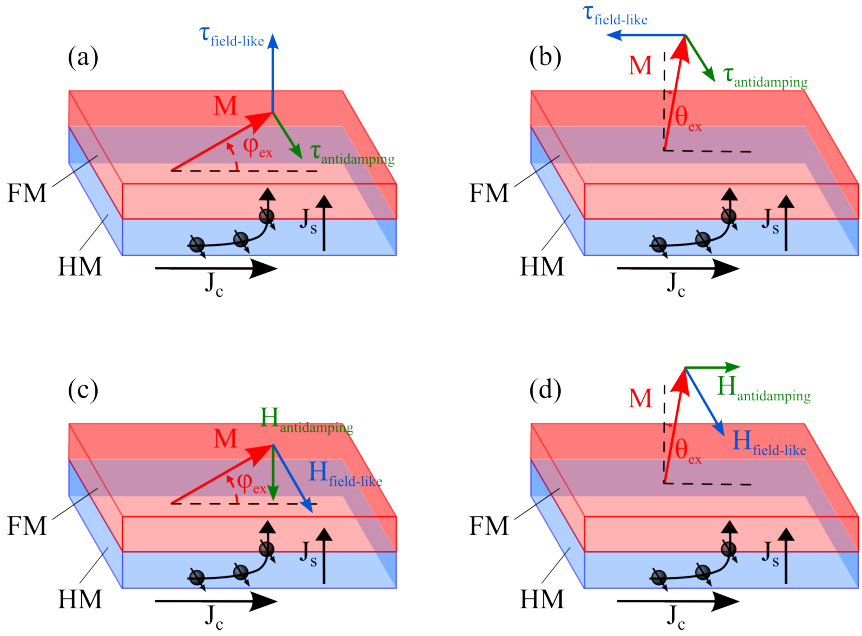

Figure 2.16: Schematic of a non magnetic heavy metal/ferromagnetic metals bilayer with (a) in-plane and (b) out-of-plane magnetisation. J_c is the charge current injected in-plane, J_s is the resulting spin current. $\tau_{\text{anti-damping}}$ and $\tau_{\text{field-like}}$ are the two torques acting on the magnetic moment. Equivalently, in panels (c) and (d) the effective fields $H_{\text{anti-damping}}$ and $H_{\text{field-like}}$ are displayed.

This relation between the torques and the originating mechanisms has proved to be not reliable in practice. The presence of an imaginary component in the interface spin-dependent resistivity results in a mixing of the two types of torques [57]. This imaginary part is seen as a phase shift of 90° for the injected spins, resulting in a rotation of the effective torque direction. In fact, Rashba and spin Hall effect can each result in both anti-damping and field-like torques. The magnitude of each of them depends on the materials and on the interface conditions, hence they are not usually known *a priori*.

Since, in general, we have $\frac{d\vec{M}}{dt} = -\mu_0\gamma_0\vec{M} \times \vec{H}_{\text{eff}}$, the torques are related to equivalent effective fields. It is sometimes useful to refer to the effective fields instead of the torques. The anti-damping effective field is proportional to $-\vec{\sigma} \times \vec{M}$. It is directed out-of-plane if $\vec{M}$ lies in the plane and along the current direction if $\vec{M}$ is perpendicular to the interface. Instead, the field-like effective field is proportional to $\vec{\sigma}$ and it is then always directed in the plane and perpendicular to the current direction. The situation is schematised in Fig. 2.16 (c) and (d).

2.3.8 Spin rectification

Spin rectification is the generation of a dc voltage following the injection of an radio-frequency current in a ferromagnetic material [58–62]. . This effect is due to non linear coupling between the current and the magnetisation dynamics that induces changes in the resistance of the sample, *i.e.*, AMR and AHE.

Under microwave excitation, the electric field and the magnetic field inside a ferromagnetic material are described by $\vec{e} = \vec{e}_0 \exp(-\imath\omega t)$ and $\vec{h} = \vec{h}_0 \exp(-\imath\omega t + \imath\Phi)$, with Φ the relative phase shift due to losses of the propagating microwave. The electric field generates a current density $\vec{j} = \vec{e}\sigma$, while the magnetic field excites magnetisation dynamics. These dynamics are in general described by $\vec{m} = \chi\vec{h}$ (see sec. 2.2). σ and χ are the high-frequency conductivity and Polder tensor respectively (see sec. 2.2). In addition to the relative phase shift Φ, there is an additional shift Θ between $\vec{h}$ and $\vec{m}$ because of the nature of the

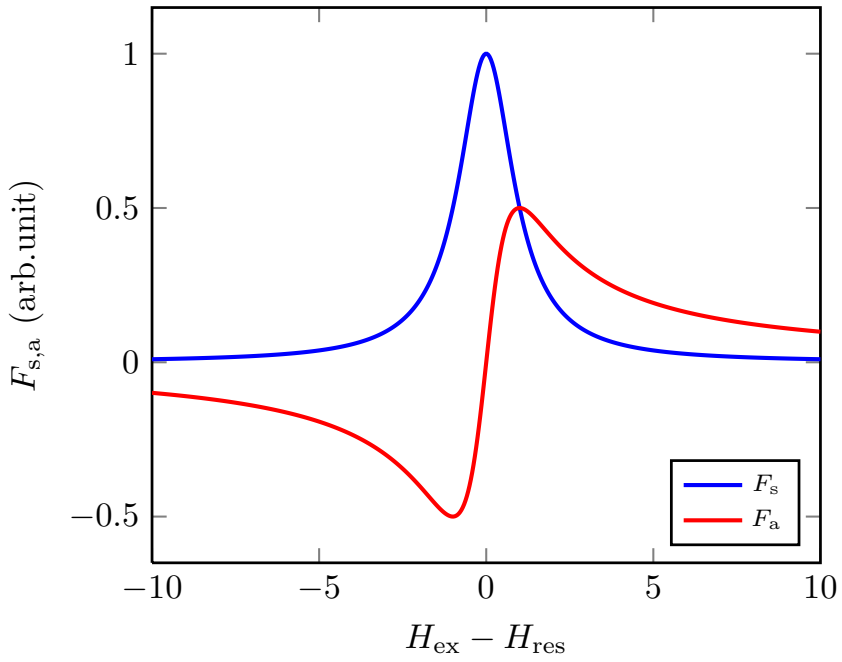

Figure 2.17: Example of symmetric and antisymmetric Lorentzian lineshapes with $\Delta = 1$.

resonance.

Following the derivation given in sec. 2.2, from the LLG equation 2.23, we can relate the transverse component of the magnetisation $\vec{m}$ to the driving rf field $\vec{h}$ through the Polder tensor as in

$$\begin{aligned}\vec{m} = \chi\vec{h} &= \begin{pmatrix} \chi_{xx} & \imath\chi_{xy} & 0 \\ -\imath\chi_{xy} & \chi_{yy} & 0 \\ 0 & 0 & 0 \end{pmatrix} \vec{h} \\ &= \begin{pmatrix} |\chi_{xx}| & |\chi_{xy}|e^{\imath\pi/2} & 0 \\ |\chi_{xy}|e^{-\imath\pi/2} & |\chi_{yy}| & 0 \\ 0 & 0 & 0 \end{pmatrix} \vec{h}\exp(\imath\Theta) \qquad (2.81) \\ &\qquad , \qquad (2.82)\end{aligned}$$

where $\Theta = \arctan[\Delta/(H_{ex} - H_{res})]$, with H_{res} and Δ the resonance field and the linewidth at constant excitation frequency. The phase Θ goes from 180° to 0° as we sweep the external field and go through the resonance, where Θ assumes the value of 90°. We can define symmetric and antisymmetric Lorentzian lineshapes as

$$\begin{aligned} F_s(H_{ex}) &= \Delta^2/[\Delta^2 + (H_{ex} - H_{res})^2] \qquad \text{and} \\ F_a(H_{ex}) &= F_s(H_{ex})(H_{ex} - H_{res})/\Delta \ , \end{aligned} \qquad (2.83)$$

respectively (see Fig. 2.17). In this way, we have $\Theta = \arctan(F_s/F_a)$ so that $F_s \propto \sin(\Theta)$ and $F_a \propto \cos(\Theta)$

and we can write the Polder tensor in eq 2.81 as $(\chi_{xx}, \chi_{xy}, \chi_{yy}) = (F_\mathrm{a} + \imath F_\mathrm{s})(A_{xx}, A_{xy}, A_{yy})$, with

$$\begin{aligned} A_{xx} &= \frac{\gamma_0 M_\mathrm{s}[M_\mathrm{s} N_y + (H_\mathrm{ex} - N_z M_\mathrm{s})]}{\alpha\omega[2(H_\mathrm{ex} - N_z M_\mathrm{s}) + M_\mathrm{s}(N_z + N_y)]} \ , \\ A_{xy} &= -\frac{M_\mathrm{s}}{\alpha[2(H_\mathrm{ex} - N_z M_\mathrm{s}) + M_\mathrm{s}\ (N_z + N_y)]} \qquad \text{and} \\ A_{yy} &= \frac{\gamma_0 M_\mathrm{s}[M_\mathrm{s} N_x + (H_\mathrm{ex} - N_z M_\mathrm{s})]}{\alpha\omega[2(H_\mathrm{ex} - N_z M_\mathrm{s}) + M_\mathrm{s}(N_z + N_y)]} \ . \end{aligned} \tag{2.84}$$

For the usual case of a thin film with in-plane applied field, we must substitute $N_x = N_z = 0$ and $N_y = 1$. Since these coefficients are all real, the components of χ include both a symmetric and antisymmetric lineshape determined by the $(F_\mathrm{a} + \imath F_\mathrm{s})$ term. However, when measuring the microwave absorption due to the resonance as in an FMR experiment, we only measure the amplitude $|m|^2 \propto F_\mathrm{s}^2 + F_\mathrm{a}^2 = F_\mathrm{s}$, hence we loose the information on the phase shift.

The rectification effect is a result of the coupling of the rf electric field (and current) to the magnetisation dynamics. In general, it follows from the formula

$$\vec{E} = \rho\vec{J} + (R_\mathrm{AMR} M_\mathrm{s}^2)(\vec{J}\cdot\vec{M})\vec{M} - R_\mathrm{AHE}\vec{J}\times\vec{M} \ , \tag{2.85}$$

where ρ is the resistivity and R_AMR and R_AHE are the AMR and AHE coefficients respectively. We can express $\vec{M}$ as $\vec{M}_\mathrm{s} + \vec{m}$ and $\vec{J}$ as $\vec{J}_0 + \vec{j}$ to separate static and rf components. We have of course $\vec{m} = \Re[\vec{m}_0 \exp(-\imath\omega t)]$. In order to find the dc rectified voltage we have to put $J_0 = 0$ and approximate eq 2.85 to the second order in both $\vec{j}$ and $\vec{m}$. In fact, since $\vec{j}$ and $\vec{m}$ oscillate periodically, their net time average is zero. Hence the terms at the first order in the expansion give no net contributions. We find

$$\vec{E} = \frac{R_\mathrm{AMR}}{M_\mathrm{s}^2}\langle(\vec{j}\cdot\vec{m})\vec{M}_\mathrm{s} + (\vec{j}\cdot\vec{M}_\mathrm{s})\vec{m}\rangle - R_\mathrm{AHE}\langle\vec{j}\times\vec{m}\rangle \ . \tag{2.86}$$

Here, the symbols $\langle\ldots\rangle$ denote time-averaging. The sample and coordinate system used are shown in Fig. 2.18. We consider a long and narrow strip of a soft ferromagnetic metal, so that we have only shape anisotropy. In this geometry, the AHE gives no voltage along the strip and it can be ignored. From eq 2.86 we can calculate the voltage across the length L of the strip as

$$\begin{aligned} V &= \int_0^L \vec{E}dz' \approx \vec{E}\cdot\vec{L} \\ &= \frac{R_\mathrm{AMR} L}{M_\mathrm{s}^2}\langle\vec{j}(\hat{z}'\cdot\vec{m})(\vec{M}_\mathrm{s}\cdot\hat{z}') + \vec{j}(\hat{z}'\cdot\vec{M}_\mathrm{s})(\vec{m}\cdot\hat{z}')\rangle - 0 \\ &= \frac{R_\mathrm{AMR} L}{M_\mathrm{s}^2}\langle\Re(j)\Re(m_x)\rangle\sin(2\theta_H) \ . \end{aligned} \tag{2.87}$$

We can use eq 2.81 and eq. 2.84 to express m_x in terms of the $\vec{h}$ field. After changing the coordinate system from $(\hat{x}, \hat{y}, \hat{z})$ to $(\hat{x}', \hat{y}, \hat{z}')$, we have

$$V = \frac{R_\mathrm{AMR} L}{2M_\mathrm{s}} j_{z'}(SF_\mathrm{s} + AF_\mathrm{a}) \ , \tag{2.88}$$

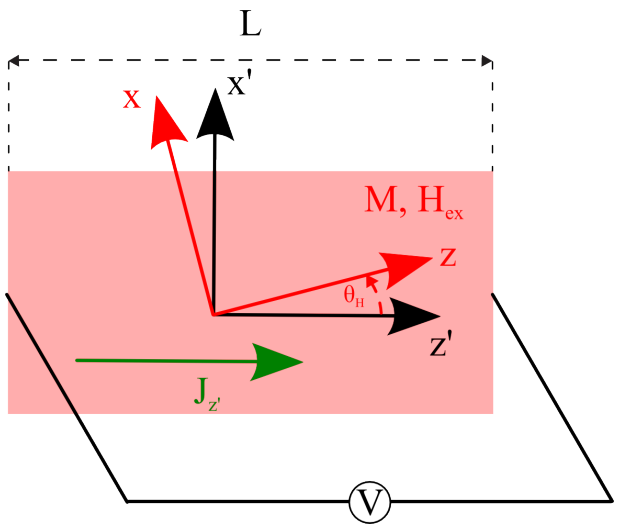

Figure 2.18: Coordinate system for a long narrow strip of a soft ferromagnetic metal. The static field H_{ex} is applied in plane at an angle θ_H with the $\hat{z}'$ axis. The rf current and electric field are along the strip length $\hat{z}'$.

with

$$\begin{aligned} S &= \sin(2\theta_H)[-A_{xx}h_{x'}\cos(\theta_H)\sin(\Phi_{x'}) \\ &\quad -A_{xy}h_y\cos(\Phi_y) + A_{xx}h_{z'}\sin(\theta_H)\sin(\Phi_{z'})] \quad \text{and} \\ A &= \sin(2\theta_H)[A_{xx}h_{x'}\cos(\theta_H)\cos(\Phi_{x'}) \\ &\quad -A_{xy}h_y\sin(\Phi_y) - A_{xx}h_{z'}\sin(\theta_H)\cos(\Phi_{z'})] \ , \end{aligned} \tag{2.89}$$

where Φ_i is the relative phase between electric and magnetic fields in the $\hat{i}$ direction. In the usual case in which the rf magnetic field is mainly in the $\hat{x}'$ direction, we have

$$V = \frac{R_{\text{AMR}}L}{2M_{\text{s}}} j_{z'}A_{xx}h_{x'}\cos(\theta_H)\sin(2\theta_H)[F_{\text{s}}\sin(\Phi) - F_{\text{a}}\cos(\Phi)] \ . \tag{2.90}$$

The lineshape can then change from a purely symmetric Lorentzian to a purely antisymmetric Lorentzian in 90° intervals of Φ. At the contrary, for the driving magnetic field along the $\hat{y}$ direction, we have

$$V = \frac{R_{\text{AMR}}L}{2M_{\text{s}}} j_{z'}A_{xy}h_y\sin(2\theta_H)[F_{\text{s}}\cos(\Phi) - F_{\text{a}}\sin(\Phi)] \ , \tag{2.91}$$

and we have the opposite situation concerning the lineshape. Since there is no way to determine Φ in experiments, the characterisation of the driving field can be practically impossible [61].

In the case of a Hall voltage measurement in the same conditions, the theoretical treatment can be made by following the same procedure used for a longitudinal voltage measurement. The only differences come from the fact that the voltage is now proportional to the out-of-plane component of the rf magnetisation m_y and we have to use the coefficient R_{AHE} instead of $R_{\text{AMR}}/M_{\text{s}}^2$. Hence we have

$$V = -R_{\text{AHE}}L\langle\Re(j)\Re(m_y)\rangle \ . \tag{2.92}$$

From the nature of the resonance it is clear that m_y is 90° out of phase with respect to m_x, hence the amplitudes of the symmetric and antisymmetric lineshapes are inverted from the previous case.

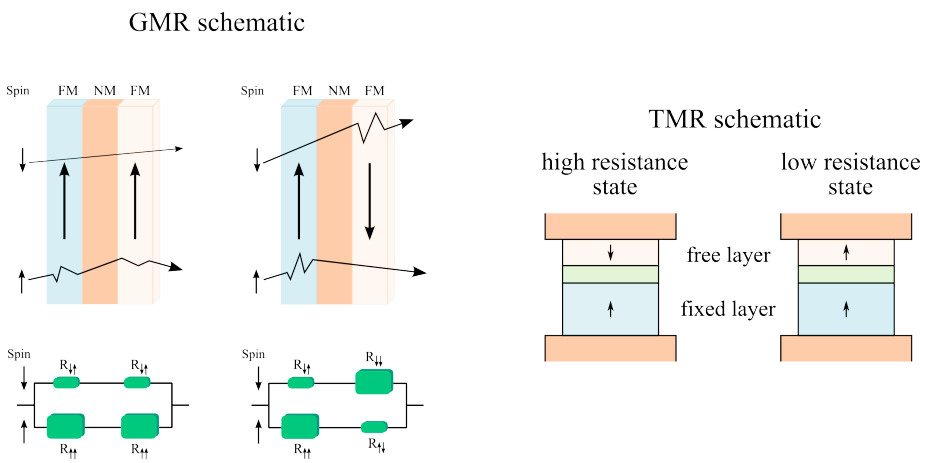

Figure 2.19: Schematics of a GMR and of a TMR cells.

A detailed review of this topic can be found in ref. [60].

2.3.9 Spin electronics

Conventional electronics has focussed only on the manipulation of the electron charge. The semiconductor industry has seen a massive development since the invention of the transistor in 1947 [63], but until recently it has ignored the fact that electron possess an intrinsic magnetic moment: its spin. Spin electronics is the branch of electronics that aims to control the spin of the electron in order to add new functionalities in devices. The discovery of the giant magnetoresistance (GMR) effect [64] in 1988 by Albert Fert and Peter Grünberg enhanced the data storage density of non-volatile magnetic memories in the form of hard disks, where the information is stored in the direction of the magnetic moment of small magnetic elements. This kind of magnetic recording has been widely used due to the fact that it is a scalable technology, *i.e.*, the magnetic moment and the field required to flip the magnetisation of a bit scale by the same amount when the volume of the magnetic element is shrunk. While this is true in principle, in practice there are some limitations to the minimum size of the magnetic elements that can be reached for device applications at the current state of the art. Some of these limitations have been discussed in sec. 1.1.

Since the discovery of the giant magnetoresistance (GMR) [64], magnetic elements have been extensively used in electronic devices, especially for fabricating non-volatile memories. GMR devices are made of two ferromagnetic layers that sandwich a non magnetic metal, as shown in Fig. 2.19. When an electric current is injected, the spin-dependent scattering of electrons travelling through the spacer in the two magnetic materials translates in different resistance values for parallel and antiparallel magnetisation configurations.

The leading device for spin electronics is the magnetic tunnel junction (MTJ) [65, 66]: it consists of two ferromagnetic layers separated by an insulating thin barrier (see Fig. 2.19). If a voltage V is applied across the junction, electrons can tunnel through the barrier and the transmission probability is strongly influenced by the available density of states (DOS) in the ferromagnetic layer on the other side. This DOS is directly connected to the magnetic state since the DOS of spin $\uparrow$ and spin $\downarrow$ electrons is different at the Fermi level. The magnetic moment of one of the layers (fixed layer) is pinned in one orientation, usually by exchange coupling with an antiferromagnet (IrMn or a synthetic antiferromagnet), while the magnetic moment of the other one (free layer) is relatively free to rotate and switch. The data is read by measuring the difference in the resistivity of the device as a function of the magnetic state, *i.e.*, when

the two layers have parallel or antiparallel magnetisations. Following Jullière [65], the tunnelling current density can be expressed as

$$J_{\uparrow\downarrow} \propto \int_0^\infty T(E) D_{\uparrow\downarrow 1}(E) D_{\uparrow\downarrow 2}(E+eV)(f(E)-f(E+eV))dE \ , \tag{2.93}$$

where $T(E)$ is the tunnelling probability, E_F is the Fermi energy, D is the DOS and $f(E)$ is the Fermi-Dirac distribution. The subscripts 1 and 2 indicate the two ferromagnetic layers, while the subscripts $\uparrow$ and $\downarrow$ refer to the respective spin sub-band. In the simple Jullière model [65], the Fermi-Dirac distribution dependence is approximated using $\int_0^\infty dE[f(E)-f(E+eV)] \approx eV$ as only small applied voltages are considered. The DOS of the two ferromagnets depends on the spin of the tunnelling electrons, and therefore on the magnetisation state of the layers. Hence, we consider a two current channels model for spin $\uparrow$ and spin $\downarrow$ electrons, with conductances

$$\sigma_\mathrm{p} = \sigma_{\uparrow\uparrow} + \sigma_{\downarrow\downarrow} \propto D_{1\uparrow} D_{2\uparrow} + D_{1\downarrow} D_{2\downarrow} \qquad \text{and} \qquad \sigma_\mathrm{ap} = \sigma_{\uparrow\downarrow} + \sigma_{\downarrow\uparrow} \propto D_{1\uparrow} D_{2\downarrow} + D_{1\downarrow} D_{2\uparrow} \tag{2.94}$$

for parallel and antiparallel magnetisations respectively. A more detailed theory [67] introduces some correction factors to these polarisation factors due to finite thicknesses of the two ferromagnetic layers. Since the spin polarisation at the Fermi level for the ferromagnet i (neglecting differences in the Fermi velocity for $\uparrow$ and $\downarrow$ electrons) is expressed as

$$P_i^0 = \frac{D_{i\uparrow} - D_{i\downarrow}}{D_{i\uparrow} + D_{i\downarrow}} \ , \tag{2.95}$$

the tunnelling magnetoresistance (TMR) ratio is given by

$$\mathrm{TMR} = \frac{R_\mathrm{ap} - R_\mathrm{p}}{R_\mathrm{p}} = \frac{G_\mathrm{p} - G_\mathrm{ap}}{G_\mathrm{ap}} = \frac{2P_1P_2}{1 - P_1P_2} \ . \tag{2.96}$$

Here R and $G = 1/R$ are the resistance and the conductance for the two configurations, respectively. The use of a MgO barrier together with crystalline CoFe ferromagnets greatly improves the TMR ratio since the MgO acts as a spin filter. In fact, the evanescent DOS in the insulating barrier presents resonant states in correspondence to the majority spins in the CoFe layers. If the magnetisations of the two electrodes are parallel, the flow of electrons is greatly enhanced by resonant tunnelling through the MgO, while if the magnetic moments are antiparallel, the current is suppressed by the absence of states in the second CoFe layer. With this method it is possible to obtain huge TMR ratio, of the order of 300 % at room temperature. The role of the spin-filtering barrier is essential since the polarisation of $3d$ ferromagnetic electrodes is not very high due to the presence of unpolarised $4s$ states at or near the Fermi level.

A particular application of a GMR or MTJ device is a spin-torque oscillator [68]. It usually features a ferromagnetic layer with fixed in-plane magnetisation and a free layer with out-of-plane magnetisation. The injection of electrons from the first into the second results in a displacement of its magnetic moment via STT and its precession around the equilibrium position, as described by the LLG equation 2.23. Since the resistance of the stack depends on the scalar product of the two magnetic moments, the injected dc current gives rise to an oscillating ac voltage. The frequency of this signal is the resonance frequency of the free layer. Therefore, it is advantageous to use a material with high PMA in order to increase the frequency of oscillation as the effective anisotropy field increases, as predicted by Kittel's law 2.38.

2.4 X-ray spectroscopy

X-ray absorption spectroscopy (XAS) has become an important tool for the characterisation of materials [69–71]. XAS is element specific and, when the signal is collected as the total electron yeld (TEY), very surface sensitive. It is also possible to obtain information on samples without long-range order, unlike in neutron diffraction experiments. Since the electronic transitions are closely related to the empty density of states, XAS is often used as for the determination of the local electronic structure of a material.

2.4.1 Interaction of x-rays with matter

A material exposed to x-rays will absorb part of the incoming photons. The absorption coefficient of x-rays shows three general features:

1. an overall decrease with increasing energy of the incoming photons,
2. sharp increases in correspondence of absorption edges
3. a series of small wiggles or oscillatory structures above those edges [70].

The first feature derives from the decrease of the imaginary part of the refractive index of materials when the photon wavelength λ decreases in the x-ray regime. In the range of photons energy above 30 eV, the optical properties of materials are related to the scattering factors of individual atoms. The refractive index is approximated by

$$n = 1 - \delta - \imath\beta = 1 - \frac{r_\mathrm{e}}{2\pi}\lambda^2 \sum_j n_j f_j \ , \tag{2.97}$$

with

$$f_j = f_1 + \imath f_2 \ , \tag{2.98}$$

r_e the classic electron radius and n_j is the number of atoms of type j per volume. The imaginary part of f_j is derived from the atomic cross section σ

$$f_2 = \frac{\sigma}{2r_\mathrm{e}\lambda} \ , \tag{2.99}$$

hence overall n has a linear dependence on λ. The real part of the refractive index in condensed matter is lower than (even if very close to) one in the x-ray regime. This is the reason why it is possible to have total reflection of the incident beam in XRR experiments at the air/sample interface (see sec. 3.7.3). Even if this means that the wavefront travels faster the light in the medium (phase velocity), the wave packet velocity (group velocity = $d\omega/dk$) cannot exceed that limit.

The energy corresponding to an edge is equal to the difference between the ground state and an excited state with a core hole. The $L_{2,3}$ edges correspond to a $2p$ ground core hole level, while the K edges correspond to an $1s$ ground level.

The third feature results from the multiple scattering arising from the wave-like behaviour of excited electrons. It will be discussed in sec. 3.4.3.

The Fermi golden rule for electronic transitions gives the transition probability W between the initial state ϕ_i and a final state ϕ_f as [23]

$$W_\mathrm{fi} = \frac{2\pi}{\hbar}|\langle\phi_\mathrm{f}|T|\phi_\mathrm{i}\rangle|^2 \delta_{E_\mathrm{f}-E_\mathrm{i}-\hbar\omega} \ , \tag{2.100}$$

where the delta function takes care that the energy difference of the states is equal to the energy of the incoming photons and T is the transition operator. The latter is a function of the scalar product of the

vector potential of the electromagnetic radiation $\vec{A}$ and the momentum of the electrons $\vec{p}$. It contains terms in $\vec{A}^2$ and $\vec{A}\cdot\vec{p}$. This expression is usually rewritten considering only the latter (dipole approximation) as

$$W_{\mathrm{fi}} \propto \sum_q |\langle\phi_{\mathrm{f}}|\vec{p}_q|\phi_{\mathrm{i}}\rangle|^2 \delta_{E_{\mathrm{f}}-E_{\mathrm{i}}-\hbar\omega} \ . \tag{2.101}$$

The polarisation q of the x-ray light is taken into account by considering the q dependent effective dipole moment $\vec{p}_q$. In the dipole approximation, it can be replaced by the position operator $\vec{r}_q$. The finite lifetime of the excited state is taken into account by substituting the delta function with a Lorentzian. By the application of T, the initial state is projected into a series of possible final states and the transition probability is evaluated. In this framework, the response of a system can be given assuming that it is in thermodynamic equilibrium before the perturbation acts on it. Therefore, it lies in its ground state and excitation arriving at successive times act independently to each other (generalised susceptibility theorem).

The atomic wavefunctions can be given by quantum numbers: our discussion involves only J and M, hence we will refer to all the other quantum numbers with the letter α. The matrix element $\langle\phi(JM\alpha)|\vec{r}_q|\phi(J'M'\alpha')\rangle$ is given, according to the Wigner-Eckart theorem, by the $3J$-symbol [23]

$$\langle\phi(JM\alpha)|\vec{r}_q|\phi(J'M'\alpha')\rangle = (-1)^{J-M} \begin{pmatrix} J & 1 & J' \\ -M & q & M' \end{pmatrix} \langle\phi(J\alpha)||\vec{r}_q||\phi(J'\alpha')\rangle \ . \tag{2.102}$$

This way the angular and radial parts can be separated into the $3J$-symbol and the reduced matrix element $\langle\phi(J\alpha)||\vec{r}_q||\phi(J'\alpha')\rangle$, respectively. A very detailed theory of atomic spectra can be found in Cowan's book (ref. [23]).

The selection rules for x-ray absorption follow directly from the triangular relations of the $3J$-symbol. An x-ray photon carry angular momentum $q = 0, \pm 1$ for linear, right circular and left circular polarisations respectively, and do not have spin momentum. Hence, the total momentum of the electron cannot change by more than 1, and the magnetic quantum number M is changed according to the polarisation of the light q. Therefore, we have

$$\Delta J = \pm 1, 0 \quad \text{and} \quad \Delta M = q \ . \tag{2.103}$$

For Bloch-like wavefunctions in the final states, J is not a good quantum number because of the effect of the crystal structure and the set (L, M_L, S, M_S) must be considered. In this case the selection rules follow directly from the simple argument that in $\langle\phi_{\mathrm{i}}|\vec{r}_q|\phi_{\mathrm{f}}\rangle\ \vec{r}_q$ is an odd function, hence ϕ_{i} and ϕ_{f} must have one odd and one even symmetries to have non zero matrix element. Therefore, their angular quantum number L must differ by 1. For the conservation of the total angular momentum we have also that M_L must differ by the photon momentum q. In addition, the photons don't carry any spin, hence the spin quantum number S is conserved. The selection rules are then given by

$$\Delta L = \pm 1 \ , \quad \Delta M_L = q \ , \quad \Delta S = 0 \quad \text{and} \quad \Delta M_S = 0 \ . \tag{2.104}$$

2.4.2 Atomic multiplets

Using the Russell-Saunders notation, the terms of a multi-electrons atomic configuration are indicated by L, S and J. If spin-orbit coupling is not considered, all terms with the same L and S have the same energy. A term is designed with the LS term symbol ${}^{2S+1}X_J$ with $X = S, P, D$, etc for $L = 0, 1, 2$, etc respectively. Indicating with upper case letters the quantum numbers of the multi-electron multiplets and with lower case letters the ones for single electrons, the possible terms for a configurations are found

considering all the possible values of L ans S as vectorial sums of the l and s of the single electrons. The general formula to determine the degeneracy of a $3d^N$ configuration is [23, 24, 72, 73]

$$\binom{10}{N} = \frac{10!}{(10-N)!N!} \ , \tag{2.105}$$

where we used the binomial coefficient $\binom{10}{N}$ that gives the number of possible subsets of N elements over a 10-element set. The $2p$ x-ray absorption edges ($L_{2,3}$ edges, corresponding to $2p \rightarrow 3d$ transitions) have final state $2p^5 3d^{N+1}$. The term symbols are found by multiplying the $3d^{N+1}$ configurations with a ^2P term symbol, corresponding to the $2p$ single hole and that comprise 6 elements. The number of possible states can become exceedingly high very fast, reaching 110 allowed transitions for 180 term-symbols for a $2p^6 3d^5 \rightarrow 2p^5 3d^6$ transition.

Hund's rules are used to find the ground state in a $3d^N$ configuration. They are:

1. term symbols with maximum spin S are lowest in energy,
2. among these terms, the one with maximum orbital momentum L is lowest,
3. in the presence of spin-orbit coupling, if the shell is less than half full the lowest is the one with $J = |L-S|$. At the contrary, if the shell is more than half full, the lowest is the one with $J = |L+S|$.

The first rule can be explained from Pauli principle. Electrons tend to avoid to occupy the same orbital in order to achieve higher separation, hence they can, and will, have the same spin. The second rule allows electrons to minimise the overlap of their orbits, hence minimising the repulsion.

The atomic wavefunctions are usually expressed as combinations of single electron wavefunctions as in a Slater determinant [24]. The energy of each term is given by the expectation value of the Hamiltonian

$$\mathcal{H} = \sum_i \frac{p_i^2}{2m} + \sum_i \frac{-Ze^2}{r_i} + \sum_{i>j} \frac{e^2}{r_{ij}} + \sum_i \xi(r_i) l_i \cdot s_i \ . \tag{2.106}$$

The Hamiltonian contains, respectively, the kinetic energy of the electrons, the electrostatic interaction with the nuclei, the electron-electron repulsion and the spin-orbit coupling. The expectation values of the first two contributions are the same for all term-symbols in a given configuration. The electron-electron repulsion is a two-electron operator and it is estimated using the Slater parameters F^2 and F^4. Since they require the knowledge of the radial wavefunctions, they are usually found with an Hartree-Fock iterative calculation or determined experimentally. The experimental value is very often reduced to 80 % of the calculated atomic value. The spin-orbit coupling splits the degeneracy of the terms with same values of L and S but different J. For the single-electron wavefunctions, l, m_l and s, m_s are not good quantum numbers any more, since the spin-orbit coupling can couple states with different values of these quantum numbers. Instead, good quantum numbers are j and m_j and the energy of a state is given by $\frac{\xi}{2}[j(j+1) - l(l+1) - s(s+1)]$. If ξ is positive, the state with the lower j lies lowest. In the many-electron case, the spin-orbit energy of the spin-orbit interactions can be estimated in the same way as $\frac{\lambda}{2}[J(J+1) - L(L+1) - S(S+1)]$, with the many-electron coefficient λ instead of ξ. We can distinguish two cases. In the first one, the spin-orbit coupling is of the same order or bigger than the electron-electron repulsion. The LS coupling scheme is not valid any more and we have to use the JJ coupling scheme to first derive the spin-orbit interaction energy and then the Coulomb electronic repulsion. This is the case of low-lying shells, such as the $2p$ ground state of $3d$ metals or the $3d$ shell of rare earth elements. In the other and far more common case, we can treat the spin-orbit coupling as a perturbation of the LS-coupled

ground state. Therefore, the spin-orbit interactions define the ground state between all possible states with the same L and S as described by Hund's third rule.

2.4.3 Crystal field

The crystal field theory approximates a material as an isolated atom surrounded by a distribution of charges that mimics the system around it. It is a representation of the electric field originating from the neighbouring atoms or molecules [24, 72, 74]. Even if this is a very simplistic model, it is extremely successful because of the use of the symmetry properties of a system and of the group theory. The symmetry of an atomic system is the perfectly spherical symmetry (SO_3)[1], while the one of a crystal lattice contains far fewer symmetry operations. In the crystal field theory, each symmetry operations or representation in SO_3 is brought into the desired symmetry group, creating a series. For example, to descend into the D_{4h} symmetry, we consider the series $SO_3 \rightarrow O_h \rightarrow D_{4h}$. The crystal field model can also be refined with the ligand field model, which takes into account the nature of the different bonds between the orbitals, hence which doesn't treat the other atoms just as point charges.

The crystal field potential V_{cr} is usually expanded in a series of normalised spherical harmonics

$$V_{\mathrm{cr}} = \sum_i \sum_l \sum_m c_{lm} Y_l^m(\theta_i, \varphi_i) R_{nl}(r_i) \ , \tag{2.107}$$

with the first summation over the i electrons of the ion and c_{lm} the coefficients for the spherical harmonics. The symmetry of the ligands around the central ion is important because the Hamiltonian must remain totally symmetric under all symmetry operations of the molecule in order for the total energy to be the same. In other words, it must span the totally symmetric irreducible representation of the point group of the molecule. Therefore, when descending into the correct symmetry, the series must end with the totally symmetric representation. The most important term in the expansion of V_{cr} is the spherically symmetric term having $l = 0$

$$V_{\mathrm{R}} = \sum_i \frac{1}{\sqrt{4\pi}} R_0(r_i) \ . \tag{2.108}$$

On the other hand, this term will only shift all the levels with the same number of electrons by the same energy, therefore it is not interesting for electric transitions. In the expansions 2.107, the harmonics of odd order do not contribute since any matrix representation of an odd potential in a basis with the same parity will vanish. In addition, if we consider d orbitals all harmonics of order higher than 4 give no contribution since the d orbital set has rank 4.

The general crystal field theory considers a central cation and negative charges surrounding it. An excellent treatment can be found in ref. [24] and [72]. The case in which those charges have positive sign is readily considered just by reversing the sign of the crystal field potential, hence of the crystal field parameters. Therefore, in the following discussion, the ordering of the levels in energy would be inverted.

Octahedral symmetry

The even harmonics of V_{cr} of order 2 are the set Y_2^m for $|m| \leq 2$. The perfect site shown in Fig. 2.20 has octahedral symmetry, point group O_h. Using Mulliken notation [75], in O_h the set spans the irreducible representation e_g and t_{2g}. The totally symmetric irreducible representation is noted as a_{1g}, hence they give no contribution to the energy. For the harmonics of order 4, Y_4^m for $|m| \leq 4$ (G representation in SO_3) we get the irreducible components a_{1g}, e_g, t_{1g} and t_{2g}. Hence, the linear combination that spans the

[1] A list of spage group symmetries can be found on page xxxiii.

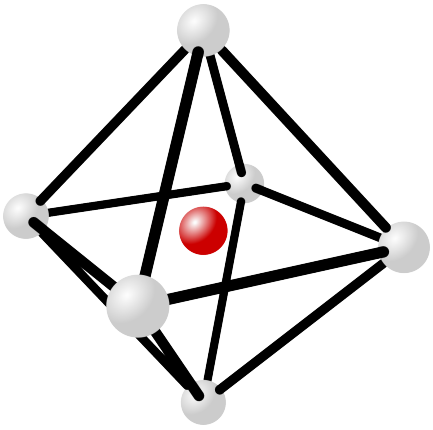

Figure 2.20: Ion in octahedral symmetry. The surrounding charges are located at $(0, d, d)$, $(0, -d, -d)$, $(0, d, -d)$, $(0, -d, d)$, $(0, 0, d)$ and $(0, 0, -d)$ with d the distance from the central ion.

totally symmetric representation a_{1g} does contribute to the total energy, following the series $G \to A_{1g}$. This combination is found to be

$$V_o = x^4 + y^4 + z^4 - \frac{3}{5}r^4 \ . \tag{2.109}$$

Under such a potential, the five-fold degenerate single-electron d orbitals splits into a two-fold degenerate e_g levels and three-fold degenerate t_{2g} levels. They are commonly expressed as the linear combinations $d_{x^2-y^2}$, d_{z^2} for e_g and d_{xy}, d_{xz} and d_{yz} for t_{2g}. By convention, the overall splitting of a single d electron under V_o is set equal to $10Dq$, where q is the electronic change and the factor D can be derived *ab initio* using self-consistent electronic calculations. Then, since the "centre of gravity" of the sum of all the energies of the terms must remain unperturbed, we obtain

$$\Delta E_{e_g} = 6Dq \quad \text{and} \quad \Delta E_{t_{2g}} = -4Dq \ . \tag{2.110}$$

Following a simple argument, one could notice that the orbitals of the e_g electrons are directed toward the vertices of the octahedron, *i.e.*, toward the ligands, while those of the t_{2g} electrons avoid these regions. Because of the Coulomb repulsion, the latter result to be more stable than the others. When it comes to many-electron configurations, two cases are considered. In the first one, called "weak field" case, we have $V_o \ll e^2/r_{ij}$. The crystal field splitting is calculated on the many-electron term-symbols, *i.e.*, one has to first find the symmetry of each term and then apply the crystal field operator to find their respective energies. The ground states for d electrons in weak field approximation are summarised in Tab. 2.1. The opposite case, the "strong field" case, the crystal field splitting parameter $10Dq$ is large enough to destroy the LS coupling of the ion. The electronic configuration is determined by the occupation numbers of the single-electron t_{2g} and e_g orbitals. The Coulomb interaction energies are evaluated afterwards by finding the Slater parameters for a t_{2g}-e_g basis. The two pictures become of course equivalent for intermediate field strength. A representation of the splitting of the electron levels as a function of the crystal field parameter is given by the Tanabe-Sugano diagram [76]. In these diagrams, the energy splitting of the terms is given as a function of the ratio $10Dq/B$ where the Racah parameter $B = \frac{9F^2+5F^4}{441}$ [77] is used instead of the single Slater parameters.

The crystal field parameter Dq is related to the coefficient of the branch $G \to A_{1g}$, usually denoted X_{40} [23, 72]. It gives the scaling between the d spherical harmonics of the SO_3 representations and the

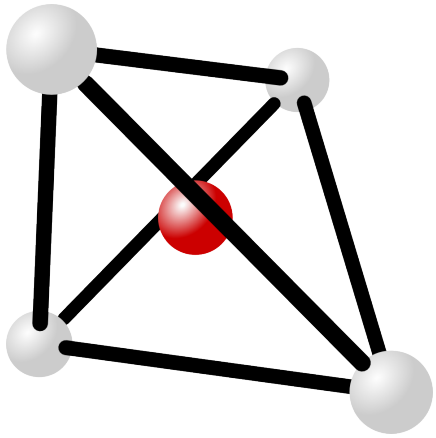

Figure 2.21: Ion in tetrahedral symmetry. The surrounding charges are located at $(-d/2, -d/2, -d/2)$, $(d/2, d/2, -d/2)$, $(d/2, -d/2, d/2)$ and $(-d/2, d/2, d/2)$, with d the edge of the cube.

octahedral orbitals represented as a_{1g} in O_h. It results is given by

$$X_{40} = \frac{\sqrt{30}}{18} 10Dq \ . \tag{2.111}$$

The tetrahedral symmetry (point group T_d, Fig. 2.21) can be easily analysed by comparison with the octahedral symmetry. The crystal field potential is identical in form to that of V_o: the only difference resides in a change of sign. Hence, the splitting of the orbitals is the same but with inverted ordering in energy, *i.e.*, e orbitals will lie lower in energy with respect to the t_2 orbitals. The value of the crystal field parameters can be estimated from the octahedral case by purely geometrical arguments. The Y_4^0 Legendre polynomial that occurs in the expansion of V_o is proportional to $\cos(\theta)_i$, the azimuthal angle of the coordinates of the surrounding charges. Therefore, while for an octahedron we have $|\cos(\theta_i)| = 1$ for the charges along $\hat{z}$ and $|\cos(\theta_i)| = 0$ for the charges in the $\hat{x}\hat{y}$ plane, for a tetrahedron we have $|\cos(\theta_i)| = \sqrt{3}/3$ for all the charges. In addition, if we consider a full cube around the ion, *i.e.*, two conpenetrating tetrahedrons we have to double the potential. It follows that

$$Dq_{\text{octahedral}} = -\frac{9}{4} Dq_{\text{tetrahedral}} = -\frac{9}{8} Dq_{\text{cube}} \ . \tag{2.112}$$

Tetragonal distortion

One of the most common deviations from the perfect octahedral crystal lattice is the tetragonal distortion (Fig. 2.22). In this case the complex contains four identical ligands arranged in a square at whose centre the ion is placed. Above and below the plane, the two other ligands are placed at different distances with respect to the previous four or are of different chemical nature. In both cases we obtain a distorted octahedron with symmetry D_{4h}. The tetragonal field V_t can be expressed as a perturbation on the octahedral field V_o. This field is given by the second and fourth order linear combinations of the spherical harmonics that now "survive" the symmetry operations in D_{4h}, while they were previously eliminated in O_h. The new series to be considered are $G \rightarrow E_g \rightarrow A_{1g}$ and $D \rightarrow E_g \rightarrow A_{1g}$. The additional crystal field parameters are Ds and Dt. Descending in symmetry from O_h to D_{4h}, the e_g orbitals splits into a_{1g} and b_{1g}, while the t_{2g} orbitals splits into b_{2g} and two-fold degenerate e_g. The perturbation on the energy

Table 2.1: Ground states in weak octahedral field for d electrons [24].

Ground state of the free ion	Octahedral states and energies in Dq-units
$d^1\ {}^2D$	${}^2T_{2g}(-4),\ {}^2E_g(+6)$
$d^2\ {}^3F$	${}^3T_{1g}(-6),\ {}^3T_{2g}(+2),\ {}^3A_{2g}(+12)$
$d^3\ {}^4F$	${}^4A_{2g}(-12),\ {}^4T_{2g}(-2),\ {}^4T_{1g}(+6)$
$d^4\ {}^5D$	${}^5E_g(-6),\ {}^5T_{2g}(+4)$
$d^5\ {}^6S$	${}^6A_{1g}(0)$
$d^6\ {}^5D$	${}^5T_{2g}(-4),\ {}^5E_g(+6)$
$d^7\ {}^4F$	${}^4T_{1g}(-6),\ {}^4T_{2g}(+2),\ {}^4A_{2g}(+12)$
$d^8\ {}^3F$	${}^3A_{2g}(-12),\ {}^3T_{2g}(-2),\ {}^3T_{1g}(+6)$
$d^9\ {}^2D$	${}^2E_g(-6),\ {}^2T_{2g}(+4)$

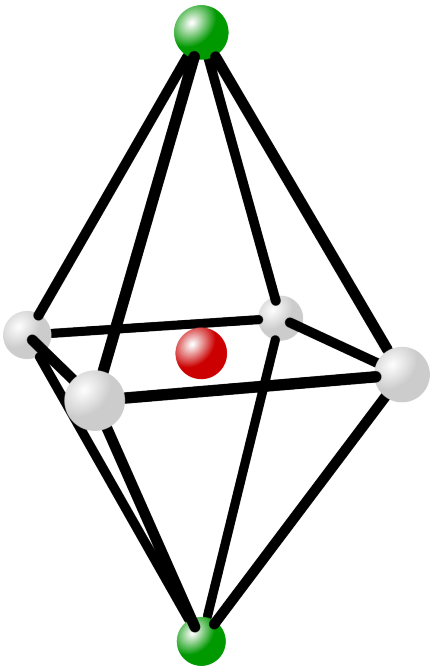

Figure 2.22: Ion in octahedral symmetry with tetragonal distortion. The surrounding charges are located at $(0, d, d)$, $(0, -d, -d)$, $(0, d, -d)$, $(0, -d, d)$, $(0, 0, d + \delta)$ and $(0, 0, -d - \delta)$ with d the distance from the central ion in octahedral symmetry and δ the tetragonal distortion.

Table 2.2: Energy of the single-electron $3d$ orbitals in strong tetragonal field

Symmetry	Energy in X-terms	Energy in D-terms	Orbitals
b_{1g}	$1/\sqrt{30}X_{400} - 1/\sqrt{42}X_{420} - 2/\sqrt{70}X_{220}$	$6Dq + 2Ds - Dt$	$d_{x^2-y^2}$
a_{1g}	$1/\sqrt{30}X_{400} + 1/\sqrt{42}X_{420} + 2/\sqrt{70}X_{220}$	$6Dq - 2Ds - 6Dt$	d_{z^2}
b_{2g}	$-2/3\sqrt{30}X_{400} + 4/3\sqrt{42}X_{420} - 2/\sqrt{70}X_{220}$	$-4Dq + 2Ds - Dt$	d_{xy}
e_g	$-2/3\sqrt{30}X_{400} - 2/3\sqrt{42}X_{420} + 1/\sqrt{70}X_{220}$	$-4Dq - Ds + 4Dt$	d_{xz} d_{yz}

Table 2.3: High-spin and low-spin parameters for $3d^4$ to $3d^7$ configurations in strong octahedral field

Configurations	High-spin	Low-spin	$10Dq$ (D)	Exchange (J)	J/D
$3d^4$	$t_{2g+}^3\ e_{g+}^1$	$t_{2g+}^3\ t_{2g-}^1$	1D	$3J_{te}$	3
$3d^5$	$t_{2g+}^3\ e_{g+}^2$	$t_{2g+}^3\ t_{2g-}^2$	2D	$6J_{te} + J_{ee} - J_{tt}$	~ 3
$3d^6$	$t_{2g+}^3\ e_{g+}^2\ t_{2g-}^1$	$t_{2g+}^3\ t_{2g-}^3$	2D	$6J_{te} + J_{ee} - 3J_{tt}$	~ 2
$3d^7$	$t_{2g+}^3\ e_{g+}^2\ t_{2g-}^2$	$t_{2g+}^3\ t_{2g-}^3\ e_{g+}^1$	1D	$3J_{te} + J_{ee} - 2J_{tt}$	~ 2

of the terms is

$$\begin{aligned} \Delta E_{a_{1g}} &= -2Ds - 6Dt \quad \Delta E_{b_{1g}} = 2Ds - Dt \\ \Delta E_{b_{2g}} &= 2Ds - Dt \quad \Delta E_{e_g} = -Ds + 4Dt\ . \end{aligned} \tag{2.113}$$

The same treatment for "weak" and "strong" crystalline fields used for the octahedral symmetry must be followed also in this case. In addition, Tanabe-Sugano diagrams for D_{4h} are readily available.

The crystal field parameters Dq, Dt and Ds are related to the coefficients of the branches $G \to A_{1g} \to A_{1g}$, $G \to E_g \to A_{1g}$ and $D \to E_g \to A_{1g}$. The branching goes from SO_3 to O_h to D_{4h}. They are indicated by X_{400}, X_{420} and X_{220}. It follows that:

$$X_{400} = 6\sqrt{30}Dq - \frac{7}{2}\sqrt{30}Dt\ , \quad X_{420} = -\frac{5}{2}\sqrt{42}Dt\ , \quad X_{220} = -\sqrt{70}Ds\ . \tag{2.114}$$

The energies of single-electron orbitals in strong tetragonal field are summarised in Tab. 2.2, in terms of both X values and D values.

High-spin/low-spin transition

Going back to a simple "strong" octahedral crystalline field, the d electrons fill the t_{2g} and e_g orbitals, starting from the former as they are lower in energy. Following Hund's rules [23], the first three electrons fill the three t_{2g} orbitals with the same spin. At this point, the fourth one can either occupy a t_{2g} orbital with opposite spin or maintain the same spin of the others and move to a higher-energy e_g orbital. In the first case, the energy increase is given by the exchange splitting derived by the Coulomb interaction of the two electrons occupying the same orbital. This energy is given by the Slater exchange parameters. In the second case, there is no exchange interaction to be considered but clearly the increase in energy is given by the crystal field parameter $10Dq$. The first is a high-spin configuration, since the total spin of the system results to be $4 \times 1/2 = 2$, while the second one is a low spin configuration, with total spin $3 \times 1/2 - 1/2 = 1$. The determination of the ground state depends on the relative strength of the crystal field versus the exchange. Tab. 2.3 summarises high-spin and low-spin states for $3d^4$ to $3d^7$ configurations.

Table 2.4: Direct product table for the O_h point group. Square brackets [ ] are used to indicate antisymmetrized products of a degenerate representation with itself.

	A_1	A_2	E	T_1	T_2
A_1	A_1	A_2	E	T_1	T_2
A_2		A_1	E	T_2	T_1
E			$A_1 + [A_2] + E$	$T_1 + T_2$	$T_1 + T_2$
T_1				$A_1 + E + [T_1] + T_2$	$A_2 + E + T_1 + T_2$
T_2					$A_1 + E + [T_1] + T_2$

2.4.4 Spin-orbit coupling

For $3d$ electrons, the value of the spin-orbit coupling constant λ is small enough to be treated as a perturbation and does affect the validity of the LS coupling scheme. The main effect of the spin-orbit coupling is the departure from the spin-only value of 2 of the Landé factor and the observation of spin-forbidden absorption bands. In fact, these transitions are observed only because of the mixing of states that would differ by $\Delta S = 1$ and would not make suitable initial and final state of an electric dipole transition.

In an octahedral field, the spin momentum branches to the group T_{1g}. In the case of weak spin-orbit coupling, the states are not scrambled and only the states with symmetry Γ for which $\Gamma \cdot T_{1g} \cdot \Gamma$ contains the irreducible representation A_{1g} will show first-order multiplet separation. For example, for a single d electron, the e_g states are not going to split, while the t_{2g} will. In the case of intermediate spin-orbit coupling, additional spin moments symmetry must be considered in order to find the basis of wavefunctions. The octahedral basis (for either weak or strong crystalline field) must be multiplied by the T_{1g} group. The new irreducible representation of the so-called double group must then be coupled following their symmetry in order to find the new set of states. For example, a single d electron e_g state will branch like $e_g \rightarrow \Gamma_8(e_g)$ and the t_{2g} states wil branch like $t_{2g} \rightarrow \Gamma_8(t_{2g}) + \Gamma_7(t_{2g})$. Hence, the Γ_7 state will not interact, while the two Γ_8 will interact at second order. The energies of the various states are found to be

$$\begin{aligned} E(\Gamma_7) &= -4Dq + \lambda \ , \\ E[\Gamma_8(t_{2g})] &= -4Dq + \sqrt{3/2}\lambda \cot(\theta) \ , \qquad \text{and} \\ E[\Gamma_8(e_g)] &= 6Dq - 1/2\lambda \cot(\theta) \ , \qquad \text{where} \\ \tan(2\theta) &= \frac{-\sqrt{6}\lambda}{10Dq + 1/2\lambda} \ . \end{aligned} \tag{2.115}$$

When the parameter λ becomes stronger than the crystal field, it will eventually completely supplant the octahedral field in determining L. The free-ion functions will be recovered and J will be a good quantum number. Even at intermediate spin-orbit strength, the wavefunctions of the states are hybridized and the expectation value of the L and S quantum number will differ. In fact, the usual "quenching" of the orbital angular momentum for d wavefunctions is reduced and the material will exhibit a finite value (even if small) of L, which will have to be taken into account.

2.4.5 X-ray absorption with atomic multiplets

The electric dipole transition yields the selection rules $\Delta J = \pm 1, 0$ and $\Delta M = q$, as discussed in sec. 2.4.1. They are only valid in the SO_3 representation of the $3d$ orbitals: in other symmetries it is necessary to

determine which matrix elements for the transition between an initial state and a final state will not end up being zero. Using group theory, this is a relatively easy task, since it is possible to find the irreducible representation of the dipole operator, $\Gamma_{\rm dip}$. Given an initial state with symmetry $\Gamma_{\rm i}$, the matrix element for the transition to the final state with symmetry Γ_f will not be zero only if the bracket $\langle\Gamma_{\rm i}|\Gamma_{dip}|\Gamma_f\rangle$ contains the totally symmetric representation A_1. This is equivalent to asking for the direct product $\Gamma_{\rm i}\otimes\Gamma_{\rm dip}$ to contain $\Gamma_{\rm f}$ or, equivalently, that the direct product $\Gamma_{\rm i}\otimes\Gamma_{\rm f}$ contains $\Gamma_{\rm dip}$. This rule is a generalisation of the even-odd symmetries rule for optical transitions discussed in sec. 2.4.1.

For example, in O_h symmetry, the electric dipole operator spans the irreducible representation T_{1u}. We can refer to the table of direct product Tab. 2.4 to find that the only allowed transitions are

$$\begin{aligned} &A_1 \to T_1 \ , \\ &A_1 \to T_2 \ , \\ &E \to T_1, T_2 \ , \\ &T_1 \to A_1, E, T_1, T_2 \ , \\ &T_2 \to A_2, E, T_1, T_2 \ . \end{aligned} \tag{2.116}$$

The spin parity of the initial and final state must be opposite, *i.e.*, an odd $_u$ state can be excited only to an even $_g$ state. This is the usual situation in $2p$ XAS, where an odd p electron is excited to an even d state. Descending in symmetry and moving towards half-full shell configurations, the number of possible transitions increases considerably. Usually the transition going from the ground state of the complex only to an excited state are considered. As mentioned before, the spin-orbit coupling can scramble the energy levels and give non zero transition probability between states where the transition would otherwise be forbidden in its absence. A typical example are the interband transitions in the visible range in transition metal oxides. These transitions, usually consisting in the forbidden $t_{2g} \to e_g$ transitions, gives the colour of transition metal complexes.

2.4.6 Charge transfer

Charge transfer effects are due to the interaction between the central ion orbitals and the ligands orbitals. In both initial state and final state, the ionic configuration is mixed with other configurations characterised by a different number of electrons [73, 78–82]. The Hamiltonian is based on the Anderson impurity model, which is, in turn, based on the Hubbard model. A review of this model can be found in ref. [73], which we wil follow in the next sections.

Initial state effects

The Anderson impurity model [78, 80, 83] describes a localised $3d$ state which interacts with delocalised electrons in the valence band. It employs the second quantisation creation and annihilation operators $a^\dagger$ and a for a specific electron. In this formalism, the hopping of an electron from the $3d$ states to an empty state in the valence band with wave vector $\vec{k}$ is given by $|\phi_0 a^\dagger_{3d} a_{v\vec{k}}\rangle$, where ϕ_0 is the ground state of the system. The number of electrons in the $3d$ and in the valence band is given by $\sum a^\dagger_{3d} a_{3d}$ and $\sum a^\dagger_v a_v$, respectively. The Hamiltonian for this system should take into account the $\vec{k}$ dependence of the valence band, but this complication is usually removed by considering a zero-bandwidth band. In more complex calculations, the bandwidth can be taken into account considering a summation of δ-like states at different

energies to recreate the entire valence band. In the simple case the Hamiltonian is given by

$$\begin{aligned}\mathcal{H}_{\text{AIM}} = \epsilon_{3d} a^\dagger_{3d} a_{3d} + U_{dd} a^\dagger_{3d} a_{3d} a^\dagger_{3d} a_{3d} + \epsilon_k a^\dagger_v a_v + t_{vd}(a^\dagger_{3d} a_v + a^\dagger_v a_{3d}) \\ + (\text{Slater integrals}) + (\text{Crystal field}) + (\text{Spin-orbit coupling}) \ . \end{aligned} \tag{2.117}$$

$$\tag{2.118}$$

The four terms are the $3d$ states energy, the correlation between $3d$ states, the energy of the valence band and the coupling of the $3d$ states with the valence band. U_{dd} is the Hubbard U interaction between $3d$ electrons that must be added to the other two-electron integrals such as the Slater parameters F^2 and F^4. U_{dd} must be taken into account in this case because of the interactions between the $3d$ orbitals of the ion and the pseudo-$3d$ valence band of the ligands. t_{vd} is the transfer integral between the $3d$ orbitals and the valence band. It can be symmetry dependent, yielding different values for $3d$ states belonging to different point groups. The effect of this Hamiltonian is to form a ground state combination of two configurations, namely $3d^N$ and $3d^{N+1}\underline{L}$, where with $\underline{L}$ we indicate the presence of an additional hole in the ligand band. In addition, the energy difference between the lowest levels in the $3d^N$ and the $3d^{N+1}$ multiplets Δ must be considered. If the hopping parameter is set to zero or Δ is too high, no charge transfer is observed, and the configurations don't mix. On the other hand, if the hopping is turned on and/or the energy barrier is reduced, the energy of the lowest state of the $3d^N$ configuration is further lowered. This state would still maintain the initial symmetry but will also feature an increasing $3d^{N+1}\underline{L}$ character. In some cases the charge transfer effect can lead to a transition to a different ground state symmetry if the $3d^{N+1}\underline{L}$ dominates, resulting for example in an high spin-low spin transition.

The energy difference between the two configuration in the initial state is given by $\Delta_{\text{i}} = \Delta$.

Final state effects

The final state Hamiltonian includes a core hole in the $2p$ levels. Therefore, its energy and interactions must be taken into account. A parameter U_{pd}, similar to U_{dd}, is introduced: this is the Hubbard potential for the overlap of the $2p$ and $3d$ orbitals that must be considered together with the Slater integrals F^2, G^1 and G^3. The additional terms in the Hamiltonian 2.117 are

$$\begin{aligned}\mathcal{H}_{2p} = \epsilon_{2p} a^\dagger_{2p} a_{2p} + U_{pd} a^\dagger_{3d} a_{2p} a^\dagger_{2p} a_{3d} + \epsilon_k a^\dagger_v a_v \\ + (\text{Slater integrals}) + (\text{Crystal field}) + (\text{Spin-orbit coupling}) \ . \end{aligned} \tag{2.119}$$

In this case, the configurations that are mixed are $3d^{N+1}$ and $3d^{N+2}\underline{L}$. The crystal field, Δ and the hopping parameters values have been reported to be slightly smaller in the final state than in the initial state. This is due to a small compression of the $3d$ wave function caused by the presence of a core hole. However, this contraction is not as significant as one would expect because of the extra $3d$ electron in the final state that increases the screening of the core hole.

The energy difference between the two configurations in the final state is given by

$$\Delta_{\text{f}} = \Delta_{\text{i}} + U_{dd} - U_{pd} \ . \tag{2.120}$$

In many cases U_{pd} is 1-2 eV larger than U_{dd}.

X-ray absorption vs x-ray Photoelectron Spectroscopy and charge transfer effects

In XAS experiments, the charge transfer model implies calculation of the initial and final state energies for both the considered configurations. Since U_{dd} and U_{pd} are close to each other, the ordering in energy of the final states is not changed. Additional dipole transition matrix elements must also be considered, theoretically forming small satellite peaks in the spectra. However, these peaks are rarely observed.

The initial state Hamiltonian in its simplest form is given by the matrix

$$\mathcal{H}_{\mathrm{i}} = \begin{vmatrix} 0 & t_{\mathrm{i}} \\ t_{\mathrm{i}} & \Delta_{\mathrm{i}} \end{vmatrix} , \tag{2.121}$$

while the final state Hamiltonian has the form

$$\mathcal{H}_{\mathrm{f}} = \begin{vmatrix} 0 & t_{\mathrm{f}} \\ t_{\mathrm{f}} & \Delta_{\mathrm{f}} \end{vmatrix} . \tag{2.122}$$

The initial state can be written as $\Phi_{\mathrm{i}} = \sin\alpha[3d^N] + \cos\alpha[3d^{N+1}]$ and the final state as a bonding state $\Phi_{\text{f-b}} = \sin\beta[2p^5 3d^{N+1}] + \cos\beta[2p^5 3d^{N+2}]$ and an antibonding state $\Phi_{\text{f-ab}} = -\cos\beta[2p^5 3d^{N+1}] + \sin\beta[2p^5 3d^{N+2}]$. The intensity of the main peak is then $\cos^2(\beta-\alpha)$ and the intensity of the satellite peak is $\sin^2(\beta-\alpha)$. For $U_{pd} \sim U_{dd}$ and $t_{\mathrm{i}} \sim t_{\mathrm{f}}$ this results in $\alpha \approx \beta$, hence the satellite peak has no intensity. The main effect of the charge transfer is given by the contraction (expansion) of the multiplets structure for positive (negative) Δ. Consider two multiplet states split by an energy δ and a charge transfer state positioned Δ above the lowest one. The charge transfer energy for the highest state is then $\Delta - \delta$. In first approximation, the energy gain for these two state is given by

$$\begin{aligned} E_{low} &= \frac{1}{2}\Delta - \frac{1}{2}\sqrt{\Delta^2 + 4t} \ , \\ E_{high} &= \frac{1}{2}\Delta - \delta - \frac{1}{2}\sqrt{(\Delta-\delta)^2 + 4t} \ . \end{aligned} \tag{2.123}$$

Therefore, the lowest energy level has the highest gain, and the overall multiplet structure is compressed. [73, 84, 85]

In $2p$ x-ray photoelectron spectroscopy (XPS) the energy levels in the final state are different with respect to XAS experiments. This is due to the fact that the $2p$ electron is excited into a high energy state (*i.e.* into vacuum) instead of into an empty $3d$ orbital [86, 87]. This means that the final state energy does not have the additional term due to U_{dd}. Therefore, we have

$$\Delta_{\mathrm{f}} = \Delta_{\mathrm{i}} - U_{pd} \ . \tag{2.124}$$

and the ordering of the levels is inverted. The satellite peak gains intensity because of the final state hybridization. The different energy levels and the transitions are schematised in Fig. 2.23.

References

[1] R. Hasegawa. *Temperature and compositional dependence of magnetic bubble properties of amorphous Gd-Co-Mo films.* Journal of Applied Physics, **46**(12):5263, 1975. doi:http://dx.doi.org/10.1063/1.321596.

[2] V. J. Minkiewicz, P. A. Albert, R. I. Potter & C. R. Guarnieri. *Magnetic properties of sputter*

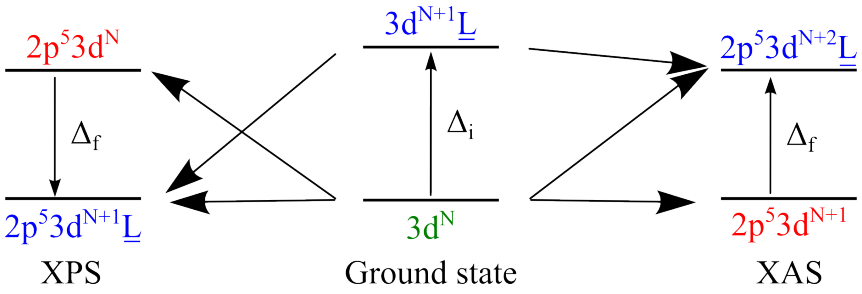

Figure 2.23: Schematic of 2*p* XAS and XPS energy levels and transitions. In XPS experiments (left) the charge transfer configuration lies below the $3d^N$ configuration. The situation is opposite for the levels in XAS experiments. From ref. [69].

deposited GdCoCu amorphous bubble films. AIP Conference Proceedings, **29**(1):107, 1976. doi: http://dx.doi.org/10.1063/1.30538.

[3] B. Huth. *Calculations of stable domain radii produced by thermomagnetic writing.* IBM Journal of Research and Development, **18**(2):100, March 1974. ISSN 0018-8646. doi:10.1147/rd.182.0100.

[4] Y. Mimura, N. Imamura & T. Kobayashi. *Magnetic properties and curie point writing in amorphous metallic films.* Magnetics, IEEE Transactions on, **12**(6):779, Nov 1976. ISSN 0018-9464. doi:10.1109/TMAG.1976.1059199.

[5] X.-G. Zhang & W. H. Butler. *Large magnetoresistance in bcc* Co/MgO/Co *and* FeCo/MgO/FeCo *tunnel junctions.* Phys. Rev. B, **70**:172407, Nov 2004. doi:10.1103/PhysRevB.70.172407.

[6] J. Slonczewski. *Current-driven excitation of magnetic multilayers.* Journal of Magnetism and Magnetic Materials, **159**(1–2):L1 , 1996. ISSN 0304-8853. doi:http://dx.doi.org/10.1016/0304-8853(96)00062-5.

[7] B. Balke, G. Fecher & C. Felser. *New Heusler compounds and their properties.* In C. Felser & G. H. Fecher, eds., *Spintronics*, pp. 15–43. Springer Netherlands, 2013. ISBN 978-90-481-3831-9. doi:10.1007/978-90-481-3832-6_2.

[8] T. Graf, C. Felser & S. S. Parkin. *Simple rules for the understanding of Heusler compounds.* Progress in Solid State Chemistry, **39**(1):1 , 2011. ISSN 0079-6786. doi:http://dx.doi.org/10.1016/j.progsolidstchem.2011.02.001.

[9] T. Graf, J. Winterlik, L. Müchler, G. H. Fecher, C. Felser & S. S. Parkin. *Magnetic Heusler Compounds.* vol. 21 of *Handbook of Magnetic Materials*, chap. 1, pp. 1 – 75. Elsevier, 2013. doi:10.1016/B978-0-444-59593-5.00001-5.

[10] H. van Leuken & R. A. de Groot. *Half-metallic antiferromagnets.* Phys. Rev. Lett., **74**:1171, Feb 1995. doi:10.1103/PhysRevLett.74.1171.

[11] H. Kurt, K. Rode, P. Stamenov, M. Venkatesan, Y.-C. Lau, E. Fonda & J. M. D. Coey. *Cubic Mn_2Ga thin films: Crossing the spin gap with ruthenium.* Phys. Rev. Lett., **112**:027201, Jan 2014. doi:10.1103/PhysRevLett.112.027201.

[12] M. Oogane, T. Kubota, Y. Kota, S. Mizukami, H. Naganuma, A. Sakuma & Y. Ando. *Gilbert magnetic damping constant of epitaxially grown co-based heusler alloy thin films.* Applied Physics Letters, **96**(25):252501, 2010. doi:http://dx.doi.org/10.1063/1.3456378.

[13] M. Oogane, T. Kubota, H. Naganuma & Y. Ando. *Magnetic damping constant in co-based full heusler alloy epitaxial films.* Journal of Physics D: Applied Physics, **48**(16):164012, 2015.

[14] E. Şaşıoğlu. *Nonzero macroscopic magnetization in half-metallic antiferromagnets at finite temperatures.* Phys. Rev. B, **79**:100406, Mar 2009. doi:10.1103/PhysRevB.79.100406.

[15] X. Hu. *Half-metallic antiferromagnet as a prospective material for spintronics.* Adv. Mater., **24**(2):294, 2012. ISSN 1521-4095. doi:10.1002/adma.201102555.

[16] M. Hakimi, M. Venkatesan, K. Rode, K. Ackland & J. M. D. Coey. *The zero-magnetization Heusler ferrimagnet.* Journal of Applied Physics, **113**(17):17B101, 2013. doi:10.1063/1.4794744.

[17] C. Hordequin, J. Nozières & J. Pierre. *Half metallic NiMnSb-based spin-valve structures.* Journal of Magnetism and Magnetic Materials, **183**(1–2):225 , 1998. ISSN 0304-8853. doi:http://dx.doi.org/10.1016/S0304-8853(97)01072-X.

[18] J. Caballero, A. Reilly, Y. Hao, J. Bass, W. P. Jr., F. Petroff & J. Childress. *Effect of deposition parameters on the CPP-GMR of NiMnSb-based spin-valve structures.* Journal of Magnetism and Magnetic Materials, **198–199**(0):55 , 1999. ISSN 0304-8853. doi:http://dx.doi.org/10.1016/S0304-8853(98)00617-9.

[19] J. E. Hirsch. *Spin Hall effect.* Phys. Rev. Lett., **83**:1834, Aug 1999. doi:10.1103/PhysRevLett.83.1834.

[20] Y. A. Bychkov & E. I. Rashba. *Oscillatory effects and the magnetic susceptibility of carriers in inversion layers.* Journal of Physics C: Solid State Physics, **17**(33):6039, 1984.

[21] J. M. D. Coey. *Magnetism and Magnetic Materials.* Cambrigde University Press, 2010.

[22] S. Blundell. *Magnetism in Condensed Matter.* Oxford Master Series in Condensed Matter Physics. Oxfors University Press, 2001.

[23] R. D. Cowan. *Theory of atomic structure and spectra.* Los Alamos series in basic and applied Sciences. University of California Press, Berkely, 1981.

[24] C. J. Ballhausen. *Introduction to ligand field theory.* McGraw-Hill series in advandec chemistry. McGraw-Hill Book Company, 1962.

[25] A. Aharoni. *Introduction to the Theory of Ferromagnetism.* International Series of Monograph on Physics. Oxford University Press, 1996.

[26] A. H. Morrish. *The Physical Principles of Magnetism.* Wiley-IEEE Press, 2001.

[27] P. Mohn. *Magnetism in the Solid State: An Introduction.* Springer Series in Solid-State Sciences. Springer, 2003.

[28] J. William Fuller Brown. *Micromagnetics.* Wiley, 1963.

[29] A. G. Gurevich & G. A. Melkov. *Magnetization Oscillations and Waves.* CRC Press, 1996.

[30] A. P. Guimarães. *Magnetism and Magnetis Resonance in Solids.* Wiley-Interscience, 1998.

[31] C. P. Slichter. *Principles of Magnetic Resonance.* Springer, 1990.

[32] D. Polder. *On the theory of ferromagnetic resonance.* The London, Edinburgh, and Dublin Philosophical Magazine and Journal of Science, **40**(300):99, 1949. doi:10.1080/14786444908561215.

[33] C. Kittel. *On the theory of ferromagnetic resonance absorption.* Phys. Rev., **73**:155, Jan 1948. doi:10.1103/PhysRev.73.155.

[34] R. Meservey & P. Tedrow. *Spin-polarized electron tunneling.* Physics Reports, **238**(4):173 , 1994. ISSN 0370-1573. doi:http://dx.doi.org/10.1016/0370-1573(94)90105-8.

[35] I. I. Mazin. *How to define and calculate the degree of spin polarization in ferromagnets.* Phys. Rev. Lett., **83**:1427, Aug 1999. doi:10.1103/PhysRevLett.83.1427.

[36] K. M. Seemann, V. Baltz, M. MacKenzie, J. N. Chapman, B. J. Hickey & C. H. Marrows. *Diffusive and ballistic current spin polarization in magnetron-sputtered $l1_0$-ordered epitaxial fept.* Phys. Rev. B, **76**:174435, Nov 2007. doi:10.1103/PhysRevB.76.174435.

[37] S. Zhang & Z. Li. *Roles of nonequilibrium conduction electrons on the magnetization dynamics of ferromagnets.* Phys. Rev. Lett., **93**:127204, Sep 2004. doi:10.1103/PhysRevLett.93.127204.

[38] A. Thiaville, Y. Nakatani, J. Miltat & Y. Suzuki. *Micromagnetic understanding of current-driven domain wall motion in patterned nanowires.* EPL (Europhysics Letters), **69**(6):990, 2005.

[39] T. McGuire & R. Potter. *Anisotropic magnetoresistance in ferromagnetic 3d alloys.* Magnetics, IEEE Transactions on, **11**(4):1018, Jul 1975.

[40] K. Ando, Y. Kajiwara, S. Takahashi, S. Maekawa, K. Takemoto, M. Takatsu & E. Saitoh. *Angular dependence of inverse spin˘Hall effect induced by spin pumping investigated in a $Ni_{81}Fe_{19}/Pt$ thin film.* Phys. Rev. B, **78**:014413, Jul 2008. doi:10.1103/PhysRevB.78.014413.

[41] O. Mosendz, J. E. Pearson, F. Y. Fradin, G. E. W. Bauer, S. D. Bader & A. Hoffmann. *Quantifying spin Hall angles from spin pumping: Experiments and theory.* Phys. Rev. Lett., **104**:046601, Jan 2010. doi:10.1103/PhysRevLett.104.046601.

[42] O. Mosendz, V. Vlaminck, J. E. Pearson, F. Y. Fradin, G. E. W. Bauer, S. D. Bader & A. Hoffmann. *Detection and quantification of inverse spin Hall effect from spin pumping in permalloy/normal metal bilayers.* Phys. Rev. B, **82**:214403, Dec 2010. doi:10.1103/PhysRevB.82.214403.

[43] V. Castel, N. Vlietstra, J. Ben Youssef & B. J. van Wees. *Platinum thickness dependence of the inverse spin-Hall voltage from spin pumping in a hybrid yttrium iron garnet/platinum system.* Applied Physics Letters, **101**(13):132414, 2012. doi:http://dx.doi.org/10.1063/1.4754837.

[44] W. Zhang, V. Vlaminck, J. E. Pearson, R. Divan, S. D. Bader & A. Hoffmann. *Determination of the Pt spin diffusion length by spin-pumping and spin Hall effect.* Applied Physics Letters, **103**(24):242414, 2013. doi:http://dx.doi.org/10.1063/1.4848102.

[45] K. Ando, S. Takahashi, K. Harii, K. Sasage, J. Ieda, S. Maekawa & E. Saitoh. *Electric manipulation of spin relaxation using the spin Hall effect.* Phys. Rev. Lett., **101**:036601, Jul 2008. doi:10.1103/PhysRevLett.101.036601.

[46] L. Liu, T. Moriyama, D. C. Ralph & R. A. Buhrman. *Spin-torque ferromagnetic resonance induced by the spin Hall effect.* Phys. Rev. Lett., **106**:036601, Jan 2011. doi:10.1103/PhysRevLett.106.036601.

[47] S. Petit, C. Baraduc, C. Thirion, U. Ebels, Y. Liu, M. Li, P. Wang & B. Dieny. *Spin-torque influence on the high-frequency magnetization fluctuations in magnetic tunnel junctions.* Phys. Rev. Lett., **98**:077203, Feb 2007. doi:10.1103/PhysRevLett.98.077203.

[48] C.-F. Pai, L. Liu, Y. Li, H. W. Tseng, D. C. Ralph & R. A. Buhrman. *Spin transfer torque devices utilizing the giant spin Hall effect of tungsten.* Applied Physics Letters, **101**(12):122404, 2012. doi: http://dx.doi.org/10.1063/1.4753947.

[49] A. Manchon & S. Zhang. *Theory of spin torque due to spin-orbit coupling.* Phys. Rev. B, **79**:094422, Mar 2009. doi:10.1103/PhysRevB.79.094422.

[50] N. Nagaosa. *Anomalous Hall effect –a new perspective–.* Journal of the Physical Society of Japan, **75**(4):042001, 2006. doi:10.1143/JPSJ.75.042001.

[51] N. Nagaosa, J. Sinova, S. Onoda, A. H. MacDonald & N. P. Ong. *Anomalous Hall effect.* Rev. Mod. Phys., **82**:1539, May 2010. doi:10.1103/RevModPhys.82.1539.

[52] M. I. Dyakonov. *Future Trends in Microelectronics: From Nanophotonics to Sensors to Energy.* Wiley-IEEE Press, 2010.

[53] S. Zhang. *Spin Hall effect in the presence of spin diffusion.* Phys. Rev. Lett., **85**:393, Jul 2000. doi:10.1103/PhysRevLett.85.393.

[54] A. Hoffmann. *Spin Hall effects in metals.* Magnetics, IEEE Transactions on, **49**(10):5172, Oct 2013. ISSN 0018-9464. doi:10.1109/TMAG.2013.2262947.

[55] V. E. Demidov, S. Urazhdin, A. B. Rinkevich, G. Reiss & S. O. Demokritov. *Spin Hall controlled magnonic microwaveguides.* Applied Physics Letters, **104**(15):152402, 2014. doi:http://dx.doi.org/10.1063/1.4871519.

[56] Garello Kevin, Miron Ioan Mihai, Avci Can Onur, Freimuth Frank, Mokrousov Yuriy, Blugel Stefan, Auffret Stephane, Boulle Olivier, Gaudin Gilles & Gambardella Pietro. *Symmetry and magnitude of spin-orbit torques in ferromagnetic heterostructures.* Nat Nano, **8**(8):587, Aug 2013. ISSN 1748-3387. doi:http://dx.doi.org/10.1038/nnano.2013.14510.1038/nnano.2013.145.

[57] J.-C. Rojas-Sánchez, N. Reyren, P. Laczkowski, W. Savero, J.-P. Attané, C. Deranlot, M. Jamet, J.-M. George, L. Vila & H. Jaffrès. *Spin pumping and inverse spin Hall effect in platinum: The essential role of spin-memory loss at metallic interfaces.* Phys. Rev. Lett., **112**:106602, Mar 2014. doi:10.1103/PhysRevLett.112.106602.

[58] H. J. Juretschke. *Electromagnetic theory of dc effects in ferromagnetic resonance.* Journal of Applied Physics, **31**(8):1401, 1960. doi:http://dx.doi.org/10.1063/1.1735851.

[59] W. G. Egan & H. J. Juretschke. *Dc detection of ferromagnetic resonance in thin nickel films.* Journal of Applied Physics, **34**(5):1477, 1963. doi:http://dx.doi.org/10.1063/1.1729604.

[60] N. Mecking, Y. S. Gui & C.-M. Hu. *Microwave photovoltage and photoresistance effects in ferromagnetic microstrips.* Phys. Rev. B, **76**:224430, Dec 2007. doi:10.1103/PhysRevB.76.224430.

[61] M. Harder, Z. X. Cao, Y. S. Gui, X. L. Fan & C.-M. Hu. *Analysis of the line shape of electrically detected ferromagnetic resonance.* Phys. Rev. B, **84**:054423, Aug 2011. doi:10.1103/PhysRevB.84.054423.

[62] H. Chen, X. Fan, H. Zhou, W. Wang, Y. S. Gui, C.-M. Hu & D. Xue. *Spin rectification enabled by anomalous Hall effect.* Journal of Applied Physics, **113**(17):17C732, 2013. doi:http://dx.doi.org/10.1063/1.4799248.

[63] J. Bardeen & W. H. Brattain. *The transistor, a semi-conductor triode.* Phys. Rev., **74**:230, Jul 1948. doi:10.1103/PhysRev.74.230.

[64] T. Valet & A. Fert. *Theory of the perpendicular magnetoresistance in magnetic multilayers.* Phys. Rev. B, **48**:7099, Sep 1993. doi:10.1103/PhysRevB.48.7099.

[65] M. Julliere. *Tunneling between ferromagnetic films.* Physics Letters A, **54**(3):225 , 1975. ISSN 0375-9601. doi:http://dx.doi.org/10.1016/0375-9601(75)90174-7.

[66] Parkin Stuart S. P., Kaiser Christian, Panchula Alex, Rice Philip M., Hughes Brian, Samant Mahesh & Yang See-Hun. *Giant tunnelling magnetoresistance at room temperature with MgO (100) tunnel barriers.* Nat Mater, **3**(12):862, Dec 2004. ISSN 1476-1122. doi:http://dx.doi.org/10.1038/nmat1256. 10.1038/nmat1256.

[67] J. C. Slonczewski. *Currents, torques, and polarization factors in magnetic tunnel junctions.* Phys. Rev. B, **71**:024411, Jan 2005. doi:10.1103/PhysRevB.71.024411.

[68] T. Silva & W. Rippard. *Developments in nano-oscillators based upon spin-transfer point-contact devices.* Journal of Magnetism and Magnetic Materials, **320**(7):1260 , 2008. ISSN 0304-8853. doi: http://dx.doi.org/10.1016/j.jmmm.2007.12.022.

[69] F. de Groot. *X-ray absorption and dichroism of transition metals and their compounds.* Journal of Electron Spectroscopy and Related Phenomena, **67**(4):529 , 1994. ISSN 0368-2048. doi:http: //dx.doi.org/10.1016/0368-2048(93)02041-J.

[70] J. J. Rehr & R. C. Albers. *Theoretical approaches to x-ray absorption fine structure.* Rev. Mod. Phys., **72**:621, Jul 2000. doi:10.1103/RevModPhys.72.621.

[71] G. van der Laan & A. I. Figueroa. *X-ray magnetic circular dichroism—a versatile tool to study magnetism.* Coordination Chemistry Reviews, **277–278**(0):95 , 2014. ISSN 0010-8545. doi:http: //dx.doi.org/10.1016/j.ccr.2014.03.018. Following Chemical Structures using Synchrotron Radiation.

[72] P. H. Butler. *Point Group Symmetry Applications: Methods and Tables.* Plenum Press, 1981.

[73] F. de Groot. *Multiplet effects in x-ray spectroscopy.* Coordination Chemistry Reviews, **249**(1–2):31 , 2005. ISSN 0010-8545. doi:http://dx.doi.org/10.1016/j.ccr.2004.03.018. Synchrotron Radiation in Inorganic and Bioinorganic Chemistry.

[74] J. H. van Vleck. *II. energetics of complexes. the magnetic behaviour of regular and inverted crystalline energy levels.* Discuss. Faraday Soc., **26**:96, 1958. doi:10.1039/DF9582600096.

[75] F. A. Cotton. *Chemical Applications of Group Theory.* Wiley-Interscience, 1990.

[76] Y. Tanabe & S. Sugano. *On the absorption spectra of complex ions. I.* Journal of the Physical Society of Japan, **9**(5):753, 1954. doi:10.1143/JPSJ.9.753.

[77] G. Racah. *Theory of complex spectra. I.* Phys. Rev., **61**:186, Feb 1942. doi:10.1103/PhysRev.61.186.

[78] J. Zaanen & G. Sawatzky. *Systematics in band gaps and optical spectra of 3d transition metal compounds.* Journal of Solid State Chemistry, **88**(1):8 , 1990. ISSN 0022-4596. doi:http://dx.doi. org/10.1016/0022-4596(90)90202-9.

[79] T. Jo & G. A. Sawatzky. *Ground state of ferromagnetic nickel and magnetic circular dichroism in Ni 2p core x-ray-absorption spectroscopy.* Phys. Rev. B, **43**:8771, Apr 1991. doi:10.1103/PhysRevB.43.8771.

[80] A. E. Bocquet, T. Mizokawa, T. Saitoh, H. Namatame & A. Fujimori. *Electronic structure of 3d -transition-metal compounds by analysis of the 2p core-level photoemission spectra.* Phys. Rev. B, **46**:3771, Aug 1992. doi:10.1103/PhysRevB.46.3771.

[81] P. Krüger & A. Kotani. *Calculation of core-level photoemission spectra of Mn films on Ag(001).* Phys. Rev. B, **68**:035407, Jul 2003. doi:10.1103/PhysRevB.68.035407.

[82] A. K. Shukla, P. Krüger, R. S. Dhaka, D. I. Sayago, K. Horn & S. R. Barman. *Understanding the 2p core-level spectra of manganese: Photoelectron spectroscopy experiments and Anderson impurity model calculations.* Phys. Rev. B, **75**:235419, Jun 2007. doi:10.1103/PhysRevB.75.235419.

[83] P. W. Anderson. *Localized magnetic states in metals.* Phys. Rev., **124**:41, Oct 1961. doi:10.1103/PhysRev.124.41.

[84] Z. Hu, G. Kaindl, S. Warda, D. Reinen, F. de Groot & B. Müller. *On the electronic structure of Cu(III) and Ni(III) in $La_2Li_{1/2}Cu_{1/2}O_4$, $Nd_2Li_{1/2}Ni_{1/2}O_4$, and Cs_2KCuF_6.* Chemical Physics, **232**(1–2):63 , 1998. ISSN 0301-0104. doi:http://dx.doi.org/10.1016/S0301-0104(98)00096-2.

[85] Z. Hu, C. Mazumdar, G. Kaindl, F. de Groot, S. Warda & D. Reinen. *Valence electron distribution in $La_2Li_{1/2}Cu_{1/2}O_4$, $Nd_2Li_{1/2}Ni_{1/2}O_4$, and $La_2Li_{1/2}Co_{1/2}O_4$.* Chemical Physics Letters, **297**(3–4):321 , 1998. ISSN 0009-2614. doi:http://dx.doi.org/10.1016/S0009-2614(98)01135-X.

[86] O. Gunnarsson & K. Schönhammer. *Electron spectroscopies for Ce compounds in the impurity model.* Phys. Rev. B, **28**:4315, Oct 1983. doi:10.1103/PhysRevB.28.4315.

[87] J. Zaanen, C. Westra & G. A. Sawatzky. *Determination of the electronic structure of transition-metal compounds: 2p x-ray photoemission spectroscopy of the nickel dihalides.* Phys. Rev. B, **33**:8060, Jun 1986. doi:10.1103/PhysRevB.33.8060.

Chapter 3

Experimental methods

3.1 Material deposition

The deposition of thin films of various materials is one of the key steps in the fabrication of solid state devices.

In this work, two different physical vapour deposition techniques have been used for the deposition of thin films of various materials: electron beam (e-beam) evaporation and sputtering.

3.1.1 Sputtering

During the sputtering process [1], a plasma (in our case an Ar plasma) is created in a high vacuum chamber and is confined by a magnet. The plasma consists of electrons, positive ions (Ar^+), and neutral atoms (Ar) [2]. The sample is placed on a grounded platter while a target consisting of the material to be deposited (sputtered) is placed in front of it.

In rf sputtering a rapidly-oscillating electric field is created. The electrons in the plasma have very small mass and are accelerated by it while heavy ions cannot react fast enough. Electrons hit the target and build up negative charge ($\pm 100\,\mathrm{V}$). This process is called self-biasing. The established dc field attracts Ar^+ ions towards the target. They knock off the atoms of the material by momentum transfer and the ejected molecules are deposited on the sample surface. In this process, secondary electrons are also produced by the various collisions and end up into the plasma. The rf plasma is usually employed if the target is an insulating material, where the application of a dc bias is not possible.

In dc sputtering, the plasma is created using a dc electric field between the target and the sample and heavy ions are accelerated towards the target by the same field. Free electrons are accelerated in the opposite direction.

In both cases, the plasma is sustained by impact ionization of the gas atoms by the accelerated electrons. When the equilibrium between the production of newly ionised atoms and the loss of them because of the bombardment is reached, a steady-state discharge is sustained.

The efficiency of the sputtering deposition is estimated by two parameters, both depending on the process gas and target material combination. The first is the sputter yield S, which is the number of sputtered atoms produced per bombarding ion atom. Hence

$$S = \frac{N_{\text{Emitted Particles}}}{N_{\text{Incident Ions}}} \ . \tag{3.1}$$

The second parameter is the secondary electron yield, *i.e.*, the number of secondary electrons produced

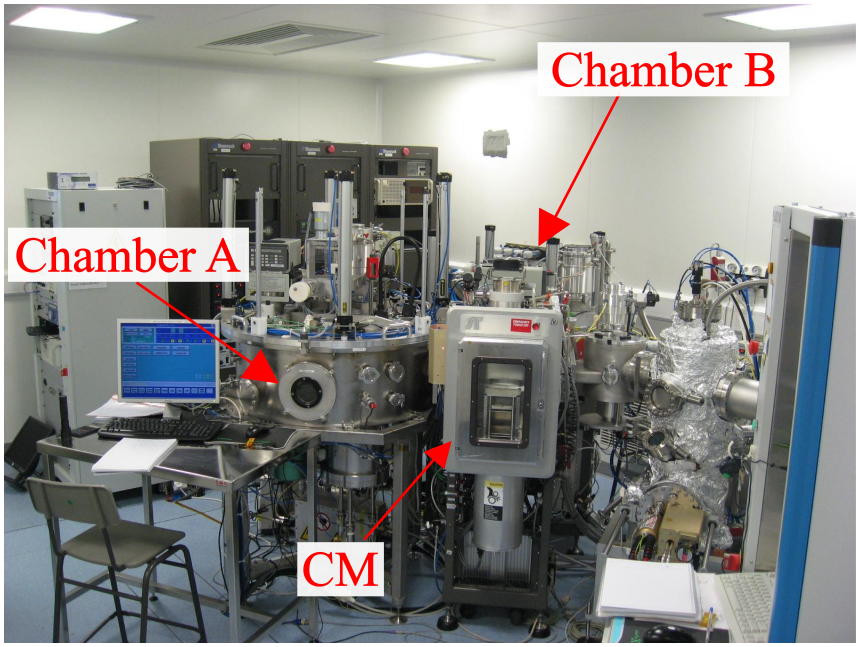

Figure 3.1: The Shamrock sputtering tool.

per bombarding ion [3, 4].

The rate of ionization of the process gas atoms can be greatly increased by using a magnetron. Permanent magnets are placed behind the target in order to create a magnetic field between the outer parts and the centre of the target. The electrons are trapped in this field and the ionization rate and the sputtering yield are enhanced. This also allows the use of lower gas pressure, which improves the directionality of the deposition due to less scattering of the target atoms on their way to the substrate. The main drawback is the non uniform consumption of the target surface, caused by the higher electronic concentration in the regions where the magnetic field is parallel to the surface (erosion region).

The substrate is placed very close to the target ($\sim$ 10 cm) in order to collect all ejected particles. The particles can have energies of up to 50 eV, much more than evaporated atoms, which improves their surface mobility on the sample surface. This results in a better surface homogeneity, but the deposition is highly non-directional because of the scattering of the target atoms with the ions in the plasma which can cause problems during lift-off processes. This issue can be addressed with an undercut resist profile (see sec. 3.2.1). The uniformity, crystallinity and roughness of the film and the rate of deposition are heavily influenced by the process parameters, such as the temperature of the substrate during deposition, the Ar gas pressure and the power injected. A high temperature usually favours the crystallization of the film, but it can lead to a rough surface profile. A high value of gas flow can result in rougher surfaces and greatly decrease the deposition rate. On the other hand, a very low Ar pressure does not allow the plasma to be ignited and sustained.

We used a high vacuum magnetron sputtering "Shamrock" cluster tool located in a class 10 000 clean room. The overall system consists of three interconnected deposition chambers: A, B and D. Chamber A is the original "Shamrock" high vacuum sputtering machine, Chamber B is a Plassys MP9000 sputter deposition system and Chamber D is a custom-built ultra high vacuum e-beam evaporation/sputter deposition system. Chamber D has never been used for the realisation of the samples of this work, hence it is not discussed further. Chamber C is only used for sample transfer. The entire tool is pictured in Fig. 3.1.

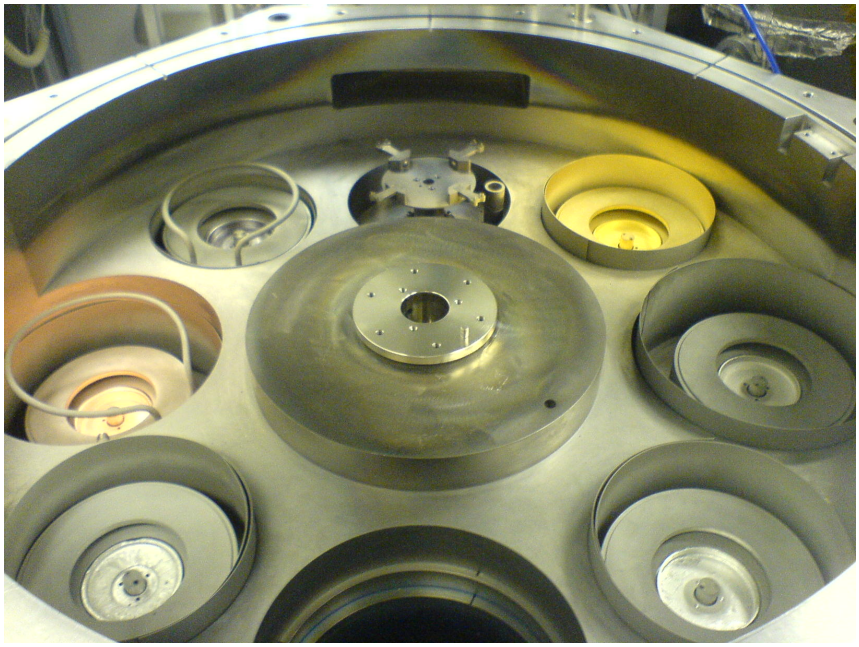

Figure 3.2: Inside view of the "Shamrock" Chamber A. On the left and the right there are the six guns, while at the top there is the wafer loader and at the bottom the ion gun.

Chamber A

The "Shamrock" Chamber A system consists of three interconnected chambers: a process module (PM) also called Chamber A (Fig. 3.2), a transfer module (TM) and a cassette module (CM). The latter is the load lock and can store up to 16 4″ wafers. The relatively small dimensions of this unit make it easier to pump it down to high vacuum quickly using a turbo molecular pump. The TM hosts the robot arm that allows the transfer of the wafers into the different chambers. It is connected to its own turbo molecular pump and CTI water pump. The PM is equipped with six three-inch Series III magnetron guns and a ion milling gun used for substrate pre-cleaning and ion etching (see sec. 3.3.2). It is possible to process 4 wafers at the same time and the deposition can be totally automated. The high vacuum is maintained by a Varian turbo molecular pump and an Oxford water pump. The base pressure is $<8 \times 10^{-8}$ Torr, while typical deposition pressures are of the order of 1-5 $\times 10^{-3}$ Torr. All six guns can operate in dc mode, while gun 5 and 6 can also operate in rf mode and a pulsed dc power supply can be used on gun 2 and 6. A motorised turntable with rotating planets is placed above the six guns. Each planet features permanent magnets that produce a uniform magnetic field of 5 mT, which is used to set the easy anisotropy axis during the growth of in-plane magnetoresistance devices. The growth rate of the individual targets must be calibrated by measuring the thickness of the material deposited in a known amount of time on a test sample. Some examples are given in Tab. 3.1.

Chamber B

Chamber B (Fig. 3.3) is a sputtering system that consists of a total of 9 guns, divided into two clusters with three guns each (Fig. 3.4), two Target Facing Target (TFT) guns (Fig. 3.5) and an rf gun. The six cluster guns are equipped with 500 W dc power supplied while the TFT and rf guns use a 300 W rf power supply with a matching circuit. The substrate can be heated up to 580 °C during the deposition. The heating is achieved by thermal radiation from a Pt wire carrying current. The system is pumped down by

Table 3.1: Typical deposition parameters for some materials used in this work

Material	Deposition chamber	Power	Ar flow (sccm)	Growth rate ($Å\,s^{-1}$)
Pt	A (dc gun)	100 W	40	0.16
Cu	A (dc gun)	100 W	25	0.48
Zr	A (dc gun)	100 W	40	0.16
$Ir_{22}Mn_{78}$	A (dc gun)	100 W	25	0.17
Ta	B (rf gun)	20 W	15	0.38
Ta	B (dc gun)	38 W	20	0.22
W	B (dc gun)	42 W	30	0.26
MgO	B (tft gun)	75 W	15	0.09
CrRu	B (rf gun)	20 W	15	0.32
Mn_2Ga	B (dc gun)	50 W	30	0.4
Ru	B (dc gun)	13 W	30	0.11
$Co_{20}Fe_{60}B_{20}$	B (dc gun)	33 W	30	0.1

Figure 3.3: Inside view of Chamber B. In clockwise direction, starting from the bottom left there are: one TFT gun, a cluster with three dc guns, the other TFT gun, the wafer loader, the other dc cluster and the rf gun.

Figure 3.4: Picture of a cluster in Chamber B with three dc guns.

a turbo molecular pump and a CTI water pump. The base pressure is about 3×10^{-8} Torr. The growth rate of the targets must be calibrated using the same procedure employed in Chamber A (see previous section).

3.1.2 Evaporation

The evaporation process consists in heating up a small quantity of the desired material to its evaporation temperature, in order to form a vapour of molecules that are deposited on the sample surface. At every temperature, there exists an equilibrium pressure of vapour above the liquid or solid material. The deposition rate will be directly proportional to the vapour pressure and reasonably high deposition rates ($1\,\text{Å}\,\text{s}^{-1}$) can be achieved with values $> 10^{-3}$Torr. A quartz crystal monitor is used to keep track of the deposition rate and layer thickness. The target material can be heated by an electrical current (thermal evaporation) or by accelerating an electron beam towards its surface (e-beam evaporation). This deposition method is highly directional, making it ideal for lift-off processes. In order to achieve this directionality and the best uniformity of the deposited layer, the distance between the target and the sample must be maximised.

Thermal evaporation is the simplest type of process: two high-current feed-throughs are used to supply current to a crucible, usually made of tungsten or molybdenum. The desired material is stored inside the crucible.

E-beam evaporation employs highly energetic electrons to heat the material. The material to be evaporated can be placed directly into a water cooled copper pocket or it can be stored into a cup-shaped crucible. The most common materials for crucibles are tungsten, molybdenum, alumina, graphite and boron nitride.

We used a Temescal FC2000 evaporation tool (Fig. 3.6). It consists of a source chamber and a product chamber. The source chamber is a high vacuum chamber with a 6 kW (10 kV, 0.6 A) electron beam gun with 6 pockets and a 2 kW (5 V, 400 A) thermal evaporation source, a Veeco ion gun and an infrared

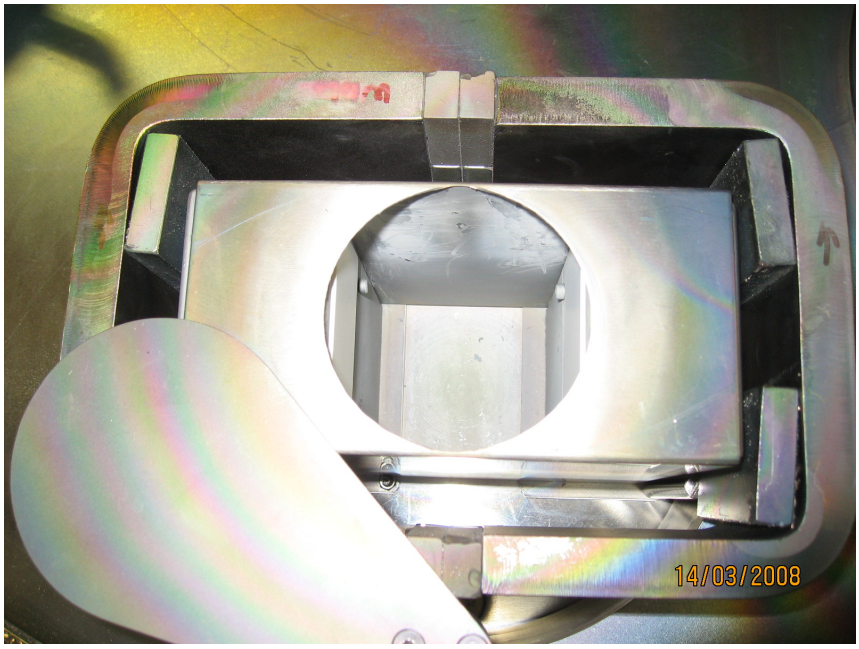

Figure 3.5: Picture of a TFT gun in Chamber B.

Figure 3.6: The Temescal FC2000 evaporation tool.

heater. The chamber is equipped with an Edwards XDS scroll pump for rough pumping and a CTI cryopump that allows a base pressure of 3×10^{-7} Torr to be reached. Typical deposition pressures are around 2×10^{-6} Torr. The product chamber is the upper portion of the source chamber enclosed by a bell-jar lid and contains the rotatable substrate holder, a water cooled deposition rate monitor and a thermocouple. A liquid nitrogen substrate cooler can also be mounted if necessary. An isolation valve separates the two chambers, allowing load-lock operations. An e-beam sweep controller allows to control the amplitude, frequency and position of the e-beam on the material pocket. In this way it is possible to choose to heat and melt the entire surface of the target material or focus the beam in one spot. The pocket selector rotates the water cooled multi-pocket copper turntable which holds the source materials (with or without crucibles). The distance between the source and the substrate is 70 cm, which makes it possible to achieve high uniformity and flatness of the deposited layer. The 3 cm dc ion source uses Ar plasma to clean or etch the substrate before the deposition (see sec. 3.3.2). Typical deposition rates are of the order of 0.5-1 $\text{Å}\,\text{s}^{-1}$.

We used the Temescal FC2000 evaporator mainly to deposit electrical contact pads on Hall bars and top contacts of MTJs and to pattern the antennas for FMR and ST-FMR measurements. We usually deposit a trilayer of Ti (5 nm)/Cu (80 nm)/Au (20 nm). The Cu layer constitutes the main part of the stack, while Ti is used to improve its adhesion and the final cap of Au protects the contact from oxidation. In addition, the Au layer improves the contact resistance with picoprobes in FMR and ST-FMR experiments. The ion gun has been used to gently clean the surface to improve the adhesion of the deposited materials and to remove oxide layers on the surface. See sec. 3.5.1 for details on the Hall voltage measurements, sec. 2.3.9 for the structure of MTJs and sec. 3.6.1 and 3.6.2 for the FMR and ST-FMR measurements.

3.2 Lithography methods

Lithography is a patterning method used to recreate a desired design on a surface. There are different types of lithography, distinguished by the way in which the pattern is created. UV lithography relies on ultra-violet light and transfers patterns typically in the micron-scale in a one-shot process via a mask. E-beam lithography is a direct write method which employs an electron beam and it is capable of producing features with better definition and of reaching the nanometric scale. All lithography techniques draw the desired design on a thin layer of resist, that has to be developed afterwards in order to reveal the pattern. Only UV lithography has been used in this project.

3.2.1 Resist types

A resist is a chemical compound used to transfer a pattern to the substrate onto which it is uniformly deposited. It usually consists of a mix of polymers and solvent and is sensitive to UV light or to an electron beam [5]. After the exposure, it must be developed using a specific chemical agent.

There are different types of resists, mainly divided into

- positive resists. Exposure to UV light or electron beams breaks the chains of polymers and makes it more soluble in the developer. After the the development, exposed areas of resist are removed.
- negative resists. Exposure to UV light or electron beams strengthen the chains of polymers by cross polymerization and makes it less soluble in the developer. The exposed areas of resist are left behind after the development.

The most important parameters that characterise a resist are sensitivity and resolution. The sensitivity is defined as the amount of light in $\text{mJ}\,\text{cm}^{-2}$ that is needed to start the chemical process that breaks or

strengthens the polymer chains. Lower sensitivity translates to lower exposure times, but it also becomes easier to have overexposure issues. The resolution is the minimum feature size achievable and it is given by the length of the polymer chain.

The deposition of the resist layer (or layers) is achieved through spin coating and successive soft-baking on a hot plate. The sample surface must be previously cleaned with isopropyl alcohol and acetone and placed in the centre of a rotating disk, called a chuck, where it is kept in place by a vacuum system. A few drops of resist are deposited on the surface and the sample is then spun for a certain amount of time. Typical spinning velocities are between 2000 and 5000 RPM, while the spinning time should be in excess of 30 s in order to achieve the best uniformity of the coating. The sample is then soft baked on a hot plate in order to evaporate the remaining solvent. If the sample has to undergo ion milling (see sec. 3.3.2) or aggressive chemical etching, it can be useful to post-bake the resist after the exposure to harden it and make it more durable. This is called a hard bake and it is performed at higher temperature and longer than for a soft bake.

3.2.2 UV lithography

Ultraviolet lithography exploits the UV light beam of a laser or a fluorescence lamp. Typical source wavelengths are 436 nm (g-line), 405 nm (h-line) and 365 nm (i-line) [6]. Mercury arc lamps are the most commonly used sources. Selected areas of an UV-sensitive resist are exposed by the radiation in order to create the desired pattern. A mask consisting of a transparent glass slab with the desired pattern etched in chromium on one side is put between the UV source and the sample with the Cr side towards the sample. The resist is irradiated only where the chromium has been removed. This procedure allows the whole sample to be patterned in a single exposure, but there is no flexibility in the pattern design, as a new mask is needed for each pattern. The resolution R, defined as the minimum feature size that can be exposed, depends on several parameters, the most important ones being the resolution of the features on the mask, exposure system quality and the photoresist used. It is given by

$$R = \kappa \frac{\lambda}{\mathrm{NA}} \ , \tag{3.2}$$

where κ is a parameter that takes into account all the process-related factors, λ is the wavelenght of the UV light and NA is the numerical aperture of the exposure system. The system quality is directly related to the characteristics of the optics and the source. Photoresists had been described in the previous section. In this context, alterations of the desired pattern can derive mainly from resist inhomogeneities, focussing problem due to a not perfectly flat surface or proximity effects. The latter are due to the unwanted overlapping of the irradiated areas for two features too close to each other. At the edges of an exposure window the dose of radiation is lower than the critical value needed to achieve complete exposure of the polymers, but the sum of the doses coming from neighbouring features can cause unwanted exposure of the area in between. The situation is schematised in Fig. 3.7. This problem can be addressed by proximity effect corrections in the pattern design.

A mask aligner is used to align the masks to the substrate. Since a complete process usually involves several steps, each pattern must be aligned with the previous ones in order to obtain the desired result. Alignment is a crucial aspect to multilevel device fabrication. The simplest type of UV lithography is contact lithography. In this case, the sample is pressed against the mask during exposure. Here the resolution is limited by the feature size of the mask used. The mask is held chrome side down in a frame below a microscope objective. The coated sample is mounted on a movable sample holder and it is aligned with respect to the mask using the microscope and three micropositioners for the $\hat{x}$, $\hat{y}$ and $\hat{\theta}$ (rotation)

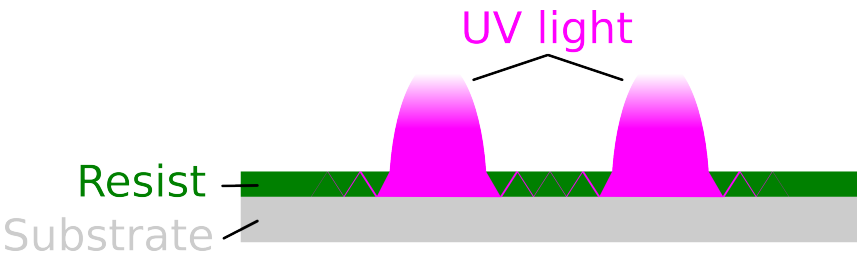

Figure 3.7: Proximity effect due to backscattering of light in UV lithography.

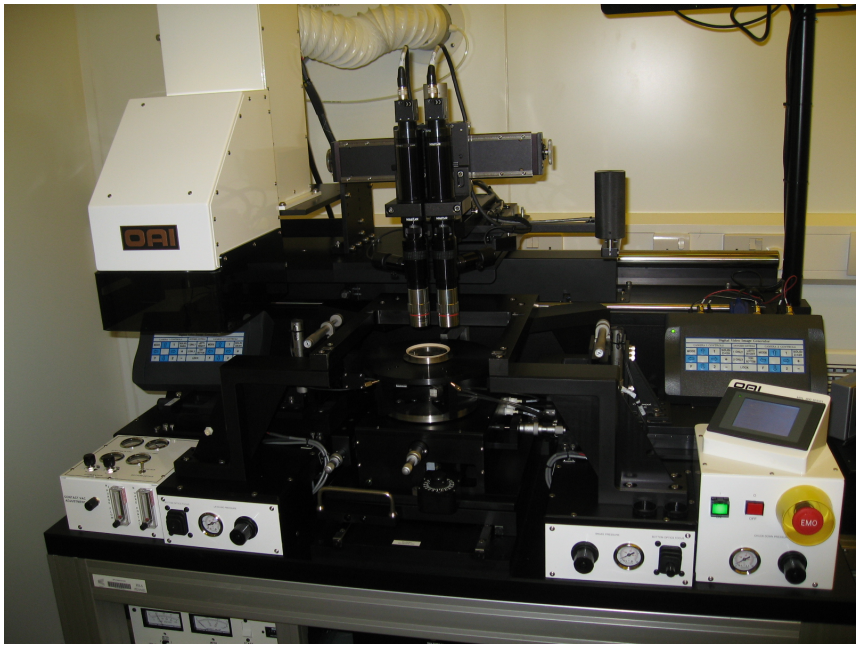

Figure 3.8: The OAI Model 800 CE mask aligner for UV lithography.

axis. Vacuum is used to keep the sample in place. Once aligned, the sample is pushed towards the mask and the contact with the mask is kept with vacuum (contact vacuum). At this point, the lamp assembly shifts on top of the sample and exposes it for the desired amount of time. The contact vacuum is the most important parameter to be maximised in order to obtain the best resolution, since a gap between the mask and the sample will cause diffraction effects. However, non-uniformities in the thickness of the resist and imperfect flatness of the mask and the sample will affect the contact vacuum. A drawback of this type of systems is the fact that the direct contact between the mask and the sample causes the formation of defects on the mask if it has to be used several times.

We used an OAI Model 800 CE mask aligner (Fig. 3.8) to perform contact photolithography. It is possible to expose up to 6" wafers using a Hg lamp. The intensity of the light is constant at $\sim$20 mW cm^{-2}. The tool is kept in a class 100 clean room.

In this work we have used UV lithography for the fabrication of three types of sample: Hall bars, MTJs and ST-FMR bars. The Hall bars have dimensions of 60 µm^2 × 20 µm^2 and 50 µm^2 × 10 µm^2. ST-FMR bars are similar to the other Hall bars but they don't need transverse contacts. On the other hand, coupled microstrips must be used as electrical contacts for GS (ground-signal) picoprobes in order to match the impedance of the source (50 Ω). The MTJ samples consist of two rows of six pillars, three of them with dimensions 4 µm^2 × 12 µm^2 and the other three with dimensions 4 µm^2 × 4 µm^2. Details of the

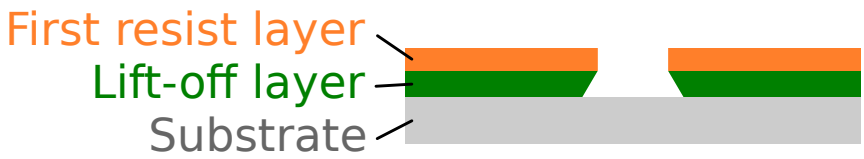

Figure 3.9: Undercut profile obtained using a double layer of resist.

fabrication of the devices are given in Appendix B, while details on the different resists used can be found in Appendix A.

3.2.3 Mask fabrication

The masks we have used are 4" soda-lime glass masks coated with CrO (8 nm)/Cr (62 nm)CrO (30 nm) layers. They have been previously spin coated with AZ1500 resist, a positive type of resist, and soft-baked.

They have been patterned using an Heidelberg DWL66 laser direct writing system. This system is kept in the class 100 clean room and it is equipped with a laser interferometer stage. The blank, resist-coated mask is kept in place at the centre of the stage using vacuum and it is moved under a laser write-head. The shutter of the write-head is opened and closed while the mask is moved accordingly to the desired design to be patterned. The design is created using layout editor such as CleWin. After exposure, the resist is developed and the chrome layer is etched using a ceric ammonium nitrate ($(NH_4)_2Ce(NO_3)_6$) and nitric acid (HNO_3) solution. This type of exposure is a serial process, hence it requires a great amount of time. The system is capable of producing mask with minimum feature size of 1 µm. During this work we fabricated all the necessary masks for the patterning of Hall bars and MTJs.

3.3 Patterning methods

In this section we will discuss the techniques used for transferring the desired pattern onto the sample surface after the lithography process.

Two methods have been used for the sample patterning: lift-off and ion milling.

3.3.1 Lift-off

The lift-off process is presented in Fig. 3.10. After the exposure and development of a resist layer with a lithographic technique, the desired material is deposited onto the sample. Subsequently the resist and the material deposited on top of it are removed in order to reveal the pattern. The shape of the resist cross section and the deposition technique greatly influence this process. In particular, it is important to obtain an undercut resist profile, as shown in Fig. 3.9, in order to have a discontinuous layer of deposited material and facilitate its removal. Thermal evaporation has better directionality while sputtering tends to cover the resist sidewalls homogeneously, making it more difficult to perform the lift-off. On the other hand, the higher kinetic energy of the sputtered atoms improves the adhesion of the material on the surface.

It is possible to use more than one layer of resist to achieve the desired resist profile. Usually this means using two different layers of resists in order to get an undercut profile, which makes it easier to lift-off the deposited material. The second layer is called lift-off Layer (LOL) and it requires a lower dose of radiation to be completely exposed with respect to the primary layer. The corresponding resist profile obtained after the development is shown in Fig. 3.9. The thickness of the deposited material should not exceed the thickness of the LOL resist.

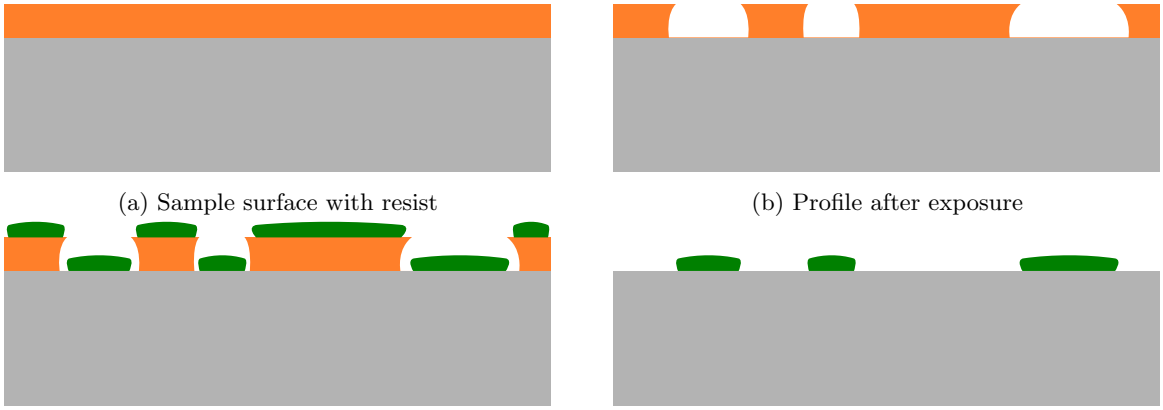

(a) Sample surface with resist

(b) Profile after exposure

(c) Material deposition

(d) Lift-off

Figure 3.10: Steps of the lift-off process.

The samples are immersed in the appropriate solvent or remover according the the resist employed. The use of a heated (up to 80 °C) ultrasonic bath may help the lift-off process, but it may lead to structural collapse, such as in the case of very high aspect ratio features. As a rule of thumb, the thickness of the resist must be at least 3 times the thickness of the deposited materials for an easy lift-off.

3.3.2 Ion milling

Ion milling is used to physically remove the portions of the sample surface that are not protected by the resist. In this case the desired material must be deposited before the lithography steps. Similar to sputtering, an Ar plasma is generated in a high vacuum chamber (see sec. 3.1.1). Unlike sputtering, the Ar^+ ions are accelerated towards the rotating sample and knock off atoms from the unprotected areas of the surface. This process has very high directionality. To prevent heating the resist (and thus making it difficult to remove), the sample stage is water-cooled and the etch process is carried out in steps with wait times. The etching process can be monitored by ion mass spectroscopy: measuring the mass of the ejected ionised atoms it is possible to recognise which layer is being etched and stop the process after the desired layers. After the main etching is completed, another step of etching at low angle of incidence is usually performed, in order to remove some of the re-deposited material from the sidewalls of the resist and improve the resist removal. Unlike the lift-off, ion milling allows for better surface flatness and sharp edges of the features. It is the technique of choice for the realisation of multilayer devices.

We used a Millatron ion milling tool (Fig. 3.11 and 3.13) that consists of a vacuum chamber, a rotatable water-cooled sample stage and an end-point detector. The plasma is generated by a CCR Technology COPRA DN250 source with an rf power supply (1.2 kW at 13.6 MHz) and a dc power supply to control the Helmholtz coils that generate the magnetic field, typically providing 2.5 A of current). A cryogenic pump is used and the base pressure is typically 2×10^{-7} Torr, while the operating pressure is $\sim 1 \times 10^{-4}$ Torr. It is a filament-less, rf inductively-coupled plasma source with a single-turn excitation electrode. The plasma is ignited by the creation of a pressure pulse, and its resonance excitation is achieved with the application of a dc transverse magnetic field of about 2 mT. An rf power of 300 W is used to create the plasma. The sample can be tilted between 0 and 90° with respect to the beam. The Hiden end-point detection (EPD) system is used to monitor the etching stage. It consists of an ion milling probe and an rf head with an amplifier. The ion milling probe is made of an energy filter, a quadrupole mass spectrometer and a secondary electron multiplier detector. The ions entering the spectrometer are deflected accordingly

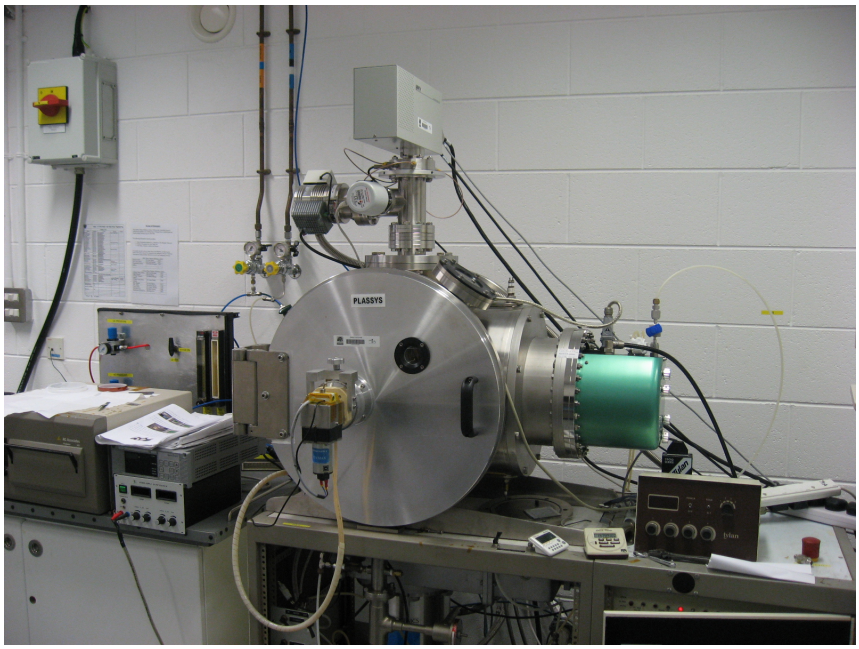

Figure 3.11: The Millatron ion milling tool.

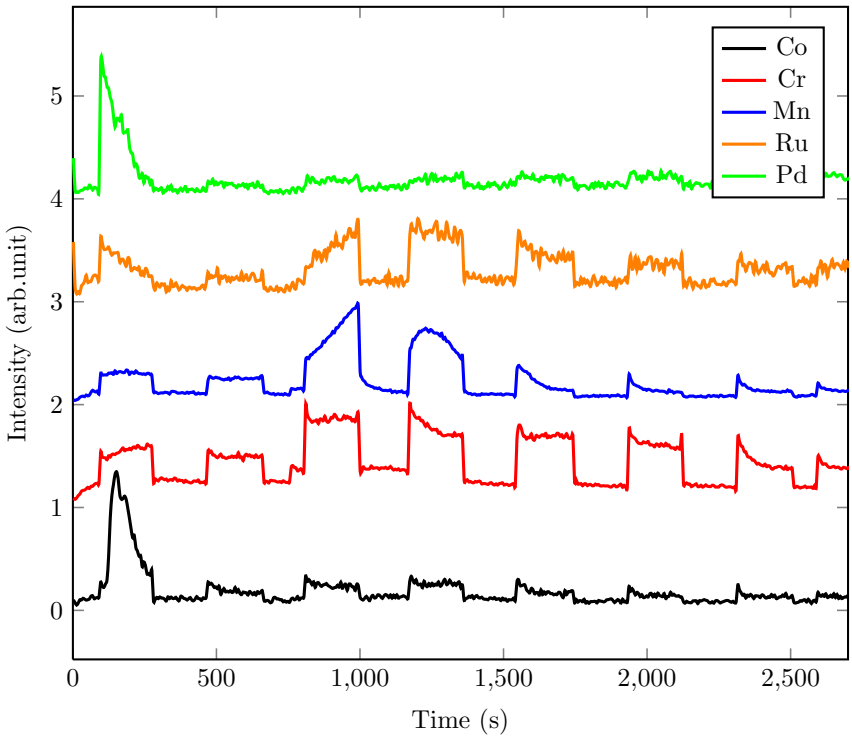

Figure 3.12: Hiden end-point-detection data from the milling of an MRG-based MTJ stack (see sec. B). The etching has been performed in steps with wait times in order to avoid the overheating of the resist. This is the reason why the curves have this particular shape.

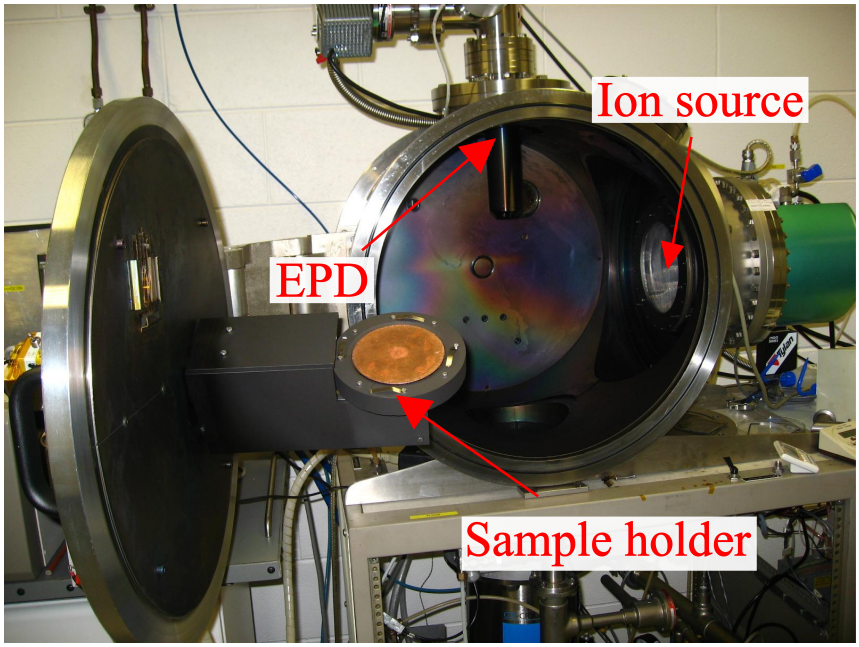

Figure 3.13: The Millatron ion milling tool chamber. On the right there is the ion gun that provides the accelerated Ar^+ particles. At the top of the chamber there is the inlet for the end-point detection.

to the mass to charge ratio m/q, and at each interval of the rf scan only one value of m/q is allowed to exit the quadrupole. The signal is collected in the multiplier detector and analysed. Fig. 3.12 shows an example of EPD data.

3.4 X-ray-based characterisation techniques

3.4.1 Light sources and monochromators

A synchrotron storage ring circulates electrons or positrons at near the speed of light. Each time these particles are accelerated, they emit x-rays. The photons emitted are monochromatised and directed towards the sample. The absorption spectra consists of the quantity of absorbed photons as a function of the beam energy. We can tune the incoming beam energy to coincide with the energy of a particular absorption edge in the material that we wish to investigate. In this work we investigated the absorption at the K-edge of Mn (6539 eV), Ru (22 117 eV) and Ga (10 367 eV) and the L-edges of Mn (649.9 eV and 638.7 eV).

X-ray absorption experiments require a source of photons with high flux, brilliance, stability and polarisation degree, as well as high energy resolution since the beam energy is swept across the absorption edge. Obviously these characteristics cannot be found in tabletop setups but are limited to synchrotron facilities. At a synchrotron facility, ultrarelativistic electrons are accelerated and injected into a storage ring, in which they circulate, producing synchrotron radiation in the form of x-rays, but without gaining further energy. A synchrotron light source also usually contains a linear accelerator (linac) and another synchrotron ring (booster): their purpose is to generate and successively accelerate the electrons before sending them to the storage ring. The radiation is projected at a tangent to the circular path and sent to experimental stations called beamlines. They can be situated in correspondence to a bending magnet at the curved portions of the storage ring or at an insertion device situated in a straight section of the ring.

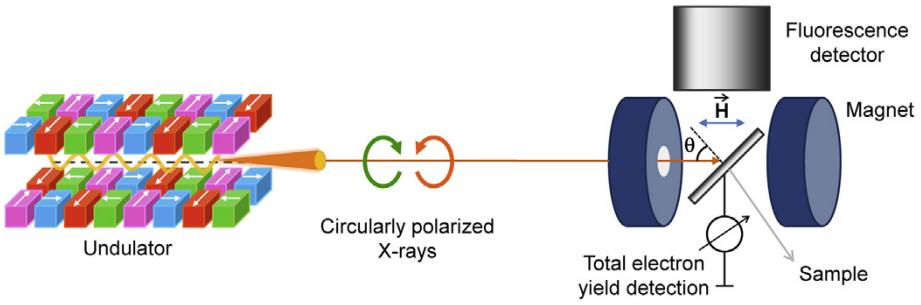

Figure 3.14: Schematic of an experimental XMCD setup at a beamline. From ref. [7].

The two configurations provide different spectra and energies of the x-rays. The radiation produced by a bending magnet is highly polarised. In an off-plane view of the electron beam in the storage ring, the particles follow an elliptical orbit, while in an in-plane view they follow only a horizontal path. Hence, the produced radiation is linearly polarised if collected in the plane of the orbit or left or right circularly polarised if collected below or above the plane. Unfortunately, the photon flux falls off very fast when moving away from the orbit plane and full circular polarisation is obtained only when it vanishes. On the contrary, the use of an insertion device such as a wiggler or an undulator, allows for the production of very high intensity and highly polarised x-rays. Wigglers and undulators consists of a periodic array of bending magnets that force the electrons to follow an oscillatory path. A helical or elliptical polarisation undulator (EPU) features a magnetic field vector that rotates around the central axis as a particle travels through the device. This results in a spiralling trajectory of the electrons and the generation of circularly polarised light. The peak energy of the x-rays depends on the vertical distance between the magnet arrays ("gap") while the left or right circular polarisation depends on the relative position ("phase") of the arrays. This way, changing between the two polarisation can take only seconds. A beamline setup with an undulator is shown in Fig. 3.14.

In a beamline, the light beam is monochromatised based on diffraction gratings (for soft x-rays) or crystals (for hard x-rays), using the Bragg condition $n\lambda = 2d\sin\theta$, where d is the grating spacing or the crystal lattice parameter. The x-rays are then focussed in the optics hutch and sent to the experimental chamber, where the sample lies. Soft x-rays reflect on mirrors and monochromators at grazing incidence, so that the polarisation is nearly completely preserved. In the experimental chamber, high magnetic fields can be obtained by using superconducting magnets, usually employed in a split coil design to apply the field parallel to the wave vector of the beam. In some stations it is possible to apply the field perpendicular to the wave vector in order to perform transverse field measurements.

3.4.2 X-ray absorption spectroscopy (XAS) and x-ray magnetic circular dichroism (XMCD)

X-ray magnetic circular dichroism (XMCD) is an optical technique based on x-ray absorption spectroscopy (XAS) performed with left and right circularly polarised light [7–10].

In the case of transition metal ions, XAS and XMCD are performed at the L-edges. They correspond to the excitations of a photoelectron from the $2p$ shell to the $3d$ shell. The energy required for this excitation to occur is of the order of 1 keV in Mn. At $T = 0$ K, the initial state is the ground state as determined by Hund's rules. Depending on the electronic configuration there can be several different final states. The energy difference between them is determined by many factors, including the spin-orbit coupling. As the spin-orbit coupling in the $2p$ shell is orders of magnitude higher than the one in the $3d$

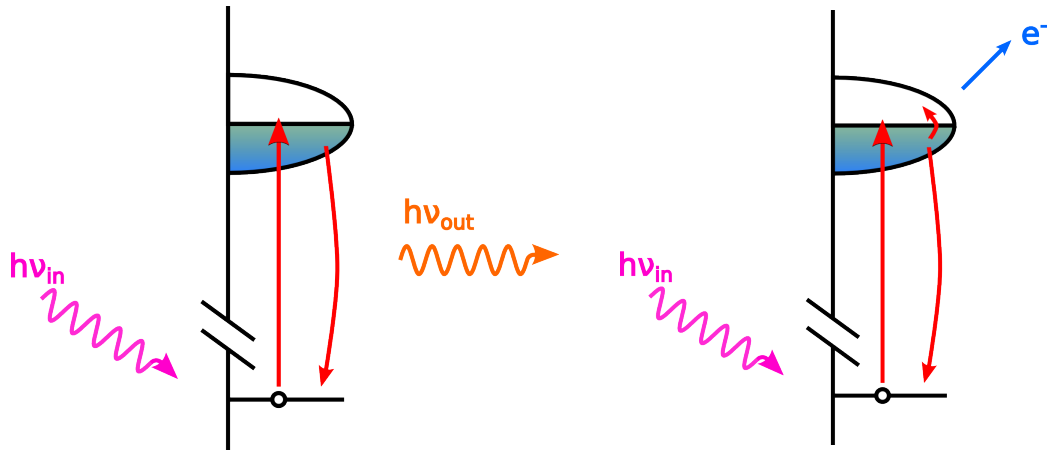

(a) Fluorescence (b) Total electron yield (TEY)

Figure 3.15: Different methods for measurements of XAS spectra.

shell (tens of eV vs tens of meV) we have two main manifolds; one corresponding to a $2p$ core hole in the $^2P_{3/2}$ state, the other corresponding to a hole in the $^2P_{1/2}$. These are the L_3 and L_2 absorption edges, respectively. For an isolated atom, the ratio between the intensities of the L_3 and L_2 absorption peaks should be equal to 2, but hybridization of the states, $3d$ spin-orbit coupling and other effects such as the charge transfer can drastically alter this value [11].

The dichroism in x-ray absorption is well described by the two step model. The first step is the absorption of the x-ray photon itself. Since the photons are circularly polarised, they carry angular momentum (± 1 for right and left polarisation respectively). For the simple LS coupling scheme, the probability of transition is derived using the dipole selection rules

$$\Delta L = \pm 1 \ , \quad \Delta M_L = q \ , \quad \Delta S = 0 \quad \text{and} \quad \Delta M_S = 0 \ , \tag{3.3}$$

where $q = \pm 1, 0$ for right/left circularly polarised light and linearly polarised light, respectively. Therefore, the absorption is different in the two cases. We will indicate the different XAS spectra as μ_0, μ_1, μ_{-1}, respectively. The XMCD spectra consists of the subtraction of the spectra $(\mu_1 - \mu_{-1})$. It is possible to determine the values of the angular momentums for the sample using the total mean XAS area and the XMCD L_3 and L_2 edge areas, applying the sum rules

$$\langle L \rangle_z = -2N_\mathrm{h} \cdot \frac{\int (\mu_1 + \mu_{-1})}{\int (\mu_1 + \mu_0 + \mu_{-1})} \ , \tag{3.4}$$

$$\langle S \rangle_{\mathrm{eff},z} = \langle S \rangle_z + \frac{7}{2} \cdot \langle T \rangle_z = \frac{3N_\mathrm{h}}{2} \cdot \frac{\int_{L3} (\mu_1 - \mu_{-1}) - 2 \int_{L2} (\mu_1 - \mu_{-1})}{\int (\mu_1 + \mu_0 + \mu_{-1})} \ , \tag{3.5}$$

where $\langle L \rangle$ and $\langle S \rangle$ are the expectation values for the orbital and spin operators, $\langle T \rangle$ the magnetic dipole operator and N_h is the total number of holes in the $3d$ band. The derived values are the projection of the momenta in the direction of incidence of the x-rays, $\hat{z}$. The isotropic XAS spectra $(\mu_1 + \mu_0 + \mu_{-1})$ is usually approximated using $\mu_0 = (\mu_1 + \mu_{-1})/2$. In $3d$ metals the magnetic dipole term is very often much smaller than the spin momentum, hence the measured effective spin moment $\langle S \rangle_\mathrm{eff}$ is approximatively equal to $\langle S \rangle$. In the limit of small $3d$ spin-orbit interactions, we have $\vec{T} = \sum_i \vec{S}_i - 3\vec{r}_i(\vec{r}_i \cdot \vec{S}_i)/r_i^2$, where the sum is performed over the i electrons and r_i is the position of the i-th electron with respect to the nucleus. In this case $\vec{T}$ is a measure of the difference between the charge quadrupole moment for spin

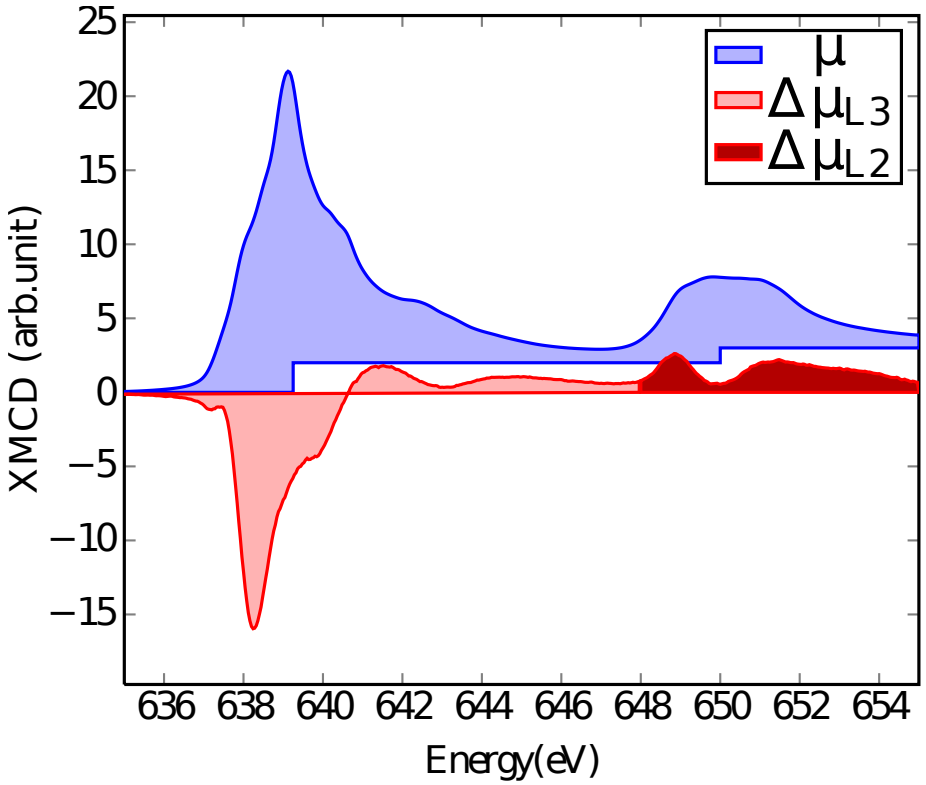

Figure 3.16: XAS(blue) and XMCD(red) signals with decomposition of the total area for L_2 and L_3 edges. The spectra shows have been taken from a Mn_3Ga sample.

$\uparrow$ and $\downarrow$ electrons, $\vec{T} = (1/2)(Q^{\downarrow} - Q^{\uparrow})\vec{S}$. Since the quadrupole moment is a second rank tensor with vanishing trace, it is possible to average out the contribution of $\vec{T}$ by measuring the XMCD over three orthogonal incidences. Alternatively, at the "magic" angle of incidence of 54.7°, $\langle T \rangle$ vanishes for cubic samples [12], as the angular dependence of $7\langle T \rangle$ is $3\cos^2\theta - 1$. The magnetic dipole term can also be seen as the result of the interaction between the spin and orbital momenta. In tetrahedral symmetry, the expectation value for $\vec{L}$ is zero for all $3d$ orbitals in the absence of spin-orbit coupling. If the latter is considered, the crystal field-split $3d$ orbitals are mixed and $\vec{L}$ assumes a finite value. Therefore, only if the spin-orbit coupling is considered, $\vec{T}$ is not zero. Because the $3d$ spin-orbit interaction is small, $\vec{T}$ is very close to zero at room temperature and can reach higher values at low temperature. In lower symmetries, the expectation value of the dipole term is not zero anymore, even in the absence of spin-orbit, coupling because of the different set of orbitals that must be considered [13]. In addition to the observation that the coupling is very small in $3d$ metals, it is worth noting that in this work we will deal with Mn^{2+} ions in the $3d^5$ ground state. In this configuration the band is half-filled, resulting in a zero expectation value of the orbital momentum even in lower symmetries such as the D_{4h} square planar symmetry, independent of the spin-orbit coupling.

The rate of the absorption can be measured by counting the x-rays emitted by the sample when it goes back to the ground state (fluorescence) or by counting the electrons excited above the Fermi level (total electron yield), as shown in Fig. 3.15. In our experiments we have chosen to measure the electron yield because it has a better signal-to-noise ratio in comparison to the fluorescence signal. On the other hand, it has to be taken into account that the measurement is more surface-sensitive, with a sampling depth of 2 nm to 10 nm.

The intensity of the XMCD signal is proportional to the exchange splitting of the bands in the direction

of the wave vector $\vec{k}$ of the incident beam. Since the bands will be split parallel to the magnetic moment, we have

$$\text{XMCD} \propto \vec{k} \cdot \vec{M} \ . \tag{3.6}$$

The signal shows a cosine dependency on the angle between the beam wave vector and the magnetisation vector $\vec{M}$. Exploiting this feature, it is possible to investigate the magnetic properties of the sample in different orientations.

In this work we used the XAS and XMCD techniques to characterise the magnetic moments of Mn-based Heusler alloys. In this kind of compound the magnetic moments are carried by the Mn atoms occupying two crystallographic inequivalent sublattices and coupling antiferromagnetically to each other. We chose to measure XMCD because it allows for the independent determination of both the spin and the orbital momentum. In addition, the contributions from the different sublattices can be extracted by exploiting the angular dependency of the signal (see sec. 4.2.2 or by fitting the data with simulated spectra (see sec. 4.3.4). These characteristics make the XAS/XMCD technique the best choice for the magnetic characterisation of our samples.

3.4.3 Extended x-ray absorption fine structure (EXAFS)

The extended x-ray absorption fine structure (EXAFS) is a measurement of the oscillations of the absorption coefficient $\mu(E)$ above the absorption edges of a material [10, 14, 15]. These oscillations are the result of the coherent interference of the backscattered electronic wavefunction from nearby atoms in a crystalline structure. Therefore, the EXAFS spectrum is usually used to evaluate the crystallographic parameters, such as the atomic distances, the crystal structure and the degree of order in it.

An electron is excited from a core level to the conduction band by the incoming high-energy photons. Usually in transition metals the K edges are used, corresponding to the $1s$-conduction band transition. In this work we investigated the EXAFS at the K-edge of Mn (6539 eV), Ru (22 117 eV) and Ga (10 367 eV). The particle is excited to the empty state in the conduction band that shows p character, due to the selection rule for optical transitions. When the photon energy exceeds the edge energy by a few tenths of eV, the final electronic wavefunction can be considered to be the one of a free electron, *i.e.*, a wave-like Bloch function with wavevector $\vec{k}$. EXAFS measurements typically consider the energy region between 25 and 1000 eV beyond the edge.

According to the Fermi golden rule (eq 2.100), the x-ray absorption coefficient μ is proportional the transition matrix element squared. For highly localised electrons, the latter is proportional to the probability $|\phi_k(r)|^2$ that the electron is found at the atom where the photon is absorbed. In the case of EXAFS, the wavefunction ψ_k can be expressed as a sum of an outgoing wave emitted at the absorbing atom plus backscattered waves coming from the nearby atoms in the crystal lattice (see Fig. 3.17). For a wave reflected straight back by an atom in the first shell of neighbours, the phase difference between these waves is about $2kR$, with $\vec{R}$ the distance between the atoms. Therefore, the wavefunction is modulated as a function of the wavelength of the outgoing wave, which is, in turn, a function of the incoming photon energy. The resulting absorption coefficient μ is modulated by the alternating constructive and destructive interferences of those waves.

The EXAFS spectrum χ is defined as

$$\chi(E) = \frac{\mu(E) - \mu_0(E)}{\Delta\mu_0} \ , \tag{3.7}$$

where μ_0 is the smoothly varying atomic-like background absorption and $\Delta\mu_0$ is a normalisation factor

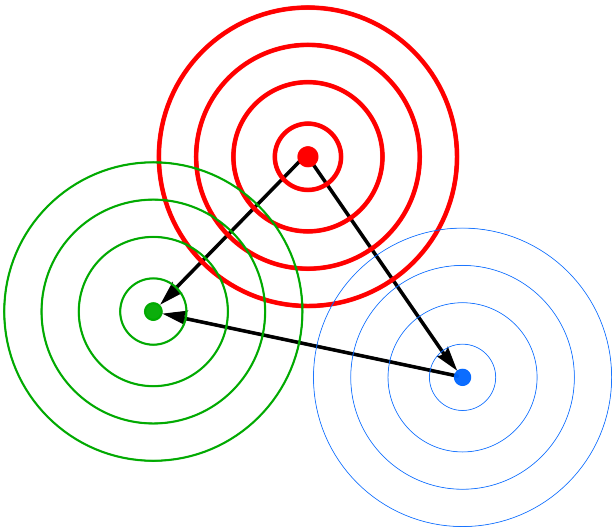

Figure 3.17: Simplified view of the multiple scattering of an outgoing wave off neighbouring atoms. The red atom is the source of the wave, which travels towards the other atoms, gets diffracted and bounces back towards the original source or towards other atoms. The amplitude of the outgoing spherical wave is weakened after each diffraction. From ref. [14]

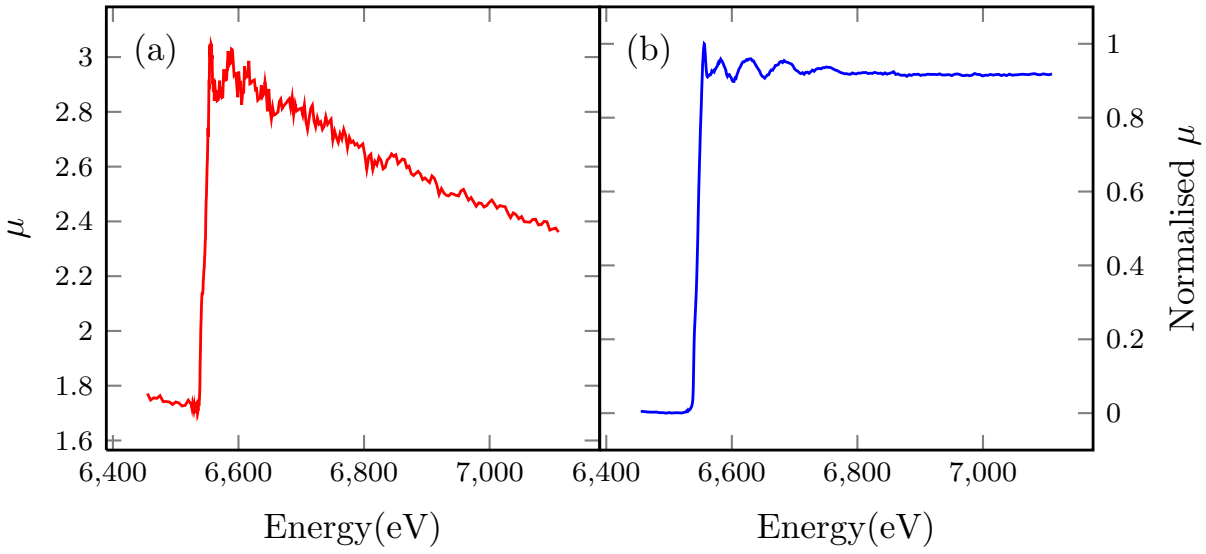

Figure 3.18: Example of EXAFS absorption spectra from the Mn K edge. a) raw data. b) corrected data: the curve have been normalised to the edge jump and the decreasing background subtracted in order to empathise the oscillations.

that arises from the increasing of the background at the absorption edge. In practice, these corrections are done only to isolate the small oscillations from the raw signal, as shown in Fig. 3.18. The wavevector of the outgoing wave is given, in first approximation, by

$$\frac{\hbar k^2}{2m} = \hbar\omega - E_\mathrm{c} + V_0 \ , \tag{3.8}$$

where $\hbar\omega$ is the photon energy, E_c is core level energy of the corresponding edge transition and V_0 is the inner potential of the solid (the work function). The latter is usually not well known but a reasonable estimate can be made and it is often negligible compared to $\hbar\omega - E_\mathrm{c}$.

The chosen absorption edge is usually the K edge since the creation of an s core hole does not split the edge because of spin-orbit coupling and the energy of the successive edge is far enough away to allow the observation of several oscillations. In an experimental station, the x-rays are usually linearly polarised and the fluorescence yield (FY) (proportional to the photons absorption) is recorded using a pixel array detector. In this case, the fluorescence yield is preferred to the total electron yeld because the latter is very surface sensitive, therefore it will not allow for the characterisation of the bulk crystal structure of the sample. The absorption is proportional to $\vec{k} \cdot \vec{e}$ with $\vec{e}$ the radiation electric field. The absorption will be modulated by the scattering of the wave front in the direction of the light polarisation. Therefore, it is possible to change the angle of incidence of the light to obtain information on the crystallographic positions along the $\hat{x}\hat{y}$ plane or towards the perpendicular $\hat{z}$ axis. X-ray linear dichroism (XLD) is the difference in absorption for different orientation of the linear light polarisation with respect to the axis of the crystal lattice. This effect is usually small but it can be detected.

In the case of thin film samples grown on a single crystal substrate, the undesired presence of diffraction peaks from the substrate can be avoided by rotating the sample around an axis perpendicular to its surface. The rotation is much faster ($> 10\,\mathrm{Hz}$) than the measurement time for one point ($> 0.3\,\mathrm{s}$). Due to the high energy of the x-rays used for K edge absorption, there is usually no need to perform the experiment under vacuum.

Single scattering

The EXAFS signal can be evaluated to a first order approximation considering only single scattering: the outgoing wave scatters from a surrounding atom directly back to the central one. The Kronig short-range-order theory [16, 17], further optimised by Sayers *et. al.* [18], express the signal as

$$\chi(k) = \sum_R S_0^2 N_R \frac{|f(k)|}{kR^2} \sin(2jR + 2\delta_\mathrm{c} + \Phi) e^{-2R/\Lambda(k)} e^{-2\sigma^2 k^2} \ . \tag{3.9}$$

Here N_R is the coordination number of the shell of atoms at distance R from the excited atom in the crystal, σ represents the temperature-dependent fluctuation in the bond length and disorder effects, $f(k) = |f(k)|e^{\imath\Phi(k)}$ is the complex backscattering amplitude, δ_c is the central atom phase shift and $\Lambda(k)$ is the energy dependent mean free path (not to be confused with the wavelength). The denominator kR^2 is the spherical wave factor that takes into account the decay of the wave while propagating. The overall amplitude factor S_0^2 can be obtained with a more detailed many-body theory calculation and it results from the response of the system to the creation of a core hole. The exponential term $e^{-2R/\Lambda(k)}$ is due to the decay of the wave related to the mean free path or finite lifetime of the particles (excited electron and core hole). The strength of this decay limits the range of atomic shells probed by EXAFS. The backscattering amplitude $|f(k)|$ and its phase $\Phi = \arg(f)$ are functions of the atoms at which the wave is scattered. In fact the scattering potential is very different for heavy and light atoms. Therefore,

it is possible, even if very difficult in some cases, to distinguish the different type of atoms in the shells surrounding the central atom. The scattering potential is calculated using a muffin-tin approximation, which consists of a spherical potential centred on each atom and a constant value in the interstitial regions. A somewhat larger contribution to the total phase shift is given by the central atom phase shift δ_c since the electron feels its potential twice. The exponential $e^{-2\sigma^2 k^2}$ is the Debye-Waller factor. It takes into account the variation of the atomic distances around the equilibrium value R_{eq} due to thermal agitations of the atoms that smears the interference pattern of the $\sin(2KR)$ term. This effect is more pronounced for higher wavelengths, hence it cuts off the EXAFS signal at wavevectors $k \sim 1/\sigma$. The Debye-Waller factor derives from the averaging over the instantaneous values of R of $\langle e^{2\imath kR} \rangle \approx e^{2\imath kR_{eq}} e^{-2\sigma^2 K^2}$. It is particularly important because it also includes effects caused by crystallographic disorder in the atomic shells, hence it can give an estimation of the quality of the crystal.

Multiple scattering

A key development in the theory and evaluation of the EXAFS came when multiple scattering was taken into account. It consists of the scattering of the outgoing wave onto multiple atoms before coming back to the original source. Accurate theories for the multiple scattering rely on the Green's function method or wavefunction approaches. Since the number of possible paths increases exponentially, it is necessary to use a fast path generation and sorting algorithm to exclude the negligible paths from the calculation. The implementation of these algorithms convoluted into the creation of the code known as FEFF [14, 19], named after the effective scattering amplitude f_{eff}. With this approach, the analysis of the data is usually performed with a Fourier transform of the signal as in

$$F(r) = \int \chi(k) W(k) k^3 e^{2\imath kR} \mathrm{d}(2k) \ , \tag{3.10}$$

where the k^3 factor is used to compensate for the rapid decrease of χ at large k values and the function $W(k)$ is a window function that smooths the signal at the boundaries k_{min} and k_{max}. An example is shown in Fig. 3.19 for $Mn_2Ru_{0.5}Ga$.

In this thesis we used EXAFS to characterise the ordering and atomic distances of Mn-based Heusler alloys. It is difficult to determine the crystal structure of these compounds using only x-ray diffraction (see sec. 3.7.3) because of the limited number of peaks detectable in such a highly symmetric crystal. In addition, the structure and the degree of order in it is very important for the magnetic properties of our samples.

3.4.4 X-ray photoelectron spectroscopy (XPS) and UV photoelectron spectroscopy (UPS)

In x-ray photoelectron spectroscopy (XPS) and UV photoelectron spectroscopy (UPS) experiments, the surface of a sample is irradiated with x-rays or UV light respectively and the emitted photoelectrons are detected and analysed with respect to their kinetic energy [20–25]. An example of XPS data is shown in Fig. 3.20. X-ray radiation is used to probe transitions from the core levels, while UV radiation is used to probe the valence bands of materials with better resolution. Synchrotron radiation can cover both spectral ranges and allow for better resolution than laboratory setups. The number of emitted electrons will be proportional to the density of states of the ground state. They are usually detected with an hemispherical analyser: an angle-integrating analyser gives information about the projected density of states in the whole reciprocal space, while a detector with small angular aperture can provide additional information on the

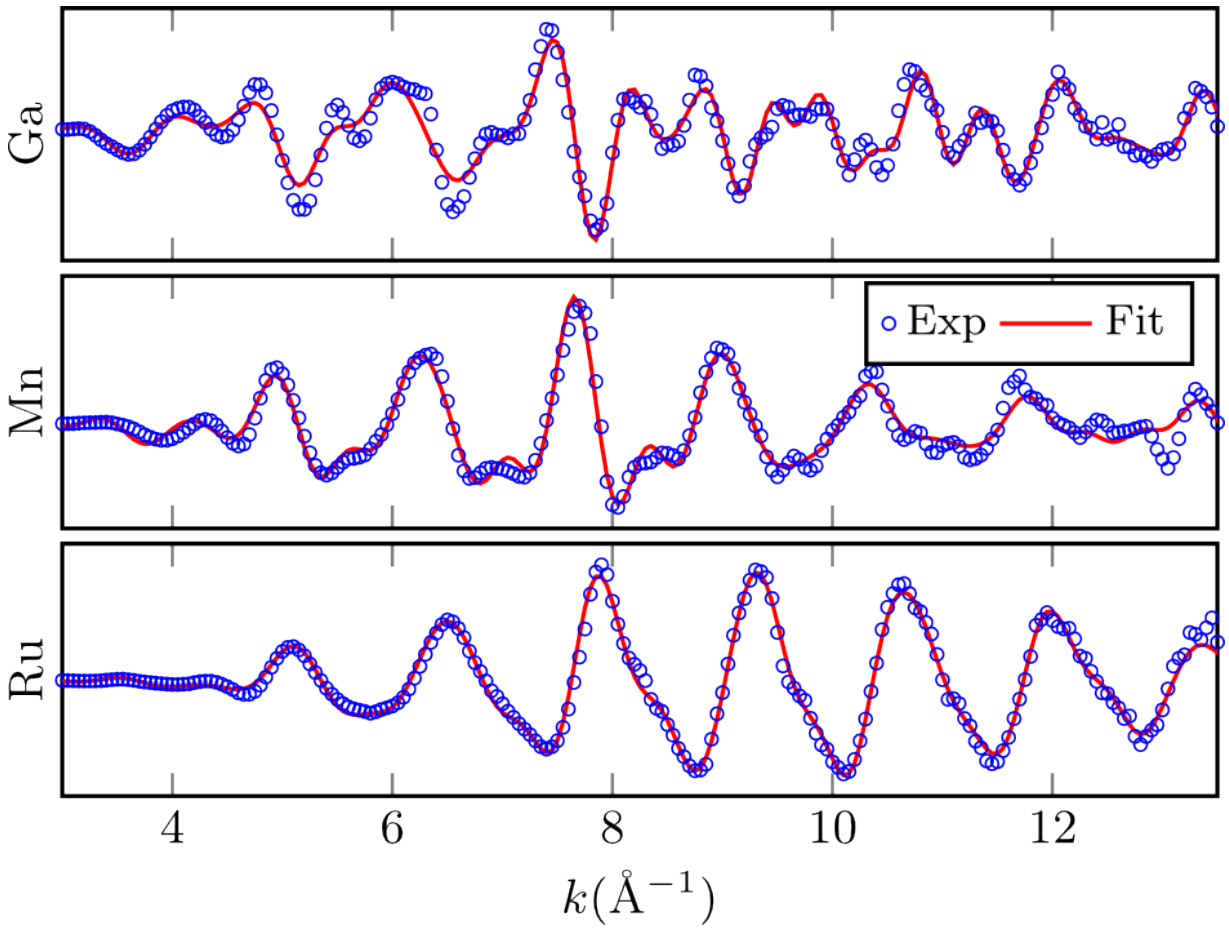

Figure 3.19: Fourier transform of corrected EXAFS signal extracted from the K edge absorption of Ga, Mn and Ru of a $Mn_2Ru_{0.5}Ga$ sample.

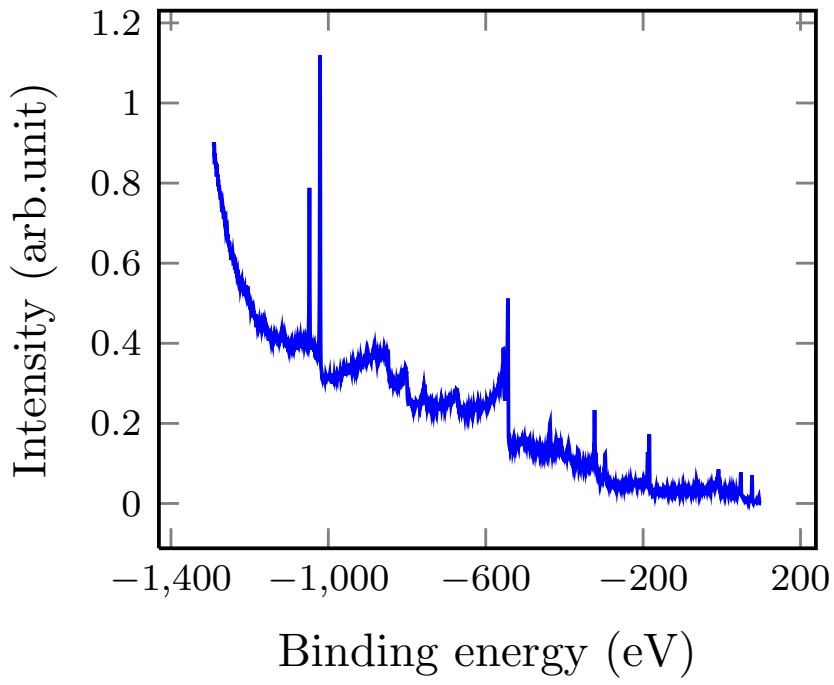

Figure 3.20: XPS data obtained using the K_α emission line of Al.

direction of the wavevector $\vec{k}$ of the photoelectrons (angle-resolved photoelectron spectroscopy, ARPES), hence allowing the determination of the band structure of the material at the cost of a lower amplitude of the signal. When performed in the UV range, the latter technique takes the name of angle-resolved UPS (ARUPS).

With reference to the treatment performed in sec. 2.4, an XPS or UPS transition does not involve the excitation of the electron in an empty valence orbital (a $3d$ orbital for $2p$ XAS for example) but instead the electron is emitted outside the material and into the vacuum. The corresponding transition for $2p$ XPS is $2p^6 3d^N \rightarrow 2p^5 3d^N$. The energy of a transition is referred to as the binding energy (BE) and it is given by BE$= E(2p^6 3d^N) - E(2p^5 3d^N)$. In first approximation this energy is the BE of the $2p$ orbital in which the core hole is created, but the creation of the hole itself modifies the electronic structure of the material and increases the measured BE. The XPS and UPS spectra can be calculated by finding the energy of the different configurations with the models discussed in sec. 2.4 or using density functional theory (DFT) algorithms. The absence of the additional electron in the valence band also enhances eventual charge-transfer effects in the spectra, with the formation of satellite peaks and shifts in the BE. XPS is a useful technique when it comes to determining the type of the bonds in a molecule. The level of ionic or covalent character of a molecular bond can be estimated by the chemical shift of the BE of a core level in an atom due to the hybridisation with the ligands orbitals. The reduced or augmented electronic charge enhances or reduces the screening of the nuclear charges, hence slightly changing the energy of the various orbitals. XPS measurements on the core levels of the same atom in different atomic environments can give information on the oxidation state of the element in the various configurations.

The photoemission process can be analysed in the framework of the three-step model: first, the core electron is excited into a final electron state within the crystal; second, the excited electron travels towards the surface; and third, the electron is emitted into the vacuum through the surface. The first step involves the calculations described above and in sec. 2.4, based on the Fermi golden rule and the

transition operator $\vec{p} \cdot \vec{A}$. The second step involves the propagation of the electron through the solid towards the surface. During this travel, some electrons will undergo scattering with other (quasi)particles, like plasmons, phonons or other electrons. Such electrons will loose the information about the energy of their initial state and, if they manage to escape into the vacuum, they will generate the secondary electron background. This background is usually evaluated employing different models, the most common being the Shirley background [26–29]. This background is proportional to the integrated photoelectron intensity at higher kinetic energies and it is usually determined by iteration of the formula

$$S_i(E) = k \int_E^\infty [j(E') - S_{i-1}(E')] \, \mathrm{d}E' \ , \tag{3.11}$$

where S_i is the i-th iteration of the Shirley background, $j(E)$ is the measured spectrum as a function of the kinetic energy of the photoelectrons and k is an arbitrary constant. As an initial approximation, a constant background S_0 is assumed and successive backgrounds S_i are calculated until the calculation converges (usually in four or five steps). The Shirley background is used because it has a physical foundation, but it is often not the best choice and alternative procedures have been proposed, based on known forms of the inelastic energy loss cross section. The Tougaard's background [30] is based on a universal inelastic loss function of the form

$$K(E - E') = \frac{B(E - E')}{(C + (E - E')^2)^2} \ , \tag{3.12}$$

where $C \approx 1643\,\mathrm{eV}^2$ and B can be used as a fitting parameter or can be calculated from the escape depth in the considered material. The corrected spectra $F(E)$ is given by

$$F(E) = j(E) - \int_E^\infty K(E - E') j(E') \mathrm{d}E' \ . \tag{3.13}$$

The scattering of the electrons on their way to the surface is the reason why XPS and UPS are, in the same way as total electron yield measurements in XAS, very surface sensitive. The third step requires the photoelectron to overcome the work function at the surface to be emitted into the vacuum. In addition, the component of the $\vec{k}$ vector parallel to the surface is conserved during the transition, while the perpendicular one is not because of the break of symmetry. This makes the accurate estimation of the initial direction of $\vec{k}$ more difficult in ARPES experiments. The kinetic energy of the photoelectron is given by

$$\frac{\hbar^2 k^2}{2m_\mathrm{e}} = \hbar\omega - \mathrm{BE} - V_0 \ , \tag{3.14}$$

with V_0 the work function of the material, that is supposed to be known. In addition, the work function of the detector must be taken into account since the photoelectrons must go through its surface in order to be detected. Therefore, an effective work function must be determined beforehand with some reference measurements on a well known material. The most common configuration for the detection employs a metallic grid on the entrance of the analyser that can be set to a variable potential, while the passing energy of the detector is kept constant. The grid voltage is then varied in order to let through only electrons with a certain kinetic energy and an energy sweep is performed. This way the resolution $\Delta E/E$ is kept constant during the scan because the analyser parameters are not modified.

The selection rules for the optical excitation follows from the group theory treatment discussed in sec. 2.4. The final state wavefunction must span the totally-symmetric representation in order to be detected by the analyser. In fact, if the final state was odd with respect to a mirror plane, a detector located in that plane would see a node of the emitted electron. The matrix transition element must also be invariant with respect to all the symmetry operations. This means that the direct product between

the initial and final state function must contain the representation corresponding to the dipole operator. Since, in general, the dipole operator depends on the polarisation of the incoming photons, it is possible to investigate the density of states of bands with different symmetries using linearly polarised light with different polarisation directions. As an alternative, it is possible to change the incidence of the incoming light with respect to the axis of the crystalline sample. A review of the possible transitions for the most common point groups has been given by Eberhardt and Himpsel [31].

For angle-resolved measurements, hemispherical detectors are used, while for angle-integrated measurements a cylindrical mirror analyser is the most common choice. The light sources for the UV range are gas discharge lamps. The discharge is created in a water- or air-cooled compartment separated by the ultra high vacuum (UHV) chamber where the sample is placed. The most commonly used type of source is the He discharge source, which is the one used in our laboratory. The He I spectral line is at 21.22 eV. XPS measurements instead requires an x-ray tube for the generation of the high energy photons. The most common anodes are Mg or Al.

We used an Omicron MultiprobeXP XPS system. It implements a monochromated Al source that exploits the K_α emission line at ∼1486 eV and an E125 hemispherical analyser. Synchrotron radiation can be used for XPS measurements, since these facilities yield a continuous spectrum of radiation extending from the far infrared to the hard x-ray regime. In addition, the spectral resolution in a beamline is much higher than the one obtainable in a laboratory setup.

3.5 Transport measurements

3.5.1 Hall voltage techniques

The Hall voltage techniques in our case mainly rely on the anomalous Hall effect (AHE). As we have seen in sec. 2.3.6, the Hall voltage in a magnetically ordered sample has two contributions, R_0 and R_{AHE}. The first is due to the normal Hall effect and it is proportional to $1/ne$, while the latter is proportional to M_z. Therefore, in our measurements we will use the AHE resistance to investigate the magnetic properties of the sample.

The sample is patterned by UV lithography into Hall bars of different dimensions or, alternatively, the transverse voltage is measured directly on an unpatterned sample by attaching silver wires on the four corners of a square sample with pressed indium (see. Fig. 3.21). An electrical current is sent through the material and the transverse voltage is detected as a function of an applied magnetic field. This magnetic field can be oriented both in-plane or out-of-plane depending on how the sample is mounted on the holder. We can measure the anomalous Hall voltage in a few different setups. One employs a GMW magnet system Model 5403 electromagnet powered by a Bouhnik power supply that allows us to apply fields up to 1.24 T. It is coupled with a one-axis rotating stage which permits us to change the orientation of the field with respect to the sample. A second setup employs a CRYOGENIC superconducting 5 T magnet. In this case, it is possible to direct the field only perpendicular or parallel to the sample surface, *i.e.*, we cannot rotate the sample with respect to the field. The Hall voltage can also be measured in a physical properties measurement system (PPMS) device from Quantum design. It allows two-axis rotation of the sample in a magnetic field up to 14 T. The sample is inserted in a cryostat where the temperature can be controlled from 2 K to 400 K. All these systems use 2400 series Keithley SourceMeters to apply the current and measure the voltage. In addition, the first setup and the PPMS can detect the Hall voltage using a lock-in technique using a Stanford Research SR830.

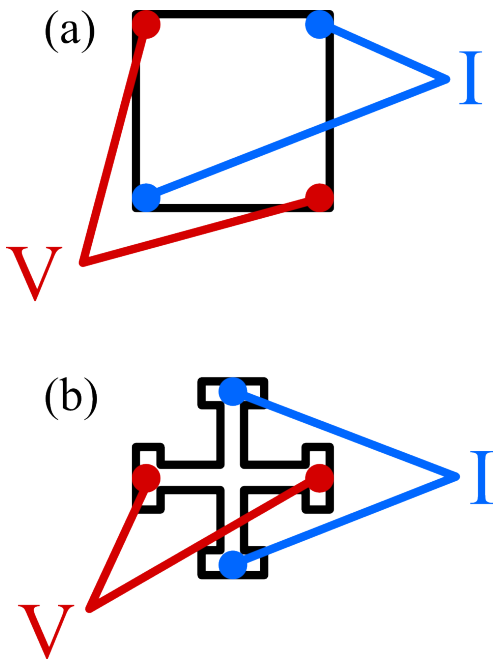

Figure 3.21: Schematic illustration of the two types of Hall voltage measurements performed on our samples. (a) Thin film with corner-contacs. (b) Patterned Hall bar.

3.6 Ferromagnetic resonance techniques

3.6.1 Ferromagnetic resonance

The ferromagnetic resonance (FMR) theory has been discussed in sec. 2.2.1. In general, the resonance frequency of a ferromagnetic material is given by the general formula known as the Kittel's law

$$\omega_{\mathrm{res}}^2 = \mu_0^2\gamma^2(H_{\mathrm{ex}} + H_{\mathrm{an}})(H_{\mathrm{ex}} + H_{\mathrm{an}} + M_{\mathrm{s}}) \ , \tag{3.15}$$

with H_{ex} and H_{an} external and anisotropy fields respectively. Therefore, it is possible to determine both the anisotropy and the saturation magnetisation by measuring the resonance frequency as a function of the applied field. We have established two different setups for the measurements of the FMR.

In the first setup (shown in Fig. 3.22 and 3.23), we use a GSG (ground-signal-ground) shorted or matched antenna to generate and detect the magnetic resonance. The antenna is patterned by lithography methods directly on the surface of a magnetic sample (Fig. 3.24 and 3.25). An rf electric current is injected using a Rohde & Schwarz ZVB vector network analyser (VNA) and consequently an oscillating Ørsted field is generated. The magnetic field acting on the magnetic layer is approximately homogeneous and directed in the plane of the sample.

The antenna is made of a thick Cu/Au bilayer and it is optimised to match the 50 Ω impedance of the cabling and generators. In order to avoid shunting of the current through the magnetic layer, a thick layer of oxide (SiO_2 or MgO) is deposited between the two surfaces. An external fixed magnetic field is applied perpendicularly to the oscillating Ørsted field and it is varied together with the frequency of the excitation. When the resonance condition is matched, the precession of the magnetisation causes the absorption of some power from the rf electromagnetic field, while, since the antenna is matched to the generator, under normal conditions there should be no absorption. The VNA allows us to measure the ratio between the injected and reflected/transmitted power, hence, by measuring it as a function of field/frequency, it is

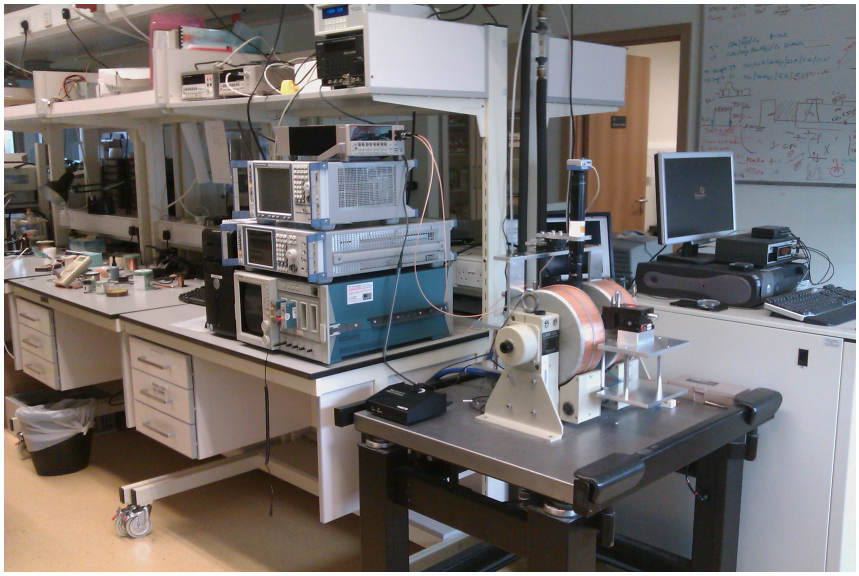

Figure 3.22: The setup for electrically-induced fmr measurements.

possible to obtain both constant-field and constant-frequency scans. This kind of measurement is usually complicated by the fact that other sources of reflections give a much higher contribution to the losses than the magnetic resonance. They derive mainly from imperfections in the patterning of the antenna, Joule losses and finite resistivity of the insulating material. In order to get rid of them, a reference spectra is measured and the actual FMR measurement consists of the subtraction between the acquired spectra and the reference one. The reference spectra is measured with a very high applied external field, in order to put the resonance condition to a frequency much higher than the available ones and to register only losses due to the additional contributions. An example broadband FMR spectra is shown in Fig. 3.26.

The second setup consists of a cavity magnetic resonance setup, also used for electron paramagnetic resonance. A microwave cavity (or rf cavity) is a resonator consisting of a closed metal structure [32]. The metal walls confine a single mode of an injected electromagnetic wave. We used rectangular and cylindrical cavities, both operating in the X-band of microwaves (8 GHz to 12 GHz). The supported electromagnetic modes are divided into transverse electric (TE) and transverse magnetic (TM) depending on which component of the wave (electric field or magnetic field) is completely perpendicular to the propagation direction. By solving the wave equation using the boundary conditions of zero electric field in correspondence to the cavity walls, it is possible to find the relation between the frequency of the modes and the dimensions and the dielectric filling of the cavity. Modes are usually labelled by three indices n,l and m, indicating the number of nodes (points where the field is zero) along the $\hat{x}$, $\hat{y}$ and $\hat{z}$ direction, respectively. For a rectangular cavity of dimensions $a \times b \times d$, the TE_{nlm} or the TM_{nlm} mode frequency is given by

$$\omega_{nlm} = \frac{c}{\sqrt{\mu_r \epsilon_r}} k_{nlm} = \frac{c}{\sqrt{\mu_r \epsilon_r}} \sqrt{\left(\frac{n\pi}{a}\right)^2 + \left(\frac{l\pi}{b}\right)^2 + \left(\frac{m\pi}{d}\right)^2}\,, \tag{3.16}$$

where c is the speed of light, μ_r and ϵ_r are the relative permeability and permittivity of the dielectric filling and k_{nlm} is the wavenumber. For a cylindrical cavity of radius R and length L, instead, TM modes have frequencies

$$\omega_{nlm} = \frac{c}{\sqrt{\mu_r \epsilon_r}} \sqrt{\left(\frac{X_{nl}}{R}\right)^2 + \left(\frac{m\pi}{L}\right)^2}\,, \tag{3.17}$$

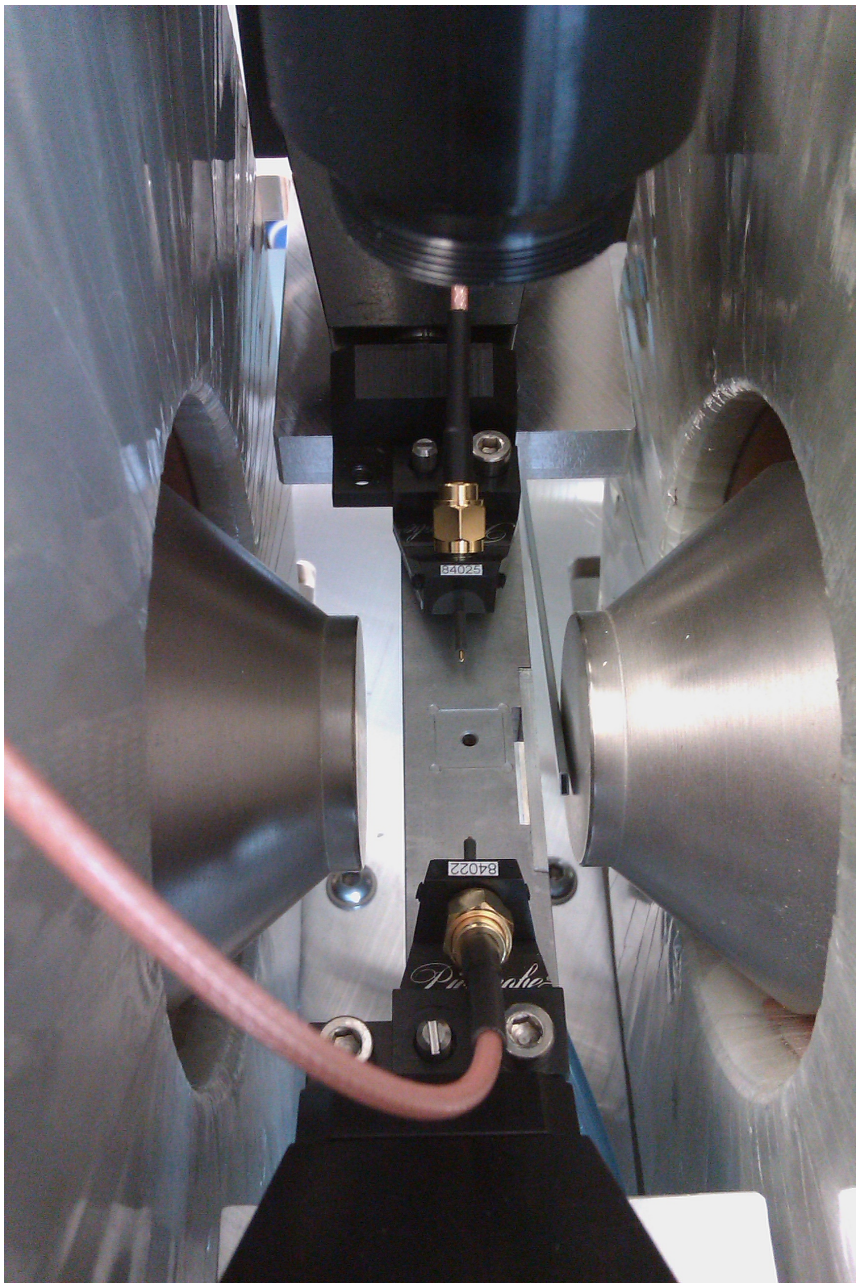

Figure 3.23: Close up view of the gap of the electromagnet setup used for FMR measurements. The two GSG probes are used to contact the lithographically defined antennas.

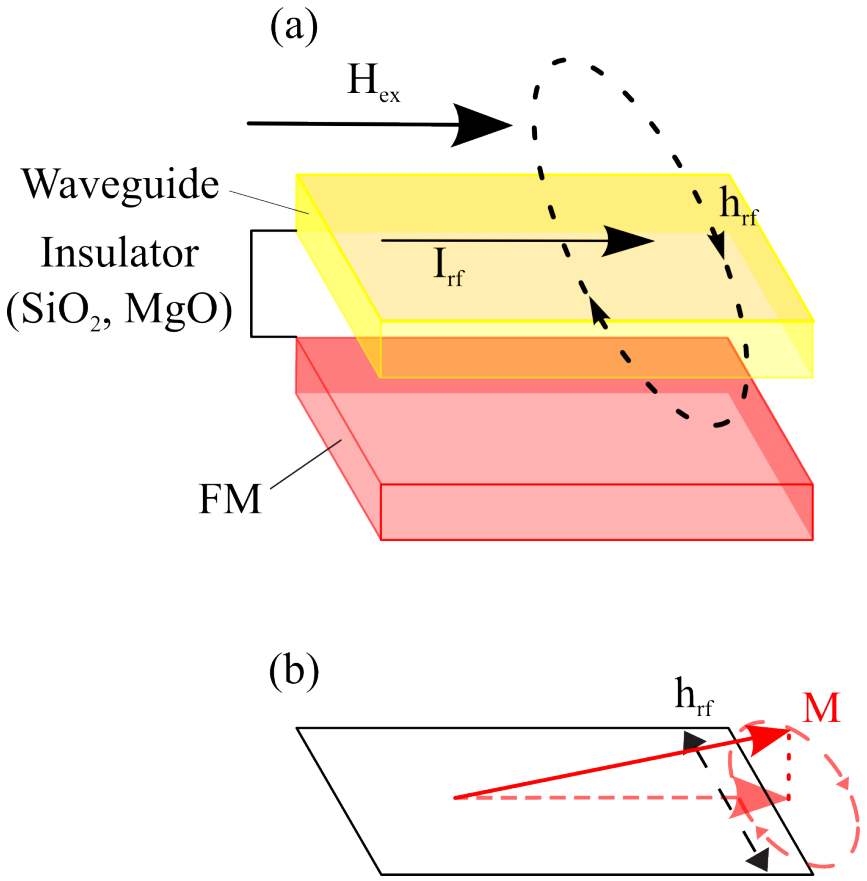

Figure 3.24: (a) Schematic illustration of the sample setups used for broadband FMR measurements. H_{ex} is the external in-plane magnetic field, I_{rf} is the rf current and h_{rf} is the resulting Ørsted field. (b) Precession of the magnetic moment M around the external field.

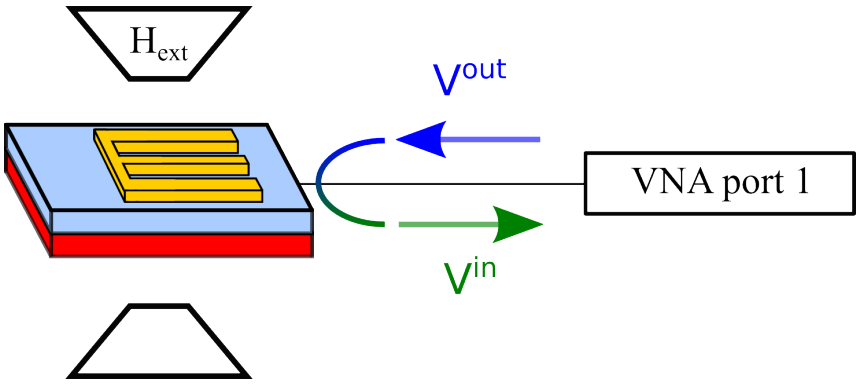

Figure 3.25: Schematic of the broadband FMR setup. An antenna is patterned on the sample and contacted using GSG picoprobes. The sample is placed in the gap of an electromagnet and connected to a vector network analyser (VNA) port, which injects an rf current in the antenna. Both magnetic field and rf frequency are swept during the measurement and the reflected signal is detected.

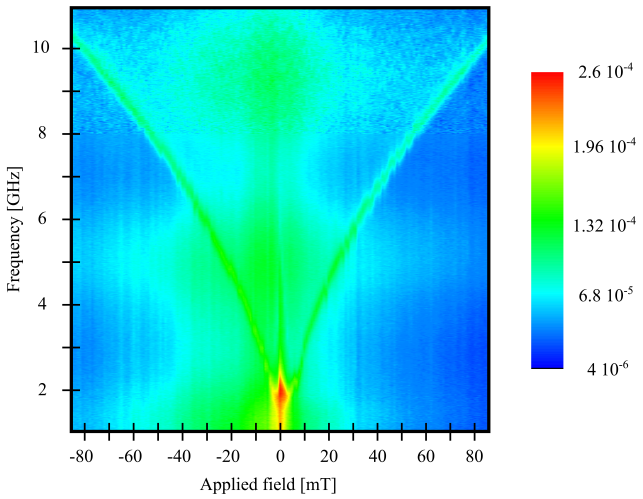

Figure 3.26: Broadband FMR spectra for a CoFeB sample with in-plane magnetisation. The noise at low field is due to the formation of magnetic domains.

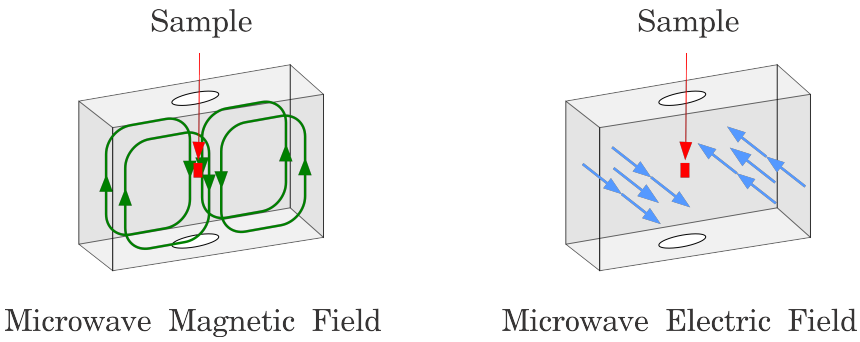

Figure 3.27: Electric and magnetic field configuration of a TE_{102} rectangular cavity used for FMR measurements.

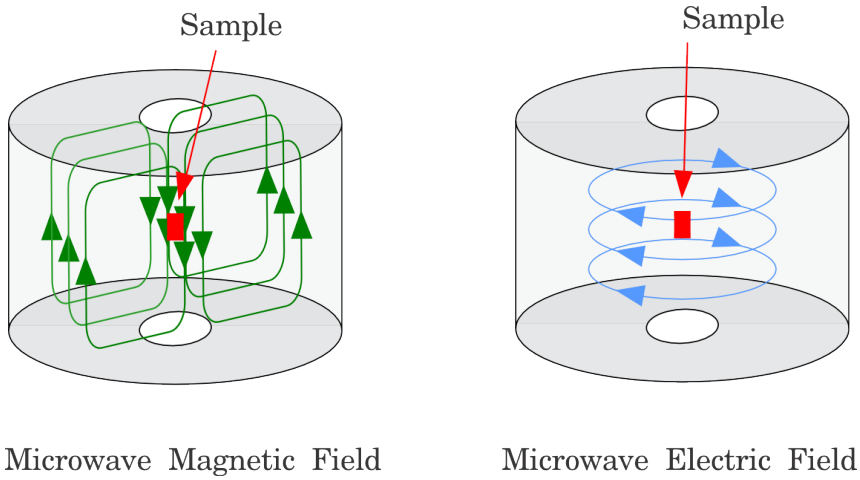

Figure 3.28: Electric and magnetic field configuration of a TE_{011} cylindrical cavity used for FMR measurements.

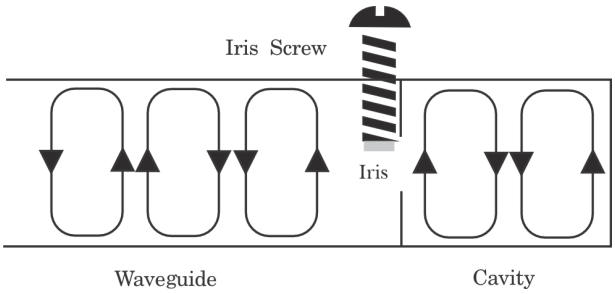

Figure 3.29: Schematic of the coupling between the cavity and the waveguide. In order to fine-tune the system, it is possible to vary the position of a teflon screw in correspondence of the iris.

while TE modes have frequencies

$$\omega_{nlm} = \frac{c}{\sqrt{\mu_r \epsilon_r}} \sqrt{\left(\frac{X'_{nl}}{R}\right)^2 + \left(\frac{m\pi}{L}\right)^2}\,, \tag{3.18}$$

where X_{nl} and X'_{nl} denotes the l-th zero of the n-th Bessel function and the l-th zero of the derivative of the n-th Bessel function respectively. The efficiency of the coupling between a cavity and the microwave signal is given by the quality factor Q, the ratio between the stored energy in the resonator and the energy loss per cycle. Microwave cavities are usually characterised by a very high Q-factor, up to 10^6. The most common sources of losses are the finite conductivity of the walls (losses by Eddy currents), power loss in the dielectric filling (in our case air), and losses resulting from deviation from a perfect geometrical shape of the resonator. In our setup we used a rectangular TE_{102} cavity (Fig. 3.27) and a cylindrical TE_{011} cavity (Fig. 3.28), both tuned to resonate at ∼9.6 GHz. The electromagnetic field configuration is chosen in order to obtain a "sweet" spot in the centre of the cavities, with almost zero electric field and maximum and uniform magnetic field. Of course, these conditions hold for a perfectly matched cavity and a point-sample. When the real sample is inserted, the matching is much less ideal. The microwave signal is generated by a klystron at the frequency of about 9.6 GHz. The frequency can be tuned coarsely by changing the length of a resonant tube at the exit of the device or, more finely, by tuning the accelerating voltage of the electron gun. The wave is sent to the cavity through waveguides and, since they are almost perfectly matched to the input signal, almost no reflection of power is observed. Any reflected power is decoupled from the input and sent to a diode by a magic tee and, since the frequency of the oscillating field is much higher than the bandwidth of the diode, a time average of the reflected signal is recorded at the output. A magnetic sample is glued on a spin-free quartz rod (containing no magnetic impurities) and inserted in the middle of the cavity. The coupling with the waveguide is tuned by changing the effective impedance using a teflon screw placed directly before the entrance iris, as shown in Fig. 3.29, in order to obtain the best coupling with the specific inserted sample. There is a trade-off between the strength of the coupling and the resolution of the measurement. The waveguide and the cavity act as coupled resonator: if the coupling is too weak, they will resonate at slightly different frequencies and produce "beats"; if the coupling is too strong, they will act as a single resonator but the damping will be enhanced and the linewidth of the resonance mode will be too high to achieve a good resolution.

Dielectric samples cause the least perturbation of the cavity, while metallic ones can drastically change its Q-factor. The cavity is placed in the gap of an electromagnet capable of applying up to 1 T perpendicular to the rf field. At the injected microwave frequency, the resonance condition is matched at a certain applied field and the reflected power from the magnetic moment precession is detected by the diode.

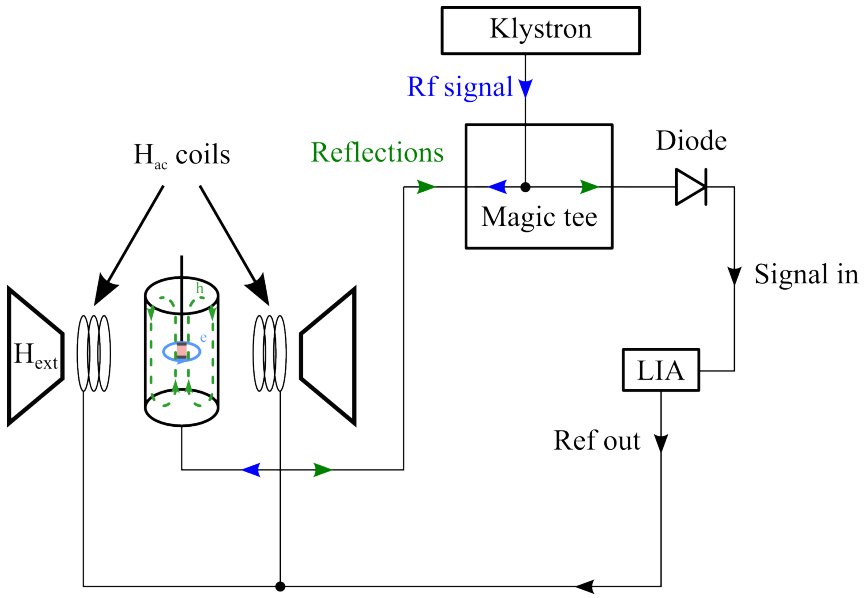

Figure 3.30: Schematic of the cavity FMR setup. The sample is placed in the centre of a microwave cavity. The rf resonance mode of the cavity (∼9.6 GHz) is excited by a klystron and the reflected power is detected using a magic tee and a diode. The cavity is placed in the gap of an electromagnet that provides a dc external field. An ac magnetic field is superimposed, modulated at the frequency (100 kHz) of the reference signal of a lock-in amplifier (LIA). The diode signal, modulated at this frequency, is detected by the LIA and recorded while the dc magnetic field is swept.

The measurement is performed by recording the reflections as a function of the external field. A small sinusoidal ac field is superposed in order to acquire the data using a lock-in technique. The derivative of the output is recorded and the resonance field and the linewidth at constant frequency are obtained. The setup in shown in Fig. 3.30.

3.6.2 Spin torque FMR

The Spin torque Ferromagnetic Resonance (ST-FMR) is a measurement technique often used to determine the resonance frequency and the spin Hall angle of a magnetic material [33–36]. The schematic of the setup is shown in Fig. 3.31. A bilayer composed of a heavy metal (HM) with high spin-orbit coupling and a soft ferromagnetic metal (FM) is patterned into strips and is placed in the gap of an electromagnet. The magnetic moment is saturated in the plane at an angle φ_H with respect to the current direction. An rf current is injected in the plane of the thin film and a dc rectified voltage is detected at the longitudinal edges of the strip as a function of the external field (see sec. 2.3.8). The magnetisation precession is excited by two different sinusoidal fields. The first one is the Ørsted field generated by the current flowing in the heavy metal layer. Since the lateral dimensions of the strip are much bigger than the thickness, this field can be considered completely oriented in the in-plane direction. The second one is the effective field arising from the spin Hall [37–40] and Rashba effects [41–43] (see sec. 2.3.7). The polarisation $\vec{\sigma}$ of the spin current J_s injected in the ferromagnetic layer points in the plane and is perpendicular to the charge current J_c direction. The spin Hall effective field is then given by $-\vec{\sigma} \times \vec{M}$ and it points out of the plane, while the field-like Rashba effective field points parallel to σ, same as the Ørsted field. The situation in schematised in Fig. 3.32.

Early reports didn't consider the scrambling of the effective fields orientations arising from the imaginary part of the spin mixing conductance for the spin Hall effect and for the Rashba effect [44]. The

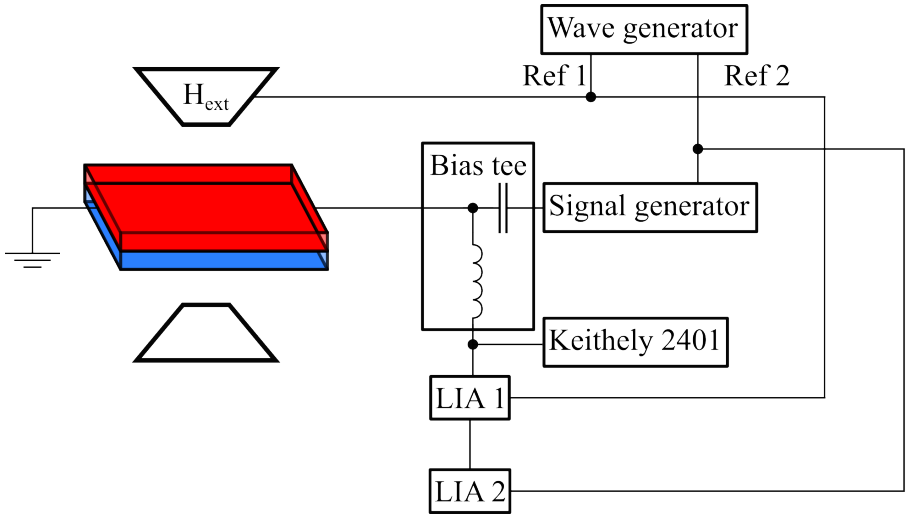

Figure 3.31: Schematic of the ST-FMR measurement setup. A signal generator sends a microwave signal into the sample through a bias tee. The source is chopped at high frequency using the first reference signal of a wave generator. The sample is placed in the gap of an electromagnet and the magnetic field is modulated at low frequency using the second reference signal of the wave generator. The rectified dc voltage produced by the sample is detected at the other end of the bias tee by two lock-in amplifiers in cascade.

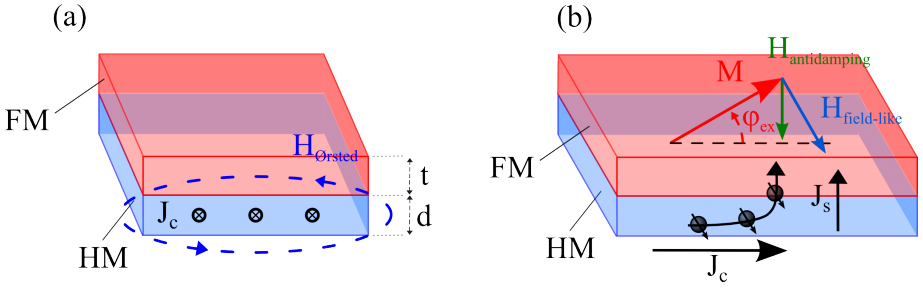

Figure 3.32: Schematic of the HM/FM bilayer used for ST-FMR measurements. (a) Front view with Ørsted field acting on the FM layer produced by the charge current in the HM layer. (b) Spin injection and effective fields acting on the magnetic moment. φ is the polar angle of the equilibrium position of the in-plane magnetic moment. The direction of the Ørsted and Rashba fields is parallel to the polarisation of the spin current, while the antidamping effective field is pointing out-of-plane.

Rashba effect is, in fact, not considered at all or assumed negligible. In addition, the relative phase between the current and the produced magnetic field is assumed to be 0, since the injected spins and the Ørsted field are in phase with the current. With such assumptions and with reference to what discussed in sec. 2.3.8, the Ørsted field will give a rectified voltage with a lineshape resembling a pure antisymmetric Lorentzian. On the contrary, the spin-orbit field (pointing out-of-plane) will result in a purely symmetric Lorenzian lineshape. The total dc signal is then a sum of the two: an asymmetric Lorentzian. Since the Ørsted field is due to the charge current while the spin Hall effect originates form the spin current, it is possible to obtain the spin Hall angle (SHA) θ_{SH} from the ratio between the amplitude of the two lineshapes after having separated them from the raw data. The coefficients of the two Lorentzians $F_{\mathrm{s}}(H_{\mathrm{ex}})$ and $F_{\mathrm{a}}(H_{\mathrm{ex}})$ (see sec. 2.3.8) are given by $S = \hbar J_{\mathrm{rf}}/(2e\mu_0 M_{\mathrm{s}} t)$ and $A = h_{\mathrm{rf}}[1 + (M_{\mathrm{s}}/H_{\mathrm{ex}})]^{1/2}$ respectively, where t is the thickness of the ferromagnetic layer. Hence the spin Hall angle is given by

$$\frac{J_{\mathrm{s}}}{J_{\mathrm{c}}} = \frac{S}{A}\frac{e\mu_0 M_{\mathrm{s}} t d}{\hbar}\left[1 + (M_{\mathrm{s}}/H_{\mathrm{ex}})\right]^{1/2} \ . \tag{3.19}$$

As shown in sec. 2.3.8, the assumptions of no field-like effective field and purely in-phase current and field excitation don't usually hold [45–50]. In addition, there is no easy way to establish the field-like torque and the phase shift for the sample under test. A Michelson interferometer-like device has been proposed to determine the relative phase between the fields, but such a device requires electrical insulation between the HM and FM layer. It has also been reported that this phase varies unreliably between apparently identical samples and that it is frequency dependent [46]. Hence, care must be taken when using this method to evaluate the SHA. Further information can be found in the paper by Harder *et. al.* (ref. [46]).

Another characterisation of the spin Hall angle can be accomplished with the same setup by injecting an additional dc current in the strip together with the rf excitation. It relies on the changes in the linewidth Δ of the resonance as a function of the anti-damping torque. As discussed in sec. 2.2.2, the anti-damping torque owes its name to the fact that it is subtracted (or summed) to the Gilbert damping. This results in an enhancement (or reduction) in the amplitude of the oscillations of the magnetisation. The linewidth is directly related to the damping. Therefore, an additional dc spin current will increase or decrease Δ [51–53], as described by the equation

$$\Delta = \frac{2\pi f}{\gamma}\left[\alpha + \frac{\sin\varphi_H}{(H_{\mathrm{ex}} + M_{\mathrm{s}}/2)\mu_0 M_{\mathrm{s}} t}\frac{\hbar J_{\mathrm{s}}}{2e}\right] \ . \tag{3.20}$$

It is then possible to evaluate the ratio between J_{s} and J_{c}. This method does not depend on the lineshape of the rectified voltage, hence the relative phase between electric and magnetic fields is not important. In addition, it evaluates only the anti-damping effective field. Therefore, the field-like effective field is not considered when calculating the SHA.

3.6.3 Inverse spin Hall effect

The inverse spin Hall effect (ISHE) is the process that converts a spin current into a charge current [54–63]. The spin current can be obtained by spin pumping from a ferromagnetic layer into a high spin-orbit coupling heavy metal. The mechanism of spin pumping by ferromagnetic resonance is schematised in Fig. 3.33 and has been discussed in sec. 2.3.4. It is the generation of a spin current from the precession of the magnetisation $\vec{M}$ in a ferromagnetic/non magnetic bilayer system. In order to perform the measurement, two electrodes are attached at the edges of the HM layer and the sample is placed in a microwave cavity as close to the centre as possible, where the rf magnetic field is at a maximum and the electric field is at a minimum. We chose to use the TE_{011} cylindrical cavity because of the higher values of rf magnetic

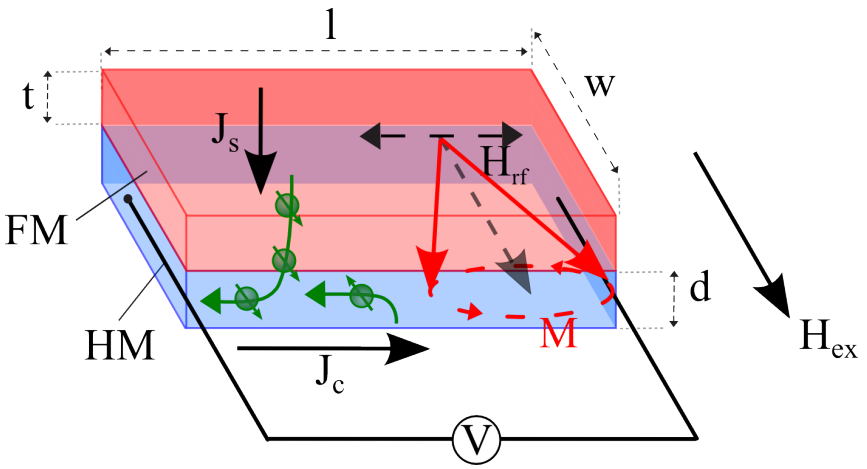

Figure 3.33: Schematic illustration of the spin pumping process achieved through ac excitation of the magnetisation of a FM layer, used in ISHE experiments. H_{ex}, h_{rf} and M are the fixed external and the rf fields and the magnetic moment, respectively. J_c and J_s are the charge and spin current, respectively.

field achievable. An external fixed magnetic field is applied along the film plane and perpendicular to the length of the sample, *i.e.*, the direction where the electrodes are connected. The FM chosen for this kind of measurements is almost always a soft ferromagnet, hence the equilibrium position of the magnetic moment is coincident with the external field. The FMR condition is given by the Kittel law 2.41 for in-plane magnetised soft material as

$$\omega^2 = \mu_0^2\gamma_0^2[H_{ex}(H_{ex} + M_s)] \ . \tag{3.21}$$

As discussed in 2.3.4, when H_{ex} and the frequency of the microwaves f fulfil the FMR condition, a pure dc spin current with polarisation σ parallel to the equilibrium magnetisation flows through the interface into the HM. There, it is converted into a transverse charge current by ISHE. This generates a transverse voltage along the strip that is detected by a voltmeter. The setup is schematised in Fig. 3.34.

The dc voltage originating from ISHE has a symmetric Lorentzian shape since it is directly proportional to the amplitude of the magnetisation oscillations $|m|^2 \propto F_s^2 + F_a^2 = F_s$ (see sec. 2.3.8). The signal is centred at the resonance field H_{res}. Ideally the sample should be placed exactly at the centre of the cavity, where the microwave electric field is negligibly small. In practice this condition is never achieved: small misalignments and field inhomogeneities in the cavity are always present, mainly because of the necessity to critically couple the impedance of the cavity + sample system and the waveguide. As can be seen in Fig. 3.35, if the sample is not placed in the exact centre, the out-of-plane component of the oscillating magnetisation $\vec{m}$ can generate an additional transverse voltage due to the anomalous Hall effect (see sec. 2.3.6). If we consider an ideal phase shift of π between the microwave electric and magnetic fields, the AHE $\propto \vec{e}(t) \times \vec{m}(t)$ will result in a signal with the shape of an antisymmetric Lorentzian. At resonance the oscillating magnetisation is $\pi/2$ out of phase compared to the rf magnetic field, hence the magnetisation is out-of-plane when the electric field is zero: no AHE signal is produced. On the other hand, before and after the resonance, the phase shift is lower or higher than $\pi/2$, and there will be a temporal overlap of the electric field and the out-of-plane magnetisation. Therefore the AHE voltage changes sign at the resonance field. The situation is schematised in Fig. 3.36. It is then possible to distinguish between the two contributions by separating the two lineshapes in the total dc voltage, that takes the shape of an asymmetric Lorentzian [54]. As already mentioned in sec. 2.3.8 and sec. 3.6.2, this kind of measurement

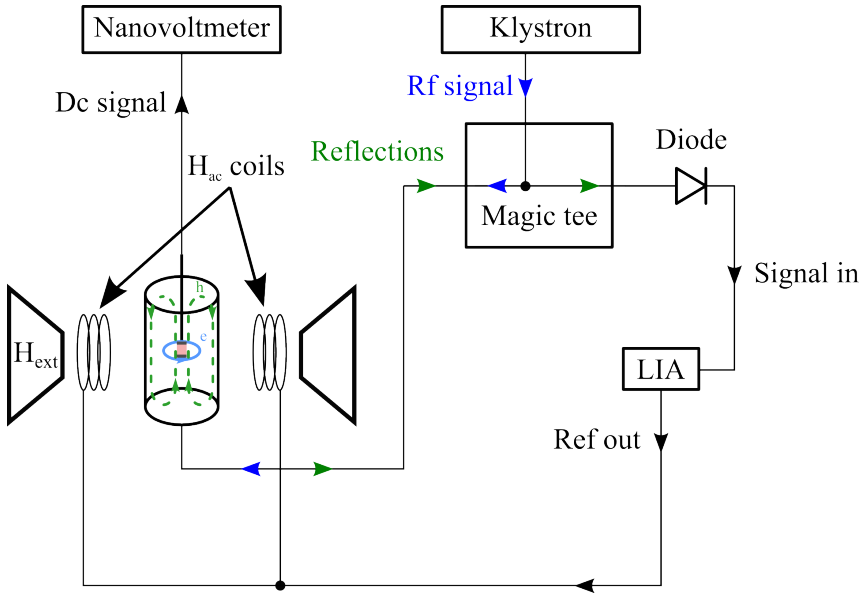

Figure 3.34: Schematic of the ISHE-spin pumping setup. The sample is placed in the centre of a microwave cavity. The rf resonance mode of the cavity (∼9.7 GHz) is excited by a klystron and the reflected power is detected using a magic tee and a diode. The cavity is placed in the gap of an electromagnet that provides a dc external field. An ac magnetic field is superimposed, modulated at the frequency (100 kHz) of the reference signal of a lock-in amplifier (LIA). The diode signal, modulated at this frequency, is detected by the LIA and recorded while the dc magnetic field is swept. The dc voltage building up at the edges of the samples is recorded by a nanovoltmeter.

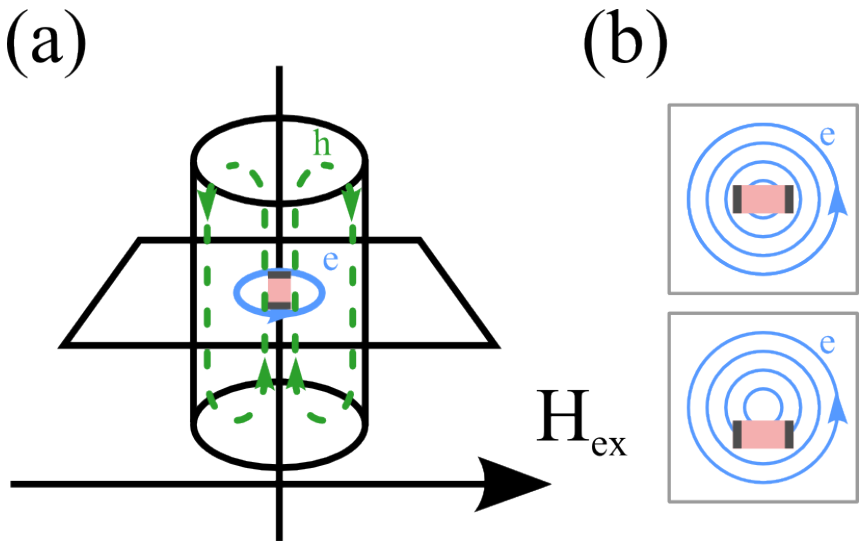

Figure 3.35: Measurement configuration for the ISHE-spin pumping in a TE_{011} cavity. (a) Schematic of the cavity with the rf $\vec{h}$ and $\vec{e}$ fields and the external $\vec{H}_{ex}$ field. The black pads on the sample represent the electrical contacts. (b) Top view of the sample in the cavity in a centred position (top) and off-centre position (bottom). The electric field seen by the sample is different in the two situations.

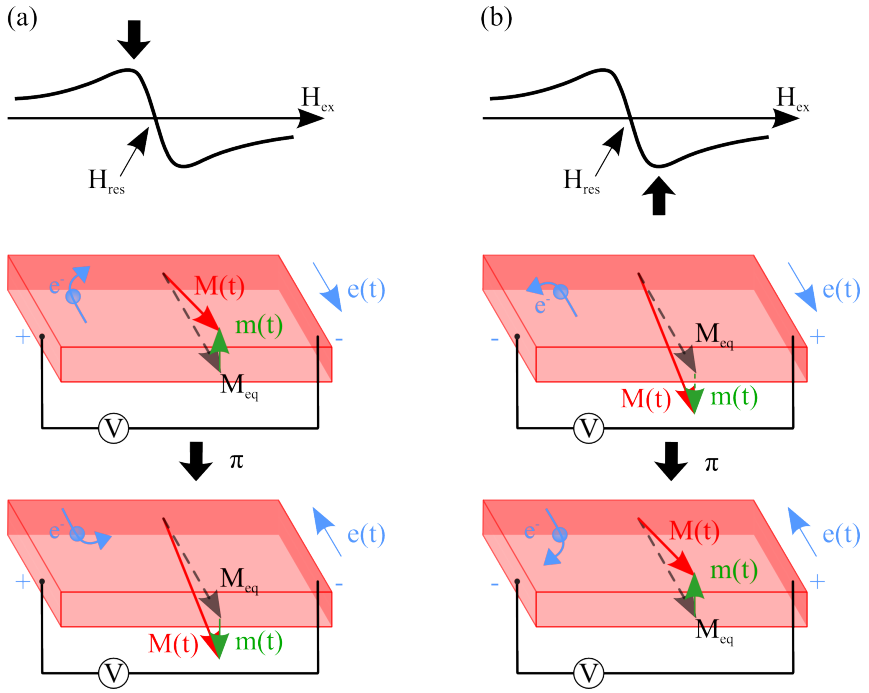

Figure 3.36: Effect of the AHE on the ISHE-spin pumping measurement. (a) Dc voltage generation induced by the AHE when $H_{ex} < H_{res}$ (b) Dc voltage generation induced by the AHE when $H_{ex} > H_{res}$. The top and bottom figures show the effect after half a period of oscillation. We suppose a phase shift of 180° between the rf electric and magnetic fields.

is reliable only if there is confidence in the relative phase between the rf electric field and the magnetic field. The relationship between the two is somewhat more reliable in a microwave cavity with respect to the injection of current in a stripline, as in a ST-FMR setup. This is due to the much higher precision achievable in the fabrication of the waveguides and cavities and by the fact that the perturbing sample occupies a very small fraction of the volume of the cavity. In a ST-FMR setup, imperfections in the lithography and in the metallic or oxide layers cause deviations from the ideal conditions. Unfortunately, we found that, even in a cavity, the phase shift can be subject to large variations if the resistivity of the sample is too high ($\geq$100 µΩ cm).

The FMR signal is measured together with the dc voltage in order to establish the parameters of the FM material like the effective saturation magnetisation M_s and the Gilbert damping α. In addition, in order to estimate the spin Hall angle, it is necessary to evaluate the interface spin-mixing conductance $g^{\uparrow\downarrow}$. This can be done because the effective damping parameter is increased by the spin pumping mechanism as discussed in sec. 2.3.4. By measuring the linewidth of the HM/FM sample and comparing it with the linewidth of a HM only sample we can use eq 2.64 to determine the effective spin-mixing conductance. For clarity, eq 2.64 is reproduced here

$$g_{\text{eff}}^{\uparrow\downarrow} = \frac{\gamma_0 \mu_0 M_s t_{\text{FM}}}{g \mu_B \omega} (\Delta H_{\text{NM/FM}} - \Delta H_{\text{FM}}) \ .$$

With reference to the equivalent circuit for the bilayer represented in Fig. 3.37, the dc voltage originating from the ISHE is given by $V = [R_{\text{FM}} R_{\text{HM}}/(R_{\text{FM}} + R_{\text{HM}})] I_c = l[\sigma_{\text{HM}} + (t_{\text{FM}}/t_{\text{HM}})\sigma_{\text{FM}}]^{-1} J_c$. R_{HM} and R_{FM} are the resistances of the HM and FM layers respectively, σ_{HM} and σ_{FM} are the respective conductivities, t_{HM} and t_{FM} are the respective thicknesses and and l is the length of the sample across

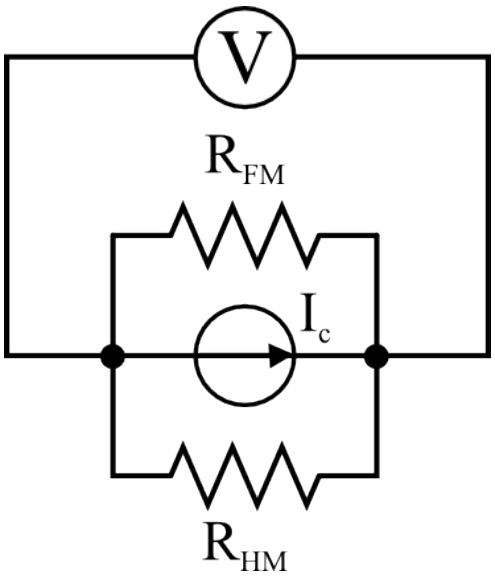

Figure 3.37: Equivalent electric circuit of the FM/HM bilayer. $R_{\rm FM}$ and $R_{\rm HM}$ are the resistances of the ferromagnetic and heavy metal layers respectively. I_c is the charge current generated by the ISHE.

the contacts. The spin current decays in the HM layer as described by eq. 2.63

$$J_{\rm s}(x) = J_{\rm s}^0 \frac{\sinh[(x - t_{\rm NM})/\lambda_{sf}]}{\sinh(t_{\rm NM}/\lambda_{sf})} \ ,$$

with

$$J_{\rm s}^0 = \frac{g_{\rm eff}^{\uparrow\downarrow}\gamma^2 h_{\rm rf}^2 \hbar \left[\mu_0 M_{\rm eff}\gamma + \sqrt{(\mu_0 M_{\rm eff}\gamma)^2 + 4\omega^2}\right]}{8\pi\alpha^2 \left[(\mu_0 M_{\rm s}\gamma)^2 + 4\omega^2\right]} \ .$$

The SHA $\theta_{\rm SH}$ is defined as

$$\theta_{\rm SH} = \frac{J_{\rm c}}{J_{\rm s}} \frac{\hbar}{2e} \ . \tag{3.22}$$

The resulting dc voltage is

$$V = \frac{l\theta_{\rm SH}\lambda_{sf} \tanh(t_{\rm NM}/2\lambda_{\rm sf})}{t_{\rm NM}\sigma_{\rm NM} + t_{\rm FM}\sigma_{\rm FM}} \left(\frac{2e}{\hbar}\right) J_{\rm s}^0 \ . \tag{3.23}$$

The rf magnetic field $h_{\rm rf}$ is determined by measuring the amplitude of the FMR absorption (peak-to-peak height of the signal) of a sample of DPPH powder inserted in the cavity together with the bilayer sample. DPPH is the common abbreviation for the organic chemical compound α-α-diphenyl-β-picryl-hydrazyl, which is a dark crystalline powder composed of stable free-radicals molecules. It is commonly used in laboratory research as a standard for the position and intensity of electron paramagnetic resonance measurements. A paramagnetic system such as the DPPH, can be described by a two spin-level system. Prior to the irradiation, the population of the lower energy spin level is higher than the population of the higher energy spin level. When the system is irradiated, transitions between ground and excited spin states occur and, in the absence of relaxation, eventually the population of the two levels would equalise. This is called absorption saturation. In an actual sample there are two main mechanisms of relaxation. The first one involves spin-lattice relaxations with time constant T_1 and is due to lattice vibrations (phonons). The second involves spin-spin relaxations with time constant T_2 and originates from dipolar and exchange interactions between spins. The values of T_1 and T_2 of DPPH are well known, as well as the value of its gyromagnetic ratio γ. The relaxation mechanisms tend to bring back the populations of the two spin

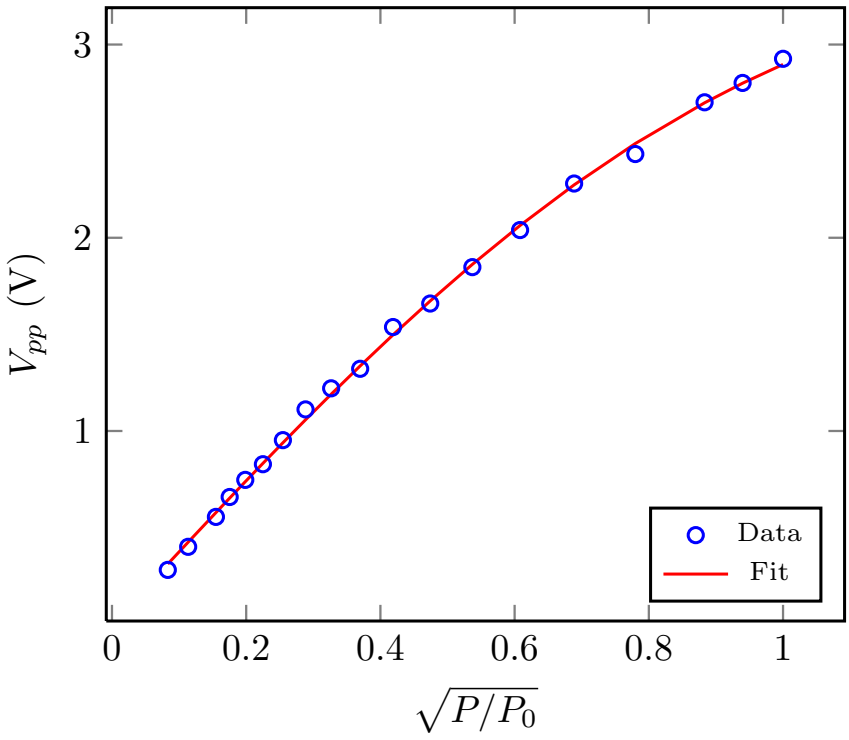

Figure 3.38: DPPH peak-to-peak height of the FMR resonance and fitting with eq 3.24.

levels to the equilibrium condition. The peak-to-peak height of the absorption is given by

$$V_{\mathrm{pp}} = b\left(a\sqrt{P/P_0}\right)\left[\frac{1}{1+\left(a\sqrt{P/P_0}\right)^2\gamma^2 T_1 T_2}\right]^{\frac{3}{2}}, \tag{3.24}$$

with $\gamma^2 T_1 T_2 = 1.211\,24 \times 10^8$ for DPPH and the rf field is given by $a\sqrt{P/P_0}$. a and b are proportionality constants. Fig. 3.38 shows an example of magnetic field calibration using eq 3.24. The measurement is performed with the DPPH powder directly attached to the sample surface because the microwave field is different for each sample due to the different losses. The magnetic field in the cavity is very small ($\sim$0.03 mT), hence it is very difficult to reach real saturation of the spin system. The resonance field of the DPPH is far higher than the resonance field of the FM materials that we studied, hence there is no interference between this measurements and the ISHE measurement. Fig. 3.39 shows an example of FMR absorption signal for the HM/FM bilayer and the DPPH. The DPPH signal is much narrower than the FM signal, as expected from a paramagnetic sample with respect to a ferromagnetic sample. To better display the data, the x axis of the second plot is on a different scale.

The measurements are performed in our cavity FMR setup as described in sec. 3.6.1, *i.e.*, with lock-in detection of the FMR resonance. The dc voltage measurements are performed using a Keithley Nanovoltmeter, Model 2182A. A special hollow spin-free quartz rod is used to insert a twisted pair of thin copper wires in the cavity and contact the edges of the sample using silver solder.

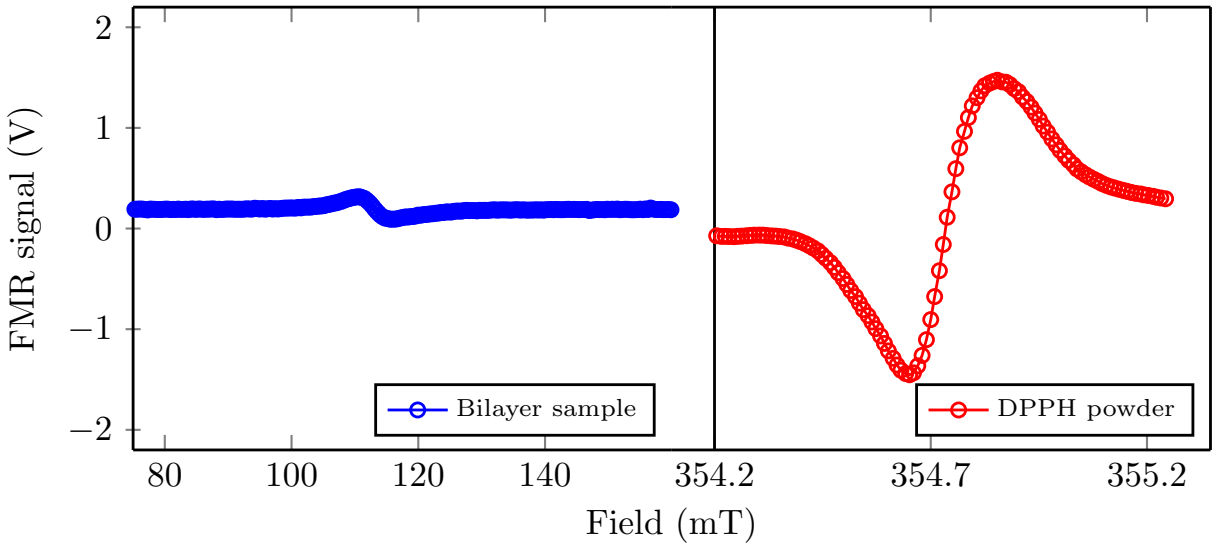

Figure 3.39: FMR signals of the bilayer FM/HM and of the DPPH paramagnetic powder. The scaling of the x axis is not the same for the two plots.

3.7 Other characterisation techniques

3.7.1 Atomic force microscope

The atomic force microscope (AFM) is a very high resolution scanning probe microscope. It consists of a cantilever with a sharp tip that is used to scan the surface of a sample mounted on an anti-vibration plate. When the tip approaches the surface it is attracted by it through contact forces or van der Waals forces and the cantilever bends elastically. The deflection of the cantilever is detected by directing a laser beam on its top surface and by tracking the position of the reflection. In order to avoid accidental collision with the surface, the tip is not kept at a constant absolute height while scanning but a feedback mechanism is employed to keep a constant tip-to-surface distance. This is made possible by piezoelectric elements connected to the cantilever, allowing control of its position. The AFM signal is then given by the feedback signal, *i.e.*, the force that it takes to keep the tip at a certain height from the surface. There are different modes of measurement that can be used with the AFM. The most common is the tapping mode, in which the cantilever is kept oscillating at its own resonance frequency and the signal is given by shifts in the frequency or in the phase of the oscillations caused by the intermittent contact of the tip with the surface. The detection is made with a lock-in technique. Another configuration is the contact mode, in which the tip is dragged along the surface and the deflection of the cantilever is measured. This method is obviously more likely to dull the tip and damage the surface of the sample. An example of AFM image in tapping mode is shown in Fig. 3.40. Cantilevers are usually made of silicon with a reflective top surface coating, while the tips can be made of different materials according on the specific sample or technique. Au coated tips are used for biological samples, diamond tips give better resistance to wear and various magnetic coatings can be used for magnetic measurements (MFM, magnetic force microscope).

3.7.2 SQUID

The superconductive quantum interference device (SQUID) is an extremely high resolution magnetometer. It exploits superconducting loops containing Josephson junctions and is based on the fact that a

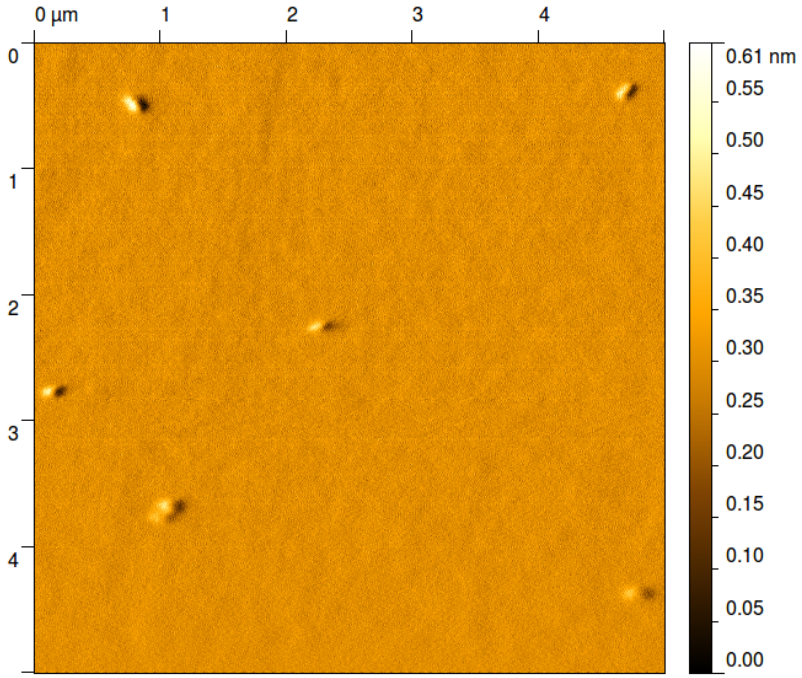

Figure 3.40: AFM scan of a MRG sample. The root mean square roughness is about 20 pm. Some particles of dust are visible.

superconducting loop can enclose only an integer number of magnetic flux quantum Φ_0. When an external field is applied, the loop will screen or increase the flux in order to get to the closest integer number of quanta. In doing so, it creates a circulating current. This current changes sign when the flux exceeds multiples of $\Phi_0/2$. The most efficient type of SQUID is the rf flux-locked: an LC circuit is coupled to the SQUID, providing additional magnetic flux. The rf current injected is used to monitor the inductance of the circuit. Any external flux, coming for example from the sample under measurement, will increase the total inductance, with minima and maxima corresponding to an increase of a flux quantum and half of a quantum, respectively. This external flux is counterbalanced by the LC circuit in order to keep the total flux in the SQUID constant. Therefore, the signal consists of the feedback provided to the LC circuit. The chosen value for the flux is one quantum Φ_0, in order to maximise the sensitivity.

The SQUID is commonly used to measure hysteresis loops of magnetic samples as a function of an applied field, both in the in-plane or out-of-plane orientations with respect to the sample surface. It is also possible to cool down the system to liquid He temperatures. We use a Quantum Design SQUID capable of applying a maximum field up to 5 T.

A SQUID magnetometer is capable of detecting magnetic moments as low as $10^{-9}\,\mathrm{A\,m^2}$, while other magnetometers like alternating gradient force magnetometers (AGFM) and vibrating sample magnetometers (VSM) are limited to $10^{-7}\,\mathrm{A\,m^2}$ and $10^{-6}\,\mathrm{A\,m^2}$, respectively. Some of the samples discussed in this work are antiferromagnets or ferrimagnets with very low magnetisation: in this case a SQUID was the only possible choice for the magnetic characterisation of the samples.

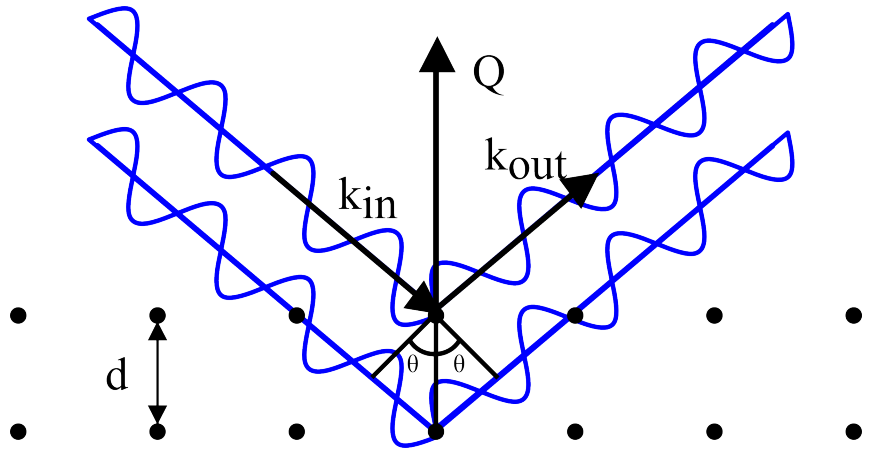

Figure 3.41: Schematic representation of Bragg's law of diffraction. Incident x-ray beams at an angle θ are reflected from parallel atomic planes with lattice parameter d.

3.7.3 X-ray diffraction and reflectometry

Characterisation of the crystal structure of thin films is commonly performed by x-ray diffraction (XRD). This technique is based on Bragg's law [64] describing the reflection of x-rays from parallel planes of atoms (see Fig. 3.41)

$$m\lambda = 2d\sin(\theta) \ , \tag{3.25}$$

where λ is the x-ray wavelenght, d is the normal distance between the planes, θ is the angle of incidence with respect to the planes and m is an integer representing the diffraction order. The waves scatter on each atom and the interference pattern is detected at a large distance from the sample. The interference is constructive if the phase shift between two reflected beams is a multiple of 2π. Bragg's law 3.25 is equivalent to the von Laue formulation

$$\vec{Q} = \vec{k}_{\text{out}} - \vec{k}_{\text{in}} \in \mathbb{R}^* \ , \tag{3.26}$$

where $\vec{k}_{\text{out}}$ and $\vec{k}_{\text{in}}$ are the wavectors of the incident and scattered beams and $\mathbb{R}^*$ is the reciprocal lattice space. The situation can be visualised using the Edwald's sphere representation (Fig. 3.42).

Each vector $\vec{Q}$ belonging to the reciprocal lattice, and consequently each corresponding peak in the diffraction pattern, is labelled by the Miller indexes (h, k, l), referring to the order of the diffraction in each crystallographic axis. In the majority of crystals, the basis of the unit cell is not composed of a single atom. Hence, additional interference between waves scattered from the atoms of the basis results in the suppression of particular peaks (forbidden peaks). For example, in a body-centered cubic (BCC) crystal, peaks with $(h^2 + k^2 + l^2)$ odd are not allowed. A more accurate description can be given by considering different form factors for the diffraction from different elements.

The angle at which a peak is found depends on the type of crystal structure of the sample and on the lattice parameters.

XRD is typically a single $2\theta - \omega$ scan ($\omega = \frac{2\theta}{2}$). Apart from giving us an indication of the crystal structure and determining the out-of-plane crystal lattice parameter of the film being studied, we can also use it to investigate the strain of the sample by analysing the shifts of the peak positions for different values of strain, the broadening of the peaks and the relative peak intensities.

Reciprocal space mapping (RSM) is a full space map of (h, k, l) or (Q_x, Q_z) space within accessible

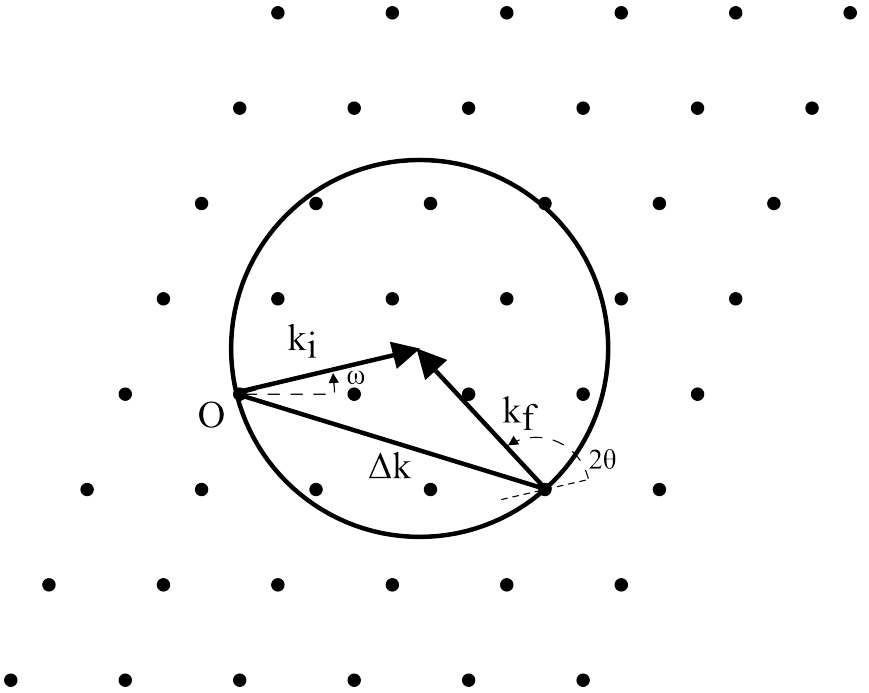

Figure 3.42: Ewald's sphere. The incident wavevector $\vec{k}_{\text{in}}$ is drawn starting from the origin of the reciprocal lattice O at the angle of incidence on the lattice. A sphere with the radius of the vector is drawn from the end of $\vec{k}_{\text{in}}$, which has angle of incidence ω. A diffraction peak is observed for all $\vec{k}_{\text{out}}$ connecting a point of the reciprocal lattice falling on the sphere and the end of $\vec{k}_{\text{in}}$. The difference between the two vectors is a reciprocal lattice vector $\vec{Q}$. The angle 2θ is the angle between the incident and outgoing vectors.

boundaries based on the measurement geometry. With this technique, it is possible to obtain more information of both in-plane and out-of-plane lattice parameters, strain and crystal structure. The drawback of RSM measurements is the large amount of time necessary to obtain a good signal-to-noise ratio and well defined lineshapes of the peaks.

The Scherrer equation

$$\tau = \frac{K\lambda}{\text{FWHM}(2\theta)\cos(\theta_{\text{B}})} \ , \tag{3.27}$$

is used to relate the size τ of the particles of crystallites in a sample to the broadening of the XRD peaks due to the finite number of cells that contribute to the scattering process. Here, λ is the wavelength of the x-rays, FWHM(2θ) is the full width at half maximum of the peak in 2θ radians and θ_{B} is the Bragg angle for the considered peak. K is a shape factor that is used to take into account the type of sample that is measured (powders, thin films, granular with different grain shapes, etc). It is always close to 1, but for thin films the most commonly used value is 0.9. The Scherrer equation gives a lower bound for the grain size, since other factors contribute to the broadening of the peaks, like the instrumental broadening, microstrain, stacking faults, antiphase boundaries and mosaicity of the substrate. In our sample, the latter contribution is the most important one: the mosaicity is the presence of terraces of atomic layers instead of a single flat surface. This can contribute largely to the peak broadening, since a thin film deposited on such a substrate will reproduce the mosaicity.

X-ray reflectivity (XRR) is used to establish the thickness, roughness and densities of the layers in a thin films sample. The x-ray beam is sent towards the materials surface at a grazing angle of incidence. Total reflection will occur below a critical angle θ_{c} (see eq. 2.97). This angle is related to the electronic density of the sample. At grazing incidence, the x-rays are reflected from the interfaces between thin

layers, between the first layer and the substrate and between the sample surface and the air. For small θ_i, the reflectivity is given by

$$R = \left| \frac{n_1 - n_2}{n_1 + n_2} \right|^2 , \tag{3.28}$$

where n_1 and n_2 are the refractive indexes of the two considered layers. The width of the maxima is related to the roughness of the surfaces.

Our system consists of a BRUKER D8 diffractometer. It uses a Cu K_α x-ray tube, a Göbel mirror and a double-bounce channel-cut Ge crystal monochromator. A 0.1 mm divergence slit and a 2.5° Soller slit are used for the final beam conditioning. On the diffracted beam side, a 1D "LynxEye" detector and a 2.5° Soller slits enable the determination of the peak positions and intensities.

References

[1] M. Ohring. *Material Science of Thin Films.* Academic Press, 2011.

[2] B. Chapman. *Glow Discharge Processes: Sputtering and Plasma Etching.* Wiley-Interscience, 1990.

[3] J. J. P. Elich, H. E. Roosendaal & D. Onderdelinden. *Precision measurements on the angular and temperature dependence of sputtering.* Radiation Effects, **14**(1-2):93, 1972. doi:10.1080/00337577208230477.

[4] K. Seshan. *Handbook of Thin Film Deposition.* William Andrew, 2012.

[5] J. R. Sheats & B. W. Smith. *Microlithography: Science and Technology.* CRC Press, 1998.

[6] S. A. Campbell. *The Science and Engineering of Microelectronic Fabrication.* Oxford University Press, 2001.

[7] G. van der Laan & A. I. Figueroa. *X-ray magnetic circular dichroism—a versatile tool to study magnetism.* Coordination Chemistry Reviews, **277–278**(0):95 , 2014. ISSN 0010-8545. doi:http://dx.doi.org/10.1016/j.ccr.2014.03.018. Following Chemical Structures using Synchrotron Radiation.

[8] P. Carra, B. T. Thole, M. Altarelli & X. Wang. *X-ray circular dichroism and local magnetic fields.* Phys. Rev. Lett., **70**:694, Feb 1993. doi:10.1103/PhysRevLett.70.694.

[9] F. de Groot. *X-ray absorption and dichroism of transition metals and their compounds.* Journal of Electron Spectroscopy and Related Phenomena, **67**(4):529 , 1994. ISSN 0368-2048. doi:http://dx.doi.org/10.1016/0368-2048(93)02041-J.

[10] H. Wende. *Recent advances in x-ray absorption spectroscopy.* Reports on Progress in Physics, **67**(12):2105, 2004.

[11] B. T. Thole & G. van der Laan. *Branching ratio in x-ray absorption spectroscopy.* Phys. Rev. B, **38**:3158, Aug 1988. doi:10.1103/PhysRevB.38.3158.

[12] J. Stöhr & H. König. *Determination of spin- and orbital-moment anisotropies in transition metals by angle-dependent x-ray magnetic circular dichroism.* Phys. Rev. Lett., **75**:3748, Nov 1995. doi:10.1103/PhysRevLett.75.3748.

[13] C. Piamonteze, P. Miedema & F. M. F. de Groot. *Accuracy of the spin sum rule in XMCD for the transition-metal l edges from manganese to copper.* Phys. Rev. B, **80**:184410, Nov 2009. doi:10.1103/PhysRevB.80.184410.

[14] J. J. Rehr & R. C. Albers. *Theoretical approaches to x-ray absorption fine structure.* Rev. Mod. Phys., **72**:621, Jul 2000. doi:10.1103/RevModPhys.72.621.

[15] J. Yano & V. K. Yachandra. *X-ray absorption spectroscopy.* Photosynthesis Research, **102**(2-3):241, 2009. ISSN 0166-8595. doi:10.1007/s11120-009-9473-8.

[16] R. d. L. Kronig. *Zur theorie der feinstruktur in den röntgenabsorptionsspektren.* Zeitschrift für Physik, **70**(5-6):317, 1931. ISSN 0044-3328. doi:10.1007/BF01339581.

[17] R. d. L. Kronig. *Zur theorie der feinstruktur in den röntgenabsorptionsspektren. iii.* Zeitschrift für Physik, **75**(7-8):468, 1932. ISSN 0044-3328. doi:10.1007/BF01342238.

[18] D. E. Sayers, E. A. Stern & F. W. Lytle. *New technique for investigating noncrystalline structures: Fourier analysis of the extended x-ray¯absorption fine structure.* Phys. Rev. Lett., **27**:1204, Nov 1971. doi:10.1103/PhysRevLett.27.1204.

[19] J. J. Rehr, J. J. Kas, F. D. Vila, M. P. Prange & K. Jorissen. *Parameter-free calculations of x-ray spectra with FEFF9.* Phys. Chem. Chem. Phys., **12**:5503, 2010. doi:10.1039/B926434E.

[20] P. Weightman. *X-ray-excited auger and photoelectron spectroscopy.* Reports on Progress in Physics, **45**(7):753, 1982.

[21] O. Gunnarsson & K. Schönhammer. *Electron spectroscopies for Ce compounds in the impurity model.* Phys. Rev. B, **28**:4315, Oct 1983. doi:10.1103/PhysRevB.28.4315.

[22] J. Zaanen, C. Westra & G. A. Sawatzky. *Determination of the electronic structure of transition-metal compounds: 2p x-ray photoemission spectroscopy of the nickel dihalides.* Phys. Rev. B, **33**:8060, Jun 1986. doi:10.1103/PhysRevB.33.8060.

[23] S. Plogmann, T. Schlathölter, J. Braun, M. Neumann, Y. M. Yarmoshenko, M. V. Yablonskikh, E. I. Shreder, E. Z. Kurmaev, A. Wrona & A. Ślebarski. *Local moments in Mn-based Heusler alloys and their electronic structures.* Phys. Rev. B, **60**:6428, Sep 1999. doi:10.1103/PhysRevB.60.6428.

[24] P. Weightman & R. Cole. *Electron spectroscopy of disordered metal alloys.* Journal of Electron Spectroscopy and Related Phenomena, **178–179**(0):100 , 2010. ISSN 0368-2048. doi:http://dx.doi.org/10.1016/j.elspec.2009.05.003. Trends in X-ray Photoelectron Spectroscopy of solids (theory, techniques and applications).

[25] P. S. Bagus, E. S. Ilton & C. J. Nelin. *The interpretation of {XPS} spectra: Insights into materials properties.* Surface Science Reports, **68**(2):273 , 2013. ISSN 0167-5729. doi:http://dx.doi.org/10.1016/j.surfrep.2013.03.001.

[26] H. Tokutaka, N. Ishihara, K. Nishimori, S. Kishida & K. Isomoto. *Background removal in x-ray photoelectron spectroscopy.* Surface and Interface Analysis, **18**(10):697, 1992. ISSN 1096-9918. doi:10.1002/sia.740181002.

[27] M. Seah. *Background subtraction: I. General behaviour of Tougaard-style backgrounds in AES and XPS.* Surface Science, **420**(2–3):285 , 1999. ISSN 0039-6028. doi:http://dx.doi.org/10.1016/S0039-6028(98)00852-8.

[28] J. Végh. *The Shirley-equivalent electron inelastic scattering cross-section function.* Surface Science, **563**(1–3):183 , 2004. ISSN 0039-6028. doi:http://dx.doi.org/10.1016/j.susc.2004.06.154.

[29] J. Végh. *The Shirley background revised.* Journal of Electron Spectroscopy and Related Phenomena, **151**(3):159 , 2006. ISSN 0368-2048. doi:http://dx.doi.org/10.1016/j.elspec.2005.12.002.

[30] S. Tougaard. *Formalism for quantitative surface analysis by electron spectroscopy.* Journal of Vacuum Science & Technology A, **8**(3):2197, 1990. doi:http://dx.doi.org/10.1116/1.577037.

[31] W. Eberhardt & F. J. Himpsel. *Dipole selection rules for optical transitions in the fcc and bcc lattices.* Phys. Rev. B, **21**:5572, Jun 1980. doi:10.1103/PhysRevB.21.5572.

[32] C. P. P. Jr. *Theory of Magnetic Resonance.* Wiley-Interscience, 1987.

[33] L. Liu, T. Moriyama, D. C. Ralph & R. A. Buhrman. *Spin-torque ferromagnetic resonance induced by the spin Hall effect.* Phys. Rev. Lett., **106**:036601, Jan 2011. doi:10.1103/PhysRevLett.106.036601.

[34] Fan Xin, Wu Jun, Chen Yunpeng, Jerry Matthew J., Zhang Huaiwu & Xiao John Q. *Observation of the nonlocal spin-orbital effective field.* Nat Commun, **4**:1799, Apr 2013. doi:http://dx.doi.org/10.1038/ncomms270910.1038/ncomms2709.

[35] C. Wang, H. Seinige & M. Tsoi. *Ferromagnetic resonance driven by an ac current: A brief review.* Low Temperature Physics, **39**(3):247, 2013. doi:http://dx.doi.org/10.1063/1.4794998.

[36] A. Ganguly, K. Kondou, H. Sukegawa, S. Mitani, S. Kasai, Y. Niimi, Y. Otani & A. Barman. *Thickness dependence of spin torque ferromagnetic resonance in $Co_{75}Fe_{25}$/Pt bilayer films.* Applied Physics Letters, **104**(7):072405, 2014. doi:http://dx.doi.org/10.1063/1.4865425.

[37] M. I. Dyakonov. *Future Trends in Microelectronics: From Nanophotonics to Sensors to Energy.* Wiley-IEEE Press, 2010.

[38] J. E. Hirsch. *Spin Hall effect.* Phys. Rev. Lett., **83**:1834, Aug 1999. doi:10.1103/PhysRevLett.83.1834.

[39] S. Zhang. *Spin Hall effect in the presence of spin diffusion.* Phys. Rev. Lett., **85**:393, Jul 2000. doi:10.1103/PhysRevLett.85.393.

[40] A. Hoffmann. *Spin Hall effects in metals.* Magnetics, IEEE Transactions on, **49**(10):5172, Oct 2013. ISSN 0018-9464. doi:10.1109/TMAG.2013.2262947.

[41] Y. A. Bychkov & E. I. Rashba. *Oscillatory effects and the magnetic susceptibility of carriers in inversion layers.* Journal of Physics C: Solid State Physics, **17**(33):6039, 1984.

[42] A. Manchon & S. Zhang. *Theory of spin torque due to spin-orbit coupling.* Phys. Rev. B, **79**:094422, Mar 2009. doi:10.1103/PhysRevB.79.094422.

[43] Mihai Miron Ioan, Gaudin Gilles, Auffret Stephane, Rodmacq Bernard, Schuhl Alain, Pizzini Stefania, Vogel Jan & Gambardella Pietro. *Current-driven spin torque induced by the Rashba effect in a ferromagnetic metal layer.* Nat Mater, **9**(3):230, Mar 2010. ISSN 1476-1122. doi:http://dx.doi.org/10.1038/nmat2613. 10.1038/nmat2613.

[44] J.-C. Rojas-Sánchez, N. Reyren, P. Laczkowski, W. Savero, J.-P. Attané, C. Deranlot, M. Jamet, J.-M. George, L. Vila & H. Jaffrès. *Spin pumping and inverse spin Hall effect in platinum: The essential role of spin-memory loss at metallic interfaces.* Phys. Rev. Lett., **112**:106602, Mar 2014. doi:10.1103/PhysRevLett.112.106602.

[45] A. Wirthmann, X. Fan, Y. S. Gui, K. Martens, G. Williams, J. Dietrich, G. E. Bridges & C.-M. Hu. *Direct phase probing and mapping via spintronic Michelson interferometry.* Phys. Rev. Lett., **105**:017202, Jun 2010. doi:10.1103/PhysRevLett.105.017202.

[46] M. Harder, Z. X. Cao, Y. S. Gui, X. L. Fan & C.-M. Hu. *Analysis of the line shape of electrically detected ferromagnetic resonance.* Phys. Rev. B, **84**:054423, Aug 2011. doi:10.1103/PhysRevB.84.054423.

[47] A. Azevedo, L. H. Vilela-Leão, R. L. Rodríguez-Suárez, A. F. Lacerda Santos & S. M. Rezende. *Spin pumping and anisotropic magnetoresistance voltages in magnetic bilayers: Theory and experiment.* Phys. Rev. B, **83**:144402, Apr 2011. doi:10.1103/PhysRevB.83.144402.

[48] L. Bai, P. Hyde, Y. S. Gui, C.-M. Hu, V. Vlaminck, J. E. Pearson, S. D. Bader & A. Hoffmann. *Universal method for separating spin pumping from spin rectification voltage of ferromagnetic resonance.* Phys. Rev. Lett., **111**:217602, Nov 2013. doi:10.1103/PhysRevLett.111.217602.

[49] W. T. Soh, B. Peng & C. K. Ong. *An angular analysis to separate spin pumping-induced inverse spin Hall effect from spin rectification in a Py/Pt bilayer.* Journal of Physics D: Applied Physics, **47**(28):285001, 2014.

[50] D.-J. Kim, S.-I. Kim, S.-Y. Park, K.-D. Lee & B.-G. Park. *Ferromagnetic resonance spin pumping in CoFeB with highly resistive non-magnetic electrodes.* Current Applied Physics, **14**(10):1344 , 2014. ISSN 1567-1739. doi:http://dx.doi.org/10.1016/j.cap.2014.07.013.

[51] K. Ando, S. Takahashi, K. Harii, K. Sasage, J. Ieda, S. Maekawa & E. Saitoh. *Electric manipulation of spin relaxation using the spin Hall effect.* Phys. Rev. Lett., **101**:036601, Jul 2008. doi:10.1103/PhysRevLett.101.036601.

[52] S. Petit, C. Baraduc, C. Thirion, U. Ebels, Y. Liu, M. Li, P. Wang & B. Dieny. *Spin-torque influence on the high-frequency magnetization fluctuations in magnetic tunnel junctions.* Phys. Rev. Lett., **98**:077203, Feb 2007. doi:10.1103/PhysRevLett.98.077203.

[53] C.-F. Pai, L. Liu, Y. Li, H. W. Tseng, D. C. Ralph & R. A. Buhrman. *Spin transfer torque devices utilizing the giant spin Hall effect of tungsten.* Applied Physics Letters, **101**(12):122404, 2012. doi:http://dx.doi.org/10.1063/1.4753947.

[54] K. Ando, Y. Kajiwara, S. Takahashi, S. Maekawa, K. Takemoto, M. Takatsu & E. Saitoh. *Angular dependence of inverse spin˘Hall effect induced by spin pumping investigated in a* $ni_{81}fe_{19}/Pt$ *thin film.* Phys. Rev. B, **78**:014413, Jul 2008. doi:10.1103/PhysRevB.78.014413.

[55] O. Mosendz, J. E. Pearson, F. Y. Fradin, G. E. W. Bauer, S. D. Bader & A. Hoffmann. *Quantifying spin Hall angles from spin pumping: Experiments and theory.* Phys. Rev. Lett., **104**:046601, Jan 2010. doi:10.1103/PhysRevLett.104.046601.

[56] O. Mosendz, V. Vlaminck, J. E. Pearson, F. Y. Fradin, G. E. W. Bauer, S. D. Bader & A. Hoffmann. *Detection and quantification of inverse spin Hall effect from spin pumping in permalloy/normal metal bilayers.* Phys. Rev. B, **82**:214403, Dec 2010. doi:10.1103/PhysRevB.82.214403.

[57] H. Nakayama, K. Ando, K. Harii, T. Yoshino, R. Takahashi, Y. Kajiwara, K. Uchida, Y. Fujikawa & E. Saitoh. *Geometry dependence on inverse spin Hall effect induced by spin pumping in* $Ni_{81}Fe_{19}/Pt$ *films.* Phys. Rev. B, **85**:144408, Apr 2012. doi:10.1103/PhysRevB.85.144408.

[58] V. Vlaminck, J. E. Pearson, S. D. Bader & A. Hoffmann. *Dependence of spin-pumping spin Hall effect measurements on layer thicknesses and stacking order.* Phys. Rev. B, **88**:064414, Aug 2013. doi:10.1103/PhysRevB.88.064414.

[59] C. Hahn, G. de Loubens, O. Klein, M. Viret, V. V. Naletov & J. Ben Youssef. *Comparative measurements of inverse spin Hall effects and magnetoresistance in YIG/Pt and YIG/Ta.* Phys. Rev. B, **87**:174417, May 2013. doi:10.1103/PhysRevB.87.174417.

[60] H. Wang, C. Du, P. Chris Hammel & F. Yang. *Spin current and inverse spin Hall effect in ferromagnetic metals probed by $Y_3Fe_5O_{12}$-based spin pumping.* Applied Physics Letters, **104**(20):202405, 2014. doi:http://dx.doi.org/10.1063/1.4878540.

[61] L. Wang, H. H. Du, C. Y. Pu, R. Adur, C. Hammel, P. & Y. Yang, F.˙ *Scaling of spin Hall angle in 3d, 4d, and 5d metals from* $Y_3Fe_5O_{12}$*/metal spin pumping.* Phys. Rev. Lett., **112**:197201, May 2014. doi:10.1103/PhysRevLett.112.197201.

[62] C. Du, H. Wang, F. Yang & P. C. Hammel. *Enhancement of pure spin currents in spin pumping* $Y_3Fe_5O_{12}$/Cu/Metal *trilayers through spin conductance matching.* Phys. Rev. Applied, **1**:044004, May 2014. doi:10.1103/PhysRevApplied.1.044004.

[63] Wei Dahai, Obstbaum Martin, Ribow Mirko, Back Christian H. & Woltersdorf Georg. *Spin Hall voltages from a.c. and d.c. spin currents.* Nat Commun, **5**, Apr 2014. doi:http://dx.doi.org/10.1038/ncomms476810.1038/ncomms4768.

[64] N. W. Ashcroft & N. D. Mermin. *Solid State Physics.* Cengage Learning, 1976.

Chapter 4

Heusler alloys

In the last few decades the increasing importance of spin electronics has directed research towards experimentation on new building blocks for future applications in high density magnetic storage and magnetic logic circuits. At present, the most used combinations of materials in magnetic tunnel junction (MTJ) devices is the CoFeB/MgO/CoFeB trilayer. With this combination it is possible to achieve more than 200 % magnetoresistance (MR) at room temperature, thanks to the spin polarisation of the ferromagnetic electrodes and, more importantly, to the spin filtering effect of the MgO barrier. Some improvements to this solution are possible. Firstly, if it has to satisfy industrial requirements, the fabrication of such a structure is only possible by depositing MgO on amorphous CoFeB and subsequently annealing at ∼350 °C in order to crystallise the CoFeB by driving the boron out to a nearby getter such as Ta. The resulting CoFe layers have low magneto-crystalline anisotropy. The weak shape anisotropy is then used for data storage but it results in poor thermal stability and data retention. An alternative solution consists in using an ultrathin layer of CoFeB on a Ta seed layer. Together with the MgO barrier on top of it, this combination creates a perpendicular magnetic anisotropy (PMA) due to interface interactions that can be exploited to obtain better thermal stability. Another limitation of this system is the difficulty of integration with multifunctional materials, for example from the oxide family (SRO, STO, BTO, LSMO, etc).

There has recently been a revived interest in the intermetallic compounds from the Heusler alloy family. This interest is due to the extremely varied physical properties that can be found within this class of material. A wide range of both full and half Heusler alloys, in their cubic $L2_1$ and $C1_b$ crystalline form, respectively, have been predicted [1–3] to be half metals with a gap Δ in the spin polarised density of states for one spin band (see Fig. 4.1), which should make them ideal candidates for spin-valves or MTJs. Unfortunately, some of these materials don't crystallise in the correct structure but in the tetragonally distorted DO_{22} structure. In addition, the high spin polarisation of the cubic alloys has only been demonstrated at low temperatures, although moderately high TMR can be maintained at room temperature.

In this chapter, we will discuss the characteristic of tetragonally distorted $Mn_{3-x}Ga$ ($0 \leq x \leq 1$) and cubic compensated ferrimagnet Mn_2Ru_xGa thin films. Since Mn_3Ga has been predicted [2] to be half metallic in its cubic form, we have grown and characterised thin films of $Mn_{3-x}Ga$ ($0 \leq x \leq 1$) on V seed layers. The use of the vanadium seed layer makes the alloys to grow in the cubic structure but the poor quality of the samples didn't allow us to obtain the desired characteristic. The results of the characterisation of these samples is discussed in Appendix D.

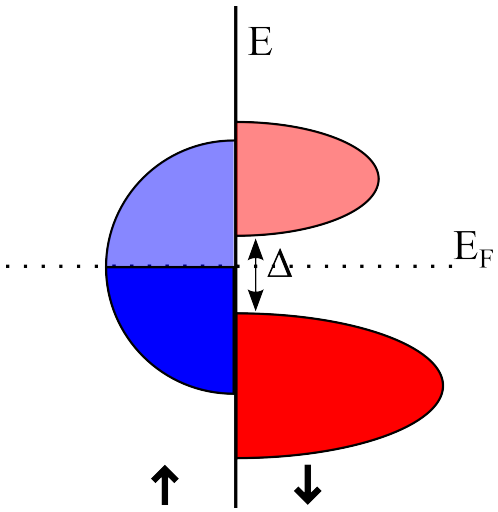

Figure 4.1: Schematic of the band structure of a half metal. The minority spin band has a gap Δ at the fermi level E_{F}.

4.1 Introduction

A Heusler compound is a ternary inter-metallic with the general formula XYZ (often called half Heusler) or X_2YZ, where X and Y typically are transition metals and Z is a main group element [4–6]. The major part of the interest in these class of materials came with the electronic structure calculations of de Groot *et. al.* [1]. He predicted that Mn-based half Heusler alloys such as NiMnSb and PtMnSb shoud be half-metallic. Later, other full Heusler compounds such as Co_2MnZ and Fe_2MnZ, with Z = Ge or Si have been proposed to be half metals [7]. A half metal features exchange-split electronic bands: while one of them crosses the Fermi level, hence behaving as a metallic band, the other presents a gap. Because of this spin gap, only one spin channel contributes to electrical conduction, resulting in, ideally, 100 % spin polarisation of an electric current. This characteristic could be easily exploited in spin electronic devices, such as MTJs or spin valves (see sec. 2.3.9), to achieve high MR or more efficient spin transfer torque effect. While other magnetic materials such as Co and Ni have a spin gap in the $3d$ band, their total spin polarisation at the Fermi level is much reduced by the presence of largely unpolarised states deriving from the $4s$ band. On the other hand, a half metal has a spin gap in the total density of states for one subband. The spin moment in Bohr magnetons per atom is then given by $M = N_\uparrow - N_\downarrow$ with $N_\uparrow$ and $N_\downarrow$ the number of spin $\uparrow$ and spin $\downarrow$ valence electrons. Since the total number of valence electrons per atom is $N_{\mathrm{v}} = N_\uparrow + N_\downarrow$ it results in

$$\begin{aligned} M &= 2N_\uparrow - N_{\mathrm{v}} \quad \text{and} \\ M &= N_{\mathrm{v}} - 2N_\downarrow \ . \end{aligned} \tag{4.1}$$

The magnetisation as a function of the number of valence electrons can be derived in the case of Heusler alloys considering the localised electrons approximation. We are going to discuss this model below, since it gives a simple view of the electronic structure in these compounds. However, it has to be kept in mind that the model fails in describing compounds with very delocalised (metallic) states or in which effects such as the charge transfer can heavily modify the electronic structure.

In a full Heusler, the Z atom has s and p valence bands that can host a total of 8 electrons. In O_h symmetry, the s orbitals span the A_{1g} representation but they are very low in energy with respect to

Table 4.1: Representation in O_h symmetry of orbitals from the $X-X$ interaction and from the Y atom. Subscripts $1, 2, 3, 4$ and 5 refer to d orbitals xy, yz, zx, $3z^2-r^2$ and x^2-y^2 and to p orbitals of $\hat{x}$, $\hat{y}$ and $\hat{z}$ symmetry, respectively. The subscripts a and b refer to the two non-equivalent X atoms in the unit cell.

Representation	$X-X$	Y
A_{1g}	$s_a + s_b$	s
A_{1u}	$s_a - s_b$	
E_g	$d_{ia} + d_{ib}$ $[i = 4, 5]$	$d_4 d_5$
E_u	$d_{ia} - d_{ib}$ $[i = 4, 5]$	
T_{2g}	$p_{1a} - p_{ib}$ & $d_{ia} + d_{ib}$ $[i = 1, 2, 3]$	$d_1 d_2 d_3$
T_{1u}	$p_{1a} + p_{ib}$ & $d_{ia} - d_{ib}$ $[i = 1, 2, 3]$	$p_1 p_2 p_3$

the other bands and they do not hybridise. The p orbitals have T_{1u} symmetry and hybridise with the p orbitals of the other atoms. Since this sp band is lower in energy with respect to the other band at the Fermi level, these orbitals are fully occupied. Since they can only be partially filled with electrons from the Z atom, d electrons from the valence bands of the X and Y atoms accommodate in these bands.

The interactions between orbitals of the different atoms are shown in Tab. 4.1 and represented in Fig. 4.2. Because of the different symmetries, the E_g orbitals at one X site can couple only to E_g orbitals of the other X or the Y site. The same applies for the T_{2g} orbitals. Considering the two X atoms, the d_1, d_2 and d_3 orbitals generate triply degenerate bonding and antibonding T_{2g} and T_{1u} orbitals, respectively. On the other hand, the d_4 and d_5 orbitals create doubly degenerate bonding E_g and antibonding and E_u orbitals, respectively. These resulting states couple with the states of the Y atoms with the same symmetry. The result is a doubly degenerate E_g level and triply degenerate T_{2g} and T_{1u} levels below the Fermi level. Above it, we have doubly degenerate E_u and E_g levels and a triply degenerate T_{2g} level. Therefore, in total the X and Y atoms generate 8 d bands for minority electrons. Hence, for a full Heusler eq. 4.1 becomes

$$M = N_\mathrm{v} - 24 \ . \tag{4.2}$$

This is usually called the Slater-Pauling rule [5]. On the other hand, in an half Heusler there is only one X atom that can hybridise its d orbitals with the Y atom and provide 5 minority d bands, as in the $X-X$ diagram of Fig. 4.2. Therefore, the Slater-Pauling rule for half Heuslers is

$$M = N_\mathrm{v} - 18 \ . \tag{4.3}$$

Because of the absence of the E_u and T_{1u} levels, the gap is usually bigger in half Heuslers than in full Heuslers. All these considerations are valid at zero temperature and without considering any mixing of the states by spin-orbit coupling. The experimentally determined spin polarisation for such materials turned out to be far less than the ideal 100 % that the theory predicts. The values for NiMnSb and Co_2MnSi turn out to be about 50 % as obtained by point-contact Andreev reflection. In addition, as anticipated in the previous section, the bulk form of several of these alloys is not the cubic $L2_1$ or $C1_b$ structure but the tetragonally-deformed DO_{22} variant.

Heusler alloys with 24 valence electrons and half Heusler with 18 electrons are particularly interesting because the Slater-Pauling rules predict zero net magnetisation for these materials [8, 9]. They should be compensated ferrimagnets: the two magnetic sublattices are antiferromagnetically coupled and the magnetic moments cancel each other. We prefer to use the word “ferrimagnets” instead of “antiferromagnets” because we reserve the latter for crystallographic-equivalent sublattices, where no net spin polarisation at the Fermi level is possible. In addition, these materials maintain their half-metallicity, *i.e.*, there is a

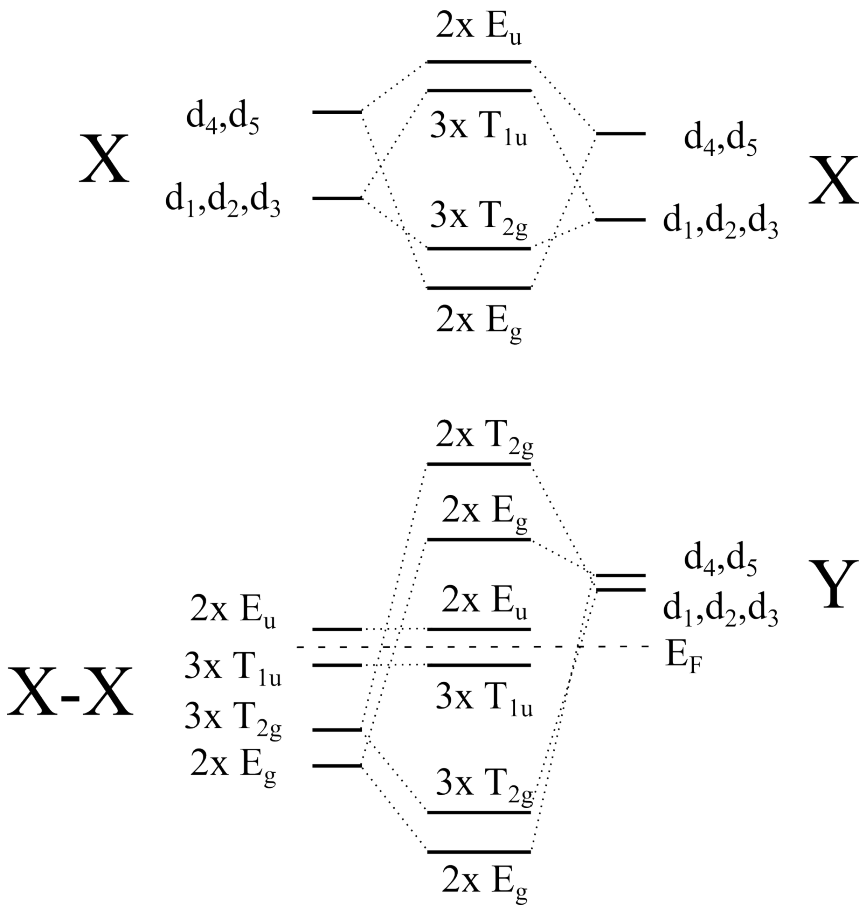

Figure 4.2: Schematic representation of the hybridisation of the d orbitals in a full Heusler alloy. The notation used is the same as in Tab. 4.1. From ref. [2].

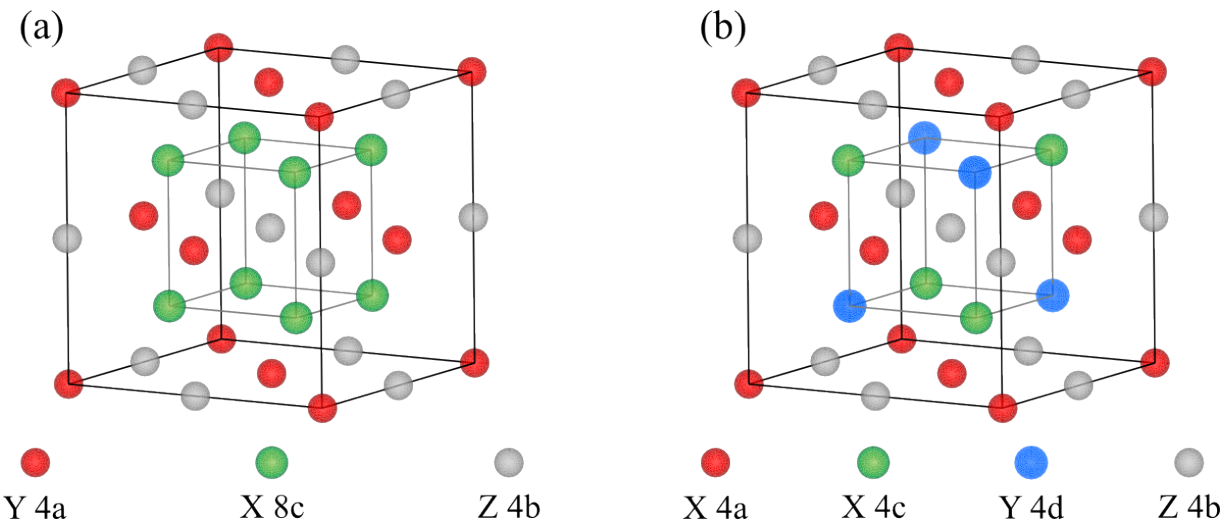

Figure 4.3: a) $L2_1$ crystal structure for a "normal" Heusler alloy b) $L2_1$ crystal structure for an "inverse" Heusler alloy.

spin gap at the Fermi level. A compensated half metal ferrimagnet would be very useful, since it would be fully spin polarised yet free from shape anisotropy, it creates no stray fields and it would be insensitive to external fields. The cubic form of Mn_3Ga (full Heusler with 24 valence electrons) has been predicted to be a compensated half metal ferrimagnet [2].

The Mn-Ga phase diagram is complex, with 15 different binary phases [10]. Furthermore, when considering the thin film form, there is additional uncertainty because of the presence of the seed layer and of the non equilibrium conditions of the deposition.

The ordered cubic $L2_1$ structure for X_2YZ Heusler alloys is illustrated in Fig. 4.3 X atoms occupy position 8c $\left(\frac{1}{4},\frac{1}{4},\frac{1}{4}\right)$, while Y and Z atoms occupy the 4a $(0,0,0)$ and 4b $\left(\frac{1}{2},\frac{1}{2},\frac{1}{2}\right)$ positions. Another structure often found in this kind of alloys is the so-called "inverse" Heusler type, where half of the atoms in position 8c are interchanged with the atoms in position 4a. The 8c position splits into two inequivalent sites 4c $\left(\frac{3}{4},\frac{3}{4},\frac{3}{4}\right)$ and 4d $\left(\frac{1}{4},\frac{1}{4},\frac{1}{4}\right)$. This way, we have X atoms in positions 4a and 4c, Y atoms in position 4d and Z atoms in position 4b. The "normal" type is favoured if X has higher number of valence electrons than Y. However, the "inverse" structure will be found if X is one of the earlier transition metal. If $X = Y$ the cubic DO_3 structure is formed.

The half Heusler structures (Fig. 4.4) are obtained by removing one of the X atoms from the crystals.

The tetragonal Heuslers are formed by taking a smaller cell from the $L2_1$ and $C1_b$ structures and stretching it along the c-axis (Fig. 4.5). This deformation is usually essential, with a c/a ratio that increases to 1.8 in the DO_{22} structure, and creates magneto-crystalline anisotropy with an easy axis. Anyway, it is found experimentally that the ordering of the X, Y and Z atoms is often less than ideal.

4.2 DO_{22} $Mn_{3-x}Ga$

4.2.1 Review of characteristics

We have grown thin-film samples of $Mn_{3-x}Ga$ on 10 mm × 10 mm $SrTiO_3$ and MgO single crystal substrates using our "Shamrock" fully automated deposition tool (see sec. 3.1.1). The films were sputtered from stoichiometric Mn_3Ga, Mn_2Ga and Mn targets onto substrates at a temperature of 350 °C. The samples

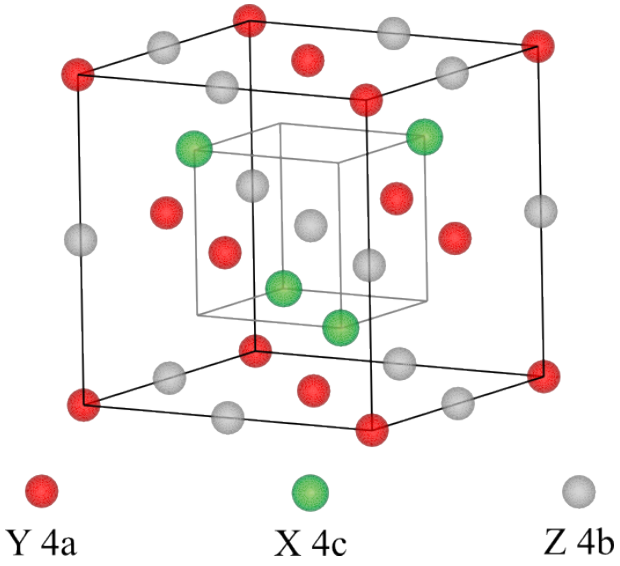

Figure 4.4: $C1_b$ crystal structure for a half Heusler alloy.

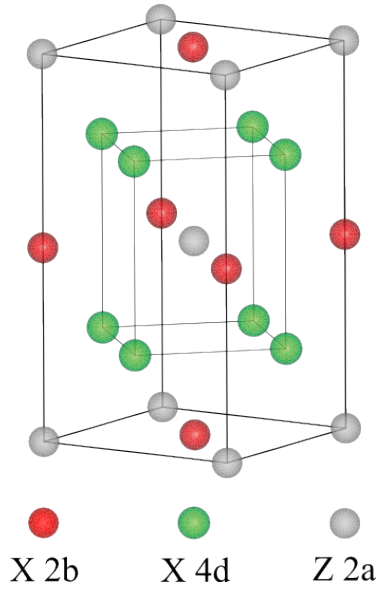

Figure 4.5: DO_{22} crystal structure for an Heusler alloy. Note that $a_{DO_{22}} \approx a_{L2_1}$
.

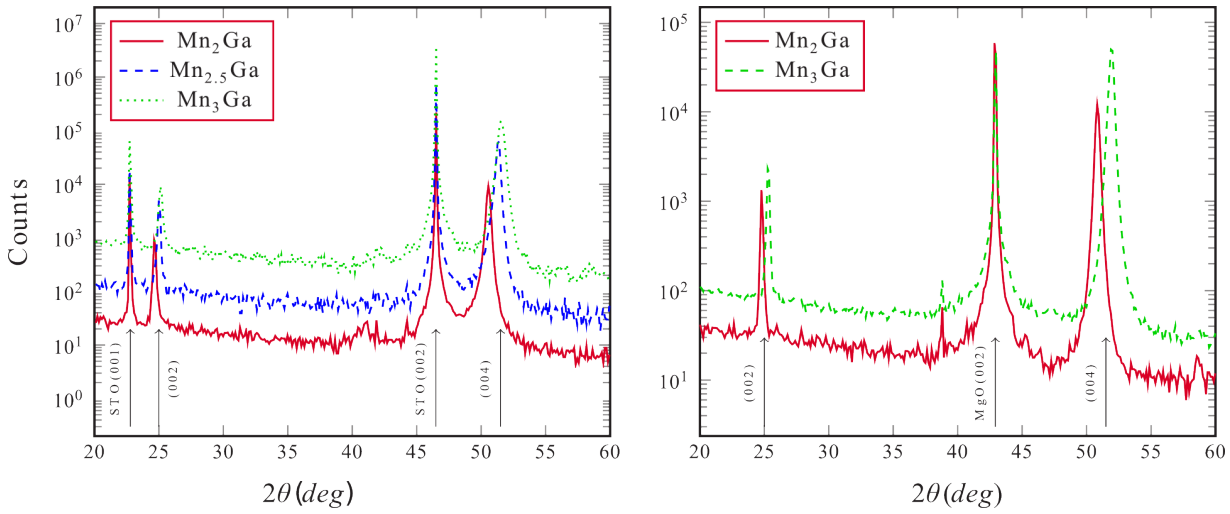

Figure 4.6: X-ray diffraction of $Mn_{3-x}Ga$ films on $SrTiO_3$ (left) and on MgO (right) substrates. The curves are offset for clarity.

were then capped with ~ 5 nm MgO. The nominal thickness of the $Mn_{3-x}Ga$ was 60 nm. Prior to further investigation, the actual thickness of the samples was determined by low-angle x-ray reflectivity. In the case of intermediate stoichiometry, $Mn_{2.5}Ga$, the samples were produced by co-sputtering from the Mn_2Ga target and a pure Mn target. Therefore, the Mn to Ga ratio is well known (and verified by inductively coupled plasma mass spectroscopy) in the cases of Mn_3Ga and Mn_2Ga, but it is likely different from the nominal $Mn_{2.5}Ga$ composition in the co-sputtered case.

The growth of the sample and previous experiments have been done by Doct. Hussein Kurt and Doct. Karsten Rode.

The crystal structure and lattice parameters were determined by symmetrical and reciprocal space map scans using our BRUKER D8 diffractometer. Mn_3Ga crystallises in the $D0_{22}$ structure, space group number 139, $I4/mmm$ with Mn in two non-equivalent sites, Wyckoff positions $2b$ and $4d$ while Ga occupies the $2a$ position. Mn spins in the $2b$ positions couple ferromagnetically to each other and antiferromagnetically to those of Mn in the $4d$ position. The overall magnetic structure is therefore expected to be a collinear ferrimagnet with alternating planes of $\uparrow$ ($4d$) and $\downarrow$ ($2b$) atoms, with both sites having their spins aligned with the crystallographic c-axis.

In Fig. 4.6 we plot the $2\theta - \theta$ x-ray diffraction diagrams of three thin films of $Mn_{3-x}Ga$ on $SrTiO_3$ and two films grown directly on MgO. Both series of samples show a high degree of texturing with the c-axis parallel to growth direction. Reciprocal space mapping and ϕ scans reveal that both series show in-plane order with the Mn_3Ga [100] in-plane direction parallel to the $SrTiO_3$ and MgO [100] directions. As can be seen from the displacement of the reflection at $2\theta \sim 52°$, the lattice c parameter is decreasing with increasing Mn content. We also recorded reciprocal space maps (RSM) around the [116] reflection of $Mn_{3-x}Ga$ to determine the in-plane lattice parameter a. A summary of the structural parameters of a selection of samples on various seed layers and compositions is given in Tab. 4.2.

As outlined above, the $Mn_{2.5}Ga$ samples are denoted by their nominal composition. The actual composition depends, among other things, on the sputtering yields of the Mn_2Ga and Mn targets. Using Vegard's law, and taking the lattice parameters for Mn_3Ga and Mn_2Ga as the solid solution end-members, we can estimate the actual composition of the $Mn_{2.5}Ga$ sample grown on $SrTiO_3$ to be $Mn_{2.77}Ga$.

The $D0_{22}$ structure, represented in Fig. 4.7, differs from the $L1_0$ structure by the ordering of Mn and

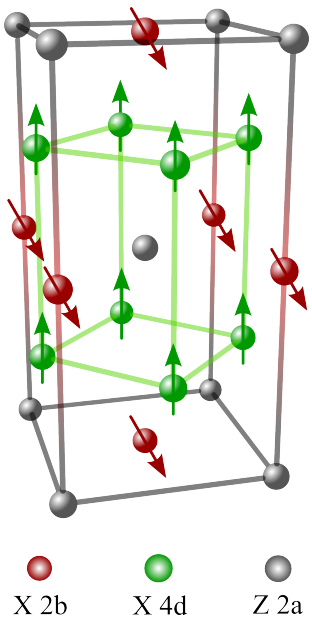

Figure 4.7: DO_{22} crystal structure of Mn_3Ga. The arrows indicate the direction of the magnetic moments on each site. In the perfectly ordered crystal, the central atom in the unit cell is always Ga.

Table 4.2: Summary of macroscopic parameters

Composition	Subs./seed	a(Å)[a]	c(Å)[a]	c(Å)[b]	S	$M_{s\perp}$[c]	$M_{s\parallel}$[c]	$M_{s\parallel}/M_{s\perp}$(%)
Mn_3Ga	$SrTiO_3$	3.92	7.08	7.0852	0.56	155	6	3.87
$Mn_{2.5}Ga$	$SrTiO_3$	3.91	7.12	7.1124	n/a	315	5	1.59
Mn_2Ga	$SrTiO_3$	3.91	7.22	7.2134	0.21	430	10	2.33
Mn_3Ga	MgO	3.92	7.04	7.0345	0.68	217	15	6.91
Mn_2Ga	MgO	3.92	7.17	7.1781	n/a	440	30	6.82
Mn_3Ga	MgO/Pt	3.91	7.06	7.0622	0.71	111	21	18.9
Mn_3Ga	MgO/Cr	n/a	n/a	6.9363	n/a	140	0	0

[a] From reciprocal space mapping.
[b] From symmetrical scans.
[c] in kA m^{-1}, 1 μ_B/formula unit $\sim$ 170 kA m^{-1}.

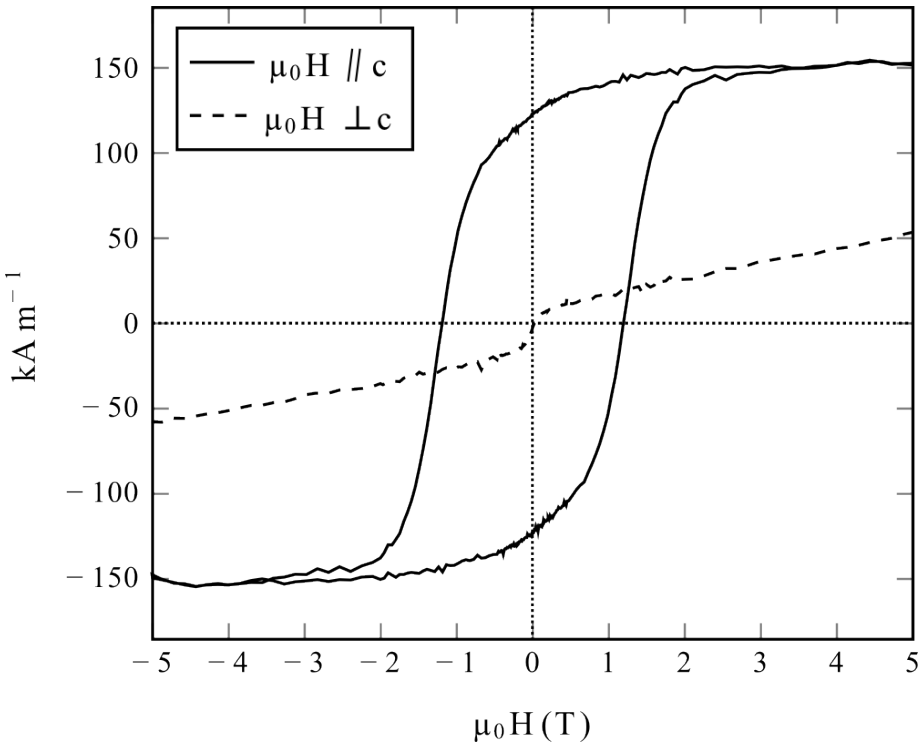

Figure 4.8: SQUID magnetometry of a Mn_3Ga thin film sample on STO at 300 K. The loop with in-plane applied field shows a small in-plane moment.

Ga in the Wyckoff 2*b* and 2*a* positions respectively. In the case where the central Ga atom in the unit cell can be either Ga or Mn, the symmetry of the unit cell is changed. This leads to a unit cell where the *a* lattice parameter is unaltered, but the *c* parameter is half that of the $D0_{22}$ structure. If this disorder is complete, this material has a c/a ratio > 1, leading to easy axis anisotropy [11, 12]. In the case of a partially ordered $D0_{22}$-like structure, the ratio $c/2a$ is < 1, suggesting that such disorder should favour an easy-plane magneto-crystalline anisotropy. A measure of the degree of 2*a* - 2*b* order is obtained by recording the integrated intensities of the x-ray diffraction [101] and [204] peaks, and normalising to the theoretical value of this ratio: the order parameter is $S = \sqrt{\left(I^{\mathrm{obs}}_{101}/I^{\mathrm{obs}}_{204}\right) / \left(I^{\mathrm{cal}}_{101}/I^{\mathrm{cal}}_{204}\right)}$.

We find that at higher values of the order parameter, the ratio between the in-plane and the out-of-plane saturation moments increases. When the disorder is complete over all three sites, the structure becomes face-centred cubic.

The macroscopic magnetic properties were measured with a Quantum Design superconducting quantum interference device (SQUID)-based magnetometer (see sec. 3.7.2), using the reciprocating sample option (RSO) and linear regression-based data reduction and also in a physical properties measurement system (PPMS) system with a vibrating sample magnetometer (VSM) insert from the same supplier. The maximum applied magnetic field is $\mu_0 H = 5.0\,\mathrm{T}$ and 14.0 T, respectively.

In Fig. 4.8, we plot the hysteresis loops of Mn_3Ga on a $SrTiO_3$ substrate with the magnetic field applied perpendicular ($\mu_0\vec{H} \parallel \vec{c}$) and parallel ($\mu_0\vec{H} \perp \vec{c}$) to the film surface. The coercive field is $\sim 1.2\,\mathrm{T}$, which is usually already an indication of very high anisotropy. The anisotropy field obtained by extrapolating the in-plane loop to the saturation magnetisation is $\mu_0 H_{\mathrm{an}} = 15\,\mathrm{T}$, corresponding to an uniaxial anisotropy energy of $1.1\,\mathrm{MJ\,m^{-3}}$. A small, soft, in-plane component of the magnetisation is clearly visible. We are confident that this contribution is not due to a secondary phase, but is rather an intrinsic property of the $Mn_{3-x}Ga$ alloys in the $D0_{22}$ structure, because it is not seen when the field is applied perpendicular

Table 4.3: Interatomic distances and magnetic coupling

Path	Distance	Coupling	Distance	Coupling
4d-4d	2.78 Å	AFM	3.55 Å	FM
2b-2b	3.94 Å	FM	4.51 Å	FM
4d-2b	2.65 Å	AFM		

to the plane. A randomly-oriented secondary phase with a soft moment should have been observed in either of the two applied field orientations. This is not the case. A perfectly oriented phase with an easy-plane, hard-axis anisotropy may be responsible for this behaviour, but in that case (a phase with almost perfect crystalline texture and occupying $\sim 10\,\%$ of the sample) we should have been able to detect it in the symmetric x-ray diffraction scans. Hence, the more likely origin is that the in-plane moment is an intrinsic property of partially-disordered $D0_{22}$ $Mn_{3-x}Ga$. In Mn_3Ga, a magnetic moment of $1\,\mu_B$ per formula unit ($2\,\mu_B$ per unit cell) corresponds to a magnetisation of $170\,kA\,m^{-1}$. The values of the c-axis magnetisation on Tab. 4.2 range from 0.6 to $1.3\,\mu_B$/fu.

Extended x-ray absorption fine structure (EXAFS) at the Mn and Ga K edges was recorded [13] at room and liquid nitrogen temperatures on the SAMBA beam-line at the SOLEIL synchrotron, France, using fluorescent detectors (Vortex50 from SIINTUSA). At low temperature we obtained a much higher signal-to-noise ratio, and hence the following results and discussion are based on the low temperature data. Furthermore, we recorded spectra at each edge with the linear polarisation of the incoming x-rays parallel ($\vec{E} \perp \vec{c}$) and perpendicular ($\vec{E} \parallel \vec{c}$) to the sample surface. Using FEFF [14, 15] to calculate a theoretical model from the ideal, perfectly ordered $D0_{22}$ structure, we simultaneously fitted the two edges with both polarisations to confirm that the local order is in agreement with that structure (see Fig. 4.9). The observed bond lengths are given in Tab. 4.3, together with the magnetic coupling expected between atoms [16, 17].

The choice of a structural model is more complicated in the case of Mn_2Ga, as we have no *a priori* knowledge of which site, 4*d* or 2*b*, will preferentially loose occupancy. Fitting the first coordination shell on the EXAFS signal for both polarisation at the Ga K-edge and assuming negligible Ga vacancies, we found that Mn vacancies are distributed over 2*b* and 4*d* sites with a occupancy of 0.56(4) and 0.72(2), respectively. Based on this result, it is possible to build a structural model and calculate the EXAFS signal for both edges and polarisations. Multiple scattering paths corroborate the hypothesis that Mn is equally lost from both sites.

4.2.2 XAS and XMCD

X-ray absorption spectroscopy (XAS) on the Mn $L_{3,2}$ edges was carried out at the SOLEIL synchrotron facility on the DEIMOS beam-line with both left and right circular polarisation in order to measure the x-ray magnetic circular dichroism (XMCD). These measurements were all carried out at room temperature, with the applied magnetic field either parallel or perpendicular to the wave vector $\vec{k}$. The detection method employed was the total electron yield (TEY) and it was not necessary to remove the capping layer since it was thin enough that it was not detrimental to the current detection. We measured XMCD by first saturating the sample as far as possible by applying 5 T perpendicular to the sample surface in the positive direction, then we reduced the applied magnetic field to 100 mT and measured absorption for both photon helicities. Then, we reversed the magnetisation by applying -5 T, followed by the application of the measurement field, -100 mT. The measurements for the case where $\mu_0\vec{H} \perp \vec{k}$ were carried out in the same fashion, but with the measurement field of ± 100 mT applied in the orthogonal direction.

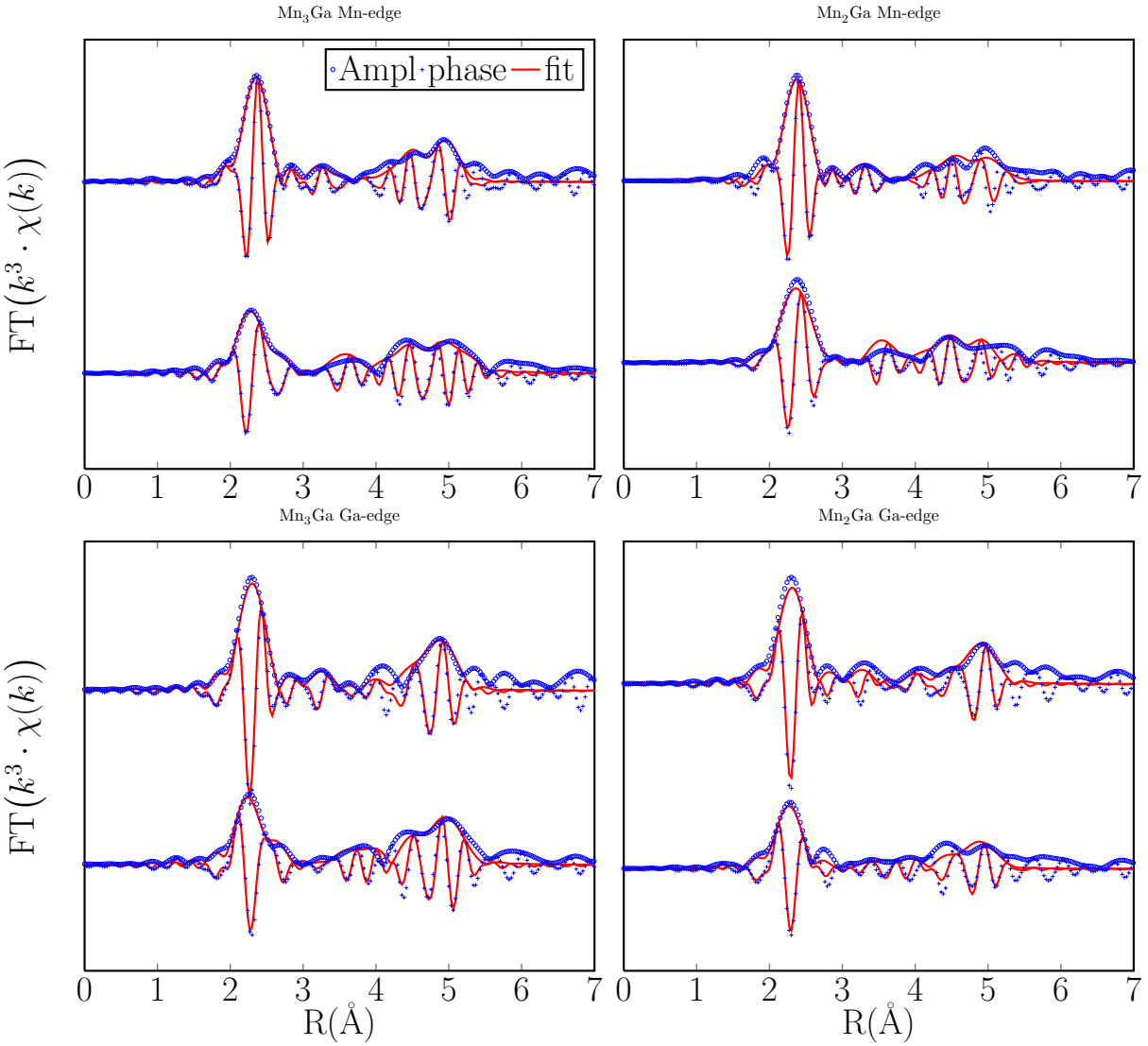

Figure 4.9: Real-space amplitude and phase of the EXAFS signal at both Mn and Ga edges. Each panel contains the experimental Fourier transform amplitude and phase (marks) and the fit based on the FEFF models as discussed in the text. Within each panel, the upper manifold corresponds to $\vec{E} \perp \vec{c}$ and the lower to $\vec{E} \parallel \vec{c}$.

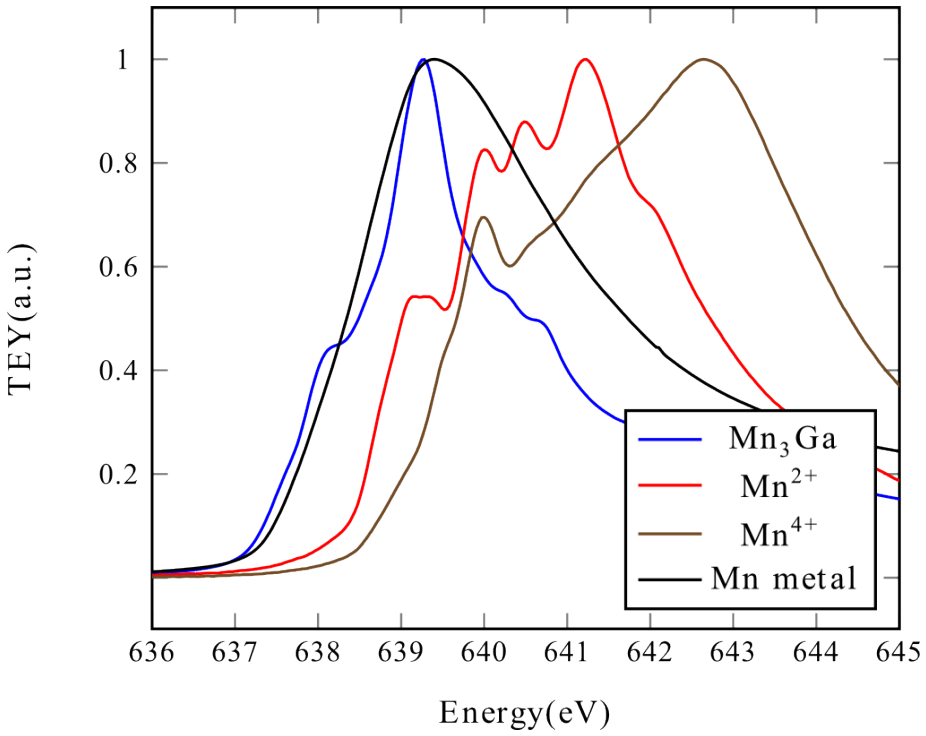

Figure 4.10: Comparison of the L_3 pre-edge of Mn in Mn_3Ga (60 nm)/MgO (5 nm), Mn^{2+}(MnO), Mn^{4+}(MnO_2) and Mn-metal.

We have seen that thin films of Mn_3Ga grown on MgO and $SrTiO_3$ substrates differ from the simple magnetic model of alternating, antiferromagnetically coupled planes. Neutron diffraction analysis point to an in-plane moment carried by the 2*b* Mn and the SQUID magnetometry confirms a magnetically soft in-plane component. This non-collinear magnetic mode, where the anisotropy seen by the two different sites is of opposite sign is most unusual.

The magneto-crystalline anisotropy is reflected in the variation of the orbital momentum when magnetised along the easy and hard axis. Transition metal *L*-edge soft x-ray spectroscopy and dichroism is a tool particularly suited to investigate this magnetic mode as it allows for the independent determination of both the spin and the orbital momentum. If furthermore, the two sites had been chemically different, the determination of the site-specific properties would have been as simple as tuning the incoming x-ray energy to the appropriate edge. Our case is a bit more intricate, as Mn is occupying both the 2*b* and 4*d* positions. Another complication of our measurement is that the accurate determination of the spin momentum is dependent on a clear separation between the L_3 and the L_2 multiplet manifolds. This is the case when the core hole 2*p* spin-orbit coupling is sufficiently high, as in Fe and Co but in the case of Mn this is not necessarily true [18]. We will see from the experimental data that there is some overlap between the two. We have chosen to fix an energy value which we define as the end of the L_3 and start of the L_2 edges. In this fashion, while the absolute value of the spin moment may be over or under-estimated, the error is completely systematic.

It has been suggested that the tetragonal distortion of the $L2_1$ Heusler structure to the $D0_{22}$ variant is due to Jahn-Teller distortion created by $Mn - d^4$ ions [19]. In Fig. 4.10 we compare the pre-edge of four different Mn-containing materials, Mn_3Ga, MnO, MnO_2 and Mn-metal. If Mn in Mn_3Ga was present in the Jahn-Teller-active configuration d^4, we should expect to observe the absorption edge shift towards that of the ionic compounds MnO and MnO_2. This is not the case, so we conclude that the tetragonal

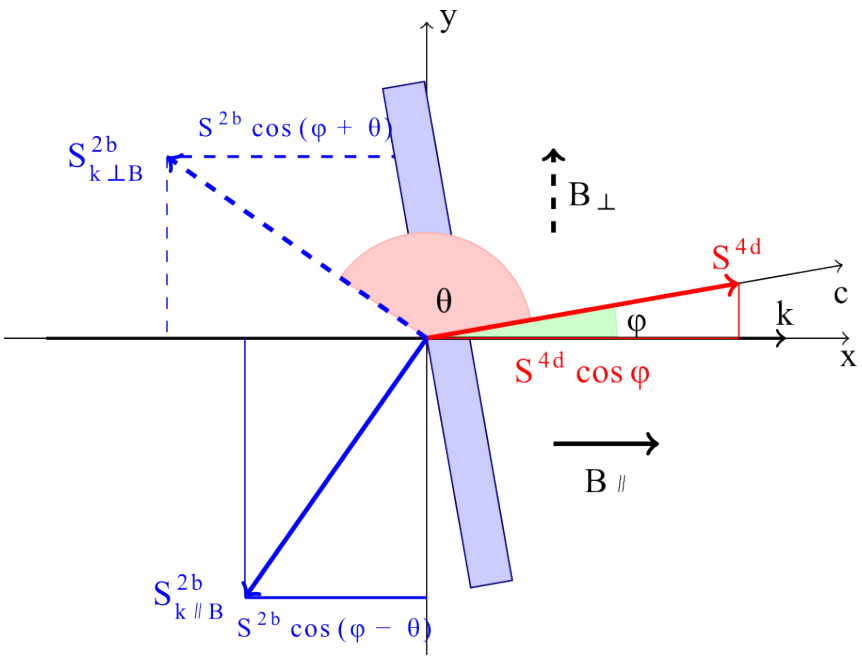

Figure 4.11: Schematic of the experimental setup for XAS and XMCD measurements with definition of the angles.

distortion in the case of Mn_3Ga is not due to Jahn-Teller-active charge configuration of the manganese. The absorption edge of Mn_3Ga is almost overlapping with that of Mn metal, indicating a strong degree of delocalisation of the *d*-band electrons. In this case, the minimisation of energy will take place through participation in the chemical bonds rather than by Jahn-Teller distortion. It is furthermore known that although some Mn-containing Heusler alloys do tetragonally distort, this is not generally true [20]; there are also examples of Heusler alloys containing no Mn which exhibit a tetragonal distortion, such as Ni_2TiGa [21].

In Fig. 4.11, we present the spin moments and their angles with respect to our choice of coordinate system for both the case where the applied magnetic field is parallel to ($\vec{H}_{\parallel}$) and perpendicular to ($\vec{H}_{\perp}$) the propagation vector $\vec{k}$ of the x-ray beam. In the figure, ϕ is the angle between the sample normal and $\vec{k}$, while θ is the angle between the spin moments on each site. In the case of a collinear arrangement of the spins, $\theta = 180°$. As can be seen from the figure, the projection of the $4d$ spin moment on the propagation vector depends only on the angle between the sample normal and $\vec{k}$ while the projection of the $2b$ spin momentum depends on both ϕ and θ, and is different depending on whether the applied field is perpendicular or parallel to $\vec{k}$. The measured magnitude of $\langle S \rangle$ as a function of the angle ϕ can then be written as

$$S_{\vec{H}\parallel}(\phi) = S^{4d}\cos(\phi) + S^{2b}\cos(\phi - \theta)\ , \tag{4.4}$$

and

$$S_{\vec{H}\perp}(\phi) = S^{4d}\cos(\phi) + S^{2b}\cos(\phi + \theta)\ . \tag{4.5}$$

The sum rules [22–25] allow the independent determination of $\langle L \rangle$ and $\langle S \rangle_{\text{eff}} = \langle S \rangle + 7/2\langle T \rangle$ where $\langle L \rangle$ and $\langle S \rangle$ are the expectation values for the orbital and spin operators, and $\langle T \rangle$ is the expectation value for the magnetic dipole operator. In the transition metal series, $\langle T \rangle$ is usually much smaller than both $\langle L \rangle$ and $\langle S \rangle$. We made an estimate of the energy of the dipole interaction in Mn_3Ga by numerical evaluation of the total energy of a crystal with in-plane and out-of-plane spins using the known atomic

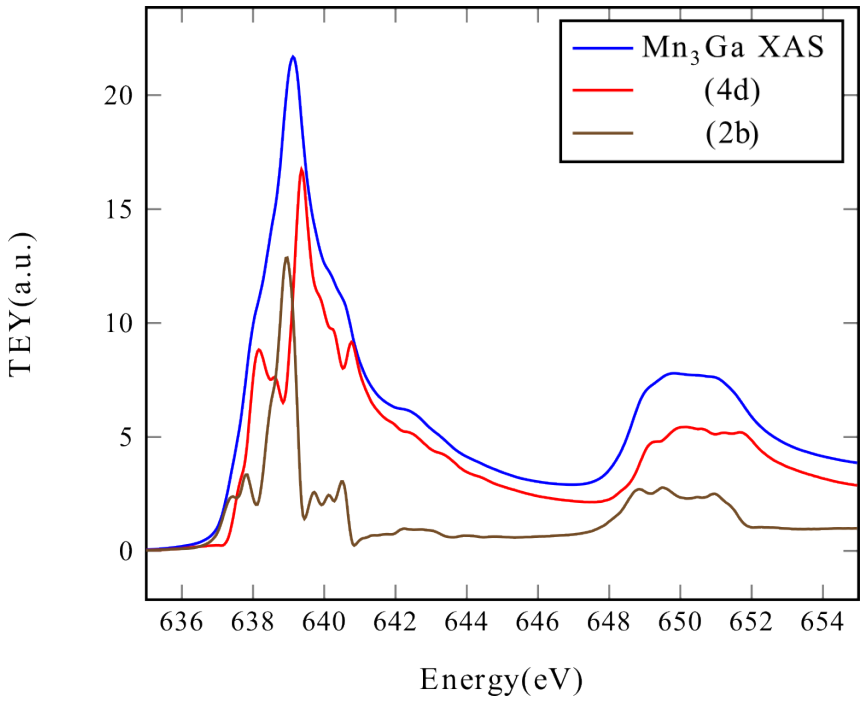

Figure 4.12: XAS spectrum of Mn_3Ga (60 nm)/MgO (5 nm) at the $L_{3,2}$ edges and the contributions from the $4d$ and $2b$ sites obtained using the decomposition method described in the text.

positions and magnetic moments We found that it corresponds to an energy $\sim 1\,\mathrm{kJ\,m^{-3}}$, or about 0.1 % of the total measured anisotropy energy. We will assume then that $\langle S\rangle_{\mathrm{eff}} = \langle S\rangle$. The number of holes in the Mn^{3d}-band can be deduced from our calculations; we find that Mn in the $4d$ and $2b$ positions have 4.82 and 4.90 holes /Mn, respectively. The $3d$ band is almost half full, confirming a negligible contribution of the magnetic dipole operator (see sec. 3.4.2).

We recorded XAS for both circular polarisations at more than eight different incidence angles ϕ in the two magnetic field configurations on samples Mn_2Ga, $Mn_{2.5}Ga$ and Mn_3Ga. Representative XAS and XMCD spectra are shown in Fig. 4.12 and 4.13, respectively.

The difference between the two magnetic configurations discussed above allows us to estimate the contribution from each site. The system of two equations (eq. 4.4 and 4.5 above) has however three unknowns, $\langle S\rangle^{4d}$, $\langle S\rangle^{2b}$ and θ. Our knowledge of the occupation ratio for the two Mn positions, obtained from the EXAFS measurements described above, makes it possible to decompose the spectra into $2b$ and $4d$ contributions. In order to do so, we must make sure that each spectrum on each sample corresponds to the same number of Mn atoms. The data reduction procedure was the following:

1. Normalise pre-edge to 1.

2. Calculate the sample-total $\langle S\rangle$ and $\langle L\rangle$ by application of the sum rules.

3. Subtract 1 from the scans and normalise post-edge to 1 thereafter.

4. By subtracting, using appropriate factors, Mn_2Ga spectra from Mn_3Ga, obtain site-specific XAS for each helicity and angle.

5. Calculate site-specific values of $\langle S\rangle$ and $\langle L\rangle$

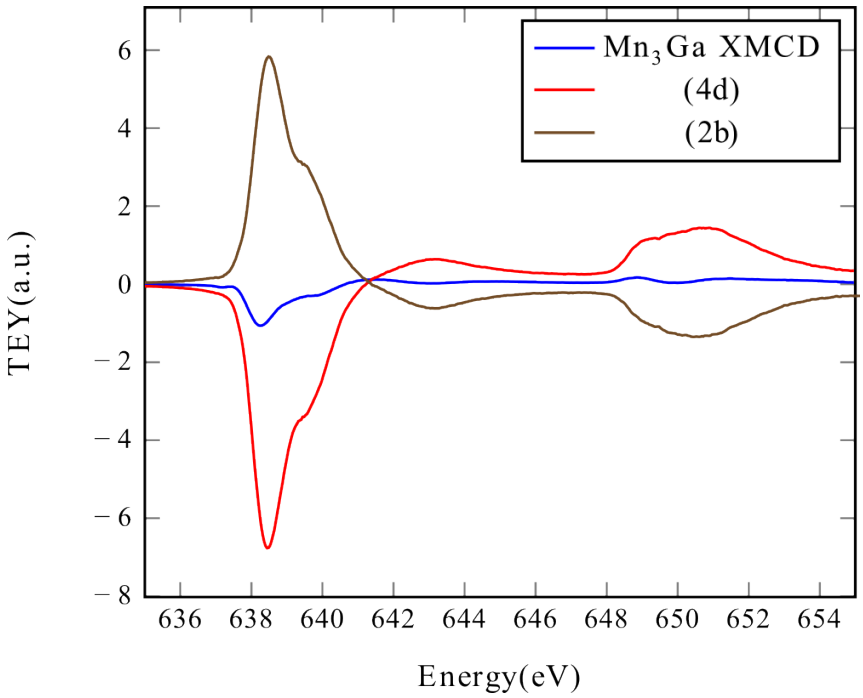

Figure 4.13: XMCD spectrum of Mn_3Ga (60 nm)/MgO (5 nm) at the $L_{3,2}$ edges and the contributions from the 4*d* and 2*b* sites obtained using the decomposition method described in the text.

The separation of the XAS and associated XMCD using the method outlined above may introduce errors in the values of both $\langle S \rangle$ and $\langle L \rangle$, in particular if the $2p \rightarrow CB$ (conduction band) absorption differs from one sample to the next. This is not our case, and we believe the errors introduced using this method is less than the overall error associated with the application of the sum rules. An experimental verification of the procedure can be obtained by the simulation of the $Mn_{2.5}Ga$ XAS and XMCD spectra. We know that analysis of the x-ray diffraction spectra of this sample indicates that its real stoichiometry is closer to $Mn_{2.77}Ga$. We used a least-square simultaneous fitting of the XAS and XMCD data of the sample using the extracted 2*b* and 4*d* contributions.

In Fig. 4.14 and 4.15 we show the results of these fits. The agreement with the experimentally observed absorption and XMCD is reasonably good, and we find from the fit that the $Mn_{2.5}Ga$ sample has composition $Mn_2Mn_{0.66}Ga$, or in other words, a fully occupied 4*d* site and a 66 % occupied 2*b* site. The slight difference (2.77 against 2.66) may be due to the different modification of the lattice parameter depending on if the loss of Mn is primarily on the 4*d* or 2*b* positions. If we base a similar analysis on the magnetisation, comparing the measured macroscopic magnetisation with the measured magnetic moment at each site (see below), we find $Mn_2Mn_{0.73}Ga$.

In Fig. 4.16 and 4.17 we plot the measured spin momentum of the Mn_3Ga sample. In Fig. 4.16, the data points are obtained by applying directly the sum rules to the experimental spectra. In Fig. 4.17, we have carried out the decomposition of each XAS spectrum as described above, and then the XMCD was calculated for each pair of helicities. We chose to use the two data sets presented in Fig. 4.16 and the data set relative to the Mn 4*d* from Fig. 4.17 for the simultaneous fitting using the appropriate cosine-dependent functions. The result of the fit is plotted as solid lines in the figures. We find a Mn 4*d* and 2*b* spin momentum of 2.67(2) μ_B and 4.74(5) μ_B, respectively, giving a net momentum of 0.6 μ_B /fu. The angle between the two spins is found to be 179.5(5)°.

We now turn to the orbital moment. As can be expected from the number of holes in the 3*d* band, the

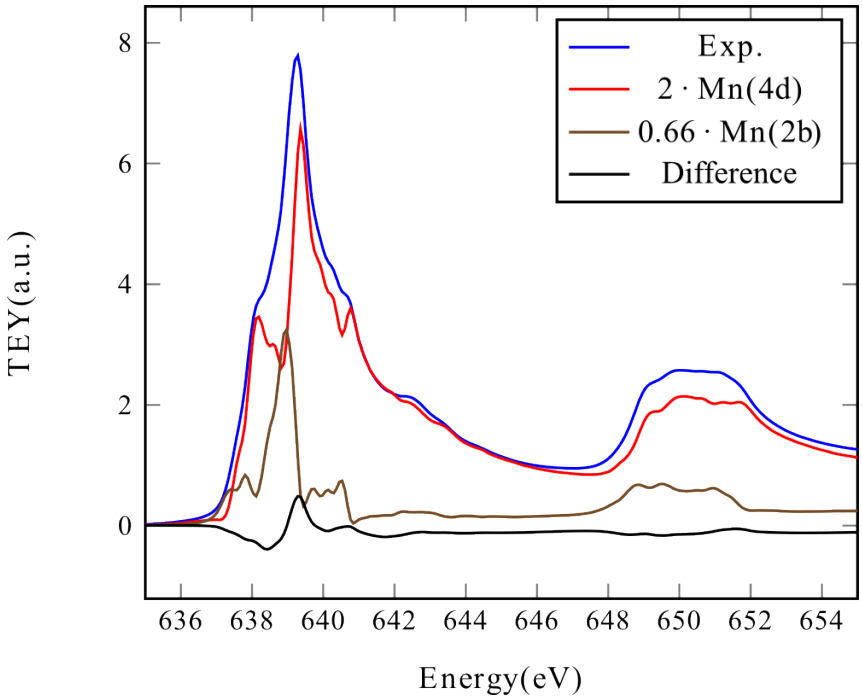

Figure 4.14: $Mn_{2.5}Ga$ (60 nm)/MgO (5 nm) experimental XAS spectra and simulation using the extracted contribution from the 4*d* and 2*b* sites.

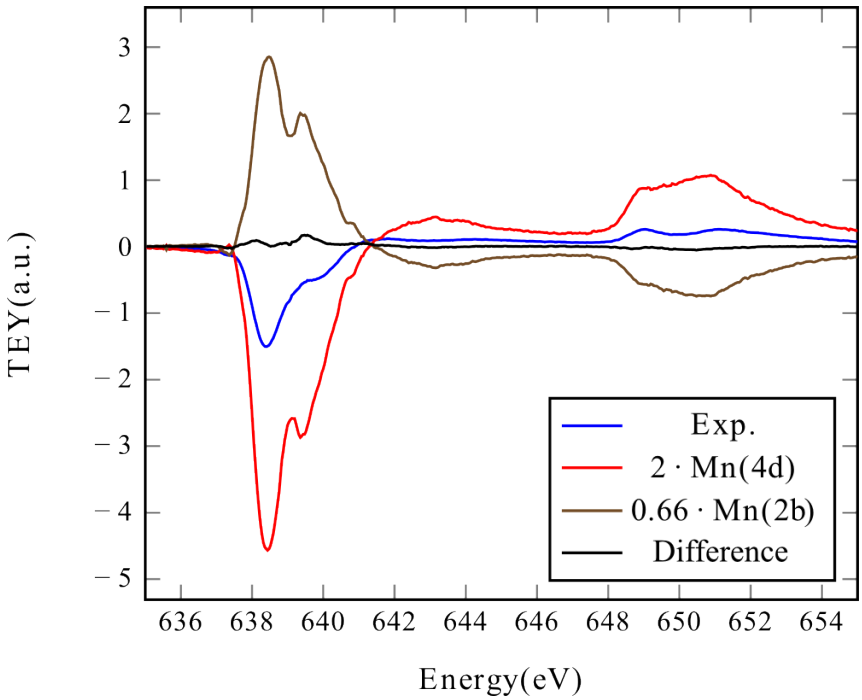

Figure 4.15: $Mn_{2.5}Ga$ (60 nm)/MgO (5 nm) experimental XMCD spectra and simulation using the extracted contribution from the 4*d* and 2*b* sites.

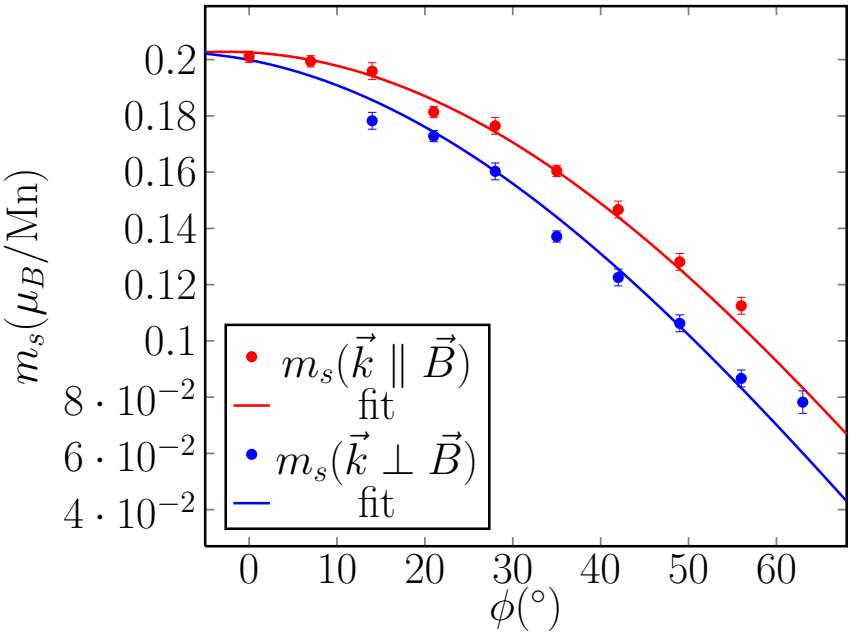

Figure 4.16: Total spin moment for Mn_3Ga (60 nm)/MgO (5 nm) with the applied magnetic field parallel and perpendicular to the wave vector $\vec{k}$. The experimental values have been extracted using the sum rules on the recorded spectra. The lines are simultaneous fits to the data in this figure and the $4d$ contribution shown in Fig. 4.17.

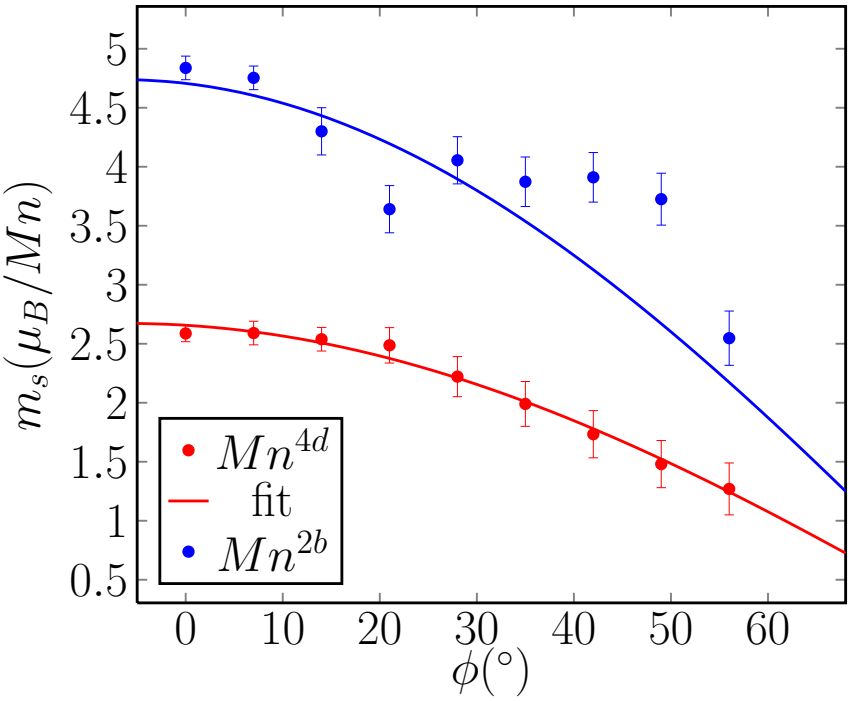

Figure 4.17: Absolute value of the sample spin moment deconvoluted to the two Mn positions. The solid line relative to the $2b$ moment is a guide to the eye, while the line relative to the $4d$ moment is a simultaneous fit using this data set and the two data sets presented in Fig. 4.16.

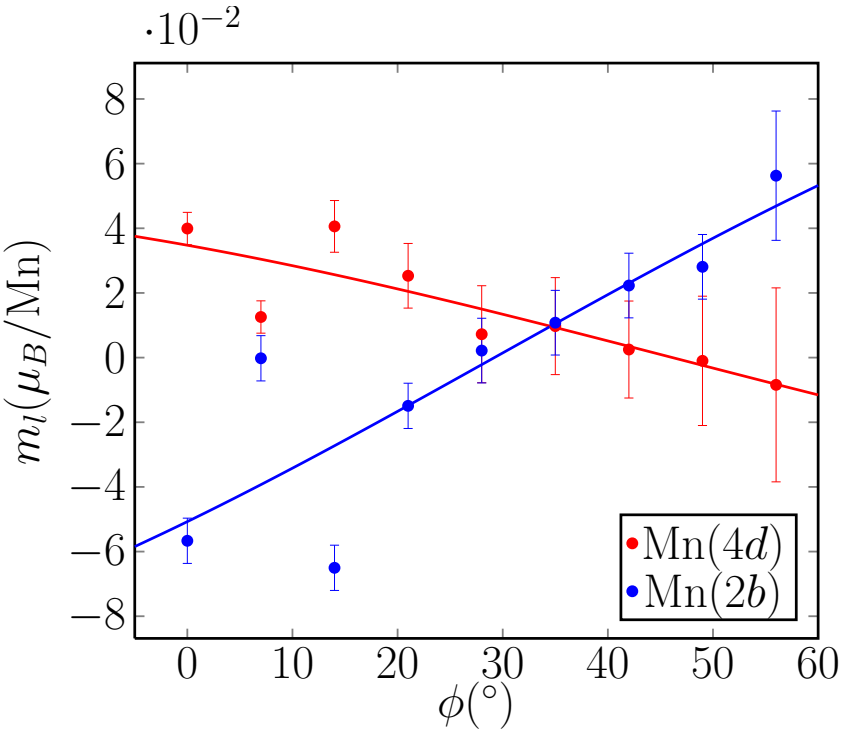

Figure 4.18: Site-specific orbital moments in Mn_3Ga (60 nm)/MgO (5 nm). The solid lines are obtained by fitting the data with a cosine function to account for the angular projection of the moment on $\vec{k}$. They allow us to determine the magnitude of the orbital moment at each Mn position.

orbital contribution to the magnetic moment is very small. Indeed, for an ion in a spherical symmetry, with $N_h = 5$, we expect the orbital momentum to be exactly zero. Furthermore, as is the case with the transition metals, the $3d$ bands in Mn_3Ga are contributing to the chemical bonding, so the orbital angular momentum is quenched, because of crystal averaging, even in lower symmetries.

In Fig. 4.18, we plot the site-specific orbital moments as a function of the angle between the wave vector $\vec{k}$ and the sample normal. Despite of the poor signal-to-noise ratio, due to the very low magnitudes, we can make an estimate of the orbital moments and their direction with respect to the sample normal, the crystallographic c-axis, coinciding with the spin direction of the Mn $4d$ ions. We find that the Mn in positions $4d$ and $2b$ carry $0.05\,\mu_B$, $0.12\,\mu_B$ and make angles of 38°, 235°, respectively. These values are obtained using the methodology for the separation of the sites described above. As previously mentioned, this may introduce small errors in the derived expectation values for $\langle S\rangle$ and $\langle L\rangle$. While $\langle S\rangle$ is big enough to make it reasonable to ignore this source of error, it is clearly not the case for the orbital momentum. In Fig. 4.19 we plot the measured total orbital momentum using the sum rules directly on the recorded spectra, and compare it to the sum of the site specific orbital moments shown in Fig. 4.18. The agreement between the two methods is very reasonable, in view of the magnitude of the signal.

The orbital moments were all measured in the configuration where the applied magnetic field is parallel to the propagation vector $\vec{k}$. The magneto-crystalline anisotropy will ensure that the magnitude of the orbital moments changes when the field is applied perpendicular to the easy axis, *i.e.*, $\vec{H} \perp \vec{k}$. In this configuration, the signal-to-noise ratio is too poor to allow us to extract the orbital momenta, and a further experiment where one can saturate the magnetisation along the hard direction is necessary in order to obtain direct evidence of the magnitude of the anisotropy. We estimate from the site specific data, that in the $\vec{H} \perp \vec{k}$ case, the orbital momentum on the $4d$ Mn is decreasing by approximately $0.02\,\mu_B$

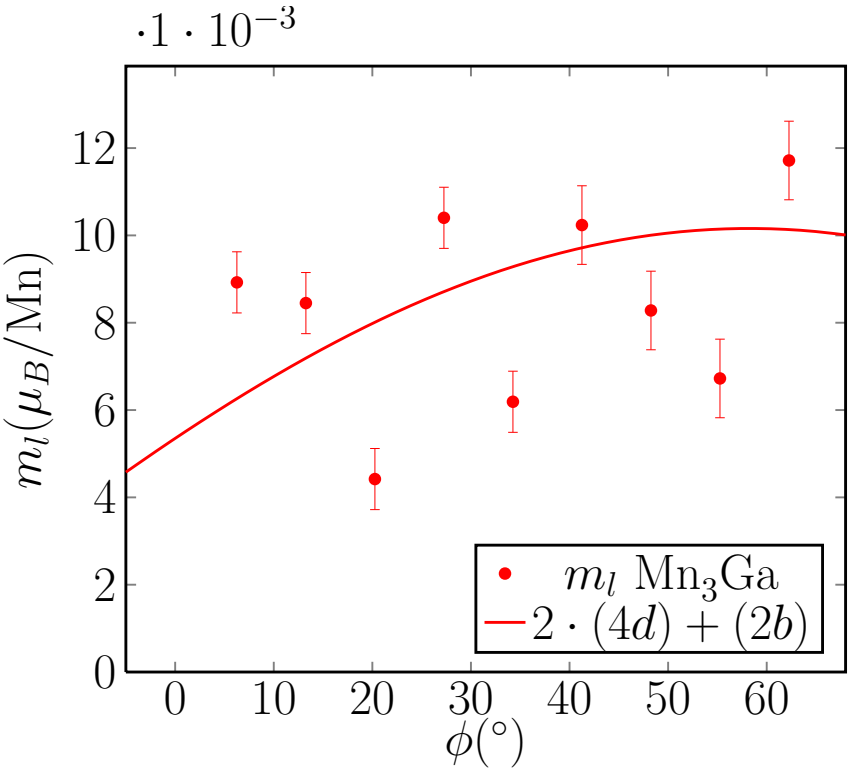

Figure 4.19: Mn_3Ga (60 nm)/MgO (5 nm) total orbital moment derived directly from the sum rules. The solid line corresponds to the sum of the site-specific orbital moments as shown in Fig. 4.18.

while it is increasing by $0.03\,\mu_B$ on the $2b$ Mn. This indicates that the two sites have different sign of the anisotropy energy, and that while Mn in the $4d$ position has easy axis anisotropy, the $2b$ position on the contrary has easy-plane anisotropy.

The experimentally observed magnetic structure is summarised in Fig. 4.20. We find, in agreement with the SQUID magnetometry, that the total magnetic moment in Mn_3Ga is about $0.2\,\mu_B$/Mn, or $0.6\,\mu_B$/fu. Furthermore, in agreement with the calculated filling of the d bands of Mn at the two positions (more than half-filled), $\vec{L} \cdot \vec{S} > 0$. We also find evidence for a non-collinear structure, although this is much less obvious in the thin films grown on $SrTiO_3$ than it is in the bulk powders, or indeed in thin films grown on MgO or on a Pt seed layer (see Tab. 4.2). The anisotropy of the orbital momentum, and hence the magneto-crystalline anisotropy indicates easy axis behaviour for the $4d$ Mn while it indicates, on the contrary, an easy-plane for the $2b$ Mn.

4.2.3 Conclusions

We have experimentally demonstrated that it is possible to use XAS and XMCD to investigate the magnetic structure of the complex system of Mn_3Ga, where Mn occupies different crystallographic sites. The decomposition of the XAS/XMCD spectra into site-specific subspectra allows us to determine the ground-state values of $\langle S \rangle$ and $\langle L \rangle$ for each site. As expected for ions with close to half-filling of the d band, the orbital momentum is close to zero. Nevertheless, we are able to make good estimates for their values, both when the applied magnetic field is parallel or perpendicular to the easy magnetic axis. From this we can build up a qualitative picture of the nature of the anisotropy on each site. While the Mn in the $4d$ sites is highly anisotropic with an easy c-axis, the $2b$ position exhibits perpendicular-to-c anisotropy.

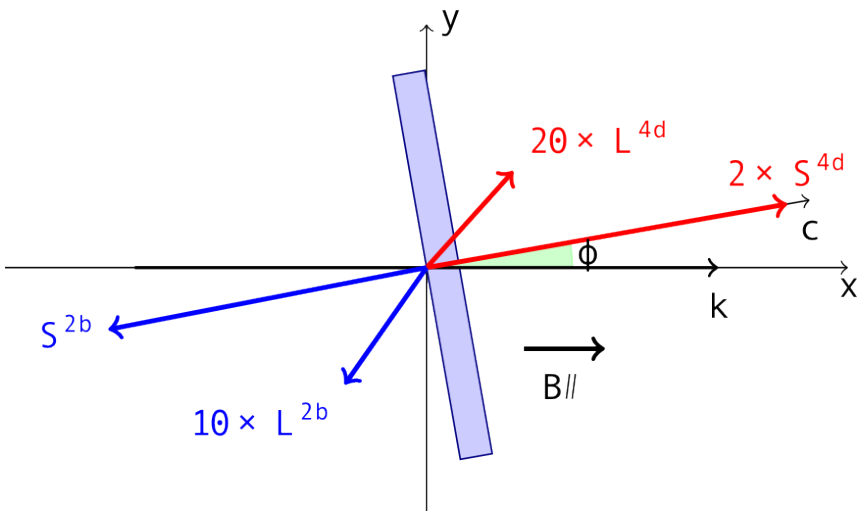

Figure 4.20: Experimentally observed, site-specific, magnetic structure of Mn_3Ga (60 nm)/MgO (5 nm). The figure is to scale, noting that the $4d$ $\vec{S}$ and $\vec{L}$ have been multiplied by a factor of 2 and 20, respectively, and the $2b$ $\vec{L}$ by a factor of 10.

The strong uniaxial anisotropy in the $4d$ position and the strong, antiferromagnetic exchange between $4d$ and $2b$ positions yields the highly anisotropic ferrimagnetic ground state.

4.3 Mn_2Ru_xGa

4.3.1 Introduction

As discussed in sec. 4.1, several Heusler alloys have been predicted to be half metals, with a gap in the spin polarised DOS for one spin subband. The magnetic moment per stoichiometric unit cell should be an integer number of Bohr magnetons and full and half Heusler alloys with the $L2_1$ and $C1_b$ structure should follow the Slater-Pauling rules

$$\begin{aligned} M &= N_\mathrm{v} - 24 \quad \text{and} \\ M &= N_\mathrm{v} - 18 \ , \end{aligned} \tag{4.6}$$

respectively. Hence, half-metallic Heuslers with $N_\mathrm{v} = 24$ and half Heuslers with $N_\mathrm{v} = 18$ are particularly interesting because they should show zero magnetic moment. Such a material could be a perfectly compensated half metal and it would be extremely useful for spin electronics applications, since it would be free from stray field and shape anisotropy, 100 % spin polarised and immune from the influence of external fields. Since the prediction by van Leuken and de Groot [8], researchers have striven to fabricate such a material. While electronic structure calculations predicted several candidates, [2, 3, 7, 26–29] attempts to realize a compensated half metal failed [28, 30, 31].

Half-metallicity is a zero-temperature property that can be spoiled by imperfect atomic order, spin-orbit coupling or finite temperature, either because of the smearing of the Fermi surface or of the different temperature dependence of the magnetisation of the two antiferromagnetically coupled sublattices. Candidate materials either turn out to have almost no moment on the transition metal atoms, or else they decompose or do not crystallise in the cubic structure and consequently exhibit a net magnetisation. Kurt

Table 4.4: Correlation between tetragonal distortion $\Delta c/a$ and thickness of MRG samples with $x \sim 1$

Sample	a(Å)	c(Å)	$\frac{c}{a} - 1$(%)
$MgO/Mn_2Ru_xGa(70\,nm)/Al_2O_3(2\,nm)$	5.956	6.065	1.84
$MgO/Mn_2Ru_xGa(34\,nm)/Al_2O_3(2\,nm)$	5.956	6.070	1.92
$MgO/Mn_2Ru_xGa(15\,nm)/Al_2O_3(2\,nm)$	5.956	6.089	2.24
$MgO/Mn_2Ru_xGa(8\,nm)/Al_2O_3(2\,nm)$	5.956	6.129	2.90
$MgO/Mn_2Ru_xGa(4\,nm)/Al_2O_3(2\,nm)$	5.956	6.172	3.62

et. al. [9] reported the growth of thin films of near-cubic Mn_2Ru_xGa (MRG), where Mn occupies two inequivalent crystallographic positions; 4*a* and 4*c*. The alloy has been identified as a zero-moment ferrimagnet with high spin polarisation, high Curie temperature T_C (550 K), with evidence of half-metallicity. The cubic crystal structure is obtained by non-equilibrium growth of the material in thin film form. The magnetic moment and the magnetic anisotropy are tunable as a function of the ruthenium concentration x.

In order to determine the Ru concentration, we deposited four MRG samples with varying Mn_2Ga target power along with a pure Ru film. The density and thickness of the samples were then measured using x-ray reflectivity. Based on the measured density and lattice parameters of these five control samples, we established a relation between the x-ray density and the Ru concentration x, against which all the samples were measured.

The growth of the sample, the patterning and the experiments have been done in collaboration with YongChang Lau, a colleague PhD student.

4.3.2 Growth and properties

The films were grown on MgO (001) substrates by dc magnetron sputtering at 250 °C substrate temperature in the Shamrock system (see sec. 3.1.1) with a base pressure of 2×10^{-8} Torr. They were obtained by co-sputtering from a Ru target and a stoichiometric Mn_2Ga target. The Ru concentration was controlled by varying the Mn_2Ga target plasma power while keeping the Ru one fixed. The samples were then capped with a protective layer of 2 nm of Al_2O_3. X-ray diffraction data are presented in Fig. 4.21. Reciprocal space mapping was used to determine the in-plane lattice constant a and we found it to be always consistent with the value of 0.5956 nm= $\sqrt{2}a_{MgO}$, meaning that Mn_2Ru_xGa grows on MgO with its unit cell rotated by an angle of 45°. The out-of-plane parameter c is found to be between 0.598 nm and 0.618 nm, depending on the Ru concentration and the film thickness. We find that c increases sharply with reducing film thickness. This confirms the cubic character of the MRG films, with a slight tetragonal distortion ($(c-a)/a = \Delta c/a$ between 1.8 % and 3.6 %).

As the crystal structure goes from the $C1_b$ of an half Heusler to the $L2_1$ of an inverse full Heusler, Mn atoms occupy the inequivalent 4*a* and 4*c* positions, while Ga atoms occupy the 4*b* position. Ru atoms increasingly fill the empty 4*c* positions as x increases. Therefore, it results that the Mn in 4*a* position is sitting in the centre of a MnGa cube and is octahedrally coordinated by the four Ga 4*b*, while the Mn in the 4*c* position is octahedrally coordinated by the Ru atoms and tetrahedrally coordinated by the Mn 4*a*.

The degree of tetragonal distortion can be controlled by growing MRG thin films on different substrates and/or substrate/seed layer combinations. Since it is not trivial to find suitable substrates or a seed layer that does not result in additional alterations of the magnetic properties, our approach to achieve this variation was to grow samples of varying thickness. We prepared MRG samples with the same Ru concentration ($x \sim 1.0$), while varying the thickness from 70 nm down to 4 nm (see Tab. 4.4). We recorded

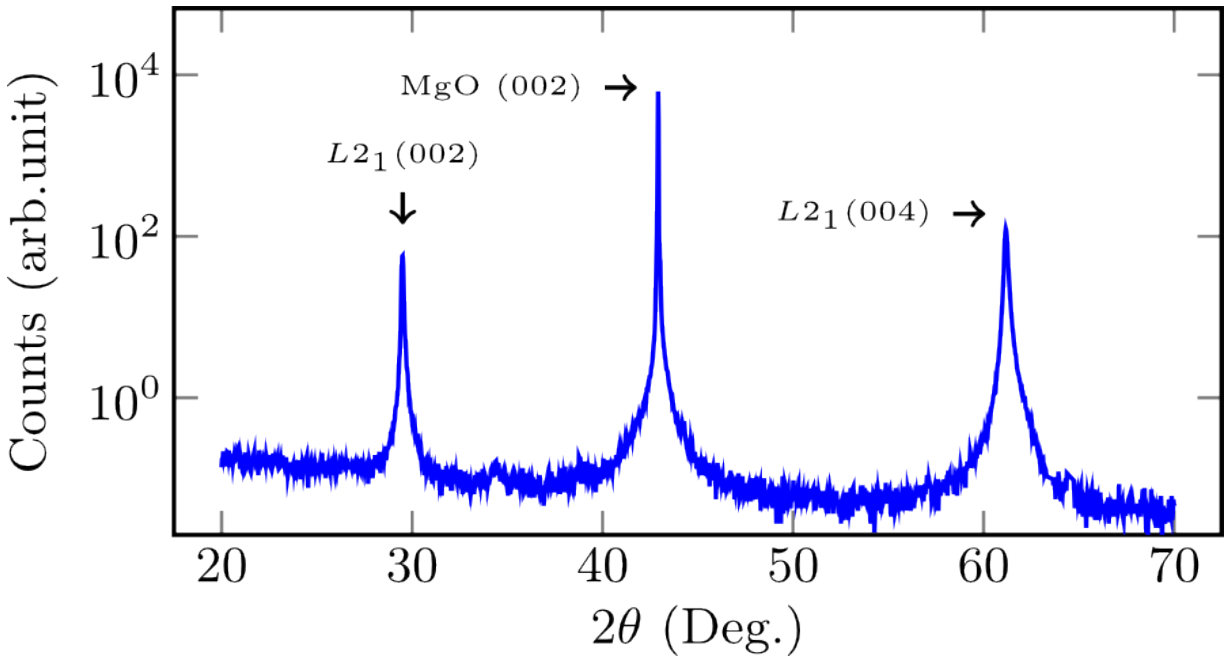

Figure 4.21: XRD pattern of $L2_1$ Mn_2RuGa grown on a MgO (001) substrate.

RSMs around the symmetric (204) reflection of MRG (Fig. 4.22) in order to determine the variation of the lattice constant c through the film thickness using Scherrer equation 3.27 of sec. 3.7.3. The reflections show no clear structure, indicating that the strain is surprisingly homogeneously distributed, and we conclude that the average $\Delta c/a$ is a good measure of the strain in the samples. The mosaic spread of the MgO substrate is too important to make a quantitative estimate of the variation of the lattice parameter c through the film thickness.

The magnetisation and magnetic anisotropy vary remarkably with Ru concentration. As x increases, the magnetic moment decrease steadily until it falls practically to zero for $x \sim 0.5$ and then rises again, as shown in Fig. 4.23. We interpret this behaviour as a change of sign of the magnetisation. According to the Slater-Pauling rules, the compensation occurs for $x = 0.5$, where the number of valence electrons is 21. Even is the unit cell has an odd number of electrons, it is not magnetic. This configuration can be by considering a doubling of the cell, with an even number of electrons in two adjacent cells, or as a superposition of quantum states with opposite spins for the last electron. The anisotropy seems to be correlated with the c/a ratio, going from in-plane to perpendicular as x increases, at a lattice parameter of 601 pm. Fig. 4.24 shows a schematic representation of the band structure at the Fermi level and the effects of Ru addition. For Mn_2Ga, *i.e.* $x = 0$, the spin gap $\Delta_\downarrow$ in the $\downarrow$ band lies a few tenths of an eV above the Fermi level. Ruthenium adds both states (6) and electrons (8) to the compound, so that the Fermi level now falls in the spin gap. Further addition of Ru lowers the minority bands at even lower energies, so that the compound looses its half-metallicity. The number of available states in each band is indicated in square brackets and their occupancy is given by the white numbers, based on measured magnetic moments. In the half-metallic region, the magnetic moment increase as a function of x with a slope of $2\,\mu_B$/f.u./Ru (red straight line in Fig. 4.23). This can be understood considering that, for each Ru atom, 2 unpaired electrons are added to the system. Therefore, if only one spin sub-band is available, the magnetic moment increases by exactly $2\,\mu_B$ f.u.$^{-1}$.

The spin polarisation at the Fermi level changes sign with respect to the magnetisation with increasing

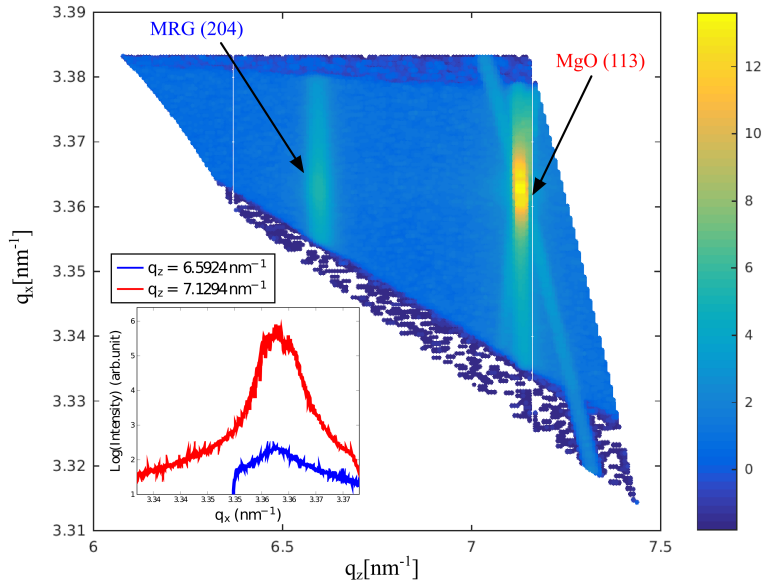

Figure 4.22: Reciprocal space mapping scan of an MRG sample around the (204) peak. The inset shows the logatimic intensity profile of the peaks at constant q_z for the MRG (204) and the MgO (113) peaks.

Ru concentration. The same effect can be achieved by changing the temperature: the two magnetic sublattices show different temperature dependence of their magnetisation. Therefore, when the temperature is varied, a sample can go through the compensation point and, further, switch the sign of its magnetisation.

The spin polarisation at the Fermi level for two samples of MRG has been measured by point contact Andreev reflection (PCAR) spectroscopy. One of them, with a value of $x \sim 1.0$ and a magnetisation of M_s =75 kA m^{-1} is in the "normal" metal region and shows a polarisation of 41 %, while the other sample, with a value of $x \sim 0.5$ and a magnetisation of M_s =21 kA m^{-1} shows 54 % spin polarisation. Although 54 % is well short of the 100 % expected for an half metal, it is close to the maximum that has been measured by PCAR on any Heusler compound. Diffusive spin polarisation measurements on bulk and thin film Heusler alloys are never much in excess of 60 %, probably because the band dispersion is different for the surface and the bulk or because of spin-orbit scattering.

4.3.3 Transport properties

The anomalous Hall voltage [32, 33] has been measured for a series of samples with the same thickness of 70 nm and therefore the same or very similar values of $\Delta c/a$ ~1.9 %. The AHE resistance changes sign at $x \sim 0.69$ (Fig. 4.25). This is consistent with a change of the sign of the spin polarisation at the Fermi level with respect to the applied external field, as discussed above. Very close to compensation, when the magnetisation is practically zero, it is almost impossible to change the magnetic state with an external magnetic field, hence the AHE voltage is a flat line, as shown in Fig. 4.25 for $x = 0.69$.

In Fig. 4.26 we show the anomalous Hall resistance of one MRG sample with $x = 1$ and $\Delta c/a$ =1.92 %. The AHE has been measured at different temperatures and it changes sign between 300 and 350 K. The magnetic compensation is achieved when the two sublattices have equal and opposite magnetisations. This occurs at some particular temperature because the sublattices show different temperature dependence. We found (see sec. 4.3.4) that the 4a magnetisation is practically constant in the range 2 to 400 K,

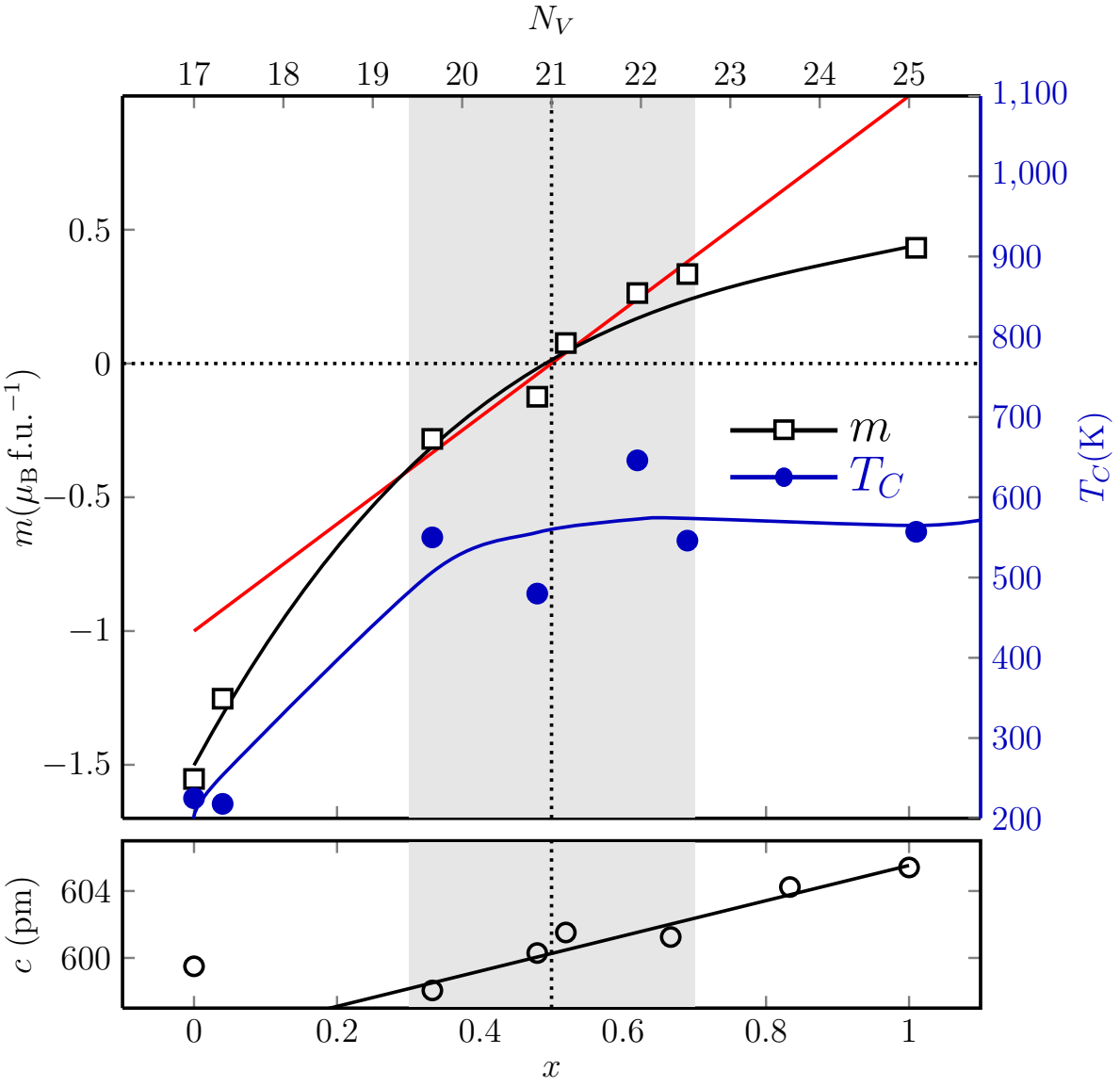

Figure 4.23: Variation of Curie temperature T_C and moment with Ru concentration x and number of valence electrons per formula unit N_v. The half-metallic region is lightly shaded. The black and blue lines are guide to the eye, while the red straight line has a slope of $2\,\mu_B$/f.u./Ru. The lower panel shows the variation of the lattice parameter c, normal to the substrate, as a function of x. The line is a linear fit of the data, excluding the first point.

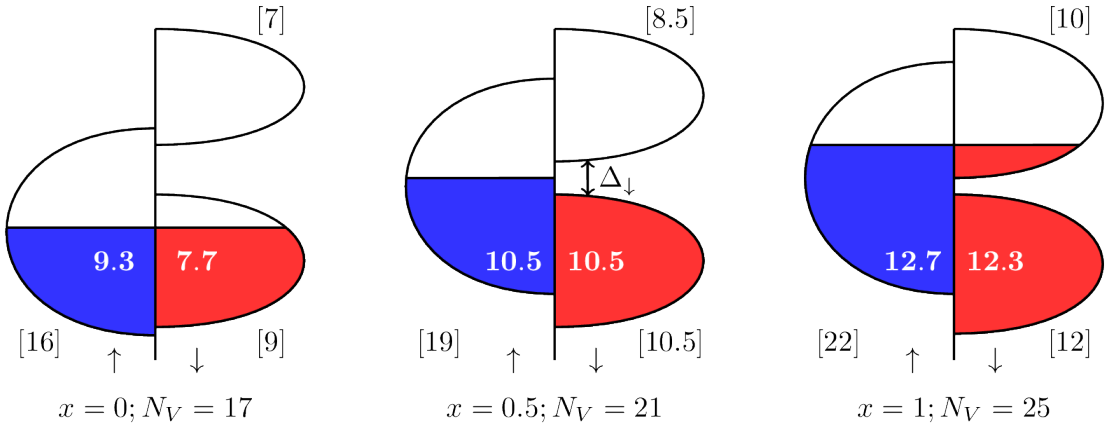

Figure 4.24: Schematic density of states showing the effect of Ru addition in Mn_2Ru_xGa, which illustrated the Fermi level crossing the spin gap. The numbers between square brackets indicate the total number of electronic states in the respective bands and the occupancy of the bands is given by the white numbers.

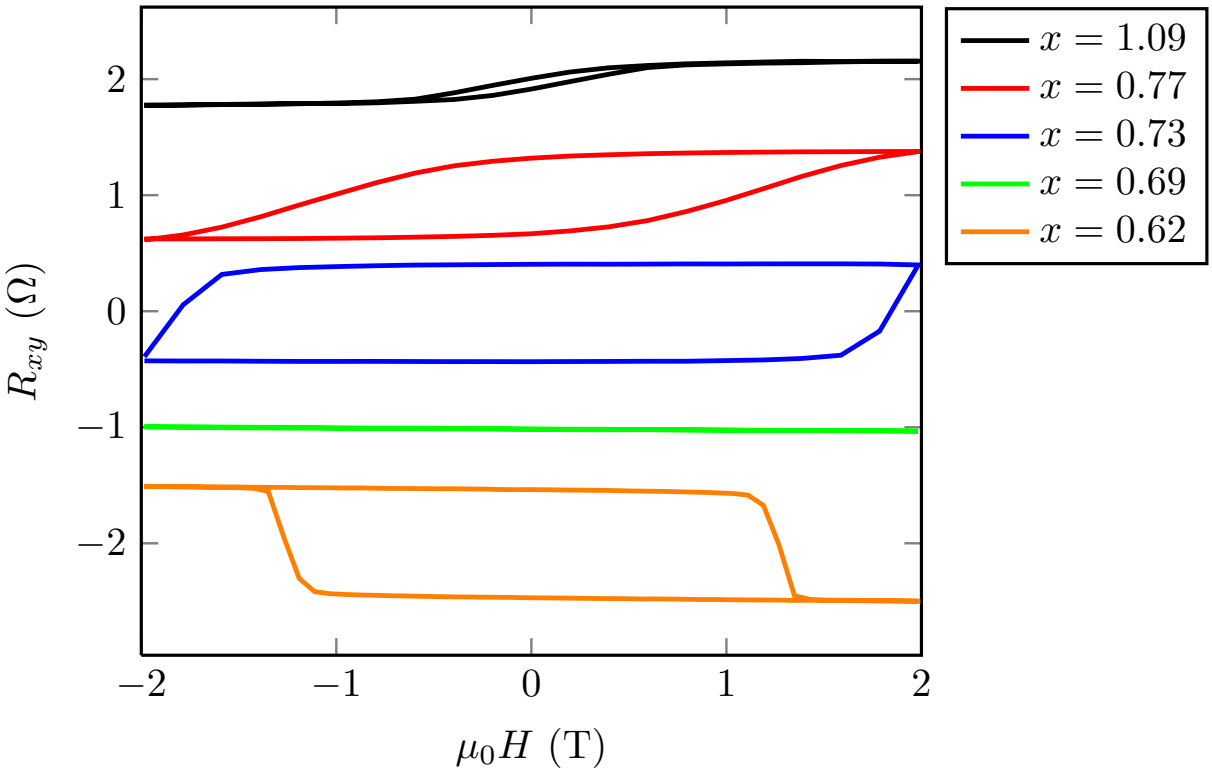

Figure 4.25: Anomalous Hall effect of Mn_2RuGa with $\Delta c/a$ =1.92 % and different x. The loops have been measured at room temperature and have been shifted for clarity. The AHE resistance changes sign between $x = 0.62$ and $x = 0.73$. At $x = 0.69$ the magnetisation is practically zero, making it almost impossible to influence it with an external magnetic field, hence the AHE voltage is a flat line. The measurements have been performed at room temperature.

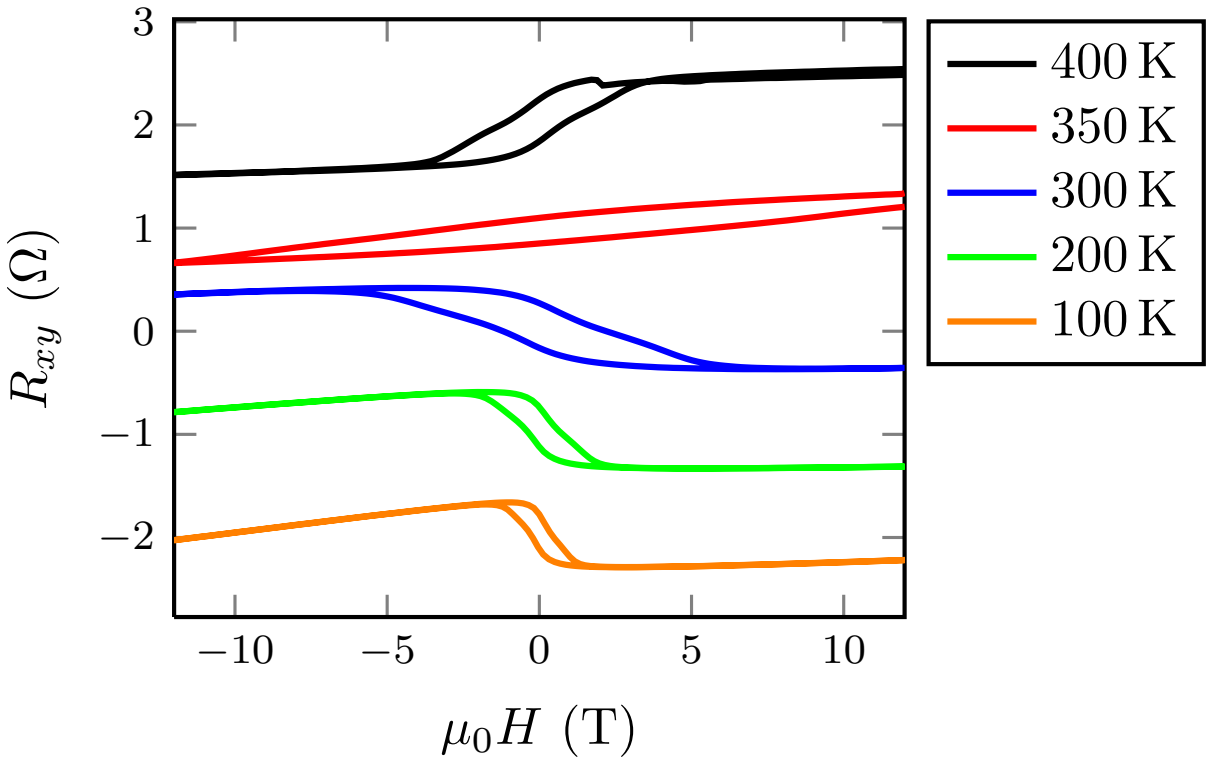

Figure 4.26: Anomalous Hall effect of Mn_2RuGa with $\Delta c/a$ =1.92 % and $x = 1$ measured at different temperatures. The loops have been shifted for clarity. The AHE resistance changes sign between 300 and 350 K.

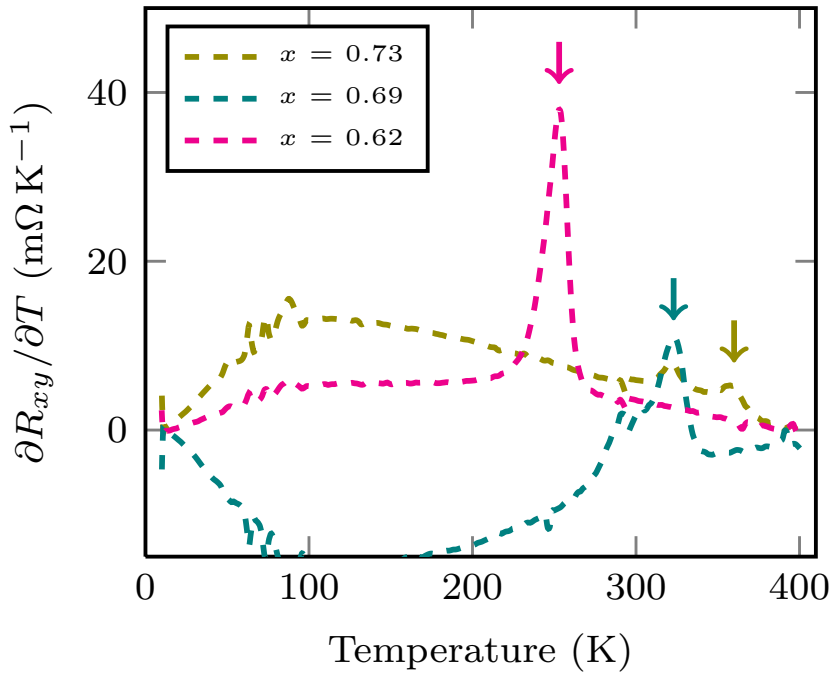

Figure 4.27: Temperature derivative of the AHE resistance $\partial R_{xy}/\partial T$ as a function of the temperature for samples of varying Ru concentration x and same $\Delta c/a$ ∼1.9 %. The maxima in the curves are indicated with arrows and correspond to the compensation temperature T_{comp}.

while the 4*c* magnetisation decreases linearly. From the plot of the temperature derivative of the AHE resistance $\partial R_{xy}/\partial T$ in Fig. 4.27 and of the coercive field in Fig. 4.28, it can be seen that the compensation temperature T_{comp} shifts to lower temperature as x is lowered. This reflects the temperature dependence of the Mn 4*c* sublattice as a function of Ru concentration (see sec. 4.3.4).

From the AHE loops, it is also clear that the coercive field H_{c} needed for the complete saturation of the sample diverges when approaching T_{comp}, since M_{s} goes to zero and there is no Zeeman energy term that can pull the moments to align with the external field.

In Fig.4.29 we show the temperature derivative of the AHE resistance $\partial R_{xy}/\partial T$ as a function of temperature the series of samples with same Ru concentration x but different strain $\Delta c/a$. The compensation temperature T_{comp} shifts to lower values as the tetragonal distortion is increased. Similar to the case of the series of samples with different x values, this behaviour reflects the different behaviour of the magnetisation for the two sublattices: when increasing the strain, the 4*c* magnetisation decrease linearly while the 4*a* magnetisation remains almost constant. Fig. 4.30 shows the corresponding variation of the coercive field H_{c}, which diverges at T_{comp}. As an example, the coercive field of the MRG sample with $\Delta c/a = 2.90\,\%$ reaches 9 T at $T_{\mathrm{comp}} \sim 200\,\mathrm{K}$.

The anomalous Hall angle (AHA) is defined as the ratio ρ_{xy}/ρ_{xx}, as discussed in sec. 2.3.6. We plot the AHA for the two series of samples together in Fig. 4.31 and 4.32 as a function of temperature. There are only slight variations in the absolute value with changing temperature. When the AHE loop is measured close to compensation, the films are not fully saturated because of the divergence of the coercivity, and hence the AHA is somewhat underestimated. In the case of the thinnest sample (4 nm), which also has the largest c/a ratio, the Curie temperature is shifted to much lower temperatures, as can be inferred from the near-zero AHA, which increases only close to 10 K. This is due to the almost complete loss of magnetic moment carried by the 4*c* Mn under tetragonal distortion. Extrapolating from our XAS/XMCD

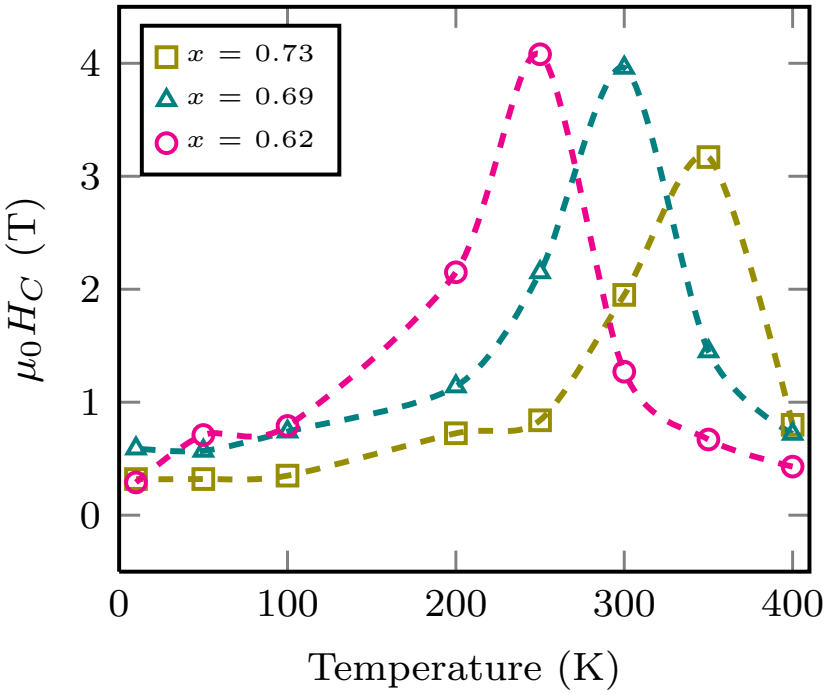

Figure 4.28: Coercive field H_c as a function of the temperature for samples of varying Ru concentration x and same $\Delta c/a$ ~1.9 %. The maxima in the curves correspond to the compensation temperature T_{comp}.

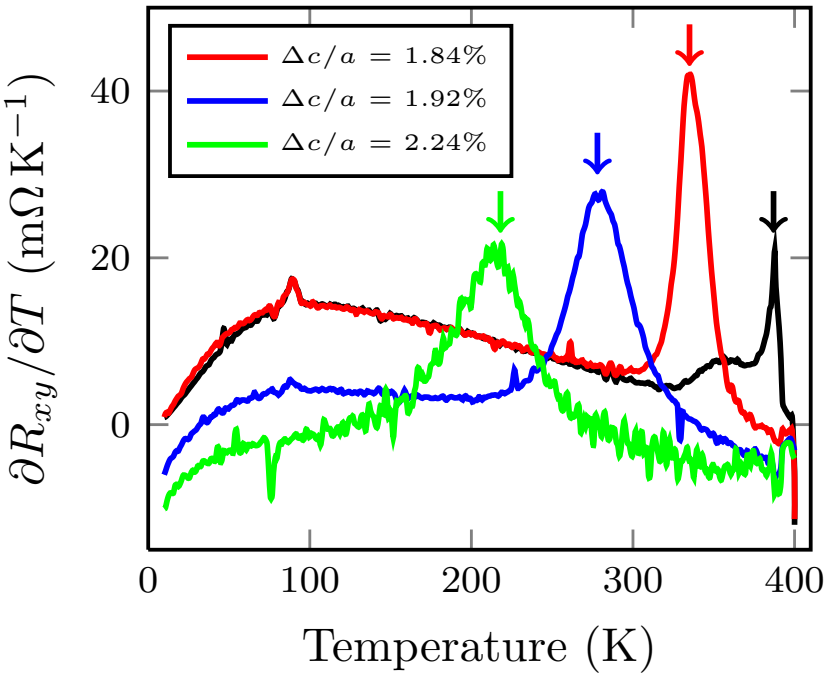

Figure 4.29: Temperature derivative of the AHE resistance $\partial R_{xy}/\partial T$ as a function of the temperature for samples of varying strain $\Delta c/a$ and same Ru concentration $x \sim 1$. The maxima in the curves are indicated with arrows and correspond to the compensation temperature T_{comp}.

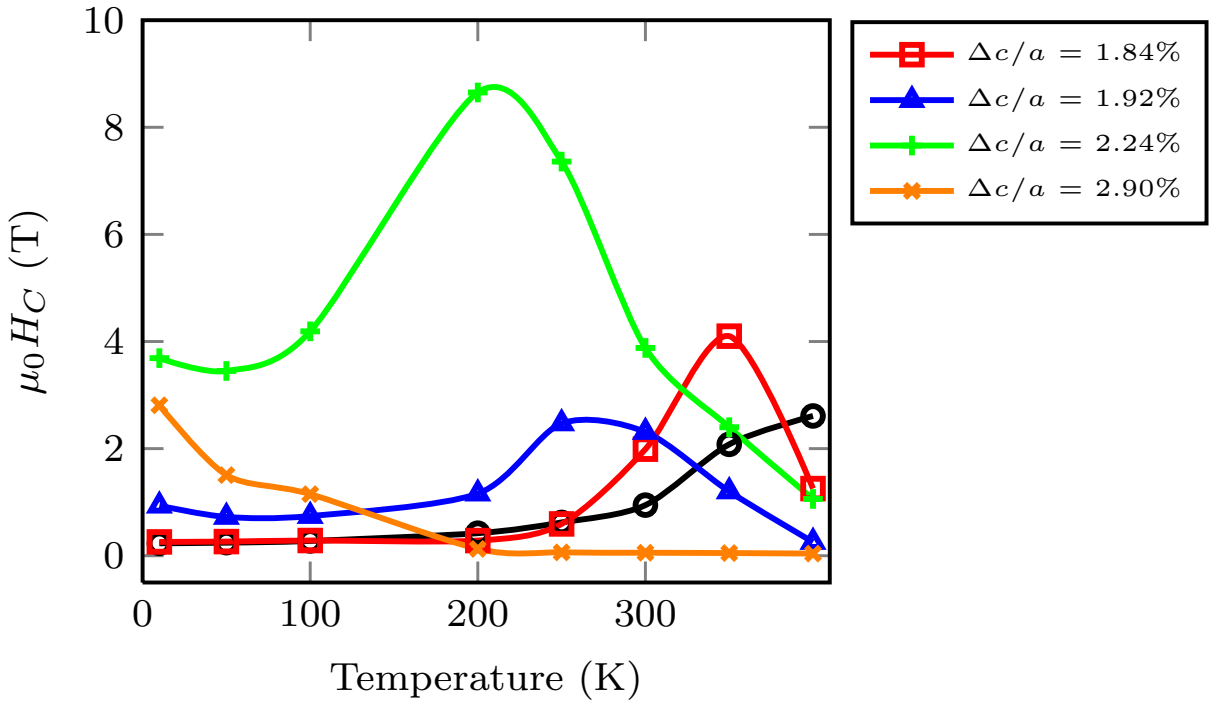

Figure 4.30: Temperature derivative of the coercive field H_c as a function of the temperature for samples of varying strain $\Delta c/a$ and same Ru concentration $x \sim 1$. The maxima in the curves correspond to the compensation temperature T_{comp}.

measurements (see sec. 4.3.4), we estimate that the zero-temperature saturation magnetisation of this sublattice under a compressive strain of 3.6 % is only 0.25 μ_B/Mn, compared to $\sim$ 1.4 μ_B/Mn in thicker samples. The much reduced magnetisation of this sublattice reduces the Curie temperature T_C from $\sim$ 550 K to $\sim$ 200 K where we first observe appreciable coercivity (see Fig. 4.30).

Fig. 4.33 shows the evolution of the AHA with varying Ru concentration x. From Fig. 4.31 it is clear that the AHA is almost constant in temperature, hence we used the data taken at 300 K for the analysis. In the figure is also shown the variation of the longitudinal and transverse resistivity ρ_{xy} and ρxx as a function of x, the latter being almost constant over the whole range. The recorded AHA ($\sim$ 7.7 %) for samples up to $x = 0.7$, which are in the half-metallic region, is about an order of magnitude larger than those found for other 3d ferromagnets at room temperature (0.2 % to 0.3 %), [34] and comparable to values recorded for amorphous rare earth transition metal alloys [35] and dilute magnetic semiconductors such as Mn:GaAs in the degenerate regime [36, 37]. A high AHE is indicative of a low carrier concentration and a high spin polarisation. The AHA increases with decreasing Ru concentration, implying that the large AHA is not due to spin-orbit scattering from the addition of Ru atoms, and as it is normalized for effects of changing electronic mobility and carrier concentration, it points to either an extremely high intrinsic contribution to the Hall signal and/or to an almost complete spin polarisation of the carriers close to the Fermi level, as is the case in Mn:GaAs [37].

We also investigated the evolution of the AHA with respect to the strain of the crystal structure (Fig. 4.34). Since there is a large variation of the AHA when Ru concentration x is varied, we compared only samples with the same values of $x \sim 1$. As the strain increases, the AHA decreases, reflecting the decreasing of the 4c magnetisation.

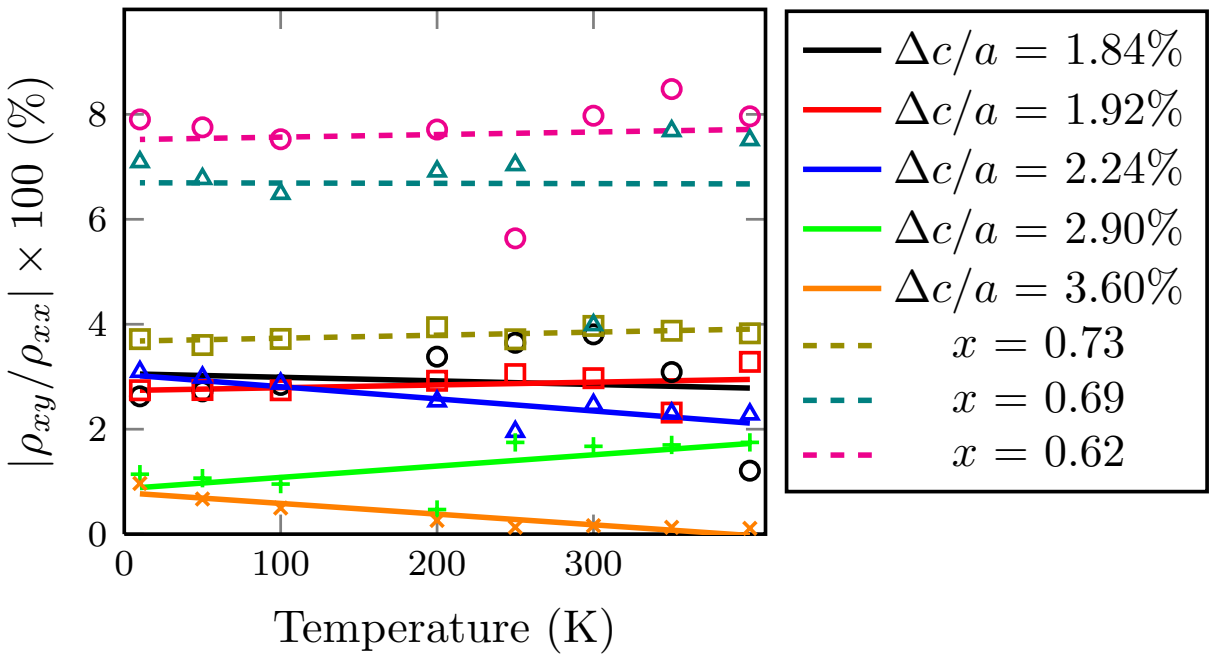

Figure 4.31: Absolute values of the anomalous Hall angle (AHA) as a function of temperature for the two sets of samples. All straight lines are obtained through linear regression of the data. The solid lines correspond to samples with same $x \sim 1$, while the dashed lines correspond to samples with same $\Delta c/a$ ~1.9 %.

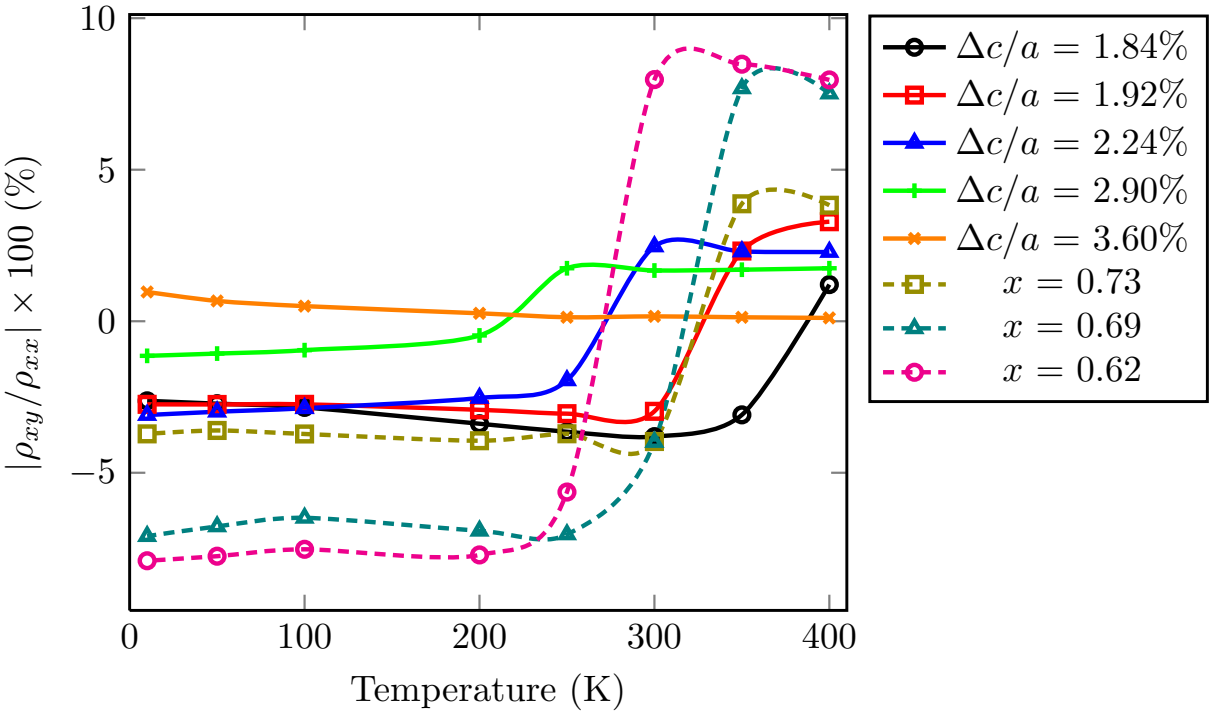

Figure 4.32: Anomalous Hall angle (AHA) as a function of temperature for the two sets of samples. The solid lines correspond to samples with same $x \sim 1$, while the dashed lines correspond to samples with same $\Delta c/a$ ~1.9 %. Negative values correspond to the switching of the magnetisation of the samples. The sample with $\Delta c/a$ =3.6 % has an estimated Curie temperature T_C of only ~200 K and it is not possible to reach compensation.

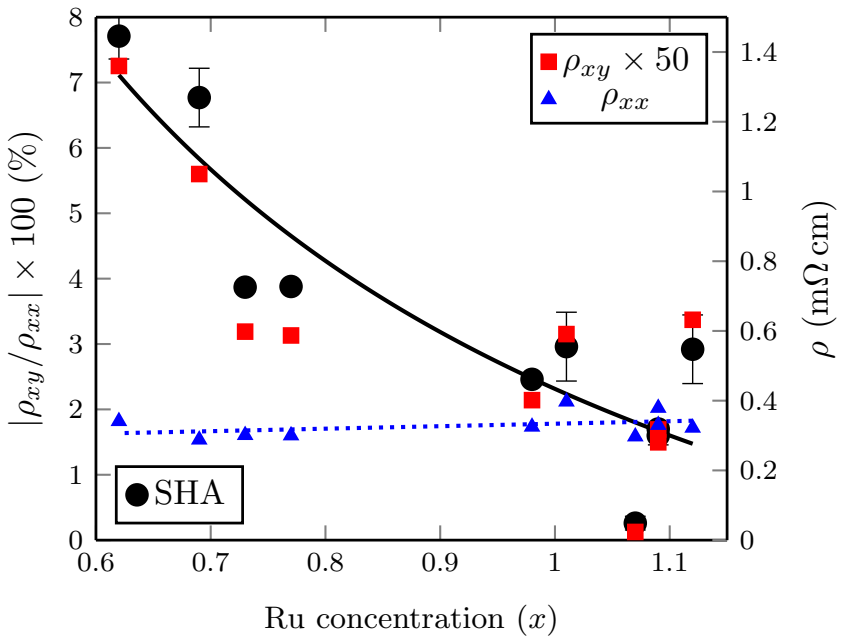

Figure 4.33: Left y axis: anomalous Hall angle (AHA) as a function of Ru concentration x, as extracted from AHE measurements at 300 K. The black line is a guide to the eye, while the blue one is a linear fit of the data. Right y axis: ρ_{xy} and ρ_{xx} as a function of x.

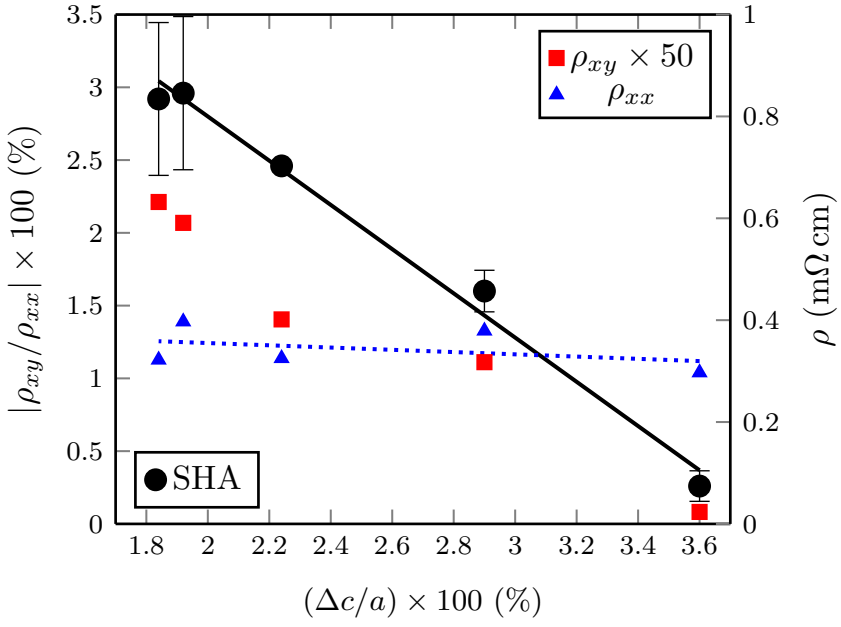

Figure 4.34: Left y axis: anomalous Hall angle (AHA) as a function of strain $\Delta c/a$, as extracted from AHE measurements at 300 K for samples with $x \sim 1$. The lines are linear fits of the data. Right y axis: ρ_{xy} and ρ_{xx} as a function of $\Delta c/a$.

Table 4.5: List of samples measured by XAS/XMCD

Sample	Ru concentration x	a(Å)	c(Å)	$\frac{c}{a}-1$(%)
$MgO/Mn_2Ru_xGa(70\,nm)/Al_2O_3(2\,nm)$	1.12	5.956	6.065	1.84
$MgO/Mn_2Ru_xGa(34\,nm)/Al_2O_3(2\,nm)$	1.01	5.956	6.070	1.92
$MgO/Mn_2Ru_xGa(15\,nm)/Al_2O_3(2\,nm)$	0.98	5.956	6.089	2.24
$MgO/Mn_2Ru_xGa(8\,nm)/Al_2O_3(2\,nm)$	1.09	5.956	6.129	2.90
$MgO/Mn_2Ru_xGa(60\,nm)/Al_2O_3(2\,nm)$	0.62	5.956	6.067	1.87
$MgO/Mn_2Ru_xGa(60\,nm)/Al_2O_3(2\,nm)$	0.69	5.956	6.073	1.97
$MgO/Mn_2Ru_xGa(60\,nm)/Al_2O_3(2\,nm)$	0.73	5.956	6.065	1.83

Conclusions

We have confirmed that for Ru concentrations in the range ~ 0.5 to 1.0, it is possible to find a compensation temperature T_{comp} where MRG thin films exhibit zero magnetisation. The sign of the anomalous Hall effect reverses at this temperature as the majority spin channel is inverted. The magnitude of the AHA is remarkably large, and cannot be attributed to the spin-orbit scattering from Ru, as it increases as x decreases. It seems to be a signature of the half metallic state. We also show that by varying the tetragonal distortion at a particular Ru concentration, it is possible to tune the compensation of the two Mn sublattices to the desired temperature range.

Recent *ab inito* calculations [38] suggested that a high anomalous Hall effect and angle could arise from "serious disorder" in MRG samples, but this cannot explain the clear inversion of the anomalous Hall loop at T_{comp}.

4.3.4 XAS ans XMCD measurements

XAS spectra on the Mn $L_{3,2}$ edges were recorded in an applied magnetic field of $\mu_0 H = 6.8\,T$ with the sample normal parallel to both the x-ray propagation vector $\vec{k}$ and the applied magnetic field. The experiments have been carried out at the SLS synchrotron facility on the X-TREME beam-line (proposal number 20140130). The list of measured samples and characteristics are reported in Tab. 4.5.

The sample temperature was varied from 2 K to 360 K. [39] We also recorded XAS spectra on the Ga $L_{3,2}$ and the Ru $M_{3,2}$ edges. We found no absorption edge in the energy range corresponding to Ga, indicating that it is close to a $3d^{10}$ configuration with no final states available in the $3d$ band. The signal to noise ratio on the Ru edges was too poor to extract any magnetic or structural information.

Normal incidence L edge x-ray absorption and dichroism allow the independent determination of the spin $2\langle S_z\rangle$ and orbital $\langle L_z\rangle$ moments via the magneto-optical sum rules. It is chemically selective due to the separation of the atomic absorption edges in energy, and specific sites can be identified due to the effect of the crystal field on the multiplet structure. The case of Mn is complicated by two main factors. First, the $2p$ spin-orbit coupling is insufficient to clearly separate the L_3 ($^2P_{3/2}$) from the L_2 ($^2P_{1/2}$) edge, and second, there is a significant degree of L_2 character in the L_3 absorption peak and vice-versa [18]. The common way to circumvent this problem is to assume that the values for the magnetic moments obtained by the sum rules have to be multiplied by a factor ~ 1.5 in the case of Mn [40], to obtain agreement with other magnetometry methods. This factor is obtained using the ratio G_{2p3d}/λ where G_{2p3d} is the $2p-3d$ multiplet interaction Slater parameter and λ is the $2p$ spin-orbit coupling. We address this problem differently. For a direct comparison with an explicit quantum mechanical core hole corrected multiplet calculation, we use the code initially written by R.D. Cowan, and further developed by T. Thole [41–43], and calculate the theoretical absorption and dichroism spectra for the two Mn

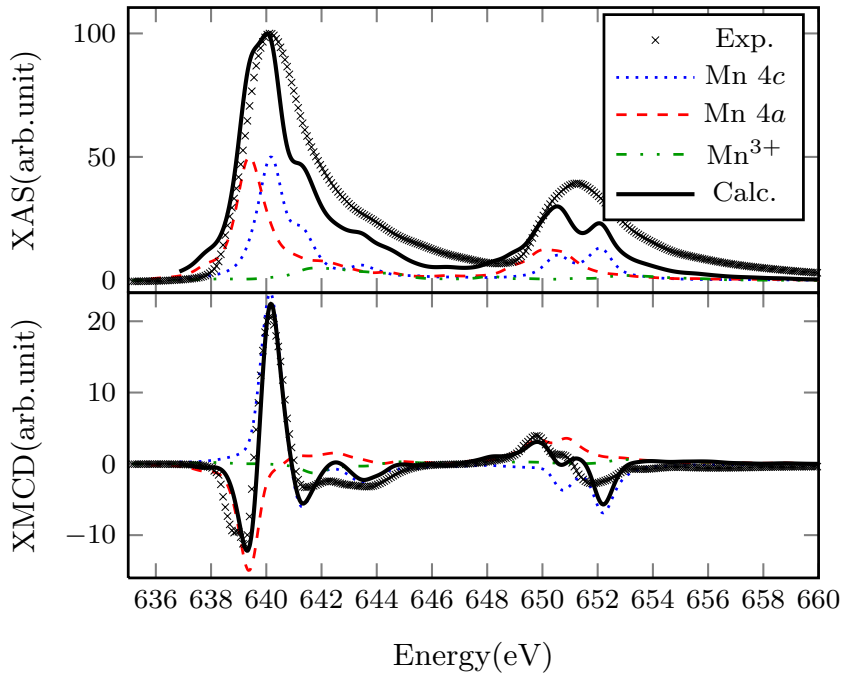

Figure 4.35: The isotropic x-ray absorption and dichroism spectra for a typical Mn_2Ru_xGa sample. The calculated contribution from each crystallographic position is shown in thin dotted/dashed lines. The dichroic spectra for each site has opposite sign for the two positions $4a$ and $4c$, confirming their antiferromagnetic ordering.

crystallographic positions [44]. The magnetic moments are then given by the calculated expectation values of $\langle S_z \rangle$ and $\langle L_z \rangle$. The experimentally observed magnetic moments are subsequently obtained by scaling the calculated dichroic signal to the observed XMCD.

In intermetallic systems, we expect a high degree of charge transfer between the different ions in the unit cell. It has however been reported that Mn in these alloys retain a partially localised electronic configuration. [13, 45, 46] We therefore based our calculated spectra on a model where Mn is in a $3d^5$ ground configuration with charge transfer by interaction with a $3d^6\underline{L}$ configuration, where $\underline{L}$ denotes a ligand hole. We used values close to what found in the literature for the transfer integrals $t_{t_{2g}} = 0.9\,\text{eV}$ and $t_{e_g} = 2.0\,\text{eV}$. The difference between the U_{dd} and U_{pd} Hubbard potentials was chosen to be 1.12 eV [47]. As discussed in sec. 4.3.2, in the Heusler structure, Mn occupies one site that is octahedrally coordinated by Ga and another that is tetrahedrally coordinated. We used 1.2 eV and 0.5 eV for the respective crystal field parameters $10Dq$. The Slater integrals were reduced to 80 % of their atomic values. The charge transfer parameters Δ were set to the values that best reproduce the experimental data: 4.0 eV and $-4.0\,\text{eV}$ for the $4c$ and $4a$ positions respectively. In Fig. 4.35 we show the experimental data along with the calculated contribution from the two, antiferromagnetically coupled, sites. We also identify a small (5 %) contribution from Mn^{3+} which we attribute to the grain boundaries in the film. An estimate of the grain surface to volume ratio can be obtained from the average grain size as measured by RSM. We find that the in-plane coherence length is $\sim 150\,\text{nm}$ implying that $\sim 2.6\,\%$ of the Mn is present in these boundaries, assuming the boundary is one atomic layer thick. We calculated this contribution as a Mn^{3+} ion with $10Dq = 0.5\,\text{eV}$. The calculated and experimental spectra show excellent agreement with each other. We find zero-temperature expectation values $2\langle S_z \rangle$ of $4.35\,\mu_\text{B}$ and $4.85\,\mu_\text{B}$ with $3d$ occupation numbers of 5.65 and 5.15 for the $4a$ and $4c$ positions respectively. The orbital momentum $\langle L_z \rangle$ and the

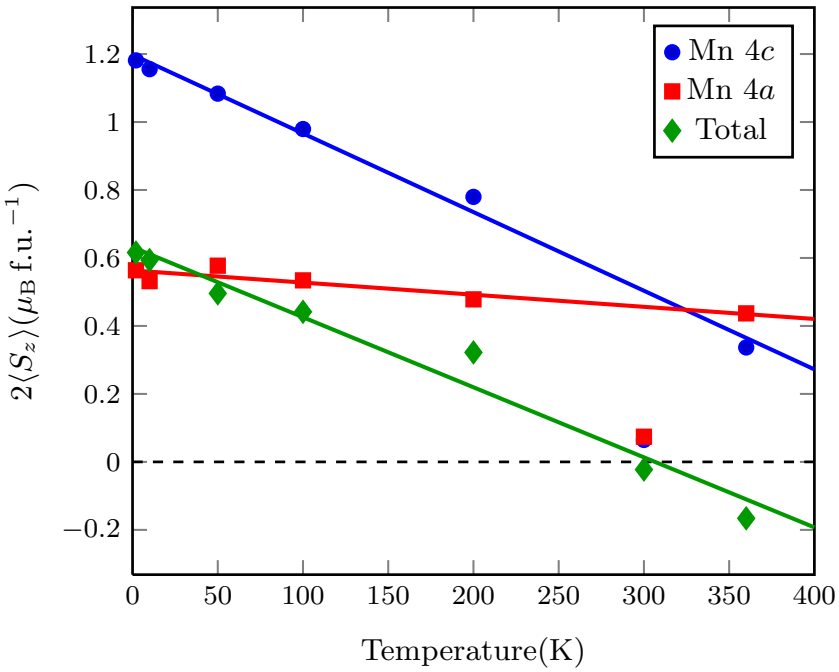

Figure 4.36: Temperature dependence of the magnetisation (absolute values) of a selected sample, with $x = 0.98$. The change of sign of the magnetisation occurs at $T_{comp} \sim 310\,K$ in good agreement with the compensation temperature measured by spontaneous Hall effect. The lines are guides to the eye only. At $T = 300\,K$, the sample is almost perfectly compensated, and we were unable to achieve even partial magnetic saturation with the maximum applied field available ($\mu_0 H = 6.8\,T$), hence the observed spin moments tend towards 0.

dipolar moment $\langle T_z \rangle$ are found to be ~ 0 for both positions, as expected for Mn in the $3d^5$ configuration. In view of recent neutron diffraction measurement [13] and DFT calculations [48] of Mn moments of related compounds, the value of $2\langle S_z \rangle$ obtained from the fits and the multiplet approximation are likely to be about 30 % too high.

In Fig. 4.36 we show the temperature dependence of the spin moments for a typical sample. There is a clear variation of the magnitudes of the moments of MRG samples with different Ru levels and c/a ratios, but the general trend is the same for all samples. The $4c$ magnetisation decreases linearly with temperature and reaches zero at an extrapolated temperature $T_C\,(4c) \sim 550\,K$ in good agreement with the behaviour reported for bulk powders of Mn_2RuGa [49]. The data for all the samples and the respective values of T_C are shown in Fig. 4.37. The $4a$ magnetisation remains almost constant over the temperature range measured. Due to this difference in temperature dependence, the sign of the magnetisation changes at a temperature that depends on both Ru concentration x and the degree of substrate-induced strain. Fig. 4.38 shows the spectra and the site-specific contributions for a sample with opposite magnetisation with respect to the sample shown in Fig. 4.35, while Fig. 4.39 shows the evolution of the XMCD of a MRG sample below, at and above the compensation temperature $T_{comp} \sim 200\,K$.

The observed site moments and saturation magnetisation are much lower than the calculated expectation values, or the values determined by neutron diffraction in tetragonal Mn_3Ga [13]. There are several reasons for this. First, the XAS/XMCD was recorded in an applied magnetic field of $\mu_0 H = 6.8\,T$, insufficient to completely magnetise the samples at all experimental temperatures, especially close to compensation, where the anisotropy field becomes very large. The nature of magnetic domains in a zero-moment material is not yet well understood. We speculate that domains are present as they are in

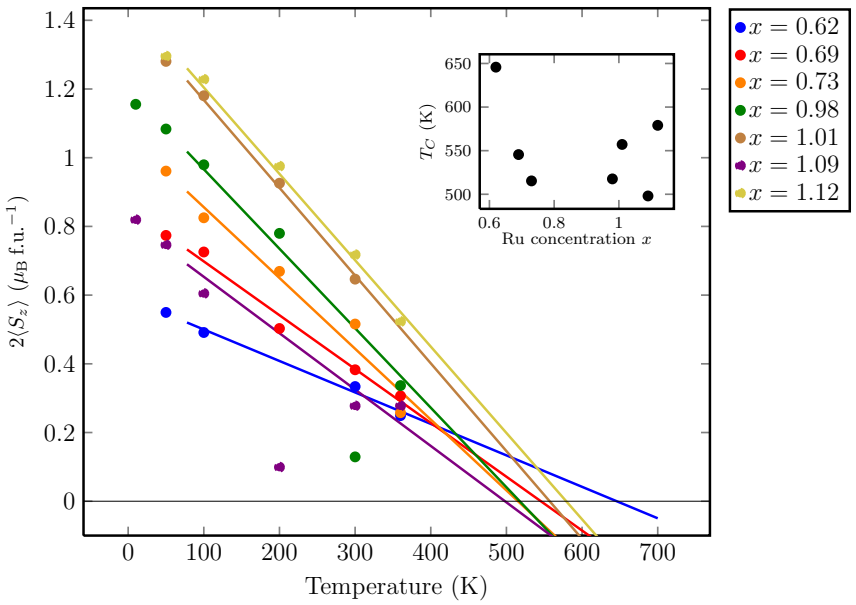

Figure 4.37: Temperature dependence of the Mn 4*c* magnetisation as a function of the temperature and linear fitting. The inset shows the extrapolated values of the Curie temperature T_C. Some data points, corresponding to the compensation temperature, have not been included in the fits since they are not reliable, as explained below.

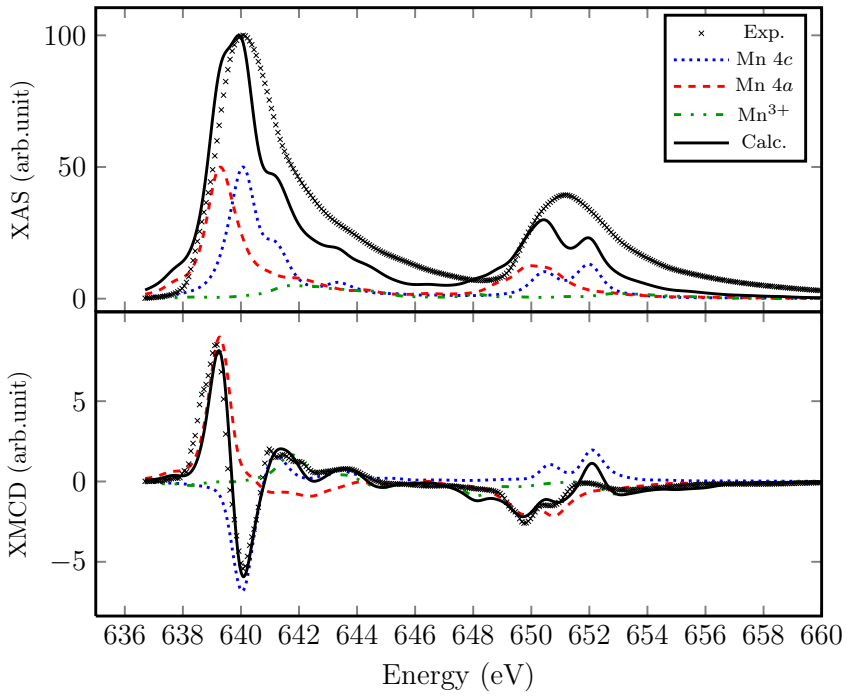

Figure 4.38: The isotropic x-ray absorption and dichroism spectra for a typical Mn_2Ru_xGa sample with switched magnetic moment. The calculated contribution from each crystallographic position is opposite with respect to the spectra of Fig. 4.35.

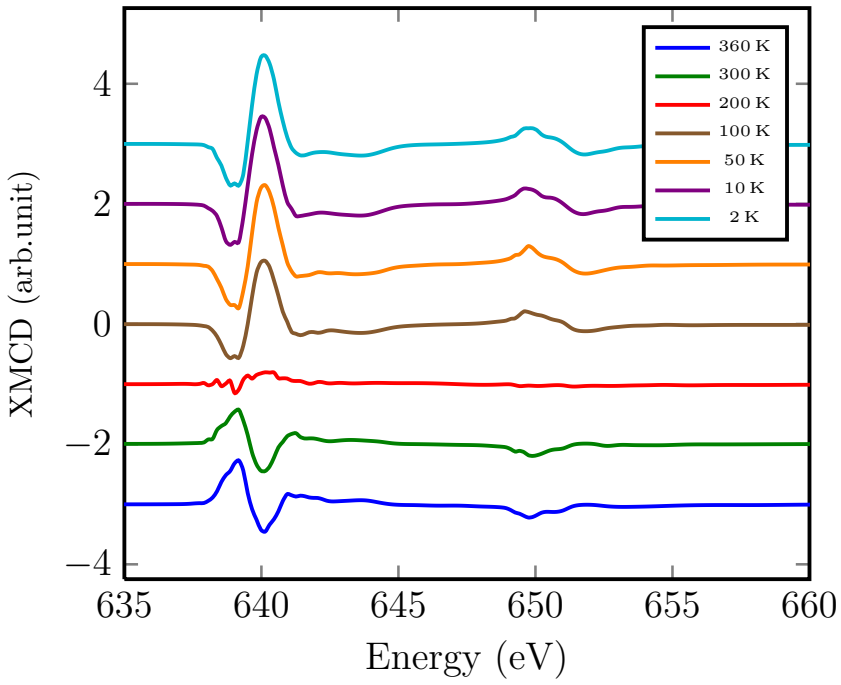

Figure 4.39: X-ray absorption spectra for samples of Mn_2Ru_xGa with $x \sim 1$ as a function of temperature. The spectra have been shifted for clarity. The features reverse at 200 K, where the magnetic moment is close to zero and no clear signal is detected.

antiferromagnets, and that the domain structure is not easily eliminated in an applied field. Second, the relatively small grain sizes (~ 150 nm) suggest that there may be a large number of anti-phase boundaries present in the samples. These are likely to couple antiferromagnetically, and hence reduce the magnetisation observed by XMCD. Third, we cannot completely exclude the possibility of a small fraction of anti-sites (Mn ($4a$) occupying the $4b$ Ga position). The two sites are equivalent by symmetry and if they coupled antiferromagnetically the XMCD of the pair would be zero.

In order to investigate the effect of the changing Ru concentration and the strain, we have chosen to extrapolate the magnetic properties to $T = 0$ K by linear regression. This extrapolation has no particular physical significance, but, as mentioned above, the linear trend in temperature is observed for all the samples measured and hence provides a good indication of their behaviour at 0 K.

In Fig. 4.40 we trace the evolution of the absolute value of the spin momentum of the $4a$ and $4c$ positions as a function of the Ru concentration x. The $4a$ magnetisation remains mostly unchanged with increasing x indicating that the Fermi level does not cross the band edges originating primarily from the corresponding reciprocal lattice position. The large spread of the values around the inferred spin momentum $2\langle S_z\rangle\,(4a) = 0.68\,\mu_B$ is due to the varying c/a ratio, discussed below.

The $4c$ position, on the contrary, exhibits a sharp increase in magnetisation between 0.60 and 0.75. The zero-temperature sign of the total magnetisation changes near $x = 0.65$. This sharp increase is followed by a change of slope for $x > 0.75$, the $4c$ magnetisation increasing moderately for $0.7 < x < 1.2$. We interpret this as follows: hybridization of bands originating from the Mn in the $4c$ position with those of Ru in $4d$ has two effects, it reduces the Mn $4c$ spin splitting and simultaneously it pulls the minority spin band down towards the Fermi level, thus changing the magnetisation of this crystallographic position. The rate of change depends on the details of the band structure, leading to an abrupt change in the $4c$ spin $\uparrow$ occupied density of states at $x \sim 0.7$ (see Fig. 4.23 and 4.24).

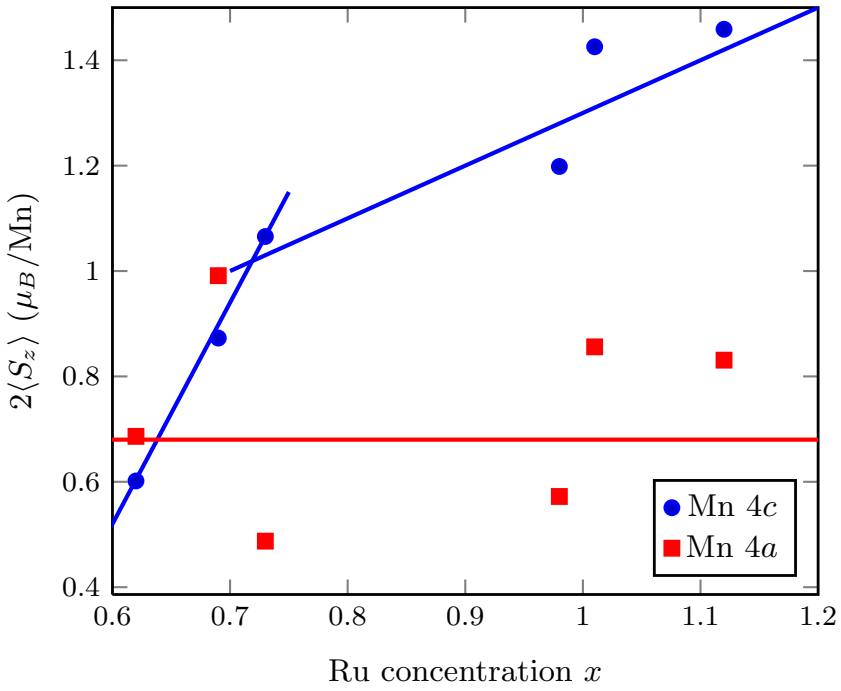

Figure 4.40: Evolution of the absolute value of the magnetic moments at of the two Mn positions, extrapolated to $T = 0\,\mathrm{K}$, with Ru concentration x. The solid lines are linear regressions to the data sets. In the case of Mn 4c, we identify a change of slope in the vicinity of $x = 0.7$, corresponding to the onset of filling the minority spin channel of Mn in this position.

We now turn to the effect of substrate-induced strain. The variation of the magnetisation in MRG is dominated by the change in Ru concentration, as can be seen in Fig. 4.40. The addition of Ru adds both electrons and states to the system as discussed above, but also provides chemical pressure, effectively modifying the strain, as observed by the change in c/a ratio. This ratio can furthermore be controlled by choosing an appropriate substrate, *or* by tuning the film thickness. In this set of experiments we have used the latter option. In order to quantify the effect of strain we therefore infer the magnetisation of a virtual sample with $x = 1.0$ for each experimental c/a ratio, following the variation shown in Fig. 4.40.

In Fig. 4.41 we plot the variation of the site-specific magnetisation as a function of the c/a ratio determined by RSM. The 4c magnetisation is decreasing with increasing c/a ratio indicating that the compressive strain provided by the MgO substrate ($\sqrt{2}a_0\,(\mathrm{MgO}) = 5.956\,\text{Å}$), gradually empties the 4c band by increasing its position in energy. Conversely, in the region of moderate strain ($c/a \sim 1.8\,\%$ to $2.0\,\%$), the 4a magnetisation increases. Above $c/a \sim 2.0\,\%$, the 4a bands deform sufficiently, changing their curvature close to the Fermi level, and a greater number of delocalised (conduction electron) states becomes available, resulting in a net decrease in the localised magnetic moment.

Conclusions

We have shown that the electronic structure of Mn_2Ru_xGa is tunable both by changing the Ru concentration x and by straining the epitaxial thin film. In order to retain high spin polarisation, the Ru concentration needs to stay below $x = 0.7$. In this regime, a moderate strain of $c/a \sim 2\,\%$ ensures that complete magnetic compensation can be achieved in the vicinity of room temperature and above, thus opening prospects of utilizing this new class of materials in spin electronic devices. The electronic structure as observed by XAS/XMCD is compatible with a half-metallic state in Mn_2Ru_xGa when $x < 0.7$. The

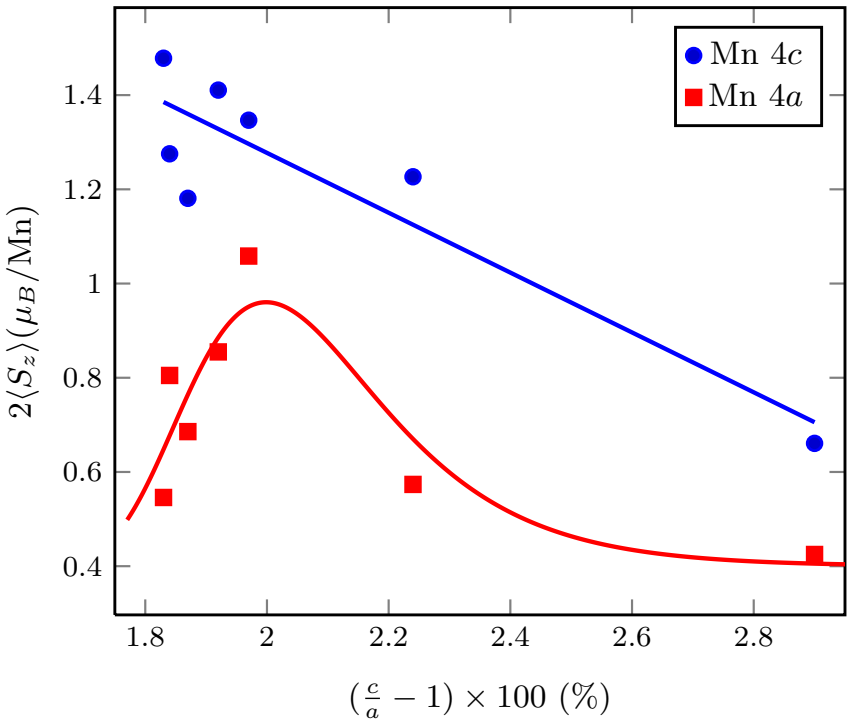

Figure 4.41: Site-specific magnetisation (absolute values) extrapolated to $T = 0\,\mathrm{K}$ as a function of c/a ratio for the samples with their spin moments translated to a virtual $x = 1.0$ Ru concentration as discussed in the text. The solid lines are guides to the eye only.

non-monotonic behaviour of the spin moment as a function of lattice strain, is a signature of a complex band structure, indicating that the rigid band, Slater-Pauling-like analysis of the magnetic properties is not adequate for MRG.

4.3.5 X-ray and UV photoelectron spectroscopy

As discussed in sec. 2.4.6, the charge transfer effect between the $3d$ orbitals of the Mn atoms and the surrounding ligands is more evident in $2p$ XPS than in XAS/XMCD measurements. The result of the XMCD analysis in sec. 4.3.4 indicates that the charge transfer is the main mechanism that drives the hybridisation of the valence d orbitals of Mn and that is at the origin of the spin gap. We expected to see some slight variations in the shape and/or position of the charge transfer peak for different Ru concentrations or temperatures. In order to analyse the evolution of these peaks, we measured $2p$ XPS on the Mn edges. The analysed samples are the same ones used for the XAS/XMCD experiment. Unfortunately, the energy resolution of our laboratory setup is around $\sim 1.0\,\mathrm{eV}$, insufficient to clearly identify charge transfer satellites (see Fig. 4.42), and hence it not possible to determine the charge transfer parameters. In Fig. 4.42, we assign the two peaks in the L_3 edge to the transitions arising from the two different sublattices. We cannot distinguish the two contributions in the L_2 edge because the peaks are intrinsically broader.

In addition we measured the UPS signal of two MRG samples with very different Ru concentration x using an He discharge lamp. One of the samples falls in the half-metallic region ($x = 0.657$), while the other is a normal ferrimagnetic metal ($x = 0.945$). There is a clear difference in the shape of the DOS near the Fermi level, as shown in Fig. 4.43, but the information that we can obtain with this setup are limited to this observation. In addition, in order to get rid of the surface contaminations and capping

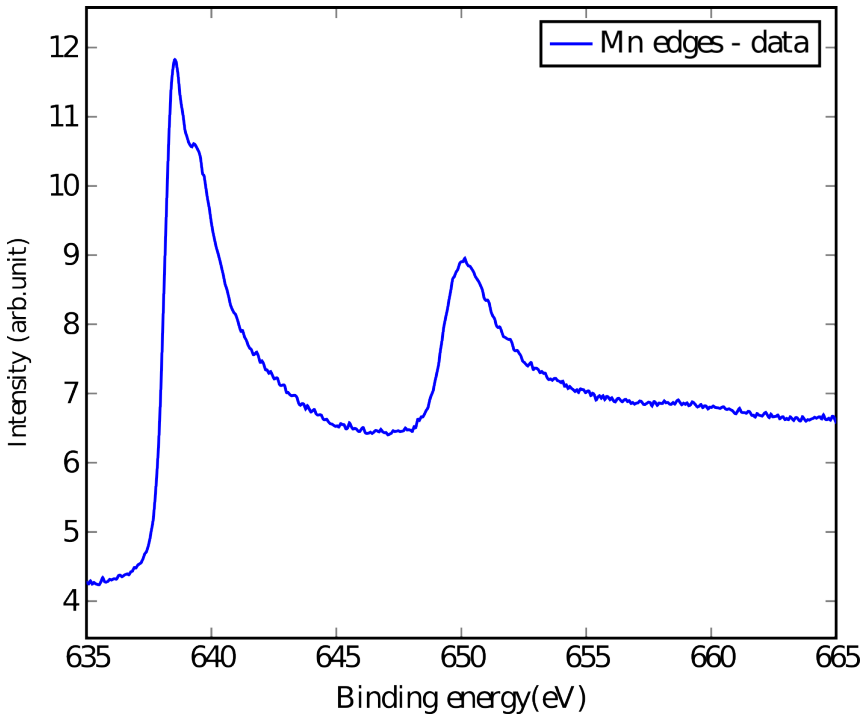

Figure 4.42: XPS spectra of a Mn_2Ru_xGa sample close to compensation. The low resolution does not allow us to clearly distinguish the position of the charge transfer satellite peak.

layer, the samples had to be etched using Ar ion milling *in situ*. We verified that this etching has a non negligible impact on the band structure of the surface, probably due to an induced atomic disorder. After annealing the etched samples at 300 °C for 1 h, the valence band DOS changed again, probably upon recrystallisation of the surface. For these reasons, we cannot unambiguously distinguish differences in the band structures of different samples.

Future work

We have submitted a proposal to the SOLEIL synchrotron to measure spin-resolved XPS and UPS (due in September 2015). A synchrotron facility provides far better energy resolution ($20000 < E/\Delta E < 70000$) coupled with the possibility of tuning the x-rays energy over a wide range of values. This will allow us to better understand the hybridisation of the $3d$ orbitals of Mn and evaluate the charge transfer parameters, consequently throwing light on the mechanism that drives the compensation of the magnetisation. Furthermore, the possibility of spin-resolved measurements of the DOS at the Fermi level will allow us to confirm the presence of a spin gap and observe the evolution of the subbands with respect to the Ru concentration x and temperature.

4.3.6 EXAFS measurements

The high symmetry of the Mn_2Ru_xGa crystal and the highly oriented (epitaxial) growth makes it impossible to infer with absolute confidence the crystal structure from XRD analysis only, since only a very limited set of reflections is available. The technique of choice in these cases is the extended x-rays absorption fine structure (EXAFS), as discussed in sec. 3.4.3. EXAFS is less sensitive to strain in the lattice parameter than XRD, but it can provide useful data on the changes in a set of samples with different

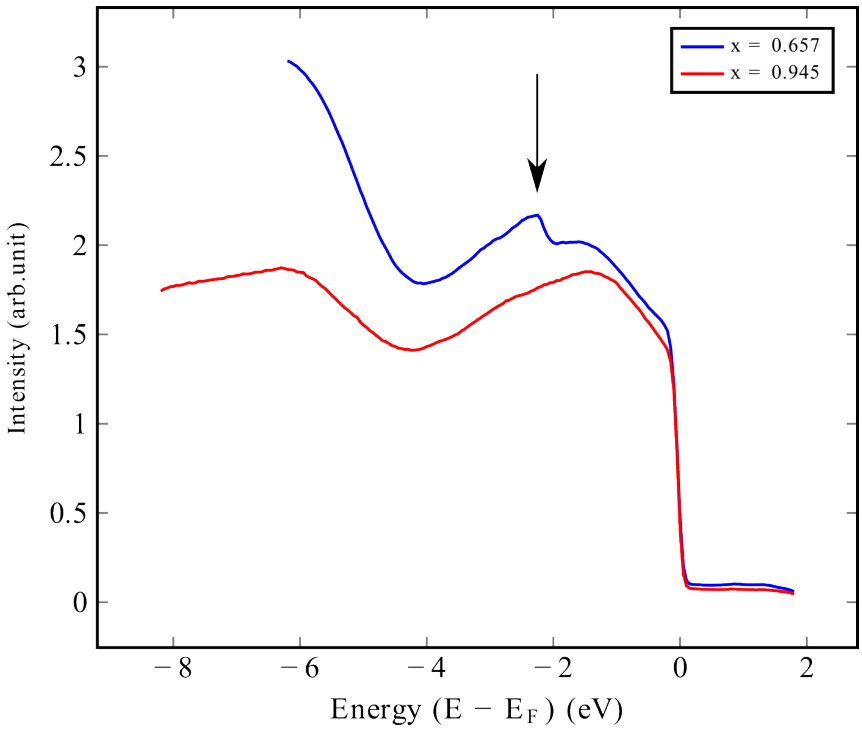

Figure 4.43: UPS spectra of two Mn_2Ru_xGa samples with different Ru concentration x. Although the spectral resolution is not very high, there is a clear difference in the valence band DOS for the two samples, indicated by the arrow.

strain. This strain has already been characterised by XRD. Together, these measurements can provide a full picture of the effect of strain, in both long-range and local ordering.

We measured EXAFS at the SOLEIL synchrotron (proposal number 20140375) at the SAMBA beamline at room temperature by fluorescence yield with a 35 pixel Germanium detector from Canberra. The monochromator was equipped with a pair of Si 220 crystals. The measured samples were part of the set already characterised by XAS/XMCD and transport measurements (see sec. 4.2.2 and 4.3.3). In particular, we focussed on the samples with similar Ru concentration x but different thickness t. The in-plane and out-of-plane crystal lattice parameters a and c, respectively, had been measured by XRD. A summary of the characteristics of the samples are reported in Tab. 4.6. The tetragonal distortion $\left(\frac{c}{a} - 1\right)$ increases as the thickness decreases.

The K edge absorption of Ru, Mn and Ga has been measured at two different angles of incidence

Table 4.6: List of samples measured by EXAFS

Sample	Ru concentration x	a(Å)	c(Å)	$\frac{c}{a} - 1$(%)
$MgO/Mn_2Ru_xGa(70\,nm)/Al_2O_3(2\,nm)$	1.12	5.956	6.065	1.84
$MgO/Mn_2Ru_xGa(34\,nm)/Al_2O_3(2\,nm)$	1.01	5.956	6.070	1.92
$MgO/Mn_2Ru_xGa(15\,nm)/Al_2O_3(2\,nm)$	0.98	5.956	6.089	2.24
$MgO/Mn_2Ru_xGa(8\,nm)/Al_2O_3(2\,nm)$	1.09	5.956	6.129	2.90
$MgO/Mn_2Ru_xGa(4\,nm)/Al_2O_3(2\,nm)$	1.07	5.956	6.172	3.62
$MgO/Mn_2Ru_xGa(60\,nm)/Al_2O_3(2\,nm)$	0.62	5.956	6.067	1.87
$MgO/Mn_2Ru_xGa(60\,nm)/Al_2O_3(2\,nm)$	0.69	5.956	6.073	1.97
$MgO/Mn_2Ru_xGa(60\,nm)/Al_2O_3(2\,nm)$	0.73	5.956	6.065	1.83

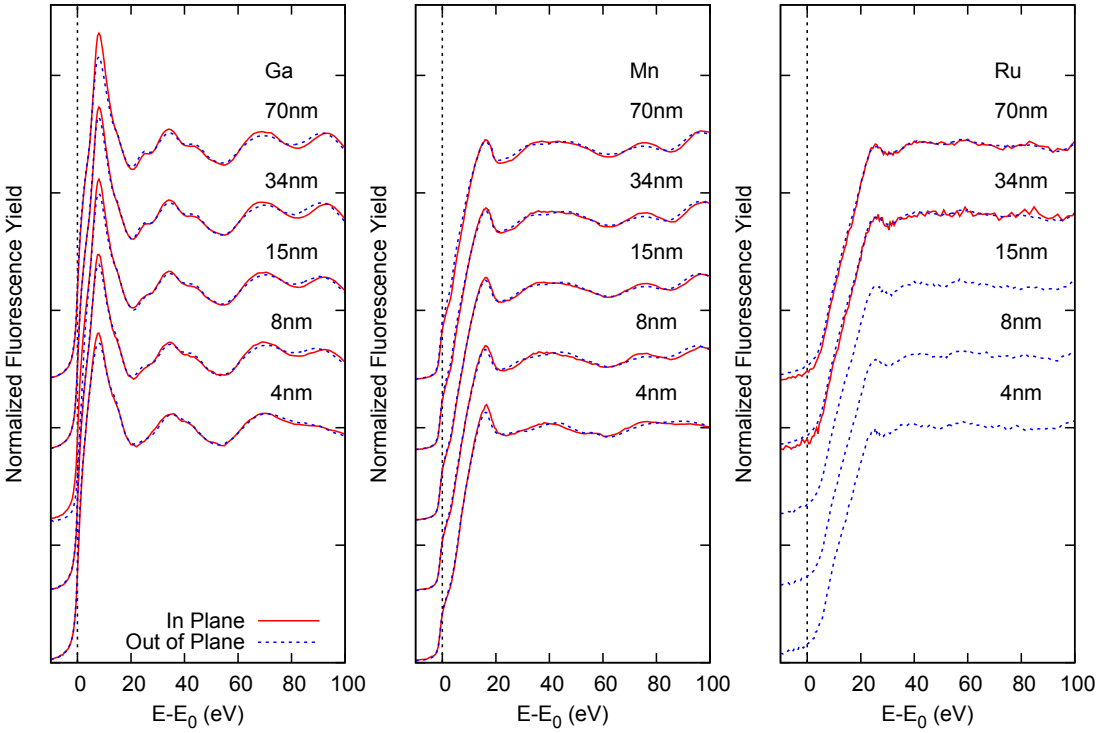

Figure 4.44: XANES and EXAFS spectra for the K edges of Ga, Mn and Ru. The data shown are for sample thickness varying from 4 nm to 70 nm and for in-plane (red, solid) and out-of-plane (blue, dotted) light polarisation. It was not possible to measure the in-plane spectra for the samples with lowest thicknesses because of the low signal-to-noise ratio, due to the extremely small interaction volume in that configuration.

with respect to the linearly polarised x-ray beam: 15° (in-plane) and 75° (out of plane) in order to obtain information on the in-plane and out-of-plane atomic configuration respectively. Unfortunately, we were not able to obtain some of the data on the Ru edge at normal incidence (15°) within acceptable quality.

XANES and EXAFS spectra and their Fourier transforms are shown in Fig. 4.44, 4.45 and 4.46, respectively. There is a progressive change of the local structure when t is varied from 4 nm to 15 nm. XANES and EXAFS show a decreasing complexity of the signal for $t \leq 15$ nm, while x-ray linear dichroism (XLD) is quite small and less evident on XANES than EXAFS (Fig. 4.44 and 4.45) while it is easier to observe on Fourier transforms (Fig. 4.46). This XLD signal is small but not negligible, as it should be in perfectly cubic crystals.

Data at the Ga K edge has been analysed starting from the detailed model obtained by reverse Monte Carlo fitting and published previously [9]. The analysis has been made by our collaborator, Doct. Emiliano Fonda, principle beamline scientist at the SAMBA beamline. The local structure around Ga atoms can be decomposed in a 1^{st} shell containing eight neighbours of Ru and Mn atoms and a 2^{nd} shell containing two non equivalent Mn atoms at different distances due to tetragonal distortion. The Mn atoms in the 2^{nd} shell are supposedly 6. The distances assume values close to each other (2.5 Å to 3.2 Å) and the same

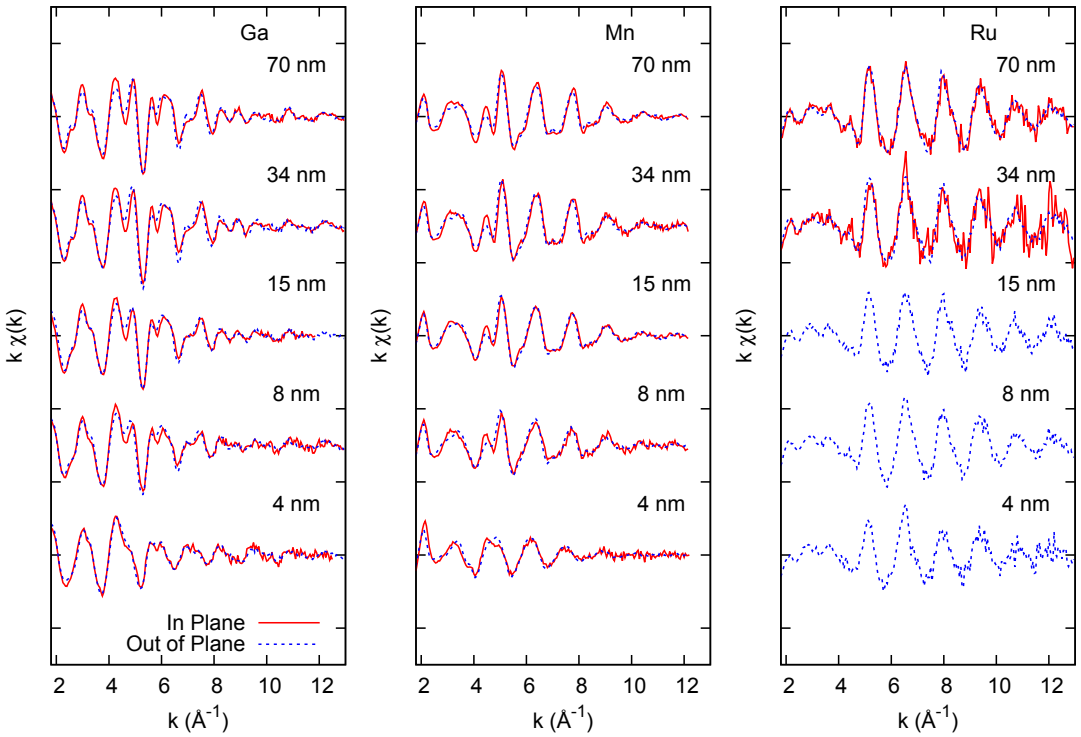

Figure 4.45: EXAFS spectra of Fig. 4.44 in reciprocal space. The data shown are for sample thickness varying from 4 nm to 70 nm and for in-plane (red, solid) and out-of-plane (blue, dotted) light polarisation. It was not possible to measure the in-plane spectra for the samples with lowest thicknesses because of the low signal-to-noise ratio, due to the extremely small interaction volume in that configuration.

Debye-Waller factor has been used for all shells. The latter turns out to be stable throughout the series at the value 8(1) 10^{-5} nm^2. The fitting are shown in Fig. 4.47.

In Fig. 4.48 the occupation of the crystalline sites and the atomic distances around Ga are shown, both in the in-plane and out-of-plane directions. The in-plane and out-of-plane occupations and distances are consistent for the thicker samples, while they deviate for $t \leq 8$ nm. In Fig. 4.48 a) the composition of the first shell has not been constrained and it remains close to a Mn/Ru ratio of 1/2 all over the range of t, except for 4 nm, where a deficiency in Mn appears. The Ga-Ru distance (Fig. 4.48 c) is somewhat constant with respect to the thickness, while the Ga-Mn one become longer at smaller t, out-of-plane as well as in-plane. The small elongation starts below 15 nm and even if the error bar is relatively large it closely follows the elongation of the c axis. The second shell distances (Ga-$Mn_{3,2}$) (Fig. 4.48 d) show a similar evolution. The in-plane distances average remains constant, while the out-of-plane distances increase at and below t =15 nm. Considering the total number of second neighbours, they decrease faster in the out-of-plane than in the in-plane direction, while attaining the same minimal value (Fig. 4.48 b). This is an unexpected result and it is certainly not an artefact, but its full significance cannot be understood without comparing Ru, Mn and Ga simulations together. This part of the analysis is still in progress.

We also measured a set of three samples with the same thickness ($\sim$ 70 nm) but different Ru concen-

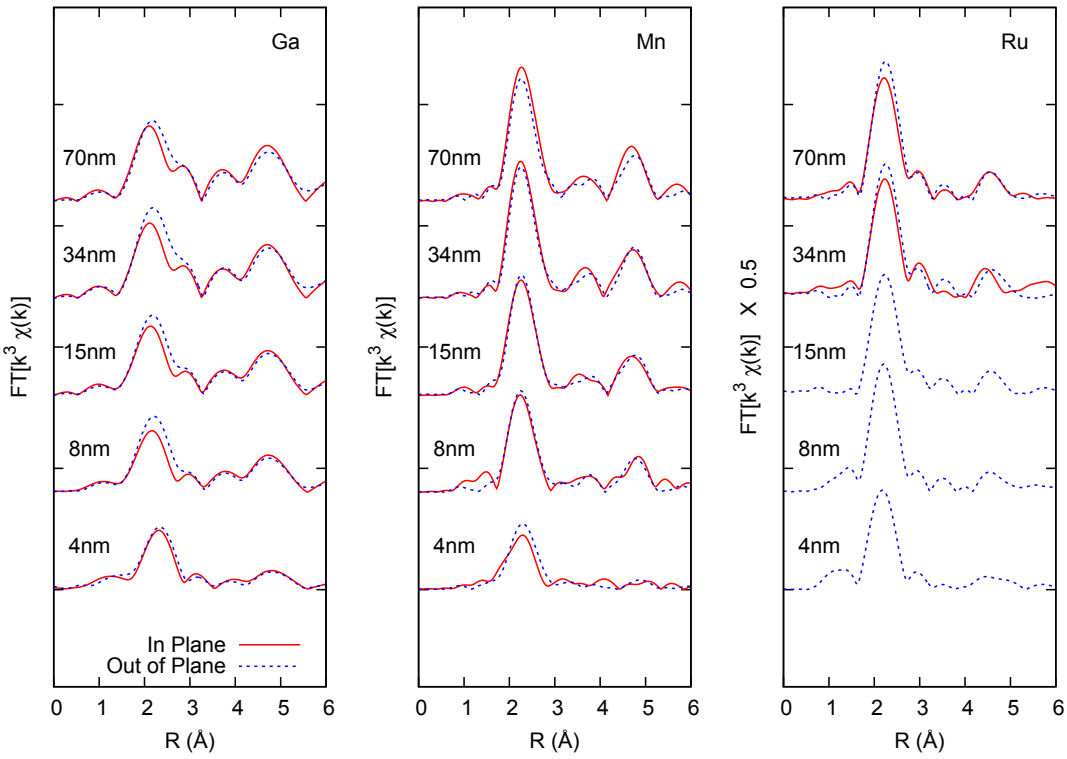

Figure 4.46: Fourier transform of the EXAFS spectra of Fig. 4.45. The data shown are for sample thickness varying from 4 nm to 70 nm and for in-plane (red, solid) and out-of-plane (blue, dotted) light polarisation. It was not possible to measure the in-plane spectra for the samples with lowest thicknesses because of the low signal-to-noise ratio, due to the extremely small interaction volume in that configuration.

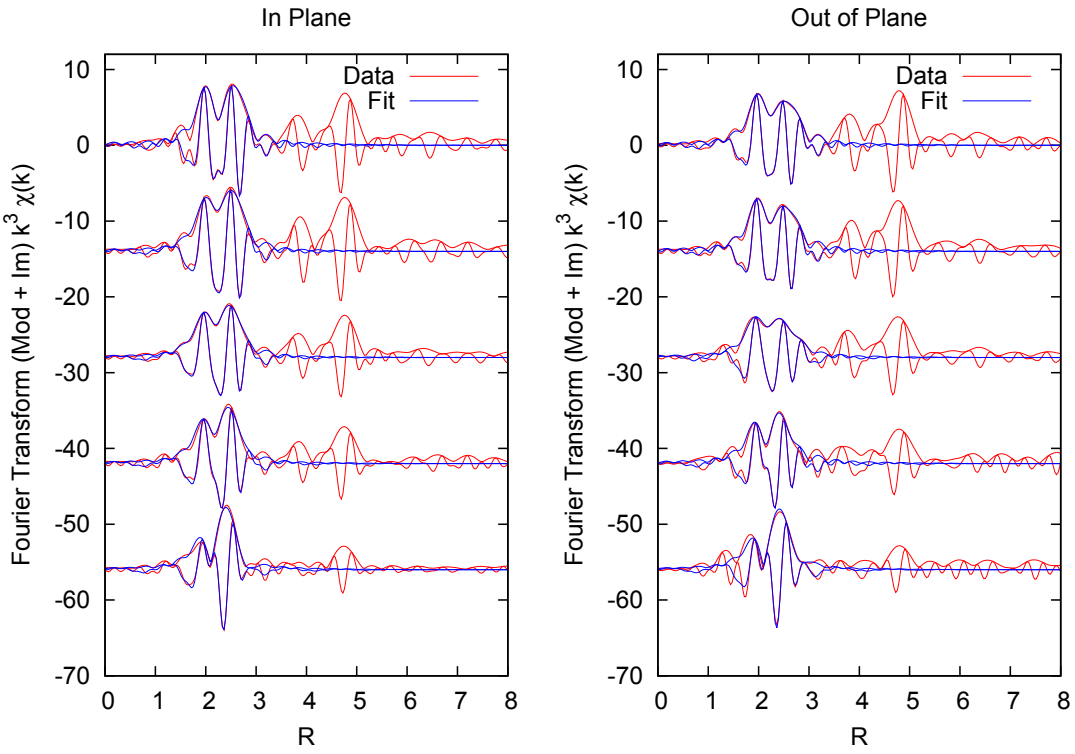

Figure 4.47: Fourier transform of the EXAFS spectra and fits using the reverse Monte Carlo model on the Ga edge. The fits consider only the 1st shell of neighbouring atoms. Both modulus and the imaginary parts of the Fourier transforms are shown.

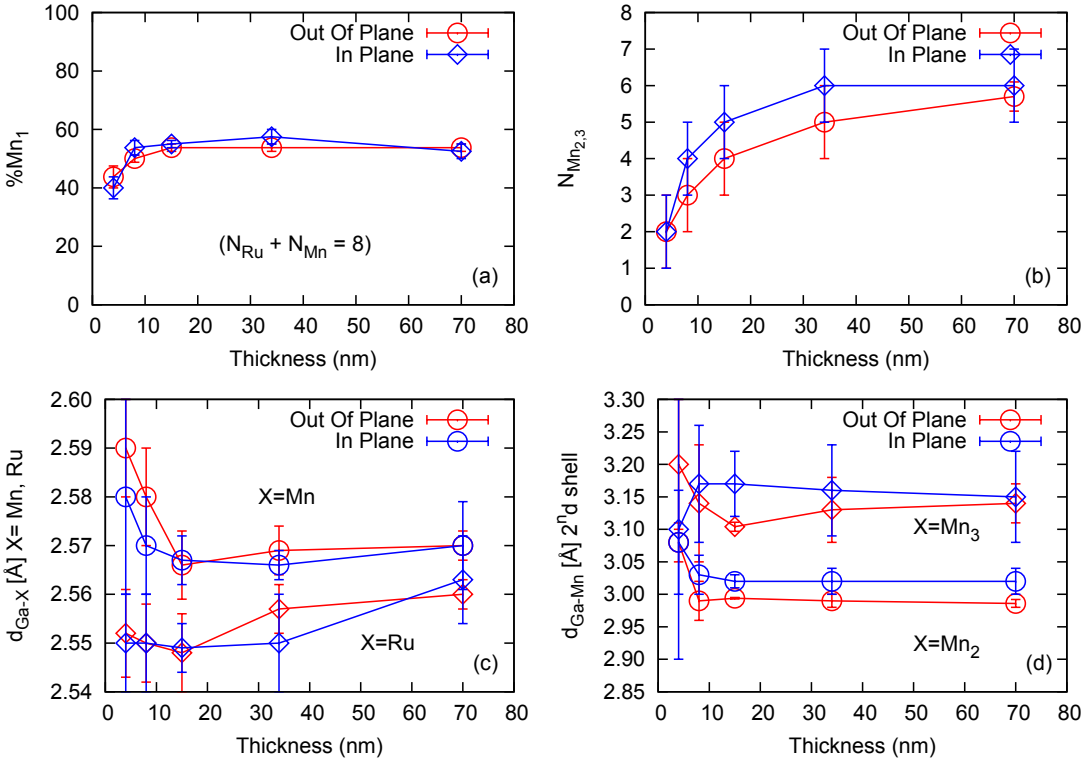

Figure 4.48: Results of the analysis of the EXAFS data for Ga. a) Percentage of Mn in the 1st shell in-plane and out-of-plane as a function of sample thickness. b) Number of Mn in the 2nd shell in-plane and out-of-plane as a function of sample thickness. c) Ga-Mn and Ga-Ru distances (1st shell) in-plane and out-of-plane as a function of sample thickness. d) Ga-Mn distances (2nd shell) in-plane and out-of-plane as a function of sample thickness.

tration x, ranging from 0.62 to 0.63, in order to analyse the different occupancy of the empty sites as Ru atoms are introduces into the compound. The data obtained with those measurements are going to be analysed last, when the occupancy and the structure of the samples with $x \sim 1$ is understood.

Conclusions

The analysis performed so far on the Ga edges seems to confirm the $C1_b$ structure, at least for the thickest samples. The Mn deficiency and the different atomic order in the thinnest samples can be the origin of the unusual XMCD data obtained, unexpectedly different from the spectra of the other samples and indicative of altered magnetic properties.

4.3.7 Mn_2Ru_xGa-based MTJ

The main application in spin electronics for a material such as a half-metallic compensated ferrimagnet would be as a magnetic layer in an MTJ structure (see sec. 2.3.9). We fabricated some junctions with an MRG layer in order to investigate their properties.

X-ray photoelectron spectroscopy

The use in the previously discussed samples of a capping layer of Al_2O_3 prevents the oxidation of Mn in the MRG layer. The electronegativity of Al is 1.61 against 1.55 for Mn, therefore the oxygen atoms tend to remain bonded to the Al atoms in the capping layer instead of diffusing in the MRG. Unfortunately, Al_2O_3 has proved not to be a good tunnel barrier for MRG-based MTJs, since it is dissolved by the developer used for the lithography process (see sec. 3.2). This results in the formation of pin-holes and, subsequently, electric shorting of the junctions. The use of a barrier of MgO, the currently employed material for spin electronics applications, is likely to lead to oxidation of the Mn atoms, since the electronegativity of Mg is only 1.31. In order to circumvent this problem, we tried to deposit a very thin dusting layer of a compatible metal to isolate the MRG layer from the oxide. It has also been shown that diffusion of Mn atoms into the barrier results in a significant lowering of the TMR [50–52]. We believe that the insertion layer could help to avoid this problem as well.

XAS is an optimum choice to study the effect of depositing an insulating oxide barrier on the MRG layer because of its surface sensitivity. We measured the Mn $L_{3,2}$ edges on samples consisting of MRG/Al/Al_2O_3, MRG/MgO and MRG/Mg/MgO together with the standard MRG/Al_2O_3 for comparison. The XAS spectra clearly show that the surface of some of them is now oxidised, as the spectra resemble closely the ones of Mn oxides. The degradation of interface is reflected in the XMCD spectra. They XAS spectra are plotted for comparison in Fig. 4.49. The MRG/MgO sample is clearly not suitable for MTJs, since the oxidation of the Mn atoms will completely change the magnetic properties of the MRG close to the interface, significantly affecting the spin polarisation and the TMR. The use of a dusting layer of Mg improves the interface quality but the spectra still show clear signs of Mn oxidation. The MRG/Al/Al_2O_3 sample looks promising but, as mentioned previously, the use of Al_2O_3 as a tunnel barrier is made complicated by lithography issues.

After these preliminary results, we have sputtered MRG samples on MgO substrates and capped the stacks with similar combinations of metal dusting layer/oxide and measured x-ray photoelectron spectroscopy with our Cu K_α source in order to obtain information on the oxidation state of the Mn atoms. The sample had been further capped with the standard Al_2O_3 layer for additional interface protection. Surface impurities and contaminations have been removed *in-situ* by gentle milling with an Ar ion-gun before the measurements. Unfortunately, the resolution of our laboratory system did not

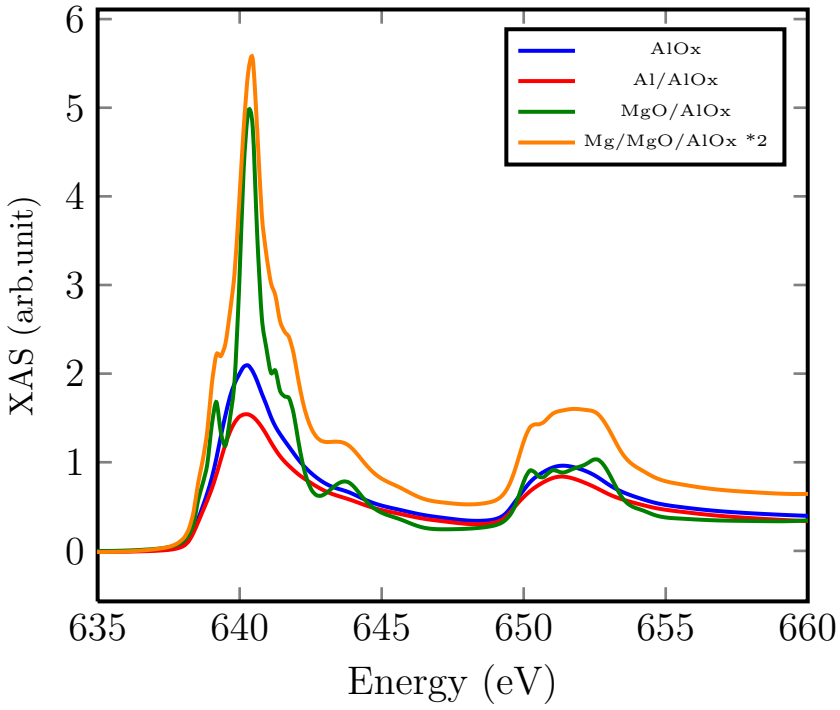

Figure 4.49: X-ray absorption spectra for samples of Mn_2Ru_xGa with different oxide capping layers. The last spectra has been rescaled for clarity. It is possible to clearly distinguish additional peaks on the $L_{3,2}$ edges that indicate the oxidation of the Mn atoms.

allow us to obtain useful information. The only sample that show a different spectra is the MRG/MgO sample, confirming that a simple MgO barrier is not compatible with MRG. The XPS spectra obtained are represented in Fig. 4.50.

Future work

As mentioned in sec. 4.3.5, we have already submitted a proposal to the SOLEIL synchrotron to measure spin-resolved XPS and UPS. The surface sensitivity of this techniques, together with the much higher energy resolution of the synchrotron facilities, will allow us to obtain more detailed information on the oxidation state of the MRG/oxide interface.

MTJ devices

We have grown MTJ stacks of Mn_2Ru_xGa on thermally oxidised Si substrates using our "Shamrock" fully automated deposition tool (Fig. 4.51). The stacks consist of CrRu (15 nm)/MRG (20 nm)/X (t nm)/MgO (4 nm)/$Co_{20}Fe_{60}B_{20}$ (1.2 nm)/Ta (0.3 nm)/$[Co(0.3\,nm)/Pd\ (0.8\,nm)]_{\times 7}$. The CrRu is used as a seed layer for the deposition of the MRG and as bottom contact. X denotes a metallic insertion layer, with X=Mg, Ru or CoFeB and $t = 0.5, 0.8$ nm the thickness of the layer. The CoFeB layer, sandwiched between MgO and Ta, shows perpendicular magnetic anisotropy (PMA). The high thickness (4 µm) of the MgO barrier has been chosen in order to avoid the formation of any pin-holes. The Co/Pd multilayer can be seen as a single magnetic layer with PMA and it is used to enhance the anisotropy of the CoFeB layer.

Since both the Co/Pd multilayer and the MRG layer show PMA, the device is a magnetic tunnel junction in which both magnetic elements have perpendicular magnetic moment. We used UV lithography,

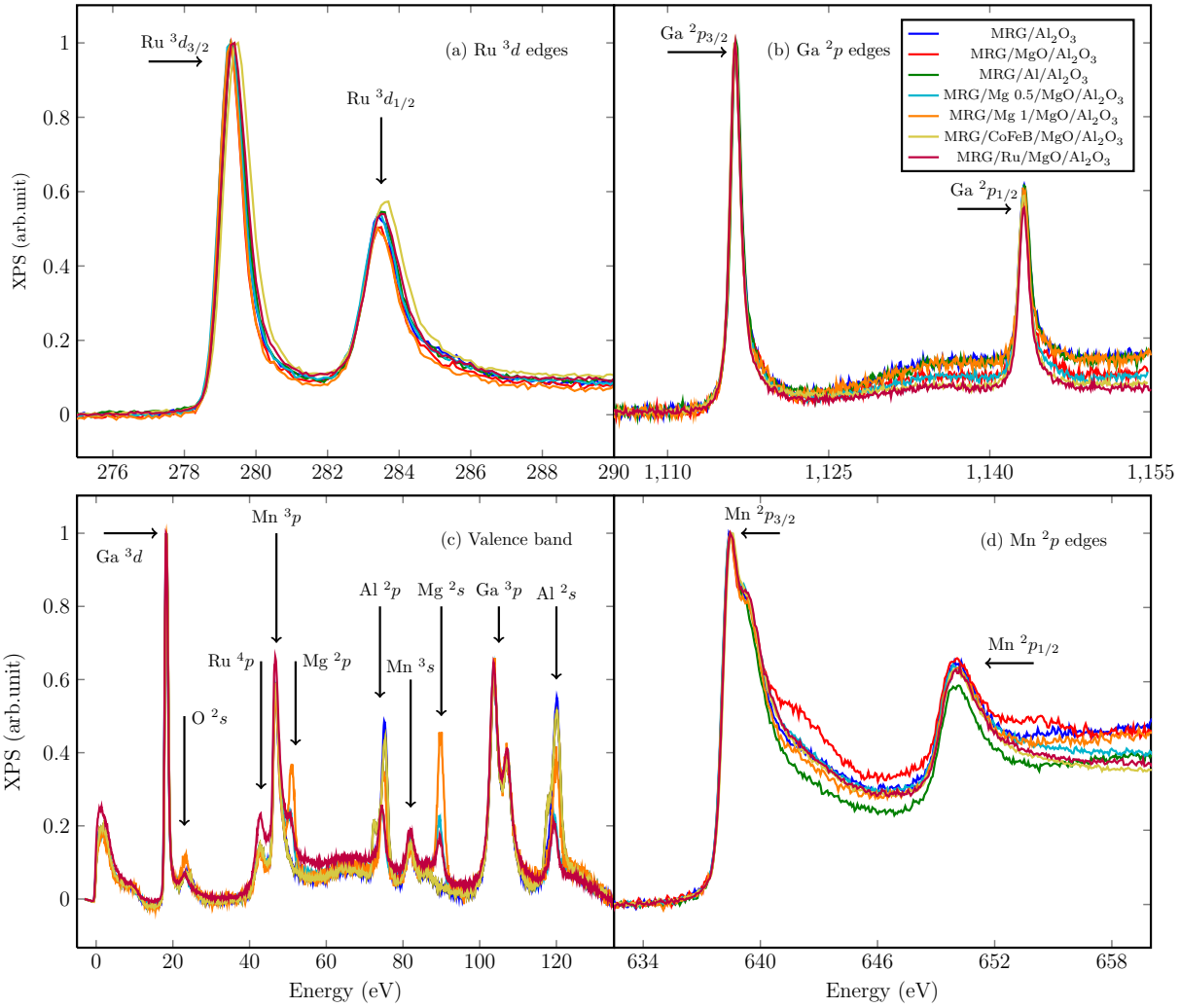

Figure 4.50: X-ray photoelectron spectra for MRG samples with different oxide capping layers. (a) Ru ^3d edges. (b) Ga ^2p edges. (c) Valence band. The double peak labelled Ga^3p consists of the $^3p_{3/2}$ and $^3p_{1/2}$ peaks. (d) Mn ^2p edges. In the last frame the effect of the Mn atoms oxidation are recognizable in the MRG/MgO/Al_2O_3 sample.

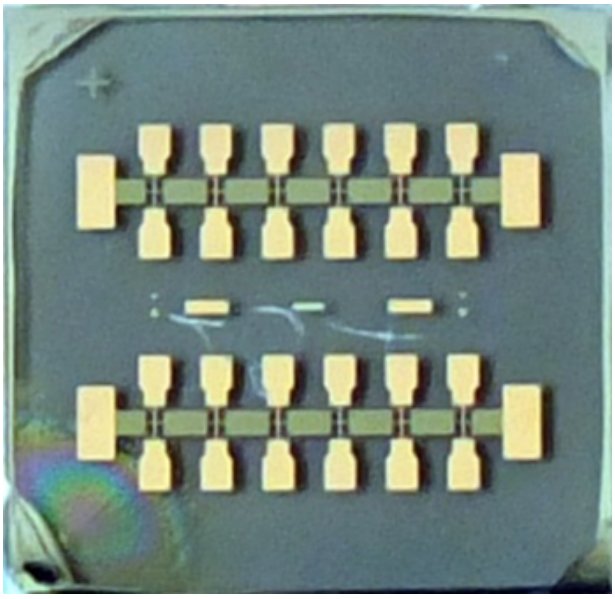

Figure 4.51: 10 mm × 10 mm sample of MRG-based MTJ stack after the patterning process. The bottom contact is in common to all the devices.

ion-milling and lift-off to pattern the samples into MTJs with nominal area of $4\times4\,\mu m^2$ and we measured the stack resistance as a function of the external perpendicular applied field. The measurements have been performed with a maximum field of 1.2 T and using a Model 6430 Keithley Sub-femtoamp Remote SourceMeter for the acquisition of the current-field curves. This has been necessary because of the high resistance of the stacks, due to the high thickness of the MgO barrier. The samples with Mg insertion showed only very small TMR ratio (1 % to 2 %) (see Fig. 4.52). The CoFeB layer acts as the free layer in this configuration and its magnetic moment switches from ↓ to ↑ and vice-versa at almost zero field. The MRG layer acts as the pinned one, switching its magnetisation accordingly to the field orientation only when it reached ∼1.1 T, at the very limits of our electromagnet.

Samples with a Ru insertion layer show no measurable TMR. This could be due to bad interface quality and/or destruction of the spin polarisation of the tunnelling electrons when travelling through the Ru layer, which possess low spin diffusion length. The CoFeB insertion has been somewhat more successful but the $R-H$ loop showed multiple magnetic switchings that indicate hybridisation of the CoFeB layer with the MRG. The loop is not easily explainable and we are not sure about its interpretation. In addition, we cannot know how the magnetic CoFeB is affecting the spin polarised tunnelling and the TMR, therefore we are not presenting this data.

We have also grown some similar MTJ stacks with Al_2O_3 as the tunnel barrier, but none of the junctions survived the patterning process: as mentioned before, NaOH and TMAH-based developers dissolve the barrier.

Conclusions

The very low TMR ratio for the MRG/Mg/MgO/CoFeB stacks, unexpected for a high spin polarised material, can be explained by the high thickness of the MgO barrier and by the limited success of the Mg insertion in suppressing the oxidation of the MRG layer, as indicated by the XAS measurements in Fig. 4.49. However, we cannot assume that the diffusion of Mn atoms into the barrier, resulting in a significant lowering of the TMR [50–52], has been completely stopped by the insertion layer. We are

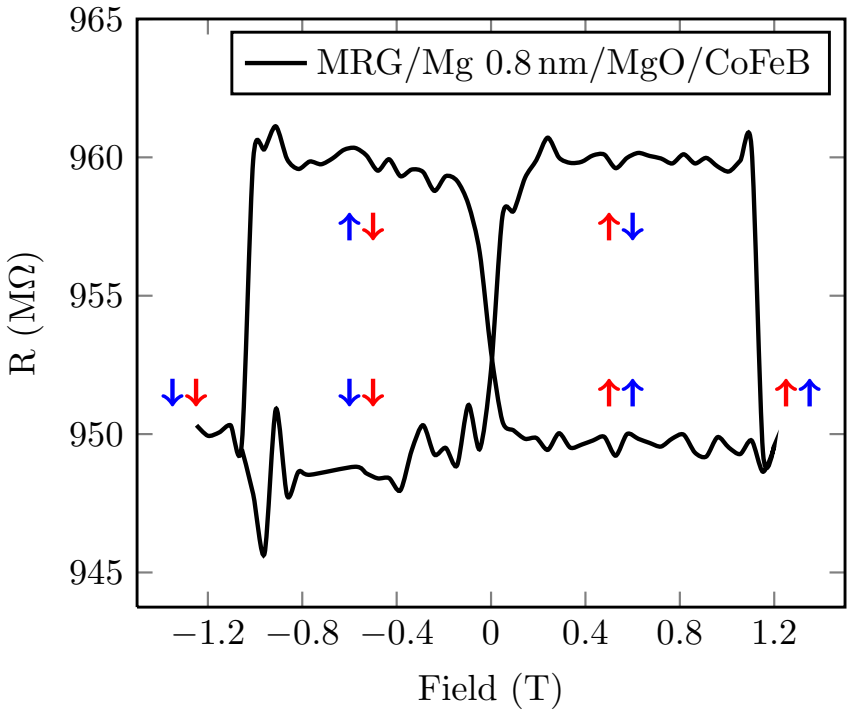

Figure 4.52: MTJ resistance as a function of the perpendicular applied field. The very high resistance of the stack make it difficult to obtain a very high signal-to-noise ratio. The arrows represent the orientation of the magnetic moment of the MRG (blue) and CoFeB (red) layers.

planning to produce MTJs with a thickness of the insulating barrier around 1 nm in order to decrease the overall electrical resistance of the stack and improve the electron tunnelling. In addition, we will test different insertion layers between the MRG and the MgO layers, such as Fe, Hf, Ti and Al.

4.4 Future work

As anticipated in sec. 4.3.7, we are investigating other possible insertion layers between the MRG and the oxide barrier in MTJ devices. We would like to employ metals such as Ti, Hf, Fe and Al and find the best configuration in order to obtain the best magnetoresistance value. In addition, we are in the process of exploring the possibilities of current-induced magnetisation switching of an MRG layer, either in a spin Hall configuration or in a MTJ nanopillar. This would be the first experimentally verified switching of an antiferromagnet with PMA and could open new scenarios in spin electronics.

In addition, we are still analysing the EXAFS data from the Ru and Mn edges and we are collaborating with the Dresden High Magnetic Field Laboratory at the Helmholtz-Zentrum in Dresden-Rossendorf (HZDR), Germany to analyse AHE and AMR with magnetic fields up to 60 T both out-of-plane and in-plane.

Regarding high frequency applications, the ferromagnetic resonance frequency is the upper limit for the switching speed in spin electronic devices such as magnetoresistive memory elements and it determines the output frequency of high-frequency generators based on STT oscillators. The current frontier for information and communication technologies is the "THz gap", as this spectral range (from 0.1 THz to 10 THz) is not easily accessible [53, 54]. Following Kittel's equation for magnetic resonance, we have $\omega_r = \mu_0\gamma\sqrt{H'_{an}(2H_{ex} + H'_{an})} \approx \mu_0\gamma\sqrt{2H'_{an}H_{ex}}$ for an antiferromagnetic sample, where $H'_{an} = 2K_u/M_{sl}$

(M_{sl} is the sublattice magnetisation) and γ is the gyromagnetic ratio. From the Curie temperature ($\sim 550\,\mathrm{K}$) and M_{sl}, we estimate the exchange field to be $\mu_0 H_{\mathrm{ex}} = 890\,\mathrm{T}$ and the sublattice anisotropy field to be approximately $\mu_0 H'_{\mathrm{an}} = 0.4\,\mathrm{T}$. Therefore the resonance frequency should be of order of 0.75 THz, putting it in the middle of the gap. We have established a collaboration with the Center for High-Power Radiation Sources at the HZDR in Dresden-Rossendorf and in particular with the Free-Electron Lasers at the ELBE (electron linear accelerator with high brilliance and low emittance) to determine the resonance frequency of the antiferromagnetically-coupled sublattices. We intend to exploit the capability of the free electron laser to produce THz radiation with high brilliance, coherence and in a large spectral range to coherently excite the resonance [55]. In addition, we have started another collaboration with the NUS Singapore University to measure time-resolved magneto-optical Kerr effect (TR-MOKE) on MRG samples. This would allow us to measure the periodic oscillations of the magnetic moments during the relaxation process after the electron had been heated above the Curie temperature. The fast demagnetising process will also give us more information on the temperature dependence of the sublattices.

As mentioned in sec. 4.3.5 and 4.3.7 we have already submitted a proposal to the SOLEIL synchrotron to measure XPS and spin-resolved UPS. This will allow us to determine the charge transfer parameters and to verify the presence of a spin gap at the Fermi level, respectively.

References

[1] R. A. de Groot, F. M. Mueller, P. G. v. Engen & K. H. J. Buschow. *New class of materials: Half-metallic ferromagnets*. Phys. Rev. Lett., **50**:2024, Jun 1983. doi:10.1103/PhysRevLett.50.2024.

[2] I. Galanakis, P. H. Dederichs & N. Papanikolaou. *Slater-Pauling behavior and origin of the half-metallicity of the full-Heusler alloys*. Phys. Rev. B, **66**:174429, Nov 2002. doi:10.1103/PhysRevB.66.174429.

[3] I. Galanakis, P. H. Dederichs & N. Papanikolaou. *Origin and properties of the gap in the half-ferromagnetic Heusler alloys*. Phys. Rev. B, **66**:134428, Oct 2002. doi:10.1103/PhysRevB.66.134428.

[4] B. Balke, G. Fecher & C. Felser. *New Heusler compounds and their properties*. In C. Felser & G. H. Fecher, eds., *Spintronics*, pp. 15–43. Springer Netherlands, 2013. ISBN 978-90-481-3831-9. doi:10.1007/978-90-481-3832-6_2.

[5] T. Graf, C. Felser & S. S. Parkin. *Simple rules for the understanding of Heusler compounds*. Progress in Solid State Chemistry, **39**(1):1 , 2011. ISSN 0079-6786. doi:http://dx.doi.org/10.1016/j.progsolidstchem.2011.02.001.

[6] T. Graf, J. Winterlik, L. Müchler, G. H. Fecher, C. Felser & S. S. Parkin. *Magnetic Heusler Compounds*. vol. 21 of *Handbook of Magnetic Materials*, chap. 1, pp. 1 – 75. Elsevier, 2013. doi:10.1016/B978-0-444-59593-5.00001-5.

[7] S. Chadov, X. Qi, J. Kübler, G. H. Fecher, C. Felser & S. C. Zhang. *Tunable multifunctional topological insulators in ternary Heusler compounds*. Nat Mater, **9**(7):541, Jul 2010. ISSN 1476-1122.

[8] H. van Leuken & R. A. de Groot. *Half-metallic antiferromagnets*. Phys. Rev. Lett., **74**:1171, Feb 1995. doi:10.1103/PhysRevLett.74.1171.

[9] H. Kurt, K. Rode, P. Stamenov, M. Venkatesan, Y.-C. Lau, E. Fonda & J. M. D. Coey. *Cubic Mn_2Ga thin films: Crossing the spin gap with ruthenium*. Phys. Rev. Lett., **112**:027201, Jan 2014. doi:10.1103/PhysRevLett.112.027201.

[10] H. Okamoto. *Phase Diagrams for Binary Alloys.* ASM International, 2010.

[11] K. Wang, A. Chinchore, W. Lin, D. C. Ingram, A. R. Smith, A. J. Hauser & F. Yang. *Epitaxial growth of ferromagnetic δ-phase manganese gallium on semiconducting scandium nitride (001).* Journal of Crystal Growth, **311**(8):2265 , 2009. ISSN 0022-0248. doi:http://dx.doi.org/10.1016/j.jcrysgro.2009.02.033.

[12] K. M. Krishnan. *Ferromagnetic δ - $Mn_{1-x}Ga_x$ thin films with perpendicular anisotropy.* Applied Physics Letters, **61**(19):2365, 1992. doi:http://dx.doi.org/10.1063/1.108245.

[13] K. Rode, N. Baadji, D. Betto, Y.-C. Lau, H. Kurt, M. Venkatesan, P. Stamenov, S. Sanvito, J. M. D. Coey, E. Fonda, E. Otero, F. Choueikani, P. Ohresser, F. Porcher & G. André. *Site-specific order and magnetism in tetragonal Mn_3Ga thin films.* Phys. Rev. B, **87**:184429, May 2013. doi:10.1103/PhysRevB.87.184429.

[14] J. J. Rehr & R. C. Albers. *Theoretical approaches to x-ray absorption fine structure.* Rev. Mod. Phys., **72**:621, Jul 2000. doi:10.1103/RevModPhys.72.621.

[15] J. J. Rehr, J. J. Kas, F. D. Vila, M. P. Prange & K. Jorissen. *Parameter-free calculations of x-ray spectra with FEFF9.* Phys. Chem. Chem. Phys., **12**:5503, 2010. doi:10.1039/B926434E.

[16] N. Yamada. *Atomic magnetic moment and exchange interaction between Mn atoms in intermetallic compounds in Mn-Ge system.* Journal of the Physical Society of Japan, **59**(1):273, 1990. doi:10.1143/JPSJ.59.273.

[17] D. Hobbs, J. Hafner & D. Spišák. *Understanding the complex metallic element Mn. I. crystalline and noncollinear magnetic structure of α-Mn.* Phys. Rev. B, **68**:014407, Jul 2003. doi:10.1103/PhysRevB.68.014407.

[18] C. Piamonteze, P. Miedema & F. M. F. de Groot. *Accuracy of the spin sum rule in XMCD for the transition-metal l edges from manganese to copper.* Phys. Rev. B, **80**:184410, Nov 2009. doi:10.1103/PhysRevB.80.184410.

[19] S. Chadov, J. Kiss & C. Felser. *Improving spin-transport by disorder.* Advanced Functional Materials, **23**(7):832, 2013. ISSN 1616-3028. doi:10.1002/adfm.201201693.

[20] P. Webster. *Magnetic and chemical order in Heusler alloys containing cobalt and manganese.* Journal of Physics and Chemistry of Solids, **32**(6):1221 , 1971. ISSN 0022-3697. doi:http://dx.doi.org/10.1016/S0022-3697(71)80180-4.

[21] A. T. Zayak, P. Entel, K. M. Rabe, W. A. Adeagbo & M. Acet. *Anomalous vibrational effects in nonmagnetic and magnetic Heusler alloys.* Phys. Rev. B, **72**:054113, Aug 2005. doi:10.1103/PhysRevB.72.054113.

[22] P. Carra, B. T. Thole, M. Altarelli & X. Wang. *X-ray circular dichroism and local magnetic fields.* Phys. Rev. Lett., **70**:694, Feb 1993. doi:10.1103/PhysRevLett.70.694.

[23] F. de Groot. *X-ray absorption and dichroism of transition metals and their compounds.* Journal of Electron Spectroscopy and Related Phenomena, **67**(4):529 , 1994. ISSN 0368-2048. doi:http://dx.doi.org/10.1016/0368-2048(93)02041-J.

[24] H. Wende. *Recent advances in x-ray absorption spectroscopy.* Reports on Progress in Physics, **67**(12):2105, 2004.

[25] G. van der Laan & A. I. Figueroa. *X-ray magnetic circular dichroism—a versatile tool to study magnetism.* Coordination Chemistry Reviews, **277–278**(0):95 , 2014. ISSN 0010-8545. doi:http://dx.doi.org/10.1016/j.ccr.2014.03.018. Following Chemical Structures using Synchrotron Radiation.

[26] S. Wurmehl, H. C. Kandpal, G. H. Fecher & C. Felser. *Valence electron rules for prediction of half-metallic compensated-ferrimagnetic behaviour of Heusler compounds with complete spin polarization.* J. of Phys.: Cond. Matter, **18**(27):6171, 2006.

[27] H. Lin, L. A. Wray, Y. Xia, S. Xu, S. Jia, R. J. Cava, A. Bansil & M. Z. Hasan. *Half-Heusler ternary compounds as new multifunctional experimental platforms for topological quantum phenomena.* Nat Mater, **9**(7):546, Jul 2010. ISSN 1476-1122. doi:10.1038/nmat2771.

[28] X. Hu. *Half-metallic antiferromagnet as a prospective material for spintronics.* Adv. Mater., **24**(2):294, 2012. ISSN 1521-4095. doi:10.1002/adma.201102555.

[29] c. Tirpanci, E. Şaşıoğlu & I. Galanakis. *Design of half-metallic Heusler-based superlattices with vanishing net magnetization.* Journal of Applied Physics, **113**(4):043912, 2013. doi:http://dx.doi.org/10.1063/1.4789361.

[30] E. Şaşıoğlu. *Nonzero macroscopic magnetization in half-metallic antiferromagnets at finite temperatures.* Phys. Rev. B, **79**:100406, Mar 2009. doi:10.1103/PhysRevB.79.100406.

[31] M. Hakimi, M. Venkatesan, K. Rode, K. Ackland & J. M. D. Coey. *The zero-magnetization Heusler ferrimagnet.* Journal of Applied Physics, **113**(17):17B101, 2013. doi:10.1063/1.4794744.

[32] N. Nagaosa. *Anomalous Hall effect –a new perspective–.* Journal of the Physical Society of Japan, **75**(4):042001, 2006. doi:10.1143/JPSJ.75.042001.

[33] N. Nagaosa, J. Sinova, S. Onoda, A. H. MacDonald & N. P. Ong. *Anomalous Hall effect.* Rev. Mod. Phys., **82**:1539, May 2010. doi:10.1103/RevModPhys.82.1539.

[34] J. W. F. Dorleijn. -. Philips Res. Rep., **31**:, 1976.

[35] T. W. Kim, S. H. Lim & R. J. Gambino. *Spontaneous Hall effect in amorphous Tb–Fe and Sm–Fe thin films.* J. of Appl.Phys., **89**(11):7212, 2001. doi:http://dx.doi.org/10.1063/1.1357117.

[36] T. Jungwirth, Q. Niu & A. H. MacDonald. *Anomalous Hall effect in ferromagnetic semiconductors.* Phys. Rev. Lett., **88**:207208, May 2002. doi:10.1103/PhysRevLett.88.207208.

[37] Y. Pu, D. Chiba, F. Matsukura, H. Ohno & J. Shi. *Mott relation for anomalous Hall and Nernst effects in* $ga_{1-x}mn_xAs$ *ferromagnetic semiconductors.* Phys. Rev. Lett., **101**:117208, Sep 2008. doi:10.1103/PhysRevLett.101.117208.

[38] I. Galanakis, K. Özdoğan, E. Şaşıoğlu & S. Blügel. *Effect of disorder on the magnetic properties of cubic* Mn_2Ru_xGa *compounds: A first-principles study.* Journal of Applied Physics, **116**(3):033903, 2014. doi:10.1063/1.4890229.

[39] C. Piamonteze, U. Flechsig, S. Rusponi, J. Dreiser, J. Heidler, M. Schmidt, R. Wetter, M. Calvi, T. Schmidt, H. Pruchova, J. Krempasky, C. Quitmann, H. Brune & F. Nolting. *X-Treme beamline at SLS: X-ray magnetic circular and linear dichroism at high field and low temperature.* Journal of Synchrotron Radiation, **19**(5):661, Sep 2012. doi:10.1107/S0909049512027847.

[40] H. A. Dürr, G. van der Laan, D. Spanke, F. U. Hillebrecht & N. B. Brookes. *Electron-correlation-induced magnetic order of ultrathin Mn films.* Phys. Rev. B, **56**:8156, Oct 1997. doi: 10.1103/PhysRevB.56.8156.

[41] R. D. Cowan. *Theory of atomic structure and spectra.* Los Alamos series in basic and applied Sciences. University of California Press, Berkely, 1981.

[42] B. Thole, G. van der Laan & P. H. Butler. *Spin-mixed ground state of Fe phthalocyanine and the temperature-dependent branching ratio in x-ray absorption spectroscopy.* Chemical Physics Letters, **149**(3):295 , 1988. ISSN 0009-2614. doi:10.1016/0009-2614(88)85029-2.

[43] E. Stavitski & F. M. de Groot. *The CTM4XAS program for EELS and XAS spectral shape analysis of transition metal L edges.* Micron, **41**(7):687 , 2010. ISSN 0968-4328. doi:http://dx.doi.org/10.1016/j.micron.2010.06.005.

[44] P. Klaer, M. Kallmayer, H. J. Elmers, L. Basit, J. Thöne, S. Chadov & C. Felser. *Localized magnetic moments in the Heusler alloy Rh_2MnGe.* Journal of Physics D: Applied Physics, **42**(8):084001, 2009.

[45] N. D. Telling, P. S. Keatley, G. van der Laan, R. J. Hicken, E. Arenholz, Y. Sakuraba, M. Oogane, Y. Ando, K. Takanashi, A. Sakuma & T. Miyazaki. *Evidence of local moment formation in Co-based Heusler alloys.* Phys. Rev. B, **78**:184438, Nov 2008. doi:10.1103/PhysRevB.78.184438.

[46] M. Meinert, J.-M. Schmalhorst, C. Klewe, G. Reiss, E. Arenholz, T. Böhnert & K. Nielsch. *Itinerant and localized magnetic moments in ferrimagnetic Mn_2CoGa thin films probed by x-ray magnetic linear dichroism: Experiment and ab initio theory.* Phys. Rev. B, **84**:132405, Oct 2011. doi:10.1103/PhysRevB.84.132405.

[47] M. Taguchi, P. Krüger, J. C. Parlebas & A. Kotani. *Theoretical study of resonant x-ray emission spectroscopy of Mn films on Ag.* Phys. Rev. B, **73**:125404, Mar 2006. doi:10.1103/PhysRevB.73.125404.

[48] L. Wollmann, S. Chadov, J. Kübler & C. Felser. *Magnetism in cubic manganese-rich Heusler compounds.* Phys. Rev. B, **90**:214420, Dec 2014. doi:10.1103/PhysRevB.90.214420.

[49] T. Hori, M. Akimitsu, H. Miki, K. Ohoyoama & Y. Yamaguchi. *Magnetic properties of $(Mn_{1-x}Ru_x)_3Ga$ alloys.* Applied Physics A, **74**(1):s737, 2002. ISSN 0947-8396. doi:10.1007/s003390101148.

[50] S. Cardoso, R. Ferreira, P. P. Freitas, P. Wei & J. C. Soares. *Influence of ta antidiffusion barriers on the thermal stability of tunnel junctions.* Applied Physics Letters, **76**(25):3792, 2000. doi:http://dx.doi.org/10.1063/1.126783.

[51] S. Cardoso, P. P. Freitas, C. de Jesus, P. Wei & J. C. Soares. *Spin-tunnel-junction thermal stability and interface interdiffusion above 300 C.* Applied Physics Letters, **76**(5):610, 2000. doi:http://dx.doi.org/10.1063/1.125833.

[52] S. Cardoso, P. P. Freitas, C. de Jesus & J. C. Soares. *High thermal stability tunnel junctions.* Journal of Applied Physics, **87**(9):6058, 2000. doi:http://dx.doi.org/10.1063/1.372611.

[53] A. H. Morrish. *The Physical Principles of Magnetism.* Wiley-IEEE Press, 2001.

[54] J. M. Chamberlain. *Where optics meets electronics: recent progress in decreasing the terahertz gap*. Philosophical Transactions of the Royal Society of London A: Mathematical, Physical and Engineering Sciences, **362**(1815):199, 2004. ISSN 1364-503X. doi:10.1098/rsta.2003.1312.

[55] Kampfrath Tobias, Sell Alexander, Klatt Gregor, Pashkin Alexej, Mahrlein Sebastian, Dekorsy Thomas, Wolf Martin, Fiebig Manfred, Leitenstorfer Alfred & Huber Rupert. *Coherent terahertz control of antiferromagnetic spin waves*. Nat Photon, **5**(1):31, Jan 2011. ISSN 1749-4885. doi: http://dx.doi.org/10.1038/nphoton.2010.259. 10.1038/nphoton.2010.259.

Chapter 5

Heavy metals, spin Hall effect and spin-orbit torques

In sec. 2.3.5, 2.3.6 and 1.1, we discussed the effects that arise from the coupling between the spin and the velocity of charged carriers. In this chapter we present a study on the efficiency of various heavy metals with high spin-orbit coupling to generating torques a magnetic moment, via spin Hall or Rashba effects. They are analysed using different methods, based on the ferromagnetic resonance or on the anomalous Hall effect of an adjacent ferromagnetic layer. These materials could be exploited in spin electronic devices to apply a torque on the magnetic moment of a ferromagnetic layer.

5.1 Literature review

The recent discovery that the magnetic moment of a single ferromagnetic (FM) layer in a device composed of the FM and of a heavy metal (HM) layer can be switched by an in-plane electric current have attracted the interest of several research groups ([1] and references within). The application of this effect in spin electronics could potentially solve the problem of having to send a high current density across an insulating barrier that bothers the spin transfer torque (STT) switching of tunnel junctions [2] (see sec. 1.1 and 1.2.2). Spin-orbit torques can lead to the switching of the magnetisation in geometries in which it was not possible with conventional STT and to unprecedented fast domain wall motion [3].

Applications of an in-plane current to systems with large spin-orbit coupling or at interfaces with breaking of inversion symmetry result in spin current generation and/or spin accumulation via the spin Hall effect [4–7] (sec. 2.3.6) or the Rashba effect [8–10] (sec. 2.3.5), respectively. Magnetisation switching induced by these mechanisms has been investigated in HM/FM heterostructures. The benchmark HM for this kind of experiment is Pt, which is relatively easy to investigate because of its resistance to oxidation, its high conductivity and its transparent interface resistance with respect to spin currents when adjacent to the majority of FMs. The current techniques employed aim to determine the ratio between the spin current and the injected charge current (the spin Hall angle θ_{SH}) in the HM, or directly the effective fields that apply a torque on the magnetisation of the FM layer. However, the evaluated parameters using different techniques vary, in some cases, by orders of magnitude. This disparity, due to differences in the preparation and measurement methods, prevents a deeper understanding of spin-orbit torques and makes it difficult to optimize their values for specific HM/FM combinations. Possible explanations of these discrepancies are different quality of the thin films in terms of crystallinity and roughness, especially at the interfaces, unreliable estimation of the spin-diffusion length or the overlooking of contributions

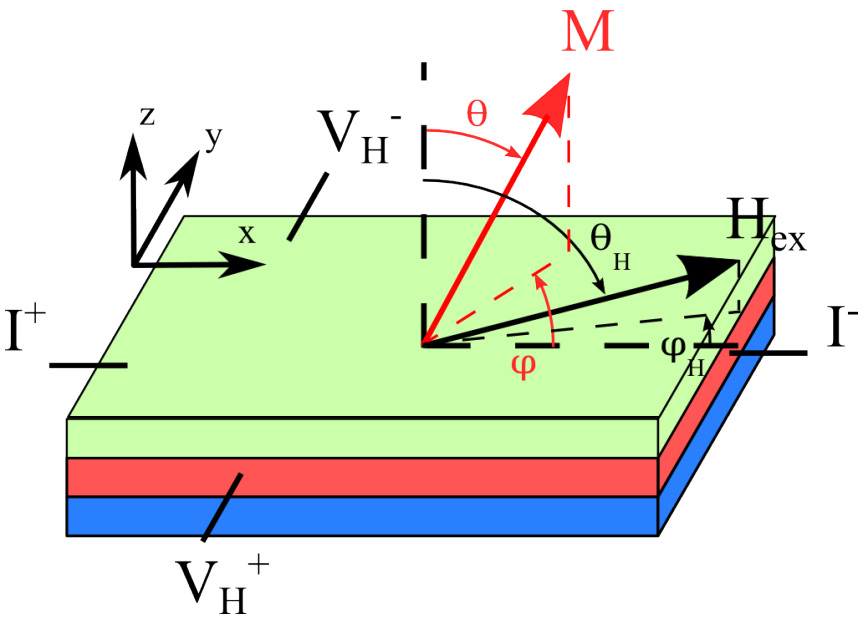

Figure 5.1: Schematic illustration of the sample and measurement geometry. A Hall bar is patterned from a stack of thin films consisting in a HM layer (blue), a FM layer (red) and an insulating oxide (green). The coordinate system uses spherical coordinates. $\vec{M}$ is the magnetisation vector and $\vec{H}_{\text{ex}}$ is the external applied field.

coming from other effects, such as the presence of field-like torques or phase shifts in rf fields.

The total current-induced spin-orbit effective field is decomposed into its longitudinal component (parallel to the injected current direction) and its transverse component (perpendicular to the injected current). They are often referred as anti-damping and field-like components. In first approximation, if we consider a perfectly transparent HM/FM interface, the imaginary part of the spin-mixing conductance is negligible (see sec. 2.3.7). In this case, the longitudinal field is due only to the spin Hall effect, while the transverse field is only due to the Rashba effect. The different sign of the fields evaluated for Ta and Pt, which have opposite sign of spin-orbit coupling, seems to endorse this picture. In real systems, the imaginary part may not be negligible and it is indeed dependent on the quality of the interface and on the HM/FM combination [11]. The result is that the two mechanisms are both playing a part in the generation of both components of the effective field (see sec. 2.3.7). In first approximation, considering the coordinate system represented in Fig. 5.1 where the charge current flows in the $\hat{x}$ direction, the polarisation of the spin current originating from the spin Hall effect is pointing in the $\hat{y}$ direction, the same direction in which the Rashba effective field is applied. Therefore, the direction of the torques is

$$\begin{aligned} \vec{\tau}_{\parallel} &\propto \vec{m} \times (\hat{y} \times \vec{m}) \ , \\ \vec{\tau}_{\perp} &\propto \vec{m} \times \hat{y} \ , \end{aligned} \tag{5.1}$$

for the anti-damping one (also called adiabatic or Slonczewski torque $\tau_{\parallel}$) and for the field-like one (also called non-adiabatic $\tau_{\perp}$), respectively. Since in general $\tau \propto \vec{m} \times \vec{H}_{\text{eff}}$, the definition of the two effective fields directly follows from 5.1

$$\begin{aligned} \mu_0 \vec{H}_{\parallel} &\propto \hat{y} \times \vec{m} \ , \\ \mu_0 \vec{H}_{\perp} &\propto \hat{y} \ . \end{aligned} \tag{5.2}$$

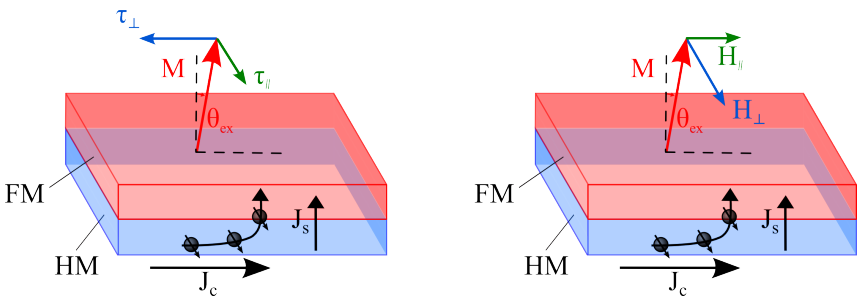

Figure 5.2: Schematic of a non magnetic heavy metal/ferromagnetic metals bilayer with out-of-plane magnetisation. On the left, $\tau_\perp$ and $\tau_\parallel$ are shown. Equivalently, the effective fields $H_\perp$ and $H_\parallel$ are displayed on the right.

Both torques and effective fields are represented in Fig. 5.2.

We studied the spin-orbit torques originating at the HM/FM interfaces using four different techniques, each of them presented in the following sections. They are based on ferromagnetic resonance (FMR) of the FM magnetic moment or on the detection of the anomalous Hall voltage [12, 13], both with dc and low frequency lock-in techniques. The anomalous Hall voltage measurements can be used to evaluate the current-induced spin-orbit effective fields acting on the magnetisation of a FM layer, while the FMR techniques are used to determine the spin Hall angle θ_{SH}.

5.2 Alternating current Hall technique

The ac Hall technique relies on the measurement of the anomalous Hall voltage arising in perpendicularly magnetised samples. We inject an ac current at low frequency (∼1 kHz) while we simultaneously detect the in-phase first harmonic and out-of-phase second harmonic signals using lock-in amplifiers [1, 14–18].

5.2.1 Theory

In this section and in the following we are going to follow the treatment of Hayashi *et. a.* (ref [17]). Considering the coordinate system of Fig. 5.1, the magnetic moment is expressed by

$$\vec{M} = M_{\mathrm{s}}\vec{m} = M_{\mathrm{s}}\left(\sin\theta\cos\varphi, \sin\theta\sin\varphi, \cos\theta\right) \ , \tag{5.3}$$

where M_{s} is the saturation magnetisation and $\vec{m}$ is the unit vector representing its direction. In the same way, the external applied magnetic field is given by

$$\vec{H}_{\mathrm{ex}} = H\left(\sin\theta_H\cos\varphi_H, \sin\theta_H\sin\varphi_H, \cos\theta_H\right) \ . \tag{5.4}$$

When an ac current is injected in the HM/FM bilayer, the spin-orbit effective fields and the Ørsted field can modify the position of the magnetisation vector with respect to its equilibrium value (θ_0, φ_0). The total magnetic energy of the system is given by

$$E = -K_{\mathrm{eff}}\cos^2\theta - K_{\mathrm{i}}\sin^2\theta\sin^2\varphi - \vec{M}\cdot\vec{H}_{\mathrm{ex}} \ , \tag{5.5}$$

where K_{eff} is the effective out-of-plane anisotropy energy

$$K_{\text{eff}} = K_{\text{u}} - \frac{1}{2}(N_z - N_x)M_{\text{s}}^2 \ , \tag{5.6}$$

where K_{u} is the uniaxial anisotropy constant and $\overline{\overline{N}}$ is the shape anisotropy tensor defined in sec. 2.2.1. Similarly, K_{i} is the in-plane shape anisotropy constant given by

$$K_{\text{i}} = \frac{1}{2}(N_x - N_y)M_{\text{s}}^2 \ . \tag{5.7}$$

Equivalently, we can define the out-of-plane and in-plane anisotropy fields

$$H_{\text{k}} = \frac{2K_{\text{eff}}}{M_{\text{s}}} \quad \text{and} \quad H_{\text{a}} = \frac{2K_{\text{i}}}{M_{\text{s}}} \ , \tag{5.8}$$

respectively. The equilibrium position of the magnetic moment is denoted by the coordinates (θ_0, φ_0) and it is determined by the minimisation of the total energy with respect to changes in θ and φ. This leads to the equations [17]

$$\begin{aligned}
&\frac{\partial E}{\partial \theta} = (K_{\text{eff}} - K_{\text{i}} \sin^2 \varphi_0) \sin\theta_0 - M_{\text{s}} H [\cos\theta_0 \sin\theta_H (\cos\varphi_0 \cos\varphi_H + \sin\varphi_0 \sin\varphi_H) - \sin\theta_0 \cos\theta_H] = 0 \quad \text{and} \\
&\frac{\partial E}{\partial \varphi} = -K_{\text{i}} \sin^2\theta_0 \sin 2\varphi_0 - M_{\text{s}} H \sin\theta_0 \sin\theta_H \sin(\varphi_H - \varphi_0) = 0 \ .
\end{aligned} \tag{5.9}$$

Note that we represent H_{ex} as H to simplify the notation. For small variation of the coordinates of the magnetic moment vector from the equilibrium position, the amplitudes of the oscillations $\Delta\theta$ and $\Delta\varphi$ resulting from the ac current can be expressed as a Taylor series with respect to the induced effective field $\Delta\vec{H}$

$$\begin{aligned}
\Delta\theta &= \sum_{i=\hat{x},\hat{y},\hat{z}} \frac{\partial\theta}{\partial H_i} \Delta H_i \ , \\
\Delta\varphi &= \sum_{i=\hat{x},\hat{y},\hat{z}} \frac{\partial\varphi}{\partial H_i} \Delta H_i \ .
\end{aligned} \tag{5.10}$$

From eq. 5.9 it results

$$\begin{aligned}
\frac{\partial}{\partial H_i}\left(\frac{\partial E}{\partial \theta}\right) &= \big[(K_{\text{eff}} - K_{\text{i}} \sin^2\varphi_0) 2\cos 2\theta_0 \\
&\quad - M_{\text{s}}(-H_x \sin\theta_0 \cos\varphi_0 - H_y \sin\theta_0 \sin\varphi_0 - H_z \cos\theta_0)\big] \frac{\partial\theta}{\partial H_i} \\
&\quad + \big[- K_{\text{i}} \sin 2\theta_0 \sin 2\varphi_0 - M_{\text{s}} \cos\theta_0 (-H_x \sin\varphi_0 + H_y \cos\varphi_0)\big] \frac{\partial\varphi}{\partial H_i} - M_{\text{s}} f_i = 0 \ , \\
\frac{\partial}{\partial H_i}\left(\frac{\partial E}{\partial \varphi}\right) &= \big[- K_{\text{i}} \cos\theta_0 \sin 2\varphi_0 + M_{\text{s}} \cos\theta_0 (H_x \sin\varphi_0 - H_y \cos\varphi_0)\big] \frac{\partial\theta}{\partial H_i} \\
&\quad + \big[- 2K_{\text{i}} \sin\theta_0 \cos 2\varphi_0 + M_{\text{s}} \sin\theta_0 (H_x \cos\varphi_0 + H_y \sin\varphi_0)\big] \frac{\partial\varphi}{\partial H_i} + M_{\text{s}} g_i = 0 \ ,
\end{aligned} \tag{5.11}$$

where

$$\begin{aligned}
&\vec{f} = (\cos\theta_0 \cos\varphi_0, \cos\theta_0 \sin\varphi_0, -\sin\theta_0) \quad \text{and} \\
&\vec{g} = (\sin\theta_0 \sin\varphi_0, -\sin\theta_0 \cos\varphi_0, 0) \ .
\end{aligned} \tag{5.12}$$

These coupled equations can be solved in order to obtain a general expression for the oscillations amplitudes but the solution is quite complex and does not have a closed formulation. Fortunately, it is possible to simplify the expressions by neglecting the in-plane anisotropy constant, considering that in the actual samples we have $|H_\mathrm{a}| \ll |H_\mathrm{ex} \sin\theta_H|$. This approximation is almost always valid for micrometric samples (such as those studied in this work), while one must verify its validity for high aspect ratio nanowires. The condition $|H_\mathrm{a}| \ll |H_\mathrm{ex} \sin\theta_H|$ results in $\varphi_0 = \varphi_H$. In addition, we consider the external field $\vec{H}$ to be applied close to one of the in-plane coordinate axis $\hat{x}$ or $\hat{y}$. With these simplifications, eq. 5.11 reduces to

$$\begin{aligned}\Delta\theta &= \frac{\cos\theta_0(\Delta H_x \cos\varphi_H + \Delta H_y \sin\varphi_H) - \sin\theta_0 \Delta H_z}{(H_\mathrm{k} - H_\mathrm{a}\sin^2\varphi_H)\cos 2\theta_0 + H\cos(\theta_H - \theta_0)} \ , \\ \Delta\varphi &= \frac{-\Delta H_x \sin\varphi_H + \Delta H_y \cos\varphi_H}{-H_\mathrm{a}\sin\theta_0\cos^2\varphi_H + H\sin\theta_H} \ . \end{aligned} \tag{5.13}$$

As discussed in sec. 2.3.7 and sec. 5.1, the longitudinal (anti-damping) effective field originates mainly from the spin Hall effect of the NM layer and is oriented in the $\hat{y}\times\vec{m}$ direction. The transverse (field-like) effective field arises mainly from the Rashba effect at the interface and is oriented in the $\hat{y}$ direction. Therefore, from eq. 5.2 we have

$$\vec{H}_\parallel = H_\parallel \hat{y}\times\vec{m} = H_\parallel \begin{pmatrix} \cos\theta \\ 0 \\ -\sin\theta\cos\varphi \end{pmatrix} \ , \tag{5.14}$$

and

$$\vec{H}_\perp = H_\perp \hat{y} = H_\perp \begin{pmatrix} 0 \\ 1 \\ 0 \end{pmatrix} \ . \tag{5.15}$$

By inserting these expressions in eq. 5.13 we get, for the longitudinal configuration ($\varphi_0 = 0$)

$$\begin{aligned}\Delta\theta &= \frac{\cos\theta_0 \Delta H_x - \Delta H_z \sin\theta_0}{H_\mathrm{k}\cos(2\theta_0) + H\cos(\theta_H - \theta_0)} = \frac{\cos^2(\theta_0)H_\parallel + \sin^2(\theta_0)H_\parallel}{H_\mathrm{k}\cos(2\theta_0) + H\cos(\theta_H - \theta_0)} \\ &= \frac{H_\parallel}{H_\mathrm{k}\cos(2\theta_0) + H\cos(\theta_H - \theta_0)} \quad \text{and} \\ \Delta\varphi &= \frac{\Delta H_y}{-H_\mathrm{a}\sin\theta_0 + H\sin\theta_H} = \frac{H_\perp}{-H_\mathrm{a}\sin\theta_0 + H\sin\theta_H} \ , \end{aligned} \tag{5.16}$$

while, for the transverse configuration ($\varphi = \pi/2$)

$$\begin{aligned}\Delta\theta &= \frac{\cos\theta_0 \Delta H_y - \Delta H_z \sin\theta_0}{H_\mathrm{k}\cos 2\theta_0 + H\cos(\theta_H - \theta_0)} = \frac{\cos\theta_0 H_\perp}{H_\mathrm{k}\cos 2\theta_0 + H\cos(\theta_H - \theta_0)} \quad \text{and} \\ \Delta\varphi &= -\frac{\Delta H_x}{H_\mathrm{a}\sin\theta_0 + H\sin\theta_H} = -\frac{\cos\theta_0 H_\parallel}{H_\mathrm{a}\sin\theta_0 + H\sin\theta_H} \ . \end{aligned} \tag{5.17}$$

The Hall voltage V_H is given by the sum of the anomalous Hall effect (AHE) and planar Hall effect (PHE) [19] contributions

$$V_\mathrm{H} = V_\mathrm{AHE} + V_\mathrm{PHE} = I_\mathrm{ac}\sin(\omega t) R_{xy} \ , \tag{5.18}$$

with

$$R_{xy} = \frac{1}{2}R_\mathrm{AHE}\cos[\theta_0 + \Delta\theta\sin(\omega t)] + \frac{1}{2}R_\mathrm{PHE}\sin^2[\theta_0 + \Delta\theta\sin(\omega t)]\sin[2\varphi + 2\Delta\varphi\sin(\omega t)] \ . \tag{5.19}$$

By using the first order Taylor expansion $\cos[\theta_0 + \Delta\theta \sin(\omega t)] \approx \cos\theta_0 - \sin\theta_0 \Delta\theta \sin(\omega t)$, it possible to express the AHE contribution in the form

$$\begin{aligned} V_{\mathrm{AHE}} &= \frac{1}{2} I_{\mathrm{ac}} \sin(\omega t) R_{\mathrm{AHE}} \cos[\theta_0 + \Delta\theta \sin(\omega t)] \\ &= \frac{1}{2} I_{\mathrm{ac}} \sin(\omega t) R_{\mathrm{AHE}} \cos\theta_0 - \frac{1}{2} I_{\mathrm{ac}} R_{\mathrm{AHE}} \sin\theta_0 \Delta\theta \sin^2(\omega t) \\ &= \frac{1}{2} I_{\mathrm{ac}} \sin(\omega t) R_{\mathrm{AHE}} \cos\theta_0 - \frac{1}{4} I_{\mathrm{ac}} R_{\mathrm{AHE}} \sin\theta_0 \Delta\theta + \frac{1}{4} I_{\mathrm{ac}} R_{\mathrm{AHE}} \sin\theta_0 \Delta\theta \cos(2\omega t) \ , \end{aligned} \tag{5.20}$$

where we used the equality $\sin^2(x) = 1/2[1 - \cos(x)]$. Therefore, the Hall voltage contains a dc signal, a first harmonic signal in phase with the injected current and a second harmonic signal 90° out of phase with respect to the current. We can determine the contribution arising from the PHE in the same way. Using the expansions around θ_0, $\sin^2[\theta_0 + \Delta\theta \sin(\omega t)] \approx \sin^2\theta_0 + \Delta\theta \sin(2\theta_0)\sin(\omega t)$ and $\sin[2\varphi_0 + 2\Delta\varphi \sin(\omega t)] \approx \sin(2\varphi_0) + 2\Delta\varphi \cos(2\varphi_0)\sin(\omega t)$ and considering only first order terms in $\Delta\theta$ and $\Delta\varphi$ we obtain

$$\begin{aligned} V_{\mathrm{PHE}} &= \frac{1}{2} I_{\mathrm{ac}} \sin(\omega t) R_{\mathrm{PHE}} \sin^2[\theta_0 + \Delta\theta \sin(\omega t)] \sin[2\varphi_0 + 2\Delta\varphi \sin(\omega t)] \\ &= \frac{1}{2} I_{\mathrm{ac}} \sin(\omega t) R_{\mathrm{PHE}} \sin^2\theta_0 \sin(2\varphi_0) + \frac{1}{2} I_{\mathrm{ac}} \sin(\omega t) R_{\mathrm{PHE}} \sin^2\theta_0 2\Delta\varphi \cos(2\varphi_0) \sin(\omega t) \\ &\quad + \frac{1}{2} I_{\mathrm{ac}} \sin(\omega t) R_{\mathrm{PHE}} \Delta\theta \sin(2\theta_0) \sin(2\varphi_0) \sin(\omega t) \\ &= \frac{1}{2} I_{\mathrm{ac}} R_{\mathrm{PHE}} \sin^2\theta_0 \sin(2\varphi_0) \sin(\omega t) + \frac{1}{2} I_{\mathrm{ac}} R_{\mathrm{PHE}} \sin^2\theta_0 \cos(2\varphi_0) \Delta\varphi \\ &\quad - \frac{1}{2} I_{\mathrm{ac}} R_{\mathrm{PHE}} \sin^2\theta_0 \cos(2\varphi_0) \Delta\varphi \cos(2\omega t) + \frac{1}{4} I_{\mathrm{ac}} R_{\mathrm{PHE}} \Delta\theta \sin(2\theta_0) \sin(2\varphi_0) \\ &\quad - \frac{1}{4} I_{\mathrm{ac}} R_{\mathrm{PHE}} \Delta\theta \sin(2\theta_0) \sin(2\varphi_0) \cos(2\omega t) \ . \end{aligned} \tag{5.21}$$

In the case of applied field being almost parallel to the current direction ($\varphi_0 = 0$, longitudinal configuration), we obtain

$$V_{\mathrm{PHE}}|_{\varphi_0=0} = \tfrac{1}{2} I_{\mathrm{ac}} R_{\mathrm{PHE}} \sin^2\theta_0 \Delta\varphi - \tfrac{1}{2} I_{\mathrm{ac}} R_{\mathrm{PHE}} \sin^2\theta_0 \Delta\varphi \cos(2\omega t) \ . \tag{5.22}$$

On the other hand, in the case of an applied field almost perpendicular to the current direction ($\varphi_0 = \pi/2$, transverse configuration), the result is

$$V_{\mathrm{PHE}}|_{\varphi_0=\pi/2} = -\tfrac{1}{2} I_{\mathrm{ac}} R_{\mathrm{PHE}} \sin^2\theta_0 \Delta\varphi + \tfrac{1}{2} I_{\mathrm{ac}} R_{\mathrm{PHE}} \sin^2\theta_0 \Delta\varphi \cos(2\omega t) \ . \tag{5.23}$$

The PHE contributes to a dc, a first harmonic and a second harmonic out of phase Hall voltage. The first harmonic component vanishes in both longitudinal and transverse configurations.

By substituting eq. 5.16 and 5.17 into eq. 5.20, 5.22 and 5.23 it is possible to find an expression for the effective fields $\Delta H_{\parallel}$ and $\Delta H_{\perp}$ as a function of the second harmonic Hall voltage.

5.2.2 Low field measurements: theory

Following again ref. [17], we consider a system with perpendicular magnetic anisotropy and in-plane anisotropy field $|H_{\mathrm{a}}| \ll |H \sin\theta_H|$. If we apply only a small in-plane external field, the equilibrium position of the magnetic moment does not deviate much from the $\hat{z}$ axis, *i.e.*, $\theta_0 = \theta_0'$ for $\vec{M}$ along $+\hat{z}$ and $\theta_0 = \pi - \theta_0'$ for $\vec{M}$ along $-\hat{z}$. Keeping only linear terms in eq. 5.9 we obtain the equation for the small

deviations from the perpendicular direction as

$$\theta_0' = \frac{H\sin\theta_H}{(H_\mathrm{k} - H_\mathrm{a}\sin^2\varphi_H) \pm H\cos\theta_H} \quad \text{and}$$
$$\varphi_0 = \varphi_H \ , \tag{5.24}$$

where the $\pm$ sign corresponds to $\vec{M}$ pointing in the $\pm\hat{z}$ direction.

Substituting eq. 5.24 into eq. 5.20 and 5.21, we obtain the amplitudes of the first and second harmonic components of the Hall voltage, V_ω and $V_{2\omega}$ respectively, as

$$V_\omega \approx \pm\frac{1}{2}R_\mathrm{AHE}I_\mathrm{ac}\left[1 - \frac{1}{2}\left(\frac{H\sin\theta_H}{H_\mathrm{k} \pm H\cos\theta_H}\right)^2\right] \ , \tag{5.25}$$

and

$$V_{2\omega} \approx -\frac{1}{4}I_\mathrm{ac}\big[\mp R_\mathrm{AHE}\left(\Delta H_x\cos\varphi_H + \Delta H_y\sin\varphi_H\right) + 2R_\mathrm{PHE}(-\Delta H_x\sin\varphi_H + \Delta H_y\cos\varphi_H)\cos(2\varphi_H)\big]\frac{H\sin\theta_H}{(H_\mathrm{k} \pm H\cos\theta_H)^2} \ . \tag{5.26}$$

These equations have been obtained using the approximations of $|H_\mathrm{a}| \ll |H\sin\theta_H|$ and $|H_\mathrm{a}| \ll |H_\mathrm{k}|$ and considering only the longitudinal and transverse configurations, *i.e.*, $\varphi_H = 0$ or $\varphi_H = \pi/2$ respectively. If the planar Hall effect was not present or negligibly small, the effective fields ΔH_x and ΔH_y could be determined separately by measuring $V_{2\omega}$ as a function of an external applied field in the $\hat{x}$ and $\hat{y}$ directions, respectively. However, the presence of the PHE mixes the contributions from the two fields in the different configurations. Therefore, in this case it is necessary to measure the Hall voltage in both configurations and derive each component from the coupled equations. In order to eliminate any dependencies on I_ac and H_k, we take the ratio between the slope and the curvature of the second and first harmonic signals, respectively. Since the external field is applied in the plane, we further substitute $\theta_H = \pi/2$ in eq. 5.25 and 5.26 to obtain the ratio ζ

$$\zeta = \left(\frac{\partial V_{2\omega}}{\partial H}\Big/\frac{\partial^2 V_\omega}{\partial H^2}\right) = -\frac{1}{2}\big[\left(\Delta H_x \mp 2\xi\cos(2\varphi_H)\Delta H_y\right)\cos\varphi_H + \left(\Delta H_y \pm 2\xi\cos(2\varphi_H)\Delta H_x\right)\sin\varphi_H\big] \ , \tag{5.27}$$

where $\xi = R_\mathrm{PHE}/R_\mathrm{AHE}$.

Defining the ratio in the longitudinal and transverse configurations as $\zeta_\parallel$ and $\zeta_\perp$ we finally have

$$\Delta H_x = -2\frac{\zeta_\parallel \pm 2\xi\zeta_\perp}{1-4\xi^2} \quad \text{and}$$
$$\Delta H_y = -2\frac{\zeta_\perp \pm 2\xi\zeta_\parallel}{1-4\xi^2} \ . \tag{5.28}$$

Using eq. 5.13 it is then possible to find that $\Delta H_x \simeq H_\parallel$ and $\Delta H_y \simeq H_\perp$ in both configurations.

Assuming that the spin Hall effect is the only contribution to the longitudinal field and that there are no other effects due to the spin Hall, it is possible to estimate the spin Hall angle of the HM material using the equation

$$\mu_0 H_\parallel = \frac{\hbar\theta_\mathrm{SH}J_\mathrm{c}}{2eM_\mathrm{s}t_\mathrm{FM}} \ . \tag{5.29}$$

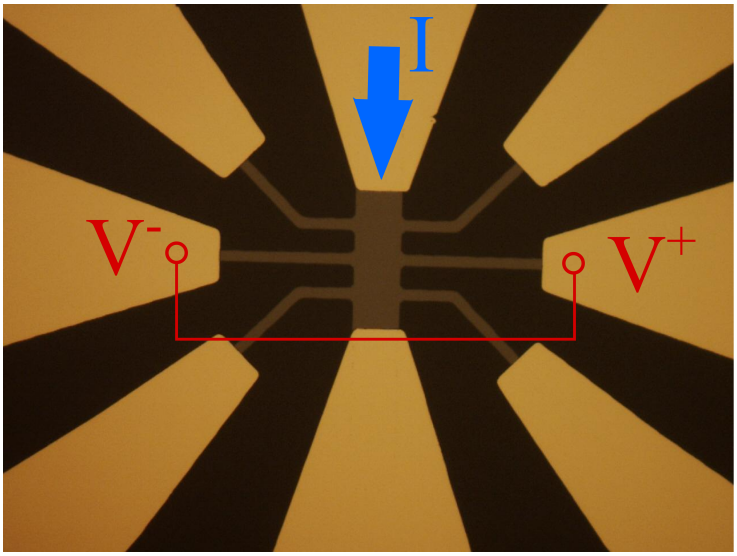

Figure 5.3: A patterned Hall bar used for spin-orbit torques measurements.

5.2.3 Samples

Our samples consist of thin films stacks of the form: Pt(5)/Hf(0.3)/$Co_{20}Fe_{60}B_{20}$(0.9)/MgO(1.6)/Ta(1), W(4)/$Co_{20}Fe_{60}B_{20}$(0.9)/MgO(1.6)/Ta(1) and Ta(4)/$Co_{20}Fe_{60}B_{20}$(0.9)/MgO(1.6)/Ta(1) (nominal thickness in nm) grown by high vacuum dc and rf sputtering on thermally oxidised Si substrates or crystalline MgO (001). The resistivity of each layer has been characterised and the value for W (between 100 and 300 µΩ cm) is consistent with the metastable β phase (A_{15} cubic). This phase is obtained due to the non-equilibrium growth condition. The sputtering process, together with the use of Si/SiO_2 substrates, stabilises the β phase in thin-films. Usually, W is present in the stable α phase, which has body-centered cubic (BCC) crystal structure and one third of the electrical resistivity (less than 25 µΩ cm) of the β phase [20]. We have also grown samples with α-W on MgO(001) substrates by sputtering at high temperature, but these samples do not show PMA even after annealing. Therefore, we have not been able to perform the harmonic Hall measurements in those samples. In the case of Ta-based samples, we grew both the α and the β or amorphous phase of Ta [21, 22]. The α phase is the most stable one and shows body-centered cubic lattice and low electrical resistivity ($15 - 60$ µΩ cm), while the β phase is metastable and has a tetragonal crystal lattice. As with the β-W phase, β-Ta has ~3.5 times ($160 - 210$ µΩ cm) the resistivity of the α phase and it is obtained in non-equilibrium deposition conditions. In order to stabilise the desired phase, the α-Ta samples were grown at high temperature (300 °C). While both W and Ta promoted PMA in the CoFeB layer, a dusting layer of Hf was deposited for the Pt-based samples to obtain PMA of the CoFeB layer on top [23]. Because of the very small thickness of the Hf with respect to its spin diffusion length, we don't expect it to produce any significant effect on the measurements, as shown by similar experiments [24] in which a Cu spacer is inserted between Pt and the magnetic layer. The topmost Ta layer completely oxidises in atmosphere and is used only to protect the MgO layer.

The films are patterned into Hall bars with dimensions $60 \times 20\,\mu m^2$ by UV lithography and Ar ion milling (see Fig. 5.3). Cu/Au contacts are deposited by e-beam evaporation and lift-off technique. Gentle Ar ion etching is carried out *in situ* prior to the deposition of the contact pads to remove the top MgO/TaOx layers and improve the interface resistance. In order to obtain PMA, the W samples are annealed in vacuum at 250 °C for 1 h under a perpendicular field of 0.8 T. Thermal annealing under similar conditions for the Pt samples results in a degradation of the PMA. The β-Ta samples also show

Table 5.1: List of samples measured with harmonic Hall measurements

Sample[a]	HM Phase	Annealed	Substrate
Pt(5)/Hf(0.3)/$Co_{20}Fe_{60}B_{20}$(0.9)/MgO(1.6)/Ta(1)	Amorphous	X	Si/SiO_2
W(4)/$Co_{20}Fe_{60}B_{20}$(0.9)/MgO(1.6)/Ta(1)	β	✓	Si/SiO_2
Ta(4)/$Co_{20}Fe_{60}B_{20}$(0.9)/MgO(1.6)/Ta(1)	β	X	Si/SiO_2
Ta(4)/$Co_{20}Fe_{60}B_{20}$(0.9)/MgO(1.6)/Ta(1)	β	✓	Si/SiO_2
Ta(4)/$Co_{20}Fe_{60}B_{20}$(0.9)/MgO(1.6)/Ta(1)	α	✓	MgO(001)

[a]Thickness in nm

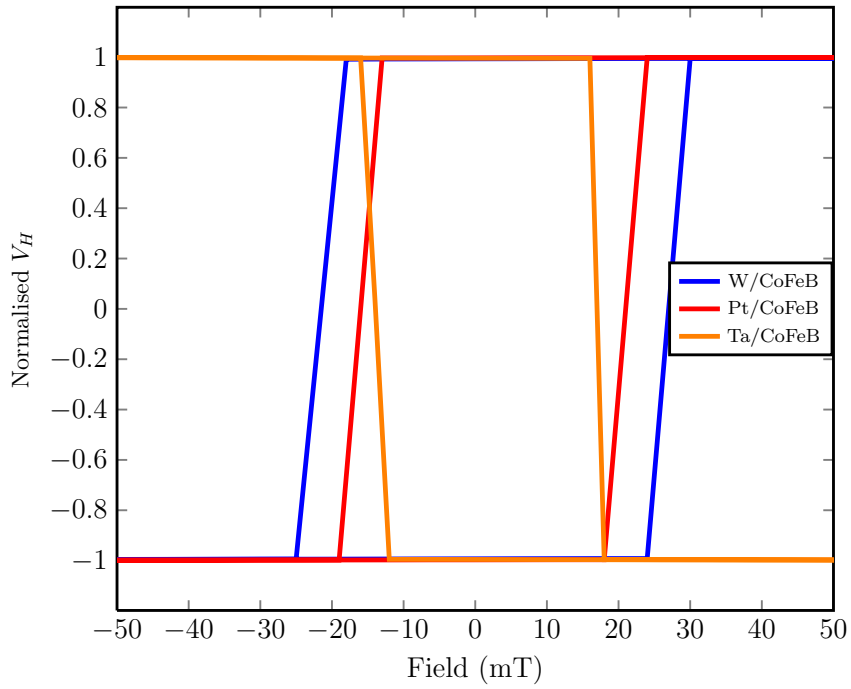

Figure 5.4: Normalised anomalous Hall signal as a function of a perpendicular applied field for W/CoFeB/MgO, Pt/CoFeB/MgO and β-Ta/CoFeB/MgO samples. The complete remanence indicates the presence of PMA.

PMA without the need for annealing, while the α-Ta samples also needed to be annealed under the same conditions. We also annealed some of the β-Ta samples at low temperature (250 °C) for 1 h in order to investigate the impact on the spin-orbit torques. The crystalline phase did not change after the annealing, since the temperature was not high enough to allow for the re-crystallisation of the material. The re-crystallisation requires 700-750 °C. All the annealing have been performed *ex situ*. A list of the samples studied is reported in Tab. 5.1.

5.2.4 Low field measurements: results

The experiments described in this section have been done in collaboration with YongChang Lau.

For the low-field harmonic Hall measurement, the sample is mounted on a rotatable holder in the gap of an electromagnet. A sinusoidal current I_{ac} is injected into the Hall bars along the $\hat{x}$ direction at a frequency of 1.234 kHz and the first (V_ω) and second harmonic ($V_{2\omega}$) signals are measured simultaneously by two lock-in amplifiers. The injected current densities have been calculated using a simple parallel

resistors model, using the measured resistivities and dimensions of the two metallic layers. The maximum current densities are $4.2 \times 10^{10}\,\mathrm{A\,m^{-2}}$ and $2.0 \times 10^{10}\,\mathrm{A\,m^{-2}}$ for W and Pt-based samples, respectively. The measurements are performed by sweeping an external magnetic field applied parallel to the current direction at $\varphi_H = 0$ (longitudinal scheme) and perpendicular to the current direction at $\varphi_H = \pi/2$ (transverse scheme). The external field H_{ex} is applied in the direction given by θ_H and φ_H (see Fig. 5.1), close to the in-plane direction ($\theta_H \sim 176^\circ$) but with a small tilt in order to keep the sample in a single domain state.

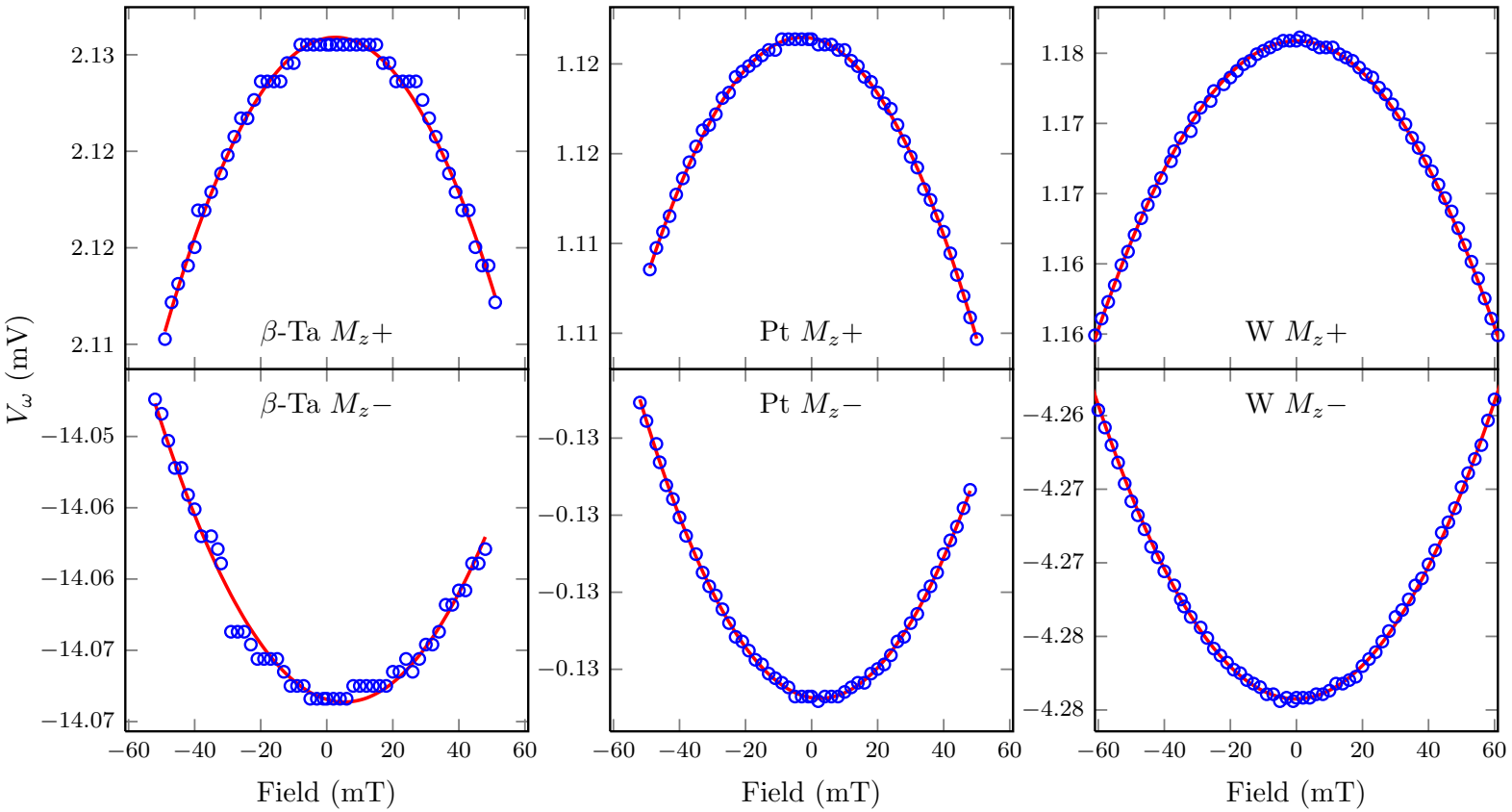

Figure 5.5: First harmonic signal V_ω as a function of the in-plane applied field for β-Ta/CoFeB/MgO, Pt/CoFeB/MgO and β-W/CoFeB/MgO samples. The data (blue circles) are fitted with a parabolic function (red curves). The upper panel corresponds to initial magnetisation pointing in the $+\hat{z}$ direction, while the lower panel corresponds to initial magnetisation pointing in the $-\hat{z}$ direction.

The second harmonic voltage $V_{2\omega}$ can be analysed using the method described in sec. 5.2.2. R_{AHE} is found by measuring the Hall voltage V_{H} as a function of the external field applied perpendicular to the sample surface (Fig. 5.4) while R_{PHE} is found by measuring V_{H} with a fixed in-plane external field (high enough to completely align the magnetic moment in its direction) and varying φ_H. In the Pt and W-based samples, the PHE contribution is unusually high: the ratio $R_{\mathrm{PHE}}/R_{\mathrm{AHE}}$ is 0.325 and 0.607 for Pt and W respectively. Hence, its contribution cannot be neglected. The Ta-based samples instead show a much lower ratio of around 0.05, that we still considered in the calculations. In both measurement configurations, V_ω does not depend on the PHE resistance and it results only from the AHE. It is given by eq. 5.20 and 5.21 as

$$V_\omega = \frac{1}{2} I_{\mathrm{ac}} R_{\mathrm{AHE}} \cos(\theta_0) \ , \tag{5.30}$$

hence it can be used to estimate the value of θ in the equilibrium position (θ_0). As discussed in the previous sec. 5.2.2, the effective fields can be estimated by using eq. 5.27 and 5.28. The first and second harmonic voltages V_ω and $V_{2\omega}$ are measured as a function of a small applied in-plane external field. The results of these measurements for the different samples are shown in Fig. 5.5, 5.6 and 5.7 for the longitudinal and transverse configurations. We don't show the first harmonic signal for both configurations because there is no qualitative difference. The labels M_z+ and M_z- indicates that the magnetic moment was originally saturated along the $\hat{z}$ and $-\hat{z}$ direction, respectively.

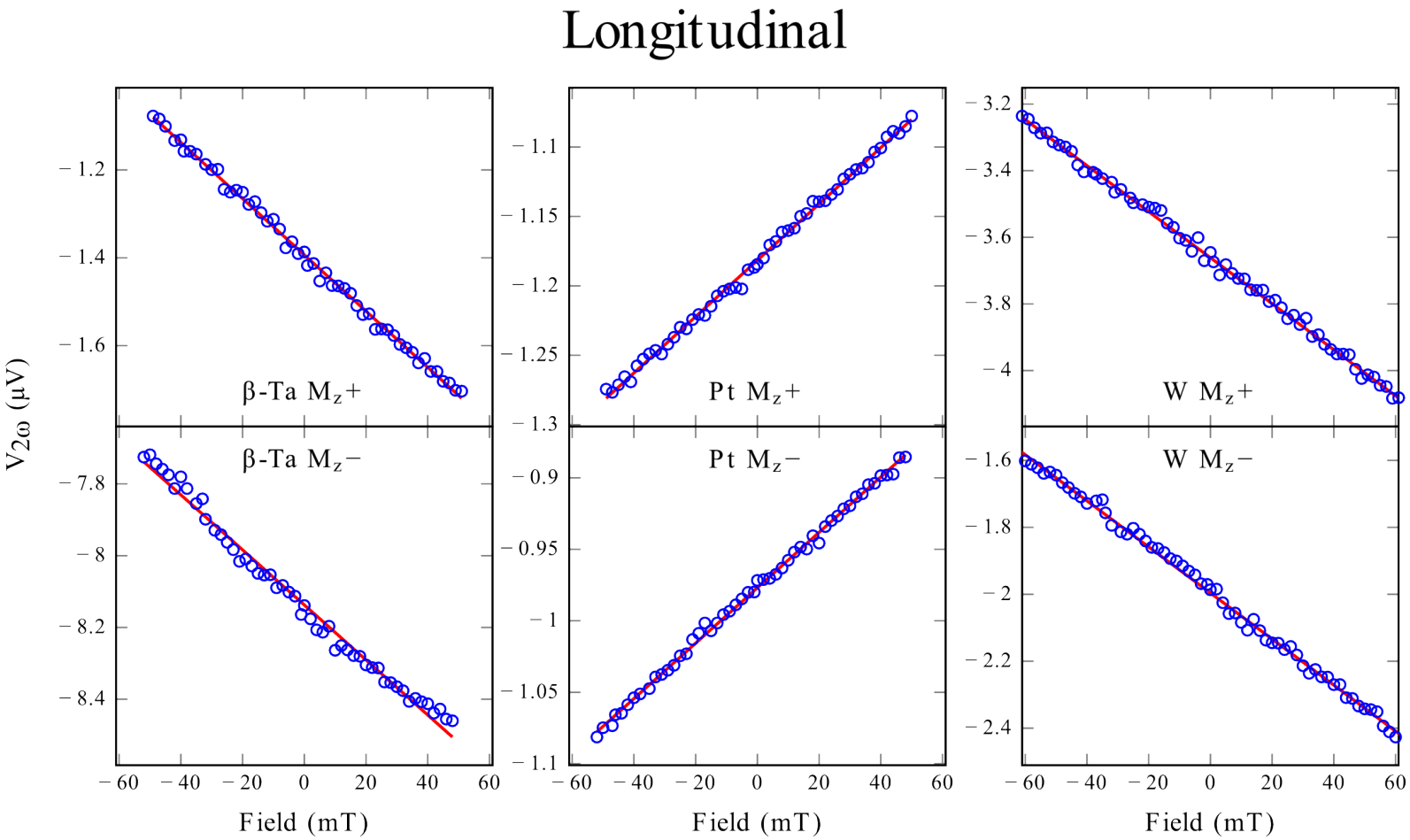

Figure 5.6: Second harmonic signal $V_{2\omega}$ as a function of the in-plane applied field in the longitudinal configuration ($\phi_H = 0$) for β-Ta/CoFeB/MgO, Pt/CoFeB/MgO and β-W/CoFeB/MgO samples. The data (blue circles) are fitted with a linear function (red lines). The upper panel corresponds to initial magnetisation pointing in the $+\hat{z}$ direction, while the lower panel corresponds to initial magnetisation pointing in the $-\hat{z}$ direction.

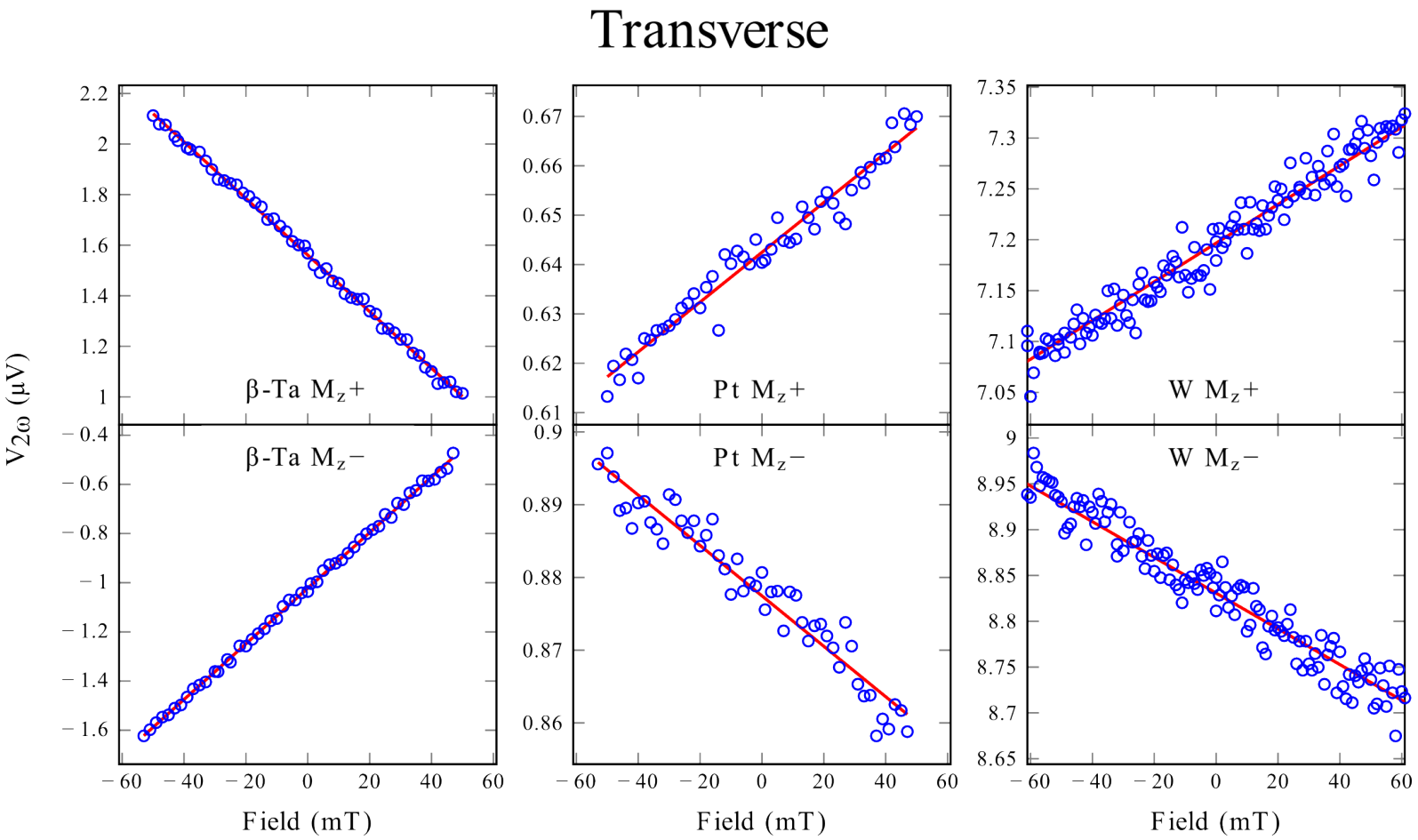

Figure 5.7: Second harmonic signal $V_{2\omega}$ as a function of the in-plane applied field in the transverse configuration ($\phi_H = \pi/2$) for β-Ta/CoFeB/MgO, Pt/CoFeB/MgO and β-W/CoFeB/MgO samples. The data (blue circles) are fitted with a linear function (red lines). The upper panel corresponds to initial magnetisation pointing in the $+\hat{z}$ direction, while the lower panel corresponds to initial magnetisation pointing in the $-\hat{z}$ direction.

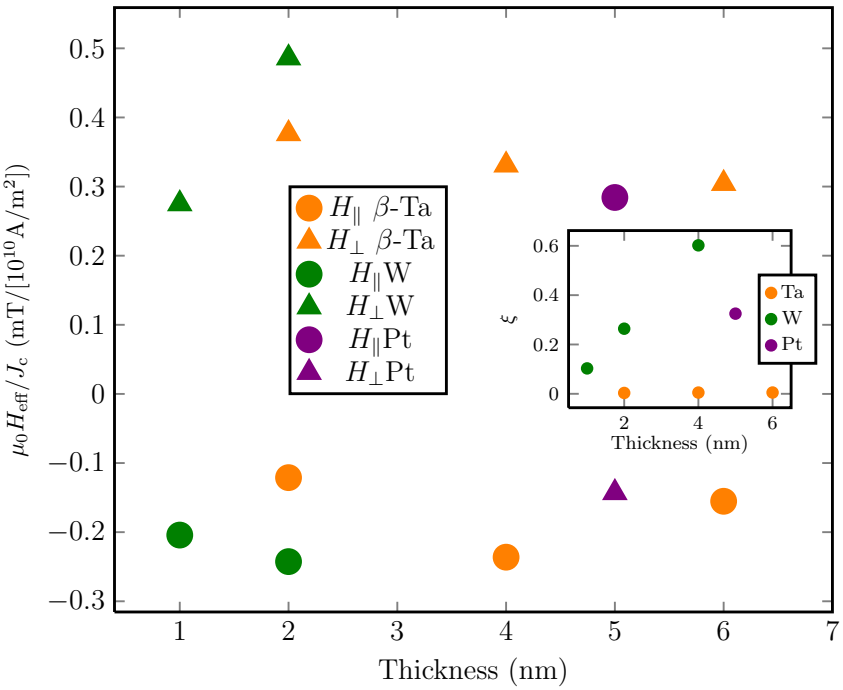

Figure 5.8: Spin-orbit effective fields $\mu_0 H_{\rm eff}$ per $10^{10}\,\mathrm{A\,m^{-2}}$ as a function of the HM layer thickness for W, β-Ta and Pt. The extracted values take into account the PHE; the ratio $\xi = R_{\rm PHE}/R_{\rm AHE}$ is shown in the inset.

As predicted by the theory, the slopes of the second harmonic signals for $\vec{M}$ pointing in the $+\hat{z}$ and $-\hat{z}$ directions are the same in the longitudinal configuration while it changes sign in the transverse one. In addition, the sign of the slope for Ta and W-based samples is opposite to the one of Pt based samples, in agreement with the simple argument that the spin-orbit coupling is opposite in Pt with respect to Ta and W. Theoretical calculations and previous measurements also result in opposite signs of spin Hall angles for these materials [15, 23, 25, 26].

Conclusions and discussion

The extracted effective fields for β-Ta, W and Pt are reported in Fig. 5.8. The values of the spin Hall angle $\theta_{\rm SH}$ can be estimated using eq. 5.29 with $M_{\rm s}$ ~1.2 MA m^{-1}. We obtain a bulk value of -0.067 and -0.038 for β-Ta and α-Ta respectively, and -0.069 and 0.093 for W and Pt, respectively. While the SHA of Pt is in good agreement with literature values [25, 27–29] and with our other measurements, the extracted valued for the other two materials are lower than expected. We don't have a simple explanation for the low value of $\theta_{\rm SH}$ for Ta in both phases, apart from pointing out that the literature is often in disagreement when it comes to the spin Hall angle [30]. In addition, it is very easy to contaminate or oxidise a thin Ta layer, therefore we cannot rule out a degradation of the Ta/FM interface and a resulting increase of the interface resistance. In addition, we report an even lower spin Hall angle (~0.012) for the samples of β-Ta that were annealed. We believe that this change is due to the degradation of the interface after annealing, probably as a result of interdiffusion of atoms between Ta and CoFeB.

Tungsten warrants a more refined discussion. We deposited a control sample with a very thick W layer in order to perform XRD measurement and determine its crystalline phase. As previously mentioned, the results show that it grows in the metastable β phase (A_{15} cubic). While the measured resistivity of the actual samples seems to endorse this hypothesis, we cannot be sure that a mixture of α and $\beta-$W

Table 5.2: Results of the low-field harmonic Hall measurements

Sample[a]	HM Phase	Annealed	θ_{SH}	Literature values
Pt/Hf/$Co_{20}Fe_{60}B_{20}$/MgO/Ta	Amorphous	X	0.093	0.04 to 0.13
W/$Co_{20}Fe_{60}B_{20}$/MgO/Ta	β	✓	−0.069	−0.01 to −0.33
Ta/$Co_{20}Fe_{60}B_{20}$/MgO/Ta	β	X	−0.067	−0.05 to −0.16
Ta/$Co_{20}Fe_{60}B_{20}$/MgO/Ta	β	✓	−0.012	−0.04 to −0.14
Ta/$Co_{20}Fe_{60}B_{20}$/MgO/Ta	α	✓	−0.038	n.a.

[a]Thickness in nm

is not present. It is not possible to measure XRD on such thin multilayers and the measurement of the electrical resistivity can be misleading due to the mixture of different contributions. A more problematic issue concerns the PHE to AHE ratio ξ. As shown in the inset in Fig. 5.8, we obtained very high values of ξ. Since the anomalous and planar Hall effect should be entirely due to the FM layer (CoFeB 0.9 nm), we didn't expect such a marked dependence on the thickness and on the type of HM on which the CoFeB is deposited. In Fig. 5.8 we didn't show the data for samples of W 4 and 3 nm since they have ratios ξ of 0.602 and 0.448, respectively, resulting in spin Hall angles of 0.9 and 1.09 (for $\xi = 0.5$ the effective fields diverge). These values are incredibly high and, more importantly, of opposite sign with respect to all the other samples and literature values. We believe that the estimation of the PHE for the W-based samples is not correct and there is another mechanism contributing to the measured planar Hall resistance that is not related to a rotation of the magnetic moment of the CoFeB layer. Additional measurements on different samples are needed in order to sort out this issue. A similar behaviour has been previously reported for W [31].

Finally, it is worth noting the high values of the transverse effective fields in comparison to the longitudinal ones. The transverse field, due to Rashba effect or to the imaginary part in the spin-mixing conductance, is the main component in the spin-orbit fields in ultrathin Ta and W, while it is less important in Pt. From our measurements we find that the ratio between the transverse and longitudinal fields is ∼0.5 for Pt and ∼2.15 and ∼2.0 for Ta and W respectively. This is due to a lower Rashba effect and better transparency of the Pt/HM interfaces with respect to Ta and W.

A summary of the results is presented in Tab. 5.2.

5.2.5 High field measurements: results

We measured the samples with the harmonic Hall technique without limiting the applied field to low values. When the magnetisation is tilted towards the in-plane direction, the $V_{2\omega}$ signal shows a peculiar shape that can be fitted with eq. 5.19 in order to obtain the spin-orbit effective fields. The first and second harmonic voltages recorded for the Pt-based sample are shown in Fig. 5.9 for both longitudinal and transverse configurations. In Fig. 5.10 the results of the α-Ta sample are shown for both longitudinal and transverse configurations.

Fig. 5.11 shows the results for the annealed β-Ta sample for longitudinal and transverse configurations, while Fig. 5.12 shows the measurements for the β Ta samples that was not annealed, for the longitudinal and transverse configurations.

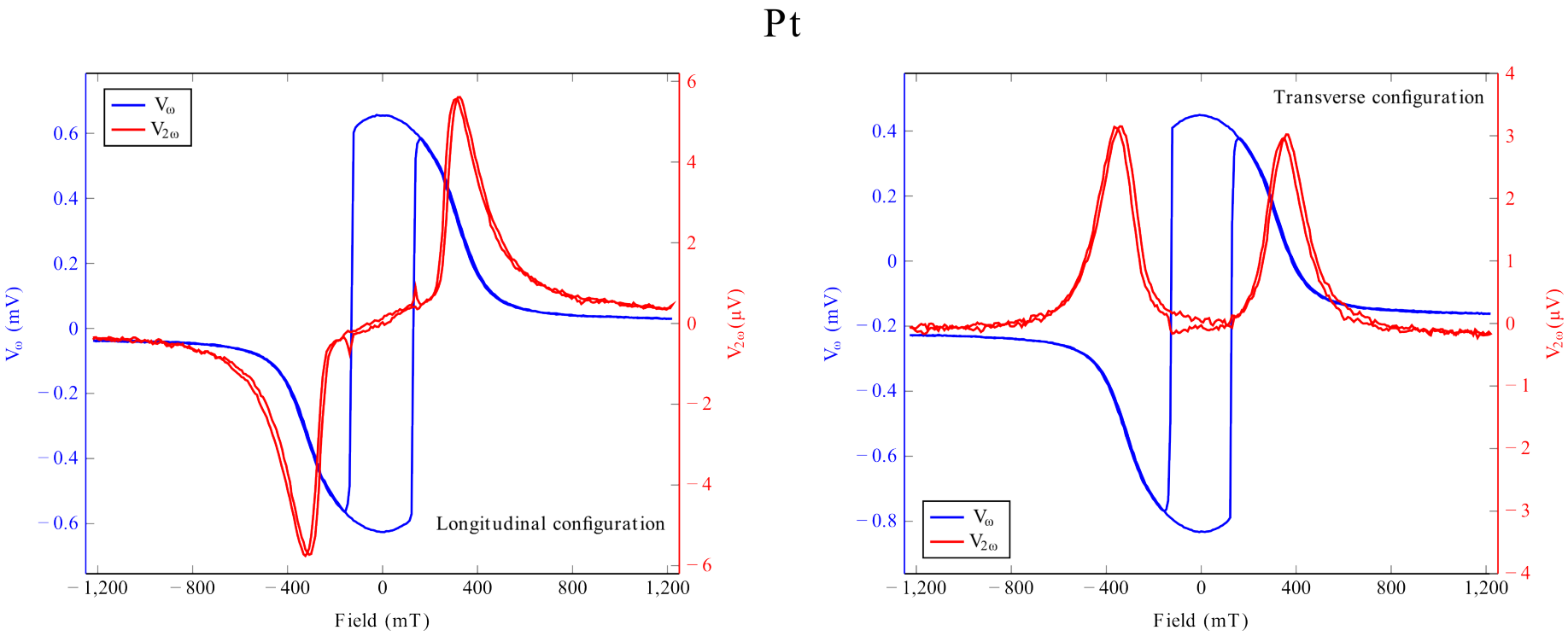

Figure 5.9: First(blue) and second (red) harmonic Hall signal as a function of the in-plane applied field ($\theta_H = 88°$) for a Pt/CoFeB/MgO sample in longitudinal ($\varphi_H = 0°$) and transverse configuration ($\varphi_H = 90°$).

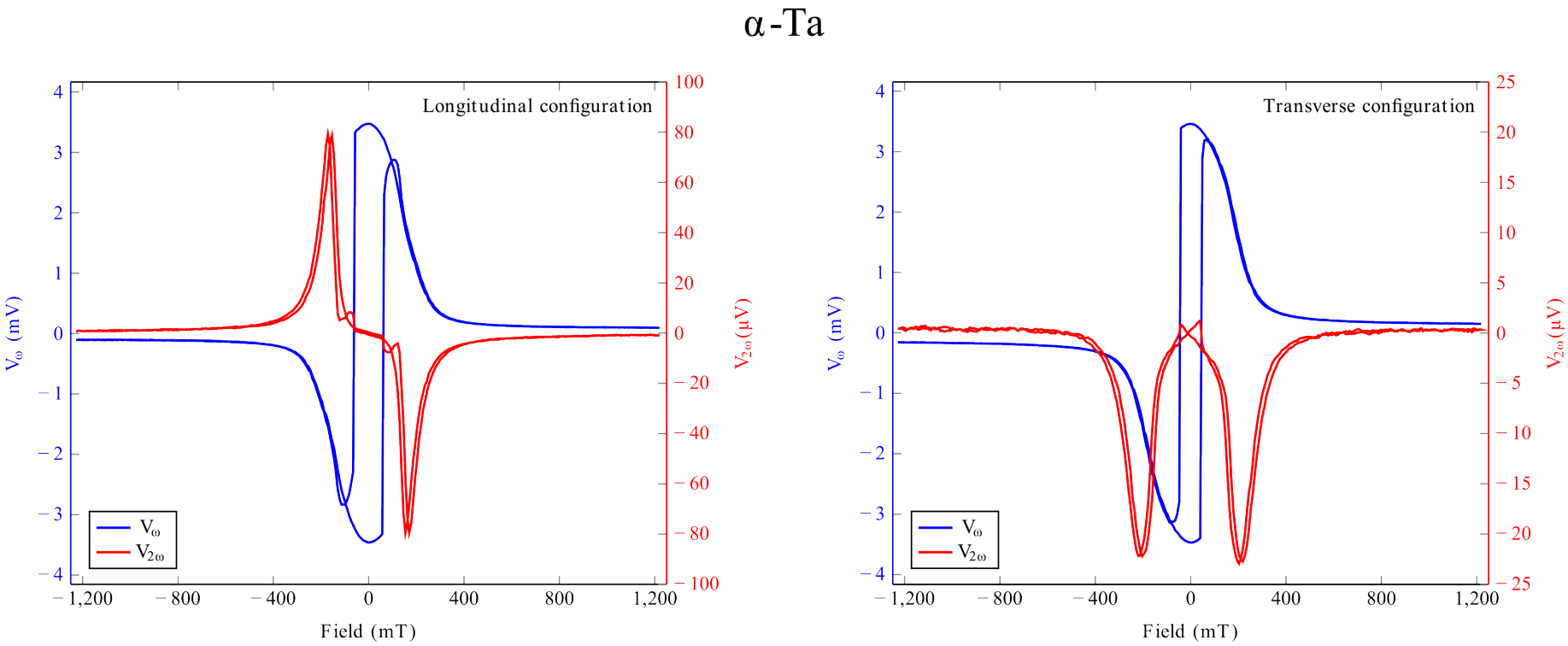

Figure 5.10: First(blue) and second (red) harmonic Hall signal as a function of the in-plane applied field ($\theta_H = 88°$) for a α-Ta/CoFeB/MgO sample in longitudinal ($\varphi_H = 0°$) and transverse configuration ($\varphi_H = 90°$).

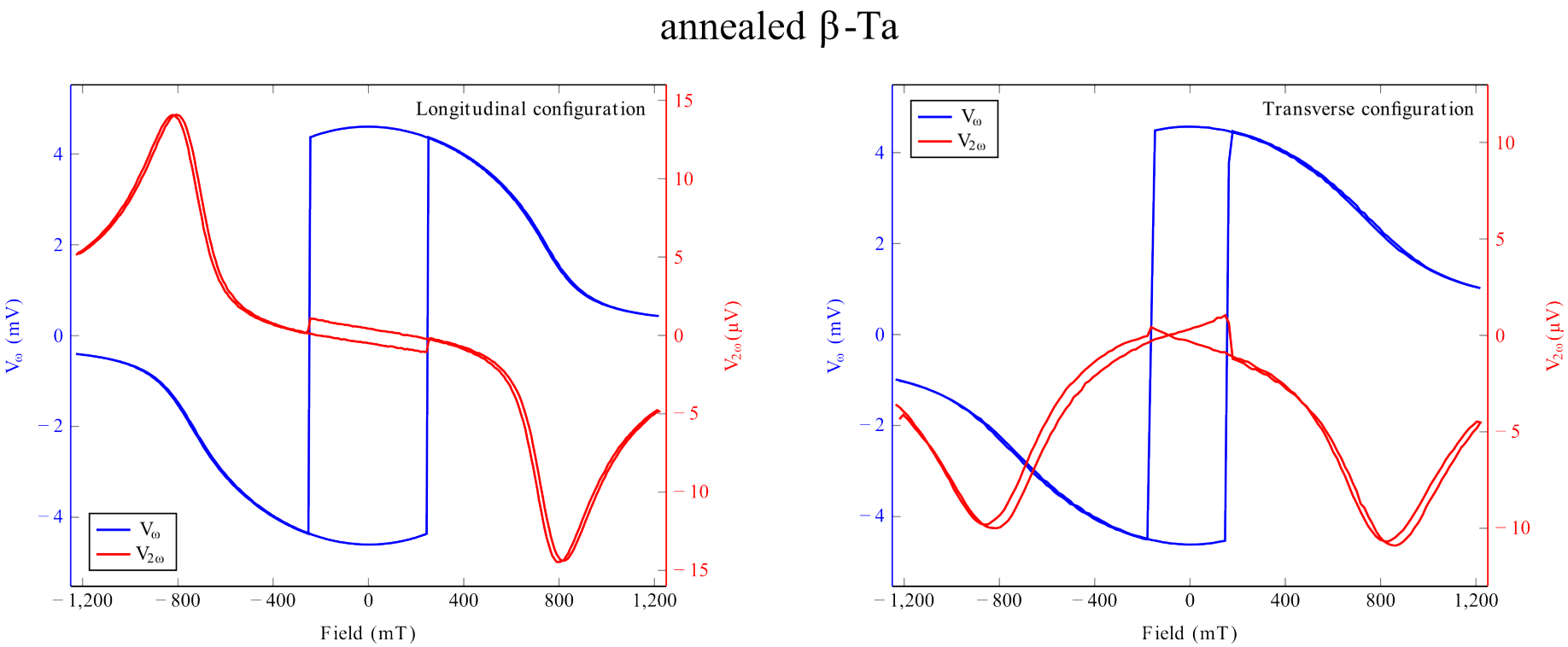

Figure 5.11: First(blue) and second (red) harmonic Hall signal as a function of the in-plane applied field ($\theta_H = 88°$) for the annealed β-Ta/CoFeB/MgO sample in longitudinal ($\varphi_H = 0°$) and transverse configuration ($\varphi_H = 90°$).

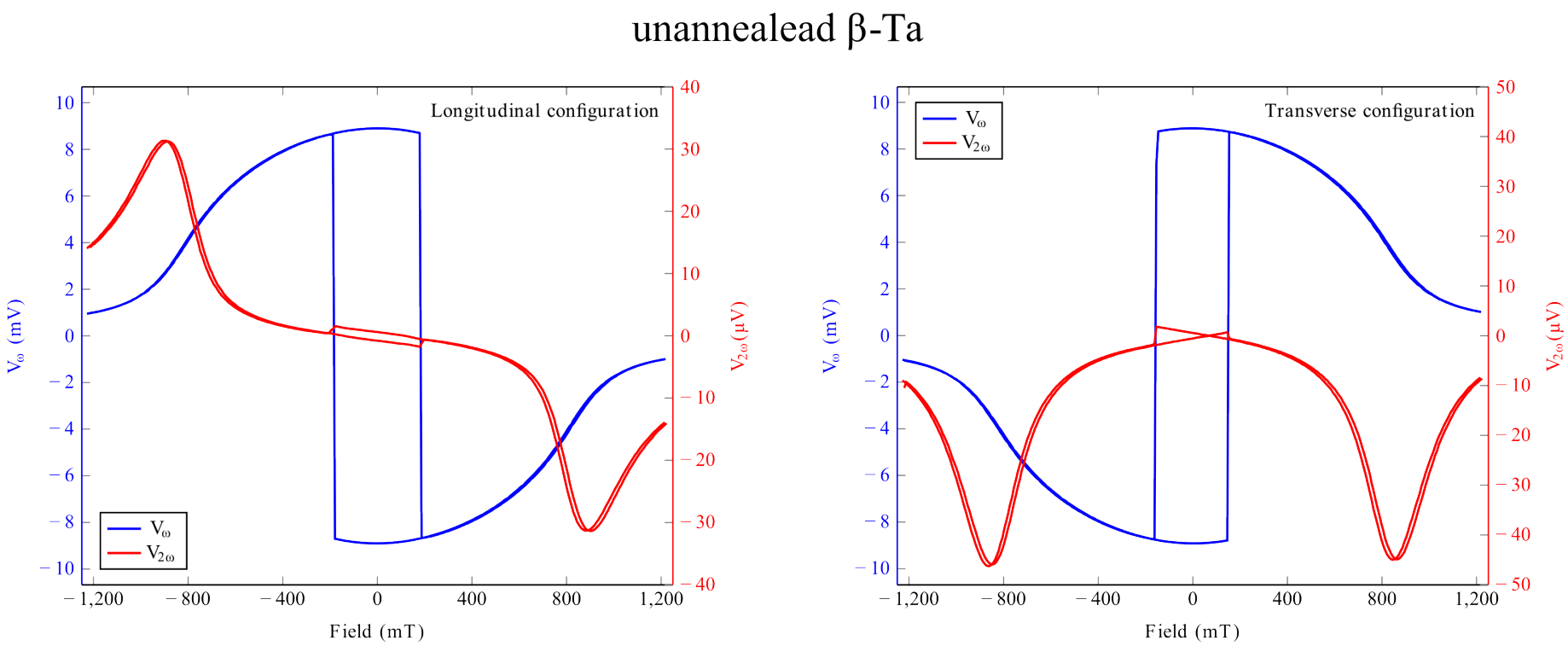

Figure 5.12: First(blue) and second (red) harmonic Hall signal as a function of the in-plane applied field ($\theta_H = 88°$) for the unannealed β-Ta/CoFeB/MgO sample in longitudinal ($\varphi_H = 0°$) and transverse configuration ($\varphi_H = 90°$).

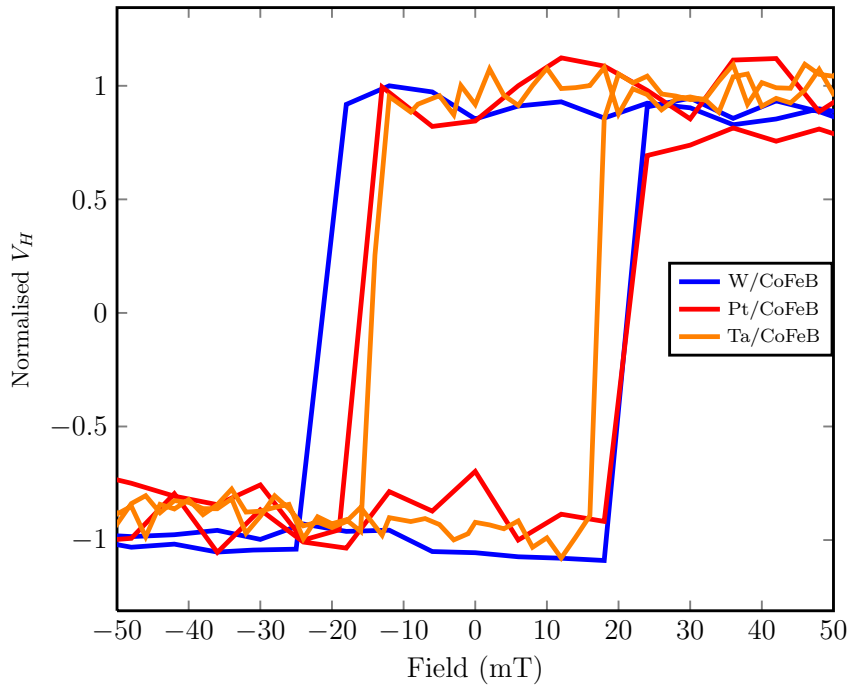

Figure 5.13: Normalised second harmonic Hall signal as a function of the perpendicular applied field for W/CoFeB/MgO, Pt/CoFeB/MgO and β-Ta/CoFeB/MgO samples. These voltages results from the anomalous Nernst effect (ANE) originating from out-of-plane temperature gradients.

The anomalous Nernst effect (ANE) is also considered in the evaluation of the effective fields [15, 18], but it could have been neglected since it is a small effect. The ANE consists in the generation of a transverse voltage as a results of the application of an in-plane thermal gradient in a perpendicularly magnetised sample. The thermal gradient generates a charge current (Seebeck effect) and, in turn, the charge current generates a transverse voltage, with the same mechanisms responsible of the AHE. With the high-field harmonic Hall method, the measurement of $V_{2\omega}$ is sensitive to sample-dependent contributions to the Hall voltage, such as misalignments in the measurement lead and thermoelectric effects. The current flowing in the device can cause inhomogeneous heating, generally corresponding to defects at the edges of the bars. In addition, the different thermal conductivities of the air and the substrate induce thermal gradients in the perpendicular direction that can give rise to a transverse voltage due to the ANE. Since the latter is modulated by the injected current, it contributes to the second harmonic signal as

$$V_{2\omega}^{\mathrm{ANE}} = I_{\mathrm{ac}} R_{\mathrm{ANE}} \frac{\cos\theta}{2} \ . \tag{5.31}$$

The asymmetry of the voltage leads, together with the Seebeck effect, can cause a constant offset in the signal. Both ANE and offset can be determined by a measurement with perpendicular applied field, as shown in Fig. 5.13, where the signal is only due to these unwanted effects. The $V_{2\omega}$ data in the longitudinal and transverse configuration can be corrected using the formula

$$V_{2\omega}^{\mathrm{corr}} = V_{2\omega}^{\mathrm{raw}} - V_{2\omega}^{\mathrm{ANE}} \frac{V_{\omega}}{2V_{\mathrm{AHE}}} - V_{\mathrm{offset}} \ . \tag{5.32}$$

The Ørsted field generated by the ac current is negligible as well. It gives an additional contribution to $\mu_0 H_{\perp}$ that is much smaller (max 0.062 mT) than the one from the spin-orbit interactions. Thermal effects

due to Joule heating are negligible as well, as proved by the verified linear dependence of the estimated fields as a function of the injected current.

Conclusions and discussion

Following the procedure discussed in sec. 5.2.1, we obtained the values of $\mu_0 H_\parallel$ and $\mu_0 H_\perp$ as a function of the magnetisation azimuthal angle. Fig. 5.14 shows the result for a Pt/CoFeB/MgO sample as a function of the injected current density in the HM layer for the longitudinal and transverse effective fields, respectively. Evaluating the mean value of $\mu_0 H_\parallel$ using the data acquired with the previous measurements we can estimate the bulk value of the spin Hall angle. Using the equation

$$\mu_0 H_\parallel = \mu_0 \hbar \theta_{\mathrm{SH}} \frac{J_\mathrm{c}}{2eM_\mathrm{s}t} \ , \tag{5.33}$$

we obtain the value of $\theta_{\mathrm{SH}}^{\mathrm{Pt}} = 0.085$ for Pt, in good agreement with our previous measurements.

Again, we report difficulties in analysing the data obtained with the W-based sample. It is not possible to fit the data using the same set of equations that proved to be correct for Pt. Even if the approximation of small deviation angles in θ and φ is not considered and the non-approximated set of equations is solved numerically, it is not possible to converge to a robust solution and the effective fields diverge for some value of θ. This is mainly due to the high value of the PHE and the ratio ξ, as reported in sec. 5.2.4. In this case, the same comments made in the previous section are still valid.

We analysed the various Ta-based samples in more detail. The calculated longitudinal and transverse effective fields as a function of the current density flowing in the HM are presented in Fig. 5.15 for α-Ta. Fig. 5.16 shows the results for annealed β-Ta, while Fig. 5.17 shows the results for the unannealed one.

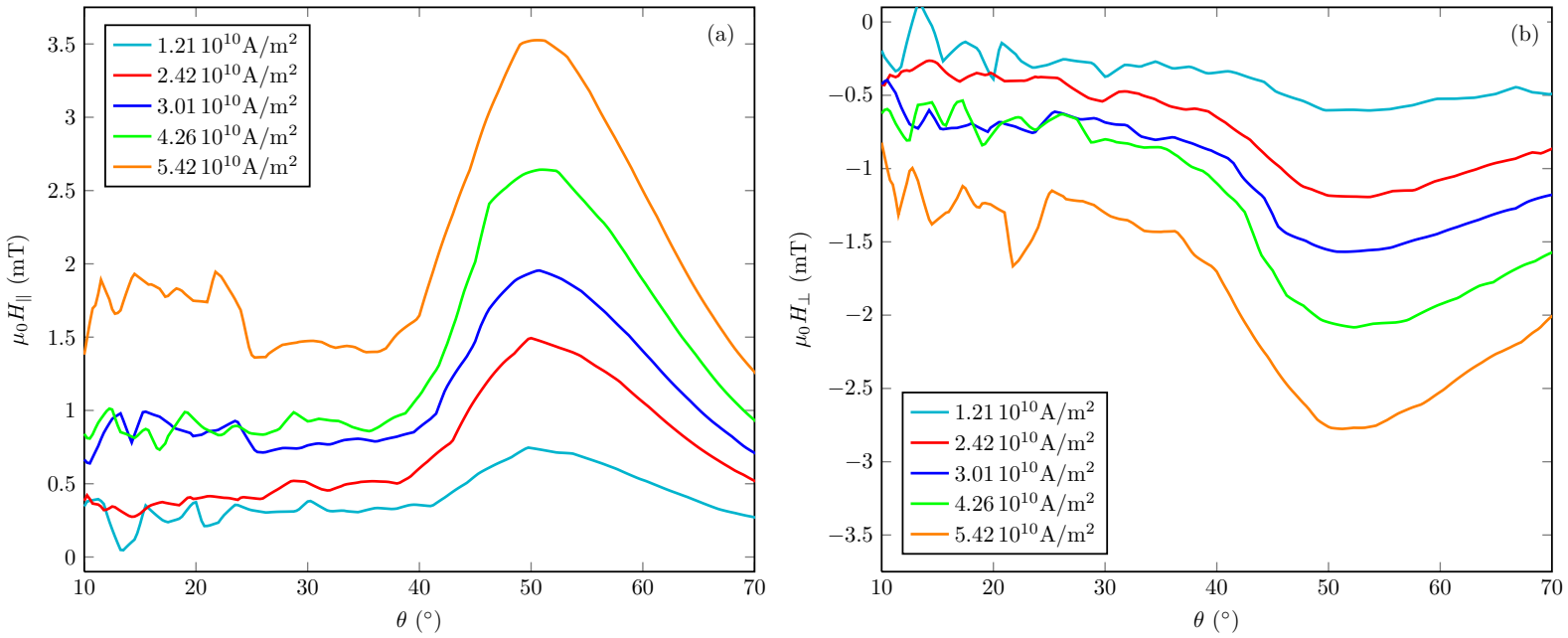

Figure 5.14: Estimated longitudinal ($\mu_0 H_{\parallel}$) (a) and transverse ($\mu_0 H_{\perp}$) (b) effective field for a Pt/CoFeB/MgO sample as a function of the injected current density.

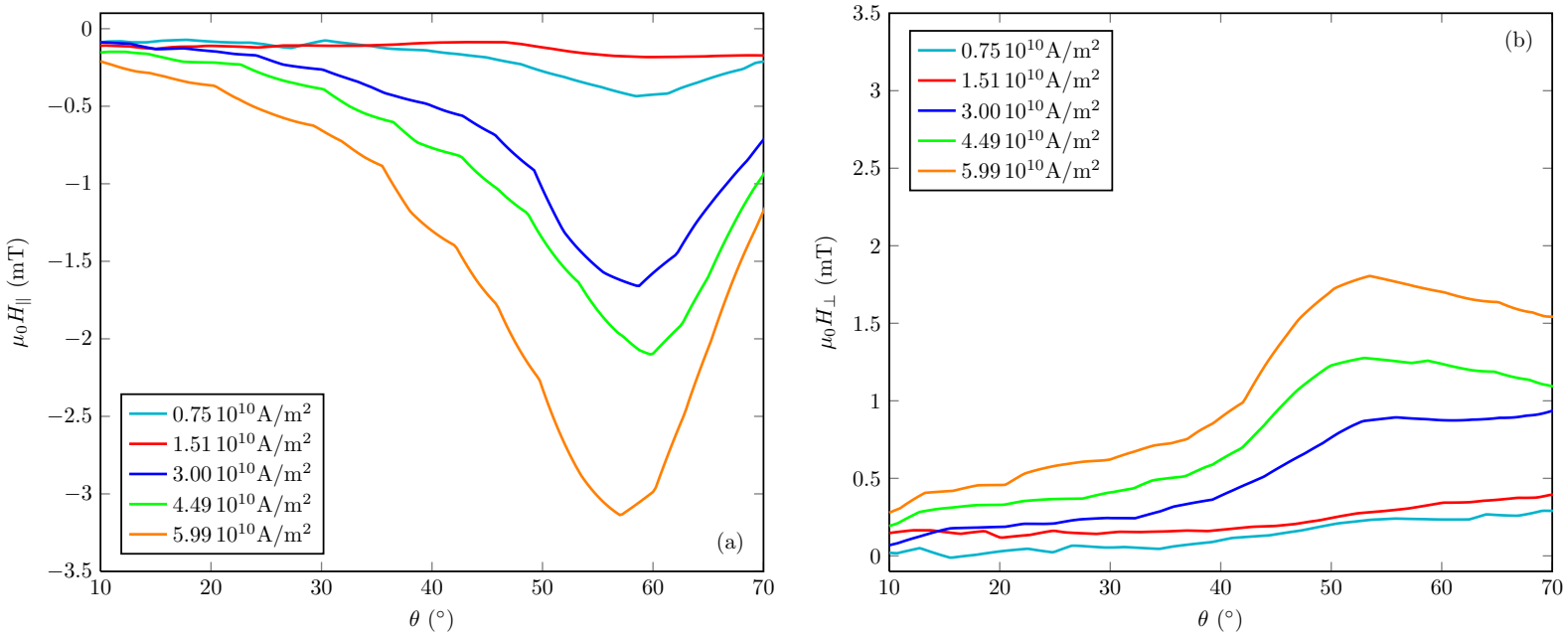

Figure 5.15: Estimated longitudinal ($\mu_0 H_{\parallel}$) (a) and transverse ($\mu_0 H_{\perp}$) (b) effective field for an annealed α-Ta/CoFeB/MgO sample as a function of the injected current density.

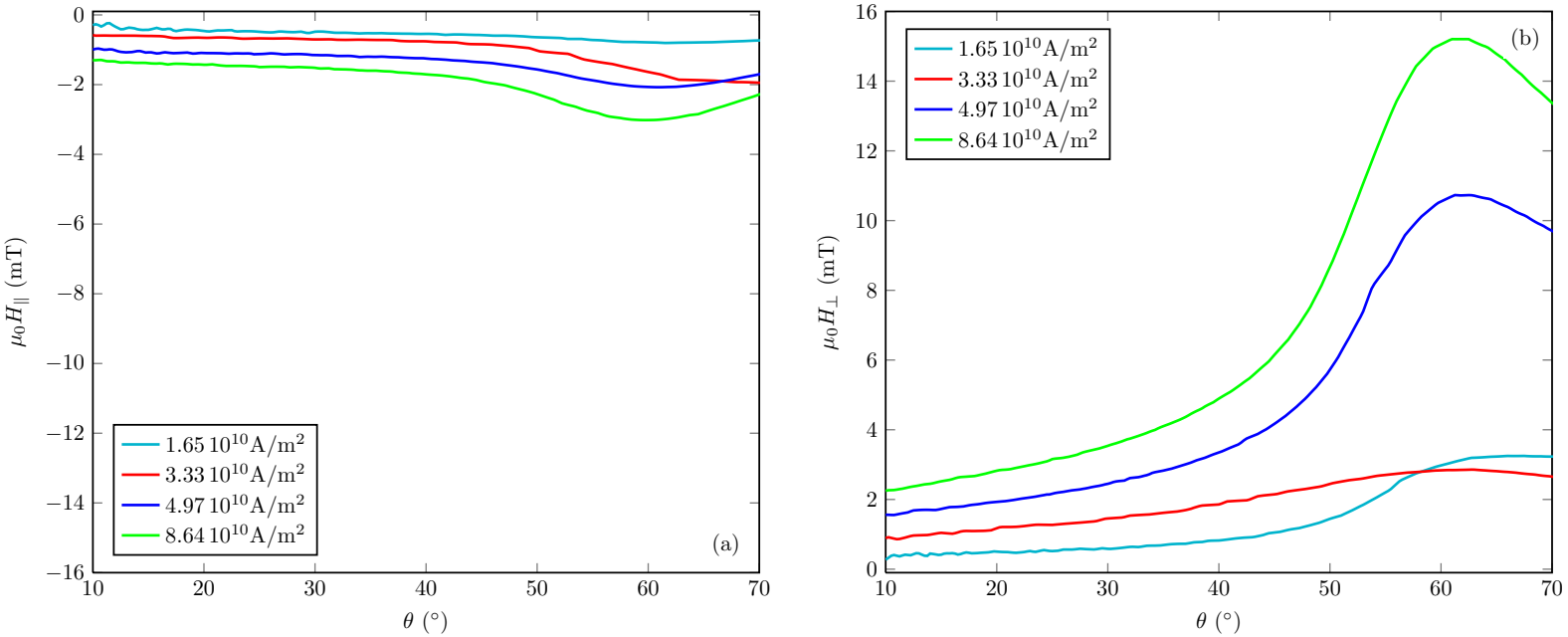

Figure 5.16: Estimated longitudinal ($\mu_0 H_\parallel$) (a) and transverse ($\mu_0 H_\perp$) (b) effective field for an annealed β-Ta/CoFeB/MgO sample as a function of the injected current density.

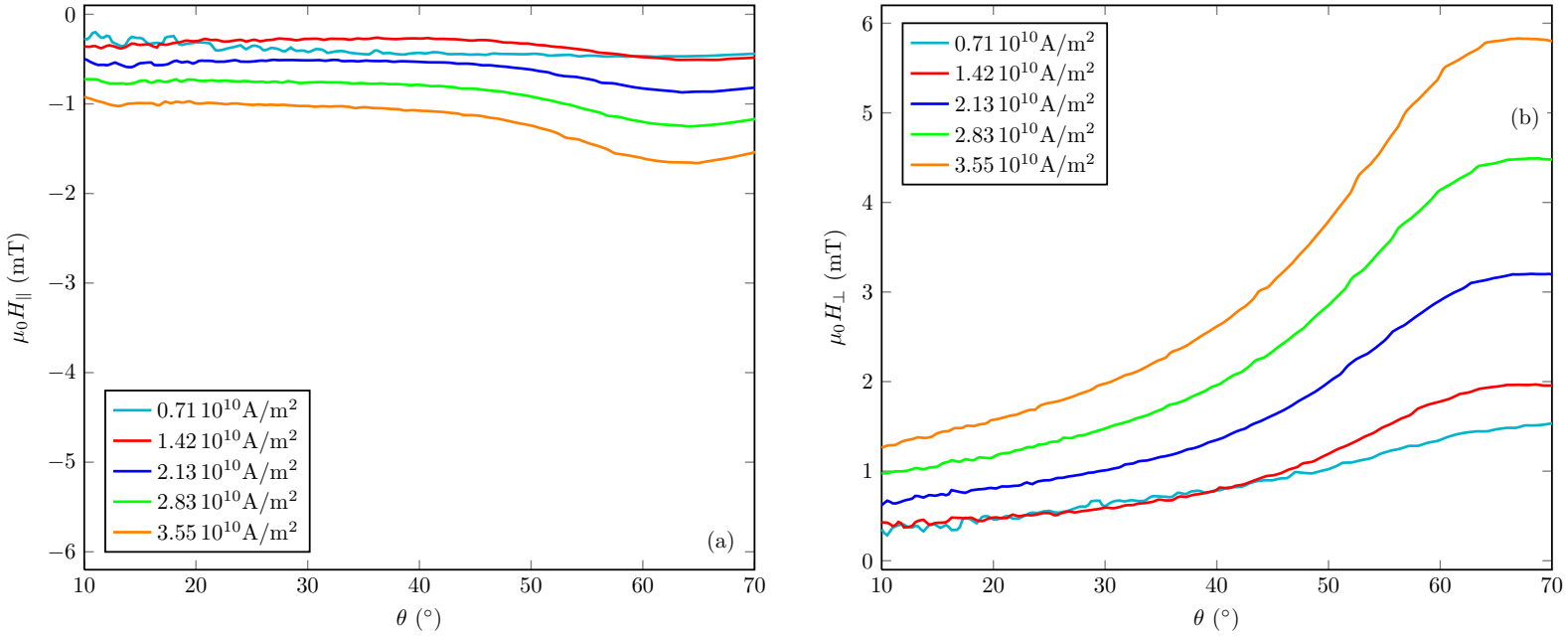

Figure 5.17: Estimated longitudinal ($\mu_0 H_\parallel$) (a) and transverse ($\mu_0 H_\perp$) (b) effective field for a unannealed β-Ta/CoFeB/MgO sample as a function of the injected current density.

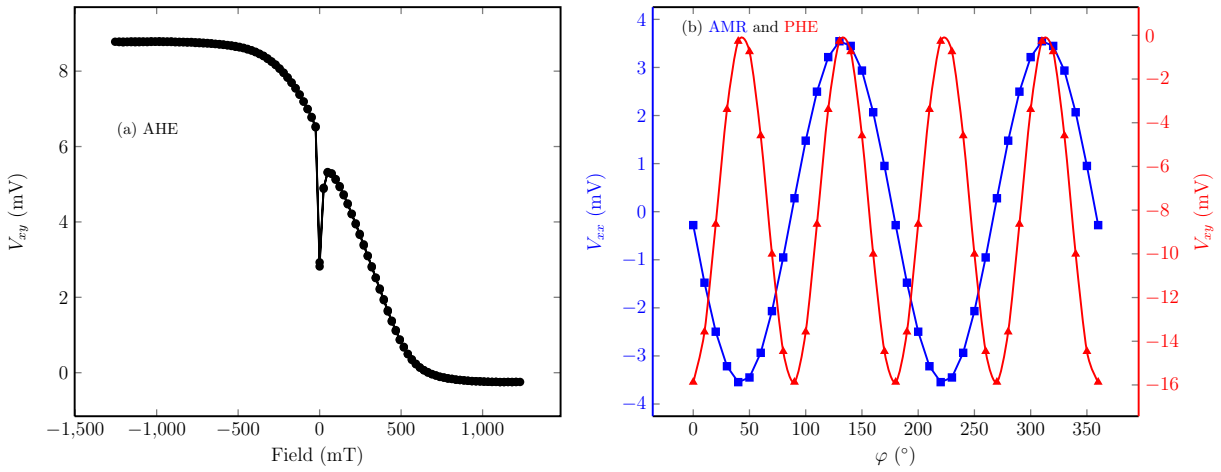

Figure 5.18: Measured AHE, AMR and PHE for a W/CoFeB/ Al_2O_3 sample. The spike at low field in the AHE loop is probably due to domain nucleation.

Again, the effective fields and the injected current follow a linear relationship. Of course, the noise level increases as the current decreases.

Using eq. 5.33 and evaluating the mean value of $\mu_0 H_\parallel$ we estimated the bulk value of the spin Hall angle for each sample. We obtained the values of $\theta_{\mathrm{SH}} = -0.026$ for α-Ta, $\theta_{\mathrm{SH}} = -0.065$ for annealed β-Ta and $\theta_{\mathrm{SH}} = -0.081$ for not-annealed β-Ta.

We found a marked angular dependence for all materials, similar to previously reports [18]. The variation of $\mu_0 H_\perp$ is unexpectedly high with respect to what we find for $\mu_0 H_\parallel$. The currently established theory for the spin-orbit torques relates $\mu_0 H_\parallel$ mainly to the SHE [32, 33], while $\mu_0 H_\perp$ results from interfacial Rashba interactions [10, 34]. Both these theories fail in explaining the observed angular dependence and no satisfying explanation has been proposed so far in the literature [18].

5.3 Planar Hall effect of HM/FM bilayers

The planar Hall effect (PHE) is a transverse voltage found in a magnetic layer, whose value is proportional to the product of the $\hat{x}$ and $\hat{y}$ components of the magnetisation $M_x M_y$ [19]. It owes its origin to the same mechanisms responsible for the AMR (see sec. 2.3.2). The PHE resistance can be expressed as

$$R_{\mathrm{PHE}} = \frac{1}{2} R_{\mathrm{PHE}} \sin^2\theta \sin(2\varphi) \ . \tag{5.34}$$

We measured the AHE, the AMR and the PHE of a series of samples in order to investigate the mechanism behind the unusually high values of the PHE/AHE ratio in W-based samples. All the samples had been deposited by rf and dc sputtering on thermally oxidised Si substrates and then patterned into Hall bars. A summary of the measured samples and the obtained results are shown in Tab. 5.3, while Fig. 5.18 shows a set of AHE, AMR and PHE data as an illustrative example. The spike at low field in the AHE loop is probably due to domain nucleation. This feature can be seen in other samples with high PHE and in-plane anisotropy (due to the shape anisotropy).

Table 5.3: PHE and AMR summary

Sample[a] (thickness in nm)	R_{AHE} (Ω)	R_{PHE} (Ω)	$\xi = R_{\mathrm{PHE}}/R_{\mathrm{AHE}}$ (%)	R_{AMR} (Ω)	$R_{\mathrm{AMR}}/R_{\mathrm{PHE}}$ (%)	R_{xx} (Ω)	Anisotropy
CoFeB(1)/Ta(4)/Al_2O_3(2)	1.987	0.115	5.79	1.10	10.05	1210.16	in-plane
CoFeB(1)/Hf(4)/Al_2O_3(2)	3.247	0.0967	2.98	1.02	10.51	3012.36	in-plane
W(4)/CoFeB(1)/Al_2O_3(2)	2.261	1.781	78.76	7.95	4.47	876.53	in-plane
Ta(4)/CoFeB(1)/Al_2O_3(2)	2.449	0.129	5.28	0.69	5.37	934.86	in-plane
Hf(4)/CoFeB(1)/Al_2O_3(2)	2.713	0.168	6.18	0.91	5.44	1294.12	in-plane
Ta(4)/W(0.3)/CoFeB(1)/Al_2O_3(2)	2.450	0.312	12.72	1.44	4.62	856.96	in-plane
W(4)/Ta(0.3)/CoFeB(1)/Al_2O_3(2)	2.095	1.393	66.50	7.23	5.19	876.54	in-plane
CoFeB(1)/Ta(0.3)/W(4)/Al_2O_3(2)	0.783	0.332	42.34	1.55	4.68	1990.00	in-plane
CoFeB(1)/W(0.3)/Ta(4)/Al_2O_3(2)	0.898	0.078	8.73	0.39	5.00	943.51	in-plane
W(4)/Ta(0.3)/CoFeB(1)/MgO(2)/Ta(1)	2.938	1.515	51.57	7.32	4.83	829.93	out-of-plane
Ta(4)/W(0.3)/CoFeB(1)/MgO(2)/Ta(1)	3.308	0.296	8.94	1.36	4.61	865.97	out-of-plane
α-Ta(4)/CoFeB(1)/MgO(2)/Ta(1)	0.592	0.036	6.06	0.191	5.31	442.31	in-plane
α-W(4)/CoFeB(1)/MgO(2)/Ta(1)	0.298	0.0425	14.28	0.182	4.30	292.96	in-plane

[a]Where not specified, Ta and W are in the β phase or amorphous.

The data show a drastic increase of the PHE resistance when β-W is the HM regardless of the configuration. The ratio between the AMR and the PHE assumes an almost constant value (around 5), confirming the common origin of these two phenomena. The addition of a dusting layer of Ta reduces the PHE resistance but does not entirely destroy the effect. On the other hand, a dusting layer of W between a Ta layer and CoFeB increases the value from $\sim$5 % to around 10 %. The stacking order of the different layers is found not to be important for the PHE, as well as the in-plane or perpendicular anisotropy of the CoFeB layer. The AHE resistance does not vary much for all samples with the exceptions of CoFeB(1)/Ta(0.3)/W(4)/Al_2O_3(2) and CoFeB(1)/W(0.3)/Ta(4)/Al_2O_3(2).

We believe that this enhancement of the planar Hall effect is due to the interface effect between W and CoFeB, resulting in either the creation of a thin magnetic layer in the W or in an enhancement of the spin-orbit coupling in the first layers of the CoFeB. Even in samples with a thin dusting layer of Ta (only 1-2 monolayers), this dusting layer might not uniformly cover the surface or it might form an alloy with W. In both cases the interfacial coupling with W would not be completely suppressed, and the enhancement is still detected.

A possible explanation relies on the creation of a W thin magnetic layer by proximity effect with the CoFeB layer, similarly to what happens at the Pt/Co interface. This layer could add its own contribution to the PHE, AHE and AMR but it has no impact on the spin Hall or Rashba mechanisms for the tilting of the total magnetic moment: the W and the CoFeB magnetic moments would be coupled together and act as a uniform magnetic layer. SQUID measurements didn't show any increased magnetisation in the W/CoFeB sample with respect to a single CoFeB layer. An enhancement of the spin-orbit interactions in a thin layer of CoFeB due to proximity or to partial alloying and interdiffusion with W does not explain the relatively unchanged value of the AHE resistance. In addition, no corrections should be made in the evaluation of the spin Hall and Rashba effective fields, hence this would not explain our difficulties in their calculation. Further experiments are necessary in order to obtain a better understanding of this phenomena.

The results of the measurements on α-Ta and α-W samples are shown in Tab. 5.3. α-Ta shows similar planar Hall resistance value with respect to β-Ta, while α-W shows much lower PHE with respect to β-W. The latter result confirms that the nature of the interfacial interaction is key to the enhanced PHE. The lower values of the anomalous Hall resistances for these two samples are due to the lower resistivity of the HM layers with respect to the FM layer: there is less current flowing in the HM layer, resulting in lower anomalous Hall resistivity. After annealing these two samples for 1 h at 250 °C, we didn't register any significant difference. The only noticeable change was the creation of PMA in the α-Ta sample.

5.4 Direct current Hall technique

The dc Hall technique [35] relies on the measurement of the anomalous Hall voltage [12, 13] when a dc current is injected in the plane of a FM/HM bilayer. An in-plane external field is applied, tilting the FM magnetic moment from the initial out-of-plane orientation resulting from PMA. The different tilt angle of the magnetisation when the current sign is reversed gives the effect of the spin-orbit effective field. For one sign of the current the effective field points in the same direction as the applied field, while for the opposite sign it points in the opposite direction [36].

The experiments described in this section have been done in collaboration with YongChang Lau.

5.4.1 Theory

Let's consider the system represented in Fig. 5.1. It consists of a FM layer with perpendicular magnetic anisotropy and a HM layer at its bottom interface. The magnetic moment is tilted from its out-of-plane equilibrium position by an external field applied in the plane ($\theta_H = \pi/2 - \delta$, with $\delta \ll 1$) and by the spin-orbit torques resulting from the injection of a dc current in the HM layer. As described in sec. 2.3.7, the spin Hall and the Rashba effects result in spin injection at the interface, that in turn produces torque on the magnetic moment.

The angle θ_H is kept close to $\pi/2$ (applied field in the $\hat{x}\hat{z}$ plane) but not strictly equal to it, in order to favour a single domain configuration of the FM, which enables us to use the macrospin model.

The measurement consists of the detection of the anomalous Hall signal (proportional to the out-of-plane component of the magnetic moment, see sec. 2.3.6) as a function of the external field while injecting an in-plane dc current in the stack. As $\mu_0 H_{\rm ex}$ is increased, the magnetisation is tilted towards the $\hat{x}\hat{y}$ plane, lowering the anomalous Hall signal.

By measuring the tilt of the magnetic moment with positive and negative applied currents, it is possible to extract the spin-orbit contribution to the torque. As described in the previous section, the Hall voltage $V_{\rm H}$ is given by the sum of the anomalous Hall effect (AHE) and planar Hall effect (PHE) contributions

$$V_{\rm H} = V_{\rm AHE} + V_{\rm PHE} = I_{\rm dc} R_{xy} \ , \tag{5.35}$$

with

$$R_{xy} = \frac{1}{2} R_{\rm AHE} \cos[\theta_0 + \Delta\theta] + \frac{1}{2} R_{\rm PHE} \sin^2[\theta_0 + \Delta\theta] \sin[2\varphi + 2\Delta\varphi] \ . \tag{5.36}$$

The small angles $\Delta\theta$ and $\Delta\varphi$ are the deviations from the equilibrium position caused by the spin-orbit torques only. We simplified this equation using the first order Taylor expansions around θ_0: $\cos(\theta_0 + \Delta\theta) \approx \cos\theta_0 - \sin\theta_0 \Delta\theta$, $\sin^2(\theta_0 + \Delta\theta) \approx \sin^2\theta_0 + \Delta\theta \sin(2\theta_0)$ and $\sin(2\varphi_0 + 2\Delta\varphi) \approx \sin(2\varphi_0) + 2\Delta\varphi\cos(2\varphi_0)$. The angles $\Delta\theta$ and $\Delta\varphi$ have opposite signs for positive and negative injected current. Therefore, we expect the spin-orbit torque to add or subtract from the field-induced torque in determining the tilting of the magnetic moment. From eq. 5.36, we obtain the following expression for the sum and the difference between the Hall resistances for applied currents of opposite signs

$$\begin{aligned}
R_{xy}^{+} + R_{xy}^{-} &= R_{\rm AHE} \cos\theta_0 + R_{\rm PHE}[\sin^2\theta_0 \sin(2\varphi_0)] \ , \\
R_{xy}^{+} - R_{xy}^{-} &= -\frac{1}{2} R_{\rm AHE} 2\Delta\theta \sin\theta_0 + \frac{1}{2} R_{\rm PHE}[4\sin^2\theta_0 \varphi \cos(2\varphi_0) + 2\Delta\theta \sin(2\theta_0)\sin(2\varphi_0)] \\
&= -R_{\rm AHE}\Delta\theta \sin\theta_0 + 2R_{\rm PHE}\sin^2\theta_0 \Delta\varphi \cos(2\varphi_0) + R_{\rm PHE}\Delta\theta \sin(2\theta_0)\sin(2\varphi_0) \\
&= R_{\rm AHE} \sin\theta_0 [\Delta\theta(-1 + 2\xi\cos\theta_0 \sin(2\varphi_0)) + \Delta\varphi(2\xi \sin\theta_0 \cos(2\varphi_0))] \ ,
\end{aligned} \tag{5.37}$$

where the superscript $\pm$ refers to positive and negative applied current and $\xi = R_{\rm PHE}/R_{\rm AHE}$. In deriving this relations we considered only first order terms in $\Delta\theta$ and $\Delta\varphi$.

In both longitudinal ($\varphi_0 = 0$) and transverse ($\varphi = \pi/2$) configurations we have

$$R_{xy}^{+} + R_{xy}^{-} = R_{\rm AHE} \cos\theta_0 \ . \tag{5.38}$$

Therefore, the sum of the Hall resistances for positive and negative currents can be used to evaluate the equilibrium polar angle θ_0. On the other hand, the difference of the Hall resistances for positive and

negative currents is given by

$$\begin{aligned} R_{xy}^{+} - R_{xy}^{-} &= R_{\mathrm{AHE}} \sin\theta_0(-\Delta\theta + 2\xi \sin\theta_0 \Delta\varphi) \quad , \quad \varphi_H = \varphi_0 = 0 \quad \text{and} \\ R_{xy}^{+} - R_{xy}^{-} &= R_{\mathrm{AHE}} \sin\theta_0(-\Delta\theta - 2\xi \sin\theta_0 \Delta\varphi) \quad , \quad \varphi_H = \varphi_0 = \tfrac{\pi}{2} \ . \end{aligned} \tag{5.39}$$

Following the treatment of sec. 5.2.1, we find from eq. 5.16 and 5.17 that the deviation angles in the longitudinal configuration are given by

$$\begin{aligned} \Delta\theta &= \tfrac{H_{\parallel}}{H_{\mathrm{k}} \cos(2\theta_0) + H \cos(\theta_H - \theta_0)} \quad \text{and} \\ \Delta\varphi &= \tfrac{H_{\perp}}{-H_{\mathrm{a}} \sin\theta_0 + H \sin\theta_H} \ , \end{aligned} \tag{5.40}$$

while, for the transverse configuration

$$\begin{aligned} \Delta\theta == \tfrac{\cos\theta_0 H_{\perp}}{H_{\mathrm{k}} \cos(2\theta_0) + H \cos(\theta_H - \theta_0)} \quad \text{and} \\ \Delta\varphi = -\tfrac{\cos\theta_0 H_{\parallel}}{H_{\mathrm{a}} \sin\theta_0 + H \sin\theta_H} \ . \end{aligned} \tag{5.41}$$

By measuring the Hall voltage in both configurations with positive and negative injected current it is then possible to solve the system of equations 5.38, 5.39, 5.40 and 5.41 in order to obtain the effective fields $H_{\parallel}$ and $H_{\perp}$.

5.4.2 Measurements results and conclusions

Our samples consist of the same Pt-based thin films stacks used for the ac Hall measurements (sec. 5.2): Pt(5)/Hf(0.3)/$Co_{20}Fe_{60}B_{20}$(0.9)/MgO (1.6)/Ta(1) (nominal thickness in nm) grown by high vacuum dc and rf sputtering on thermally oxidised Si substrates.

The 60 × 20 µm^2 Hall bars were patterned by UV lithography and Ar ion milling. Cu/Au have been chosen for the contacts as usual, and have been deposited by e-beam evaporation and lift-off technique. The interfacial Hf dusting layer is sufficient to achieve PMA, without thermal annealing, which results in a degradation of the PMA.

The results of the measurement data analysis are shown in Fig. 5.19. We determine that the data recorded is only reliable to infer the two spin-orbit effective fields in the range $\theta = 30°$ and $65°$ and we do not trust the quality of the data outside this range. When the magnetic moment is almost completely out-of-plane or almost parallel to the plane the difference between the Hall voltages with positive and negative current is below the noise level. From the average value of $\mu_0 H_{\parallel}$ we estimate a spin Hall angle of 0.067, in agreement with previous measurements. It is important to note that the noise in this kind of measurement is higher than in other techniques. This is the reason why only Pt have been measured this way.

5.5 Current-induced switching of PMA structures

The electric manipulation of the magnetic moment of a ferromagnetic layer in a FM/HM bilayer is not only restricted to small deviations from the equilibrium position. The switching of the magnetisation of the FM layer in both in-plane and perpendicularly magnetised samples has been observed [1, 32, 35, 36] when an in-plane current of sufficient amplitude is injected. The case of PMA layers is of particular

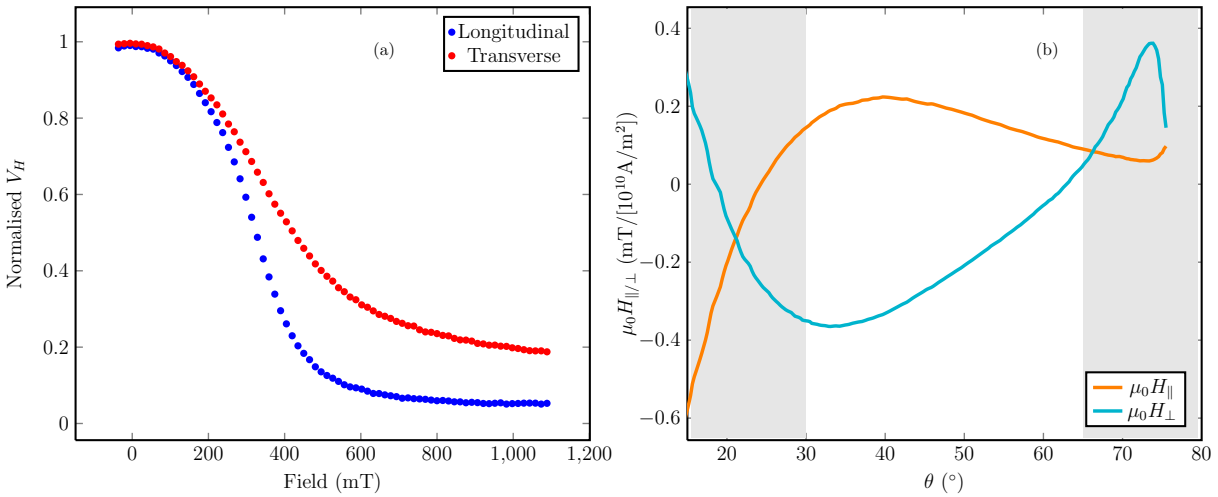

Figure 5.19: Results from dc Hall measurements on a Pt/CoFeB/MgO/Ta sample. (a): normalised Hall voltage V_{H} as a function of an in-plane applied field for longitudinal and transverse configurations. (b): estimated effective fields $\mu_0 H_{\parallel}$ and $\mu_0 H_{\perp}$ as a function of θ(direction of the FM magnetic moment). The grey areas indicate the regions where the data are not reliable.

interest because of its potential application in current magnetic data storage devices.

The experiments described in this section have been done in collaboration with YongChang Lau.

5.5.1 Theory

We consider once again the perpendicularly magnetised FM/HM stack represented in Fig. 5.1. A current injected along the $\hat{x}$ direction will, as discussed in sec. 2.3.6, generate a pure spin current from the HM layer towards the $\hat{z}$ direction, which will in turn transfer angular momentum to the FM layer. If this current is sufficiently large, it will reverse the magnetisation of the FM layer from $+\hat{z}$ to $-\hat{z}$ or vice-versa. This process is only possible if a weak in-plane external field is applied parallel to the injected current ($\hat{x}$ direction). The switching is irreversible, but it is possible to bring the magnetic moment back to the initial state by inverting the current direction, since the switching direction is given by the sign of the scalar product $\vec{J} \cdot \vec{H}_{\mathrm{ex}}$.

The first explanation of this effect has been given in a simple macrospin picture using the Stoner-Wohlfarth model [32]. The equilibrium position of the magnetisation as a function of the applied field and the spin-orbit torque τ_{so} can be found by imposing zero total torque as in

$$\tau_{\mathrm{tot}} = \tau_{\mathrm{so}} + \mu_0 H_{\mathrm{ex}} \sin(\theta_H - \theta) - \mu_0 H_{\mathrm{an}} \sin\theta \cos\theta = 0 \ , \tag{5.42}$$

with $\mu_0 H_{\mathrm{an}}$ the effective anisotropy field in the perpendicular direction and θ_H close to $\pi/2$ (in-plane external field). Considering the main contribution for the spin-orbit torque coming from the spin Hall effect, the torque is given by $\tau_{\mathrm{so}} \propto \vec{m} \times (\hat{y} \times \vec{m}) \propto \hat{y}$. As the current is increased at a constant external field, the effect of the spin Hall torque is to rotate the magnetic moment in the $\hat{y}\hat{z}$ plane until, when the current reaches a critical value J_{cr} that is related to the anisotropy strength and the spin Hall angle, an abrupt hysteretic switching is observed. The in-plane external field is necessary since it slightly tilts the magnetisation, giving a component parallel to the current direction that allows the torque from the spin Hall effect to produce a perpendicular equivalent field. This field breaks the $\hat{y}\hat{z}$ symmetry and enables the switching [3].

Although giving a reasonable qualitative explanation of the process, this simple macrospin model has proved inadequate when it comes to providing a quantitative understanding of the reversal process. The current-induced equivalent field needed to switch the magnetisation of a sample with PMA should be of the order of $H_{\mathrm{an}}/2$. The anisotropy field is usually large for PMA samples while the switching occurs for much lower current-induced fields. The cause of this behaviour is that the reversal is caused by (thermally assisted) domain walls depinning and propagation instead of the coherent rotation of a macrospin [35]. This process requires much lower effective fields, due to the much higher susceptibility of the domain walls as soon as the effective pinning field is overcome. This mechanism is well known in magnetism since it is easily seen in the difference between the anisotropy field and the coercive field in a sample with uniaxial anisotropy (see sec. 2.1.6). In a simple macrospin model, the anisotropy field and the coercive field should assume the same value, while in reality the coercive field is always smaller due to the lower domain walls depinning field. The stability factor for the depinning, taking into account the spin Hall torque and Joule heating, can be written as a function of the injected current as [35]

$$\Delta^* = \left[\frac{E_{\mathrm{p}}(J)}{k_{\mathrm{B}}(T_0 + \kappa J^2)}\right]\left[1 - \frac{H^z_{\mathrm{ex}} + H^z_{\mathrm{SH}}(J)}{H^z_{\mathrm{p},0}(J)}\right] , \tag{5.43}$$

where H^z_{ex} is an out-of-plane applied field, $T_0 = 295\,\mathrm{K}$, E_{p} is the depinning energy barrier, H_{SH} is the spin Hall effective field and $H^z_{\mathrm{p},0}$ is the effective depinning field in the absence of thermal fluctuations. Since we have $H_{\mathrm{SH}} \propto \vec{m} \times \hat{y}$, the effective field will possess a perpendicular component H^z_{SH} only if $\vec{m}$ has an $\hat{x}$ component. It has been shown [3] that, in order to obtain an effective displacement of a domain wall in a PMA material, the wall has to be of the Néel type (where the magnetisation rotates in the $\hat{x}\hat{z}$ axis) rather than the Bloch type (where the magnetisation rotates in the $\hat{y}\hat{z}$ axis). Since Bloch walls are energetically favourable in thin magnetic layers, the in-plane applied field necessary to obtain a m_x component of the magnetisation in the wall width. Moreover, it has been shown [33] that at the interfaces of a HM/FM/Oxide multilayer there can be a strong Dzyaloshinskii-Moriya interaction (DMI), due to the broken symmetry of the interfaces. Domain walls therefore have a fixed chirality, left- or right-handed (see Fig. 5.20(a)). depending on the sign of the DMI.

If only DMI is present, the in-plane magnetisation at the centre of a domain wall on all sides of an enclosed domain will not have the same direction over all the length of the wall. Therefore, the spin-orbit effective field will have different orientations at different locations and the net effect will only be a displacement of the domain wall in one direction. In order to obtain the expansion or the annihilation of the domain, it is necessary to apply an in-plane field that will break the DMI-induced chirality and force a m_x component along all sections of the wall (see Fig. 5.20). The signs of this magnetic field and of the current determine the resulting magnetic state, *i.e.*, the switching is governed by the sign of the scalar product $\vec{J} \cdot \vec{H}_{\mathrm{ex}}$.

5.5.2 Measurement results

We measured the current-induced switching of PMA samples in stacks of Pt(5)/Hf(0.3)/$Co_{20}Fe_{60}B_{20}$(0.9)/MgO(1.6)/Ta(1), and W(4)/$Co_{20}Fe_{60}B_{20}$(0.9)/MgO(1.6)/Ta(1) (nominal thickness in nm) grown by high vacuum dc and rf sputtering on thermally oxidised Si substrates. Those samples are the same as these used for the ac and dc Hall measurements. They have been patterned into Hall bars by UV lithography as described in the previous sections (see Appendix B).

The samples have been placed in the gap of an electromagnet with the applied field in the plane and parallel to the injected current. The measurement was performed as follows. A constant magnetic field

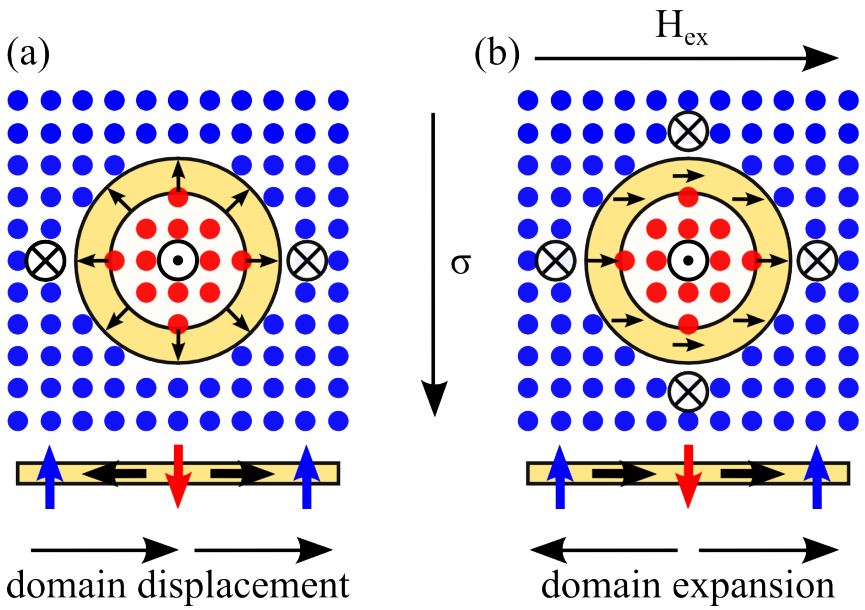

Figure 5.20: Schematic illustration of an up-down domain wall (red dots = down moments, blue dots = up moments). In (a) the Dzyaloshinskii-Moriya interaction (DMI) fixes the chirality (left-handed) of the domain walls. The directions of the spin Hall effective fields acting on the left and right sections on the wall is indicated, where we have $m \approx \pm m_x$. In this case, there is no domain nucleation/annihilation but only a displacement, hence no reversal of the magnetisation is possible. In (b) an external field is applied along $\hat{x}$, imposing the chirality of the domain walls. Therefore, nucleation or annihilation of the domain is possible under the effect of a spin-orbit field. From ref. [35].

is applied in plane on a sample with out-of-plane magnetic moment, saturated prior to the measurement. A current pulse of duration 10 ms is then sent into the Hall bars. Injecting pulses of current instead of a constant dc signal reduces the heating of the sample, allowing it to dissipate the heat before the following pulse. After the pulse, a low dc current (0.1 mA or $10^9 \mathrm{A\,m^{-2}}$) is applied in order to measure the anomalous Hall voltage, therefore probing the magnetic configuration of the bar. This current is chosen to be low in order to avoid any additional effect on the magnetisation state and avoid additional heating. Using this method, it is possible to measure the anomalous Hall voltage using the same probing current and with the sample at room temperature, if it had enough time to cool down after the current pulse. The results are shown in Fig. 5.21 for a sample of W/CoFeB/MgO.

Conclusions

We were able to switch the magnetic moment of a PMA magnetic layer using the spin-orbit torques of the HM layers. As predicted by the theory, the reversal direction is given by the sign of the dot product $\vec{J} \cdot \vec{H}_{\mathrm{ex}}$. In addition, the relatively low current densities at which the switching is observed confirms the inadequacy of the macrospin model. No switching is observed with no applied field or for in-plane applied field perpendicular to the current direction. The nature of the switching (due to the domain wall depinning) does not allow for any reliable estimation of the spin-orbit torques acting on the magnetic moment.

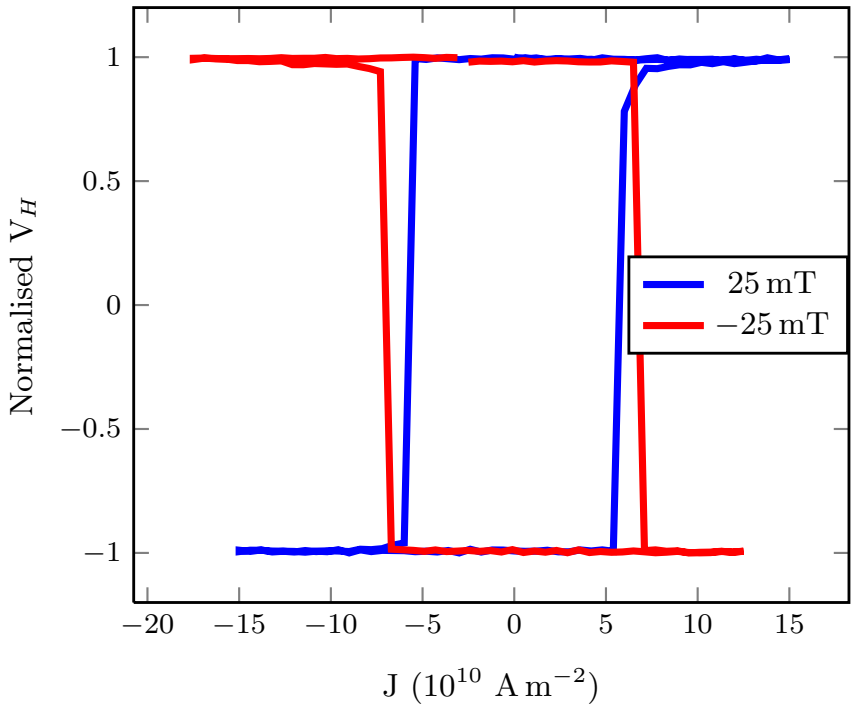

Figure 5.21: Current switching of the magnetisation of W/CoFeB/MgO as a function of an injected pulsed current with 25 mT and −25 mT longitudinal applied field $\mu_0 H_{\text{ex}}$.

5.6 Ørsted field calculation

The Ørsted field is calculated using the method described in ref. [17]. We consider a conductive layer of width w and thickness d represented in red in Fig. 5.22. The centre of the $\hat{z}$ axis is placed in correspondence to the top surface of the layer, the $\hat{y}$ axis centre is located at the centre of the layer along the width direction and the $\hat{x}$ axis is parallel to the current direction. The $\hat{y}$ and $\hat{z}$ components of the Ørsted field (in mT) at every coordinate (y, z) in the red layer is given by

$$
\begin{aligned}
B_y(y,z) &= \tfrac{I}{wd}\left[U_y^+(y,z) - D_y^+(y,z) + U_y^-(y,z) - D_y^-(y,z)\right] \times 10^{-4}\ , \\
U_y^\pm(y,z) &= 2(z+d)\arctan\left[\tfrac{w/2\pm y}{2}\right] + \left(\tfrac{w}{2}\pm y\right)\ln\left[\left(\tfrac{w}{2}\pm y\right)^2 + (z+d)^2\right]\ , \\
D_y^\pm(y,z) &= 2z\arctan\left[\tfrac{w/2\pm y}{2}\right] + \left(\tfrac{w}{2}\pm y\right)\ln\left[\left(\tfrac{w}{2}\pm y\right)^2 + z^2\right]\ , \\
B_z(y,z) &= \tfrac{I}{wd}\left[U_z^+(y,z) - D_z^+(y,z) - U_z^-(y,z) + D_z^-(y,z)\right] \times 10^{-4}\ , \\
U_z^\pm(y,z) &= 2\left(\tfrac{w}{2}\pm y\right)\arctan\left[\tfrac{z+d}{w/2\pm y}\right] + (z+d)\ln\left[\left(\tfrac{w}{2}\pm y\right)^2 + (z+d)^2\right]\ , \\
D_z^\pm(y,z) &= 2\left(\tfrac{w}{2}\pm y\right)\arctan\left[\tfrac{z}{w/2\pm y}\right] + (z+d)\ln\left[\left(\tfrac{w}{2}\pm y\right)^2 + z^2\right]\ .
\end{aligned}
\tag{5.44}
$$

In order to obtain the average field in the magnetic (red) layer placed above the conductive heavy metal (blue) layer, it is necessary to integrate the field along $\hat{y}$ from $-w/2$ to $w/2$ and along $\hat{z}$ from 0 to t, the thickness of the magnetic layer.

For all our measurements the Ørsted field was found to be negligibly small. The maximum value was in W-based samples; $\mu_0 H_{\text{Ørsted}} = 0.062\,\text{mT}$. Therefore, the Ørsted field can be neglected in all our calculations of the transverse effective fields.

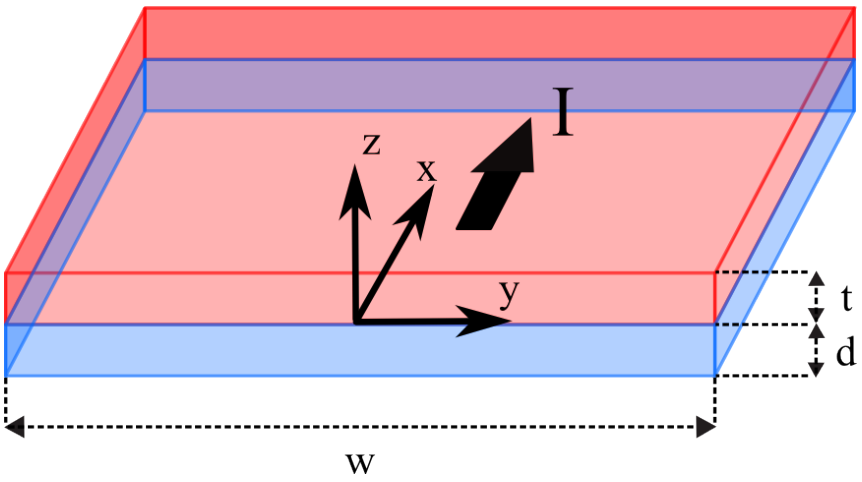

Figure 5.22: Schematic illustration of the coordinate system for the calculation of the Ørsted field. The current is assumed to flow in the bottom (blue) layer, while the profile of the field is calculated in the upper layer (red).

5.7 Spin torque-FMR technique

5.7.1 Theory

A third method used to measure the spin Hall angle of a material is the spin torque ferromagnetic resonance (ST-FMR) [24, 30, 37, 38], discussed in sec. 3.6.2. The samples used for this technique are bilayers consisting of a heavy metal with high spin-orbit coupling and a soft ferromagnetic layer with in-plane magnetisation. When an rf current is injected in the stack, the spin-orbit torques and the Ørsted field arising from the current flowing in the HM layer excite the precession of the magnetisation of the FM layer. As a result of the (weak) spin-orbit coupling in the latter, the resistance of the stack varies because of the anisotropic magnetoresistance (AMR) effect as $(\vec{M}\cdot\vec{J})\vec{M}$ [39]. This variation of the resistance happens at the same frequency of the rf current that provides the excitation for the precession. The coupling between the injected current and the oscillation of the resistance results in the generation of a dc voltage across the sample. Following the derivation presented in sec. 3.6.2 and in ref. [30], this dc voltage is maximised for an in-plane applied field with $\varphi_H = 45°$ and is given by the equation

$$V_{\rm dc} = -\frac{1}{4}\frac{dR}{d\varphi_H}\frac{\gamma_0 I_{\rm rf}\cos\theta}{\Delta 2\pi (df/dH_{\rm ex})|_{H_{\rm ex}=H_{res}}}[SF_{\rm s}(H_{\rm ex}) + AF_{\rm a}(H_{\rm ex})]\ , \tag{5.45}$$

where $F_{\rm s}(H_{\rm ex}) = \Delta^2/[\Delta^2 + (H_{\rm ex} - H_{res})^2]$ is a symmetric Lorentzian centred at H_{res} with linewidth Δ, $F_{\rm a}(H_{\rm ex}) = F_{\rm s}(H_{\rm ex})(H_{\rm ex} - H_{res})/\Delta$ is an antisymmetric Lorentzian, $S = \hbar J_{\rm rf}/(2e\mu_0 M_{\rm s} t)$, $A = H_{\rm rf}[1 + (M_{\rm s}/H_{\rm ex})]^{1/2}$, H_{res} is the resonance field and t is the thickness of the ferromagnetic layer.

Therefore, the shape of the dc voltage as a function of the external field is an asymmetric Lorentzian; the sum of a symmetric and an antisymmetric Lorentzian, centred at the resonant field (Fig. 5.23). The symmetric Lorentzian results from the transverse (anti-damping) torque, while the antisymmetric one results from the longitudinal (field-like) torque. As discussed in sec. 5.1 early studies considered the symmetric signal as coming only from the spin Hall effect, while the asymmetric one only from the Ørsted field. With these assumptions, it is possible to evaluate the spin Hall angle using the ratio between the coefficients S and A. Later, it was found that this ratio is heavily influenced by the longitudinal torque resulting from the Rashba field or from a non transparent interface resistance. In addition, the unknown

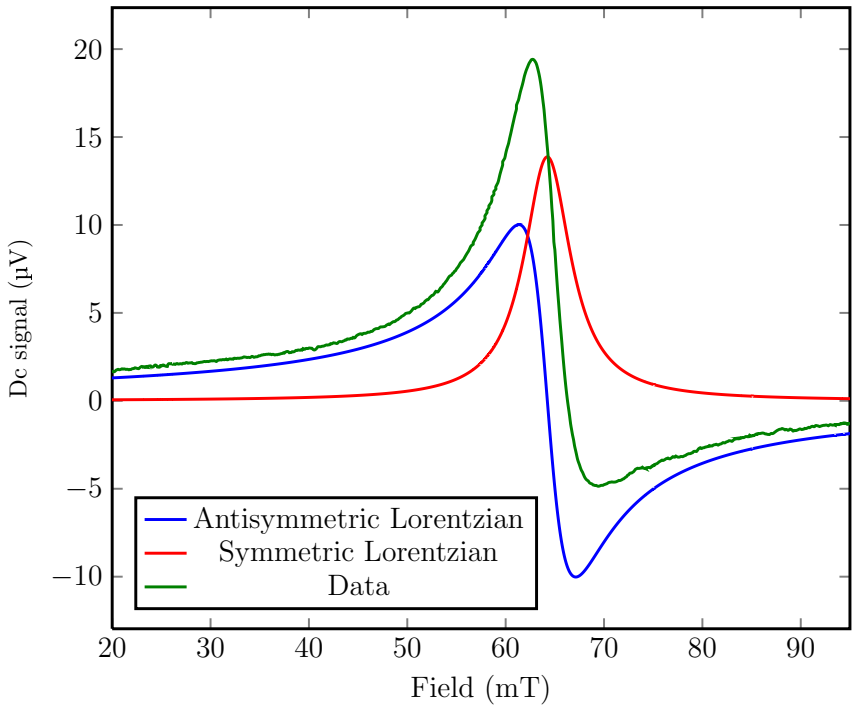

Figure 5.23: ST-FMR signal for a W/CoFeB sample. The measured dc voltage is decomposed into an antisymmetric and a symmetric Lorentzians.

relative phase shift between the rf current and the magnetisation precession mixes the two Lorentzians even in the absence of a longitudinal torque. This phase is theoretically 0° but in practise it can assume very different values, especially when dealing with high resistive samples such as the ones with W or Ta. It has also been shown that is is sample dependent. Therefore, it is not possible to calibrate the phase shift even by using reference samples with no heavy metal layer such as Cu/FM bilayers (see Fig. 5.24) [40].

A different approach consists of injecting a dc current together with the rf one. In this case it is possible to measure the variation of the linewidth Δ of the dc signal as a function of the dc current. The linewidth is directly related to the Gilbert damping parameter α. Therefore, the slope of the linewidth vs current gives information about the anti-damping torque alone [41–43]. In this kind of measurement the lineshape of the signal and the phase between rf current and magnetic moment precession are not important. In the first approximation, the transverse (anti-damping) torque is only due to the spin Hall effect. Therefore, it should be possible to extract the spin Hall angle from this kind of measurement, using the equation (see sec. 3.6.2)

$$\Delta = \frac{2\pi f}{\gamma_0}\left[\alpha + \frac{\sin\varphi_H}{(H_{\mathrm{ex}} + M_{\mathrm{s}}/2)\mu_0 M_{\mathrm{s}} t}\frac{\hbar\theta_{\mathrm{SH}} J_{\mathrm{c}}}{2e}\right] . \tag{5.46}$$

In addition, it is possible to estimate the spin diffusion length λ of the HM layer by measuring the spin Hall angle of samples with different thicknesses of the HM layer t and by fitting the data with the equation [30]

$$\theta_{\mathrm{SH}}(t)/\theta_{\mathrm{SH}}(\infty) = 1 - sech(t/\lambda) . \tag{5.47}$$

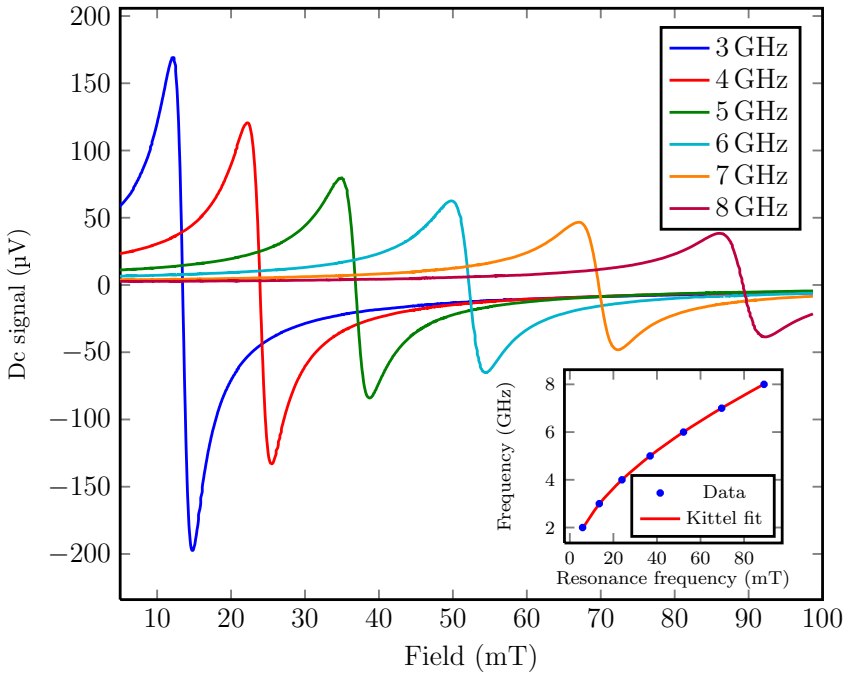

Figure 5.24: ST-FMR signal for a Cu (10)/NiFe (10) sample (thickness in nm). The measured dc voltage has an almost perfect antisymmetric lineshape, with the best results obtained at the frequency of 7 GHz. The inset shows a plot of the excitation frequency against the resonance field and the fit using Kittel law 2.38.

5.7.2 Results

We performed ST-FMR measurements on Pt and W-based samples with 10 nm thick NiFe and CoFeB layers respectively in order to evaluate the SHA and the spin diffusion lengths λ_W and λ_{Pt} [38]. The samples are patterned into Hall bars of various dimensions using UV lithography and ion milling. After another step of lithography, thick Cu/Au contact are then deposited by thermal evaporation and lift-off. Before the deposition a gentle Ar ion etch is performed *in situ* in order to remove any oxidised layer and improve the electric contact at the interface.

The magnetic moment is saturated in-plane by applying a magnetic field at a certain angle φ_H with respect to the current direction. An rf current is injected in the plane of the layers using a GS (ground signal) probe connected to a Rohde&Schwarz SMF 100A signal generator. The resulting rf and dc voltage are separated from each other using a bias tee. The measurement is performed with a double modulation lock-in technique. The rf current is chopped at a high frequency (1.234 kHz) while the external field is modulated at a much lower frequency (17 Hz), in order to avoid any overlap of the signals. The output is then demodulated using two Stanford Research SR830 lock-in amplifiers in cascade.

We estimated the spin diffusion length λ of Pt and W as shown in Fig. 5.25 and 5.26. We obtain the values of $\lambda_{Pt} \sim 1.25$ nm and $\lambda_W \sim 1$ nm.

Conclusions

Using the equation (see sec. 3.6.2)

$$\frac{J_s}{J_c} = \frac{S}{A}\frac{e\mu_0 M_s t d}{\hbar}\left[1 + (M_s/H_{ex})\right]^{1/2} , \tag{5.48}$$

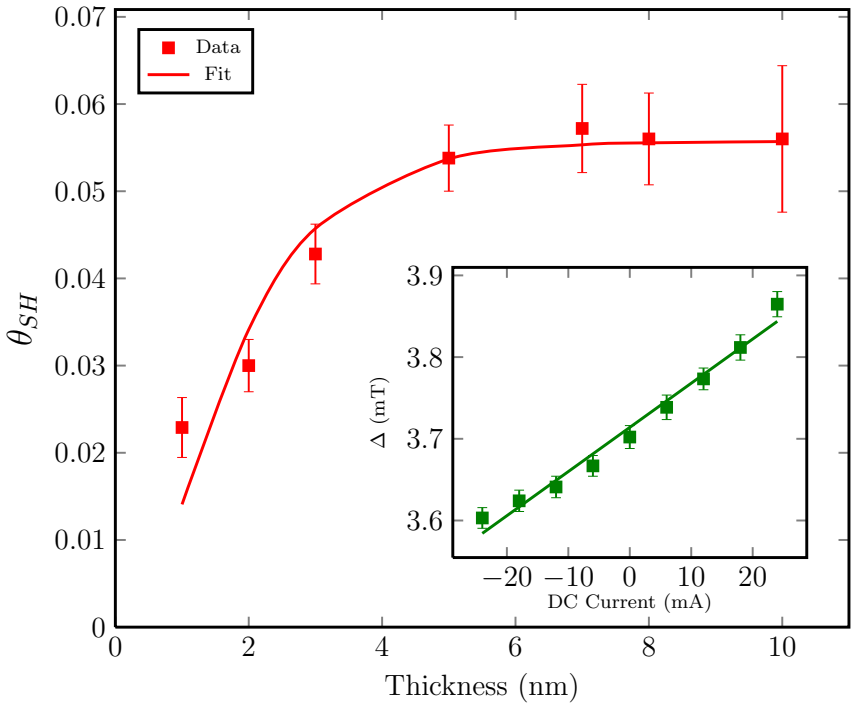

Figure 5.25: Thickness dependence of the spin Hall angle of Pt, fitted using eq. 5.47. The inset shows a representative dataset for the change in the linewidth Δ with the injected dc current.

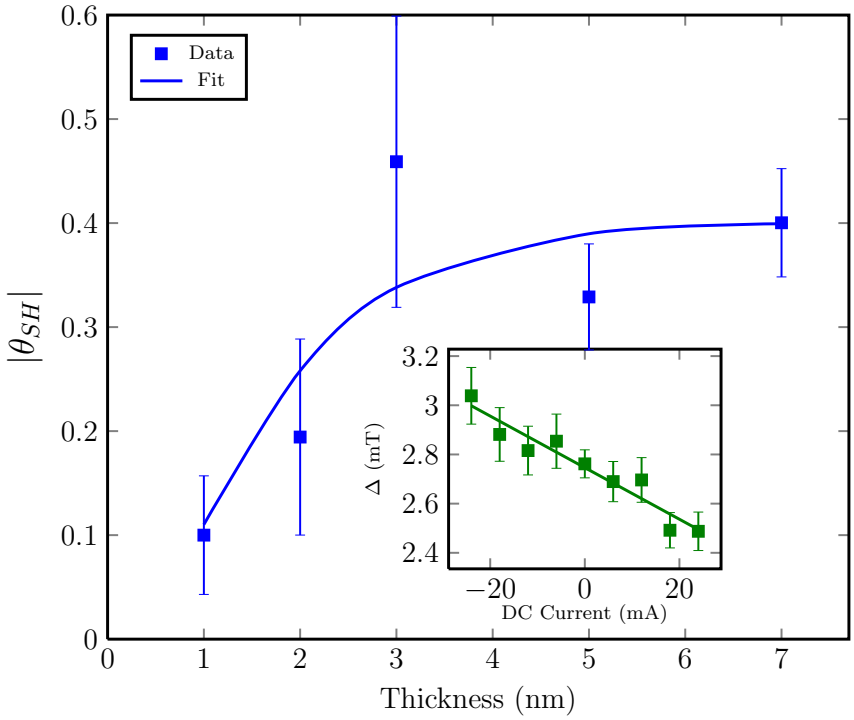

Figure 5.26: Thickness dependence of the spin Hall angle of W (absolute value), fitted using eq. 5.47. The inset shows a representative dataset for the change in the linewidth Δ with the injected dc current.

and eq. 5.47 we can extrapolate the bulk values $\theta_{SH}^{Pt} = 0.055$ and $\theta_{SH}^{W} = -0.384$. These consistent values of the spin Hall angle with opposite sign for Pt and W are in good agreement with previously published results [23, 25] and our previous estimates.

5.8 ISHE and Spin pumping technique

The spin pumping techniques and the inverse spin Hall effect (ISHE) [25–29, 44–48] have been described in sec. 2.3.4 and 3.6.3, respectively. For this type of experiment, the samples consist of HM/FM bilayers, where the FM is a soft ferromagnet that shows in-plane magnetisation due to shape anisotropy. We measured the ISHE signal of Pt/NiFe samples in our TE_{011} cavity as previously described, with a fixed frequency of 9.87 GHz for the rf electromagnetic field and varying the dc magnetic field. The stacks have been grown by dc sputtering in high vacuum on MgO or Al_2O_3 substrates. We found that it is important to use dielectric substrates in order to avoid any unnecessary perturbation of the cavity. The resistivity of each layer has been characterised individually and we obtained $\rho = 55.7\,\mu\Omega\,\text{cm}$ and $\rho = 20.4\,\mu\Omega\,\text{cm}$ for NiFe and Pt, respectively. A small amount of DPPH powder has been placed on the surface of the samples in order to calibrate the amplitude of the rf magnetic field as explained in sec. 3.6.3. Its value varied depending on the sample, but it was in the order of 0.03 mT. The samples were cut in order to fit the entrance of the cavity, with their length about 4 mm.

As discussed in sec. 3.6.3, ISHE measurements rely on the detection of the voltage generated in the HM layer when the applied field matches the resonance conditions for the FM layer. This voltage is due to the spin dependent scattering in the HM and to the injected spin current originating from the spin pumping from the FM layer. The signal of interest must be extracted from the raw data by fitting the lineshape as a sum of a symmetric and an antisymmetric Lorentzian. In order to obtain useful information, the relative phase between the electric current and the oscillating magnetic field must be known. In an rf cavity this phase should be $\pi/2$, so that the symmetric Lorentzian is due only to the ISHE, while the antisymmetric Lorentzian is due only to the AHE, but in practice this relationship is not always satisfied. In order to verify the validity of the technique, we measured the dc voltage in a sample consisting only of a NiFe layer. As shown in Fig. 5.27, the signal has an almost completely antisymmetric lineshape. Since there is no HM layer, it must result only from the AHE: the measured lineshape proves that the phase between the electric current and the oscillating magnetic field is $\sim \pi/2$.

Fig. 5.29 shows the ferromagnetic resonance (FMR) signal for the same NiFe-only sample and for a Pt/NiFe sample as a function of the applied dc field. The resonance appears at ∼120 mT. The Pt/NiFe sample signal has broader linewidth, resulting from the additional damping due to the spin pumping from the NiFe layer into the Pt layer, as discussed in sec. 3.6.3. Fig. 5.28 shows the dc voltage for the Pt/NiFe sample, divided into symmetric and antisymmetric lineshapes. The effective magnetisation of the FM layer has been deduced fitting the resonance frequency to Kittel law eq. 2.38 for an in-plane magnetised soft material. Using eq. 2.64, 3.22 and 3.23 with the parameters $\lambda_{NM} = 1.25\,\text{nm}$, $\mu_0 \Delta H_{NM/FM} = 7\,\text{mT}$ and $\mu_0 \Delta H_{FM} = 3.3\,\text{mT}$ we obtain a spin Hall angle for bulk Pt of 0.077, in good agreement with literature values [27, 44] and our previous characterisation.

One of the issues related to this technique concerns the conductivity mismatch between the FM and the HM layers. The equivalent circuit of the bilayer is represented in Fig. 3.37, sec. 3.6.3. The two layers are considered as two resistances in parallel through which the charge current is flowing. If the conductivity of the FM layer is much higher than the one of the HM layer, the latter will shunt the current and the signal coming from the ISHE will be more difficult to detect and analyse. In addition, the difference in the linewidths of the FMR signals becomes smaller and hard to detect. That is not the case in the Pt/NiFe

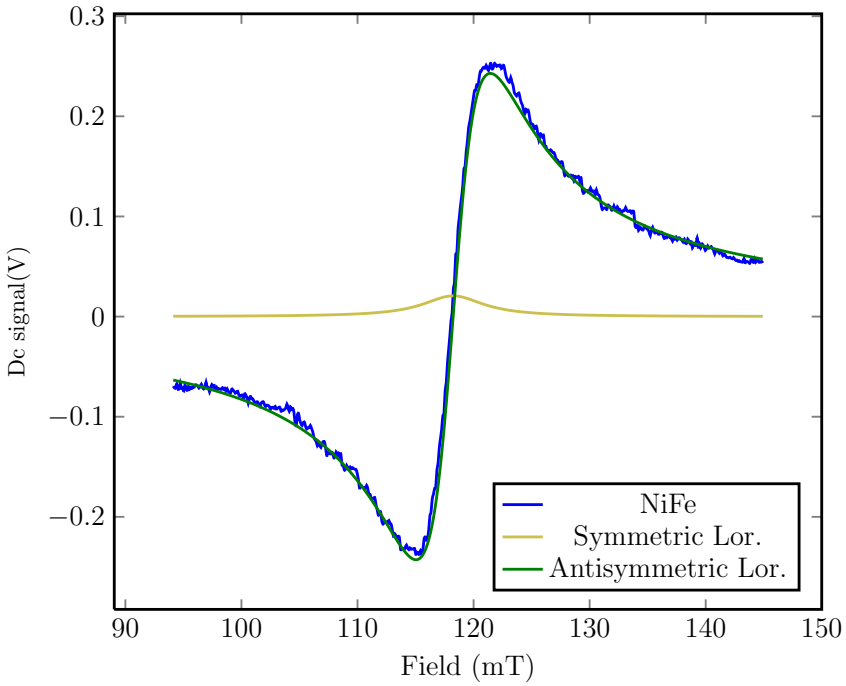

Figure 5.27: Dc voltage signal of a NiFe-only sample measured in the rf cavity. The signal, originating from the anomalous Hall effect, has an almost completely antisymmetric lineshape, indicating that the phase between the electric and magnetic field is $\pi/2$.

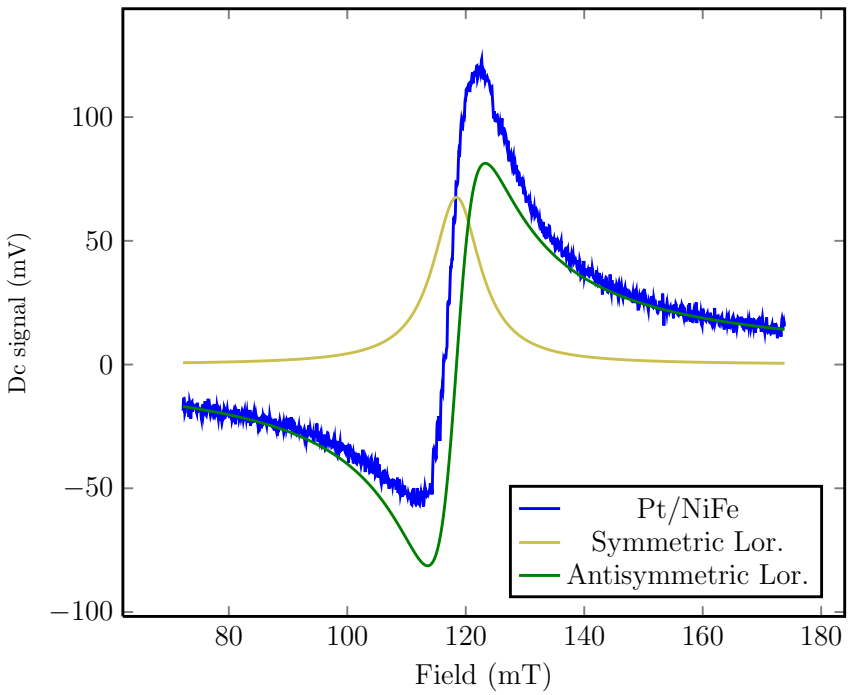

Figure 5.28: Dc voltage signal of a Pt/NiFe sample measured in the rf cavity. The signal is divided into an antisymmetric Lorentzian, arising from the AHE, and a symmetric Lorentzian, arising from the ISHE.

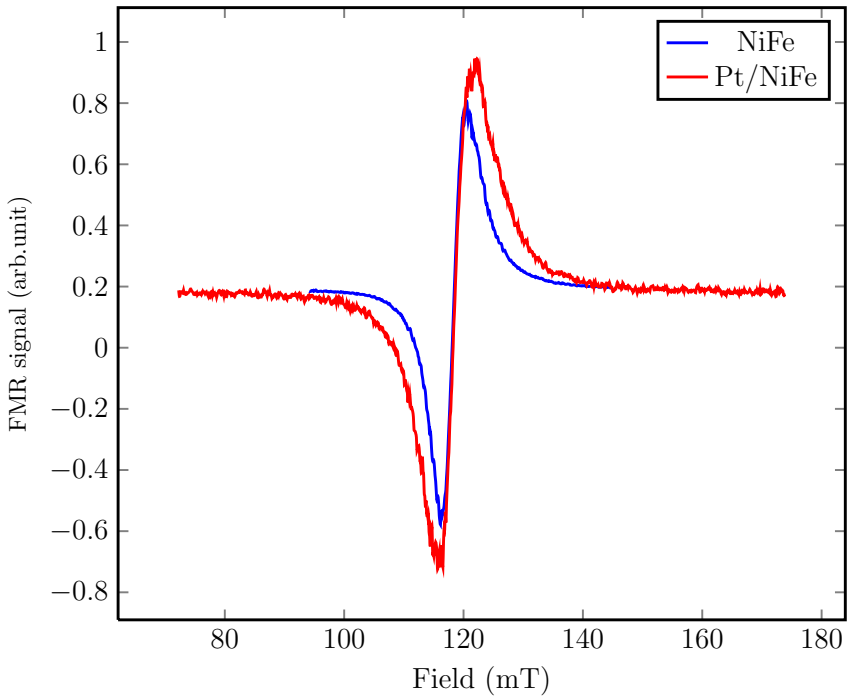

Figure 5.29: Ferromagnetic resonance of the NiFe-only and the Pt/NiFe sample. The latter shows a broader linewidth, resulting from the additional damping due to the spin pumping.

bilayer: the conductivities of the two materials are similar.

On the other hand, when we tried to measure a Ta/NiFe sample the high resistivity of Ta ($\sim$140 µΩ cm) with respect to the one of NiFe didn't allow us to obtain reliable measurements. Therefore, we prepared samples of Ta/CoFeB bilayers on MgO and Al_3O_2 substrates. The resistivity of CoFeB is around 170 µΩ cm, comparable to the one of Ta, and its magnetic properties are similar to the ones of NiFe. Its higher magnetisation shifts the resonance field to $\sim$70 mT, but there is still no magneto-crystalline anisotropy for thick layers. Unfortunately, the measurements performed on a CoFeB-only sample, in order to verify the phase shift between the electric and magnetic fields, showed that the ideal condition of a $\pi/2$ shift is not verified for this material. As clearly shown in Fig. 5.30, the measured dc voltage has a strong symmetric component and the ratio between the asymmetric and symmetric Lorentzians implies a phase between the electric current and the magnetic field of about 20°. In addition, the same measurement on nominally identical samples didn't give the same result. The phase shift can vary of ±4° from sample to sample.

We have measured the Ta/CoFeB samples following the procedure of reference [49], *i.e.*, taking into account the phase shift of CoFeB by subtracting the symmetric lineshapes present in the bilayer and monolayer samples (Fig. 5.31 and 5.32). Using the value of $\lambda_{NM} = 1$ nm, $\mu_0\Delta H_{NM/FM} = 2.72$ mT and $\mu_0\Delta H_{FM} = 2.33$ mT we obtain a spin Hall angle varying from 0.083 to 0.05 depending on the phase shift assumed.

5.8.1 Conclusions

We found that the ISHE-spin pumping technique is reliable if the FM and HM layers have similar resistivity and if the phase between electric current and magnetic field is known. While the first condition can be achieved by choosing the appropriate HM/FM materials combination, it is not possible to determine the

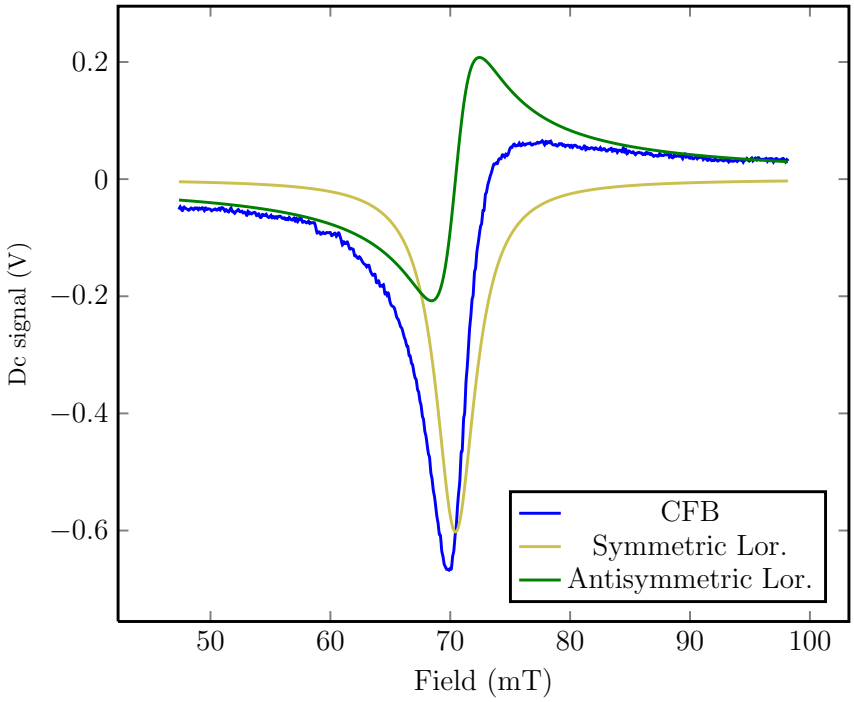

Figure 5.30: Dc voltage signal of a CoFeB-only sample measured in the rf cavity. The signal is a mixture of antisymmetric and symmetric Lorentzians, indicating that the phase between the electric and magnetic field is ∼20°.

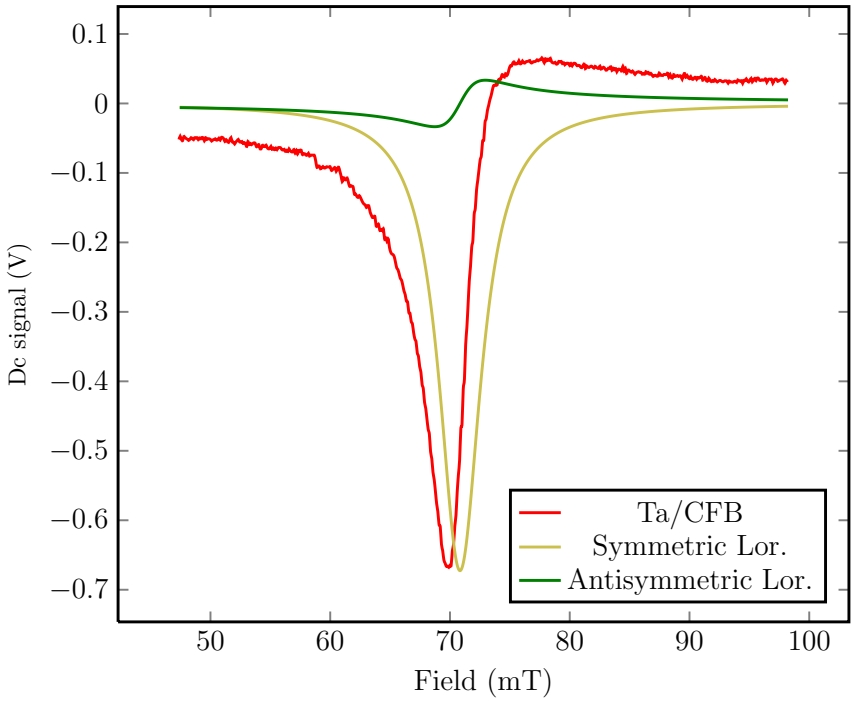

Figure 5.31: Dc voltage signal of a Ta/CoFeB sample measured in the rf cavity. The signal is divided into an antisymmetric Lorentzian.

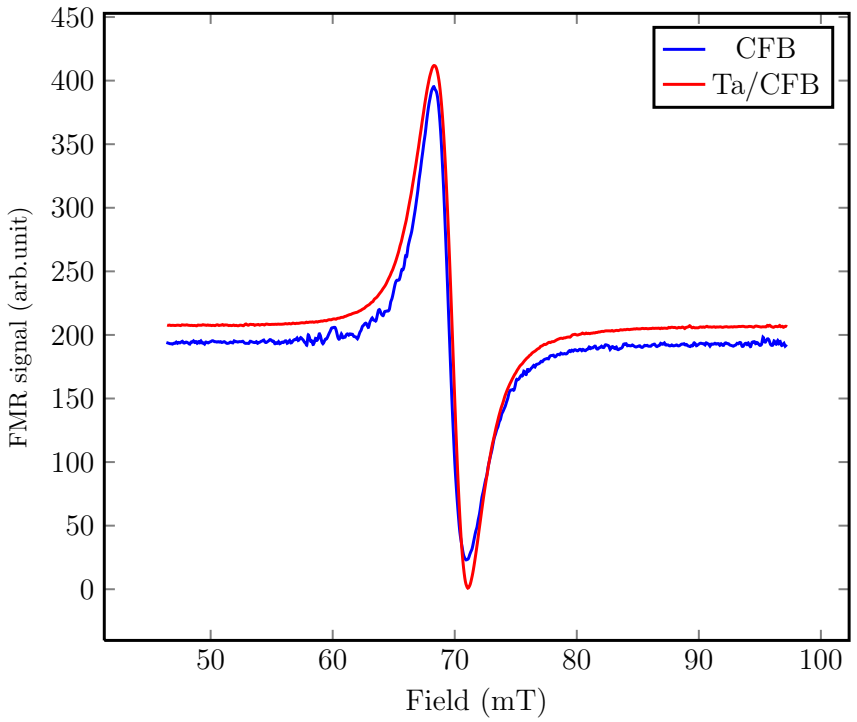

Figure 5.32: Ferromagnetic resonance of the CoFeB and the Ta/CoFeB sample. The latter shows a broader linewidth, resulting from the additional damping due to the spin pumping effect.

phase shift unambiguously. In the case of the Pt/NiFe samples the phase seems to assume the ideal value of $\pi/2$ in the control sample. While there is no assurance that it doesn't change dramatically in the HM/FM samples, the obtained value for the spin Hall angle is in agreement with our previous measurements. In the case of the Ta/CoFeB samples, the degree of uncertainty in the phase-shift doesn't doesn't allow for a very reliable determination of the spin Hall angle of a material, and other techniques have to be used.

5.9 Future work

The investigation of the effective fields and torques arising from spin-orbit interaction is still a lively and ever-changing field of research. The next steps of research should focus on the understanding of the proximity-induced PHE in W/CoFeB stacks. Apart from the intrinsic scientific interest, finding the answer to this question will allow to better interpret the behaviour of these materials and quantify the effectiveness of the spin Hall and Rashba effects.

The insulating ferrimagnet yttrium iron garnet (YIG, $Y_3Fe_5O_{12}$), grown on gadolinium gallium garnet (GGG, $Gd_3Ga_5O_{12}$) (111) substrates, has proved to be an excellent substitute for a conventional FM layer. Since it is perfectly insulating, the use of YIG will allow to perform ISHE measurement without having any electric current in the FM layer [25, 26, 29]. This will eliminate any difficulties in the determination of the current density flowing in the HM layer and in the separation of the lineshapes, since no AHE will be present. In addition, the recent discovery of the spin Hall magnetoresistance effect in ferromagnetic insulator/normal metal stacks [50–52] provides another method of characterisation of these materials. The optimisation of YIG will make it possible to develop this technique.

References

[1] C. O. Avci, K. Garello, C. Nistor, S. Godey, B. Ballesteros, A. Mugarza, A. Barla, M. Valvidares, E. Pellegrin, A. Ghosh, I. M. Miron, O. Boulle, S. Auffret, G. Gaudin & P. Gambardella. *Fieldlike and antidamping spin-orbit torques in as-grown and annealed Ta/CoFeB/MgO layers*. Phys. Rev. B, **89**:214419, Jun 2014. doi:10.1103/PhysRevB.89.214419.

[2] J. Slonczewski. *Current-driven excitation of magnetic multilayers*. Journal of Magnetism and Magnetic Materials, **159**(1–2):L1 , 1996. ISSN 0304-8853. doi:http://dx.doi.org/10.1016/0304-8853(96)00062-5.

[3] Haazen P. P. J., Murè E., Franken J. H., Lavrijsen R., Swagten H. J. M. & Koopmans B. *Domain wall depinning governed by the spin Hall effect*. Nat Mater, **12**(4):299, Apr 2013. ISSN 1476-1122. doi:http://dx.doi.org/10.1038/nmat3553. 10.1038/nmat3553.

[4] M. I. Dyakonov. *Future Trends in Microelectronics: From Nanophotonics to Sensors to Energy*. Wiley-IEEE Press, 2010.

[5] J. E. Hirsch. *Spin Hall effect*. Phys. Rev. Lett., **83**:1834, Aug 1999. doi:10.1103/PhysRevLett.83.1834.

[6] S. Zhang. *Spin Hall effect in the presence of spin diffusion*. Phys. Rev. Lett., **85**:393, Jul 2000. doi:10.1103/PhysRevLett.85.393.

[7] A. Hoffmann. *Spin Hall effects in metals*. Magnetics, IEEE Transactions on, **49**(10):5172, Oct 2013. ISSN 0018-9464. doi:10.1109/TMAG.2013.2262947.

[8] Y. A. Bychkov & E. I. Rashba. *Oscillatory effects and the magnetic susceptibility of carriers in inversion layers*. Journal of Physics C: Solid State Physics, **17**(33):6039, 1984.

[9] A. Manchon & S. Zhang. *Theory of spin torque due to spin-orbit coupling*. Phys. Rev. B, **79**:094422, Mar 2009. doi:10.1103/PhysRevB.79.094422.

[10] Mihai Miron Ioan, Gaudin Gilles, Auffret Stephane, Rodmacq Bernard, Schuhl Alain, Pizzini Stefania, Vogel Jan & Gambardella Pietro. *Current-driven spin torque induced by the Rashba effect in a ferromagnetic metal layer*. Nat Mater, **9**(3):230, Mar 2010. ISSN 1476-1122. doi:http://dx.doi.org/10.1038/nmat2613. 10.1038/nmat2613.

[11] J.-C. Rojas-Sánchez, N. Reyren, P. Laczkowski, W. Savero, J.-P. Attané, C. Deranlot, M. Jamet, J.-M. George, L. Vila & H. Jaffrès. *Spin pumping and inverse spin Hall effect in platinum: The essential role of spin-memory loss at metallic interfaces*. Phys. Rev. Lett., **112**:106602, Mar 2014. doi:10.1103/PhysRevLett.112.106602.

[12] N. Nagaosa. *Anomalous Hall effect –a new perspective–*. Journal of the Physical Society of Japan, **75**(4):042001, 2006. doi:10.1143/JPSJ.75.042001.

[13] N. Nagaosa, J. Sinova, S. Onoda, A. H. MacDonald & N. P. Ong. *Anomalous Hall effect*. Rev. Mod. Phys., **82**:1539, May 2010. doi:10.1103/RevModPhys.82.1539.

[14] Kim Junyeon, Sinha Jaivardhan, Hayashi Masamitsu, Yamanouchi Michihiko, Fukami Shunsuke, Suzuki Tetsuhiro, Mitani Seiji & Ohno Hideo. *Layer thickness dependence of the current-induced effective field vector in Ta—CoFeB—MgO*. Nat Mater, **12**(3):240, Mar 2013. ISSN 1476-1122. doi:http://dx.doi.org/10.1038/nmat3522. 10.1038/nmat3522.

[15] Garello Kevin, Miron Ioan Mihai, Avci Can Onur, Freimuth Frank, Mokrousov Yuriy, Blugel Stefan, Auffret Stephane, Boulle Olivier, Gaudin Gilles & Gambardella Pietro. *Symmetry and magnitude of spin-orbit torques in ferromagnetic heterostructures.* Nat Nano, **8**(8):587, Aug 2013. ISSN 1748-3387. doi:http://dx.doi.org/10.1038/nnano.2013.14510.1038/nnano.2013.145.

[16] M. Jamali, K. Narayanapillai, X. Qiu, L. M. Loong, A. Manchon & H. Yang. *Spin-orbit torques in Co/Pd multilayer nanowires.* Phys. Rev. Lett., **111**:246602, Dec 2013. doi:10.1103/PhysRevLett.111.246602.

[17] M. Hayashi, J. Kim, M. Yamanouchi & H. Ohno. *Quantitative characterization of the spin-orbit torque using harmonic Hall voltage measurements.* Phys. Rev. B, **89**:144425, Apr 2014. doi:10.1103/PhysRevB.89.144425.

[18] Qiu Xuepeng, Deorani Praveen, Narayanapillai Kulothungasagaran, Lee Ki-Seung, Lee Kyung-Jin, Lee Hyun-Woo & Yang Hyunsoo. *Angular and temperature dependence of current induced spin-orbit effective fields in Ta/CoFeB/MgO nanowires.* Sci. Rep., **4**, Mar 2014. doi:http://dx.doi.org/10.1038/srep0449110.1038/srep04491.

[19] H. Tang, R. Kawakami, D. Awschalom & M. Roukes. *Giant planar Hall effect in epitaxial (Ga,Mn)As devices.* Phys. Rev. Lett., **90**:107201, Mar 2003.

[20] P. Petroff, T. T. Sheng, A. K. Sinha, G. A. Rozgonyi & F. B. Alexander. *Microstructure, growth, resistivity, and stresses in thin tungsten films deposited by rf sputtering.* Journal of Applied Physics, **44**(6):2545, 1973. doi:http://dx.doi.org/10.1063/1.1662611.

[21] M. H. Read & C. Altman. *A new structure in tantalum thin films.* Applied Physics Letters, **7**(3):51, 1965. doi:http://dx.doi.org/10.1063/1.1754294.

[22] L. A. Clevenger, A. Mutscheller, J. M. E. Harper, C. Cabral & K. Barmak. *The relationship between deposition conditions, the beta to alpha phase transformation, and stress relaxation in tantalum thin films.* Journal of Applied Physics, **72**(10):4918, 1992. doi:http://dx.doi.org/10.1063/1.352059.

[23] C.-F. Pai, M.-H. Nguyen, C. Belvin, L. H. Vilela-Leão, D. C. Ralph & R. A. Buhrman. *Enhancement of perpendicular magnetic anisotropy and transmission of spin-Hall-effect-induced spin currents by a Hf spacer layer in W/Hf/CoFeB/MgO layer structures.* Applied Physics Letters, **104**(8):, 2014.

[24] Fan Xin, Wu Jun, Chen Yunpeng, Jerry Matthew J., Zhang Huaiwu & Xiao John Q. *Observation of the nonlocal spin-orbital effective field.* Nat Commun, **4**:1799, Apr 2013. doi:http://dx.doi.org/10.1038/ncomms270910.1038/ncomms2709.

[25] H. Wang, C. Du, P. Chris Hammel & F. Yang. *Spin current and inverse spin Hall effect in ferromagnetic metals probed by $Y_3Fe_5O_{12}$-based spin pumping.* Applied Physics Letters, **104**(20):202405, 2014. doi:http://dx.doi.org/10.1063/1.4878540.

[26] L. Wang, H. H. Du, C. Y. Pu, R. Adur, C. Hammel, P. & Y. Yang, F.˙ *Scaling of spin Hall angle in 3d, 4d, and 5d metals from* $Y_3Fe_5O_{12}$*/metal spin pumping.* Phys. Rev. Lett., **112**:197201, May 2014. doi:10.1103/PhysRevLett.112.197201.

[27] K. Ando, Y. Kajiwara, S. Takahashi, S. Maekawa, K. Takemoto, M. Takatsu & E. Saitoh. *Angular dependence of inverse spin˘Hall effect induced by spin pumping investigated in a $Ni_{81}Fe_{19}/Pt$ thin film.* Phys. Rev. B, **78**:014413, Jul 2008. doi:10.1103/PhysRevB.78.014413.

[28] O. Mosendz, J. E. Pearson, F. Y. Fradin, G. E. W. Bauer, S. D. Bader & A. Hoffmann. *Quantifying spin Hall angles from spin pumping: Experiments and theory.* Phys. Rev. Lett., **104**:046601, Jan 2010. doi:10.1103/PhysRevLett.104.046601.

[29] C. Hahn, G. de Loubens, O. Klein, M. Viret, V. V. Naletov & J. Ben Youssef. *Comparative measurements of inverse spin Hall effects and magnetoresistance in YIG/Pt and YIG/Ta.* Phys. Rev. B, **87**:174417, May 2013. doi:10.1103/PhysRevB.87.174417.

[30] L. Liu, R. A. Buhrman & D. C. Ralph. *Review and Analysis of Measurements of the Spin Hall Effect in Platinum.* ArXiv e-prints, Nov. 2011.

[31] Torrejon Jacob, Kim Junyeon, Sinha Jaivardhan, Mitani Seiji, Hayashi Masamitsu, Yamanouchi Michihiko & Ohno Hideo. *Interface control of the magnetic chirality in CoFeB/MgO heterostructures with heavy-metal underlayers.* Nat Commun, **5**, Aug 2014. doi:http://dx.doi.org/10.1038/ncomms565510.1038/ncomms5655.

[32] L. Liu, O. J. Lee, T. J. Gudmundsen, D. C. Ralph & R. A. Buhrman. *Current-induced switching of perpendicularly magnetized magnetic layers using spin torque from the spin Hall effect.* Phys. Rev. Lett., **109**:096602, Aug 2012. doi:10.1103/PhysRevLett.109.096602.

[33] Emori Satoru, Bauer Uwe, Ahn Sung-Min, Martinez Eduardo & Beach Geoffrey S. D. *Current-driven dynamics of chiral ferromagnetic domain walls.* Nat Mater, **12**(7):611, Jul 2013. ISSN 1476-1122.

[34] T. Suzuki, S. Fukami, N. Ishiwata, M. Yamanouchi, S. Ikeda, N. Kasai & H. Ohno. *Current-induced effective field in perpendicularly magnetized Ta/CoFeB/MgO wire.* Applied Physics Letters, **98**(14):, 2011.

[35] O. J. Lee, L. Q. Liu, C. F. Pai, Y. Li, H. W. Tseng, P. G. Gowtham, J. P. Park, D. C. Ralph & R. A. Buhrman. *Central role of domain wall depinning for perpendicular magnetization switching driven by spin torque from the spin Hall effect.* Phys. Rev. B, **89**:024418, Jan 2014. doi:10.1103/PhysRevB.89.024418.

[36] L. Liu, C.-F. Pai, Y. Li, H. W. Tseng, D. C. Ralph & R. A. Buhrman. *Spin-torque switching with the giant spin Hall effect of tantalum.* Science, **336**(6081):555, 2012. doi:10.1126/science.1218197.

[37] C. Wang, H. Seinige & M. Tsoi. *Ferromagnetic resonance driven by an ac current: A brief review.* Low Temperature Physics, **39**(3):247, 2013. doi:http://dx.doi.org/10.1063/1.4794998.

[38] A. Ganguly, K. Kondou, H. Sukegawa, S. Mitani, S. Kasai, Y. Niimi, Y. Otani & A. Barman. *Thickness dependence of spin torque ferromagnetic resonance in $Co_{75}Fe_{25}$/Pt bilayer films.* Applied Physics Letters, **104**(7):072405, 2014. doi:http://dx.doi.org/10.1063/1.4865425.

[39] T. McGuire & R. Potter. *Anisotropic magnetoresistance in ferromagnetic 3d alloys.* Magnetics, IEEE Transactions on, **11**(4):1018, Jul 1975.

[40] M. Harder, Z. X. Cao, Y. S. Gui, X. L. Fan & C.-M. Hu. *Analysis of the line shape of electrically detected ferromagnetic resonance.* Phys. Rev. B, **84**:054423, Aug 2011. doi:10.1103/PhysRevB.84.054423.

[41] K. Ando, S. Takahashi, K. Harii, K. Sasage, J. Ieda, S. Maekawa & E. Saitoh. *Electric manipulation of spin relaxation using the spin Hall effect.* Phys. Rev. Lett., **101**:036601, Jul 2008. doi:10.1103/PhysRevLett.101.036601.

[42] S. Petit, C. Baraduc, C. Thirion, U. Ebels, Y. Liu, M. Li, P. Wang & B. Dieny. *Spin-torque influence on the high-frequency magnetization fluctuations in magnetic tunnel junctions.* Phys. Rev. Lett., **98**:077203, Feb 2007. doi:10.1103/PhysRevLett.98.077203.

[43] C.-F. Pai, L. Liu, Y. Li, H. W. Tseng, D. C. Ralph & R. A. Buhrman. *Spin transfer torque devices utilizing the giant spin Hall effect of tungsten.* Applied Physics Letters, **101**(12):122404, 2012. doi: http://dx.doi.org/10.1063/1.4753947.

[44] O. Mosendz, V. Vlaminck, J. E. Pearson, F. Y. Fradin, G. E. W. Bauer, S. D. Bader & A. Hoffmann. *Detection and quantification of inverse spin Hall effect from spin pumping in permalloy/normal metal bilayers.* Phys. Rev. B, **82**:214403, Dec 2010. doi:10.1103/PhysRevB.82.214403.

[45] H. Nakayama, K. Ando, K. Harii, T. Yoshino, R. Takahashi, Y. Kajiwara, K. Uchida, Y. Fujikawa & E. Saitoh. *Geometry dependence on inverse spin Hall effect induced by spin pumping in* $Ni_{81}Fe_{19}$*/Pt films.* Phys. Rev. B, **85**:144408, Apr 2012. doi:10.1103/PhysRevB.85.144408.

[46] V. Vlaminck, J. E. Pearson, S. D. Bader & A. Hoffmann. *Dependence of spin-pumping spin Hall effect measurements on layer thicknesses and stacking order.* Phys. Rev. B, **88**:064414, Aug 2013. doi:10.1103/PhysRevB.88.064414.

[47] C. Du, H. Wang, F. Yang & P. C. Hammel. *Enhancement of pure spin currents in spin pumping* $Y_3Fe_5O_{12}$/Cu/Metal *trilayers through spin conductance matching.* Phys. Rev. Applied, **1**:044004, May 2014. doi:10.1103/PhysRevApplied.1.044004.

[48] Wei Dahai, Obstbaum Martin, Ribow Mirko, Back Christian H. & Woltersdorf Georg. *Spin Hall voltages from a.c. and d.c. spin currents.* Nat Commun, **5**, Apr 2014. doi:http://dx.doi.org/10.1038/ncomms476810.1038/ncomms4768.

[49] D.-J. Kim, S.-I. Kim, S.-Y. Park, K.-D. Lee & B.-G. Park. *Ferromagnetic resonance spin pumping in CoFeB with highly resistive non-magnetic electrodes.* Current Applied Physics, **14**(10):1344 , 2014. ISSN 1567-1739. doi:http://dx.doi.org/10.1016/j.cap.2014.07.013.

[50] H. Nakayama, M. Althammer, Y.-T. Chen, K. Uchida, Y. Kajiwara, D. Kikuchi, T. Ohtani, S. Geprägs, M. Opel, S. Takahashi, R. Gross, G. E. W. Bauer, S. T. B. Goennenwein & E. Saitoh. *Spin Hall magnetoresistance induced by a nonequilibrium proximity effect.* Phys. Rev. Lett., **110**:206601, May 2013. doi:10.1103/PhysRevLett.110.206601.

[51] Y.-T. Chen, S. Takahashi, H. Nakayama, M. Althammer, S. T. B. Goennenwein, E. Saitoh & G. E. W. Bauer. *Theory of spin Hall magnetoresistance.* Phys. Rev. B, **87**:144411, Apr 2013. doi:10.1103/PhysRevB.87.144411.

[52] M. Althammer, S. Meyer, H. Nakayama, M. Schreier, S. Altmannshofer, M. Weiler, H. Huebl, S. Geprägs, M. Opel, R. Gross, D. Meier, C. Klewe, T. Kuschel, J.-M. Schmalhorst, G. Reiss, L. Shen, A. Gupta, Y.-T. Chen, G. E. W. Bauer, E. Saitoh & S. T. B. Goennenwein. *Quantitative study of the spin Hall magnetoresistance in ferromagnetic insulator/normal metal hybrids.* Phys. Rev. B, **87**:224401, Jun 2013. doi:10.1103/PhysRevB.87.224401.

Chapter 6

Conclusions and outlook

In this thesis we investigated the properties of new materials and new multilayer systems with a particular focus on their possible application in spin electronics devices.

The discovery and mastery of new functional materials is a major driving force of technological innovation. For example, the discovery of the electromagnets allowed the electrification of the world in the 19th century while in the 20th century, the right choice of ferromagnetic and insulating layers made it possible to realise magnetic memories and store the entire wealth of human knowledge on magnetic hard disks in server farms across the world. In the first part of this work we focussed on Mn-based Heusler alloys, an interesting class of materials which shows properties like perpendicular magnetic anisotropy, high spin polarisation and low moments. We analysed the magnetic configuration of $Mn_{3-x}Ga$ thin films, finding it more complex than a simple collinear ferrimagnet. One of the two antiferromagnetically coupled sublattices is slightly canted towards an in-plane direction; this small component able to rotate freely in the plane. The high PMA of these alloys translates in very high ferromagnetic resonance frequency, which should be exploited in the future for the realisation of high-frequency spin-torque oscillator. In addition, nowadays the most important limitation of electronic devices is not the floating point operations per second rate of the processors but the capability of the connection lines (bus) to transport information back and forth to the memory cache. The upper limit of the speed for the read and write operations of a magnetic data cell is given by the ferromagnetic resonance frequency. In this framework, the use of high PMA materials like Mn_3Ga would allow for a faster reading and writing of the data, improving the overall performances of electronic devices. Furthermore, as the lateral size of a data cell shrinks following Moore's law, the ferromagnetic layers in MTJ devices need very high perpendicular anisotropy to maintain enough thermal stability to be used for applications. The commonly used CoFeB does not have bulk PMA, but it only relies on the weak surface anisotropy to obtain perpendicular magnetisation. The use of materials with bulk PMA, like Mn_3Ga would make it possible to solve the stability problem and realwhich smaller devices.

We also fabricated thin films of the first experimental example of a half metallic zero-moment ferrimagnet Mn_2Ru_xGa (MRG) and the structural, magnetic and transport properties have been investigated in detail, allowing us to obtain a comprehensive understanding of the complex structure of this Heusler alloy. The compensation of the magnetic moments of the two sublattices has been confirmed and a variety of evidence for half metallicity has been found. Its compensation temperature can be tuned by varying the Ru content x and/or the strain. This material is very promising for use in spin electronics, in particular in MTJ devices. It would make possible to move away from the CoFeB/MgO/CoFeB structure, solving several fabrication problems and, at the same time, it will open new possibilities thanks to its tunability.

The use CoFeB and MgO is made necessary by the relatively small spin polarisation of common ferromagnetic materials. The spin-filtering effect of the MgO barrier increases the effective spin polarisation of the CoFeB layers, which by themselves reach 40 % at most, up to almost 100 %, resulting in very high TMR ratio. In addition, the CoFeB/MgO interface is responsible for the PMA of the former. The growth of highly crystalline and ultra-thin MgO layers by sputtering is definitely not an easy task: MgO is a highly hygroscopic material and the slightest presence of water in a high vacuum chamber will compromise the crystallinity of the films. The implementation of MRG would remove the need for the MgO barrier, since its very high spin polarisation should result in sufficiently high TMR without spin filtering. As mentioned before, the weak CoFeB surface anisotropy is not enough to assure the scalability of the devices down to a few nanometres of lateral dimension. Due to its slightly distorted crystal structure and very low (or even zero) net magnetisation, MRG will maintain PMA even at the smallest dimensions. Having zero magnetic moment, it is not influenced by external perturbation and it doesn't create any stray field. This removes the possibility of cross-talk between magnetic layers of the same device of between adjacent devices. On the other hand, it is necessary to improve the performance of MRG-based MTJ devices. At present, oxidation of the Mn atoms, surface roughness and interdiffusion at the insulating barrier are problems that have to be overcome in order to make MRG compatible with the actual state-of-the-art technology. While the Curie temperature is found to be around 500 K - 600 K, Mn is known to oxidise easily and diffuse into other materials upon annealing. The degradation of the MRG/oxide barrier interface drastically reduces the spin polarisation and, consequently, the TMR.

In the second part of this work, the spin-orbit torque resulting from the current-induced spin accumulation in high Z metals such as Pt, Ta and W have been investigated. The use of spin-orbit torque to manipulate the magnetisation of a free magnetic layer in devices is an appealing alternative to the standard spin transfer torque mechanism. The latter is effective in nanosized junctions but has some major issues: the required critical current flowing through the ultra-thin insulating barrier can cause dielectric breakdown and the switching from antiparallel to parallel configuration is easier than the opposite one. By growing the free layer on top of a material with high spin-orbit coupling it is possible to exploit the spin-orbit torque to manipulate the magnetic moment without having to send it through the oxide barrier. The current is, in this case, sent in the plane and not perpendicular to the stack, and does not travel into the insulating barrier. In addition, the switching would be symmetric. The spin Hall effect and the Rashba effect have been characterised using different methods, with the pro and cons of each addressed. The harmonic Hall technique, in particular, has proved to be the most reliable and versatile in determining the current-induced effective fields. The spin-orbit torque switching of perpendicular ferromagnetic layers with an external applied field has already been demonstrated, but further improvement is needed to enable its use in spin electronic devices. In particular, it is necessary to find a scalable and efficient way to realize zero external field switching and to reduce the minimum current density needed for the switching. While finalising this work, we made some progress in the realisation of zero external field switching by spin Hall torque, which brings us one step closer to the application of this effect in devices.

Appendix A

Resist details

S1813 positive resist

S1813 is a high resolution positive resist for g-line UV lithography. The maximum resolution is well below 1 µm and has good adhesion and thickness uniformity. A nominal thickness of 1.3 µm is achieved after 30 s of spin coating at 3000 RPM. The sensitivity is between 90 and 150 mJ cm^{-2}. A primer is usually not necessary when processing Si/SiO_2 wafers, while it may be necessary when the resist is used directly on quartz or glass. It can be removed with acetone or Microposit 1165 remover (N-methyl-2-pyrrolidone) and it is developed by the Microposit MF319 developer, a sodium-based alkaline solution. This resist requires pre-exposure soft bake for 1.5 min at 120 °C.

Ma-N 1420 negative resist

The ma-N 1420 negative resist is an i-line photoresist with a resolution of 1.5 µm. The nominal thickness after spin coating at 3000 RPM is 2 µm. The typical dose required is around 500 mJ cm^{-2}. It can be removed by acetone or ma-Rem 404S remover and it is developed by the ma-D 533S, a tetramethylammonium hydroxide (TMAH, $N(CH_3)_4^+$ OH^-)-based solution. The required pre-exposure soft bake is for 2 min at 105 °C. It doesn't require post-exposure bake.

LOR 10B positive LOL

The LOR 10B is a positive photoresist used as a lift off layer in combination with the S1813 resist. It gives a thickness of about 1.3 µm when spin coated at 2000 RPM. This thickness must be higher than the thickness of the deposited material in order to obtain a good lift-off. The sensitivity of the LOR 10B is very high compared to S1813, resulting in an undercut profile. The resist must be soft-baked at 120 °C for ∼2 min.

Appendix B

Device fabrication steps

In this section we will present the steps involved in the fabrication of the devices used in this work. We will further discuss the realisation of Hall bars and MTJs in the next sections. We will not discuss the samples for ST-FMR experiments since their fabrication is very similar to that of the Hall bars, but a schematic of the samples is shown in Fig. B.1.

B.0.1 Hall bars

Hall bars were patterned on Heusler alloy films in order to characterise them by anomalous Hall effect measurements (see sec. 2.3.6) and on heavy metal/ferromagnetic metal/oxide trilayers for spin Hall effect measurements (see sec. 3.5.1). These samples have been deposited on Si/SiO_2 or MgO (001) substrates. The Hall bars have dimensions of $60\,\mu m^2 \times 20\,\mu m^2$ and $50\,\mu m^2 \times 10\,\mu m^2$. Two electrical contacts are patterned at opposide edges in the longitudinal direction, while three pairs of contacts are patterned in the transverse direction equally spaced along the bars. A step-by-step representation of the fabrication process is shown in Fig. B.2.

1. Hall bars patterning:
    - Ma-N 2403 negative photoresist is spun on the full stack at 3000 RPM for 30 s.
    - The resist is soft baked at 105 °C for 2 min.
    - The sample is exposed for 23 s using the OAI mask aligner. In this step the Hall bars are defined.
    - The photoresist is developed for ∼60 s in ma-D developer and rinsed in DI water.
    - The sample is etched in the Millatron down to the substrate with the rf power at 300 W. After the main etching at almost normal incidence, a final brief etch at low angle is performed.
    - The resist is stripped using acetone or ma-Rem 660 remover.
2. Contact patterning:
    - S1813 positive photoresist is spun on the sample at 5000 RPM for 45 s.
    - The resist is soft baked at 115 °C for 1.5 min.
    - The sample is exposed for 6 s using the OAI mask aligner. In this step the contacts are defined.
    - The photoresist is developed for ∼35 s in MF319 developer and rinsed in DI water.

Figure B.1: Schematic of a sample used for ST-FMR experiments. The red bar of magnetic material is contacted by two coupled microstrips. The contacts make a 45° turn in order to make it possible to apply the field with an angle of 45° in the plane with respect to the bar using our rf setup.

- A trilayer consisting of Ti(5 nm)/Cu(80 nm)/Au(20 nm is deposited in the Temescal evaporator. Prior to metal deposition, the ion gun is used to etch the oxide layer/clean the surface (∼2 min at 38 W).
- The lift-off is performed using acetone or 1165 remover.

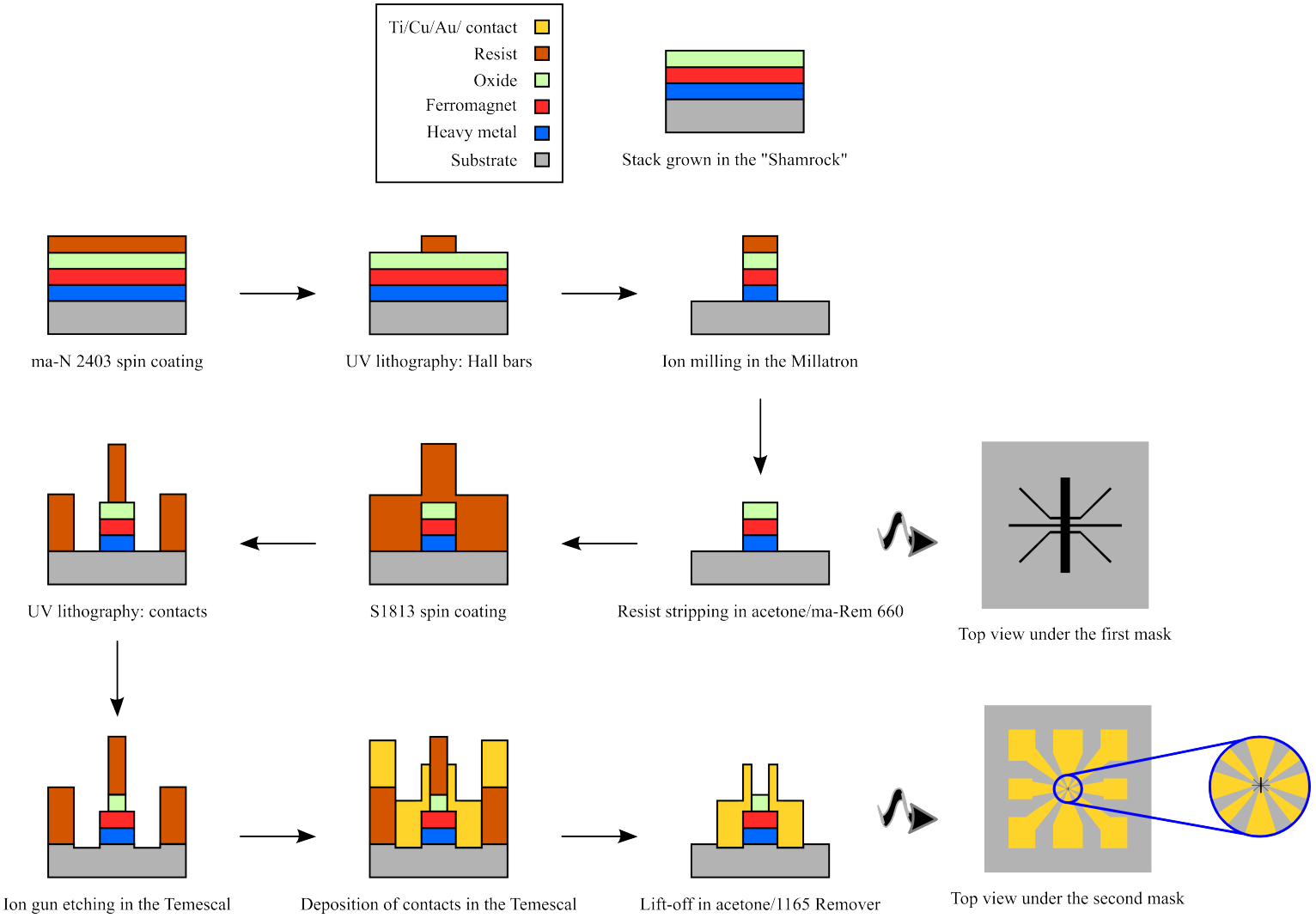

Figure B.2: Step-by-step fabrication process of the Hall bars samples for spin Hall measurements.

B.0.2 MTJ samples

Magnetic tunnel junctions have been fabricated using an Heusler alloy (Mn_2Ru_xGa, MRG) as the hard magnetic element in order to characterise the tunnelling magnetoresistance of this kind of device (see sec. 4.3.7). The exact stack composition varied during this thesis but a typical stack is composed of: CrRu(15 nm)/MRG(20 nm)/X/MgO/$Co_{20}Fe_{60}B_{20}$(1.2 nm)/Ta(0.3 nm)[Co(0.3 nm)/Pd(0.8 nm)]$_{\times 7}$ or MRG(20 nm)/X/MgO/$Co_{20}Fe_{60}B_{20}$(1.2 nm)/Ta(1 nm)/$Co_{20}Fe_{60}B_{20}$(1 nm)/MgO(1 nm)/Ta(1 nm). X is an insertion layer used to prevent the oxidation of the MRG layer. The thicknesses of this layer and of the MgO layer varied between samples. The top stacks are designed to have perpendicular magnetic anisotropy. These samples have been deposited on MgO (001) substrates. They consist of two rows of six pillars, three of them with dimensions 4 µm^2 × 12 µm^2 and the other three with dimensions 4 µm^2 × 4 µm^2. The bottom layers of each row has two contact, while there are two top contact for each single MTJ. Both two-point and four-point measurements can be performed. A step-by-step representation of the fabrication process is shown in Fig. B.3.

1. Bottom contacts:
   - S1813 negative photoresist is spun on the full stack at 5000 RPM for 45 s.
   - The resist is soft baked at 115 °C for 1.5 min.
   - The sample is exposed for 6 s using the OAI mask aligner. In this step the bottom contacts are defined.
   - The photoresist is developed for ∼35 s in MF319 developer and rinsed in DI water.
   - The sample is etched in the Millatron down to the substrate with the rf power at 300 W. After the main etching at almost normal incidence, a final brief etch at low angle is performed. The EPD is used to monitor the etching.
   - A layer of SiO_2 is deposited in the "Shamrock" in order to planarise the surface as much as possible. The thickness of the oxide is comparable to the total thickness of the stack.
   - The resist is stripped using acetone or 1165 remover.
2. Pillars patterning:
   - Ma-N 2403 negative photoresist is spun on the full stack at 3000 RPM for 30 s.
   - The resist is soft baked at 105 °C for 2 min.
   - The sample is exposed for 23 s using the OAI mask aligner. In this step the pillars are defined. In addition, the bottom contacts are protected from the following etching.
   - The photoresist is developed for ∼60 s in ma-D developer and rinsed in DI water.
   - The sample is etched in the Millatron down to or just below the oxide barrier layer. The EPD is used to stop the process at the right moment, also using the previous EPD data as reference. The rf power is set to 300 W. After the main etching at almost normal incidence, a final brief etch at low angle is performed. Additional care is taken to avoid overheating the resist by using a multiple etch-and-cool cycle, since the removal of the resist from small size features is particularly difficult.
   - A layer of SiO_2 is deposited in the "Shamrock" in order to electrically insulate the top and bottom contacts. The thickness of the oxide is comparable to the total thickness of the stack. The nature of the sputter deposition covers the sidewalls of the pillars.

- The resist is stripped using acetone or ma-Rem 660 remover.

3. Contact patterning:

   - S1813 positive photoresist is spun on the sample at 5000 RPM for 45 s.
   - The resist is soft baked at 115 °C for 1.5 min.
   - The sample is exposed for 6 s using the OAI mask aligner. In this step the contacts are defined in correspondence of the bottom contact and the top of the pillars.
   - The photoresist is developed for ∼35 s in MF319 developer and rinsed in DI water.
   - The sample is loaded in the Temescal evaporator. First, the ion gun is used for gently cleaning the surfaces (∼20 s at 38 W). Afterwards, a trilayer consisting of Ti(5 nm)/Cu(80 nm)/Au(20 nm) is deposited.
   - The lift-off is performed using acetone or 1165 remover.

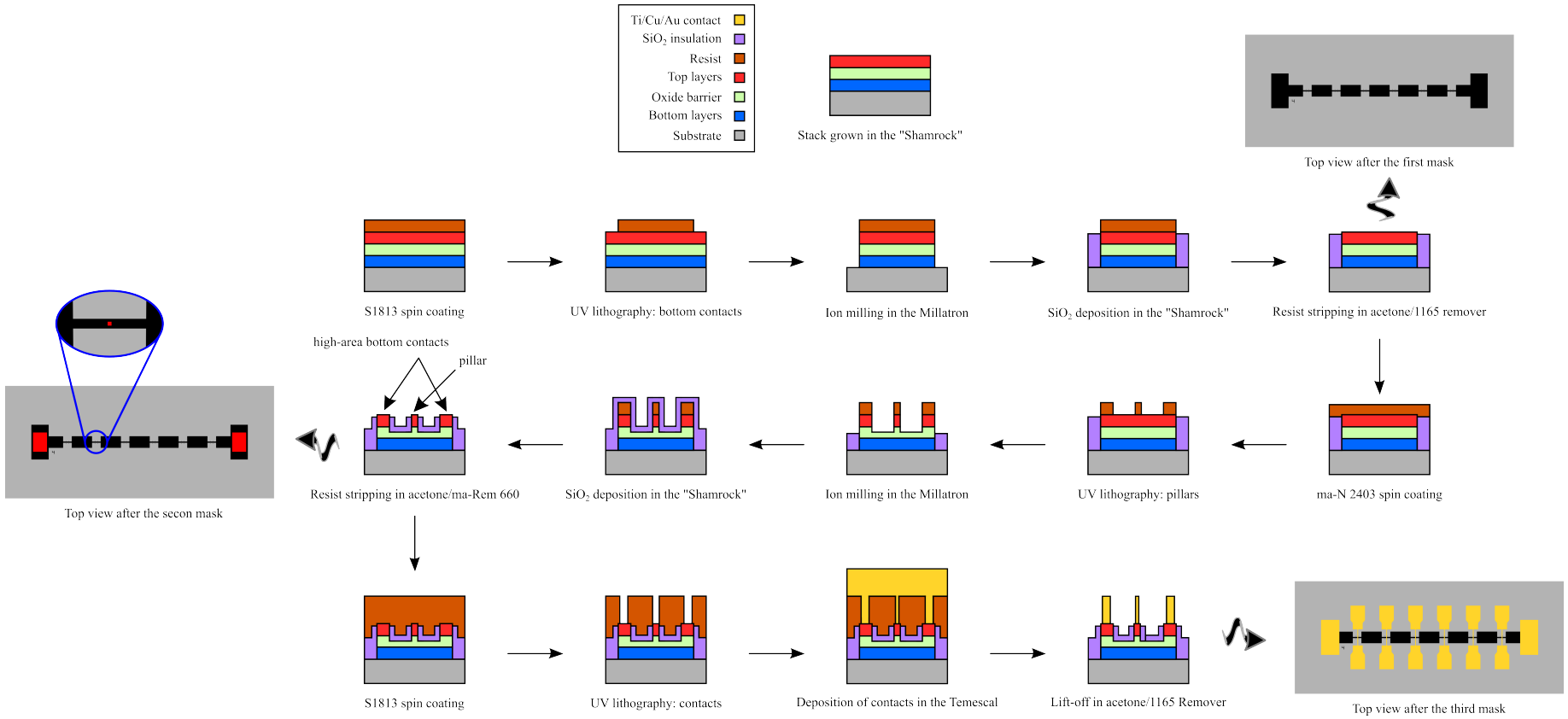

Figure B.3: Step-by-step fabrication process of the MTJ samples.

Appendix C

Beamline details

In this work we performed EXAFS experiments at the SAMBA beamlines at the SOLEIL synchrotron and XAS/XMCD experiments at the DEIMOS beamline at the SOLEIL synchrotron and at the X-TREME beamline at the SLS synchrotron. The main characteristics of these beamlines are:

- SAMBA (www.synchrotron-soleil.fr/Recherche/LignesLumiere/SAMBA):
  - Energy range: 4-43 keV.
  - Energy resolution: 6×10^{-5} at 15 keV.
  - Source: bending magnet.
  - Flux: 2.8×10^{11} Phot/s/0.1bw at 15 keV.
  - Optics: sagittal focusing monochromator between two bendable cylindrical mirrors.
  - Beam size at the sample: $200\,\mu m^2 \times 300\,\mu m^2$.
  - Detectors: Canberra 35-elements monolithic planar Ge pixel array detector, multi-elements Ge detector or a Vortex silicon drift detector, TEY.
  - Light polarisation: linear.
  - Maximum magnetic field: n.a.
  - Temperature range: ancillary cryostats for liquid He or N_2 are available.
- DEIMOS (www.synchrotron-soleil.fr/Recherche/LignesLumiere/DEIMOS):
  - Energy range: 350-2500 eV.
  - Energy resolution: 6000-10 000.
  - Source: APPLE II insertion device or EMPHU65 insertion device.
  - Flux: 6×10^{12} Phot/s/0.1bw at 750 eV.
  - Optics: two mirrors with two incidence angles, plane-grating monochromators (PGM) with variable groove depth (VGD) gratings or multilayer gratings, post-focusing Wolter system.
  - Beam size at the sample: $80\,\mu m^2 \times 80\,\mu m^2$ or $800\,\mu m^2 \times 800\,\mu m^2$ with the two-mirror stage in the Wolter system.
  - Detectors: absorption in TEY and FY.
  - Light polarisation: circular left/right and linear.

  - Maximum magnetic field: ± 7 T along the beam direction, ± 2 T perpendicular to it.
  - Temperature range: 1.5-350 K.

- X-TREME (www.psi.ch/sls/xtreme/xtreme):
  - Energy range: 400-1800 eV.
  - Energy resolution: >5000
  - Source: APPLE II insertion device.
  - Flux: 4.7×10^{12} Phot/s/0.1bw at 700 eV.
  - Optics: two mirrors with two incidence angles, plane-grating monochromators (PGM) with variable groove depth (VGD) gratings, refocussing mirror after the slit.
  - Beam size at the sample: exit slit size x 230 µm.
  - Detectors: absorption in TEY and FY.
  - Light polarisation: circular left/right and linear.
  - Maximum magnetic field: ± 6.8 T along the beam direction, ± 2 T perpendicular to it.
  - Temperature range: 2-370 K.

Appendix D

$C1_b$ $Mn_{3-x}Ga$

D.0.3 Review of characteristics

Similarly to what we have done for the DO_{22} $Mn_{3-x}Ga$ samples, we have grown thin-film samples of $Mn_{3-x}Ga$ on MgO single crystal substrates introducing a seed layer of vanadium (001). The samples were grown by co-sputtering of a Mn_2Ga and a Mn_3Ga targets at 300 °C and then capped with $\sim$ 2 nm Al_2O_3. The nominal thickness of the $Mn_{3-x}Ga$ was 60 nm. As before, the actual thickness of the samples was determined by low-angle x-ray reflectivity prior to the investigation. The crystal structure and lattice parameters were again measured by symmetrical and reciprocal space map scans using our BRUKER D8 diffractometer.

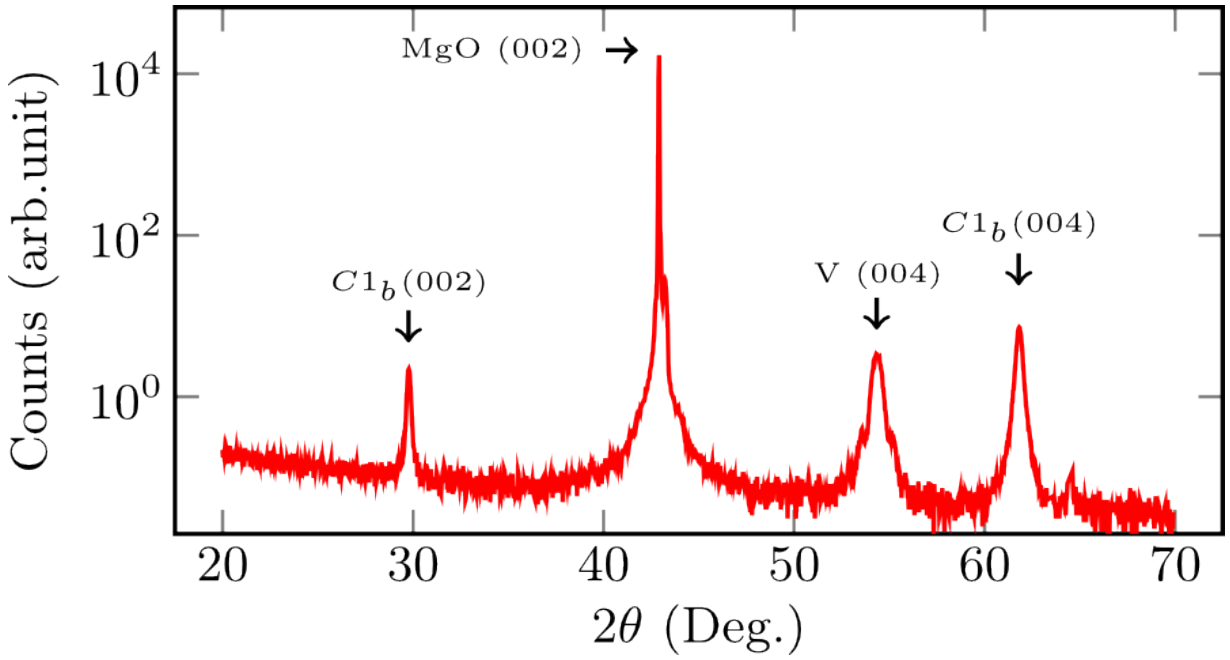

Figure D.1: XRD pattern of $C1_b$ Mn_2Ga grown on a V (001) seed layer.

Mn_3Ga in its cubic $C1_b$ structure (Fig. 4.4 has been predicted to be a compensated half metal, *i.e.*, a ferrimagnet with zero magnetisation and 100 % spin polarisation at the Fermi level [1]. The cubic $C1_b$ phase of Mn_2Ga or Mn_3Ga has not been observed in the bulk or in thin film form when directly grown on a crystalline MgO substrate. We had been able to obtain cubic $Mn_{3-x}Ga$ in thin film form by inserting

the vanadium seed layer. In the half Heusler Mn_2Ga, the Mn atoms occupy the $4a$ and $4c$ crystal sites, while the Ga atoms occupy the $4b$ position (see sec. 4.1 and Fig. 4.4). Adding Mn atoms, the empty $4d$ sites are filled, until the lattice positions are completely occupied in the full Heusler Mn_3Ga (see Fig. 4.3). Unfortunately, the thin films have a very granular and discontinuous structure that makes it difficult to determine their properties and makes them unsuitable for direct application in electronic devices.

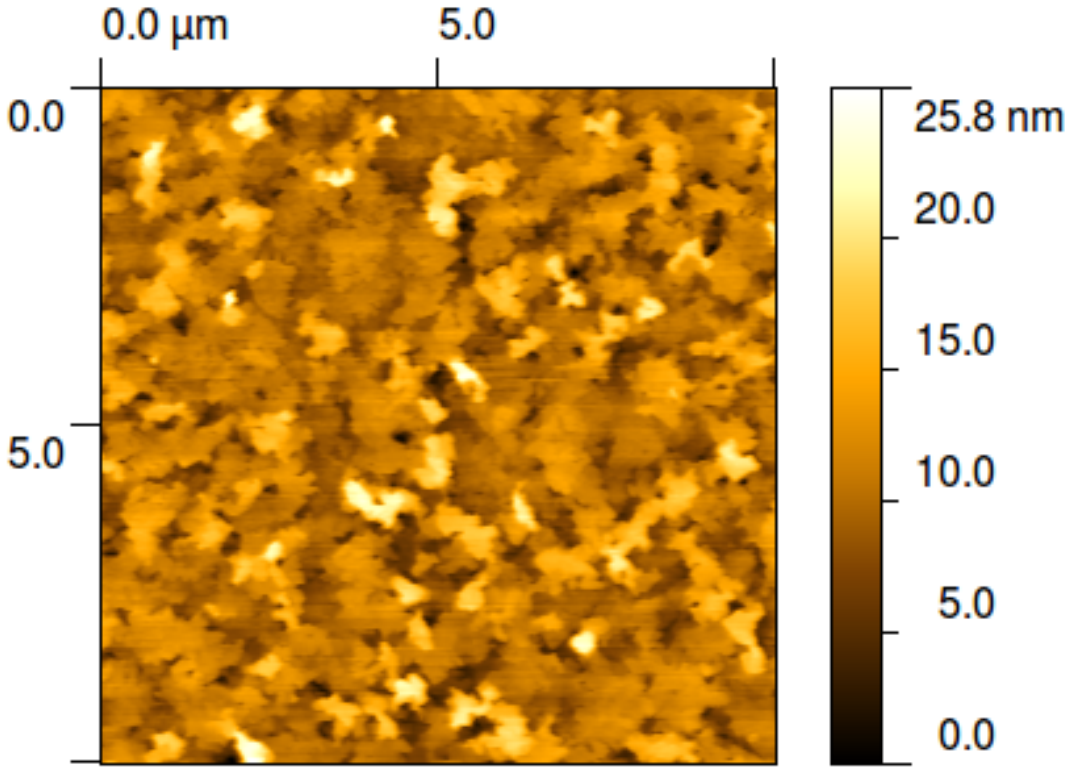

Figure D.2: Atomic force microscope scans of a 10 x 10 µm surface area of Mn_3Ga sample. The film is granular and discontinuous, with several pin-holes.

We were able to measure the spin polarisation by point contact Andreev reflection (PCAR): we found a value of 40 % but the discontinuous nature of the films make this result not very reliable.

Another confirmation of the granular nature of the sample comes from the XPS spectra that we obtained with our laboratory setup. As discussed in sec. 3.4.4, the escape depth of photoelectrons is only a few nanometres. In the experiment we recorded a strong signal coming from the $2p$ V peaks that shouldn't have been detectable underneath 25 nm of continuous $Mn_{3-x}Ga$ film.

D.0.4 XAS and XMCD

We measured XAS/XMCD at the SLS synchrotron facility on the X-TREME beam-line on a series of $Mn_{3-x}Ga$ samples. The Mn $L_{3,2}$ edges were recorded in an applied magnetic field of $\mu_0 H = 6.8\,\mathrm{T}$ with the x-ray propagation vector $\vec{k}$ and the applied magnetic field normal to the surface of the samples. The temperature have been varied between 50 and 360 K. We investigated 5 samples, nominally Mn_2Ga, $Mn_{2.25}Ga$, $Mn_{2.5}Ga$, $Mn_{2.75}Ga$ and Mn_3Ga. The recorded XAS and XMCD spectra are shown in Fig. D.4

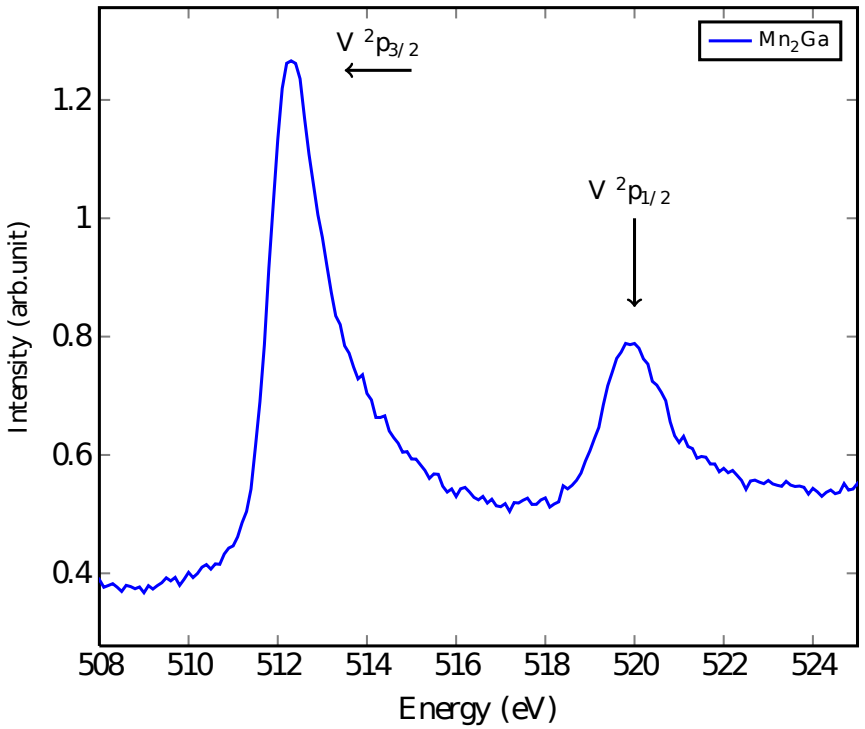

Figure D.3: XPS spectra of a Mn_2Ga showing the $2p$ peaks of V. The presence of these peaks is a further confirmation of the granular nature of the thin film.

and D.5.

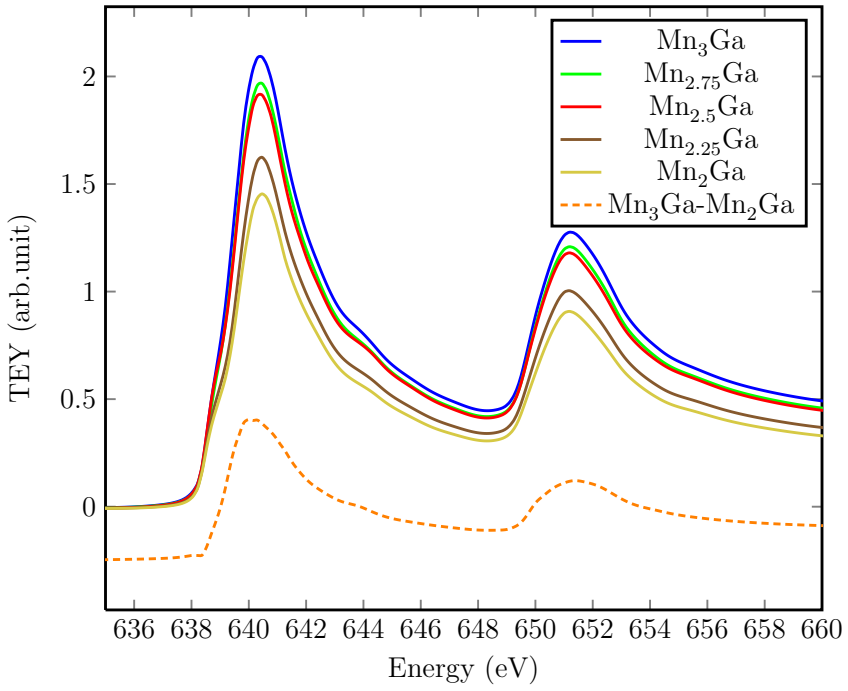

Figure D.4: XAS spectra for $Mn_{3-x}Ga$ samples. The curve in orange is the difference between the Mn_3Ga and Mn_2Ga spectra, that we attribute to the additional Mn atoms in the first alloy. No clear spectral signature due to these atoms is visible.

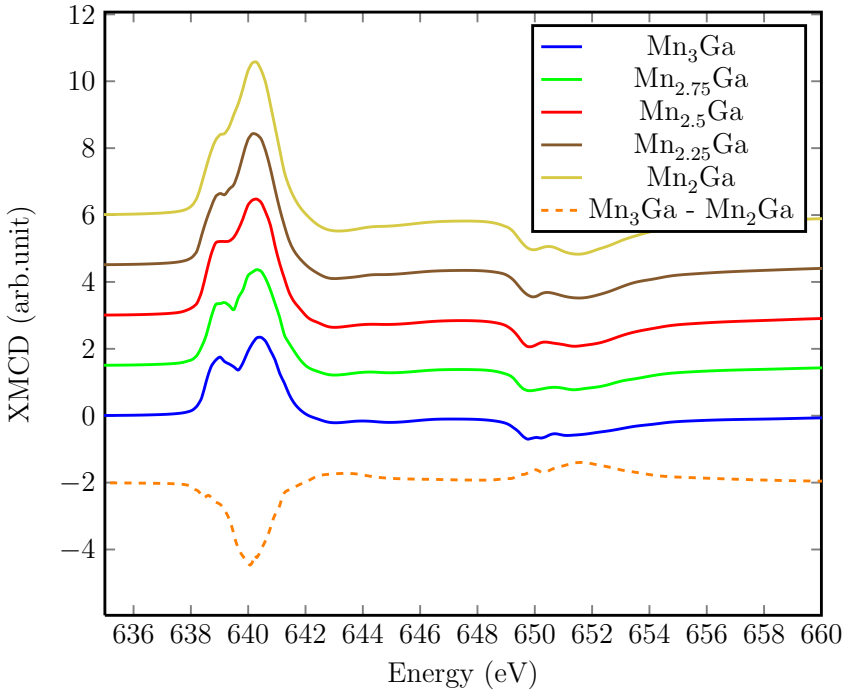

Figure D.5: XMCD spectra for $Mn_{3-x}Ga$ samples. The curve in orange is the difference between the Mn_3Ga and Mn_2Ga spectra, that we attribute to the additional Mn atoms in the first alloy. This signal resemble the one of a tetrahedrally coordinated Mn atom.

The XAS spectra don't show any trend when varying Mn content x at all temperatures, indicating that there is no change of crystal symmetry or charge distribution. As expected, the signal increases monotonically with x. On the other hand, the XMCD spectra show a clear evolution, especially in the L_3 peak. It is possible to evaluate the contribution of the additional Mn atoms by taking the difference between the Mn_3Ga and the Mn_2Ga spectra. We used an atomic multiplet code, initially written by R.D. Cowan, and further developed by T. Thole [2–4], to simulate the spectra of the various alloys. It is possible to identify the additional contribution as the one coming from a tetrahedrally coordinated Mn atom, in agreement with the expected occupation of the crystal lattice [5]. The fitting of the XAS and XMCD spectra with the atomic multiplet code is shown in Fig. D.6 and D.7 respectively. The agreement between the simulations and the data is not perfect: this is mainly due to the inability of the code to replicate the heavy broadening of the peaks in a metallic compound and probably to the disordered nature of the lattices.

The magneto-optical sum rules allow for the independent determination of the spin $2\langle S_z\rangle$ and orbital $\langle L_z\rangle$ momentums, as discussed in sec. 3.4.2. We applied the sum rules on the measured spectra: the orbital momentums are near zero for all the compounds, as expected for Mn in a $3d^5$ configuration and in a cubic crystal. The values for the spin momentums are reported in Tab. D.1. The Slater-Pauling rules (eq. 4.2 and 4.3) predict a momentum of 1 and $0\,\mu_B$ f.u.$^{-1}$ for Mn_2Ga and Mn_3Ga respectively. The measured values are much higher and we don't observe the expected trend with respect to the Mn content. In fact, the spin momentum $2\langle S_z\rangle$ remains almost constant around $2\,\mu_B$ f.u.$^{-1}$ for all values of x and temperatures.

When it comes to the application of the sum rules, the case of Mn is more complicated than the other elements because the spin-orbit coupling of the $2p$ orbitals is not high enough to clearly separate the L_3 ($^2P_{3/2}$) from the L_2 ($^2P_{1/2}$) edge. In addition, there is a significant degree of L_2 character in the L_3 absorption peak and vice-versa [6]. We adopted the same method used for the analysis on the DO_{22}

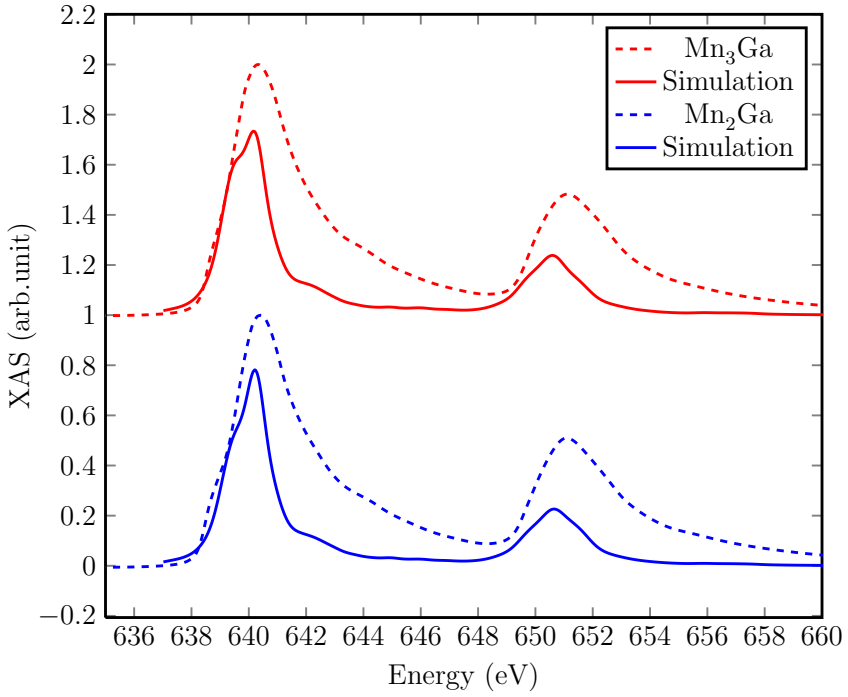

Figure D.6: Fit of the XAS spectra for Mn_2Ga and Mn_3Ga. The Mn_3Ga one shows more contribution from a tetrahedrally coordinated site.

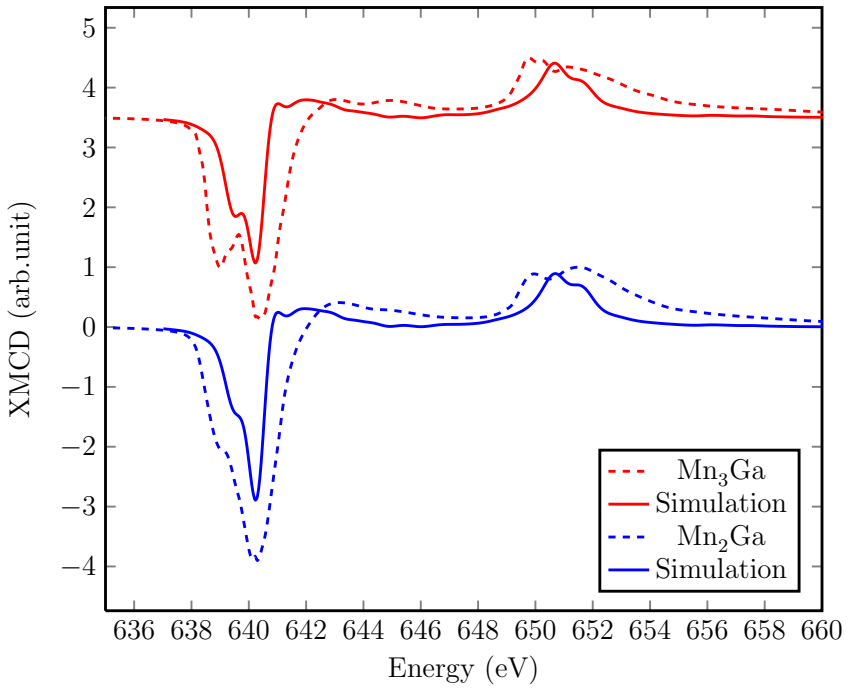

Figure D.7: Fit of the XMCD spectra for Mn_2Ga and Mn_3Ga. The Mn_3Ga one shows more contribution from a tetrahedrally coordinated site.

$Mn_{3-x}Ga$, *i.e.*, we have chosen to fix an energy value which we define as the end of the L_3 and start of the L_2 edges. This way, while the absolute value of the spin momentum may be over or under-estimated, the error is completely systematic.

The Mn_2Ga, $Mn_{2.5}Ga$ and Mn_3Ga samples have been measured in our SQUID in order to determine the magnetic moment and compare with the results obtained with the sum rules. Fig. D.8 shows the magnetisation loops as a function of the applied external field, both out-of-plane and in-plane. Since the in-plane lattice parameter a is slightly higher than the out-of-plane one, c, they show easy-plane anisotropy. The values for the magnetic moments are reported in Tab. D.1: the agreement with the XMCD values is reasonable, especially for the first two samples, but they are both far off from the theoretically predicted values.

Table D.1: List of samples measured by XAS/XMCD

Sample	a (Å)	c (Å)	$2\langle S_z\rangle^{a}$ (μ_B f.u.$^{-1}$)	$2\langle S_z\rangle^{b}$ (μ_B f.u.$^{-1}$)
MgO/V(17 nm)/Mn_2Ga(25 nm)/Al_2O_3(2 nm)	5.968	5.835	2.14	2.2
MgO/V(17 nm)/$Mn_{2.25}Ga$(25 nm)/Al_2O_3(2 nm)	5.968	5.826	2.08	n.a.
MgO/V(17 nm)/$Mn_{2.5}Ga$(25 nm)/Al_2O_3(2 nm)	5.968	5.831	2.21	2.1
MgO/V(17 nm)/$Mn_{2.75}Ga$(25 nm)/Al_2O_3(2 nm)	5.968	5.825	1.95	n.a.
MgO/V(17 nm)/Mn_3Ga(25 nm)/Al_2O_3(2 nm)	5.968	5.837	1.824	1.4

[a] From XMCD sum rules.
[b] From SQUID measurement.

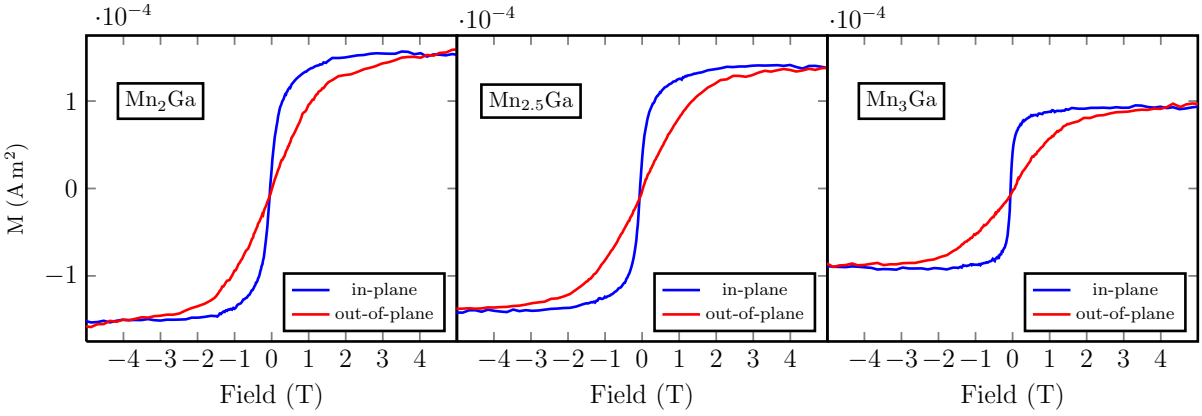

Figure D.8: SQUID data for Mn_2Ga, $Mn_{2.5}Ga$ and Mn_3Ga measured with applied out-of-plane and in-plane field at room temperature.

D.0.5 Conclusions

We believe that the poor quality of the films has altered the magnetic properties of the samples. With all probability there is a high degree of disorder in the occupation of the crystalline sites. In addition, there is the possibility that the V atoms have diffused in the layer above and further modified the magnetic properties. Vanadium is usually in a $3d^3$ configuration, which is very stable in a tetrahedrally coordinated site such as the empty $4d$ position.

We believe that cubic Mn_3Ga and related alloys are potentially very interesting for spin electronics applications, but the growth conditions must be optimised in order to obtain continuous and reasonably smooth films. There are key features for the realisation of actual devices. As these alloys strongly favours, the tetragonal DO_{22} structure, this objective is not easy to achieve.

References

[1] R. A. de Groot, F. M. Mueller, P. G. van Engen, and K. H. J. Buschow. New class of materials: Half-metallic ferromagnets. *Phys. Rev. Lett.*, 50:2024–2027, Jun 1983.

[2] Robert Duane Cowan. *Theory of atomic structure and spectra*. Los Alamos series in basic and applied Sciences. University of California Press, Berkely, 1981.

[3] B.T. Thole, G. van der Laan, and P. H. Butler. Spin-mixed ground state of Fe phthalocyanine and the temperature-dependent branching ratio in x-ray absorption spectroscopy. *Chemical Physics Letters*, 149(3):295 – 299, 1988.

[4] Eli Stavitski and Frank M.F. de Groot. The CTM4XAS program for EELS and XAS spectral shape analysis of transition metal L edges. *Micron*, 41(7):687 – 694, 2010.

[5] P Klaer, M Kallmayer, H J Elmers, L Basit, J Thöne, S Chadov, and C Felser. Localized magnetic moments in the Heusler alloy Rh_2MnGe. *Journal of Physics D: Applied Physics*, 42(8):084001, 2009.

[6] Cinthia Piamonteze, Piter Miedema, and Frank M. F. de Groot. Accuracy of the spin sum rule in xmcd for the transition-metal l edges from manganese to copper. *Phys. Rev. B*, 80:184410, Nov 2009.

Publications

- N. Thiyagarajah, Y.-C. Lau, D. Betto, K. Borisov, J. M. D. Coey, P. Stamenov and K. Rode, *Giant spontaneous Hall effect in zero-moment Mn_2Ru_xGa*, Applied Physics Letters 106, 122402, 2015.

- D. Betto, N. Thiyagarajah, Y.-C. Lau, C. Piamonteze, M.-A. Arrio, P. Stamenov, J. M. D. Coey, and K. Rode, *Site-specific magnetism of half-metallic Mn_2Ru_xGa thin films determined by x-ray absorption spectroscopy*, Phys. Rev. B 91, 094410, 2015.

- D. Betto and J.M.D. Coey, *Vortex state in ferromagnetic nanoparticles*, Journal of Applied Physics 115, 17D138, 2014.

- K. Rode, N. Baadji, D. Betto, Y.-C. Lau, H. Kurt, M. Venkatesan, P. Stamenov, S. Sanvito, J. M. D. Coey, E. Fonda, E. Otero, F. Choueikani, P. Ohresser, F. Porcher, and G. Andr, *Site-specific order and magnetism in tetragonal Mn_3Ga thin films*, Physics Review B 87, 184429, 2013.